

IFMASS 10



FUNDAMENTALS OF FRACTURE MECHANICS AND STRUCTURAL INTEGRITY ASSESSMENT METHODS

This monograph contains the lectures presented at the Tenth International Fracture Mechanics Summer School held on mountain Zlatibor, Serbia, 23rd to 27th June 2008.

Editor: S. Sedmak

Belgrade, 2009

This monograph is published with the financial support of the
Ministry of Science and Technological Development of the Republic of Serbia

Jointly published by the
Faculty of Mechanical Engineering (MF), University of Belgrade
Faculty of Technology and Metallurgy (TMF), University of Belgrade
Society for Structural Integrity and Life (DIVK)
Institute for Materials Testing IMS, Belgrade

© 2009 MF, TMF, DIVK and IMS
All rights reserved.

This work is protected under copyright by MF, TMF, DIVK and IMS.
No part of this publication may be reproduced, stored in a retrieval system, or transmitted in any form or
by any means, electronically, mechanically, photocopying, recording or otherwise, without the prior
written permission of the publishers MF, TMF, DIVK and IMS.

Edited, reviewed and corrected by:
Prof. Dr. Stojan Sedmak

Reviewed by:
Prof. Dr. Vitomir Djordjević
Prof. Dr. Endre Romhanji

Graphics and text arrangement:
Boris Hriberšek

First edition 2009

Circulation: 400 copies

Printed by Printing Office of the Faculty of Technology and Metallurgy, University of Belgrade.

To contact the Publisher
Prof. Dr. Stojan Sedmak
Society for Structural Integrity and Life
Bulevar vojvode Mišića 43, room 258
11000 Belgrade, Serbia
Tel. XX-381-11-2631845
E-mail: Sedmak@divk.org.rs
<http://divk.org.rs>

CIP – Каталогизacija у публикацији
Народна библиотека Србије, Београд

620.172.24:62-112.81(082)
539.42(082)

INTERNATIONAL Fracture Mechanics Summer School (10 ; 2008 ; Zlatibor)

Fundamentals of Fracture Mechanics and Structural Integrity Assessment Methods : this monograph contains the lectures presented at the Tenth International Fracture Mechanics Summer School – IFMASS 10, held on mountain Zlatibor, Serbia, 23th to 27th June 2008. / editor S. [Stojan] Sedmak ; [organizers] Faculty of Mechanical Engineering ...[et al.]. – 1st ed. -Belgrade : Faculty of Mechanical Engineering: Faculty of Technology and Metallurgy : Society for Structural Integrity and Life :Institute for Materials Testing, 2009 (Belgrade : Faculty of Technology and Metallurgy, Research and Development Centre of Printing Technology). – [6], 346 str. :ilustr. ; 24 cm

Tiraž 400. – Str. [3-4]: Preface / Stojan Sedmak. – Bibliografija uz svaki rad.

ISBN 978-86-82081-19-7 (IMS)

1. Mašinski fakultet (Beograd), 2. Tehnološko-metalurški fakultet (Beograd), 3. Društvo za integritet i vek konstrukcija (Beograd) 4. Institut za ispitivanje materijala Srbija (Beograd) a) Металне конструкције - Интегритет – Зборници b) Механика лома – Зборници
COBISS.SR-ID 170781708

PREFACE

Tenth International Fracture Mechanics Summer Schools (IFMASS 10) had been organized in 2008, on the mountain Zlatibor, in Serbia. Following established tradition, organisers decided to publish the monograph

“Fundamentals of fracture mechanics and structural integrity assessment methods”

This book is the tenth in IFMASS monograph series. First four volumes had been published in Serbian, the fifth one in English and a shortened version in Serbian, sixth and seventh in Serbian, and last three in English. This enabled an extended use of IFMASS books not only in former Yugoslavia and its federal states, but also world wide. Last three editions are also available on internet, DIVK site divk.org.rs.

The role of IFMASS is accomplished in the best way, and it served not only for education, but also as a forum to present the achievements and exchange the ideas regarding theoretical, experimental and numerical development of fracture mechanics, and structural integrity and life assessment. Very important in that sense was the joint Yugoslav–USA project “Fracture Mechanics of Weldments”, performed by six institutions from former Yugoslavia and the National Institute of Standards and Technology (NIST), Boulder, Colorado (USA) that started in 1982 and ended in 1992. The IFMASS 5 attracted in Dubrovnik 145 participants and 24 lecturers recognised in the power industry world-wide and monograph “The Application of Fracture Mechanics to Life Estimation of Power Plant Components” had been published in English by EMAS Publisher.

Unfortunate events started in 1991, disturbed IFMASS in its mission. However, even in these circumstances, two Schools had been organized successfully. It was the time when foreign lecturers hesitated to come to our country, but IFMASS still saved its importance, attracting 137 participants and 8 foreign contributions out of 25 given lectures at IFMASS 7 in 1997. Unfortunate events culminated in 1999 with NATO bombardment which delayed monograph publishing until 2000. Next important event was founding of the Society for Structural Integrity and Life (DIVK) in 2001. New Society reactivated IFMASS, and next three Schools were organized.. It is to underline that, in addition to IFMASS, important position in considering the topics connected with fracture mechanics and allied field has now DIVK journal “Structural Integrity and Life”, also available on the internet.

The activities motivated by DIVK members are of great importance for further development in Serbia in the field of structural integrity and life in industry, and in the same time present the base for education, research and investigation.

Among about 150 DIVK active members most of the lecturers for IFMASS 10 had been recruited. Some of them used to be participants in former IFMASSs. This resource of experts in DIVK is significant support for development, and many institutions and laboratories where they are engaged represent important experimental base for scientific work, in the same time serving to solve the industrial problems. Let us mention DIVK members from Military Technical Institute (VTI), Institute for Material Testing IMS, Goša Institute, Mechanical Engineering Faculty (Mf), Belgrade, Faculty of Technology and Metallurgy (TMF), Belgrade, from many DIVK donator members, like Electricity of Serbia, TENT, GOŠA FOM, Beogradske Elektrane, (Serbian heating company), Belgrade. Important support in DIVK activities comes from SME companies and innovation institutions

It is worth to mention that in this environment, involved through IFMASS and DIVK, new ideas might be realized, and one example can illustrate this in the best way. Innovation centre SYSTEM DC 90 , a small enterprise, recently promoted a new laboratory for research in earthquake engineering based on fracture mechanics and fatigue testing, consisting of two servohydraulic devices and vibrating table and organized first Summer Scientific Workshop Colony. Servo hydraulic closed loop testing machine (force ± 5000 kN, displacements ± 265 mm), with a vertical frame for 5000x3000x1000 mm sized samples, (Figure left) is located outdoor, smaller device with vibrating table (Figure right) were designed and produced in Serbia. (More details can be found in “Structural Integrity and Life”, Vol. 9, 3/2009).



Belgrade, October 2009.

Prof. Dr. Stojan Sedmak
IFMASS 10 editor

Contents

Preface	1
A Sedmak: Failures of structures in service	3
P Agatonović Fracture mechanics in the plastic range.....	19
M Mićunović Ductile failure criteria under multiaxial loading	45
M Rakin Micromechanical constitutive equations for ductile fracture prediction	69
Z Burzić, M Burzić Fatigue analysis using fracture mechanics	87
D Kozak, N Gubeljak Theoretical basis of structural integrity and life	107
P Agatonović Simplifications for conservative structural integrity assessment.....	125
V Grabulov, D Momčilović Significance of Fracturemechanic testing for structural integrity of welded joints.....	145
M Arsić Practical aspects of pressure vessels integrity	163
K Gerić Microstructural analysis of crack tip region	179
S Kuzmanović, A Koro, N Njuhović Application of non-destructive testing procedures for structural integrity assessment ...	191
T Maneski, V Milošević-Mitić The Analysis of the stress-state in constructions in exploitation	203
N Trišović Dynamic characteristics modification in the mechanical structures reanalysis.....	225
M Kirić, M Srećković Modern approach to control and nondestructive testing methods	237
N Gubeljak, J Predan, T Valh, D Valh Continuous monitoring and structure integrity assessment	261
N Radović Role of particles in fracture mechanics: Evolution of one approach	285
Lj Milović Steels for elevated temperature application: Heat-Affected-Zone specifics	297
M Wnuk Discrete and fractal aspects of fracture.....	309
S Sedmak Crack analysis at nano level	323

Other IFMASS titles

- IFMASS 1 *Uvod u mehaniku loma i konstruisanje sa sigurnošću od loma*, Edited by S. Sedmak, published by GOŠA Institute and TMF, Belgrade 1981 (in Serbian)
- IFMASS2 *Savremeni aspekti projektovanja i izrade posuda pod pritiskom i cevovoda*, Edited by S. Sedmak, published by GOŠA Institute and TMF, Belgrade 1982 (in Serbian)
- IFMASS 3 *Mehanika loma zavarenih spojeva*, Edited by S. Sedmak, published by GOŠA Institute and TMF, Belgrade 1984 (in Serbian)
- IFMASS 4 *Perspektive razvoja i primene mehanike loma*, Edited by S. Sedmak, published by GOŠA Institute and TMF, Belgrade 1986 (in Serbian)
- IFMASS 5 *The Application of Fracture Mechanics to Life Estimation of Power Plant Components*, Edited by S. Sedmak, published by EMAS Ltd. and TMF, Belgrade 1990 (in English)
- Primena mehanike loma u oceni preostalog veka komponenti termoenergetske opreme*, Edited by S. Sedmak, published by GOŠA Institute and TMF, Belgrade 1991 (in Serbian)
- IFMASS 6 *Eksploatacija prslina u posudama pod pritiskom i rezervoarima*, Edited by S. Sedmak, and A. Sedmak, published by TMF, UN European Centre of Peace and Development, and GOŠA Institute, Belgrade 1994 (in Serbian)
- IFMASS 7 *Ekperimentalne i numeričke metode mehanike loma u oceni integriteta konstrukcija*, Edited by S. Sedmak and A. Sedmak, published by TMF, GOŠA Institute, and Yugoslav Welding Association, Belgrade 2000 (in Serbian)
- IFMASS 8 *From Fracture Mechanics to Structural Integrity Assessment*, Edited by S. Sedmak and Z. Radaković, published by DIVK and TMF, Belgrade 2004 (in English)
- IFMASS 9 *The Challenge of Materials and Weldments*, Edited by S. Sedmak, Z. Radaković and J. Lozančić, published by Faculty of Mechanical Engineering (MF), DIVK, TMF and GOŠA Institute, Belgrade 2008 (in English)

FAILURES OF STRUCTURES IN SERVICE

Aleksandar Sedmak

University of Belgrade, Faculty of Mechanical Engineering, Belgrade, Serbia
asedmak@mas.bg.ac.rs

Jasmina Lozanović

University of Belgrade, Innovation Centre of the Faculty of Mechanical Engineering, Belgrade, Serbia

1. INTRODUCTION

Despite great improvements in design, manufacturing, inspection and maintenance procedures, failures of structures still occur, often with great human and economic loss. Since this lecture provides an introduction to the subject of failure analysis, the general methodologies involved in carrying out such an analysis are illustrated by two case studies. Failure analysis can be an absorbing subject to those involved in investigating the cause of an accident, but the capable investigator must have a thorough understanding of mode of operation of the components involved, as well as knowledge of the possible failure modes. A properly performed investigation should lead to a rational scenario of the sequence of events occurred in the failure as well as to an assignment of responsibility, either to the designer, the manufacturer, the operator or the maintenance and inspection organization involved. A successful investigation may also result in improvements in design, manufacturing, inspection and maintenance procedures.

Since prehistoric times, failures have often resulted in taking one step back and two steps forward, but sometimes with severe consequences for the designers and builders. This can be illustrated by the Code of Hammurabi, which was written in about 2250 BC /1, 2/: “If a builder build a house for a man and do not make its construction firm, and the house which he has built collapse and cause the death of the owner of the house, that builder shall be put to death. If it causes the death of a son of the owner of the house, they shall put to death a son of that builder. If it destroys property, he shall restore what ever it destroyed, and because he did not make the house which he built firm and it collapsed, he shall rebuild the house which collapsed at his own expense.”

The failure analysis of bridges, viaducts, cathedrals, pressure vessels, aircraft vehicles and other structures resulted in better design, improvement of materials and construction procedures. Mechanical components, such as wheels and axles, were improved through empirical insights gained through experience, and these improvements worked out quite well, but not always. An example of an evolved design that did not work out well is related to the earthquake that struck Kobe, Japan, in 1995. That area of Japan had been free of damaging earthquakes for some time, but had been visited frequently by typhoons. To stabilize homes against the ravages of typhoons, the local building practice was to use a rather heavy roof structure. However, when the earthquake struck, the collapse of heavy roofs caused considerable loss of life and property damage. The current design codes for this area have been revised to reflect a concern for both typhoons and earthquakes.

Stress analysis plays an important role both in design and in failure analysis. Ever since the advent of the industrial revolution, concern about the safety of structures has

resulted in significant advances in stress analysis. The advent of the high-speed computer has led to further rapid advances in the use of numerical methods of stress analysis using the finite element method (FEM), and improved knowledge of material behavior has led to advances in development of constitutive relations based upon dislocation theory, plasticity, and mechanisms of fracture.

Design philosophies such as safe-life and fail-safe have also been developed, particularly in the aerospace field.

For a safe-life, a structure is designed as a statically determined structure intended to last without failure for the designed lifetime of the structure. To guard against premature failure, the component should be periodically inspected during its in-service lifetime.

In the fail-safe approach, the structure is designed in such a way that if one member of the structure were to fail, there would be enough redundancy built into the structure that an alternate load path would be available to support the loads, at least until the time of the next inspection. Consideration must also be given to the spectrum of loading that a structure will be called upon to withstand in relation to the scatter in the ability of materials to sustain these loads. As indicated in Fig. 1, danger of failure is present when these two distributions overlap. In addition, new fields such as fracture mechanics, fatigue research, corrosion science, and nondestructive testing have emerged. Important advances have also been made in improving the resistance of materials to fracture. In the metallurgical field, these advances comprise better alloy design and control of chemistry, and improvements in metal processing and heat treatment.

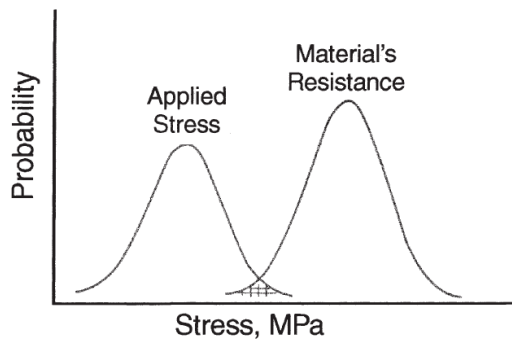


Figure 1: Schematic frequency distributions showing the applied stresses and material resistance

The failure analyst often has to determine the nature of a failure; for example, was it due to fatigue or to an overload? In many cases, a simple visual examination may suffice to provide the answer. In other cases, however, the examination of a fracture surface (fractography) may be more involved and may require the use of laboratory instruments such as the light microscope, the transmission electron microscope, and the scanning electron microscope. Many of today's investigations are quite costly and complex, and require a broad range of expertise as well as the use of sophisticated laboratory equipment. Many investigations are also carried out by manufacturers to ensure that their products perform reliably. In addition, a number of companies now exist for the purpose of carrying out failure analyses to assist manufacturers and power plant owners, as well as to aid in litigation. The results of many of these investigations are made public, and thus provide useful information as to the nature and cause of failures, but unfortunately, the results of some investigations are sealed as part of a pretrial settlement to litigation.

Today, the reliability of engineered products and structures is at an all-time high, but this reliability often comes with a high cost. In fact, in the nuclear industry, compliance with regulations intended to maximize safety may be so costly as to warrant the taking of a reactor out of service. It is also important for manufacturers to be aware of the state of the art as well as the latest standards. The number of manufacturers of small planes has dwindled because of product liability losses incurred when it was shown that their manufacturing procedures did not meet the current state-of-the-art safety standards. To guard against product failures, a number of firms now are organized in such a way that failure analysis is a line function rather than a staff function, and a member of the failure analysis group has to sign off on all new designs before they enter the manufacturing stage.

Two typical examples are selected to illustrate the significance of failure case studies and the benefits which can be gained for structure design and service improvement.

2. THE ALEXANDER KIELLAND PLAT FORM DISASTER

On the evening of 27th March, 1980, the Alexander Kielland, a drilling rig converted into an accommodation platform and located in the North Sea, started to capsize and within 20 minutes had overturned killing 123 of 212 people on board /3/. The reason for the failure was later traced to a small 6 mm fillet weld which joined a non load-bearing flange plate to one of the main bracings. The purpose of the flange plate was to hold a sonar device used in connection with drilling operations; ironically, the platform was never actually employed as a drilling rig. This case study is concerned with the possible factors that contributed to the failure of the weld.

The Alexander L. Kielland was a mobile platform of the pentagon type and was designed and built in France at the Dunkirk Shipping Yards. The rig was ordered by the Norwegians in 1973 and delivered in 1976. It was originally built as a drilling rig, but during its entire operation it was utilized instead as an accommodation platform. Initially, its capacity was 80 beds, and in April, 1978, this had been increased to 348. Altogether, eleven platforms of this type have been built, nine are still in service in the North Sea.

The characteristic form of a pentagon platform design is shown in Fig. 2. The main concern herein is the D column and the bracing D-6. A detail of this part of the rig is given in Fig. 3.a, which shows the location of the sonar flange plate, welded to the main bracing (D-6), Fig. 3.b. The D-6 bracing is 24 m long, circular, hollow beam of diameter 2.6 m and thickness 26 mm. It is left open to the sea and allowed to contain sea water in order to increase the rig's stability. For that, the bracing contains an elongated opening (300 x 800 mm) on the bottom of the bracing next to the sonar flange plate. Both the air hole and elongated opening were fitted with flanges to reduce the stress concentrations.

The production schedule was such that the assembly work was divided between two teams, one team being responsible for the main welding and fitting operations and the other taking care of the welding and fitting of ancillary equipment. In this respect, for example, the welding of the flanges to the elongated opening and air hole was included among the duties of the main installation team, while the welding of the non load-bearing sonar flange plate was the responsibility of the other team. Furthermore, it was not considered necessary in the design work to carry out any stress analysis of the sonar flange plate fitting, although a stress analysis of, e.g., the oval hole flange plate was carried out. This turned out to be a vital omission. The main braces were of a welded construction and made from Nb -microalloyed fine-grained steel.

2.1. The construction and fitting of the sonar flange plate

As shown in Fig. 3.b, the flange plate is essentially a short, circular, hollow cylinder, 325 mm in diameter, wall thickness 20 mm and 228 mm long. Similar flange plates were fitted to three of the main braces, i.e. B-5, D-6 and A-5. The flange plate material was fine-grained pearlitic-ferritic steel, shaped by bending and butt welding. The profile of the butt weld was of an X form, welded from both inside and outside employing 2 runs on the inside and up to four on the outside. The welding procedure applied was Manual Metal Arc (MMA), using flux-covered electrodes.

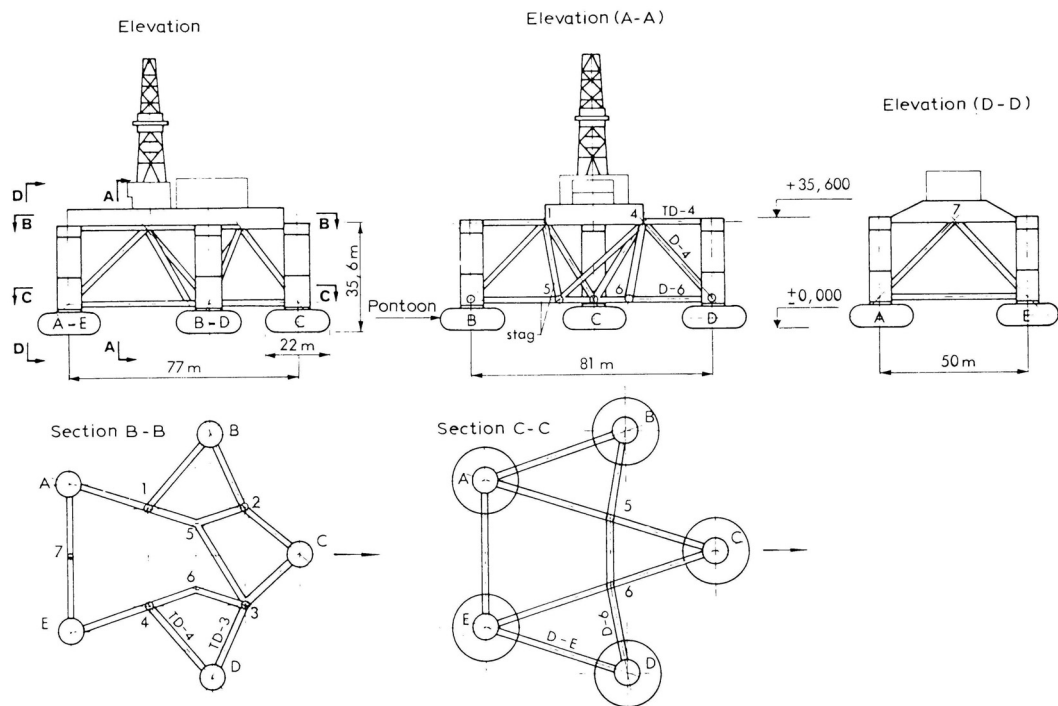


Figure 2: General design view of a pentagon type platform

The sonar flange plate was located at a flame-cut hole in the bracing, of approximately 3-5 mm larger diameter than the flange itself. The flange plate was then welded in position using MMA welding of 2-3 runs per weld, employing fillet welds both inside and outside the main brace plate, Fig. 3.b. Flux-covered basic electrodes, 5 mm in diameter, were selected. The weld's dimension 'a' was 6 mm, but the number of runs per weld was not specified. Preheat was neither specified nor employed.

2.2. Capsize of the Alexander Kielland

On the 27th March, 1980, the day of the disaster, the weather in the North Sea was stormy with mist and rain and visibility down to about a kilometre. It was cold, with an air temperature of 4-6°C and a sea temperature of 6°C. As the day progressed the weather deteriorated, with the wind blowing at 20 m/s, churning up waves of 6-8 m in height. About half an hour later, at 6.28 p.m., the radio officer on board the Kielland heard a loud thump from below. Not too much notice was paid to begin with, since such noises are not unusual in heavy seas. Soon after the first thump, however, came another and this was followed by a definite listing of the platform. Minutes after the second thump was heard,

the platform had already listed over to an angle of 30-35° from the horizontal. Indeed, it was apparent that only the anchor wire, 'as taut as a violin string', prevented the platform from turning over completely. At 6.53 p.m., 24 minutes after the 'Mayday' was sent out, it was recorded that the Alexander Kielland had completely overturned.

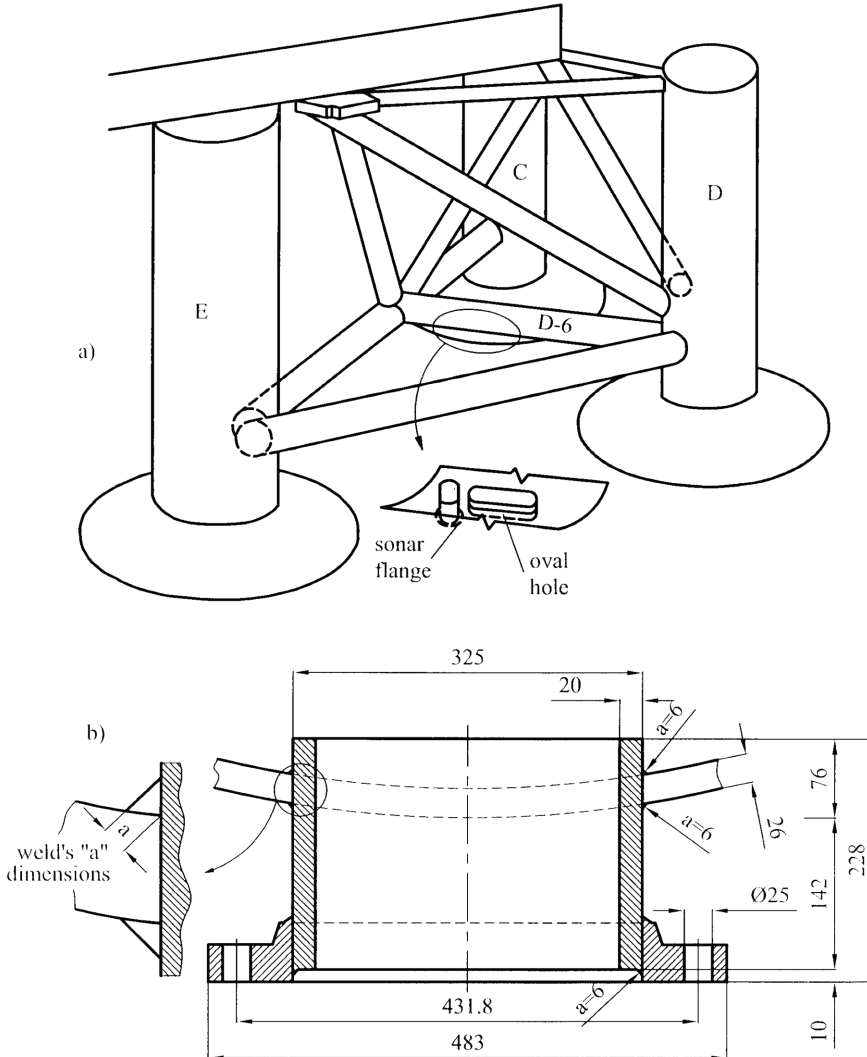


Figure 3: a. A detail of the rig, with the location of the sonar flange plate
 b. A detail of the flange plate as welded to the main bracing (D-6)

It was later established by the Norwegian Commission that investigated this incident, that the first thump heard by the radio officer was certainly caused by the fracture of the main brace, D-6. Then followed, in rapid succession, presumably due to overloading, failures of the other bracings which connected column D to the platform. The positions of the various bracings fractures are shown in Fig. 4. The spacing of the latter fractures led the Commission to conclude that failure of bracings other than D-6 was due to bending.

The failure in bracing D-6, which initiated the structural failure, was clearly due to fatigue. Indeed, it was later established that prior to the final fracture, the crack had grown to a length of over 5 m, or ca. 2/3 the circumference of the bracing! Figure 3.b. is a

detail from the flange plate region which shows that the main fracture had occurred quite independently of the main butt weld of the main bracing (shown to the right); it is, however, clearly associated with the fillet weld of the flange plate. Studies of the characteristic river patterns of the main fracture confirmed this.

2.3. Metallographic examination of the sonar flange plate welds

A metallographic examination of the fractured D-6 bracing revealed (amongst other things) the following factors:

1. The butt welded joint of the sonar flange plate contained both toe and root cracks, the latter extending the whole length of weld. Lamellar tearing of material was also noticed.
2. Secondary cracking associated with the butt weld was observed at the cross-over between the butt weld and the fillet weld.
3. The quality of the butt weld was generally poor, exhibiting unsatisfactory penetration of the base material.

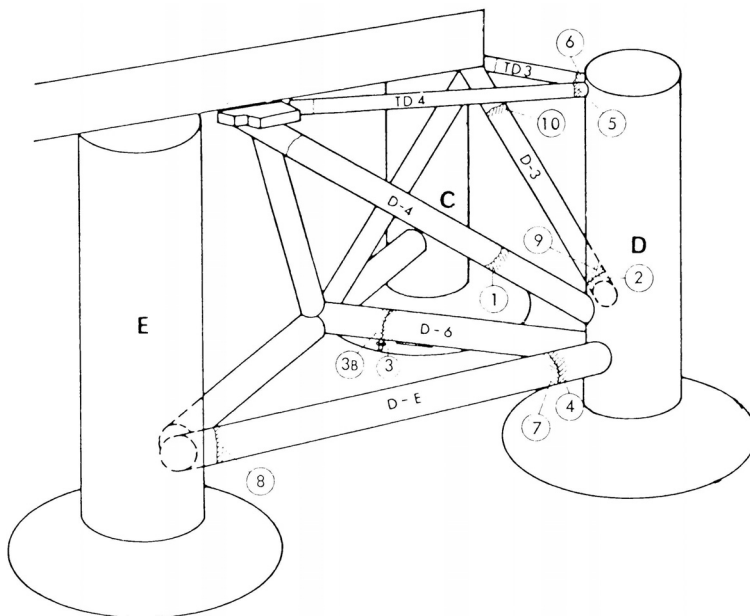


Figure 4: The various locations of fracture, indicated by 1 to 9

4. The quality of the fillet welds, connecting the flange plate to the main bracing, was generally poor, showing insufficient penetration and uneven profiles.
5. Significant amounts of lamellar tearing of the flange plate material were observed in association with the fillet welds. However, there was no evidence of lamellar tearing in the bracing plate material.
6. Cracks running parallel to the edges of the fillet welds and joining up with the main fracture were observed (see Fig. 5 and Fig. 6).
7. Several small cracks were found associated with the fatigue initiation point I, as presented in Fig. 5. The appearance of these cracks indicates cold cracking.
8. Small traces of paint, of the type originally used in the Dunkirk Yards, were discovered on the fracture surface of the fillet weld, implying that some cracking had been present in this weld already during manufacture of the rig and prior to it going to sea.

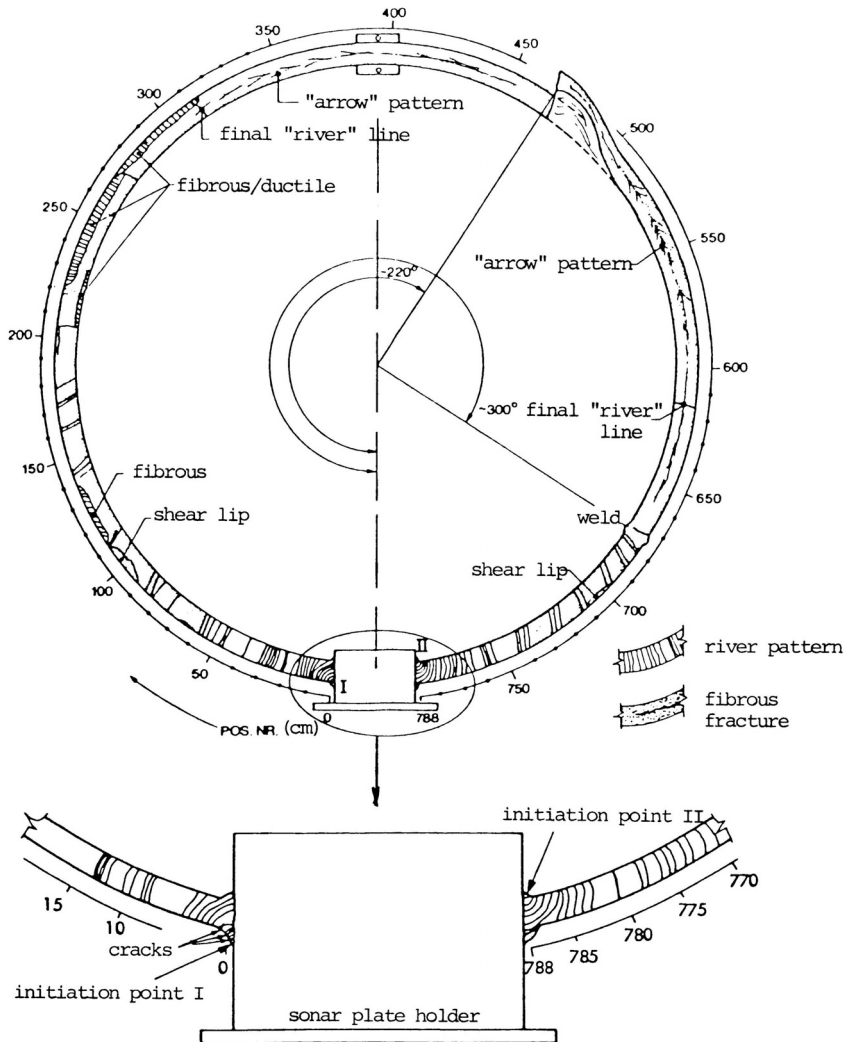


Figure 5: Scheme of crack development on the fracture surface of

9. Hardness measurements were carried out on the fillet-welded joint, and these results are given in Fig. 7. The maximum hardness is associated with the HAZ of cylindrical part, reaching values of 350 HV, compared with about 160 HV in the base material. The hardness of the as-solidified weld metal lies between these values.

10. Microstructural and mechanical properties of both the flange plate and bracing plate materials are summarized in Table 1. Note that although the grain sizes in both materials are small, the transverse (through-thickness) properties of the flange plate material are exceptionally poor. Fatigue life experiments were also carried out on the main bracing material, giving satisfactory values for the stress ranges expected.

11. Stress analysis of the effect of the sonar flange hole on stress concentration in the bracing material, with and without the flange plate in position, was carried out. This showed that if the flange plate had not been present the stress concentration would almost double, reaching a value of about three times that of the mean stress in the bracing. If the flange plate had been intact, the maximum stress concentration would be about 1.8.

12. Examination of bracing A-5; B-5, also with sonar flanges, revealed no signs of failure.

2.4. Analysis of weld thermal cycle effects on the bracing and flange plate materials

The material of main bracing was Nb -microalloyed, fine grained, high strength steel, Table 1. In normalized conditions the steel contains a fine dispersion of NbC precipitate which stabilizes and refines the grain size. The carbon content is high (0.17%), giving the steel its fairly high C_{equiv} value (0.41). Aluminium (0.044 wt %) is mainly present as a deoxidizer, there evidently being little or no nitrogen present to form AlN or Nb(CN).

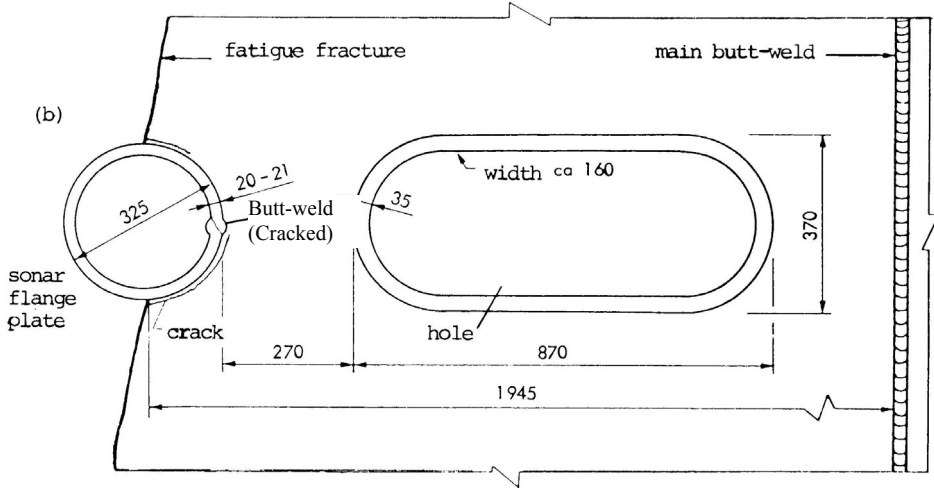


Figure 6: Crack initiating in a fillet weld of sonar flange plate and ending in cracked butt weld. The position of final fatigue fracture is indicated

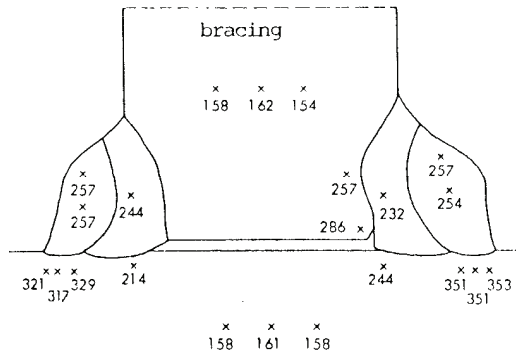


Figure 7: Hardness distribution in failed fillet welded joint between bracing and flange plate

The continuous cooling diagram for the steel is similar to that shown in Fig. 8 (for the 0.19% C content), in which it is seen that the relatively high cooling rates of MMA welding are likely to give a mainly bainitic microstructure. The presence of Nb, if it is in solution in the austenite, further tends to promote the lower bainite transformation. In other words, this alloy is a typical example of today's sophisticated steels which aim to possess the ideal combination of high strength and acceptable weldability.

The solubility temperature of NbC in steel is given by equation

$$\log_{10} [\%Nb][\%C] = 2.96 - 7510 / T \quad (1)$$

and thus it is estimated to be $T \sim 1150^\circ\text{C}$. During a rapid thermal cycle, as in welding, the carbide is effectively superheated. On this basis, knowing the welding energy Q used

$$Q / RT_m = 23.2 \text{ (for Nb)} \quad (2)$$

when carrying out the fillet weld, it may be estimated whether or not the NbC is likely to have gone into solution.

According to the data available, the fillet weld was carried out with a 5 mm covered (basic) electrode of the type OK 48.30, manufactured by ESAB. The following data for this electrode is recommended: current 200-260 A, voltage 24 V. Assuming an efficiency of 0.8 for MMA welding procedure, an input energy of about 0.7-0.8 MJ m⁻¹ can be calculated. This corresponds to a Δt_{8-5} of about 2-3s, giving a temperature of solution for NbC of cca. 1270 °C

Table 1: Summary of microstructural and mechanical properties of applied base materials

Property	Main bracing	Flange plate
Composition (approx.)	0.17wt%; 0.32 Si; 1.37Mn; 0.044 Al; 0.029 Nb	Not specified
C_{equiv}	0.41	Not specified
Grain size (normalized)	ASTM 11.5 (ca. 8 μm)	ASTM 10.7 (ca. 7 μm)
Micro-structural features	1.Banded, ferritic-pearlitic 2.Slag content low, mainly MnS, finely distributed	1.Banded, ferritic-pearlitic 2.Slag content fairly high; Mainly MnS in extreme rolled-out form
σ_y (rolling direction)	345-353 N mm ⁻²	Not specified
σ_t (rolling direction)	506-518 N mm ⁻²	Not specified
σ_t (transverse direction)	419-474 N mm ⁻²	215-437 N mm ⁻²
Area reduction (rolling Direction)	30-34 %	Not specified
Area reduction (transverse)	6-13 %	1-7 %
Impact strength (Charpy)		
0°C	83 J	Not specified
-40 °C	36 J	16 J

The implications of this are threefold. In the first place, it means that grain growth in the HAZ at temperatures above ca. 1270°C can occur. In addition, it is likely that Nb in solution tends to promote the lower transformation products on cooling. Finally, the very rapid cooling rate through 800-500°C predicted for this welded joint ($\Delta t_{8/5}=2-3$ s) tends to promote the martensite transformation in this steel.

Taking into account estimated cooling time and peak temperature, it can be predicted that the maximum austenite grain size for this weld energy-input (assuming a thick-plate condition) is of the order of ca. 30-35 μm , compared with ca. 8 μm for the ferritic base material. Thus, the Nb in solution in the region of the HAZ and the high cooling rate are both likely to produce a hard bainitic - martensitic microstructure in the HAZ of the bracing material. The conclusion is supported by the hardness measurements (Fig. 7) carried out on the fillet weld in question.

The presence of a number of small, underbead cracks in the vicinity of the HAZ of the fillet weld in the bracing material is intriguing, primarily because of cold cracks. The use of a basic electrode should normally keep the hydrogen content at a low value. On the other hand, it has been well established that the stress concentration at the weld was likely to be high and the microstructure is likely to contain martensite. On this basis, cold cracks of the fillet weld cannot be ruled out, even in the presence of low hydrogen levels.

Unfortunately, no chemical analysis for flange plate material was available. Micrographs show that the steel contains a highly banded, ferritic-pearlitic microstructure of a somewhat finer grain size than that of the bracing material (see Table 1). On the other hand, the MnS-inclusion content is not only higher than for the bracing material, but is present in the undesirable shape of long, rolled out laths. This, of course, gives the material its very poor transverse ductility (1-7%). It is therefore hardly surprising that significant lamellar tearing was observed in connection with both the fillet and butt welds.

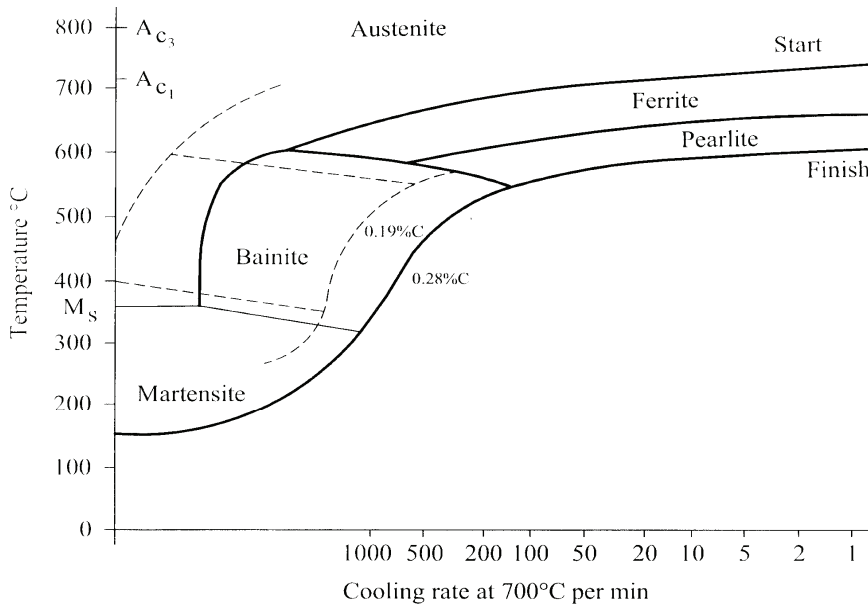


Figure 8: Continuous cooling diagram for microalloyed steel containing 0.19%C

The root cracks and toe cracks reported for the butt weld are presumably due to cold (hydrogen) cracking. Assuming the use of the same basic electrodes as specified for the fillet weld, cold cracking problems should not normally occur, although it is not known whether the electrodes were properly dried prior to use. Another possible contributory cause to these cracks may be in the form of liquation cracking, this often arising if elongated MnS particles intersect the fusion zone, as seems likely in the case of the butt weld. In any case, the hardness measurements in the HAZ of this material (Fig. 7) are somewhat higher than for the bracing material HAZ. This suggests the presence of a significant amount of the bainitic-martensitic structure, susceptible to cold cracking.

2.5. Mechanism of failure: main conclusions

There appears to be a number of factors which could possibly have contributed to the failure of the D-6 bracing, with the resulting capsizing of the Alexander Kielland platform. Of these the following are probably the most important:

1. The considerable amounts of lamellar tearing in the flange plate and the extensive root crack in the butt weld both contribute to the weakening of the sonar flange-plate in its capacity as structural strengthener. This, together with the resulting increased stress concentration at the hole, evidently induced cracking (or caused existing cracks to grow) around the periphery of the flange plate in the fillet weld.
2. The poor profile of the fillet weld contributed to reduced fatigue strength of the weld.

3. The rapid cooling rate of the fillet weld, the dissolution of NbC precipitates, and some grain growth in the HAZ of the bracing plate, all (together with the increased stress concentrations) helped produce just the conditions likely to give rise to cold cracking.

4. Given the presence of cold cracks in the fillet welds, the increase in stress concentration due to weakening of the flange plate, the poor weld profile, and the cyclic stresses experienced at sea then all the necessary conditions for fatigue crack growth appear to be present.

As with most case studies, there are some unanswered questions. For example, why did significant cracking occur in bracing D-6, but not in bracings A-5 and B-5, which also contained sonar flange plates? A possible variable might be proper drying of the electrodes for the fillet weld, particularly because this weld was considered of secondary importance at the manufacturing stage. It is also not clear that the loading conditions are the same for all three bracings under normal service at sea, and this may be another important variable.

3. FRACTURE OF CARRIAGE MONOBLOCK WHEELS

The monoblock wheel was fractured radially in the zone corresponding to chuck marks, Fig. 9. The data from report /4/ revealed that the wheel had been installed on 26th January, 1998 the tread diameter was reduced from 920 to 908 mm on 16th March, and machined further to 890 mm on 15th May. After that the wheel had been broken with tread diameter about 890 mm. This information points to possible braking problems.

It should be emphasised that a 5 mm gap was present in the fracture area (Fig. 9). The gap indicates the presence of residual compressive stresses, in one wheel area at least.

The facts regarding breaking of this wheel, i.e. the influence of the brake shoe insert (Fig. 9) that imparted traces of over-heating on the wheel and the insert itself are of an equal importance. It should be mentioned that even more visible traces of braking are found on N°6 wheel from the same bogie, only that this wheel was without chuck marks.



Figure 9: Fractured monoblock wheel

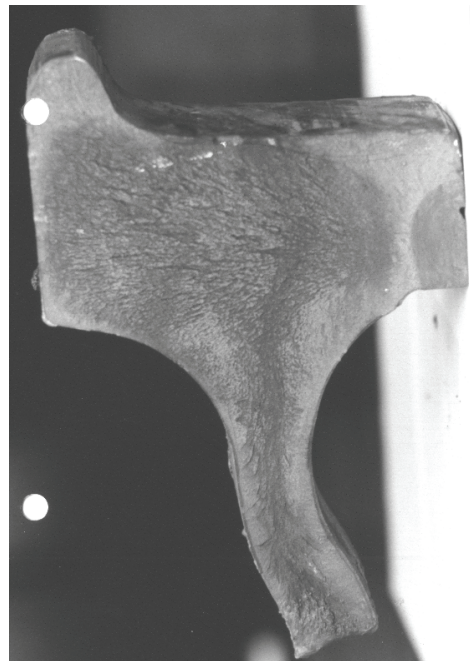


Figure 10: The appearance of fractured wheel surface

The following action had been performed:

1. Investigation and analysis of the causes of wheel fracture.
2. Establishment of the crack growth rate brought about by material fatigue. Assessment of whether the cracks could have been detected before fracture (during routine inspection) is based on this.

Parts of fractured wheel, i.e. sample taken from the fractured zone, were used for fracture investigation and analysis. The wheel material sample was also used to determine the crack growth rate during fatigue stressing.

3.1. Fracture analysis

A sample for fracture analysis had been taken from UV 7929/114 wheel. Visual inspection gave the following results:

- a 14x35 mm fatigue caused crack was noticed in the lower left corner on the wheel rim;
- ridges (scores) in the rest of the rim and flange (directed toward the fracture source, i.e. fatigue crack), as typical signs of brittle fracture;
- traces of plastic deformation on the wheel tread surface.

Part of the fracture surface is examined by a scanning electronic microscope (SEM) in order to detect possible material texture faults and to examine fractured surface in detail. This examination failed to reveal any fault.

Chemical analysis was performed by an ordinary wet process, and results are shown here in Table 2. It is clear from the results that the composition is in accordance to UIC 812-3, Table 2 regulation (R7T Steel).

Table 2: Chemical composition of wheel sample

C	Si	Mn	P	S	Cr	Cu	Mo	Ni	V	Cr+Mo+Ni
0.53	0.36	0.72	0.021	0.022	0.18	0.24	0.03	0.06	0.03	0.27

3.2. Mechanical properties

Impact toughness was tested on Charpy pendulum machine using standard V2-notched specimen. Total energy was separated into the crack initiation and crack growth energies.

The specimens were sampled in two directions, transversal and longitudinal in respect to wheel circumference. The results, presented in Table 3, reveal low impact toughness values, especially low crack growth energy.

Table 3: Results of impact tests performed on Charpy Pendulum machine

Sample	Specimen	Total impact energy E, J	Crack initiation energy E _{inic} , J	Crack growth energy E _{growth} , J
U1	1	19,0	18,1	0,9
U2	2	14,4	13,7	0,7
U3	3	18,5	17,2	1,3
P1	1	15,8	14,5	1,3
P2	2	15,8	14,7	1,1
P3	3	17,7	16,2	1,5

3.3. Material fatigue test

Fatigue testing was performed in accordance with ASTM E647 Standard, by three points bending of standard Charpy specimens, on a Resonating High-Frequency Pulsating

machine CRACKTRONIC in the load-control mode. Test results enabled to relate fatigue crack growth rate (da/dN) and stress intensity factor (ΔK), as plotted in Fig. 11.

One should notice an extremely high crack growth rate, which caused the specimen fracture after very small increase of the stress intensity factor range ΔK , from the initial, threshold, value ($\Delta K_{th} \approx 18 \text{ MPa}\sqrt{\text{m}}$), to the final value ($\Delta K_{max} \approx 20 \text{ MPa}\sqrt{\text{m}}$). The number of cycles spent for crack initiation was $N_i \approx 200,000$, whereas the number of cycles for crack growth and final fracture was $N_k \approx 20,000$.

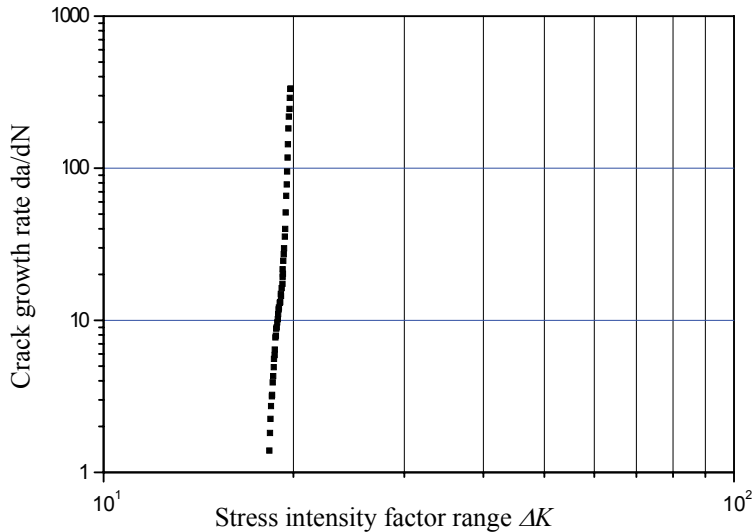


Figure 11: Relationship crack growth rate da/dN vs. stress intensity factor range ΔK

3.4. Analysis of rupture causes

According to the visual inspection and SEM examination one can conclude that the final fracture was brittle. The basic macroscopic fracture appearances that indicated such a conclusion are negligible plastic deformation (existing only near tread surface) and the existence of ridges which indicate the initial fracture location (fatigue crack). Moreover, it should be noted that the existence of ridges indicates a quasi-static character of final fracture. Microscopic fracture characteristics are in accordance with this, since the SEM examination hasn't indicated the presence of plastic deformation either.

Consequently, the fracture occurred in two steps: first, a fatigue crack appeared, which further developed in a stable manner to a critical value; in the second phase, under the effect of a quasi-static load, the unstable fatigue crack propagation preceded the final fracture, which was brittle and occurred within a short time interval, i.e. very fast.

The above given number of cycles can not taken as exact because of the different conditions in service and in fatigue laboratory test. While the fatigue test load is a simple one and consist of alternate bending and stretching with the same (constant) amplitude, in service a wheel is subjected additionally to variable thermal stress at each braking. Mechanical load is relatively simple and causes stresses ranging from a maximal compressive one (wheel/rail contact) to zero, while thermal shock are more complex and bring about different stress states in different wheel parts. In the area of the wheel where fatigue crack appeared, the thermal shock due by braking causes cyclic stresses ranging from maximal tensile to a compressive stress of lower intensity /4/. Contrary to that, at

cooling, which is much slower than heating, the process is reversed, but the stresses are of a lower intensity due to the slower temperature change.

Furthermore, one should also consider the influence of residual stresses which are caused by braking in a similar manner as the thermal shock stresses due to uneven heating and cooling, only that they have the quasi-static and not the cyclic character. The residual stresses developed in this manner are tensile, also relatively high, in the tread surface layer and compressive, relatively low, in the rest of the wheel, the fatigue crack zone included. Combined action of all mentioned stresses (mechanical, thermal and residual) is obviously such that there is a resulting cyclic-stress which can cause the initial fatigue crack, located at the highest stress concentration/chuck mark, to develop to its critical size. It is also obvious that there is the resulting quasi-static tensile stress at braking, which can cause the crack of a critical size to propagate in unstable manner till brittle fracture of the wheel.

For the next analysis several facts and data had to be considered.

Impact toughness testing indicated an extremely low resistance to crack growth, only about 1 J, accompanied by a low resistance to crack initiation (about 15 J). However, impact loads are not typical for railroad wheels, but they can be involved.

Fracture toughness, obtained using 30 mm thick CT specimens, is $K_I = 104.9 \text{ MPa}\sqrt{\text{m}}$, but the thickness requirement for valid K_{Ic} was not satisfied. Since thickness requirement would be satisfied for fracture toughness value $64.2 \text{ MPa}\sqrt{\text{m}}$, it is accepted that the real value of plane strain fracture toughness is in the range $64.2 < K_{Ic} < 104.9 \text{ MPa}\sqrt{\text{m}}$ /4/.

Fatigue tests indicated very small resistance to crack growth corresponding to only 20,000 cycles for crack propagation before fracture, where the stress intensity factor range ($\Delta K \approx 20 \text{ MPa}\sqrt{\text{m}}$) is much lower than its critical value ($K_{Ic} = 64.2 \text{ MPa}\sqrt{\text{m}}$) and the corresponding stress range ($\Delta\sigma = 87 \text{ MPa}$) is much lower than the yield stress, being for this steel class $R_{ch} = 500 \text{ MPa}$.

Using these data it is possible to evaluate the tensile quasi-static stress for the brittle fracture of the wheel having a fatigue crack of approximately semi-elliptic form, modelled in Fig. 13, of crack length $c = 14 \text{ mm}$ and crack depth $a = 35 \text{ mm}$.

It was calculated that the value of remote tensile stress is $\sigma = 282.5 \text{ MPa}$, sufficient to produce brittle fracture. The tensile stress of this magnitude may appear during wheel braking by the brake system used in the considered case.

3.5. Assessment of the possibility of crack detection before fracture

According to fatigue tests, the number of cycles during fatigue crack propagation till fracture is about 20,000. The corresponding range of stress-intensity factor applied was $\Delta K \approx (18 \text{ to } 20) \text{ MPa}\sqrt{\text{m}}$, which corresponds to the stress amplitude $\sigma = 79.2 - 88 \text{ MPa}$ that can be achieved only during braking process, since in normal service stress in this wheel is much lower /4/. For that, the applicable cycle number for crack growth monitoring is determined by braking application. However, since the given number of cycles is very small, the likelihood of crack detection before fracture is negligible, because frequent wheel examination by non-destructive methods should be required. It is reasonable to conclude that material having such a high rate of crack growth, used in condition when brake shoe is acting upon wheel tread surface, does not allow crack monitoring before fracture in a satisfactory manner.

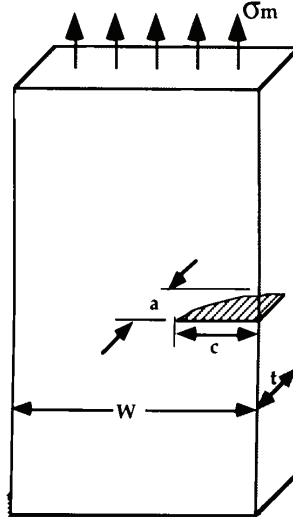


Figure 12: Model of tensile plate with an edge surface crack

For the evaluation of remote tensile stress $\sigma (= \sigma_m)$, necessary for the final fracture, rectangular plate is assumed, of thickness $t = 50$ mm and width $w = 135$ mm in cross section, through which contained semi-elliptic crack, 14×35 mm in size will propagate in the material of plane strain fracture toughness $K_{Ic} = 64.2$ MPa \sqrt{m} .

The procedure based on linear elastic fracture mechanics for the angle position $\phi = 0$ included following equations used in a sequence /4/:

$$\sigma_m = \frac{K}{F \sqrt{\frac{\pi a}{Q}}}; \quad \sigma_m = 282.5 \text{ MPa} \quad (3) \quad Q = 1 + 1.464 \left(\frac{c}{a} \right)^{1.65} = 1.323 \quad (4)$$

$$F = \left[M_1 + M_2 \left(\frac{a}{t} \right)^2 + M_3 \left(\frac{a}{t} \right)^4 \right] g_1 g_2 f_\phi f_w \quad (5)$$

$$M_1 = \sqrt{\frac{c}{a}} \left[1.08 + 0.03 \left(\frac{c}{a} \right) \right] = 0.69; \quad M_2 = 0.375 \left(\frac{c}{a} \right)^2 = 0.06; \quad M_3 = -0.25 \left(\frac{c}{a} \right)^2 = -0.04$$

$$g_1 = 1 + \left[0.08 + 0.4 \left(\frac{c}{t} \right)^2 \right] (1 - \sin \phi)^3 = 1.11, \quad g_2 = 1 + \left[0.08 + 0.15 \left(\frac{c}{t} \right)^2 \right] (1 - \cos \phi)^3 = 1$$

$$f_\phi = \left[\left(\frac{c}{a} \right)^2 \sin^2 \phi + \cos^2 \phi \right]^{\frac{1}{4}} = 1, \quad f_w = \left[\sec \left(\frac{\pi c}{2W} \sqrt{\frac{a}{t}} \right) \right]^{\frac{1}{2}} = 1; \quad F = 0.788$$

3.6. Conclusion

The examination and analysis of the carriage monoblock wheel fracture causes allows the following conclusions:

- Fatigue crack emerged under the influence of cyclic stresses induced by braking and is situated at the highest stress concentration location, chuck marks.

- Fatigue crack propagated under the influence of the same cyclic-stresses. The fatigue crack growth rate is so high that it is practically impossible to monitor it.

- Unstable quasi-static propagation is caused by maximal tensile stress in a single braking cycle. The required remote tensile stress level (282.5 MPa) is achievable with the applied braking system.

The general conclusion based on the above analysis is that in the present combination of material with low resistance to fatigue crack growth and a braking system producing high tensile stresses a reliable monitoring of crack growth for fracture prevention is not possible. High susceptibility to stress concentration of fatigue crack initiation, i.e. a small number of cycles before crack appearance, indicates a need to avoid wheel fastening by chucks during machining procedure. The following actions have been recommended:

- change machining practices;
- change braking system; and
- perform a detailed analysis of wheel stress state.

Detailed analysis means the calculation of stress-state caused by mechanical loading and thermal shocks using finite element analysis, as well as the measurement of residual stresses by ultrasonic and magnetic methods.

4. FINAL REMARKS

It is clear from presented crack parameters and their application that three aspects have to be involved for the analysis of in-service structural failures: theoretical, numerical modelling and experimental. The scope of necessary knowledge and skill is large. In theoretical sense at least mechanics, mathematics, physics, material science, theory of elasticity, theory of plasticity, fracture mechanics are inevitable. Examples show that not only basic knowledge, but also skill and experience are required to solve complicated problems of stress and strain analysis, including simplifications and assumptions which must be introduced when exact solution is not possible. Finally, all obtained solutions and results must be verified by experiments, far from being simple, especially in the case of full scale testing. This is also to add the complex standard testing of cracked specimens and metallography, demanding in performance and result analysis.

Fracture mechanics and its parameters significantly contributed to improve structure integrity by crack significance and residual life assessment, but also in design, including materials properties improvement and development of new materials, /5/.

ACKNOWLEDGEMENTS

The authors gratefully acknowledge the financial support from the Serbian Ministry of Science under the project OI 144027 “Special topics in fracture mechanics of materials”.

REFERENCES

1. McEvily, A., *Metal Failures: Mechanisms, analysis, prevention*, ISBN 0-471-41436-0
2. Harper, R. F., *Code of Hammurabi*, University of Chicago Press, (1904).
3. Easterling, K. *Introduction to the Physical Metallurgy of Welding* 2nd edition. Butterworths, London, (1992).
4. Report 12-29-12.03/2000: *Report on causes of failure of mono block railroad wheel*, Faculty of Mechanical Engineering, Belgrade (2000) (in Serbian *Izveštaj o stručnom nalazu uzroka pucanja monoblok točka na putničkim kolima, ŽTP Beograd*)
5. Nichols, R. W., *Use of Fracture Mechanics as an Engineering Tool*, The 1984 ICF Honour Lecture. Sixth International Conference on Fracture, ICF 6, New Delhi, India (1983).

FRACTURE MECHANICS IN THE PLASTIC RANGE

Petar Agatonović

D-85244 Röhrmoos, Deutschland

P.Agatonovic@t-online.de

1. INTRODUCTION

Fracture mechanics plays today a substantial role in the area of the investigation and justification of structure integrity and in this respect it is very important instrument of the engineering technology. With the help of fracture mechanics the relationships between stress, crack size and material resistance to fracture can be calculated and evaluated for different relationships. Here, a critical value of any one of the quantities can be determined if the other two are known. For the purposes of the prediction and control, fracture mechanics provides the adequate mathematical relationships between these variables in the moment of failure. For example, if the design stress in the structure and the fracture toughness of the material are specified, one can determine the critical flaw size leading to the fracture. Compared to the traditional mode of integrity calculation that relates applied stresses, for example, to the yield strength of the material, this is fully new approach to the solution of the problem.

Within of the given structure the stresses are typically determined by the design, while the fracture toughness is a property of the material. All materials contain flaws which sizes and locations eventually can be determined by non-destructive testing method. Resistance to fracture is the basic property of material contains the flaw. Main goal of corresponding calculations in the design is the evaluation of the severity of the cracks, existing in the structural elements, regarding the possible fracture and failure. Procedure is based on principle that the failure appears when the applied load producing the growth of the detected crack is larger than the material resistance to crack extension.

Key industries for economy any state depend very much on safe operation of plant equipment and structures. General trend in the development and design methods is to allow plastic loading with the aim not only to use properly modern materials of higher strength, but also to extend the lifetime of the structure with the help of damage tolerance, based on fracture mechanics methods. In this way, on the basis of integrity assurance the large economic advantages can be achieved.

To this end, Linear Elastic Fracture Mechanics (LEFM) methods for the evaluation of crack effect at load levels below and near yield strength, have been almost exclusively used. They are adequate for some application but not effective and even dangerous in many other situations, because they do not guarantee results on the safe side. But, a sudden failure, as assumed in LEFM regime, is a rare event, although very spectacular since it occurred by fast unstable crack propagation, in a most dangerous way, More typical is the structural failure, accompanied by a plastic deformation and slow crack extension, known as 'ductile failure' or 'plastic collapse'. The plasticity effect in this case can be explained considering energy nature of the fracture. Moreover, since in such a case, a part of energy is spend for plastic deformation and the stress state is changed in

the plastically deformed section, an accurate evaluation of the conditions for the failure is only possible if the both contributions, elastic and plastic, are considered separately.

Therefore, significant errors can appear if plasticity effect is ignored, especially in the case of ductile materials, typical and recommended for heavy loaded structures.

As strong engineering tool for the evaluation of crack significance, fracture mechanics offers, if reasonably used, useful solutions with required reliability. To achieve applicable and reliable results the adequate knowledge and skill are necessary. Inadequate results in fracture mechanics applications are mainly the consequence of uncertain assumptions and inaccurate data, and not of the fracture mechanics methods. Fracture mechanics will not help without the necessary attention and information concerning loading, stress state, crack data and material characteristics.

2. BASIC APPROACHES

2.1. First developments

Looking back to the history of fracture mechanics development the impression dominates, that the elastic plastic treatment was from the beginning one of the main directions. The first theoretical treatment of the crack effect has been performed by English already in 1913. He defined the stresses at crack tip as reciprocal to the tip radius size, which therefore for infinite sharp cracks become also infinite. Therefore, every element with the crack, regardless how small crack is and how small is its loading must be broken. This could not be the satisfying solution. To solve this dilemma Griffith (1920) approached to the solution in the other way, connecting the fracture with the energy necessary to form crack. He assumed that the crack growth require some surface energy taken from strain energy of the local stresses release when the crack grows. The fracture occurs when the reduction in strain energy is sufficient to prevail material resistance. This is essentially a restatement of the first law of thermodynamics.

If the plate in Fig. 1 is under state of constant tension (displacement $\Delta = \text{const.}$), prerequisite for crack growth is:

$$-\left(\frac{\partial U}{\partial a}\right)_{\Delta} \geq \frac{dW}{da} \quad (1)$$

where U is the elastic energy (per thickness unit) contained in the plate in an account of its tension, and W is the work necessary for growth of a crack of initial length a . Based on this solution stress at crack tip becomes final value and no more depend on tip radius only (assuming that the crack is really sharp).

Irwin and Orowan improved this solution in 1948 considering plastic deformations in the vicinity of the crack tip. Irwin defined the term on the left of side of expression (1) as the energy release rate or crack growth force, G , necessary to extend the crack and the term on the right as the material characteristics called fracture toughness, R . According to the definition, the energy release rate (G) is the energy quantity per unit length along the crack contour that is disclosed from the elastic energy of the body and the loading system when the new crack surface is created. If the crack, under fixed grip conditions (constant displacement), extends for an increment da , the stored energy decreases by dU . For this incremental crack extension to occur, dU must be at least as large as dW (the work required to fracture the material and create new crack surface).

The Griffith model, based on energy, with some modifications, is still applied today.

If the driving force G is larger than material resistance R , the crack growth becomes unstable. If $G = R$ the crack growth can be stable or unstable, that depends on material and loading configuration, i.e. the way how G changes with the crack growth. This behaviour is described using so called resistance curve (R -curve, Fig. 2). The driving force is presented by a series of G versus crack length lines for various load levels. Most materials have the resistance curve R that grows depending on the crack size increase. In this case, up the loading increase at to the P_2 level nothing happens, because the material resistance is larger than the driving force. Only when the loading reaches P_3 level, the crack grows for a small amount in accordance to the resistance curve curvature. When the load reaches P_4 the unstable situation is established. Because the material resistance is not sufficient to prevent it, the crack continuously grows, frequently up to final fracture.

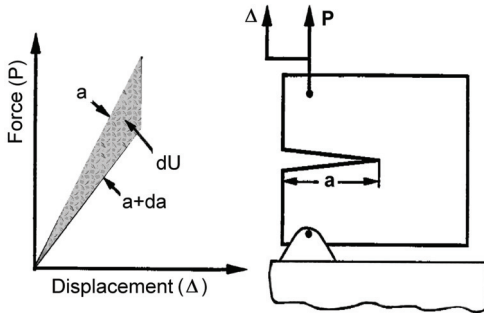


Figure 1. Condition for crack growth

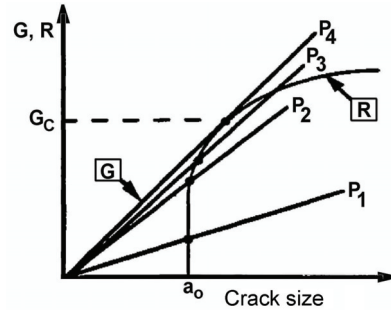


Figure 2. Scheme of (un)stable crack growth

In accordance to it one can write:

$$G = R \quad \text{and} \quad \frac{dG}{da} \leq \frac{dR}{da} \quad (2)$$

At the same time, Irwin showed that for these conditions the equivalent relationship exists between energy and stress intensity factor K for linear elastic materials.

$$G = \frac{K^2}{E'} \quad (3)$$

where $E' = E$ (Young's modulus) for plane stress and $E' = E/(1 - \nu^2)$ for plane strain; ν is Poisson's ratio. Anyhow, the stress intensity approach is commonly applied in LEFM.

2.2. Elastic-plastic features of the material

Inelastic strains appear in the material on the basis of dislocations. Inelastic deformations are of irreversible character. The rules based on the classic plasticity theory decompose total deformation to elastic and plastic parts with corresponding relationship for each of them. The total strain is the sum of its elastic and plastic components:

$$\varepsilon = \varepsilon_e + \varepsilon_p \quad (4)$$

Classic plasticity theory is based on following elements:

- A yield surface defining elastic limit of a material in a multiaxial stress state that defines if the body will react in elastic or plastic way (Fig. 3).
- A hardening rule that defines material behaviour during yielding, i.e. the way in which the resistance to the plastic strain grows together with inelastic strains.
- A flow rule defining the magnitude and direction of the plastic strain development.
- Elastic unloading criteria that models irreversible features of the body.

The conditions defining growth of plastic strain through the yielding surface, with the parameters k and α defining its size and position in stress space are shown in Fig. 3, so that variation of them allows different kinds of material behaviour to be described.

Accordingly, any change in inelastic strains depends not only on stress state but also on yield surface, which defines the state of the material and varies as the inelastic strain is generated. This point out to the fact that the development of inelastic strains is always accompanied by a change in the microstructure of the material, causing the change in the material response, including the fracture mechanics parameters.

There are many different criteria which define yield surface change, as the main conditions for the origin of inelastic strains, but for the purposes of the fracture mechanics the criteria von Mises and Tresca are generally used.

A Tresca or maximum shear stress criterion is based on the observation that the materials fracture in shear planes, what is suitable for the application to metals.

$$f(\sigma_{ij}, \varepsilon_p) = \max\{|\sigma_1 - \sigma_2|, |\sigma_2 - \sigma_3|, |\sigma_3 - \sigma_1|\} - \sigma_{YS}(\varepsilon_p) = 0 \quad (5)$$

Von Mises criteria, also named maximum distortion energy criteria, takes in consideration that the hydrostatic stresses in material doesn't affect yielding and doesn't participate in fracture, what is an important characteristics of materials, particularly metallic.

$$f(\sigma_{ij}, \varepsilon_p) = \sqrt{\frac{1}{2}[(\sigma_1 - \sigma_2)^2 + (\sigma_2 - \sigma_3)^2 + (\sigma_3 - \sigma_1)^2]} - \sigma_{YS}(\varepsilon_p) = 0 \quad (6)$$

In both criteria for $f(\sigma_{ij}, \varepsilon_p) < 0$ the material deforms elastically, for $f(\sigma_{ij}, \varepsilon_p) = 0$

plastically. The yield stress σ_{YS} may increase during plastic straining, as a function of a measure of total plastic strain ε_p . Experiments have shown that if a solid is plastically deformed, unloaded, and again re-loaded to produce next plastic strains, its resistance to plastic flow will be increased by strain hardening. So, if the inelastic deformation leads to the material hardening, than the yield surface increase or move in the stress space.

Obviously, it is possible to describe strain hardening in an appropriate way by definition how, depending on plastic strain, the yield surface changes its form and position. Previously described way of yield surface size increase is so called isotropic hardening, which however, is not adequate for the application in case of cyclic loading, because it does not account for the Bauschinger effect; that is the hardening by the loading in one direction has the consequence of softening if loaded in opposite direction. In this case the application of so-called kinematic hardening is more appropriate, by which the yield surface moves in load direction without size change.

However, material behaviour in the case of cyclic loading is much more complex and under elevated temperature further complicated by time dependent inelastic strain (creep).

Let us look back on the flow rule. If the stress state is on the yield surface, and stress slightly increases, this rule defines direction and size for the development of plastic strain increment. As already stated this increment only appears for loading increase. Since the plastic strain increment is dependent on total stress and not on stress increment. this theory is known as incremental theory of plasticity or flow theory. During loading the stress follows non-linear line (Fig. 4), and in case of unloading the strains are elastic.

For the purposes of fracture mechanics the theory of non-linear elastic deformation (deformation theory), by which loading and unloading follows the same curve, is

frequently used. Although here is not plastic material considered, if the loading is proportional, the incremental and deformation theories produce the same results.

2.3. Micro mechanisms of fracture

For the application of the fracture mechanics in general, and particularly for elastic-plastic fracture mechanics, it is important to establish the difference between brittle and ductile fractures. Modes of fracture in steel and in its welded joint are transgranular cleavage, microvoid coalescence and intergranular fracture, or their combinations.

Cleavage is rapid, unstable fracture usually of brittle materials, and ductile tearing (microvoid coalescence) occurs in a slow, stable manner. Intergranular cracking can be ductile or brittle. It is usually associated with a corrosive environment, grain boundary segregation, or both. The fracture toughness parameters depend on fracture mechanisms.

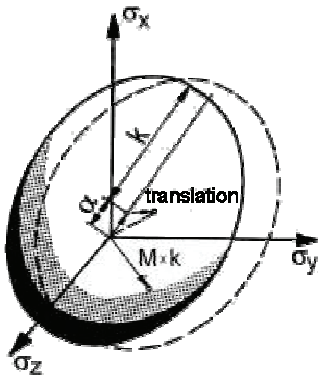


Figure 3. Yield surface

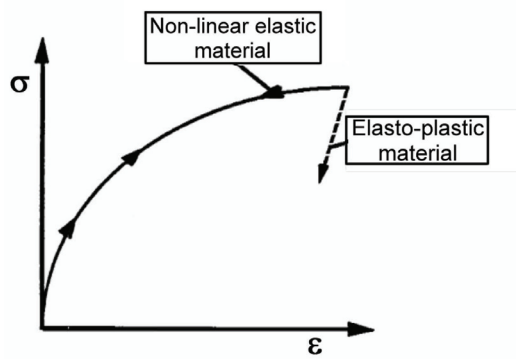


Figure 4. Elastic-plastic and non-linear elastic material

Brittle fracture takes place by rapid crack extension and negligible plastic deformation, with even, flat fracture surfaces. For most brittle crystalline materials, crack propagation corresponds to the successive breaking of atomistic bonds along well defined crystallographic (or cleavage) planes (in case BCC iron it is 100). For fracture to occur, the cohesive strength of material must be prevailed and the tearing occurred when the local stress is high enough to drive micro crack to grow locally in microstructure, at carbides or inclusions). Transgranular fracture means that the crack grows through the grains, changed the direction from grain to grain, in dependence of the atomic orientation in particular grains. It is logical that, when the crack reaches the boundary of the new grain, it searches new direction of the lowest resistance for further growth.

The places in the microstructure where the tearing occurs depend on the alloy and heat treatment. In mild steels cleavage usually initiates at grain boundary carbides. In quenched and tempered steels critical places are spherical carbide or inclusion. Susceptibility to cleavage fracture is enhanced by almost any factor that increases the yield strength, such as low temperature, a triaxial stress state, radiation damage, high strain rate, and strain aging. In ferritic steels, cleavage occurred at low temperature, with temperature increases the fracture become ductile, based on microvoid coalescence.

The growth of the ductile crack is accompanied with significant plastic deformation and the ductile fracture reveals characteristic coarse fracture surface. The mechanism of crack growth is shown in Fig. 5. At the beginning plastic deformations cause formation of small micro cavities in material at inclusions. In the next process development the

cavities grow and they coalesce. Final fracture took place when remain material between the cavities breaks (tearing): the critical deformation necessary provokes the cavities coalescence formed around the inclusions. The microvoid coalescence fracture surface has a fibrous appearance based on tearing between the cavities. Figure 6 compares the appearances of two fracture types under the scanning electron microscope.

3. ELASTIC-PLASTIC FRACTURE MECHANICS (EPFM)

In the narrower sense, linear elastic fracture mechanics is applicable only for materials that break in the fully brittle manner. However, almost all structural components are made from materials of at least minimum ductility.

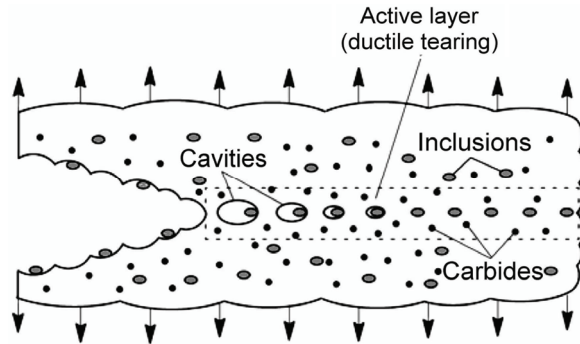


Figure 5: Phenomenology of ductile fracture

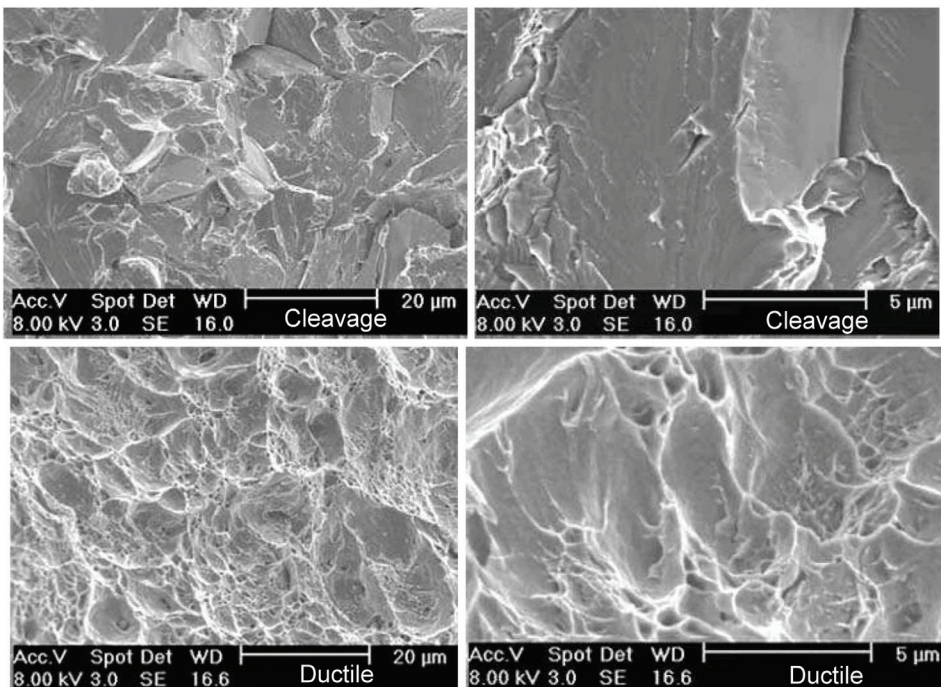


Figure 6: Fracture appearance (up fracture by cleavage; down by microvoid coalescence)

Treatment of the plasticity by EPFM falls into two main categories:

- Simple correction of the LEFM theory under the conditions of small scale yielding on the crack tip where the plastic volume is contained up to the fracture in elastic material.

- Application of material and loading parameters that allow for nonlinear behaviour.

Simple correction of stress intensity factor based on so-called plastic zone at crack tip has been proposed by Irwin. This idea was further developed from many authors. First real elastic-plastic parameter, crack opening displacement, has been proposed by Wells in 1961, and the J -integral is proposed by Rice few years latter. Both parameters are in the relationship; about this will be told more in the subsequent discussions.

Based on the formula for the calculation of stresses at the crack tip

$$\begin{bmatrix} \sigma_x \\ \sigma_y \\ \tau_{xy} \end{bmatrix} = K_{\theta=0} \frac{\cos \frac{\theta}{2}}{\sqrt{2\pi r}} \begin{bmatrix} 1 - \sin \frac{\theta}{2} \sin 3\frac{\theta}{2} \\ 1 + \sin \frac{\theta}{2} \sin 3\frac{\theta}{2} \\ \sin \frac{\theta}{2} \sin 3\frac{\theta}{2} \end{bmatrix} + \text{“negligible” terms of higher order} \quad (7)$$

with
$$K_{\theta=0} = \sigma \sqrt{\pi a} \quad (7a)$$

it is easy to establish that just at the tip $1/\sqrt{r}$ singularity exists and this relationship predicts infinite stresses at the crack tip, which no one material is able to resist.

Accordingly, analysis based on $\sigma = f(K, r)$ with the aim to compare with the strength properties of the material (to evaluate safety margin) does have no sense. Based on this, it is decided that K is „better“ parameter and fracture mechanics is born.

This was possible, because the structural materials deform plastically above the yield stress and this limits, through the stress redistribution and crack blunting, this kind of development of the maximal stresses. However, this feature of structural materials is not considered by elastic analysis, which becomes inadequate. Even worse, stress redistribution leads to stress increase on remain part ahead the crack tip and raised values of the stress intensity factor, so that the solution goes to the unsafe side.

3.1. Limits of LEFM (crack tip plasticity)

To avoid described situation, Irwin takes the increase of the effective K_I in consideration through the increase of crack size against its real values

$$K_{eff} = Y\sigma \sqrt{\pi a_{eff}} \quad (8)$$

Effective crack length a_{eff} is obtained adding plastic zone size r_y to the actual length

$$a_{eff} = a + r_y \quad (9)$$

The correction is calculated based on stress in the crack plane ($\theta=0$):

$$\sigma_{yy} = \frac{K_I}{\sqrt{2\pi r}} \quad (10)$$

For plane stress conditions ($\sigma_{zz} = 0$), material yields when $\sigma_{yy} = \sigma_{YS}$, (yield strength for uniaxial tension). Part in which materials stress field does not harden is cut, as shown in Fig. 7. After substitution in (10) it follows

$$r_y = \frac{1}{2\pi} \left(\frac{K_{eff}}{\sigma_{YS}} \right)^2 \quad (11)$$

Similarly, the correction for plane strain condition will produce lower value:

$$r_y = \frac{1}{6\pi} \left(\frac{K_{eff}}{\sigma_{YS}} \right)^2 \quad (12)$$

Calculation of K_{eff} is iterative process that, however, very fast leads to the end values. The correction is in reality also dependent on material hardening (n) and geometry.

In fact, calculation process in LEFM is the same, independent on plane stress or strain conditions (or between), but the toughness values (that must be evaluated experimentally) are higher if the conditions are not plane strain. This increase is accompanied with sometimes large errors, and it is better to use the K_{Ic} values. Methods of LEFM meet the limits if the stress is higher than the half of yield strength. It should be recognize that the calculation results are more and more on the unsafe side.

Corresponding relationships and mechanisms can be explained graphically in a simple way using stress-strain diagram for specimen with the crack (Fig. 8). It is not difficult to note that because of additional plastic deformations the amount of energy spent is larger. Physical mechanisms of energy dissipation are based on plastic deformation in the vicinity of crack tip for metals, micro cracks for ceramics, fibre pull-out for composites and even on the basis of material heating and/or on all that. For that, convincing energy ends to be only crack surface energy $G = dWdA$ as in the case of LEFM conditions. In plastic deformations, as known, not only crack tip but also the volume near to the tip or even near to the all net section take part, and this must be considered ($dWdV$).

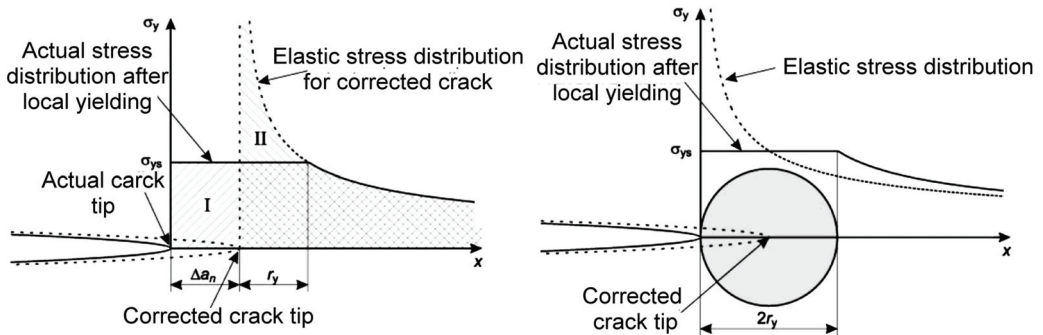


Figure 7. Irwin's correction for the plastic zone

As already accentuated, introduced energy is not only spent on crack growth and fracture. Total energy after loading to the point (P, Fig. 8) corresponds to the area under the curved (OPS). The energy amount $(dWdV)_p$ spent for the plastic deformation become visible only after unloading, in which the remain recoverable part of energy is released ($dWdV$), that is lower than the total energy. It corresponds to the triangle UPS. It is to note that unloading path slope of crack extension differs from the initial one. This appears as the consequence of reduced stiffness due to the net section area reduction. At failure, assumed in point F, only the recoverable energy is available and, therefore, relevant as the measure of the failure resistance. It is directly related to the J -integral and G . However, this energy cannot be measured in this way, because the specimen is broken.

In LEFM conditions energy release rate G is proportional to K , as given in Eq. (3). This is not valid for ductile materials, and in EPFM other parameters are necessary.

There are two main development branches in EPFM: crack tip opening displacement (CTOD, δ), popular in Great Britain and Europe, and J -integral, from the beginning

mostly applied in USA. It is interesting that these two parameters are related in definite functional way, so that both could be applied, and proper application must lead to the same results. This, however, does not mean that the both procedures are the same.

3.2. *J* - integral

The stress-strain relationships in the theory of plasticity are much more complex than that for elastic theory. For example, when a material deforms elastically, it is possible based on current strains to determine current stresses and vice-versa. In case of plasticity this is not possible, because the material response to plastic deformations is history dependent. For that, the same combination of deformations can include different stress states. Based on this, it is not possible to achieve analytical solution for the crack tip stress field, similar to the solution for linear elastic materials. It is necessary to use the approximate solutions, like for non-linear elastic material or for deformation theory (Chapter 2.2.). Given solution certainly does not have general character, especially for the cases of 3-dimensional geometry, but there are many situations in which non-linear elastic material model supply solid approximation for real material behaviour.

Rice utilised this approximation to derive the *J* path independent integral (Fig. 9), a parameter that describes the conditions near the crack tip in a proper way.

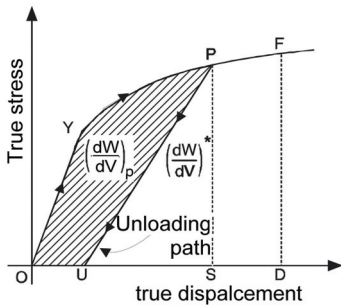


Figure 8. Energy for crack growth

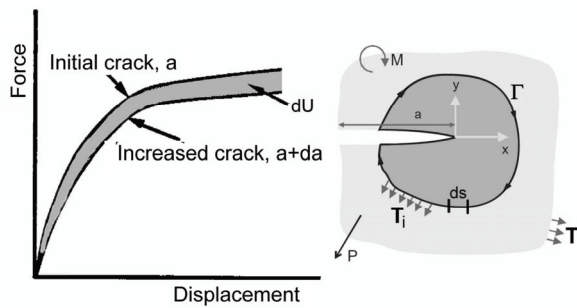


Figure 9. Elements for *J* - integral evaluation

In fact, class of path independent integrals was earlier known, but not applied to the solution of fracture mechanics problems. The *J* - integral value is obtained by integrating the following expression along an arbitrary closed path (Fig. 9) around the tip of a crack

$$J = \int_{\Gamma} \left(W dy - T \frac{\partial u}{\partial x} ds \right) \quad (13)$$

where Γ represents the path of integration (it is important to observe that within Γ there is no singularity), and W is the strain energy density. Furthermore, T is the traction vector, u is the displacement vector and ds increment along the path contour. For non-linear elastic materials Rice showed that the value of *J* is independent of the integration path as long as the contour encloses the crack tip.

J represents energy release rate of nominal potential energy depending on crack growth (for thickness unit of crack contour) for non-linear elastic body. *J* can also be imagined as the energy that flows into crack tip.

$$J = - \left(\frac{\partial U}{\partial a} \right)_{\Delta} \quad (14)$$

where U is the deformation energy for thickness unit, and Δ deformation in the direction of loading. Under LEFM conditions J become identical with energy release rate ($J = G$).

Based on this, J becomes parameter describing stress intensity similar to K in LEFM. Hutchinson and Rice and Rosengren independently derived a crack tip stress and strain solution for nonlinear elastic materials, which became known as the HRR solution. The HRR solution was derived for materials with power law stress-strain relationship

$$\frac{\varepsilon}{\varepsilon_o} = \alpha \left(\frac{\sigma}{\sigma_o} \right)^n \quad (15)$$

where σ_o is a reference value of stress (usually), $\varepsilon_o = \sigma_o/E$, and α and n are material constants. The HRR stress and strain fields near the tip of the crack are given by

$$\sigma_{ij} = \sigma_o \left(\frac{EJ}{\alpha \sigma_o^2 I_n r} \right)^{1/(n+1)} g_{ij}(n, \theta) \quad (16)$$

$$\varepsilon_{ij} = \alpha \frac{\sigma_o}{E} \left(\frac{EJ}{\alpha \sigma_o^2 I_n r} \right)^{n/(n+1)} h_{ij}(n, \theta) \quad (17)$$

where I_n is a dimensionless constant that depends on n , and g_{ij} and h_{ij} are dimensionless functions of n and θ . These parameters also depend on stress state (plane stress or plane strain). For a linear elastic material, $n = 1$ and stress varies as J/r ($= G/r$ or K/\sqrt{r}) which is consistent with the elastic solution for K .

As with the stress intensity factor K for linear elastic materials, J completely characterizes the crack tip stresses and strains in nonlinear elastic materials. Thus J is an adequate fracture mechanics parameter for elastic-plastic materials, as long as the nonlinear elastic assumption gives a reasonable approximation of real material behaviour.

Real relationships are, as shown in Fig. 10, somewhat more complex. Part (a) illustrates the state in case of small scale yielding that corresponds to LEFM regime. The region moderately close to the crack tip, where the crack tip stress and strain fields are in conformance with the calculation with K , is the region controlled by K and with slope that corresponds to the solution based on $1/\sqrt{r}$ dependence. Somewhat closer to the crack tip, in the plastic zone, is the J controlled region where the slope of the change corresponds to $1/(n+1)$. The small area very close to the crack tip is the large strain region where the HRR solution is no longer valid. A log-log plot has been selected to show these relationships more clear. It should not forget, that in the solution for K (7) there are other terms of high order neglected that outside the K controlled region gain in the importance. However, in case of small scale yielding crack can be characterised with K or J , because of analytical relationship between this two parameters in form

$$J = \frac{K^2}{E} \quad (18)$$

With the loading increase the K controlled region gradually disappears (b in Fig. 10), but there is still remain the region in which the HRR solution is valid. This also means that the application of K is no more adequate and the situation at the crack tip can be only characterised by J . However, the evaluation of K values based on

$$K_{eff} = \sqrt{JE'} \quad (19)$$

is possible, even though the effective K value does not have any connection with the stress distribution around crack tip shown by broken line in Fig. 10 b).

In addition, region on the tip, not controlled by the solution is becoming much larger, HRR solution is no more valid in this area due to the crack blunting. It is favourable that the stresses in the large strain region are lower than predicted by the HRR singularity.

Under large scale yielding conditions, Fig. 10c, the calculations both with K and J are no more valid. If the material is sufficiently ductile to experience this state before fracture, than the stresses at the tip are significantly favourable, not only because of lower values (than predicted by both J and K theory) but also because of a loss in triaxiality.

The sizes of the J and K controlled regions depend on the size and geometry of the structure with the crack. Based on larger dimensions these regions in case of real structures exist considerable longer, and because of this for the evaluation of material characteristics the specimen must satisfy corresponding conditions for its validity to the real structures be guaranteed. For example, for K_{Ic} evaluation different standards require that the specimen dimensions fulfil the following requirement:

$$B, b \geq 2.5 \left(\frac{K_{Ic}}{\sigma_{YC}} \right)^2 \quad (20)$$

where B is the specimen thickness and b the size of the uncracked ligament. Comparison with the plastic zone correction shows that these should be no more than 1/50 of specimen characteristic dimensions.

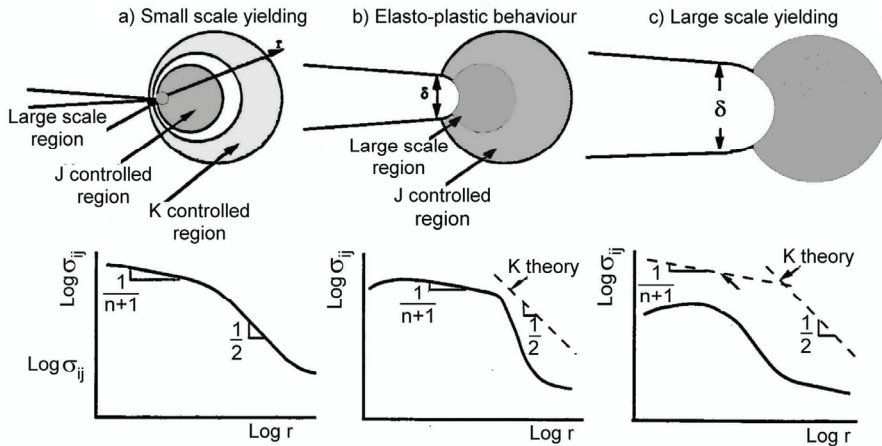


Figure 10: Scheme of the effect of plastic deformation on the crack tip stress field

For J_{Ic} evaluation requirements concerning the specimen size are different:

$$B, b \geq \frac{25J}{\sigma_Y} \quad (21)$$

where σ_Y is the flow stress, defined as the average between the yield and tensile strengths.

For mild steels with $\sigma_Y = 350$ MPa, $K_{Ic} = 250$ MPa \sqrt{m} and $E = 210$ GPa according this requirement, specimen size for K_{Ic} evaluation should be $B, b > 1.28$ m

For J_{Ic} evaluation, however sufficient sizes of the specimen are:

$$b > 25 \frac{J_{Ic}}{\sigma_Y} = 25 \frac{K_{Ic}}{E} \frac{(1-\nu^2)}{\sigma_Y} \quad b > 0.02 \text{ m}$$

It can be seen from this comparison that the experiment for J_{Ic} evaluation is simpler. Also it is clear that the requirement for K_{Ic} cannot absolutely be fulfilled, even when the structure is in LEFM regime. This difference between test specimen and real structure is shown in Fig. 11. Small laboratory specimen and a large structure are loaded to the same applied J . The plastic zone in the small specimen is too large to be K controlled, but the plastic zone for the structure is small compared to structural dimensions. Thus, the structure has both K and J controlled regions, but the specimen has only a J controlled region. Clear, in situation like this, it is possible to measure a J_{Ic} value on the small specimen, convert this value to an equivalent K_{Ic} using Eq. (18), and apply this K_{Ic} to the structure ignoring, however, the fact that further from the crack tip, the stress fields are different because the stresses in the small specimen are influenced by its small size.

In spite of the situation like this, one can not expect that the parameters obtained by the specimen of the full ligament in plastic regime can be easily transferred to the large structure when plastic zone is limited to the relatively small area around the crack tip.

Furthermore, the name „stress intensity factor“ is in some way inadequate, because it has dimensions, and these are, at the same time, without definite physical sense:

$$Dim[K] = \frac{N}{m^{3/2}}$$

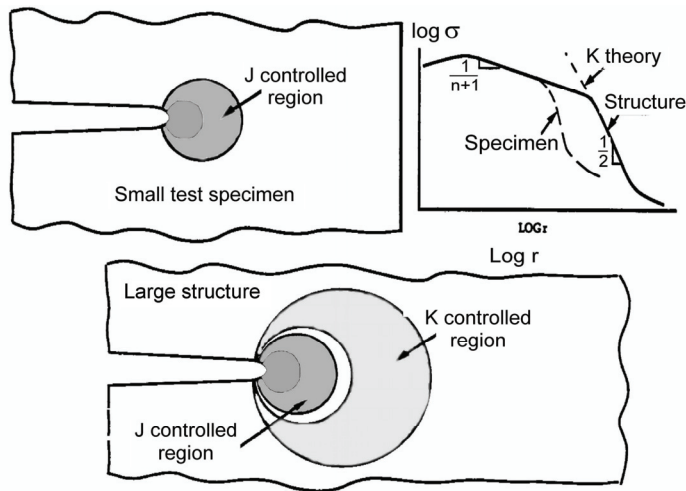


Figure 11: Comparison of J and K controlled areas for test specimen and large structure

Even the squaring of this relationship

$$Dim[K^2] = \frac{N^2}{m^3}$$

do not lead to the successful solution. Only after division with E-modulus (Eq. 18)

$$Dim\left[\frac{K^2}{E} = J = G\right] = \frac{N^2}{m^3} \cdot \frac{m^2}{N} = \frac{N \cdot m}{m^2} = \left[\frac{Energy}{Area}\right]$$

the physical sense of the notion „specific energy“ is in accordance with the theories of fracture appearance. Previous relationship could be further cleared, if considered that one of K -parameters after division by E gives the corresponding relative deformation $\varepsilon(K_\varepsilon)$.

$$J = \frac{K^2}{E} = K \cdot \frac{K}{E} = K_\sigma \cdot K_\varepsilon \quad (22)$$

On the basis of total strains can this proposed relationship, achieved based on elastic solution, be generalised by including the plastic deformation too

$$\varepsilon = \varepsilon_e + \varepsilon_{pl} \quad (23)$$

It is obvious that any solution for the conditions at the crack tip must include, behind the solution for stress state, the strain state too, as the J - integral does.

Although the standards for the material testing based on J -integral exist, at this point will be useful, showing the way how to treat experimental results for the evaluation of J -integral, to be familiarized with the these basic characteristics of the material.

Results of testing specimens are critical value of J_{Ic} –integral and J - R curve, defined as the J vs. crack extension, Δa , over defined range of validity. The integral values can, dependent on material, considerable exceed the critical values (J_{Ic}). During the test measured are the pairs of J and Δa values and plotted in the diagram. The results are sensitive to the initial crack size a_0 . To ensure that the initial crack length is accurate, the standard calls for a_0 to be adjusted by fitting a third order polynomial to the J vs. Δa data:

$$a = a_{0Q} + \frac{J}{2\sigma_Y} + BJ^2 + CJ^3$$

and extracting an adjusted new calculated a_0 , called a_{0Q} . If the new value differs from the measured by more than $0.01W$ the data are invalid. If not, the new diagram should be designed where all points are corrected by new values $\Delta a = a_{0Q} - a$ (Fig. 12). Even with no visible physical crack growth, the crack will appear to have grown due to crack tip blunting. To account for this, the "blunting line" is drawn given by

$$J = 2\sigma_Y \Delta a$$

Then the exclusion lines are defined parallel to the blunting line, at 0.15 and 1.5 mm offset. Critical value is evaluated ($J_Q = J_{Ic}$, if the requirements are met), however, in cut of the parallel line shifted at the 0.2 mm offset with results line. If all test conditions are met the data between limits (1.5 mm) should be interpolated by exponential curve

$$J = C_1 \Delta a^{C_2}$$

Slope that defines the increase of resistance above J_Q depends on many factors, considered later on. Although this increase can be used the safest application is based on critical value that defines initiation of real crack growth.

Fracture mechanics based on J - integral application certainly has advantages in relationship to K . Moreover, this is also true concerning fatigue crack growth analysis, taking in consideration that between the both parameters the direct dependence in linear range exists. However, this means, at the same time, that the introduction of ΔJ at the place of ΔK does not have strong reasons. Even though is well known that ΔJ application can extend the range of linear log-log dependence out of ΔK (Fig. 13), regime of high crack growth rates do not have large importance for the calculation of total number of cycles to the fracture or the contribution within of the total life. Moreover, taking in consideration that J is based on deformation theory that does not consider cyclic loading (unloading), the main question is if this parameter is „better“ than K . In the same time, the evaluation of small cracks (with high stresses) is not sufficient examined in this respect.

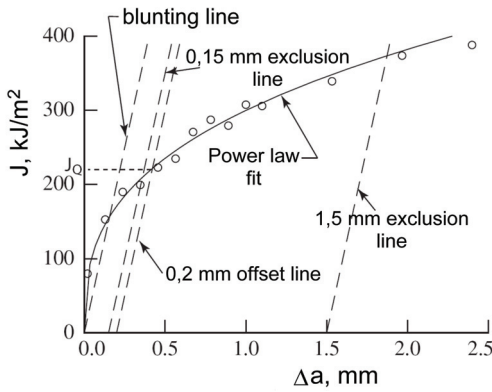


Figure 12. J - R curve evaluation based on test results

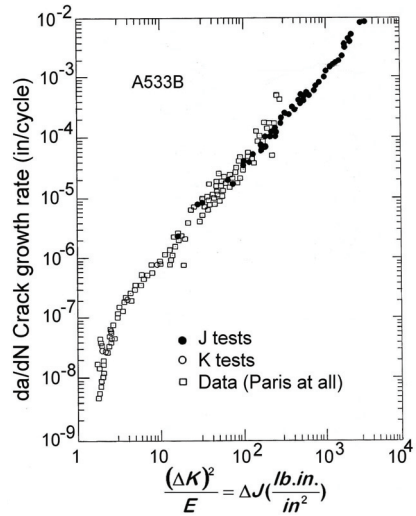


Figure 13. Crack growth rate vs. ΔJ

3.3. Crack opening displacement

In the late 1950s, Wells applied Irwin’s stress intensity concept to measure the fracture resistance of medium strength structural steels, and found that they materials exhibited a high degree of plastic deformation prior to fracture. This was good news for designers, indicating high toughness in these steels, but was bad news for fracture mechanics application because it meant that LEFM is not applicable to typical structural steels.

Wells noticed on tested specimens that the crack faces open strongly prior to fracture so that this can be accurately measured. Based on these observations he proposed in 1961 crack opening displacement as a fracture toughness criteria. Crack opening displacement (COD) was defined on its tip, Fig. 14. Today is usual to measure crack opening at surfaces positioned at 90° at crack tip (CTOD). Both measurements give similar results.

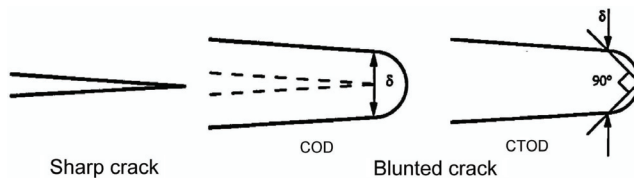


Figure 14: Crack opening displacement (COD) and crack tip opening displacement (CTOD)

To verify the concept Wells showed that under the condition of plane stress and small scale yielding between K_I and CTOD (δ) analytical dependence exists in form

$$\delta = \frac{K_I^2}{\sigma_{YS} E} \tag{24}$$

Although this parameter was intended for the application outside LEFM, it was certainly useful to found it in accordance with the valid facture mechanics relationships. Similarly the relationship between J and CTOD can also be established in form:

$$J = \sigma_{YS} \delta$$

Based on HRR solution the same relationship can be written in slightly different form, but so that is not limited to LEFM range

$$J = \frac{\sigma_o \delta}{d_n} \quad (25)$$

where d_n is dimensionless constant that depends on material characteristics (ε_o , ν , α) and stress state (plane stress or plane strain). In fact d_n depends strong on n and weak on σ_o/ε . For plane strain is $d_n \approx 0.3 - 0.65$ and for plane stress: $d_n \approx 0.5 - 1.07$ (max for $n \rightarrow \infty$). Because the structural steels of medium strength usually have n in the range 8 to 12, the d_n value for such materials under plane strain conditions is approximately 0.5.

Similar experiments (K_{Ic} , K_{R} , and J_{Ic} , $da/\Delta N$) serve for the evaluation of material fracture resistance, but test with CTOD have found application mainly in offshore structures. Calculation based on CTOD is carried out in the same way as in the case of J -integral. So calculated design curve is recommended (Fig. 15) in standards.

The application of this curve is appropriate for ductile fracture with large deformation. In case of brittle materials the measurements are less accurate, and the application is inconvenient. One of the most stimulating reasons of CTOD application is the expectation that for heterogeneous materials, like welded joints, this can be more usable.

However, CTOD procedure in case of under matched welded structures predicts significantly lower values for crack driving force as in reality, and for overmatching cases the use of base metal tensile properties will produce over-conservative predictions. Especially for the case of under matching if $\varepsilon_f/\varepsilon_Y > 0.5$ the application should be avoided.

3.4. Analysis of tearing instability

Until now the use of different parameters of fracture has been concentrated on crack initiation at critical values of J , K or $CTOD$. However, the ductile materials possess the growing resistance curve in form $(J, K, CTOD) = f(\Delta a)$ that indicates the fracture must not appear at initiation or when the critical values as J_{Ic} has been achieved. Depending on the geometry and loading, slow, stable crack growth is often observed prior to fracture instability. The analysis of crack growth up to the instability point is important for calculation of the maximum load carrying capacity of fractured structure or component and understanding of crack tearing is important in practice. Nevertheless, the attention should be given to the fact that for some materials, as the aluminium alloys, the resistance curve is almost with no increase.

Figure 16 shows that instable crack growth appears when the driving force change rate, expressed by the slope which depends on loading and crack growth, exceeds the increase in material resistance. However, conditions in this respect depend on the way how a structure is loaded. When the load is fixed, the crack driving force increases with crack extension. Because of this, the load controlled structure is more prone to the instability. If the deformation of the structure is constant, the crack driving force falls with the crack growth, so that the probability of stable crack growth is significantly higher. In reality many structures are under conditions somewhere between. To make this more clearly these two extremes are compared in Fig. 17.

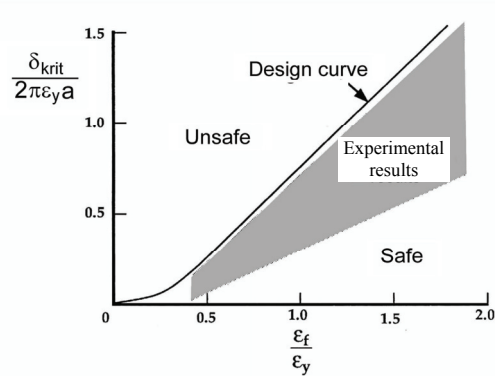


Figure 15. CTOD Design curve

Paris and Hutchinson have developed a detailed instability analysis that takes account of structural compliance. Their approach has been incorporated into the EPRI elastic-plastic fracture handbook. Dimensionless tearing modules are defined for the calculation slopes of the crack driving force and material resistance, in the form:

$$T_{JR} = \frac{E}{\sigma_o^2} \frac{dJ_R}{da} \quad (26)$$

where J_R is the J value according to the resistance curve. Value of applied T depends on partial derivative for J at the place of nominal displacement:

$$T_j = \frac{E}{\sigma_o^2} \left(\frac{\partial J}{\partial a} \right)_{\Delta T} \quad (27)$$

The conditions for stable and unstable crack extension are as follows:

$$T_j < T_{JR} \quad (\text{stable})$$

$$T_j \geq T_{JR} \quad (\text{unstable})$$

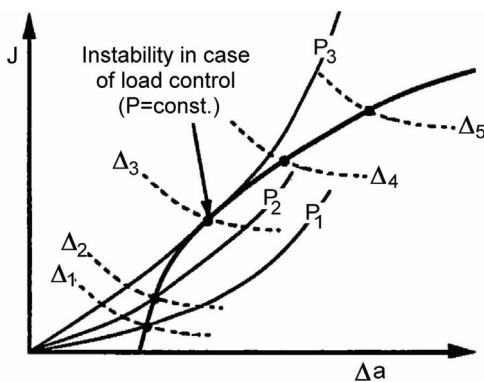


Figure 16. Evaluation of growth instability

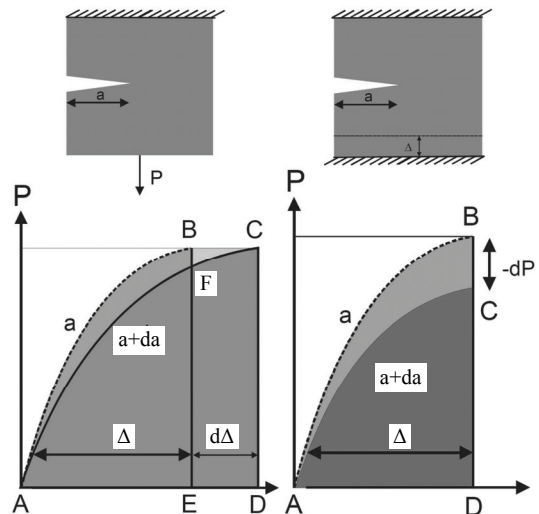


Figure 17: Comparison of tearing instability for load or displacement control

4. SIZE AND THICKNESS INFLUENCE

It is very important for successful calculation and results evaluation to be guaranteed that the material resistance curve relative to the crack growth is independent on geometry. For that it is necessary to know the limits for the parameters and used method, accurately define its application boundaries and, if necessary, to correct the method for parameters estimation in order to extend application limits and assure the use of existing methods.

Application of J-integral has been significantly extended in last years. However, some uncertainties still exist that must be eliminated for further extension of application. Most important is to consider the constraint effects when evaluate the parameters of the crack growth for material. This is the preposition for successful application of described methods also in case of 3-dimesional cracks and structures of different thickness.

When the structure or specimen containing a crack is exposed to increasing load, they pass through different regimes and different methods could be adequately applied. The conditions of small scale yielding (SSY) are established for the crack tip plastic zone infinitely small compared to other dimensions and LEFM is applicable since the crack is embedded in an elastic volume. However, by the further load level increase the plastic deformations cause the reduction of constraint at the crack tip. In the moment when the global and local deformation interact, the crack tip stresses and strains no more increase in proportion to one another and in dependence on only single parameter. At these large deformations, equivalence of single parameter characterisation of fracture driving force (i.e. K , J and δ) does not ensure identical stresses and strains distribution at crack tip for different cracked geometries. The general term “size effect“ includes complex geometry and loading effects on the stress state at crack tip and material fracture toughness, when fracture can appear at different load level. In essence this effect is based on size influence to the relationships between macroscopic fracture parameters and the crack driving force at micro scale. Early fracture mechanics research addressed size effect to establish size and deformation limits below which the geometry independence of fracture toughness is assured. If the corresponding requirements are fulfilled, a single parameter is sufficient for unique description of the stresses and strains state near crack tip. In this range the LEFM application with the simple plasticity correction of crack size is appropriate. In general this analysis produces over conservative results. However, increase in fracture resistance in dependence on geometry could not be taken into account in this way and other methods based on application of two parameters become necessary.

The breakthrough in this respect has come through the new methods and increased computing power, which has enabled crack tip stress distributions to be examined in detail and without simplifications concerning material non-linear behaviour. The series of different procedures had been developed, directed to the consideration of parameter variations in dependence on constraint and difference in geometry. Decisions in this respect are also supported with experimental results that showed large differences in R -curves in dependence on geometry and loading conditions. Idea that the ductile tearing resistance could be described by only one representative curve was given up.

The need for a quantification of the constraint and local stress states effect on ductile fracture become evident, making unavoidable an additional parameter for fracture resistance. The term “constraint effect” in fracture mechanics commonly designates the influence on the crack-tip stress field imposed by the loading configuration and geometry. The main cause of constraint is the degree h of crack tip stress triaxiality, that is the size

of the mean volume (hydrostatic) stress σ_m relative to the resulting von Mises effective stress, σ_e , i.e. $h = \sigma_m/\sigma_e$. According to plastic theory laws, especially in case of metals, the mean „hydrostatic“ stress of the system will never cause yield, no matter how large the stress. Therefore, the size of plastic increments depends only on components of the so-called deviatoric stress, and in the case $h = 1$ plastic deformation will not occur.

Complexity of the conditions for volume cracks shows the results of FEM-calculation for surface crack in Fig. 18. Near the surface the yielding is free and h takes minimal values. However, the value of the constraint parameter h increase inside the crack, what is not difficult to imagine, and in case of cylinder under pressure the maximal values is even between surface and depth (ligament) of the crack. The consequences of this are shown in Fig. 19. In spite of load increase the values of J - integral at the surface are on account of plasticity in decrease and only after crossing into full plasticity increase arise that, however, fall back compared to the crack depth position. Obviously, the application of elastic solution (K) is not sufficient to evaluate relationship along crack contour.

High degree of constraint leads to the faster fracture. Because the energy introduced in system (the value is measured by J - integral) is dissipated based on plastic deformation in smaller extent, and therefore stay available for fracture initiation. It is obvious that the constraint is significant parameter for fracture mechanics to establish the safe fracture criteria. But, important problem exist, because of the constraint conditions for specimens, which are small, compared to the real structure, so that the data transfer could be unsafe.

The constraint effect is observed from early beginning of the fracture mechanics development. Limitation to the 2-dimensional through crack showed the consequences already by the selection of specimens. However, former only two extreme cases, plane stress and plane strain has been shown to be insufficient.

Figure 20 shows that, due to different conditions on the external surfaces and inside of the specimen the size of the plastic zones is different, and material resistance at specimen surfaces is higher than inside it. In Fig. 21 various forms of fracture surfaces for 2-dimensional specimens are shown. An initially straight front bends at ends with the growth before the instable fracture onset. Interior to the plate, there prevails a high constraint effect leading to crack growth profile similar to the beginning. At specimen edges there is no constraint and the energy is more dissipated in distortion.

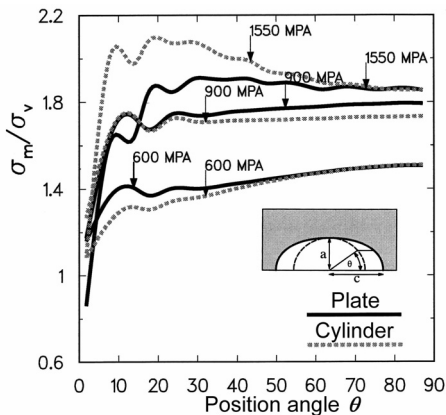


Figure 18. Degree of constraint along crack profile (comparison of plate and cylinder)

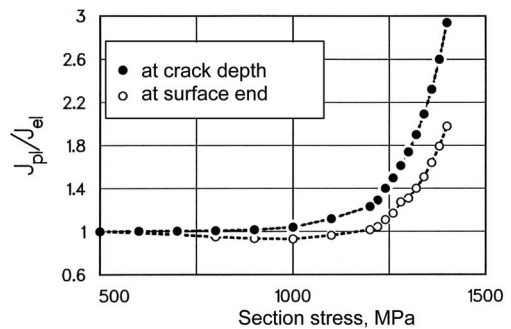


Figure 19. J - integral development for situations in Fig. 18

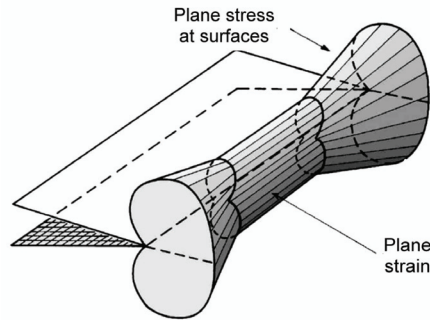


Figure 20: Through thickness plastic zone in a plate

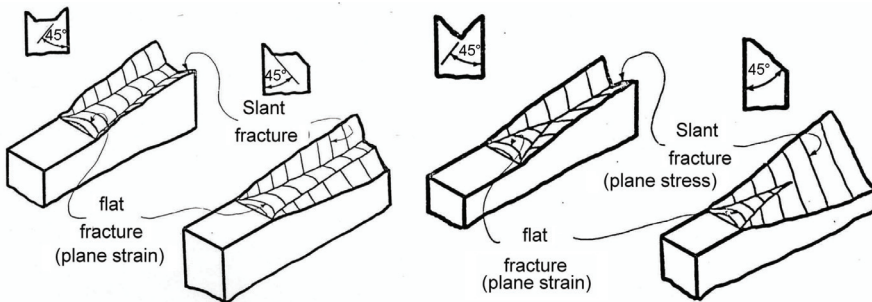


Figure 21: Typical forms of the fracture surface for plate or thin wall structure

The crack surface is observed to rotate in this region so as to make an angle of approximately 45° with load direction. These inclined portions of the crack surface near the plate surfaces are known as "shear lips". The proportions of each type of crack surface depend on material properties (yield strength, strain hardening exponent), specimen geometry (crack length, plate thickness) and loading. The proportion of the fracture surface associated with slant fracture or shear lips increases with decreasing plate thickness and in very thin plates in which the shear lips merge into each other the fracture surface completely rotate to 45° . The initial straight fracture line decreases with increase in load level, showing the dependence of the behaviour on load level.

The postulates that "plane strain condition" are in all cases on the safe side cannot be fully accepted, as it refers only to "out-of-plane" constraint which are normal to the crack growth direction, and does not allow for explaining the effects of varying "in-plane" constraint in the direction of crack growth. Anyway, specimens for fracture toughness measurement the corresponding requirements in both directions must be fulfilled.

Although, the constraint problem is connected to the stress state in space and to the effect of hydrostatic stresses, the first attempts to take this phenomenon into account were based on the solutions for K and J . As known the solution based on K is realised by neglecting higher terms in the solution, and the solution for J with the assumption for non-linear elastic material. Based on this, the parameters T -stress and Q -factor has been involved to consider the neglected parts of the solution and so ignored effects of geometry and load level. Application of these parameters have demonstrated that scatter of experimental data can be significantly reduced by correcting for constraint effects.

The two-parameter formulation based on the T -stress approach is defined through the expansion of the linear elastic stress field about the crack tip using the form

$$\sigma_{ij} = \frac{K_I}{\sqrt{2\pi r}} f_{ij}(\theta) + T \delta_{li} \delta_{lj} \quad (28)$$

T -stress in the above formula is not singular term, as is the case with the first term (based on K). The T -stress, as a homogeneous uniaxial stress field acting parallel to the crack, obviously increase for small scale yielding (SSY) the constraint, contributing to the triaxiality of the near-tip region. Also, surprising on a first glance, there is experimental and numerical evidence that T correlates with the constraint effect even for large scale yielding (LSY). However, based on its origin from the elastic solution the correlation is only qualitative, and the connection with the J - integral solution is not possible.

For the J - integral another solution is proposed. The solution is based on Q -factor that can be evaluated comparing the FEM and HRR solutions for the same case.

$$Q = \frac{\sigma_{\theta\theta} - (\sigma_{\theta\theta})_{HRR}}{\sigma_Y} \quad \text{for } \theta = 0, \quad r_0 = \frac{2J}{\sigma_o} \quad (29)$$

Herein the first is the „real“ stress $\sigma_{\theta\theta}$ taken from FEM-solution, and second one which is based on HRR-solution. Distance r_0 from the crack tip to the calculation point of this factor is selected to avoid the region of crack blunting where J solution is not valid.

Based on (29) it can be also written

$$\sigma_{\theta\theta} = (\sigma_{\theta\theta})_{HRR} + Q\sigma_Y \quad (30)$$

With the development of plastic deformation factor Q become negative and this means that the stress values reduce compared to the calculation based on J . In general Q is a function of geometry, work hardening, and deformation level. For instance, in the centre cracked tension geometry Q quickly reaches value of 1, whereas, in deeply cracked bending, Q remains close to zero well in the range of general yielding (Fig. 22).

Determination of Q is complicated, because it requires a very detailed elastic-plastic finite element analysis. The most attractive feature of T is that it can be determined from an elastic finite element analysis. Factor d_n , appearing in the general relationship between J and δ (25) is also known to be constraint-dependent, and this means it can serve as a parameter to characterize constraint. The factor can be determined either by a finite-element analysis or experimentally. As a displacement-related quantity it is easier to be determined than the Q -factor. Unfortunately, its values can be used only for orientation.

In this field further investigations are necessary. Application of Q is not always successful and, because it requires complicated FEM-calculations, can be the source of deviation and uncertainties. If this calculation exists, the evaluation of h can give the better survey of general situation of the structure. Moreover, variable calculations at the same model are accessible for the sensitivity analysis and design optimisation.

5. EPFM PROCEDURES FOR THE INTEGRITY ASSESSMENT

At the beginning it is necessary here to warn design engineers that the characteristics taken to define strength of materials, like yield strength, tensile strength, elongation at fracture, do not have nearly anything with the integrity of the structures jeopardized by the cracks and by the crack growth under service loads.

For many structures and before all for plant vessels and pipes, metal constructions **and similar** is the application of ductile, yielding materials practical. Application of LEFM is under these conditions, due to the large plastic volumes formed around crack tip that considerable influence their behaviour, usually not adequate for such structures,

particularly in the ranges where the solution based on stress intensity factor K should be valid.

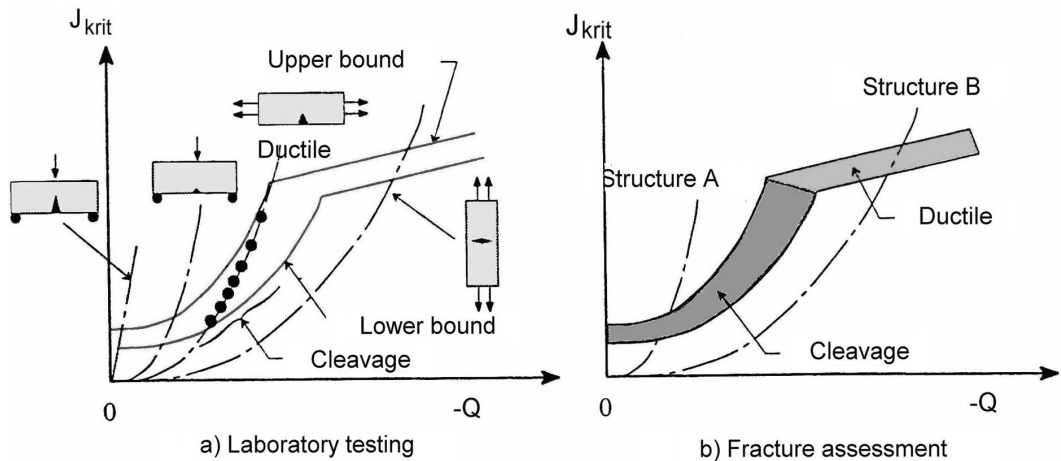


Figure 22: Scheme of J-Q approach (structure A → brittle fracture, structure B → ductile fracture)

Corresponding EPFM approaches for reliable structural integrity in this case are:

1. Solution based on evaluation of stresses and strains at crack tip (for example based on HRR solution) and corresponding J - integral as criterion.
2. Crack opening displacement as criterion.
3. Failure Assessments Diagram (FAD), based on fracture mechanics and considers failure due to plastic collapse.

First two approaches are based on determination of crack driving force (CDF) and the corresponding procedure can be summed up in following way:

1. Calculate J - integral or Crack Tip Opening Displacement (CTOD) δ in dependence on loading and geometry.
2. The critical values of J - integral (J_{Ic}) and CTOD (δ_{Ic}) can be determined empirically by testing standard specimens.
3. Calculated values of J - integral should not be higher than J_{Ic} or CTOD values should not exceed the critical δ_{Ic} considering required safety margins.

Accordingly, fracture mechanics based on J and δ application follows the same way as in the case of LEFM and K application. It is expected then that critical conditions at the crack tip are accurately described by J (or δ), so that both parameters can be used for the crack evaluation. Previously discussed limits in this respect should not be overlooked.

5.1. Stress-strain diagrams of material

Important parameter for the calculation that, at the same time, presents the essential difference to the LEFM procedure is the evaluation and consideration of the elastic-plastic material behaviour under load. Although the same material and measurement are applied, this curve is not the same for different methods. Based on use of different interpretations of the measurements (Fig. 23), the same curve can not be used, since this will be not in agreement with method requirements. Most often assumption of this curve is based on true or engineering stress and strain, Ramberg-Osgud curve (Fig. 24):

$$\frac{\varepsilon}{\varepsilon_{Y_0}} = \frac{\sigma}{\sigma_{Y_0}} + \alpha \left(\frac{\sigma}{\sigma_{Y_0}} \right)^n \quad \varepsilon = \frac{\sigma}{E} + \left(\frac{\sigma}{\sigma_{Y_0}^n} \right) \sigma^n = \frac{\sigma}{E} + \frac{1}{F} \sigma^n = \varepsilon_e + \varepsilon_{pl} \quad (31)$$

5.2. Procedure for J evaluation using EPRI handbook

J - integral calculations based on HRR solution is developed for different cases from General Electric Company and publish in form of Electric Power Research Institute (EPRI) Handbook in 1981 year. Calculation is based on separate elastic and full plastic solutions calculation that are than combined to become end results in form

$$J_{tot} = J_{el} + J_{pl} \quad (32)$$

where the elastic part is based on elastic stress intensity factor for effective crack size a_{eff} :

$$J_{el} = \frac{K_I^2 (a_{eff})}{E'} \quad (33)$$

However, the correction of the crack size based on plastic zone radius is very often neglected, because of the low difference of only 5 % or less.

For the calculation of plastic part Eqs. (16) and (17) are rewritten to obtain

$$J = \alpha \varepsilon_0 \sigma_0 I_n r \left(\frac{\sigma_{ij}}{\sigma_0} \right)^{n+1} \sigma_{ij}^{n+1} (n, \theta) \quad (34)$$

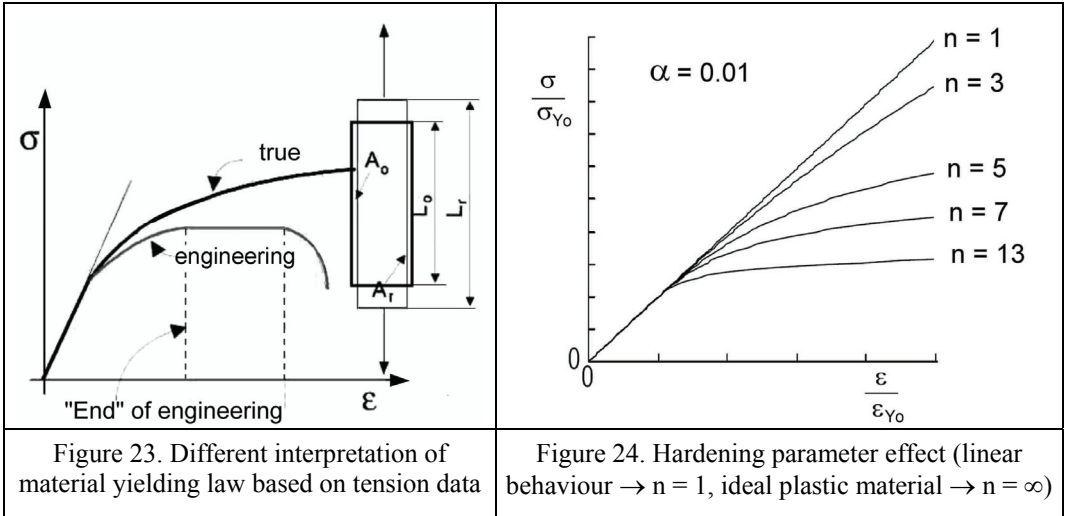
Since the nominal stress changes proportional to the load change in a structure, it is

$$J = \alpha \varepsilon_0 \sigma_0 h L \left(\frac{P}{P_0} \right)^{n+1} \quad (35)$$

Here is the parameter h dimensionless and depends on the geometry and material curve exponent n ; L is characteristic length of the structure and P_0 characteristic loading of the structure. L and P_0 can be defined arbitrary and h is determined based on numerical analysis in dependence on configuration which is examined. EPRI-Handbook contains detailed data tables for many characteristic cases.

5.3. Failure assessment diagram (FAD)

Previous assessment methods that consider only fracture mechanics parameters like J and δ , are independent on yielding conditions and plastic collapse of the structure. For that, starting from two limiting cases, methods are developed that combine corresponding criteria of pure brittle and pure ductile failure in form of Failure Assessment diagrams (FAD). Because of complex behaviour, solutions for real conditions, between these two limiting cases, are only possible through the interpolation or approximation. Accordingly, FAD in its classical, simplest form is based on interpolation between two independent solutions: failure due to the crack, predicted based on LEFM and failure due to the plastic collapse in critical section that is predicted with plastic analysis.



There exist different methods for the construction of this diagram, but here we want to use for the presentation one of the simplest that is developed and verified for the design of the ARIANE 5 Booster case by author. Since the majority of other FAD construction methods is also less accurate, it is very reasonable to use this simple **and robust** method.

Abscissa of the FAD represents the plasticity effect. To this end the ordinate is given as the ratio between actual nominal load σ and nominal load at the yielding level σ_Y

$$L_r = \frac{\sigma}{\sigma_Y} \quad (36)$$

FAD ordinate is a measure of proximity to LEFM failure due to crack driving force depending on plasticity level (L_r). Based on (22) this can be estimated by the relationship

$$K_r = \frac{\sigma}{\sqrt{\sigma E(\varepsilon_e + \varepsilon_{pl})}} \quad (37)$$

It should be mentioned that designation with K_r should be not confused with the stress intensity factor, because K_r is dimensionless value and represents factor of relative reduction of critical fracture resistance characteristics (K_{Ic} , J_{Ic} , δ_{Ic} , K_R) for given L_r value.

It follows after substitution from (36) $\rightarrow \sigma = L_r \sigma_Y$ and material curve $\sigma = B \Delta \varepsilon_{pl}^n$

$$K_r = \sqrt{\frac{L_r \sigma_Y}{E \left[\frac{L_r \sigma_Y}{E} + \left(\frac{L_r \sigma_Y}{B} \right)^{1/n} \right]}} \quad (38)$$

Based on this solution corresponding FAD curve is designed in Fig. 25. Up to the stress increase to about 70 % of yield stress the material resistance to fracture is not changed, and after that there it is significantly reduced based on net section yielding.

Failure assessment diagram has been firstly proposed from Central Electricity Generating Board (CEGB) in Great Britain, based on which the known R-6 method was developed. From first publishing 1976 it passed different improvements and revisions and today is well developed and include data necessary for practical application. However, the results of calculation based on R-6 can be sometimes inadmissible conservative.

For this method (Option 2) $K_r = f(L_r)$ is defined with the following formula

$$K_r = \left[\frac{E \varepsilon_{ref}}{L_r \sigma_Y} + \frac{L_r^3 \sigma_Y}{2E \varepsilon_{ref}} \right] \quad (39)$$

FAD in R-6 is cut at someone level of L_r , that depends on material properties.

Elastic-plastic crack driving force evaluated based on the EPRI procedure can also be presented in FAD form. For this purpose, first are defined the ratios

$$J_r = \frac{J_e(a)}{J_e(a_{eff}) + J_{pl}} \quad \text{and} \quad S_r = \frac{P}{P_o} \quad (40)$$

The equivalent K_r is equal to the square root of J_r . Results are compared in Fig. 26.

In the FAD both possible effects based on comparison of crack driving force with the parameters of material toughness and plastic collapse are considered in the same time.

Complete R-6 procedure contains different levels, each of increasing complexity, assuming to be less conservative than that of lower level, applied in dependence of the results and significance of the case. However analyses based on resistance curve (Fig. 15) may give more accurate results and demonstrate the sensitivity of the problem.

Structural integrity assessment always includes the safety factor. Evaluation of the reliability level is complex, especially in fracture mechanics that includes more parameters. Starting from the base definition that safety factor is the ratio of load leading to failure and expected load of the structure, the safety factor in the FAD is accepted as the ratio of segments OB/OA (Fig. 27). But, safety factor based on crack must consider that the stress values are dependent on square root of crack size. For that so accepted safety factor must be proved in detail.

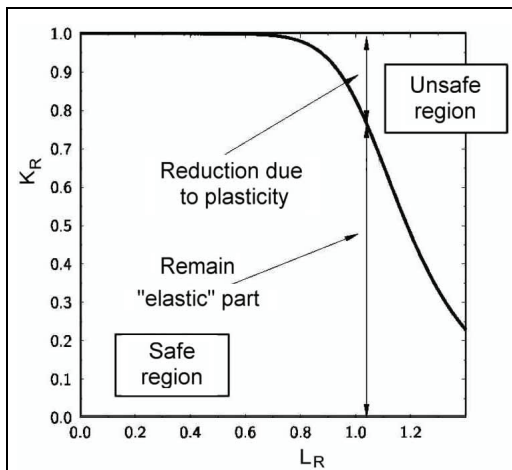


Figure 25. Failure assessment diagram-FAD

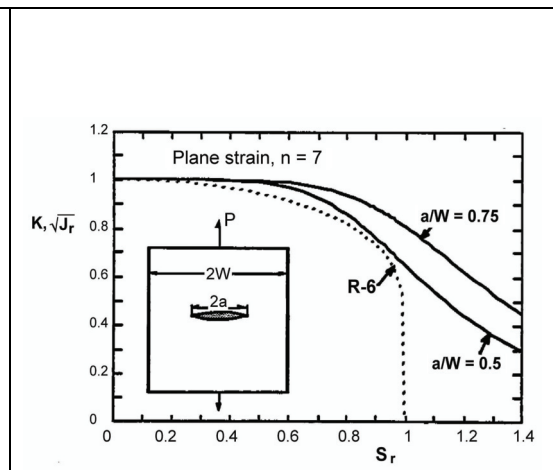


Figure 26. Comparison of FAD for EPRI and R-6

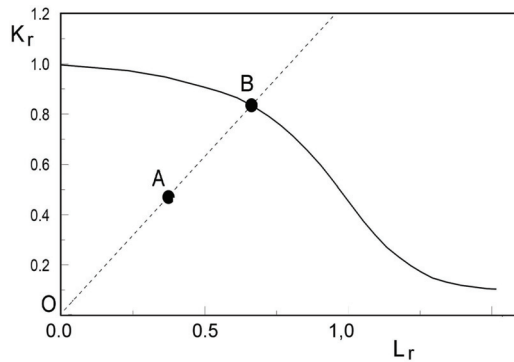


Figure 27: Procedure for determination of safety margins

6. END REMARKS

When the nominal stresses significantly exceed half of yield strength, pure LEFM-analysis does not consider the risk of underestimation of the crack driving force and the results could be unsafe. When the plasticity correction is not considered, the results of LEFM do not give any warning and results validity is questionable. In most complex cases is better to carry out a robust EPFM analysis, giving valid results from LEFM to EPFM. In case of corresponding conditions elastic-plastic analysis passes in linear elastic one and in this way not only become simpler, but gives the results without ambiguity.

REFERENCES

1. Agatonovic, P.: Fracture Case Studies –Basic Principles, in From Fracture Mechanics to Structural Integrity Assessment, IFMASS 8, 2003, Ed. S. Sedmak and Z. Radakovic, pp. 159–192.
2. Agatonovic, P.: Different strategies of remnant strength and life assessment, IVK (2/2001), pp. 5-89.
3. Agatonovic, P.: Die Restfestigkeit bestimmen, Spannungs-Dehnungs-Annäherung – ein neues Verfahren, Materialprüfung 41(1999), pp. 24-30.
4. Agatonovic, P.: K_I mittels Spannungs-Dehnungs-Annäherung abschätzen: Verifikation des Verfahrens, Materialprüfung 41(1999), pp. 77-84.
5. Agatonovic, P.: Development of residual strength evaluation tool based on stress-strain approximation, International Journal of Fracture 98, pp. 129-152.
6. Agatonovic, P. and T.K.Henriksen: Development of Residual Strength Prediction Tools for the Structure Integrity of Launchers Based on Elasto-Plastic Fracture Mechanics, Conf. on Spacecraft Structures, Materials and Mechanical Testing, 1996, ESA/ESTEC.
7. Agatonovic, P. and U. Clormann: Analytical Prediction and Test Verification of the Multiaxial Behaviour of High-strength Steel for Lightweight Structures, Proc. Int. Symp. “Advanced materials for lightweight structures” ESTEC, ESA SP-336, Oktober 1992.
8. Agatonovic, P and N. Taylor: Optimisation of a Life Prediction Method for Environmental Assisted Damage of Components Operating at High Temperature, Kyoto, 1991.
9. Agatonovic, P. and M. Windisch: Role of Combined Numerical and Experimental Investigation in the Justification of the Structure Integrity and Damage Tolerance of Space Structure, ESA Int. Symp. Spacecraft Structures and Mechanical Testing, Noordwijk, NL, 24-26th April 1991.
10. Agatonovic, P. et al.: Anwendung kleiner Proben mit Oberflächenriss zur Vorhersage der Tragfähigkeit von rissbehafteten Bauteilen, In Werkstoffprüfung 1990, Bad Nauheim DVM Dezember 1990, pp. 213-222.

11. Agatonovic, P. and M. Windisch: Non-Linear Fracture Analysis of Specimens and Components with Surface Cracks, 5th Int. Conf. Numerical Methods in Fracture Mechanics, 23-27 April 1990 in Freiburg.
12. Anderson, T. L.: Elastic - plastic fracture mechanics: a critical review, (part 1) ssc-345, Ship structure committee, April 1990,
13. Brocks, W. and W. Schmitt: The second parameter in J-R curves: Constraint or Triaxiality, Second Symposium on Constraint Effects, ASTM STP 1244, 1994.
14. Dodds R.H., C. Fong Shih and T. L. Anderson: Continuum and micromechanics treatment of constraints in fracture, Int. Journ. of Fracture 64, 101-133, 1993.
15. Milne, I. et al: Assessment of the Integrity of Structures Containing Defects, Int. J. Pres. Ves. & Piping 32 (1988) 3-104.
16. Mirzaei M.: Fracture Mechanics Lecture Notes: 3, Dept. of Mechanical Eng., TMU, <http://www.modares.ac.ir/eng/mmirzaei/FM.htm>
17. Kumar, V. et al: An engineering approach for elastic-plastic fracture analysis, EPRI NP-1931, 1981
18. Shih, C.F.: Small scale yielding analysis of mixed mode plane strain crack problems, AFOSR Tech. Report 73-1692, 1973.
19. Wnuk, M.P.: Limit analysis of cracked pressure vessel, IFMASS 2, 1982, Ed. S.Sedmak, pp. 51-78
20. Zehnder, A.L.: Lecture Notes on Fracture Mechanics, Dept. of Theoretical and Applied Mechanics, Cornell University, Ithaca, NY 14853, January 7, 2008.

DUCTILE FAILURE CRITERIA UNDER MULTIAXIAL LOADING

Mićunović Milan

Mechanical Engineering Faculty, Kragujevac, Serbia

mmicun@sezampro.rs

1. INTRODUCTION

Frequently is necessary to go deeply into plastic range before severe accidents occur for design of nuclear reactors and some chemical plants. Such a reserve is needed to sustain the course of hypothetical core melt accidents, potential containment failure modes and sequences leading to radioactive release. An analogous situation appears in stamping plants operating on ductile mild ferritic steels where a large plastic strain without fracture is needed in order to form complicated shell parts of a car body. Ductile fracture as combination of normal cracking, delamination and fracture along shear-bands might be divided into two categories: tensile type and shear type failure. It is affected by:

1. history of stress, strain and temperature including their actual values and strain rate,
2. grain size as well as grain boundaries relative strength,
3. size of the considered structure or specimen, and
4. strain distribution (strain gradients).

Concerning history effects it is likely that the comment of McClintock is still valid: with not even an understanding of the difference between monotones shear and tensile fracture it is not surprising that the effects of varying stress history are not understood. In order to clarify at least partly the significance of history diverse stress directions and non proportional paths are necessary. As a single scalar measure of failure advance equivalent plastic strain is not convenient. Instead Davis triaxiality factor T_f (ratio of first stress invariant and Mises equivalent stress) being for isotropic materials: 0 for shear, 1 for uniaxial tension and 2 for equibiaxial tension appears to be much more appropriate.

Existing criteria might be classified into:

1. maximum tensile stress (here maximum of largest principal engineering stress corresponds to maximum load) leading to diffuse instability criterion,
2. hole-growth criterion which is built by means of intrinsically statistical theory with some inevitable simplification,
3. connection of localization to yield surface corners appearance and development,
4. maximum shear stress criterion useful for crystal grains or grain boundaries but not poly-crystals, and
5. forming limit diagrams (FLD) being successfully applied to metal sheet forming where for isotropic materials $\sqrt{3} \leq T_f \leq 2$ (i. e. $0.5 < \sigma_2/\sigma_1 < 1$).

2. EXISTING MODELS OF DUCTILE FAILURE CRITERIA

2.1. McClintock's model of growing touching holes

As a background for his calculations McClintock had experimental evidence concerning coalescence of holes appearing not only in metals like copper, but also in plastics. Typically, holes look like "wolf's ear" connecting during growth to each other either

across (leading to normal fracture) or along a typical ear shape hole (leading to delamination). The third mode of shear type is not considered in his paper /23/.

Assumptions

A1-1: Rate independent rigid plastic material is assumed which obeys associativity of flow rule based on Mises yield surface. In this case the following equation holds in terms of true stress deviator and total true strain deviator

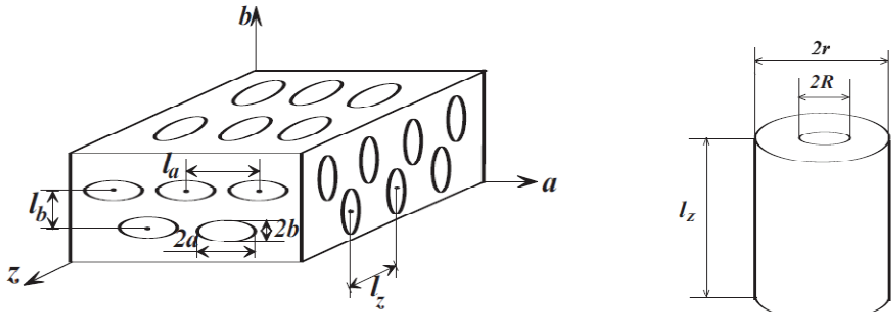
$$d\boldsymbol{\varepsilon}' = d\lambda \mathbf{T}', \quad d\lambda = \frac{3}{2} \frac{d\bar{\boldsymbol{\varepsilon}}}{\bar{\boldsymbol{\sigma}}} \quad (1)$$

where “rigidity” means $\boldsymbol{\varepsilon} = \boldsymbol{\varepsilon}_p$ (i.e. total and plastic strains are assumed to be approximately equal for advanced plastic strain at fracturing process), and

$$\bar{\boldsymbol{\sigma}}^2 = 3/2 \operatorname{tr} \mathbf{T}'^2 d\bar{\boldsymbol{\varepsilon}}^2 = 2/3 \operatorname{tr} d\boldsymbol{\varepsilon}'^2$$

Are equivalent stress and equivalent increment of total strain (increment of plastic accumulation path), respectively.

A1-2. Three mutually perpendicular elliptically cylindrical holes (Fig. 1.a) are assumed to exist such that each hole surrounded by a solid material with cross section of diameters equal to average spacing between holes forms a cell.



a. Three sets of mutually perpendicular elliptical cylindrical holes

b. McClintock's representative annular cylinder

Figure 1: An illustrative damaged specimen

For instance, for a cell whose axis is with growth extending along axis b , the corresponding relative growth factor is defined as follows

$$\Phi_{zb} = \left(\frac{b}{l_b}\right) / \left(\frac{b_0}{l_{b0}}\right) \equiv F_{zb} / F_{zb0}$$

If $F_{zb}^f = 1/2$, then the zb -fracture begins due to coalescence of z -holes into b -direction and $\Phi_{zb}^f = F_{zb}^f / F_{zb0} = 1/2 / F_{zb0}$. In general, for the whole set $\Phi_{ij} = F_{ij} / F_{ij0}$ the fracture begins when $\max_{i,j} (F_{ij}) = 1/2$.

Finally McClintock proposed a logarithmic, additive and normalized, damage measure

$$\eta_{ij} = \ln \Phi_{ij} / \ln \Phi_{ij}^f \quad (2)$$

which at fracture became unity. Its additivity is guaranteed only if Lagrangian approach with fixed reference configuration is accepted. Otherwise in the terminology of FEM, if updated (i.e. variable) reference configuration is employed, then it is not additive any more. A modified damage measure

$$h_{ij}^o = \ln F_{ij} / \ln F_{ij}^f$$

can be used instead, and typical diameter of a hole and its eccentricity are denoted by

$$R := \frac{a+b}{2}, \quad e := \frac{a-b}{a+b}.$$

A1-3. Strain hardening was assumed to be described by Ramberg-Osgood rule, i.e.

$$\bar{\sigma} = \sigma_1 \bar{\varepsilon}^n \quad (3)$$

where σ_1 is equivalent stress at $\bar{\varepsilon} = 1$ and as before $\bar{\varepsilon}^2 = 2/3 \text{ tr } \varepsilon'^2$ is equivalent total strain, respectively. Moreover, Mises yield surface and associativity of flow rule was accepted even at fracturing. As two special cases of the above hardening model he takes: $n = 0$, as obvious non-hardening case, and $n = 1$, which he claims to be equation corresponding to linear viscoelastic behaviour.

A1-4. Rotation of principal axes of stresses is assumed to be negligible during stress history, which means that only principal stresses and strains considered (as mentioned at the beginning of this subsection the analysis is not intended to describe shears but only normal strains).

A1-5. Plastic zone covers all the considered body, and thermal effects are neglected.

Analysis

1. McClintock first derived change of his damage measure, Eq. (2), for circular cylindrical parallel holes in non-hardening plastic material ($\bar{\sigma} = \text{const}$, i.e. $n = 0$).

Assuming, moreover, absence of plastic volume change for a representative circular cylinder (Fig. 1.b) and integrating radial equilibrium equation for axisymmetric generalized plane strain he obtained following analytical solution, /23/- Eq. (11):

$$\ln \frac{R}{R_0} = \frac{\bar{\varepsilon}\sqrt{3}}{2} \sinh \left[\frac{\sqrt{3}}{2} \frac{\sigma_a + \sigma_b}{\bar{\sigma}} \right] + \frac{\varepsilon_a + \varepsilon_b}{2} \quad (4)$$

2. On the other hand, for a linear viscoelastic material obeying the evolution equation

$$\dot{\varepsilon}' = \frac{1}{2\mu^\#} \mathbf{T}' \quad (5)$$

where $\mu^\# = \text{const}$ is viscosity coefficient, under the condition of constant stress deviator we have $\bar{\sigma} = \bar{\sigma}t/3\mu^\#$. The corresponding solutions, according to /17/, now read

$$\ln \frac{R}{R_0} = 3\bar{\varepsilon} \frac{\sigma_a + \sigma_b}{\bar{\sigma}} + \frac{\varepsilon_a + \varepsilon_b}{2} \quad (6)$$

$$e = \frac{\sigma_a - \sigma_b}{\sigma_a + \sigma_b} + \left(e_0 - \frac{\sigma_a - \sigma_b}{\sigma_a + \sigma_b} \right) \exp \left[\frac{-3\bar{\varepsilon}}{2} \frac{\sigma_a + \sigma_b}{\bar{\sigma}} \right] \quad (7)$$

3. Taking Eqs. (1) and (5) as two limiting cases of the power hardening Eq. (3), corresponding to $n=0$ and $n=1$, respectively, next interpolation is introduced in /23/

$$\ln \frac{R}{R_0} = \frac{\bar{\varepsilon}\sqrt{3}}{2(1-n)} \sinh \left[\frac{\sqrt{3}(1-n)}{2} \frac{\sigma_a + \sigma_b}{\bar{\sigma}} \right] + \frac{\varepsilon_a + \varepsilon_b}{2} \quad (8)$$

$$e = \frac{\sigma_a - \sigma_b}{\sigma_a + \sigma_b} + \left(e_0 - \frac{\sigma_a - \sigma_b}{\sigma_a + \sigma_b} \right) \exp \left(\frac{-\sqrt{3}\bar{\varepsilon}}{1-n} \sinh \left[\frac{\sqrt{3}(1-n)}{2} \frac{\sigma_a + \sigma_b}{\bar{\sigma}} \right] \right) \quad (9)$$

Which, reduces to Eqs. (4), (6) - (7) in the mentioned limiting cases. By means of identity $b = R(1 - e)$ and of logarithmic (true) strain $\varepsilon_b = \ln(l_b/l_{b0})$ from Eq. (2)

$$\eta_{zb} \ln \phi_{zb}^f = d \ln \left(\frac{1-e}{1-e_0} \right) - d\varepsilon_b \quad (10)$$

Neglecting influence of eccentricity, i.e. the second term on right-hand-side (RHS) for constant stress state we have

$$\frac{d\eta_{zb}}{d\bar{\varepsilon}} \ln \phi_{zb}^f = \frac{\sqrt{3}}{2(1-n)} \sinh \left[\frac{\sqrt{3}(1-n) \sigma_a + \sigma_b}{2 \bar{\sigma}} \right] + \frac{3 \sigma_a - \sigma_b}{4 \bar{\sigma}} \quad (11)$$

Let either stress components are constant or a proportional stress path is considered. Then the above equation is integrated up to value $\eta_{zb}^f = 1$ to give equivalent fracture strain when z-holes coalesce in b-direction

$$\bar{\varepsilon}^f = \ln(\phi_{zb}^f) \left(\frac{\sqrt{3}}{2(1-n)} \sinh \left[\frac{\sqrt{3}(1-n) \sigma_a + \sigma_b}{2 \bar{\varepsilon}} \right] + \frac{3 \sigma_a - \sigma_b}{4 \bar{\sigma}} \right) \quad (12)$$

Assuming in the case of plane tension $-1 < m \equiv \sigma_b/\sigma_a < 1$, corresponding to triaxiality factor, /11/

$$0 < T_f = tr \mathbf{T} / \bar{\sigma} < 2 \quad (13)$$

the above equation permits graphical representation of fracture strain derived by critical growth factor versus triaxiality. It should be noted that triaxiality factor for the case of isotropy and plane stress by its values delimits some characteristic regions:

- $T_f = 0, (\sigma_1 = -\sigma_2)$ -simple shear,
- $T_f = 1, (\sigma_2 = 0)$ -uniaxial tension,
- $T_f = \sqrt{3}, (\sigma_1 = 2\sigma_2)$ -plane strain,
- $T_f = 2, (\sigma_1 = \sigma_2)$ -equibiaxial tension.

According to McClintock's results /4/ and his criterion the smallest fracture strain is obtained for equibiaxial stress state and the largest for shear when $\sigma_b = -\sigma_a$.

2.2 Diffuse plastic instability

According to Ref. /2/ a nonuniform strain field may develop twofold: (a) thinning during tension loads occurs very gradually in dimensions comparable with specimen dimensions and, (b) it occurs in a region comparable with sheet (or specimen) thickness. The first is called diffuse instability whereas for the second phenomenon the name localized instability is chosen. Due to above distinction the diffuse instability could appear mainly when cylindrical specimen are used.

Assumptions

A2-1. The material considered is assumed to be strain hardening rigid plastic obeying assumptions A1-1 and A1-3. Moreover, multiaxial stress state is restricted to be homogeneous, i.e. uniform in terminology of Ref. /20/.

A2-2. The basic assumption lies in the principle of maximum rate of plastic work as stated in Ref. /19/:

$$\int_V (\mathbf{T}'_{actual} - \mathbf{T}'): \dot{\varepsilon}'_{actual} dV \geq 0 \quad (14)$$

According to Hill's terminology throughout this subsection the subscript "actual" is used to denote actual or true quantities like stress and strain (the word "actual" is used here instead of "true" to avoid confusion). Likewise \mathbf{T}'_{actual} and $\dot{\varepsilon}'_{actual}$ are actual stress and actual strain deviators, respectively. These two must be related through the strain

hardening curve (i.e. “universal” flow curve) $\bar{\sigma} = f(\bar{\varepsilon})$. Time rate of actual stress is singled out by the requirement that it must be compatible with the current rate of strain hardening, by tangent to the strain hardening curve. It must be noted that this statement does not hold for arbitrary assumed or virtual deviatoric stresses and strains, \mathbf{T}' and ε' .

This assumption implicitly states that actual and virtual stress and strain coincide until actual instant of time (denoted by $\tau = 0$). Then these two may split such that actual stress increment remains tangent to actual stress trajectory, whereas virtual stress may be oblique with respect to it. If the condition of Eq. (14) is not satisfied, then bifurcation leading to plastic instability takes place.

A2-3. The strain tensor used almost exclusively by Hill /29/ is logarithmic Eulerian (true) strain tensor which in terms of its proper directions $\vec{i}_1, \vec{i}_2, \vec{i}_3$ has the form (with summation over repeated indices implied), $\varepsilon = \vec{i}_k \otimes \vec{i}_k \ln \lambda_k \equiv \vec{i}_k \otimes \vec{i}_k \varepsilon_k$, where $\lambda_1, \lambda_2, \lambda_3$ are principal stretches. For a parallelepiped with edges L_1, L_2, L_3 is $\lambda_k = L_k/L_{0k}$ ($k = 1,2,3$). The conjugate stress tensor is Cauchy stress such that work increment equals $\delta W = \mathbf{T} : \delta \varepsilon$. According to this assumption $tr \varepsilon = 0$, $tr \dot{\varepsilon} = 0$ for advanced plastic strains. This means that elastic strains are negligible and plastic incompressibility holds.

A2-4. For proportional plane stress paths $m = \sigma_2/\sigma_1 = const$ the onset of diffuse instability appears when $\dot{\sigma}_1/\sigma_1 = \dot{\varepsilon}_1$, $\dot{\sigma}_2/\sigma_2 = \dot{\varepsilon}_2$. This means that previous assumption holds and that maximum of two in-plane engineering stresses appear simultaneously when diffuse instability begins.

Analysis

1. Hillier used the Hill's principle, Eq. (14) in the following way /20/. According to assumption A2-2 we must have at $\tau = 0$ the equalities:

$\mathbf{T}' = \mathbf{T}'_{actual}$, $\bar{\sigma} = \bar{\sigma}_{actual}$, $e' = e'_{actual}$, as well as $\dot{e}' = \dot{e}'_{actual}$ where the last equality follows from Eq. (1). Now, differentiating Eq. (14) with respect to time, replacing the above equalities in it and taking account stress homogeneity, it is

$$\dot{\bar{\sigma}}_{actual} \geq \dot{\bar{\sigma}} \quad (15)$$

The inverse sign of inequality would mean instability. Therefore, the instability condition may be written as follows

$$\frac{1}{Z_{actual}} = \frac{1}{\bar{\sigma}_{actual}} \frac{d\bar{\sigma}_{actual}}{d\bar{\varepsilon}_{actual}} \leq \frac{1}{\bar{\sigma}} \frac{d\bar{\sigma}}{d\bar{\varepsilon}} = \frac{1}{Z} \quad (16)$$

The limiting value of Z where this becomes equality is referred to as the critical subtangent (Fig. 2.a).

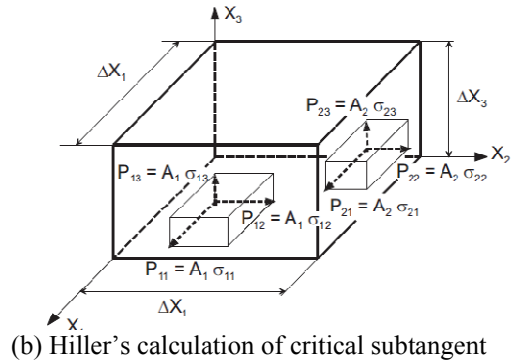
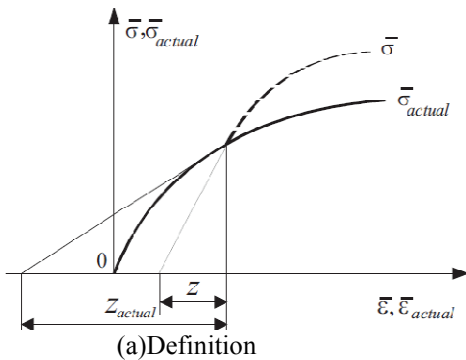


Figure 2: Notion of critical subtangent

2. Considering a rectangular block whose sides are exposed to forces (Fig. 2.b) $\vec{P}_\alpha = A_\alpha \vec{t}_\alpha$ (Greek indices employed indicating no summation) induced by uniform stresses

$$\vec{t}_k = \mathbf{T} \cdot \vec{n}_k \equiv \mathbf{T} \cdot \vec{l}_k = \sigma_{kl} \vec{l}_l$$

Hillier has derived the next expression for the critical subtangent

$$\frac{1}{Z} = \frac{9}{4} \frac{1}{\bar{\sigma}^3} \left[\frac{1}{A_\alpha} \frac{\partial P_{\alpha j}}{\partial e_{mn}} \sigma'_{mn} \sigma'_{ij} \delta_{\alpha i} + \sigma_{\alpha j} \sigma'_{ij} \sigma'_{\alpha \beta} \delta_{\alpha \beta} \delta_{\alpha i} \right] \quad (17)$$

under the assumption that sides of the block are not influenced by shearing strains

$$\frac{1}{A_\alpha} \frac{\partial A_\alpha}{\partial e_{\alpha \delta}} = -\delta_{\alpha \beta} \quad (18)$$

The application of critical subtangent formula lies practically in extremum values of loads i.e. $dP_\alpha = 0$ for diverse loading situations.

3. Let a rectangular block of dimensions $\Delta X_1, \Delta X_2, \Delta X_3$, (Fig. 2.b), be subject to uniform plane stresses $\sigma_{11}, \sigma_{22} = m\sigma_{11}, \sigma_{33} = 0, \sigma_{12} = k\sigma_{11}, \sigma_{23} = 0, \sigma_{31} = 0$. Then application of Eq. (17) to a Ramberg-Osgood material obeying Eq. (3), under critical loads $\partial P_{\alpha k} / \partial e_{mn}$ gives the next value for critical subtangent /20/

$$Z = \frac{4(1 - m + m^2 + 3k^2)^{3/2}}{(1 + m)(4 - 7m^2 + 3k^2)} \quad (19)$$

which has been derived for case of normal strains i.e. for $k = 0$ by Swift (1957). In the most special case of uniform tension, when $m = 0$ and $k = 0$ critical subtangent corresponds to necking initiation (when engineering stress is maximum). Then Eq. (19) specializes into $Z = 1$. The corresponding "uniform" strain is easily derived in the sequel (by means of $\bar{\sigma} = \sigma_{11} > 0$)

$$\begin{aligned} dP_{11} &= A_1 d\sigma_{11} + dA_1 \sigma_{11} = P_{11} \left(\frac{d\sigma_{11}}{\sigma_{11}} + \frac{dA_1}{A_1} \right) = 0 \\ \frac{dA_1}{A_1} &\approx -de_{11} \equiv -d\bar{\varepsilon}, \frac{d\bar{\sigma}}{\bar{\sigma}} = \frac{n}{\bar{\varepsilon}} \Rightarrow \left(\frac{n}{\bar{\varepsilon}_u} - 1 \right) d\bar{\varepsilon} = 0 \end{aligned}$$

such that

$$\varepsilon_u = n \quad (20)$$

Replacing this value into the definition of critical subtangent, Eq. (16) allows $Z = 1$. In the special case when $k \rightarrow \infty$ corresponding to pure shear $\sigma_{11} = \sigma_{22} = 0; \sigma_{12} \neq 0$, formula (19) fails, giving $Z \rightarrow \infty$ and the corresponding $\bar{\varepsilon}_u \rightarrow \infty$. Suppose, following Hill, Ref. /28/ that an initially anisotropic material deforms plastically according to the following yield function

$$2f = \frac{1}{h(\bar{\varepsilon}P)} \mathbf{T} : \mathcal{A} : \mathbf{T} = \frac{1}{h(\bar{\varepsilon}P)} \mathcal{A}_{ijkl} \sigma^{ij} \sigma^{kl} \equiv \frac{2}{3} \frac{\bar{\sigma}^2}{h(\bar{\varepsilon}P)} = 1 \quad (21)$$

where are: \mathcal{A} - fourth rank tensor of constants depending on material symmetries (it will be specified in the sequel for orthotropic as well as transversely isotropic materials), $\bar{\sigma}$ - equivalent stress, $\bar{\varepsilon}_p$ - equivalent strain and h - scalar function describing "isotropic" hardening, $\bar{\sigma} = \bar{\sigma}(\bar{\varepsilon}_p)$, capable to account only for homogeneous inflation of the yield surface. Hill claims that \mathcal{A} in general case is specified by six constants determined by initial yield stresses for tensions and shears with respect to principal material directions.

For this claim he did not give an account to material symmetries in an invariant form, but the claim is correct since all stress eigenvalues are uniquely determined by means of its proper invariants. Accepting associate flow rule and using the identity $\mathbf{T} : \partial_{\mathbf{T}} f = 1$, we arrive at evolution equations for plastic strain increments

$$d\varepsilon_p = d\lambda \partial_{\mathbf{T}} f = \bar{\sigma} d\bar{\varepsilon}_p \partial_{\mathbf{T}} f = \bar{\sigma} Z \partial_{\mathbf{T}} f \quad (\partial_{\mathbf{T}} f : d\mathbf{T})$$

or, equivalently

$$df = d\lambda \frac{\partial f}{\partial \sigma^{ij}} = \bar{\sigma} d\bar{\varepsilon}_p \frac{\partial f}{\partial \sigma^{ij}} = \bar{\sigma} Z \frac{\partial f}{\partial \sigma^{ij}} \frac{\partial f}{\partial \sigma^{kl}} d\sigma^{kl} \quad (22)$$

Here the use has been made of the following definitions

$$df = \frac{\partial f}{\partial \sigma^{ij}} d\sigma^{ij} + \frac{\partial f}{\partial \varepsilon_p} d\varepsilon_p = \quad (23)$$

$$\hat{d}W_p = \sigma^{ij} d\varepsilon_{ij} = d\lambda \sigma^{ij} \frac{\partial f}{\partial \sigma^{ij}} = d\lambda \text{ and } d\bar{\varepsilon}_p := \frac{\hat{d}W_p}{\bar{\sigma}} \quad (24)$$

for consistency condition, elementary plastic work and equivalent plastic strain increment. At this point Hill's stability postulate, Ref. /19/, is invoked stating in its local form that at a bifurcation point (Fig. 2) the following equality holds

$$\dot{\mathbf{T}} : \dot{\varepsilon}_p = \text{tr}\{\dot{\varepsilon}_p \cdot \mathbf{T} \cdot \dot{\varepsilon}_p\} \quad \text{or} \quad \dot{\sigma}^{ij} \dot{\varepsilon}_{pij} = \sigma^{ij} \dot{\varepsilon}_{pj k} \dot{\varepsilon}_{pil} \delta^{kl} \quad (25)$$

for rigid plastic materials (i.e. materials where elastic strain is so smaller than plastic strain that it may be neglected i.e. $\varepsilon \approx \varepsilon_p$). In above equality $\dot{\mathbf{T}}$ is time rate of true stress, whereas $\dot{\varepsilon}_p$ is time rate of Eulerian true plastic strain tensor. Combining above equations we arrive at the following critical subtangent already written by Hill /29/ and by Ref. /21/ in terms of principal stresses.

$$Z_H = \frac{df}{d\bar{\sigma}} \sigma^{mn} \frac{\partial f}{\partial \sigma^{mn}} \left(\sigma^{ij} \frac{\partial f}{\partial \sigma^{ik}} \frac{\partial f}{\partial \sigma^{jl}} \delta^{kl} \right)^{-1} \quad (26)$$

Equating this with the definition of subtangent from the ‘‘universal’’ hardening curve

$$Z = \bar{\sigma} \frac{d\bar{\varepsilon}_p}{d\bar{\sigma}} \quad (27)$$

we obtain limit strains $\bar{\varepsilon}_u$ (‘‘uniform’’ strains) for diverse loading conditions. It should be noted that from Eq. (26) there follows previous expression for Z . Obviously less general expressions for uniaxial tension, equibiaxial tension etc. follow automatically reducing the corresponding stress components to zero. However, we must not forget that critical subtangent approach is restricted heavily by assumption on existence of universal curve $\bar{\sigma} = \bar{\sigma}(\bar{\varepsilon}_p)$ excluding from Eq. (25) mixed stress-plastic strain invariants responsible for kinematic and more general types of hardening.

4. Korhonen, 1978, used for orthotropic materials from Hill's yield condition:

$$2f := \frac{1}{h(\bar{\varepsilon})} \frac{2}{3} \bar{\sigma}^2 = F(\sigma_2 - \sigma_3)^2 + G(\sigma_3 - \sigma_1)^2 + H(\sigma_1 - \sigma_2)^2 = 1 \quad (28)$$

He further obtained the critical diffuse subtangent in the following form (with identities $R_1 \equiv H/G$, $R_2 \equiv H/F$)

$$Z_H = \frac{\sqrt{2}}{\sqrt{3}} \frac{(R_1 + R_2 + R_1 R_2)^{1/2} \{m^2(1 + R^2)R_1 - 2mR_1 R_2 + (1 + R_1)R_2\}^{3/2}}{m^3 R_1^2 (1 + R_2)^2 - m^2 R_1^2 R_2 (2 + R_2) - m R_2^2 R_1 (2 + R_1) + R_2^2 (1 + R_1)^2} \quad (29)$$

for plane stress with ratio of principal stresses equals to $m = \sigma_2/\sigma_1$ which with notations $c \equiv 1 + 1/R_1$, $b \equiv 1 + 1/R_2$, may be written in the following more compact form

$$Z_H = \sqrt{\frac{2}{3} \frac{\sqrt{b+c-1}(c-2m+bm^2)^{3/2}}{c^2 + b^2m^3 - m(2c-1) - m^2(2b-1)}} \quad (30)$$

According to the above definition of equivalent stress and definition of equivalent plastic strain, we have

$$\begin{aligned} \bar{\sigma} &= \frac{\sqrt{2}}{\sqrt{3}} (R_1 + R_2 + R_1R_2)^{-1/2} \{R_1\sigma_2^2 + R_2\sigma_1^2 + R_1R_2(\sigma_1 - \sigma_2)^2\}^{1/2} = \\ &= \left(\frac{3/2}{b+c-1} \right)^{-1/2} (c\sigma_1^2 + b\sigma_2^2 - 2\sigma_1\sigma_2)^{1/2} \end{aligned} \quad (31)$$

$$\begin{aligned} d\bar{\varepsilon} &= \frac{\sqrt{2/3}}{\sqrt{R_1R_2}} \left(\frac{R_1 + R_2 + R_1R_2}{1 + R_1 + R_2} \right)^{1/2} \{R_1d\varepsilon_1^2 + R_2d\varepsilon_2^2 + R_1R_2d\varepsilon_3^2\}^{1/2} = \\ &= \sqrt{\frac{2}{3}} \left(\frac{b+c-1}{bc-1} \right)^{1/2} (bd\varepsilon_1^2 + cd\varepsilon_2^2 + 2d\varepsilon_1d\varepsilon_2)^{1/2} \approx d\bar{\varepsilon}_p \end{aligned} \quad (32)$$

such that evolution equations, so called Levi-Mises equations, read

$$\frac{d\varepsilon_1}{c\sigma_1 - \sigma_2} = \frac{d\varepsilon_2}{b\sigma_2 - \sigma_1} = -\frac{d\varepsilon_3}{(c-1)\sigma_1 + (b-1)\sigma_2} = \frac{3d\bar{\varepsilon}}{2(b+c-1)\bar{\sigma}} \quad (33)$$

The solution procedure covers integration of Eq. (33), which is elementary for proportional paths where $m = \text{const}$, which allows subsequently the equivalent limit strain.

At this place, however, limit strains are checked according to equality $Z_D = Z_H$. It was assumed that $\bar{\sigma} = c\bar{\varepsilon}^n$, which allows from Eq. (27) the relation $\bar{\varepsilon}_u = nZ$ for uniform (i.e. limit) equivalent strain.

It should be mentioned that in the report /4/ for the sake of illustration the following materials are considered: (1) orthotropic, with $R_1 = 1/0.38$, $R_2 = 1/0.3092$ (rolled, by aluminium killed steel); (2) transversely isotropic with $R_1 = R_2 = 1/0.35$; (3) transversely isotropic with $R_1 = R_2 = 1/2$; (4) isotropic with $R_1 = R_2 = 1$. Two Ramberg-Osgood exponents, $n = 0.431$ and $n = 0.148$ are taken. Results are plotted on Fig.1.5 and 1.6. It was remarked that for a small value of n limit curves are almost coincident.

Note N-1

Consider an orthotropic material. For it an invariant yield function in the form /31/

$$2f := \frac{2\bar{\sigma}^2}{3h} = 2 \frac{2r_1 + 2r_2 - 1}{4 + r_1 + r_2} \left\{ 2J_2 + \frac{3}{2r_1 + 2r_2 - 1} [(1 - r_2)A_{\sigma_1}^2 + (1 - r_1)A_{\sigma_2}^2] \right\} = 1$$

is chosen with, $A_{\sigma_1} = (\bar{a}_1 \otimes \bar{a}_1) : \mathbf{T}'$, $A_{\sigma_2} = (\bar{a}_2 \otimes \bar{a}_2) : \mathbf{T}'$, as stress invariants in privileged directions, while r_1 and r_2 depend on initial yield stresses in material principal directions Ref. /31/.

Here, strain increment invariants in privileged directions are $dA_{\varepsilon_1} = (\bar{a}_1 \otimes \bar{a}_1) : d\varepsilon_p$, $dA_{\varepsilon_2} = (\bar{a}_2 \otimes \bar{a}_2) : d\varepsilon_p$, so that Levi-Mises equations are given by

$$\frac{d\varepsilon_1}{c\sigma_1 - \sigma_2} = \frac{d\varepsilon_2}{b\sigma_2 - \sigma_1} = -\frac{d\varepsilon_3}{(c-1)\sigma_1 + (b-1)\sigma_2} = \frac{3d\bar{\varepsilon}}{(2+b+c)\bar{\sigma}} \quad (34)$$

By means of $m = \sigma_2/\sigma_1$ we get the expression for critical subtangent as follows

$$Z_H = \frac{1}{\sqrt{3}} \frac{\sqrt{2+b+c}(c-2m+bm^2)^{3/2}}{c^2 + b^2m^3 - m(2c-1) - m^2(2b-1)}$$

differing from the corresponding Korhonen's expression by $\sqrt{2+b+c}/\sqrt{2b+2c-2}$, a constant, which in the case of isotropy becomes 1. Accordingly, uniform (limit) strain concordant with the above expressions differs from Korhonen's limit strain also up to this constant. In the case of isotropy $b = c = 2$ both limit strains coincide.

Here one may draw following conclusions:

- the method is easy for application and gives good results for bodies whose characteristic dimensions are all of the same order of magnitude;
- its inability to account for strain rate effects is a serious shortcoming;
- the assumption about simultaneous maxima of engineering in-plane principal stresses should be checked by experiments (some experimental data, in fact, demonstrate that indeed their maxima are not simultaneous -Albertini /6/).

2.3. Localized necking in thin sheets

Physically, the formation of a neck in a sheet requires deformation in a thin zone where the material does not change in length along the zone because of the constraint of rigid shoulders on each side, Ref. /2/.

- The main contribution to be considered here is that of Hill /29/.
- Its application to anisotropic sheets was done in /21/.

Assumptions

A3-1. Let a necking strip of width B appears in a sheet with velocity of its propagation inclined by an angle ψ (Fig. 3), Hill /29/. Assumption rigid plasticity (i.e. negligible elastic strain) and plastic incompressibility (cf. A2-3) deformation gradient reads:

$$\mathbf{F} = \begin{Bmatrix} 1+st & 0 & 0 \\ ct & 1 & 0 \\ 0 & 0 & 1/(1+st) \end{Bmatrix} \quad (35)$$

Here, material coordinate frame is chosen to coincide X_2 -axis with the strip, whereas $s \equiv v \sin\psi/B$, $c \equiv v \cos\psi/B$. Then eigenvalues of stretching tensor $\mathbf{D} = \dot{\boldsymbol{\epsilon}}$ are

$$\dot{\epsilon}_1 = \frac{v(1+s)}{2B(1+st)}, \quad \dot{\epsilon}_2 = -\frac{v(1-s)}{2B(1+st)}, \quad \dot{\epsilon}_3 = \frac{vs}{B(1+st)} \quad (36)$$

Hill in /29/ neglects the bracket in the denominators under the assumption that $|st| \ll 1$. The proper directions of $\dot{\boldsymbol{\epsilon}}$ are oblique with respect to the strip by angle of $(2\pi - \psi)/4$. Orientation of velocity discontinuity found from the above relationships:

$$\sin\psi = \frac{\dot{\epsilon}_1 + \dot{\epsilon}_2}{\dot{\epsilon}_1 - \dot{\epsilon}_2} \quad (37)$$

delimits applications of this method only to time instants when:

$$\dot{\epsilon}_1 > 0, \quad \dot{\epsilon}_2 < 0. \quad (38)$$

A3-2. For localized necking in sheets $|\dot{L}_1/\dot{L}_3| \ll 1$ and $|\dot{L}_2/\dot{L}_3| \ll 1$ such that maximum of largest principal engineering stress gives

$$\frac{\dot{\sigma}_1}{\sigma_1} \approx -\frac{L_2\dot{L}_3}{L_2L_3} = -\dot{\epsilon}_3 \quad (39)$$

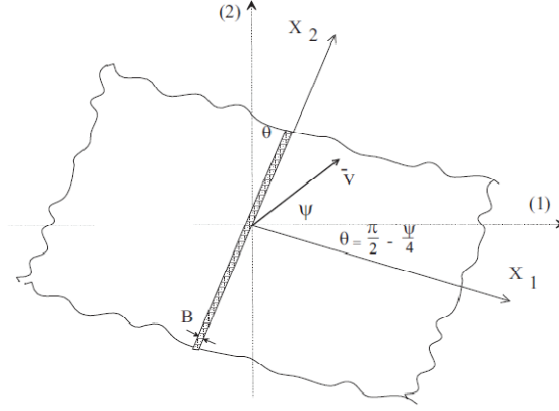


Figure 3: Principal stretching direction for a localized strip in rigid plastic thin sheet

Then proportionality of stress path requires $\dot{\sigma}_2/\sigma_2 = \dot{\sigma}_1/\sigma_1$ i.e $\dot{\sigma}_2/\sigma_2 = -\dot{\epsilon}_3$. Thus, localized necking commences with simultaneous maximum of two in-plane principal engineering stresses.

A3-3. Hill postulated yield function for plane stress in the form.

$$f(\sigma_1, \sigma_2) - F(W) \leq 0 \quad (40)$$

where equality stands for plasticity and inequality for elasticity. The so called consistency condition states that $\dot{f} - \dot{F} = 0$ should hold as well. According to his main assumption, localized instability commences when

$$F'(W) \leq \frac{\dot{f}}{\dot{W}} = \frac{\partial f}{\partial \sigma_1} + \frac{\partial f}{\partial \sigma_2} \quad (41)$$

The last equality follows from the assumption A3-2.

Analysis

1. Consider an orthotropic material (Note N-1) having equivalent stress and equivalent strain (according to Korhonen):

$$\begin{aligned} \bar{\sigma} &= \left(\frac{3}{2b + 2c - 2} \right)^{1/2} (c\sigma_1^2 + b\sigma_2^2 - 2\sigma_1\sigma_2)^{1/2} \\ d\bar{\epsilon} &= \frac{1}{\sqrt{3}} \left(\frac{2b + 2c - 2}{bc - 1} \right)^{1/2} (bd\epsilon_1^2 + cd\epsilon_2^2 + 2d\epsilon_1d\epsilon_2)^{1/2} \\ f(\sigma_1, \sigma_2) = \bar{f}(\bar{\sigma}) &\Rightarrow \frac{\partial f}{\partial \sigma_1} + \frac{\partial f}{\partial \sigma_2} = \frac{d\bar{f}}{d\bar{\sigma}} \frac{c - 1 + m(b - 1)}{(c - 2m + bm^2)^{1/2}} \left(\frac{3}{2b + 2c - 2} \right)^{1/2} \end{aligned} \quad (42)$$

Such that (with $m \equiv \sigma_2/\sigma_1$).

$$\dot{f} - \dot{F} = \frac{d\bar{f}}{d\bar{\sigma}} \dot{\bar{\sigma}} - F'(W)\dot{W} = \frac{d\bar{f}}{d\bar{\sigma}} - F'(W)\bar{\sigma}\dot{\bar{\epsilon}} = 0 \quad (43)$$

Thus

$$F'(W) = \frac{d\bar{f}}{d\bar{\sigma}} \frac{1}{\bar{\sigma}} \frac{d\bar{\sigma}}{d\bar{\epsilon}} = \frac{1}{Z} \frac{d\bar{f}}{d\bar{\sigma}} \quad (44)$$

where Z is the subtangent found from universal curve $\bar{\sigma} = \bar{\sigma}(\bar{\epsilon})$. If the universal flow is of Ramberg-Osgood type (A1-3), then

$$\bar{\varepsilon}_u = nZ = n \sqrt{\frac{2}{3}} \sqrt{b+c-1} \frac{(c-2m+bm^2)^{1/2}}{c-1+m(b-1)} \quad (45)$$

Its in-plane components are found from definition of equivalent strain and Levi-Mises equations as follows:

$$\varepsilon_{1u} = n \frac{c-m}{c-1+m(b-1)}, \quad \varepsilon_{2u} = n \frac{bm-1}{c-1+m(b-1)} \quad (46)$$

such that the straight line

$$\varepsilon_{1u} + \varepsilon_{2u} \leq n \quad (47)$$

delimits uniform strain state as instability onset. The above equation has been already written in Ref. /1/ for isotropic solids. Here, it is shown that the same equation holds for orthotropic solids as well. It is worthy to note that the same result holds irrespective of the definition of equivalent stress and equivalent strain used. In the special case of uniaxial stress tension $m = 0$, uniform equivalent strain is reduced to

$$(\bar{\varepsilon}_u)^{uni} = nZ^{uni} = n \sqrt{\frac{2}{3}} \sqrt{b+c-1} \frac{\sqrt{c}}{c-1} \quad (48)$$

Following Ref. /11/ let us define ductility as ratio of general limit strain versus limit strain at uniaxial tension:

$$\mathcal{M} = \frac{\bar{\varepsilon}_u}{(\bar{\varepsilon}_u)^{uni}} \quad (49)$$

This universal measure of instability onset is easily calculated from above formulae:

$$\mathcal{M} = \frac{\sqrt{1-2m/c+m^2b/c}}{1+m[(b-1)/(c-1)]} \equiv T_f^* \quad (50)$$

where a modified triaxiality factor

$$T_f^* = \frac{1+m(b-1)/(c-1)}{\sqrt{1-2mc/c+m^2b/c}} \quad (51)$$

reduces to the known form $T_f = tr \mathbf{T}/\bar{\sigma}$ in the special case of isotropy when $b = c = 2$.

At the end of this subsection the following comments seem necessary:

- The point that the assumption A3-1 is not connected to the other assumptions and the analysis subsequently presented above seems interesting. Thus, if the above criterion is valid, then its validity is not necessarily restricted to strain range $\dot{\varepsilon}_1 > 0$, $\dot{\varepsilon}_2 < 0$.
- At first sight the assumption A3-1 seems unquestionable and physically well grounded. However, if elastic strains are not neglected, then the results hold only for plastic but not for total strain. On the other hand, plastic volume change could also be significant at advanced plastic strains due to holes development and coalescence.

2.4. Localized instability due to initial geometric imperfections

Here it is assumed that material instability originates from an initial thinning developing catastrophically into fracture.

In this field fundamental is the contribution of Marciniak and Kuczynski /22/. In the literature dealing with the subject their approach is denoted by M-K for brevity.

Another paper to be considered is /21/. It is also purely analytical aiming to compare criteria dealt with diffuse and localized instability.

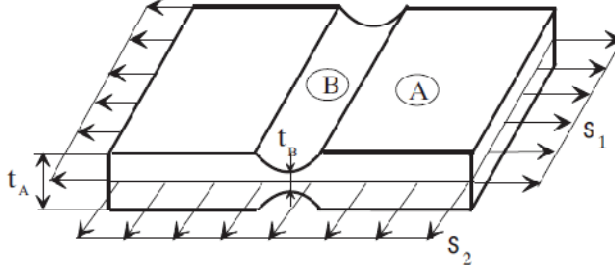


Figure 4: The thin sheet with groove of Marciniak and Kuczynski /22/

Assumptions

A4-1. For the plane sheet specimen considered (Fig. 4) an initial geometric imperfection given by two symmetric very shallow grooves $1 - t_{B_0}/t_{A_0} \ll 1$ is assumed. Moreover, a plane tension is considered such that one of principal stresses is along the groove whereas, the other is perpendicular to it such that stress state is close to equibiaxial (i.e. $\sigma_1 > \sigma_2 > (\sigma_1/2) > 0$, $\tau_{12} = \tau_{23} = \tau_{31} = 0$).

A4-2. Rigid rate independent plasticity of transversely isotropic material (its direction being normal to the sheet) is accepted with evolution equations

$$d\varepsilon_1 = [(R + 1)\sigma_1 - R\sigma_2]d\lambda, \quad d\varepsilon_2 = [-R\sigma_1 + (R + 1)\sigma_2]d\lambda, \quad d\varepsilon_3 = -(\sigma_1 + \sigma_2)d\lambda \quad (52)$$

originating by the associate flow rule from the following yield function

$$2f \stackrel{\text{def}}{=} \frac{2}{3} \frac{\bar{\sigma}^2}{h(\bar{\varepsilon})} = 1 \quad (53)$$

where $h(\bar{\varepsilon})$ is hardening function. Here equivalent stress and equivalent strain increment are respectively given by

$$\bar{\sigma} = \frac{\sqrt{3}}{\sqrt{2}} \frac{1}{\sqrt{2+R}} \{ (R+1)(\sigma_1^2 + \sigma_2^2) - 2R\sigma_1\sigma_2 \}^{\frac{1}{2}} \quad (54)$$

$$d\bar{\varepsilon} = \frac{\sqrt{2}}{\sqrt{3}} \sqrt{\frac{2+R}{1+2R}} \{ d\varepsilon_1^2 + d\varepsilon_2^2 + R d\varepsilon_3^2 \}^{\frac{1}{2}} \quad (55)$$

which follow from Korhonen's expressions assuming that $R_1 = R_2 = R$. Their product amounts to the infinitesimal increment of plastic work, i.e.

$$d\bar{\varepsilon} := \frac{dW_p}{\bar{\sigma}} \approx d\bar{\varepsilon}_p \quad (56)$$

The two formulae (54) and (55), are also derived directly from the book of Hill /28/ (chapter on anisotropic plasticity) with the yielding anisotropy parameter

$$R = 2 \frac{\sigma_{y_3}^2}{\sigma_{y_1}^2} - 1 \quad (57)$$

($\sigma_{y_1} = \sigma_{y_2} \neq \sigma_{y_3}$ are uniaxial yield stresses in indicated directions). Apart from a typographic mistake in $d\bar{\varepsilon}$ (where on RHS in M-K they have $\varepsilon_1^2 + d\varepsilon_2^2 + d\varepsilon_3^2$), constants in $\bar{\sigma}$ and $d\bar{\varepsilon}$ are slightly different here, but it does not influence the final results.

A4-3. For proportional stress paths with constant ratio of two in-plane principal stresses $m := \sigma_2/\sigma_1 = \text{const}$) we obtain

$$\frac{d\varepsilon_3}{d\varepsilon_2} = \frac{1+m}{r-(r+1)m} \equiv \alpha \quad (58)$$

equivalent stress - equivalent strain relationship

$$\bar{\sigma} = c_1(\varepsilon_0 + \bar{\varepsilon})^n \quad (59)$$

Analysis

1. Cutting the specimen, depicted in Fig. 4, along the grooves across the minimal cross section and writing equilibrium equations Marciniak and Kuczynski have obtained $\sigma_{1A}t_A = \sigma_{1B}t_B$. For the grooved cross section stress path is in general non-proportional. Thus, they introduced an additional scalar function

$$u = \frac{\sqrt{3}}{\sqrt{2}} \frac{1}{\sqrt{R+1}} \frac{\sigma_{1B}}{\sigma_B} \quad (60)$$

whose variability is responsible for non-proportionality. Inserting it into the above expression for $\bar{\sigma}$ and differentiating leads to

$$\frac{du}{u} = \frac{d\bar{\sigma}_A}{\bar{\sigma}_A} - \frac{d\bar{\sigma}_{1B}}{\bar{\sigma}_B} - d\varepsilon_{3A} - d\varepsilon_{3B} \quad (61)$$

where strain increment components perpendicular to sheet plane are

$$d\varepsilon_{3A} = \frac{dt_A}{t_A}, \quad d\varepsilon_{3B} = \frac{dt_B}{t_B}$$

From the assumption A4-1 there follows that $d\varepsilon_{3A} < 0$, $d\varepsilon_{3B} < 0$. Then two principal stresses in the grooved cross section are connected by

$$\frac{\sigma_{2B}}{\sigma_{1B}} = \frac{R}{R+1} + \frac{\sqrt{2R+1}\sqrt{1-u^2}}{R+1} \frac{1}{u} \quad (62)$$

Here, the authors tacitly assumed that stress state is nearer to equibiaxial case leading to $\alpha < 0$, $d\varepsilon_2 > 0$. Then Eqs. (52) allow

$$\begin{aligned} d\bar{\varepsilon}_B &= \sqrt{\frac{1+2R}{1+R}} \sqrt{\frac{2}{3}} (1-u^2)^{-1/2} d\varepsilon_2 \\ d\bar{\varepsilon}_{3B} &= -\left(\frac{\sqrt{1+2R}}{1+R} u(1-u^2)^{-1/2} + \frac{1}{1+R} \right) d\varepsilon_2 \end{aligned} \quad (63)$$

Now, inserting Eq. (63) into Eq. (61) and taking into account Eq. (59) in its differential form, Marciniak and Kuczynski obtained the following integral-differential equation

$$\frac{du}{u} = \left\{ \frac{1}{A_1 + B_1 \varepsilon_2} + E_1 + (1-u^2)^{-1/2} \left(C_1 u - \frac{1}{D_1 + B_1 \int (1-u^2)^{-1/2} du} \right) \right\} d\varepsilon_2 \quad (64)$$

with constants

$$\begin{aligned} A_1 &= \sqrt{3} \left(1 + \alpha + \frac{1+R}{2} \alpha^2 \right)^{-1/2} \frac{\varepsilon_0}{2n}, & B_1 &= \frac{1}{1+R} + \alpha \\ C_1 &= \frac{\sqrt{2R+1}}{R+1}, & D_1 &= \frac{\sqrt{3}}{2} \left(\frac{1+R}{1+2R} \right)^{1/2} \frac{\varepsilon_0}{n}, & E_1 &= \frac{1}{1+R} + \alpha \end{aligned} \quad (65)$$

Its solution depends mostly on initial value of geometric imperfection

$$u_0 = \left\{ \frac{1 + 2R}{1 + R} \right\}^{1/2} \{(1 + R)(1 + m^2 f_0^2) - 2Rmf_0\}^{1/2} \quad (66)$$

where $f_0 \equiv t_{1B}^0/t_{1A}^0$. The criterion of instability onset is postulated by the equality

$$\frac{d\bar{\varepsilon}_A}{d\bar{\varepsilon}_B|_{\bar{\varepsilon}_A=\bar{\varepsilon}_{MK}^*}} = 0$$

giving the limit strain $\bar{\varepsilon}_{MK}^* = \bar{\varepsilon}_u$. For a very ductile steel sheet with $m = 1$; $R = 1$; $n = 0.2$ and $\varepsilon_0 = 0.00136$ the authors have found that $0.98 < f_0 < 0.99$ fits experimental limit strain $\bar{\varepsilon}_A^* \approx 0.82$, (cf. Figure 1.5 in M-K, 1967). When $f_0 \rightarrow 1$, then $\bar{\varepsilon}_{MK}^* \rightarrow \infty$. The above, here given, formulae are slightly different than the corresponding in Ref./22/ correcting their typographical mistakes and applying the invariant formulation given Ref./22/.

In the paper /22/ the authors analysed in detail also the other factors influencing $\bar{\varepsilon}_{MK}^*$ such as m , n , ε_0 and R . They gave the important note that a linear initial distribution of voids could have similar effect as initial geometric imperfection f_0 .

2. In paper /21/ Korhonen considered localized instability in the same way as in previous text for isotropic and transversely isotropic metal sheets using Eq. (64) in Ref./22/, corrected for their typographical mistakes. He did not try, however, to derive these equations for the case of orthotropy which is usually induced by rolling of car body sheets.

On the other hand he wanted to compare diffuse instability criterion with the localized instability criterion.

After solving some typical stress states and some characteristic material symmetry, Korhonen drew following conclusions:

- a minimum in M-K limit curves in $(\varepsilon_1, \varepsilon_2)$ diagrams - forming limit diagrams (FLD) may appear near plane strain states where $\varepsilon_2 \approx 0$, $\varepsilon_3 \approx -\varepsilon_1$ caused by $\sigma_1 \approx 2\sigma_2$ in the considered cases of isotropy and transverse isotropy;
- M-K limit curves are higher when R in Eq. (62) is smaller, i.e. when ratio of in-plane yield stress versus normal-to-plane yield stress (σ_{y1}/σ_{y3}) decreases;
- sensitivity of M-K limit curves to material anisotropy is higher than sensitivity of Hill's (i.e. diffuse) limit curves;
- according to M-K limit curves maximal limit strains there appear during equibiaxial tension, whereas in Hill's limit curves a maximum between equibiaxial tension and plane strain usually appears
- Hill's necking subtangent is heavily influenced by the shape of function i.e. $\bar{\sigma} = \bar{\sigma}(\bar{\varepsilon}_p)$.

Its dependence on strain rate as well as temperature are often indispensable.

3. The best way to see applicability of a criterion is to apply it at diverse stress states and a real material. For this sake let us consider an by aluminium killed steel sheet, made of C0148P5 (JUS standard) equivalent to DIN St 24 of following chemical composition

	C	Mn	Si	P	S	Al
standard	0.08	0.45	traces	<0.03	<0.03	<0.02
measured	0.05	0.21	traces	0.012	0.019	0.07

and large randomly oriented ferritic grains oriented in rolling direction. Stress-strain relations at strain rate of about $8 \times 10^{-3} s^{-1}$ obtained from tension tests read

$$\begin{aligned} \sigma &= c_1(\varepsilon_{01} + \varepsilon^{n1}) \equiv 388.3(0.456 + \varepsilon^{0.448}) \quad (\text{rolling direction}) \\ \sigma &= c_2(\varepsilon_{02} + \varepsilon^{n2}) \equiv 405.2(0.444 + \varepsilon^{0.428}) \quad (\text{transverse to rolling}) \end{aligned} \quad (67)$$

$\sigma = c_3(\varepsilon_{03} + \varepsilon^{n3}) \equiv 418(0.4337 + \varepsilon^{0.417})$ (direction inclined by 45°) according to experiments and a best fit made in Ref./9/. Although the above functions are not suitable for small strains, when $\varepsilon \rightarrow 0$, $(d\sigma/d\varepsilon) \rightarrow \infty$ they permit determination of material constants r_1 and r_2 appearing in expressions for equivalent stress and equivalent strain. Indeed, rewriting them in the following form reminding us to the “universal” stress-strain curve

$$\begin{aligned}\bar{\sigma}\mathcal{K}_1 &= c_1[\varepsilon_{01} + (d\varepsilon/\mathcal{K}_1)^{n1}], & \bar{\sigma}\mathcal{K}_2 &= c_2[\varepsilon_{02} + (d\varepsilon/\mathcal{K}_2)^{n2}] \\ \bar{\sigma}\mathcal{K}_3 &= c_3[\varepsilon_{03} + (d\varepsilon/\mathcal{K}_3)^{n3}]\end{aligned}\quad (68)$$

where

$$3\mathcal{K}_1^2 = \frac{2+b+c}{c}, \quad 3\mathcal{K}_2^2 = \frac{2+b+c}{b}, \quad 3\mathcal{K}_3^2 = \frac{2+b+c}{5b+5c-12}$$

we may find in this case $c = 1.38$; $b = 1.3092$; $n = (1/3)(0.448 + 0.428 + 0.417) = 0.431$.

Deflections from universality given by $(n_i - n_j)/n_j$ are 6.92% and 4.46%, whereas measured by $(c_i\mathcal{K}_i^{-1-n_i} - c_j\mathcal{K}_j^{-1-n_j})/(c_j\mathcal{K}_j^{-1-n_j})$ amount even to 12.05% and 58.29%. This indeed gives rise dramatically to the question how correct is it to use a single curve $\bar{\sigma} = \bar{\sigma}(\bar{\varepsilon})$ for advanced strains.

Similar conclusion for cruciform specimen has been drawn before in Albertini et al. /26/ by simultaneous measurements of $(\varepsilon_1, \sigma_1)$ and $(\varepsilon_2, \sigma_2)$ diagrams.

4. A comprehensive graphical representation of results of M-K analysis for orthotropic materials with diverse type of line imperfections has been given in /4/. In this report results of M-K analysis are also compared with results of Hill's localized necking.

Concluding this subsection it is possible to say:

- Range of applicability of Hill-Korhonen criterion is wider than that of M-K criterion, since for the later McClintock's assumption of rigid shoulders along the groove is essential ingredient (equivalent to $\varepsilon_{2A} = \varepsilon_{2B}$). Linearity of FLD by means of $\varepsilon_{1u} + \varepsilon_{2u} \leq n$, Eq. (53), for all materials is doubtful and should be examined by experiments.
- Ductility \mathcal{M} found from Hill-Korhonen's criterion is insensitive to Ludwick exponent n , whereas \mathcal{M} found from M-K analysis is highly sensitive to value of n .

2.5. Gurson's approach to ductile rupture by void nucleation and growth

In this subsection Gurson's paper /18/ is analysed with some additional modifications concerning strain hardening of matrix materials, being neglected in /18/.

Assumptions

A5-1. Let the average (“macroscopic”, which means measurable) stress and strain be denoted by T and whereas matrix stress and its strain be \mathbf{T}_M and ε_M . Then, for either cylindrical or spherical voids and whole matrix plastified (i.e. Plastically deformed) he derived the following yield function

$$f = (\bar{\sigma}/\bar{\sigma}_M)^2 + 2\omega \cosh\left(\frac{\mathcal{X} \operatorname{tr}\mathbf{T}}{2\bar{\sigma}_M}\right) - 1 - \omega^2 = 0 \quad (69)$$

where $\mathcal{X} = \sqrt{3}$ for cylindrical and $\mathcal{X} = 1$ for spherical voids, while ω is volume fraction of voids, total volume of voids divided by body volume. Main assumptions in Eq. (69) are: (a) random voids are idealized by a single void; (b) matrix is rigid perfectly plastic and obeys Mises flow rule. Then integration leading to macroscopic stress when axisymmetric deformation takes place brings to Eq. (69).

Tvergaard /24/ modified the above yield function by two coefficients, q_1 ; q_2 , as follows

$$f = (\bar{\sigma}/\bar{\sigma}_M)^2 + 2\omega q_1 \cosh\left(\frac{1}{2} \mathcal{X} q_2 \frac{\text{tr}\mathbf{T}}{\bar{\sigma}_M}\right) - 1 - (q_1\omega)^2 = 0 \quad (70)$$

He suggested $q_1 = 1.5$, $q_2 = 1$ as an improvement.

A5-2. Void behaviour is governed by the following evolution

$$\dot{\omega} = (1 - \omega)\text{tr}\dot{\epsilon} + \mathcal{B}_1\dot{\bar{\epsilon}}_M + \mathcal{B}_1\dot{\bar{\epsilon}}_M + \mathcal{B}_2\text{tr}\dot{\mathbf{T}} \quad (71)$$

where first term is responsible for void growth, while $\mathcal{B}_1 > 0, \mathcal{B}_2 > 0$ describe void coalescence according to /24/. It is assumed here that void coalescence appears at some critical ω^* when instability abruptly leads to fracture. According to Gurson's assumptions $\omega^* = 1$, but Anderson, 1977, suggests $\omega^* = 0.25$ for the growth of a spherical void in the stress field in front of a crack tip. In the sequel \mathcal{B}_1 and \mathcal{B}_2 are neglected (Gurson assumed $\mathcal{B}_1 = 0, \mathcal{B}_2 = 0$).

A5-3. Equality of plastic work by matrix stress and strain versus work done by average stress and strain leads to

$$\text{tr}\{\mathbf{T}\dot{\epsilon}\} = (1 - \omega)\bar{\sigma}_M\dot{\bar{\epsilon}}_M \quad \text{or} \quad \sigma^{ij}\dot{\epsilon}_{ij} = (1 - \omega)\bar{\sigma}_M\dot{\bar{\epsilon}}_M \quad (72)$$

A5-4. An associate flow rule is postulated in the common form

$$\dot{\epsilon} = \Lambda \frac{\partial f}{\partial \mathbf{T}} \quad \text{or} \quad \dot{\epsilon}_{ij} = \Lambda \frac{\partial f}{\partial \sigma_{ij}} \quad (73)$$

In the standard way scalar function Λ is found either from consistency condition $\dot{f} = 0$ (rate independent plasticity) or it is a given function of stress and plastic strain (viscoplasticity).

Analysis

In the sequel it is supposed that $\mathcal{X} = 1$, i.e. voids have approximately spherical shape. Consider as in /18/ perfectly plastic matrix characterized by:

$$\bar{\sigma}_M = \sigma_0 = \text{const} \quad (74)$$

in plastic range. Then time differentiation of Eq. (69) combined with Eqs. (71) and (73) gives us plastic modulus Λ in the following form:

$$\Lambda = \mathcal{A}_1^0 \dot{\bar{\sigma}} + \mathcal{A}_2^0 \text{tr}\dot{\mathbf{T}} \quad (75)$$

where the coefficients are:

$$\mathcal{A}_1^0 = 2 \frac{\bar{\sigma}}{\bar{\sigma}_M^2} \left[6 \frac{\omega}{\bar{\sigma}_M} (1 - \omega)(\omega - C_1) S_1 \right]^{-1}, \quad \mathcal{A}_2^0 = \frac{\omega}{\bar{\sigma}_M} S_1 \left[6 \frac{\omega}{\bar{\sigma}_M} (1 - \omega)(\omega - C_1) S_1 \right]^{-1} \quad (76)$$

and denotations used

$$S_1 \equiv \sinh\left(\frac{\text{tr}\mathbf{T}}{2\bar{\sigma}_M}\right), \quad C_1 \equiv \sinh\left(\frac{\text{tr}\mathbf{T}}{2\bar{\sigma}_M}\right). \quad (77)$$

The governing differential equations are obtained inserting (75) in Eqs.(71) and (73)

$$\dot{\epsilon}_1 = (\mathcal{A}_1^0 \dot{\bar{\sigma}} + \mathcal{A}_2^0 \text{tr}\dot{\mathbf{T}}) \left(\frac{2\sigma_1 - \sigma_2}{\bar{\sigma}_M^2} + \frac{\omega S_1}{\bar{\sigma}_M} \right), \quad (78)$$

$$\dot{\epsilon}_2 = (\mathcal{A}_1^0 \dot{\bar{\sigma}} + \mathcal{A}_2^0 \text{tr}\dot{\mathbf{T}}) \left(\frac{2\sigma_2 - \sigma_1}{\bar{\sigma}_M^2} + \frac{\omega S_1}{\bar{\sigma}_M} \right), \quad (79)$$

$$\dot{\omega} = 3S_1 \frac{\omega(1-\omega)}{\bar{\sigma}_M} \left(\mathcal{A}_1^0 \bar{\sigma} + \mathcal{A}_2^0 tr \mathbf{T} \right) \quad (80)$$

Their integration for given stress history $\sigma_1(t), \sigma_2(t), \sigma_3(t)$, gives limit strains $\varepsilon_1(t^*), \varepsilon_2(t^*)$, where temporal onset of instability is found from $\omega(t^*) = \omega^*$. Numerical results of such an integration and the corresponding diagrams are given in /4/.

3. SOME COMMENTS ON EXPERIMENTAL EVIDENCE

The principal question is how to identify experimental problems of interest from the comprehensive literature on the localization and ductile failure. An effort is made to give a concise approach, since there are not clear boundaries between different applications.

3.1. Forming limit diagrams (FLD)

Due to their importance for applications in automotive industry there is a general agreement on main items, although sometimes misleading and wrongly interpreted.

Azrin and Backofen concluded /8/:

- the upper bound for limit strain is obtained from the condition $d\varepsilon_{1A}/d\varepsilon_{1B} = 0$ (M-K recommendation), whereas the lower bound corresponds to initiation of non-proportionality, i.e. $d\varepsilon_{2B}/d\varepsilon_{1B} \neq const$ (equivalent to $du \neq 0$);
- for AISI 301 commence of the upper bound comes abruptly (upper and lower bound almost coincide), dislike to ferritic steels where such a transition is smooth;
- the dependence of limit strain on strain ratio $d\varepsilon_{1B}^*/d(\varepsilon_{2A}/\varepsilon_{1A})$ is positive for ferritic steels, slightly negative for AISI 301 and almost constant for brass;
- making an artificially produced through (i.e. a straight scratch) they concluded that initial imperfection must be larger than in M-K theory.

Ghosh and Backofen report /10/:

- pronounced influence of strain history, as given by prestraining in diverse directions $\varepsilon_{2A}/\varepsilon_{1A}$ and then uniaxially pulled by $\sigma_{1A} \neq 0$, on limit strains;
- with respect to "orange peel" on surface their main outcome was that local neck did not evolve from early strain-induced roughening.

Tadros and Mellor in their paper /14/:

- show that localized neck is accompanied by a large increase of surface roughness for rimming steel, aluminium and soft 70/30 brass;
- conclude that experimentally found limit strains are lower than theoretically predicted instability strains (by M-K analysis);
- found initial imperfection f_0 in M-K theory fitting experimental data and theoretical curve;
- state that Hill's equations for plastic orthotropic materials with yield function defined by means of modified equivalent stress are reasonable for the killed steel but fail for aluminium and 70/30 brass;
- assume that deformation is uniform up to the general instability point.

The last conjecture is still open since it depends mainly on physical model and initial geometrical imperfection.

Aleksandrović /7/ has also investigated non-proportional stress paths taking special account to abrupt change of principal axes between phases and trying to apply some quasi-theoretical best-fit connecting experimental points of different phases, following /9/.

3.2 Some experiments concerning ductile failure

It is very important to understand conditions for specific mode of instability.

Manjoine from his experiments derived the following conclusions /11/:

- He defined ductility \mathcal{M} and Davis triaxiality factor T_f as

$$\mathcal{M} \stackrel{\text{def}}{=} \frac{\bar{\varepsilon}}{(\bar{\varepsilon})_{uniax}}, \quad T_f = \frac{tr\mathbf{T}}{\bar{\sigma}} \quad (81)$$

and claims that they are roughly in inverse proportion; more precisely he assumed

$$\mathcal{M} = \min\{1/T_f, 2^{1-T_f}\} \quad (82)$$

i.e. lower of the two curves dependent on T_f .

- For elevated temperatures, long service life and small strain rates two major modes of damage leading to failure hold: (a) crack initiation and growth by a maximum principal stress history and (b) accumulation of shear strain up to strain instability.
- With reference to strength of grains and their boundaries mode (a) corresponds to grains stronger than their boundaries (appearing at lower strain rates and higher temperatures), whereas mode (b) is inverse to the above.

According to this, he suggested the following damage evolution equation

$$\mathcal{M} = f \left\{ \sum (t_i/t_r)_{\sigma_{max}}, \quad \sum (\varepsilon_i/\varepsilon^*)_{\varepsilon, \mathbf{T}} \right\} \quad (83)$$

where t_r is rupture time at fixed maximum principal stress, $\sigma_{max} \equiv \sigma_M$, ε^* is limit strain at given strain rate, $\dot{\varepsilon}$, and true stress, \mathbf{T} .

For a ductile alloy “D” ultimate strength (corresponding to maximal principal engineering stress) decreases slowly with temperature for $0^\circ F - 400^\circ F$; is practically constant in the interval $400^\circ F - 800^\circ F$ and then steeply decreases until $1400^\circ F$.

(Lindholm et al, /35/) performed biaxial tensile experiments (tension-torsion) on beryllium and titanium specimens with following remarks:

- ductility is significantly reduced under biaxial tensile stresses, opposite to low-carbon steels where critical subtangent $Z = 2$ for equibiaxial and $Z = 1$ for uniaxial tension;
- precompression could exhaust ductility and to lead to brittle fracture in subsequent tensile loading (such a conclusion seems strange since compressive loading closes voids and by plastic volume change should increase ductility);
- more generally strain history defined by diverse prestraining strain states (most primitively by Bauschinger effect) influences limit strains very much;
- confirm mentioned importance of surface roughness on failure detection and grain size;
- ductility for the tested materials is maximal for pure shear, whereas smaller and equal for uniaxial tension and equibiaxial tension but minimal for $\sigma_1/\sigma_2 = 0.5$; and
- they promote Mogi's criterion dependent on stress invariants as follows

$$f(\bar{\sigma}, T_f, \sigma_{max}, \tau_{max}) = (A + B)\bar{\sigma}T_f + B\bar{\sigma}^2 + C(\tau_{max} - 2\sigma_{max}) = 1 \quad (84)$$

where $\sigma_{max} \equiv \sigma_1$, $\tau_{max} \equiv \sigma_1 - \sigma_3$, and $\sigma_1 > \sigma_2 > \sigma_3$ are principal stresses.

Vavakin et al. /15/ investigated short term creep by staircase temporal stress loading programs (Fig. 5. a and b) as well as by hold times at M–P and P–M nonproportional paths in Hochenemser experiment (Fig. 5. c – vertices D_1 , D_2 as hold points). Their conclusion follows a previous experiments by Zhukov and Rabotnov /16/ and confirms existence of short creep processes at abrupt change of stress trajectories.

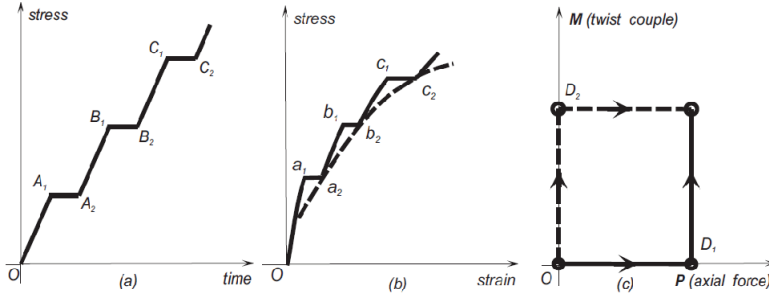


Figure 5: Subfigures (a) and (b) show staircase stress paths aimed to detect static yield surface /15/, while at subfigure (c) Hohenemser classical non-proportional stress paths are shown

Schwer et al reported experiments on cylindrical tanks under and without internal pressure when hit, locally to a spot, radially by a stream mild detonating fuze /13/. They concluded that deformability is considerably reduced by internal pressure. The relationship of this experiment to an experiment by means of biaxial Hopkinson bar in Dynamic material testing laboratory in JRC-Ispira was discussed in /5/.

Mason et al measured continuously during Hopkinson bar experiment change of temperature in order to calibrate Γ in the equation for transfer of plastic work into heat /12/

$$d\theta \approx -\frac{\Gamma}{\rho c_p} \hat{d}W_p \quad (85)$$

under assumption of adiabatic conditions and small elastic strain as in Ref. /33/. The measurement was performed by high speed infrared detectors. Although such an experiment is not devoted to failure, measurement of detecting temperature is important, /25/.

Multiaxial tests aimed to characterize inelastic behaviour of steel and other materials by means of sophisticated specimen (like “bicchierino” and cruciform specimen, Ref. /32/) have been made in Dynamic material testing laboratory of the Institute of nuclear safety (JRC) in Ispira during last years. The accumulated experience allows a new more profound insight into most interesting material behaviour at complex stress paths leading to multiaxial stress as well as strain states. From this experience and other experimental as well as theoretical work two principal features should be on-line detected during each test namely

- time dependent change of temperature; and
- plastic volume change, especially at advanced stage of failure process.

The obtained results are presented in /32/ and the other reports by Mićunović for this for this laboratory covering multiaxial stress-strain histories, as well as in small to high strain rate ranges.

4. CONCLUDING REMARKS

Some results to be noted are the following:

- Clear procedure of treatment of test records obtained by strain gauge as well as photo recorded grid measurements is given. This procedure given in the appendix shows how to get correct stress and strain measures at finite strains, static as well as dynamic tests in order to perform constitutive modelling and localization analysis. The corresponding program is written in MATLAB-code in such a way that once Lagrangian total strain

components EKL and engineering stress components are known, then all tensorial quantities and invariants are calculated.

- Constitutive modelling by Johnson-Cook (JC) /30/, Armstrong-Zerilli (AZ) /27/ and simplified Zener-Hollomon (ZH) models, are improved to include higher strain rates.
- A manifold of existent localization criteria like McClintock's, Hill-Korhonen's, Marciniak-Kuczynski is applied to same real materials (mainly aluminium killed steel) as well as some hypothetical materials. A special attention is paid to Gurson's fracture criterion which allowed for higher values of fracture strains than found by experiments. It should be noted, however, that in recent research of M.M. with coworkers these strains are significantly smaller when thermal effects are taken into account.

Some additional conclusions are also have to be considered:

- Manjoine's triaxiality T_f , which accounts also on trace of stress tensor, is one of the most important analytical parameters for damage characterization and monitoring.
- Identification of constitutive models based on the associate flow rule, as (JC), (AZ) and (ZH) model may be considered as successful since all the models permitted calibration of separate as well as simultaneous consideration of groups G_1 and G_2 . Such an ability originated from the fact that a linear relationship between equivalent plastic strain rate and equivalent stress rate $\dot{\varepsilon}_p^{eq} = \exp(-\mathcal{N})\dot{\sigma}^{eq}$ has been found and the corresponding universal material constant \mathcal{N} calibrated. It is called "universal" since its value does not depend on constitutive model chosen for the analysis. Another "universality" introduced by relationships of the type $\sigma^{eq} = \Phi(\varepsilon_p^{eq}, \dot{\varepsilon}_p^{eq})$ fails. It had been shown that AZ-approach based on dislocation mechanics is superior over the others two.
- The model based on tensor functions has shown its superiority far above all the mentioned models even in its simplest version with only three material constants. Not only its highest correlation coefficients but its best qualitative agreement with experiments was very good. Such a model has been shown to be solely able to cover small, medium and high strain rates at shear, uniaxial tension by traditional cylindrical specimen as well as biaxial tension by cruciform specimen tests /34/, whereas all traditional associate flow rule models with "universal" flow rule assumption failed.

Let us note at the end of this review that for the sake of brevity non-proportional stress histories given in /4/ are not included here. As mentioned in the introduction they are very important for all plastically deforming real structures.

REFERENCES

Reviews on ductile fracture criteria

1. Dodd, B. and Bai, Y. (1987): *Ductile Fracture and Ductility*, London, Academic Press.
2. McClintock, F. A. (1971): *Plasticity Aspects of Fracture*, in: Liebowitz. H., (ed.), *Fracture*, Academic Press, Vol.III, pp. 48-227.
3. Manjoine, M. J. (1971): *Multiaxial stress and fracture*, in: Liebowitz. H.,(ed.), *Fracture*,Academic Press, Vol.III, pp. 265-309.
4. Mićunović, M. *Study of Ductile Failure Criteria Under Multiaxial Loading*, Contract No5364-93-06 ED ISP YU, Final Report, JRC CEC - Ispra, Italy 1999.
5. Mićunović, M. *Study of Ductile Failure Criteria Under Multiaxial Loading* (Biaxial Hopkinson Tests), Contract No 5364-93-06 ED ISP YU, Final Report, JRC CEC - Ispra, Italy
Experimental papers dealing with ductile fracture
6. Albertini, C. (1994): *Private communication*.

7. Aleksandrović, S., (1993): *Formability of thin sheets for non-monotonous plastic deformation processes*, MSc-thesis, Fac.Mech.Engng., Kragujevac.
8. Azrin, M. and Backofen, A. (1970): *The deformation and failure of a biaxially stretched sheet*, Metal. Transactions, 1, pp.2857-2865.
9. Devedzić, B. and Stefanović, M., (1987): *Effects of the friction and deformation path on stretch-formability of sheet metal*, 2nd Int.Conf.Technology of Plasticity, Stuttgart, pp.437-444.
10. Ghosh, A.K., and Backofen, A. (1973): *Strain hardening and instability in biaxially stretched sheets*, Metal. Transactions, 4, pp.1113-1123.
11. Manjoine, M. J. (1982): *Creep-rupture behaviour of weldments*, Welding Research Supplement, February, pp. 50-57.
12. Mason, J.J., Rosakis, A.J. and Ravichandran, G. (1992): *On the strain and strain-rate dependence of the fraction of plastic work converted to heat: an experimental study using high speed infrared detectors and the Kolski bar*, SM Report 92-33.
13. Schwer, L.E., Holmes, B.S. and Kirkpatrick, S.W. (1988): *Response and failure of metal tanks from impulsive spot loading: experiments and calculations*, Int. J. Solids Structures, Vol.24, No. 8., pp. 817-833.
14. Tadros, A. K. and Mellor, P. B. A. (1978): *An experimental study of the in-plane stretching of sheet metal*, Int. J. Mech. Sci., Vol. 20., pp. 121-134.
15. Vavakin, A.S., Viktorov, V.V., Mohel, A.N. and Stepanov, L.P. (1986): *On creep influence on plastic deformation of steel during complex loading*, (in Russian), in: Physics of Strength and Plasticity, ed. S. N. Zhurkov, Nauka, St. Petersburg, pp. 142-148.
16. Zhukov, A.M., and Rabotnov, Yu. N. (1954): *Research on plastic deformation of steel during complex loading*, (in Russian), MTT, vol. 18., pp. 105-112.

Analytical papers dealing with ductile fracture

17. Berg, C. A. (1962): *The motion of Cracks in Plane Viscous Deformation*, ASME Proceedings of the Fourth U.S. National Congress of Applied Mechanics, Vol. 2., pp. 885-892.
18. Gurson, A.L., (1977): *Continuum Theory of Ductile Rupture by Void Nucleation and Growth: Part I - Yield Criteria and Flow Rules for Porous Ductile Media*, J.Engng.Materials Technol.Vol.99, p.2-15.
19. Hill, R., (1957): *On the Problem of Uniqueness in the Theory of a Rigid Plastic Material - III*, J.Mech.Phys.Solids Vol. 5, p. 153-161.
20. Hillier, M. J. (1963): *Tensile Plastic Instability under Complex Stress*, Int. J. Mech. Sci., Vol.5, pp.57-67.
21. Korhonen, A. S. (1968): *On the Theories of Sheet Metal Necking and Forming Limits*, ASME J. Engng. Mat. Technology, Vol. 100., pp. 303-309.
22. Marciniak, Z. and Kuczyński, K., (1967): *Limit strains in the processes of stretch-forming sheet metal*, Int. J. Mech. Sci., Vol. 9, No. 9, p. 609-620.
23. McClintock, F. A. (1968): *A Criterion for Ductile Fracture by the Growth of Holes*, ASME J.Appl. Mech., Vol. 35., pp. 363-371.
24. Tverdaard, V. (1982): *On localization in Ductile Materials containing Spherical Voids*, Int. J. Fracture, Vol.18, pp. 237-252.

General references related to the subject

25. Albertini, C., Montagnani, M and M. Mićunović (1989): *Viscoplastic Behaviour of AISI 316 H-Multiaxial Experimental Results in:* Hadjian (ed.), Transactions of SMIRT-10, Los Angeles
26. Albertini, C., Montagnani, M and M. Mićunović: (1991): *Viscoplastic behaviour of AISI 316H: multiaxial experimental results and preliminary numerical analysis*, Nuclear Engineering and Design, 130, pp. 205-210.
27. Armstrong, R and Zerilli, F. (1988): *Dislocation mechanics based analysis of material dynamics behaviour*, J. de Physique, 49, pp. C3-59.
28. Hill, R. (1950): *The Mathematical Theory of Plasticity*, Oxford :Clarendon.

29. Hill, R., (1952): *On Discontinuous Plastic States with Special Reference to Localized Necking in Thin Sheets*, J.Mech.Phys.Solids Vol. 1, p. 19-30.
30. Johnson, G. R. and Cook W. H. (1983): in: Proceedings of the Seventh Int. Symp. On Ballistics, The Hague, p. 541.
31. Mićunović, M., (1985): *A Yield Condition for Anisotropic Materials*, Transactions Of SMIRT-8, 243-250, North-Holland, Amsterdam.
32. Mićunović, M., Nikezić and Rubesa, D. (1991): Contract No 4020-90-06 ED-ISP-YU: *Influence of Irradiation on the Inelastic Behaviour of AISI 316 Austenitic Stainless Steels Described by Uniaxial Dynamic Experiments and Constitutive Equations* - final report.
33. Mićunović, M. (1992): *On the thermal elastoplastic transition in viscoplasticity of metals*, Facta Univ. Ser. Mech. Autom. Contr. and Rob. (Univ. of Niš), Vol.1, No.2, p.155.
34. Mićunović, M., Albertini, C. and Montagnani, M., (1997): *High strain rate viscoplasticity of AISI 316H stainless steel from tension and shear experiments*, (in: Solid Mechanics) Scientific Meetings of the Serbian Academy of Sciences and Arts, Dept. Techn. Sci., Vol. LXXXVII, Book 3, pp97-106.
35. Lindholm, U.S., Yeakly, L.M. and Davidson D.L., (1974): *Biaxial strength on beryllium and titanium alloys*, Report AFML-TR-74-172.

A. STRESS AND STRAIN MEASURES

A.1. General stress and strain measures used to describe plastic behaviour

Kröner's decomposition rule:

$$\mathbf{F} = \mathbf{F}_E \mathbf{F}_P, \quad F_E = [1 + \alpha(\Theta - \Theta_0)] F_e \quad (\text{A.1})$$

Deformation gradient tensor:

$$\mathbf{F} = \mathbf{1} + \text{GRAD } \vec{u} \quad (\text{A.2})$$

$$\mathbf{F} = \begin{Bmatrix} 1 + \frac{\partial u_1}{\partial X_1} & \frac{\partial u_1}{\partial X_2} & \frac{\partial u_1}{\partial X_3} \\ \frac{\partial u_2}{\partial X_1} & 1 + \frac{\partial u_2}{\partial X_2} & \frac{\partial u_2}{\partial X_3} \\ \frac{\partial u_3}{\partial X_1} & \frac{\partial u_3}{\partial X_2} & 1 + \frac{\partial u_3}{\partial X_3} \end{Bmatrix} \equiv \begin{Bmatrix} 1 + u_{11} & u_{12} & u_{13} \\ u_{21} & 1 + u_{22} & u_{23} \\ u_{31} & u_{32} & 1 + u_{33} \end{Bmatrix}$$

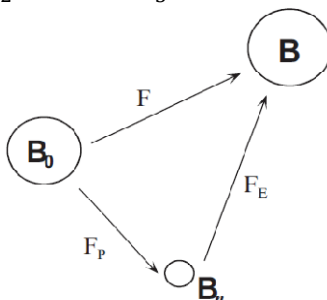


Figure A1: Kröner's deformation decomposition

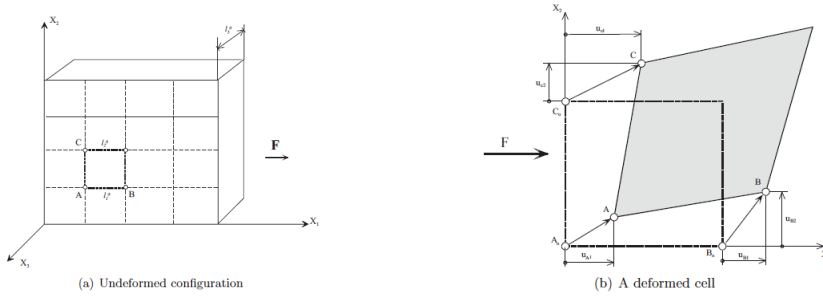


Figure A2: In-plane grid measurements.

Lagrangian total strain tensor:

$$2\mathbf{F} = \mathbf{F}^T \mathbf{F} - \mathbf{1} = \begin{Bmatrix} E_{11} & E_{12} & E_{13} \\ \text{sym} & E_{22} & E_{23} \\ & & E_{33} \end{Bmatrix} \quad (\text{A.3})$$

Eulerian total strain tensor:

$$2\mathbf{e} = \mathbf{1} - \mathbf{F}^{-T} \mathbf{F}^{-1} = \mathbf{F}^{-T} \mathbf{E} \mathbf{F}^{-1} \quad (\text{A.4})$$

Lagrangian plastic strain tensor:

$$\mathbf{E}_p = [1 - 2\alpha(\Theta - \Theta_0)]\mathbf{E} - \alpha(\Theta - \Theta_0)\mathbf{1} - \mathbf{F}^{-T} \mathbf{E}_e \mathbf{F} \quad (\text{A.5})$$

Eulerian plastic strain tensor (under the assumption $\mathbf{F}_e = \mathbf{R}_e \mathbf{U}_e$, $\mathbf{R}_e = \mathbf{1}$):

$$\mathbf{e}_p = [\Theta - \Theta_0]\mathbf{e} - \alpha(\Theta - \Theta_0)\mathbf{1} + \mathbf{E}_e \mathbf{e} + \mathbf{e} \mathbf{E}_e - \mathbf{E}_e \quad (\text{A.6})$$

Hill's logarithmic plastic strain tensor:

$$\varepsilon_p = \frac{1}{2} \ln(\mathbf{F}_p \mathbf{F}_p^T) \quad (\text{A.7})$$

Cauchy (true) stress tensor and its deviator:

$$\mathbf{T} = \begin{Bmatrix} \sigma_1 & 0 & 0 \\ 0 & \sigma_2 & 0 \\ 0 & 0 & 0 \end{Bmatrix}, \quad \sigma_1 = \frac{F_1}{A_1}, \quad \sigma_2 = \frac{F_2}{A_2} \quad (\text{A.8})$$

$$\mathbf{T}' = \frac{1}{3} \begin{Bmatrix} 2\sigma_1 - \sigma_2 & 0 & 0 \\ 0 & 2\sigma_2 - \sigma_1 & 0 \\ 0 & 0 & -\sigma_1 - \sigma_2 \end{Bmatrix} \quad (\text{A.9})$$

Mises equivalent true stress (compare (A9)):

$$\sigma_{eq} = \sqrt{\frac{3}{2} \text{tr}\{\mathbf{T}'^2\}} = \sqrt{\sigma_1^2 + \sigma_2^2 - \sigma_1 \sigma_2} \quad (\text{A10})$$

Second Piolo-Kirchhoff stress tensor

$$\mathbf{S} \approx \mathbf{T} - \mathbf{E}_e \mathbf{T} - \mathbf{T} \mathbf{E}_e \quad (\text{A11})$$

Hooke's law:

$$\mathbf{E}_e = \frac{1}{E} [(1 + \nu)\mathbf{S} - \nu \mathbf{1} \text{tr}\mathbf{S}] \quad (\text{A.12})$$

$$\mathbf{E} \mathbf{E}_e = (1 + \nu)(\mathbf{T} - \mathbf{E}_e - \mathbf{T} \mathbf{E}_e) - \nu \mathbf{1} \text{tr}(\mathbf{T} - \mathbf{E}_e \mathbf{T} - \mathbf{T} \mathbf{E}_e) \quad (\text{A.13})$$

should be solved iteratively to find \mathbf{E}_e from \mathbf{T} : Nominal (engineering) stress tensor:

$$\mathbf{T}^{eng} = (\det \mathbf{F}) \mathbf{T} \mathbf{F}^{-T} \quad (\text{A.14})$$

Mises equivalent engineering stress (from (A.14)):

$$\sigma_{eq}^{eng} = \sqrt{\frac{3}{2} \text{tr}\{\mathbf{T}'_{eng}{}^2\}} \quad (\text{A.15})$$

Plastic stretching tensor (plastic “strain rate”).

$$2\mathbf{D}_P = \dot{\mathbf{F}}_P \mathbf{F}_P^{-1} + \mathbf{F}_P^{-T} \dot{\mathbf{F}}_P^T \quad (\text{A.16})$$

Equivalent plastic strain rate:

$$\dot{\varepsilon}_{eq}^P = \sqrt{\frac{2}{3} \text{tr}\mathbf{D}_P^2} \quad (\text{A.17})$$

Special case of small strains - applicable to strain gage measurements

$$\begin{aligned} & \begin{Bmatrix} \varepsilon_{11} & 0 & 0 \\ 0 & \varepsilon_{22} & 0 \\ 0 & 0 & \varepsilon_{33} \end{Bmatrix} \approx \begin{Bmatrix} u_{11} & 0 & 0 \\ 0 & u_{22} & 0 \\ 0 & 0 & u_{33} \end{Bmatrix} \\ \mathbf{E} \begin{Bmatrix} \varepsilon_{11}^E & 0 & 0 \\ 0 & \varepsilon_{22}^E & 0 \\ 0 & 0 & \varepsilon_{33}^E \end{Bmatrix} & \approx \begin{Bmatrix} \sigma_{11} - \nu\sigma_{22} & 0 & 0 \\ 0 & \sigma_{22} - \nu\sigma_{11} & 0 \\ 0 & 0 & -\nu\sigma_{11} - \nu\sigma_{22} \end{Bmatrix} \\ & \begin{Bmatrix} \varepsilon_{11}^P & 0 & 0 \\ 0 & \varepsilon_{22}^E & 0 \\ 0 & 0 & \varepsilon_{33}^P \end{Bmatrix} \approx \begin{Bmatrix} \varepsilon_{11} - \varepsilon_{11}^E & 0 & 0 \\ 0 & \varepsilon_{22} - \varepsilon_{22}^E & 0 \\ 0 & 0 & \varepsilon_{33} - \varepsilon_{33}^E \end{Bmatrix} \\ & \begin{Bmatrix} D_{11}^P & 0 & 0 \\ 0 & D_{22}^P & 0 \\ 0 & 0 & D_{33}^P \end{Bmatrix} \approx \begin{Bmatrix} \dot{\varepsilon}_{11}^P & 0 & 0 \\ 0 & \dot{\varepsilon}_{22}^P & 0 \\ 0 & 0 & \dot{\varepsilon}_{33}^P \end{Bmatrix} \end{aligned}$$

Invariants appearing in evolution equations

$$s_2 = \text{tr}\{\mathbf{T}'^2\} = \frac{2}{3}(\sigma_1^2 + \sigma_2^2 - \sigma_1\sigma_2) \equiv \frac{2}{3}\sigma_{eq}^2$$

$$s_3 = \text{tr}\{\mathbf{T}'\varepsilon_p\} = \frac{1}{27}[(2\sigma_1 - \sigma_2)^3 + (2\sigma_2 - \sigma_1)^3 + (\sigma_1 + \sigma_2)^3]$$

$$\begin{aligned} \mu_1 = \text{tr}\{\mathbf{T}'\varepsilon_p\} &= \{(2\sigma_1 - \sigma_2)\log p_1 + (2\sigma_2 - \sigma_1)\log p_2 - (\sigma_1 + \sigma_2)\log p_3\} \equiv \\ &\equiv \sigma_1 \log p_1 + \sigma_2 \log p_2 \end{aligned}$$

$$\begin{aligned} \mu_2 = \text{tr}\{\mathbf{T}'^2\varepsilon_p\} &= \frac{1}{9}\{(2\sigma_1 - \sigma_2)^2\log p_1 + (2\sigma_2 - \sigma_1)^2\log p_2 + (\sigma_1 + \sigma_2)^2\log p_3\} \equiv \\ &\equiv \sigma_1(\sigma_1 - 2\sigma_2)\log p_1 + \sigma_2(\sigma_2 - 2\sigma_1)\log p_2 \end{aligned}$$

$$(\dot{\varepsilon}_{eq}^P)^2 = \frac{4}{3}\left[\left(\frac{\dot{p}_1}{p_1}\right)^2 + \left(\frac{\dot{p}_2}{p_2}\right)^2 + \frac{\dot{p}_1\dot{p}_2}{p_1 p_2}\right] \equiv \frac{4}{3}(\dot{\varepsilon}_{p11}^2 + \dot{\varepsilon}_{p22}^2 + \dot{\varepsilon}_{p11}\dot{\varepsilon}_{p22})$$

$$(\varepsilon_{eq}^P)^2 = \frac{4}{3}[(\log p_1)^2 + (\log p_2)^2 + \log p_1 \log p_2] \equiv \frac{4}{3}(\varepsilon_{p11}^2 + \varepsilon_{p22}^2 + \varepsilon_{p11}\varepsilon_{p22})$$

It must be taken into account that

$$\dot{\varepsilon}_{eq}^P \neq \frac{d}{dt}\varepsilon_{eq}^P$$

unless for proportional plastic strain paths where $\varepsilon_{p22} = m_p \varepsilon_{p11}$ with $m_p = \text{const}$:

MICROMECHANICAL CONSTITUTIVE EQUATIONS FOR DUCTILE FRACTURE PREDICTION

Marko Rakin

*University of Belgrade, Faculty of Technology and Metallurgy, Belgrade, Serbia
marko@tmf.bg.ac.yu*

Bojan Međo

University of Belgrade, Faculty of Technology and Metallurgy, Belgrade, Serbia

1. INTRODUCTION

Ductile fracture mechanism in metallic materials develops through three stages - nucleation of voids, their growth and eventual coalescence. This mechanism is characterised by a local development of damage, hence it does not depend on the analysed geometry. There are two main mechanisms of void nucleation in metallic materials: particle cracking and debonding from the metallic matrix. The void existence in the material causes local stress and strain concentration in the surrounding matrix. Under the external loading, the void changes its shape and volume (void growth stage), which makes the analysis of the above-mentioned fields very complicated.

Void coalescence occurs during the localization of the plastic deformation on microscopic level - in the intervoid ligaments. The plane of localization depends on the orientation of the ligament between two voids with respect to the loading direction. An example of void coalescence, in steel A508, is given in Fig. 1.

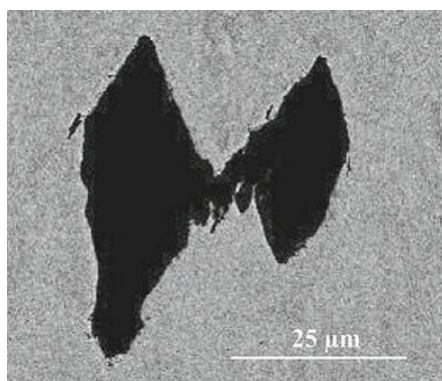


Figure 1: Void coalescence in steel A508 /1/

Elastic-plastic fracture mechanics (EPFM) cannot reliably describe the complex process of ductile fracture in metallic materials. Therefore, parameters that reflect the local nature of damage process should be introduced. Local approach uses such parameters, and is able to describe the fracture process in a way close to the actual phenomena in the material. It is based on micromechanical models of microscopic damage, with the aim to explain and predict the macroscopic failure of structure.

The correct use of the micromechanical models should include a close interaction of microstructural examination, material characterisation, fracture mechanics testing and numerical calculations. Having in mind that the parameters used for damage

quantification are determined locally, the aim is to achieve so-called *transferability* of the model parameters to different geometries.

As another advantage in comparison with EPFM global approach, local approach can be used for prediction of ductile fracture initiation in geometries without initial cracks, because reaching the critical value of the damage parameter will eventually lead to crack initiation at some critical location - with high values of triaxiality or plastic strain.

Local approach to ductile fracture is used here for assessment of the crack growth initiation and its stable growth in welded joints made of high-strength low-alloyed steel. Presented results include the analysis of the influence of the overmatched joint width, finite element size and formulation and initial crack length on ductile fracture initiation.

2. MODELS BASED ON THE GROWTH OF AN ISOLATED VOID

Uncoupled modelling of ductile fracture is based on the analysis of the growth of an isolated void in a material under the external loading. Such simplification is appropriate in case when the number of voids in the metallic matrix during the initial stage of fracture is small, and the distance between them is large. Therefore, the stress and strain concentration around the void should not affect other voids.

The assumption of the uncoupled modelling is that the void presence does not significantly alter the behaviour of the material; for that the damage parameter is not incorporated into the constitutive equation, with frequently used von Mises plastic yield criterion. A very important issue is defining the conditions for the loss of load-carrying capacity of the material due to the damage caused by ductile fracture mechanism.

The model of Rice and Tracey /2/, modified by research group Beremin /3/, states that the void growth is strongly dependent on stress-field multiaxiality and plastic deformation of the material:

$$\ln\left(\frac{R}{R_0}\right) = 0.283 \int_0^{\varepsilon_{eq}^p} \exp\left(\frac{3\sigma_m}{2\sigma_{eq}}\right) d\varepsilon_{eq}^p \quad (1)$$

where R stands for the actual mean void radius, R_0 is its initial value, σ_m/σ_{eq} represents the stress triaxiality, and ε_{eq}^p is the equivalent plastic strain. Significant influence of stress triaxiality on damage parameter and ductile fracture initiation can be seen from Eq. (1), because the increase of σ_m/σ_{eq} directly causes the increase of void growth ratio R/R_0 .

Another modification of the Rice - Tracey model was proposed by Huang /4/, by introducing $\sigma_m/\sigma_{eq} = 1$ as the limit value for high stress triaxiality and separating the expressions defining the void growth for the two cases

$$\ln\left(\frac{R}{R_0}\right) = 0.427 \int_0^{\varepsilon_{eq}^p} \left(\frac{\sigma_m}{\sigma_{eq}}\right)^{1/4} \exp\left(\frac{3\sigma_m}{2\sigma_{eq}}\right) d\varepsilon_{eq}^p \quad \text{for } \sigma_m/\sigma_{eq} \leq 1 \quad (2)$$

$$\ln\left(\frac{R}{R_0}\right) = 0.427 \int_0^{\varepsilon_{eq}^p} \exp\left(\frac{3\sigma_m}{2\sigma_{eq}}\right) d\varepsilon_{eq}^p \quad \text{for } \sigma_m/\sigma_{eq} > 1 \quad (3)$$

Starting from the model of Rice and Tracey, Chaouadi et al. /5, 6/ proposed another damage parameter for development of ductile fracture in the material - *damage work*, which is the work due to the plastic deformation, taking into account the change of volume at the local level around the void. This new parameter can be expressed as:

$$W_d = \int_0^{\varepsilon_{eq}^p} \left(\sigma_{eq} d\varepsilon_{eq}^p + 3\sigma_m \frac{dR}{R} \right) \quad (4)$$

As already mentioned, one of the problems in application of the uncoupled approach is the treatment of the final stage of damage until the final failure. Beremin research group /3/ proposed a rather simple way to define the failure criterion, by integrating Eq. (1) from zero to the experimentally determined strain at fracture ε_f :

$$\ln\left(\frac{R}{R_0}\right)_c = 0.283 \int_0^{\varepsilon_f} \exp\left(\frac{3}{2} \frac{\sigma_m}{\sigma_{eq}}\right) d\varepsilon_{eq}^p \quad (5)$$

where $(R/R_0)_c$ is the critical void growth ratio. Similar procedure can also be applied to the expressions of Huang and Chaouadi.

It is very important to choose the appropriate location in the structure where the Eq. (5) is applied. That should be the critical location (or locations) in a structure, e.g. crack tip, stress concentrators or regions with high stress triaxiality. The value of the critical void growth ratio decreases with increase of triaxiality, but this change isn't significant, which was a conclusion of the round robin project /7/ dedicated to local approach to fracture. According to Chaouadi et al. /5, 6/, parameter W_{dc} (critical damage work) exhibits even less pronounced dependence on stress triaxiality. However, the results obtained using the parameters W_{dc} and $(R/R_0)_c$ do not differ significantly, because the damage work concept is derived on the basis of the model of Rice and Tracey.

Simple numerical procedure and possibility to use the results of a finite element analysis for many post-processing routines are advantages of the uncoupled approach, favourable for engineering assessment /8, 9/. However, significant disadvantages of this approach are modelling of the final stage of ductile fracture - void coalescence, and nucleation of so-called secondary voids during the increase of the external loading.

3. MODELS BASED ON THE YIELD CRITERION OF A POROUS MATERIAL

The coupled approaches to material damage and ductile fracture initiation consider material as a porous medium, taking into account the influence of voids on the stress-strain state and plastic flow of the material. The existence of voids in the plastically deforming metallic matrix is quantified through a scalar quantity - void volume fraction or porosity f :

$$f = \frac{V_{voids}}{V} \quad (6)$$

where V_{voids} is volume of all voids in the analysed material volume V .

Based on the work of McClintock /10/ and Rice and Tracey /2/, Gurson /11/ derived several models of void-containing unit cells, obtaining the yield criterion of a porous material that became the basis for many often-used models of coupled approach:

$$\phi = \frac{3S_{ij}S_{ij}}{2\sigma_Y^2} + 2f \cosh\left(\frac{3\sigma_m}{2\sigma_Y}\right) - [1 + f^2] = 0 \quad (7)$$

This constitutive equation is based on the assumption that the behaviour of the material is isotropic - i.e. it can be treated as a continuum "weakened" by the existence of voids. The parameter f is calculated during the processing procedure, because it is directly

incorporated into Eq. (7). The influence of the mean stress σ_m on the plastic flow of the material is another important property of the Gurson criterion.

3.1. Gurson-Tvergaard-Needleman model (GTN)

Thomason /12/ and Tvergaard /13/ have shown that Gurson yield criterion can capture the influence of the voids on the material damage during the early stage of ductile fracture (growth of voids), but the results deviate from the experimental ones with the increase of the external loading. To improve the material behaviour assessment in the final stage of fracture, Tvergaard /13/ modified the original Eq. (1), introducing two parameters of the constitutive model, $q_1 \geq 1$ and $q_2 \geq 1$, into the parts containing the void volume fraction f and mean stress σ_m . Also, the yield stress is replaced by the current yield stress of the material matrix σ , to take the material hardening into account. The basic equation of the Gurson-Tvergaard-Needleman model (GTN) is:

$$\phi = \frac{3S_{ij}S_{ij}}{2\sigma^2} + 2f^* q_1 \cosh\left(\frac{3q_2\sigma_m}{2\sigma}\right) - \left[1 + (q_1 f^*)^2\right] = 0 \quad (8)$$

where f^* is so-called damage function, proposed by Tvergaard and Needleman /14/:

$$f^* = \begin{cases} f & \text{for } f \leq f_c \\ f_c + K(f - f_c) & \text{for } f > f_c \end{cases} \quad (9)$$

f_c is the critical void volume fraction, corresponding to the initiation of their coalescence, and K is parameter that represents the loss of load-carrying capacity of the material (sudden drop of force at the force - diameter reduction diagram):

$$K = \frac{f_u^* - f_c}{f_F - f_c} \quad (10)$$

Void volume fraction at final fracture is denoted as f_F , while $f_u^* = 1/q_1$ is the value of damage function at the moment of fracture.

Parameters q_1 and q_2 intensify the influence of f and σ_m on the plastic flow of the material, favouring the development of damage, especially for large values of triaxiality and porosity. Tvergaard /13/ proposed the values $q_1 = 1.5$ and $q_2 = 1$, as the values most suitable for high-strength steels.

Gurson-Tvergaard-Needleman model was used for analysis of ductile fracture of various metallic materials; e.g. pressure vessel steel by Rakin et al. /15, 16/, welded joints by Rakin et al. /17/ and Dobrojević et al. /18/.

Gao et al. /19/ analysed the influence of the yield strain and hardening exponent on the parameters q_1 and q_2 for Cr-Mo pressure vessel steel. Their results are given in Table 1.

Table 1: Values of q_1 and q_2 , depending on the hardening exponent n and ratio σ_Y/E /19/

n	$\sigma_Y/E = 0.001$		$\sigma_Y/E = 0.002$		$\sigma_Y/E = 0.004$	
	q_1	q_2	q_1	q_2	q_1	q_2
5	1.96	0.781	1.87	0.800	1.71	0.836
6.7	1.78	0.833	1.68	0.856	1.49	0.901
10	1.58	0.902	1.46	0.931	1.29	0.982

Dutta et al. /20/ proposed another approach - dependence of q_2 on the distance of the point from the crack tip, r :

$$q_2 = 1 + q_{2a} e^{-(r/l_c)/q_{2b}} \quad (11)$$

This dependence is determined from the condition that the parameter set of the GTN model should be used for determining the crack growth initiation, but also its stable growth in steel SA333 Gr.6. Here, q_{2a} and q_{2b} are two new constants, defining the variation of q_2 in the vicinity of the crack tip.

Parameter f_F can be determined from microstructural observation of the fracture surfaces, but this is a very difficult procedure. Zhang et al. /21/ has shown, using the unit cell model, that f_F depends on f_0 , and can be approximately calculated as:

$$f_F \approx 0.15 + 2f_0 \quad (12)$$

Determination of the critical void volume fraction f_c is very important for application of Eq. (9). Different techniques are proposed in /22 – 24/ for determining its value. Rakin /25/ and Rakin et al. /15, 26/ have shown an experimental-numerical procedure based on the examination of the round tensile specimen.

In the initial stage of ductile fracture of steel, the voids nucleate mostly around the non-metallic inclusions. Therefore, the initial porosity is often assumed to be equal to the void volume fraction of non-metallic inclusions f_v , which can be determined by quantitative microstructural analysis, briefly described in the next chapter.

The increase of the void volume fraction can be separated into the growth of the existing voids:

$$\dot{f}_{growth} = (1 - f) \dot{\varepsilon}_{ii}^p \quad (13)$$

and nucleation of the new (often called secondary) voids under external loading:

$$\dot{f}_{nucleation} = A_N \dot{\varepsilon}_{eq}^p \quad (14)$$

where $\dot{\varepsilon}_{ii}^p$ is the plastic part of the strain rate tensor.

$$\dot{f} = \dot{f}_{growth} + \dot{f}_{nucleation} \quad (15)$$

The increase of the external loading causes further growth of voids and their eventual coalescence, leading to final fracture.

Chu and Needleman /27/ proposed the following expression for nucleation of secondary voids, using normal distribution:

$$A_N = \frac{f_N}{s_N \sqrt{2\pi}} \exp \left(-\frac{1}{2} \left(\frac{\varepsilon_{eq}^p - \varepsilon_N}{s_N} \right)^2 \right) \quad (16)$$

where f_N denotes the volume fraction of secondary-void forming particles, ε_N is the mean strain at void nucleation (the strain for which 50% particles are broken or separated from the matrix) and s_N is the standard deviation of this value. Changing the standard deviation causes the change of the interval width corresponding to the nucleation of most voids.

When applying this approach to quantify the void nucleation, one should have in mind that it is a simplified procedure, and that variety of sizes and types of particles makes this mechanism very difficult to be modelled exactly. Therefore, instead of a unique model to

describe the process of ductile fracture in most metallic materials, the aim is to derive an approach capable of taking into account the specific properties of the examined material.

3.2 Complete Gurson model (CGM)

As already explained, the GTN model describes the material as a continuum weakened by the presence of voids. Such representation corresponds to so-called homogeneous deformation mode. Damage function (9) can be used to model the loss of load-carrying capacity of the material, but it cannot be directly linked with the actual processes during the last stage of ductile fracture. Thomason /28/ proposed a more realistic failure criterion, which is based on the analysis of deformation in the intervoid ligaments - localised deformation mode. Localized deformation state of void coalescence differs from the homogenous deformation state during void nucleation and growth. For small values of external load, homogeneous state is dominant, because the intervoid ligaments are large. With further increase of load, plastic strain grows, and these ligaments become thinner. Therefore, the stress needed for localised deformation decreases. When this stress is equal to the stress needed for the homogeneous deformation, the void coalescence starts.

Zhang et al. /21/ made a significant modification of the GTN model - they applied the Thomason's void coalescence criterion based on the plastic limit load model (with the assumption that all the voids remain spherical during the increase of the external loading), thus introducing the complete Gurson model - CGM. Criterion for determining the instant when void coalescence starts is:

$$\frac{\sigma_1}{\sigma} > \left(\alpha \left(\frac{1}{r} - 1 \right) + \frac{\beta}{\sqrt{r}} \right) (1 - \pi r^2) \quad (17)$$

Here, σ_1 is the maximum principal stress, $\alpha = 0.1$ and $\beta = 1.2$ are constants introduced by Thomason /28/. Zhang et al. /21/ proposed a linear dependence of α on hardening exponent n for elastic-plastic materials that exhibit strain hardening.

In Eq. (17), r represents the void space ratio /21/, i.e. the ratio of the void radius and the intervoid distance:

$$r = \sqrt[3]{\frac{3f}{4\pi} e^{\varepsilon_1 + \varepsilon_2 + \varepsilon_3}} / \left(\frac{\sqrt{e^{\varepsilon_2 + \varepsilon_3}}}{2} \right) \quad (18)$$

where ε_1 , ε_2 and ε_3 are principal strains. Therefore, the critical void volume fraction f_c is not a material constant in CGM - but the material response at void coalescence. The value of f_c depends on the strain field, so it is not necessary the same in all finite elements and in all integration points within one element. According to the CGM, ductile fracture initiation is fully determined by Eqs. (8) and (9), with the criterion for void coalescence (17).

Micromechanical models for ductile fracture prediction described in Chapters 2 and 3 are continuously being improved through many on-going investigations, national and international research projects. One of the aims is application of local approach to ductile and cleavage fracture in structural integrity assessment, as shown in /29/.

4. CRACK GROWTH MODELLING

Besides the analysis of ductile fracture initiation, local approach can be used for stable crack growth modelling. In case some of the uncoupled micromechanical models are used, crack growth can be modelled using the node release technique, controlled by the

critical value of damage parameter in the element ahead the crack tip. Similar procedure can be applied for the coupled models, using the critical value of appropriate damage parameter. This group of models offers another possibility - advance of the crack can be regarded as loss of material load-carrying capacity in the ligament ahead the crack tip. As the criterion for ductile fracture initiation is satisfied, the element ahead the current crack tip fails, according to the equations of the used micromechanical model. This approach is used in given example, and the criterion for the crack growth is determined by the CGM.

Unlike the coupled micromechanical models, where the influence of the voids is defined through void volume fraction (porosity), there are techniques that include modelling of each void, using a very refined mesh around them. This approach is used by Tvergaard and Hutchinson /30/ and Tvergaard /31/, and the mesh in the part of the ligament in front of the crack tip is shown in Fig. 2.

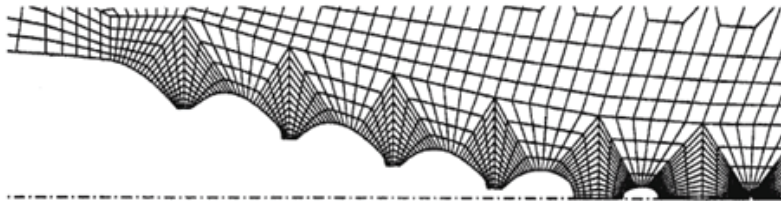


Figure 2: Modelling of the voids in front of the crack tip /31/

Crack growth is modelled by node release technique; nodes are released at critical value of the ligament thickness, see /30 – 32/. This way of crack growth modelling is very time-consuming and requires significant computational resources. However, only a small number of voids can be analysed, which is why it cannot be used for real components and specimens. On the other hand, this method is very useful for detailed analysis of the void size and distribution effects on the fracture process and material behaviour.

5. PREDICTION OF DUCTILE FRACTURE IN WELDED JOINT

5.1. Material properties

An example of application of the CGM is presented through the analysis of the crack initiation and stable growth in NIOMOL 490 high-strength low-alloyed (HSLA) steel welded joints. For details about the welding process and experimental procedure see /33/.

Chemical composition of the base metal (BM) and weld metal (WM) are given in Table 2. Tensile properties and true stress - true strain curves of BM and WM, determined on round tensile specimens, are given in Figure 3. Overmatched welded joint of the mismatch ratio $M = R_{p0.2}(\text{WM})/R_{p0.2}(\text{BM}) \approx 1.19$ had been prepared.

Table 2: Chemical composition of the base metal and weld metal

Material	C	Si	Mn	P	S	Cr	Mo	Ni
Base metal (BM)	0.123	0.33	0.56	0.003	0.002	0.57	0.34	0.13
Weld metal (WM)	0.04	0.16	0.95	0.011	0.021	0.49	0.42	2.06

The presence of sulphides, oxides, silicates and complex inclusions in tested materials is determined by microstructural analysis. Both BM and WM contain a significant fraction of oxides. Microphotograph with several such clusters in BM is shown in Fig. 4.

The volume fraction of non-metallic inclusions f_v is determined as the mean value for all measurement fields, taken successively on surfaces of prepared samples (ASTM

E1245-89 standard and /34/), by quantitative microstructural analysis using optical microscope, based on the equality with surface fraction of detected inclusions $A_A/34/$:

$$f_v = A_A = \frac{A_i}{A_T} \quad (19)$$

where A_i is the area of inclusions and A_T is the measurement field area.

For determining the mean free path between non-metallic inclusions λ according to ASTM E1245-89 standard, in each measurement field five horizontal measuring lines are drawn, and the number of interceptions of inclusions per measurement line unit, N_L , is determined. The mean free path is mean edge-to-edge distance between inclusions:

$$\lambda = \frac{1 - A_A}{N_L} \quad (20)$$

The final value of λ is determined, in the same way as the volume fraction of non-metallic inclusions f_v , as the mean value for all measurement fields.

The values of f_v and λ for both materials are given in Table 3.

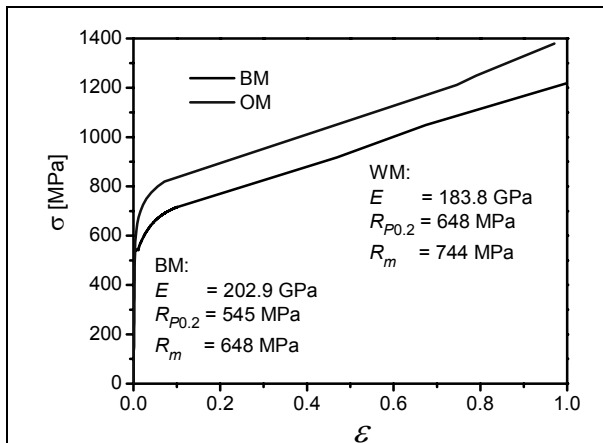


Figure 3. Tensile properties and true stress - true strain curves of BM and WM at room temperature

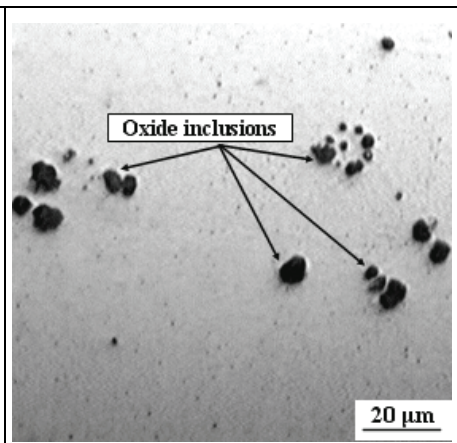


Figure 4. Microphotograph of oxides in base metal

Table 3: Volume fraction f_v and mean free path between non-metallic inclusions λ

Material	f_v	λ [μm]
BM	0.012164	103.1336
WM	0.006342	157.4719

5.2. Finite element model

Single-edge notched bend (SENB) specimens are used for examination of the welded joints, with different width of WM (and joint) $2H$: 6, 12 and 18 mm, Fig. 5. Crack tip opening displacement (CTOD) values are determined, both experimentally and by numerical calculations, using δ_5 concept /35/.

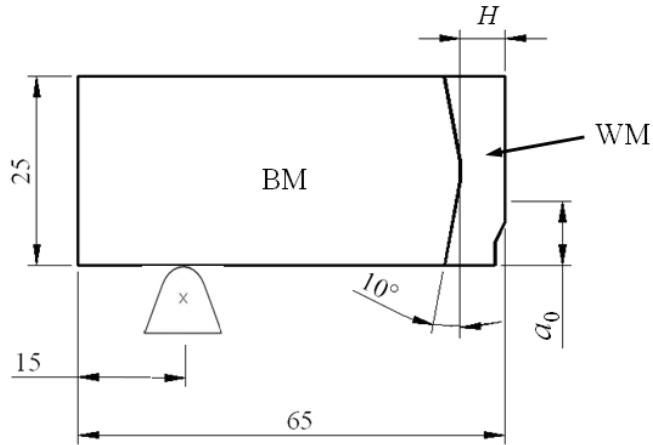


Figure 5: Dimensions of the SENB specimen and weld metal ($2H = 6, 12$ and 18 mm)

The specimen is analysed under plane strain conditions, and the finite element (FE) mesh is shown in Fig. 6, with magnification of the region near the crack tip. Crack tip is modelled using a refined FE mesh without singular elements. Finite element software package ABAQUS (www.simulia.com) is used for numerical analysis, and the CGM is applied through user material subroutine created by Zhang, based on /21/. The initial void volume fraction f_0 is set as equal to f_v , according to /25, 36/. FE calculations are carried out with the values of Tvergaard constitutive parameters $q_1 = 1.5$ and $q_2 = 1$. External loading is defined by prescribing displacement of the rigid body, which is in contact with the model (position A, Fig. 6). Contact is also used for defining the boundary conditions for support (position B). It is important to note that the heat affected zone (HAZ) is not taken into account, based on /37, 38/, since the crack is located in the weld metal, along the axis of symmetry of the joint. Coupled approach to ductile fracture (the GTN model) was also used in /17, 18/ for assessment of ductile fracture initiation in these joints.

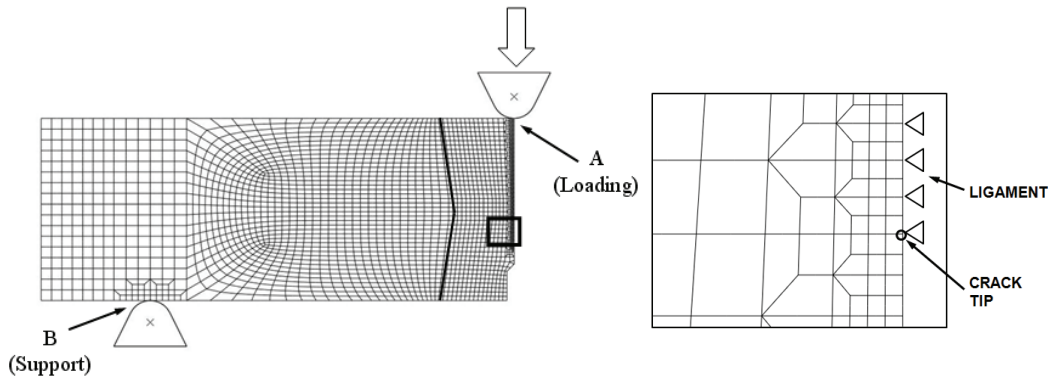


Figure 6: FE mesh of one half of SENB specimen (left) and detail around the crack tip (right)

5.3. Crack growth initiation

Distribution of void volume fraction f near the crack tip at the crack growth initiation is shown in Fig. 7 for the joint 6 mm wide and 20-node elements with reduced integration and size 0.15×0.15 mm. Concentration of large values very close to the crack tip is obvious. One can also see a large variation of f in the elements near the crack tip.

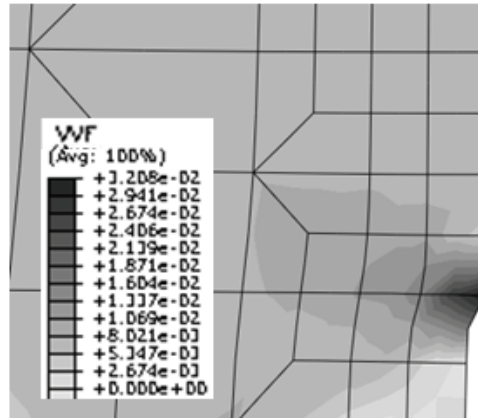


Figure 7: Distribution of void volume fraction f near the crack tip at the crack growth initiation

The influence of the finite element size, formulation and integration order on the results of the crack growth initiation analysis on SENB specimen is considered in this section. In addition to the adopted FE size 0.15×0.15 mm (corresponding to the mean free path between the inclusions in WM, according to /15, 25/), two other FE sizes are considered: 0.3×0.3 mm and 0.075×0.075 mm. The results obtained in /39/ using these sizes of 8-noded elements with reduced (2x2) integration are given in Fig. 8. CTOD value at the crack growth initiation ($CTOD_i$) is determined when damage parameter f reaches critical value f_c at the integration point nearest to the crack tip, see /15, 40/. Nucleation of the secondary voids is not taken into account here, but will be analysed later on.

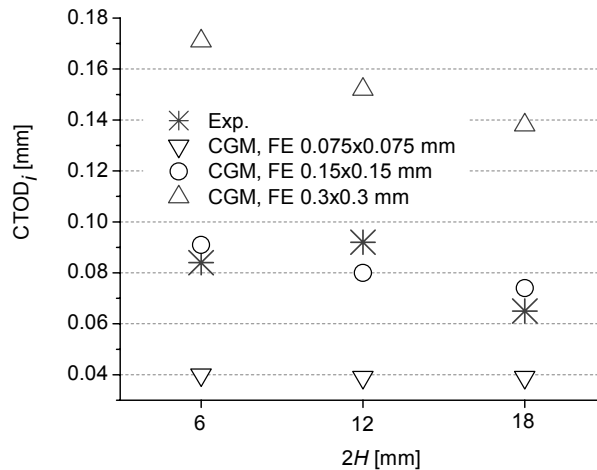


Figure 8: The influence of element size on the $CTOD_i$ values, 8-noded FE with reduced integration

Calculation with FE size 0.3×0.3 mm gives higher material resistance than the real one, while the opposite is obtained with FE size 0.075×0.075 mm. It is clear that FE size similar to the mean free path between the inclusions is the most suitable in this case.

Besides the FE size ahead the crack tip, formulation of the element and the integration order should also be taken into account. The results obtained using various elements with dimensions 0.15×0.15 mm (Fig. 9) imply that the integration order has a strong influence on predicted $CTOD_i$ values. The use of 8-noded elements with full integration leads to much smaller values, which are very close to those obtained with 8-noded elements with

reduced integration and dimensions 0.075x0.075 mm. These two elements have similar distance between integration points, so these results are in agreement with the conclusions of Rakin /25/, that distance between integration points, instead of the FE size, should be related to the mean free path between the void-nucleating particles.

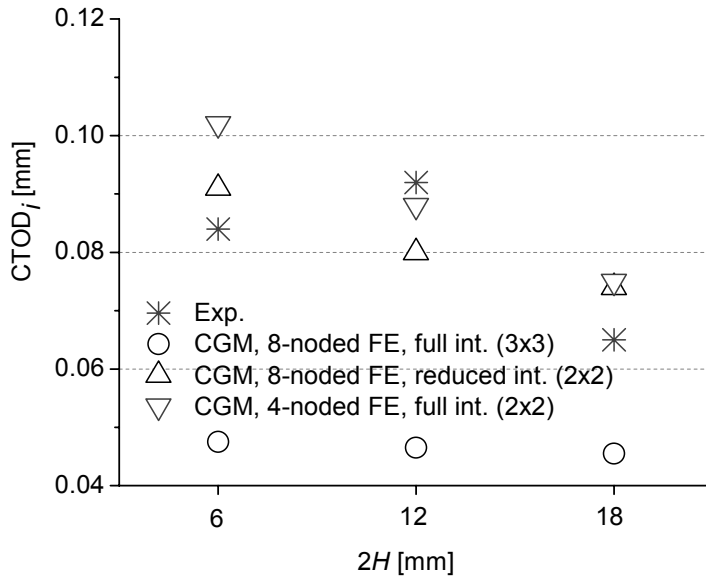


Figure 9: The influence of interpolation and integration on the $CTOD_i$ values (FE 0.15x0.15 mm)

On the other hand, for the same number of integration points and distance between them, prediction of ductile fracture initiation is not much affected by the change of the interpolation order. Result obtained using 8-noded and 4-noded elements with 2x2 integration do not differ significantly, as can be seen in Fig. 9.

5.4. Stable crack growth

Stable crack growth is modelled by development of damage in the ligament ahead the crack tip. The criterion for the loss of load-carrying capacity of the material is defined applying the CGM. The FE meshes are created using 4-noded elements with full (2x2) integration and dimensions in the ligament 0.15x0.15 mm. Deformed mesh of the specimen of joint width 12 mm, for load line displacement $v_{LL} = 1.6$ mm, is shown in Fig. 10.

The influence of the joint width on the crack growth can be seen in Fig. 11, where the ligament meshes in front of the crack tip for three analysed widths are given. Dark colours represent high values of void volume fraction (porosity) f , in elements that have already lost their load-carrying capacity. The current crack length is determined by multiplying the number of failed elements with their dimension in crack growth direction (which is 0.15 mm for the meshes in Fig. 11). It can be concluded that the influence of the geometry is similar as for the crack growth initiation - increase of the joint width reduces the fracture resistance. This dependence can be seen as the increase of the crack length, having in mind that three porosity fields given in Fig. 11 correspond to the same value of the load line displacement $v_{LL} = 1.6$ mm.

The results obtained by crack growth modelling are shown in Fig. 12 - 16, on force F - crack tip opening displacement CTOD diagrams. Experimentally obtained curves for the three joint widths are compared with the results obtained using von Mises plastic yield

criterion and the CGM. First of all, it can be seen that the load-carrying capacity of the material is overestimated if damage due to the voids is not taken into account (von Mises criterion). These results can be improved using the node release technique, as explained, but in this analysis it is chosen to model the crack growth by development of damage in the ligament, using the CGM. It is shown that this procedure can give appropriate results, and predict the weakening of the material caused by the nucleation, growth and coalescence of voids during the process of ductile fracture. Very good agreement with experimental data is achieved for 6 and 12 mm wide joints, while certain differences exist in case of the widest joint (18 mm), where the estimated values of force are larger, but with correct trend that reflects the loss of load-carrying capacity of the material.

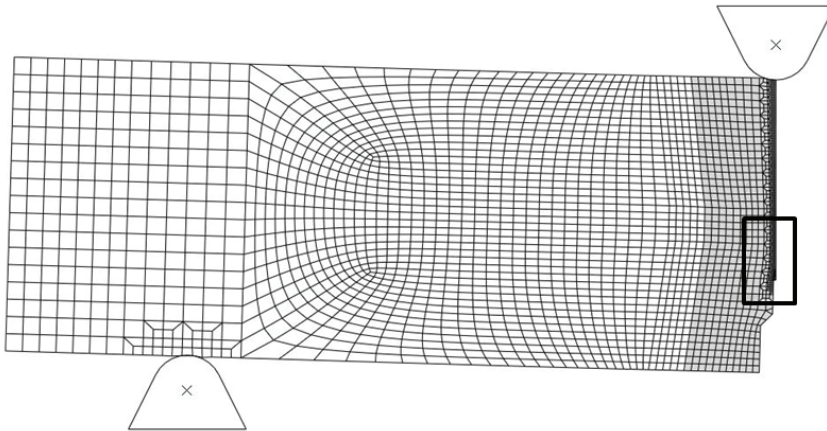


Figure 10: Deformed FE mesh of one half of SENB specimen, joint width 12 mm

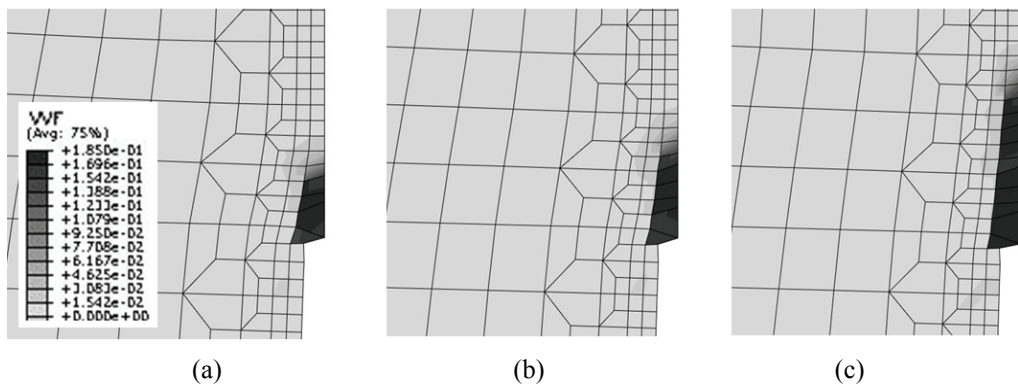


Figure 11: Detail of deformed FE mesh in the ligament in front of the crack tip, joint width 6 mm (a), 12 mm (b) and 18 mm (c)

The influence of the secondary voids formed around the Fe_3C particles on the crack growth initiation is also analysed using the CGM. Volume fraction of these particles in the weld metal, $f_N = 0.002257$, is determined using the lever rule /41/. Results obtained using the approach of Chu and Needleman /27/ are shown in Fig. 15. The adopted values of ϵ_N and s_N are 0.3 and 0.1, respectively. It is concluded that secondary voids in the analysed weld metal do not contribute to the decrease of the load-carrying capacity. Such behaviour is not a surprise, having in mind the low contents of carbon, and therefore also Fe_3C particles.

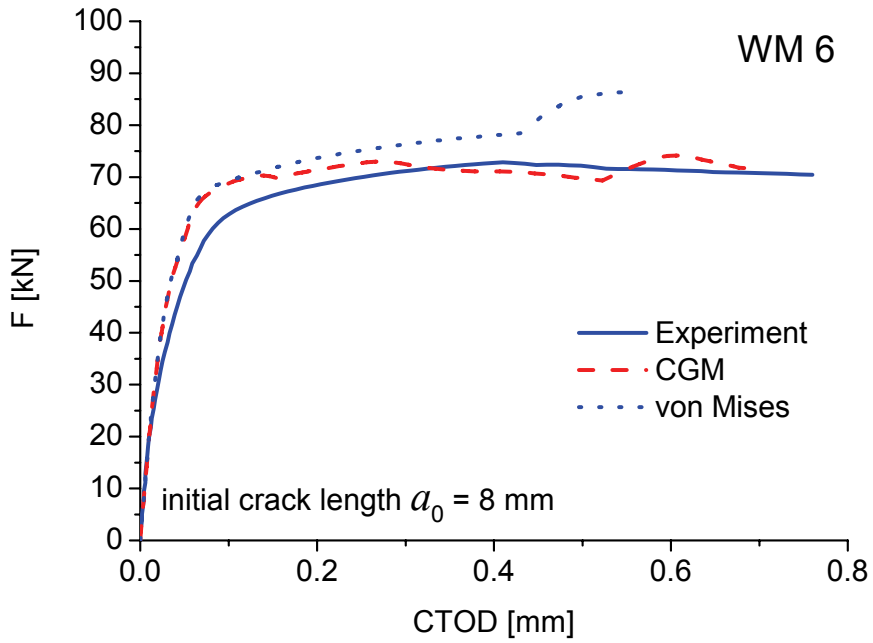


Figure 12: F -CTOD curves obtained experimentally, using von Mises criterion (without crack growth) and the CGM (with crack growth) for joint width 6 mm

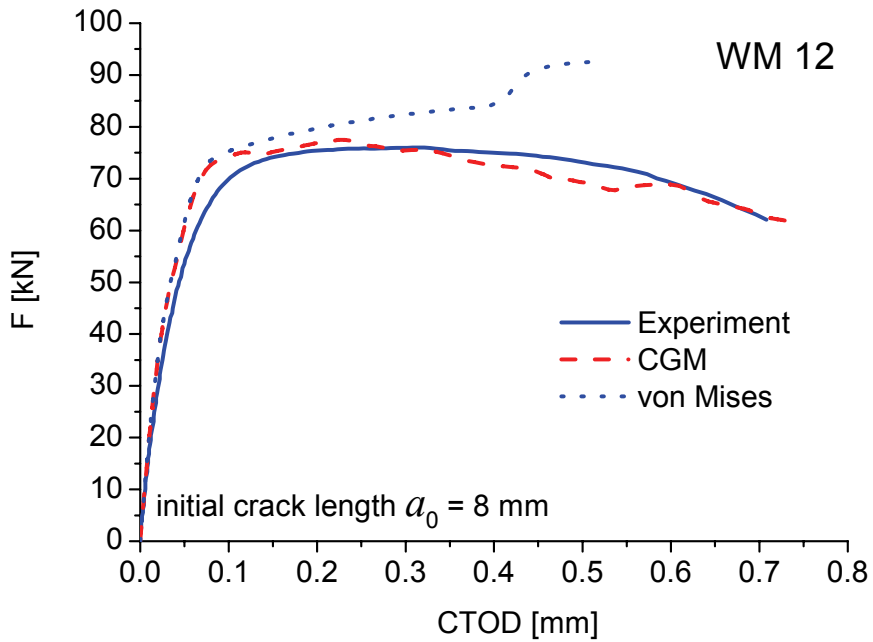


Figure 13: F -CTOD curves obtained experimentally, using von Mises criterion (without crack growth) and the CGM (with crack growth) for joint width 12 mm

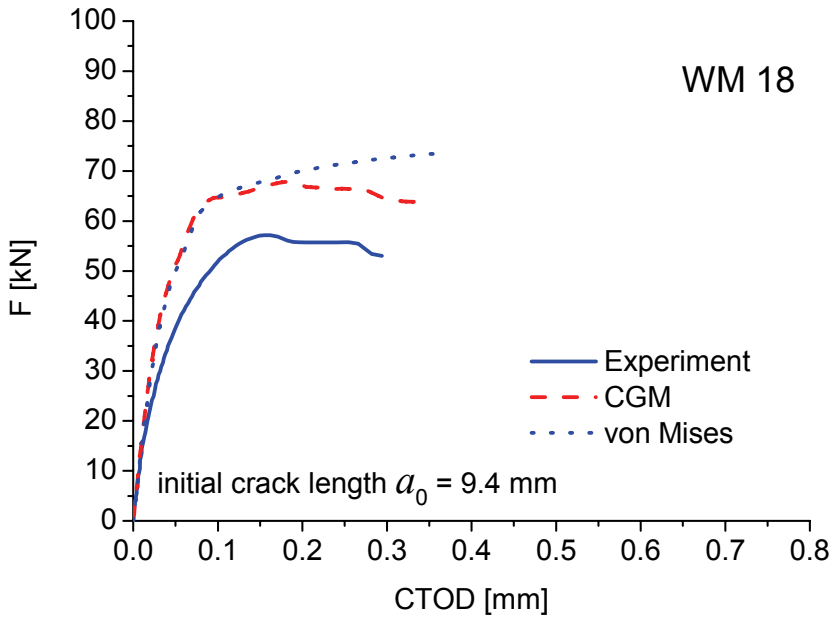


Figure 14: F -CTOD curves obtained experimentally, using von Mises criterion (without crack growth) and the CGM (with crack growth) for joint width 18 mm

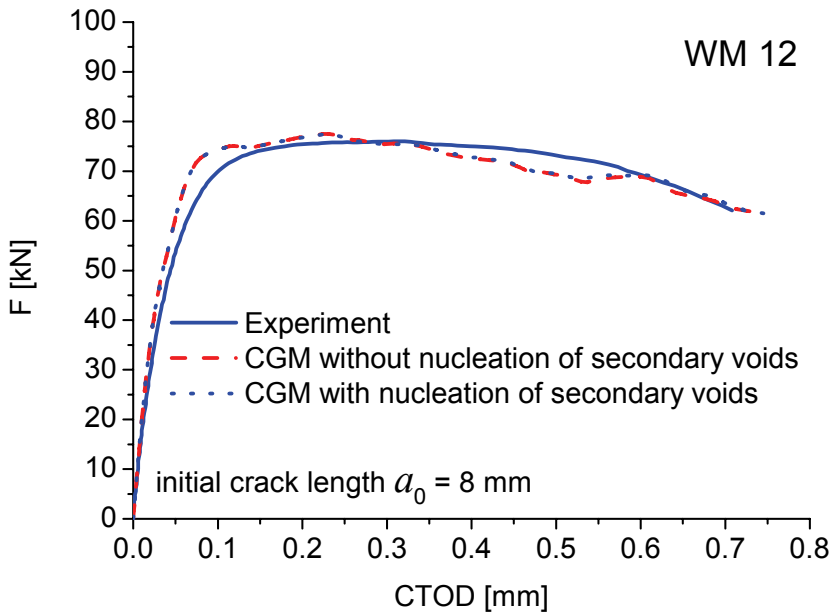


Figure 15: F -CTOD curves obtained experimentally and using the CGM, with and without nucleation of secondary voids, for joint width 12 mm

The influence of an important dimension of the specimen, initial crack length a_0 , is analysed for two SENB specimens of joint width 6 mm, for $a_0 = 8$ mm and $a_0 = 10.4$ mm, corresponding to the experimentally measured lengths. F -CTOD curves obtained experimentally and using the CGM are given in Fig. 16. It is clear that the difference in behaviour of these two specimens can be assessed using the CGM, and that damage modelling in the ligament is in good agreement with actual material behaviour.

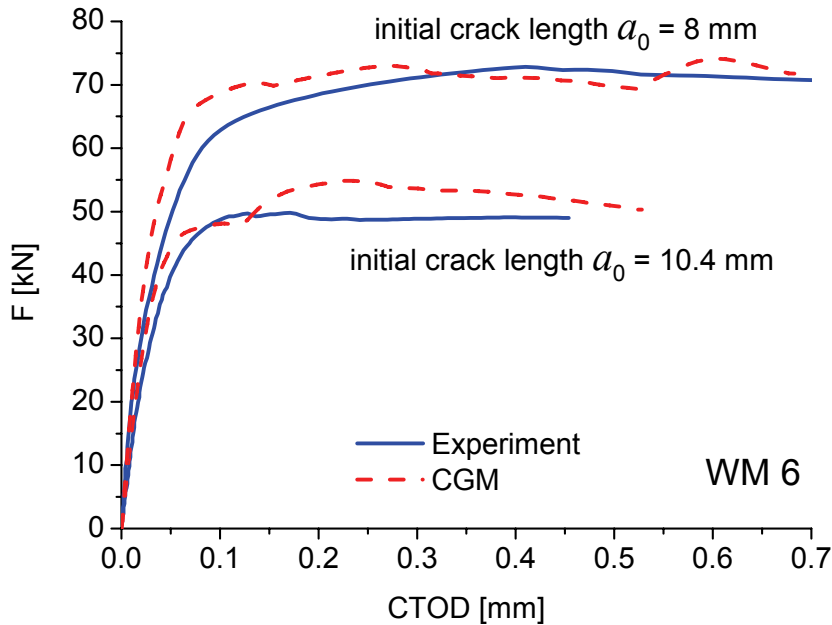


Figure 16: F -CTOD curves obtained experimentally and using the CGM for joint width 6 mm and different initial crack lengths

6. CONCLUSIONS

An overview of the uncoupled and coupled micromechanical models of local approach to ductile fracture has been given in this lecture. One of the coupled models, the complete Gurson model, has been used for analysis of ductile fracture initiation in overmatched welded joints made of high-strength low-alloyed steel of yield strength 545 MPa. SENB specimens have been investigated. Metallographic observation has been used to quantify the volume fraction of non-metallic inclusions f_v and mean free path between the inclusions λ in the base metal and weld metal. Initial void volume fraction f_0 has been set as equal to f_v . CTOD at the moment of the crack growth initiation on SENB specimen has been measured experimentally and calculated using the local approach.

It is found that the CGM enables determination of the crack growth initiation in analysed welded joints. Damage parameter distribution exhibits only local character near the crack tip, but the size of finite elements strongly influences the results. In addition, the effect of integration order of the elements exists, while the interpolation order of the element (quadratic or linear) does not influence the results significantly.

Analysis of the stable crack growth has shown that the loss of load-carrying capacity of the material in the ligament due to the crack growth can be assessed using the CGM. The results have been obtained by observing the damage in the elements along the crack line, without releasing the nodes. The influence of the joint width is predicted correctly, except for the widest joint, that exhibit certain deviations on force - crack tip opening displacement diagram. The influence of the crack length can also be estimated using the CGM. Nucleation of secondary voids around Fe_3C particles doesn't affect the behaviour of the joints, because the percentage of carbon in the weld metal is rather low.

ACKNOWLEDGEMENTS

The authors gratefully acknowledge the financial support from the Serbian Ministry of Science under the project OI 144027 and Slo-Serb. bilateral project "Failure prevention of inhomogeneous materials and structures" (together with Slovenian Ministry of Science). The lecturers would also like to thank N. Gubeljak for the results of the tensile and fracture mechanics tests, Z.L. Zhang for the CGM user subroutine, M. Dobrojević for useful suggestions and I. Cvijović - Alagić for help in microstructural analysis.

REFERENCES

1. Pineau, A., "Modelling ductile to brittle fracture transition in steels - micromechanical and physical challenges". International Journal of Fracture, Vol. 150, (2008), pp. 129-156.
2. Rice, J.R., Tracey, D.M., "On the ductile enlargement of voids in triaxial stress fields". Journal of the Mechanics and Physics of Solids, Vol. 17, (1969), pp. 201-217.
3. Beremin, F.M., "Experimental and numerical study of the different stages in ductile rupture: application to crack initiation and stable crack growth". In: Three-dimensional Constitutive Relations and Ductile Fracture, North-Holland Publications, Amsterdam, (1981), pp. 185-205.
4. Huang, Y., "Accurate dilatation rates for spherical voids in triaxial stress fields". Transactions ASME: Journal of Applied Mechanics, Vol. 58, (1991), pp. 1084-1086.
5. Chaouadi, C., de Meester, P., Vandermeulen W., "Damage work as ductile fracture criterion". International Journal of Fracture, Vol. 66, (1994), pp. 155-164.
6. Chaouadi, R., De, Meester P., Scibetta, M., "Micromechanically modeling of ductile fracture toughness of reactor pressure vessel steels". In: Proceedings of the 1st European Mechanics of Materials Conference on Local Approach to Fracture, EUROMECH-MECAMAT'96, Fontainebleau (1996) pp. 126-138
7. Mudry, F., Di Fant, M., "A round robin on the measurement of local criteria". Irsid, St. German, (1993).
8. Zrilić, M., Rakin, M., Milović Lj., Burzić Z., Grabulov V., "Experimental and numerical evaluation of steamline behaviour using local approach". Metallurgy, Vol. 46, (2007), pp. 87-92.
9. Zrilić, M., Rakin, M., Sedmak, A., Aleksić, R., Cvijović, Z., Arsić, M., "Ductile fracture prediction of steam pipeline steel". Materials Science Forum, Vol. 518, (2006), pp. 537-542.
10. McClintock, F.A., "Ductile rupture by the growth of holes". Journal of Applied Mechanics, Vol. 35, (1968), pp. 363-371.
11. Gurson, A., "Continuum theory of ductile rupture by void nucleation and growth: Part I - yield criteria and flow rules for porous ductile media". Journal of Engineering Materials and Technology, Vol. 99, (1977), pp. 2-15.
12. Thomason, P.F., "Three-dimensional models for the plastic limit-loads at incipient failure of the intervoid matrix in ductile porous solids". Acta Metallurgica, Vol. 33 (1985) pp. 1079-1085
13. Tvergaard, V., "Influence of voids on shear band instabilities under plane strain conditions". International Journal of Fracture, Vol. 17, (1981), pp. 389-407.
14. Tvergaard, V., Needleman, A., "Analysis of the cup-cone fracture in a round tensile bar", Acta Metallurgica, Vol. 32, (1984), pp. 157-169.
15. Rakin, M., Cvijović, Z., Grabulov, V., Putić, S., Sedmak, A., "Prediction of ductile fracture initiation using micromechanical analysis". Engineering Fracture Mechanics, Vol. 71, (2004), pp. 813-827.
16. Rakin, M., Cvijović, Z., Sedmak, A., Sedmak, S., "Analysis of the transferability of micro-mechanical parameters of damage of steel under the conditions of ductile-fracture initiation". Materials Science, Vol. 38, (2002), pp. 104-113.

17. Rakin, M., Gubelj, N., Dobrojević, M., Sedmak, A., “*Modelling of ductile fracture initiation in strength mismatched welded joint*”. Engineering Fracture Mechanics, Vol. 75, (2008), pp. 3499-3510.
18. Dobrojević, M., Rakin, M., Gubelj, N., Cvijović, I., Krunić, N., Sedmak, A., “*Micromechanical analysis of constraint effect on fracture initiation in strength mismatched welded joints*”. Materials Science Forum, Vol. 555, (2007), pp. 571-576.
19. Gao, X., Faleskog, J., Shih, C.F., Dodds, R.H., “*Ductile tearing in part-through cracks: experiments and cell-model predictions*”. Engineering Fracture Mechanics, Vol. 59, (1998), pp. 761-777.
20. Dutta, B.K., Guin, S., Sahu, M.K., Samal, M.K., “*A phenomenological form of the q_2 parameter in the Gurson model*”. International Journal of Pressure Vessels and Piping, Vol. 85, (2008), pp. 199-210.
21. Zhang, Z.L., Thaulow, C., Ødegård, J., “*A complete Gurson model approach for ductile fracture*”. Engineering Fracture Mechanics, Vol. 67, (2000), pp. 155-168.
22. Bernauer, G., Brocks, W., “*Numerical round robin on micro-mechanical models – Results*”. ESIS TC8, GKSS Research Center, Geesthacht, (2000).
23. Sun, D.Z., Kienzler, R., Voss, B., Schmitt, W., “*Application of micro-mechanical models to the prediction of ductile fracture*”. In: Fracture Mechanics, 22nd Symposium, Vol. II, ASTM STP 1131, (1992), pp. 368-378.
24. Steglich, D., Brocks, W., “*Micromechanical modeling of damage and fracture of ductile metals*”. Fatigue and Fracture of Engineering Materials and Structures, Vol. 21, (1998), pp. 1175-1188.
25. Rakin, M., “*The analysis of ductile fracture initiation in structural steel using micromechanical models*”. Ph.D Thesis (in Serbian), Faculty of Technology and Metallurgy, Belgrade (2003)
26. Rakin, M., Sedmak, A., Zrilić, M., Putić, S., Sedmak, S., “*Analysis of crack growth initiation and stable growth in low-alloyed pressure vessel steel*” (In Serbian). Procesna tehnika, Vol. 19, (2003), pp. 78-81.
27. Chu, C., Needleman, A., “*Void nucleation effects in biaxially stretched sheets*”. Journal of Engineering Materials and Technology, Vol. 102, (1980), pp. 249-256.
28. Thomason, P.F., “*Ductile fracture of metals*”. Pergamon Press, Oxford, (1990).
29. Rakin, M., Sedmak, A., “*Micromechanical analysis in structural integrity assessment*”. In: Monograph of the 9th International Fracture Mechanics Summer School (IFMASS 9), Faculty of Mechanical Engineering, Society for Structural Integrity and Life, Faculty of Technology and Metallurgy, GOŠA, Belgrade, (2008), pp. 85-104.
30. Tvergaard, V., Hutchinson, J.W., “*Two mechanisms of ductile fracture: void by void growth versus multiple void interaction*”. International Journal of Solids and Structures, Vol. 39, (2002), pp. 3581-3597.
31. Tvergaard, V., “*Discrete modelling of ductile crack growth by void growth to coalescence*”. International Journal of Fracture, Vol. 148, (2007), pp. 1-12.
32. Kim, J., Gao, X., Srivatsan, T.S., “*Modelling of crack growth in ductile solids: a three-dimensional analysis*”. International Journal of Solids and Structures, Vol. 40, (2003), pp. 7357-7374.
33. Gubelj, N., Scheider, I., Koçak, M., Oblak, M., Predan, J., “*Constraint effect on fracture behaviour on strength mis-matched weld joint*”. In: Proceedings of the 14th European Conference on Fracture (ECF 14), Vol I, Krakow, (2002), pp. 647-655.
34. Underwood, E.E., “*Quantitative Metallography*”. In: ASM Metals Handbook, Vol. 9, ASM International, (1986), pp. 123-134.
35. GKSS: “*Displacement gauge system for applications in fracture mechanics*”. Patent Publication, GKSS Research Center, Geesthacht, (1991).

36. Rakin, M., Cvijović, Z., Grabulov, V., Kojić, M., “*Micromechanism of ductile fracture initiation - void nucleation and growth*”. Facta Universitatis; Series: Mechanical Engineering, Vol. 1, (2000), pp. 825-833.
37. Schwalbe, K. H., “*Basic engineering methods of fracture mechanics and fatigue*”, GKSS Forschungs- zentrum, Geesthacht, (2001).
38. Schwalbe, K.H., Ainsworth, R.A, Eripret, C., Franco, C., Gilles, P., Koçak, M., Pisarski, H., Wang, Y.Y., “*Common views on the effects of yield strength mis-match on testing and structural assessment*”. In: Mis-matching of Interfaces and Welds, GKSS Research Center, Geesthacht, (1997), pp. 99-132.
39. Međo, B., Rakin, M., Gubeljak, N., Sedmak, A., “*Application of complete Gurson model for prediction of ductile fracture in welded steel joints*”. Key Engineering Materials, Vol. 399, (2009), pp. 13-20.
40. Rakin, M., Cvijović, Z., Grabulov, V., Gubeljak, N., Sedmak, A., “*The influence of micro-structure on ductile fracture initiation in low-alloyed steel*”. Materials Science Forum, Vol. 453-454, (2004), pp. 175-180.
41. Awerbuch, J., “*Fundamentals of mechanical behaviour of materials*”. Wiley Custom Publishing, Philadelphia, (2001).

FATIGUE ANALYSIS USING FRACTURE MECHANICS

Zijah Burzić

*Military Technical Institute, Belgrade, Serbia,
zijah_burzic@vektor.net*

Meri Burzić

Institute GOŠA, Belgrade, Serbia

1. INTRODUCTION

Fatigue properties offer information for structural life assessment in many engineering applications. They are a critical element in the path relating the materials of construction to the components and must take into account many influences to reflect the actual situation. In application, fatigue requests a detail analysis, trying to assess what will occur at a particular location of a component or assembly under cyclic loading.

The topic of fatigue properties is very broad and is typically based on testing coupons. To be applicable, determined properties must support proper fatigue design approach. Three general approaches to fatigue design are considered here, and their individual property requirements are described. The purpose is to provide the basic insights necessary to examine those properties that can be found, review some of the common presentation formats, and recognize their inherent characteristics, which may be critical in actual application. The susceptibility of mechanical properties to variation through microstructural manipulation and structural consideration can be substantial.

The testing for property characterisation is reviewed briefly, with the discussion of relations between material, property, and structure. Three sections cover specific properties to the major design approaches: stress-life, strain-life, and fracture mechanics, with selected examples of properties that reflect some detail of each approach.

Fatigue life assessment is obviously one of the main areas requiring properties development. Basically, data for test coupons are only good for life assessment of test coupons; other structures may not be as amenable to assessment. The substantial amount of scatter in results is one of the contributing features to these difficulties. Verification of life estimations should be considered as an important activity to confirm the calculations. For the sake of brevity, only the constant-amplitude loading will be discussed. But, it is essential to understand that variable-amplitude loading can produce different rankings than constant-amplitude results. Another concession to brevity is that within the fracture mechanics area, only plane-strain state is included /1/.

2. FATIGUE DESIGN PHILOSOPHY

Fatigue properties have to be consistent with one of three general fatigue design philosophies (Table 1). Each of these has a concomitant design methodology and at least one way of representing testing data that provide the properties of interest.

These "lifing" or assessment techniques correspond to the historical development and evolution of fatigue technology over the past minimum 150 years.

Table 1: Basic design philosophy and methodology with principal testing method

Design philosophy	Methodology	Principal testing data description
Safe-life, infinite-life	Stress-life	Stress - number of cycles, $S-N$
Safe-life, finite-life	Strain-life	Strain - number of cycles, $\epsilon-N$
Damage tolerant	Fracture mechanics	Crack growth rate-stress intensity factor range, $da/dN-\Delta K$

The safe-life, infinite-life philosophy is the oldest approach to fatigue. It is developed based on August Wöhler's work on railroad axles in Germany in the mid-1800s /2/. The design method is stress-life, generally presented by $S-N$ (stress vs. number of cycles to failure). Failure in $S-N$ testing is typically defined by total separation of the sample.

Applicability of the stress-life method is restricted to the homogeneous continuum, assuming no cracks in it. However, some design guidelines for weldments, which inherently contain discontinuities, offer reduced residual life for a variety of process and joint types that generally follow the safe-life, infinite-life approach /3/. The advantages of this method are simplicity and ease of application. It is best applied in or near the elastic range, addressing constant-amplitude loading situations in what has been called the long-life (hence infinite-life) regime.

The stress-life approach is best applied to components similar to the test samples in shape and size, important for total separation as a failure criterion. It is applicable ferrous metals, especially steels. Other materials may not respond in a similar manner.

Through the 1940s and 1950s, mechanical designs pushed to further extremes in advanced machinery, resulting in higher loads and stresses, including the plastic regime of material and a more explicit consideration of finite lived components. Then the description of local events in terms of strain made more sense and resulted in the development of assessment techniques that used strain as a determining quantity. The general data presentation is in terms of $\epsilon-N$ (log strain vs. log number of cycles to failure). The failure criterion is the detection of a "small" crack or some equivalent measure related to a change in load-deflection response, although failure may also be defined by separation.

The use of strain is a consistent extension of the stress-life approach. As with the safe-life, infinite-life approach, the strain-based safe-life, finite-life philosophy relies on the "no cracks" restriction of continuous media. While more complicated, this technique offers advantages: it includes plastic response, addresses sound approach for finite-life, can be generalized to different geometries and variable amplitudes, and can account for a variety of other effects. The strain-life method is better suited to handling a greater diversity of materials. Because it does not necessarily attempt to relate to total failure (separation) of the part, but can really initiation for final failure, it has a substantial advantage over the stress-life method. But this method is more complex, and has more complicated proprietary descriptions.

The ability to generate and model both $S-N$ and $\epsilon-N$ data effectively is very important. From a design standpoint, there are some circumstances where inspection is not a regularly used practice, unfeasible, or sometimes physically impossible.

In both presented techniques substantial assumption is continuity ("no cracks"). But it is far from reality. Many components, assemblies, and structures, have crack-like discontinuities induced during service or repair or as a result of primary or secondary processing, fabrication, or manufacturing, which could not be detected because of limited susceptibility of applied non-destructive testing equipment. However, defective parts can

to bear load and can operate safely for extended periods of time. Developments from the 1960s and before have produced the third design philosophy, damage tolerant. It is intended expressly to address the issue of "cracked" components.

When a crack is present, an alternative controlling quantity is involved, as mode I stress intensity factor range, (ΔK_I), a function of crack location, orientation, and size within the geometry of the part. This fracture mechanics parameter is then related to the potential for crack extension under the imposed cyclic loads for subcritical growth or the initiation of unstable fracture. It is quite different from the other two approaches. Property descriptions for the crack extension under cyclic loading are typically $da/dN - \Delta K_I$ curves (log crack growth rate vs. log stress-intensity range), Table 1.

The advantage of the damage tolerant design philosophy is the ability to treat cracked objects in an appropriate fashion. The previous methods only allow for the immediate removal of cracked structure, and here the number of cycles of crack growth over a range of crack sizes can be estimated and fracture to be predicted. The clear tie of crack size, orientation, and geometry to non-destructive testing (NDT) is also a benefit. Disadvantages are connected with complexity in development and modelling of property data, and required numerical integration for crack growth. The predicted lives are influenced by the initial crack size, requiring quantitative determination of detection probability for each type of NDT method used.

3. INFINITE-LIFE CRITERION (*S-N* CURVE)

Safe-life design based on the infinite-life criterion reflects the classic approach to fatigue. It was developed through the 1800s and early 1900s because complex machinery of that time increasingly produced dynamic loads, followed by increasing number of failures. The safe-life, infinite-life design philosophy was the first to address this need.

The stress-life or *S-N* approach is one of a safe-life, infinite-life regime. It is categorized as a "high cycle fatigue", with most considerations based on maintaining elastic behaviour in the examined object. The "no cracks" is accepted, although all test results inherently include the influence of the discontinuity population present in the object.

In this period steel was dominant metallic structural material (land transportation, power generation, constructions). The "infinite-life" aspect of this approach is related to the asymptotic behaviour of steels, many of which exhibited a fatigue limit or "endurance" limit at a high number of cycles ($>10^6$). Most other materials do not exhibit this response, displaying a continuously decreasing stress-life response, even at a great number of cycles (10^6 to 10^9), more correctly described by fatigue strength at a given number of cycles. Figure 1 shows a schematic comparison of these two characteristic results. Many machine design texts cover this method to varying degrees /4-8/.

What about the *S-N* data presentation? Stress is the controlling quantity in this method. The most typical formats for the data are to plot the log number of cycles to failure (sample separation) versus either stress amplitude (S_a), maximum stress (S_{max}), or stress range (ΔS) /9, 10/. Figure 2 provide plots for three constant-*R* value tests (*R* is the ration of minimum and maximum stress in a cycle, the second dynamic variable). Note the apparent reversal of the effect of *R*, although the data are identical. Clearly, while the analytical result must be identical regardless of which graphic means is employed, the visual influence in interpretation varies with the method of presentation.

Mean stress influence is important, and design approach must consider it. According to Bannantine et al. /7/, the archetypal mean stress (S_m) versus stress amplitude (S_a)

presentation displays mean stress effects in the safe-life, infinite-life regime, proposed by Haigh. The Haigh diagram is a plot of real data, but it requires an enormous amount of information. More convenient means to show the same information incorporates the Haigh diagram with S_{max} and S_{min} axes to produce a constant-life diagram (Fig. 3).

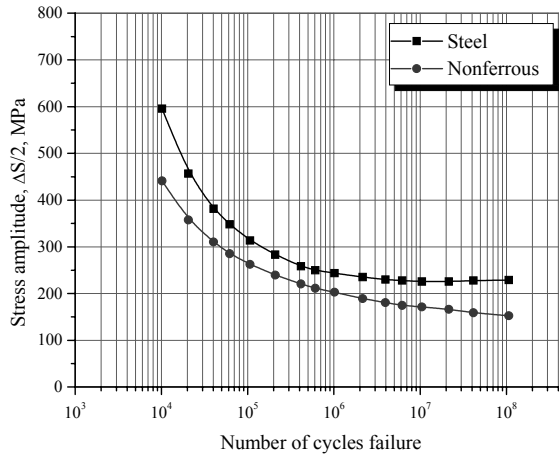


Figure 1: Schematic S - N representation of materials having asymptotic fatigue limit behaviour (up) and those displaying a fatigue strength response - continuously decreasing property (down)

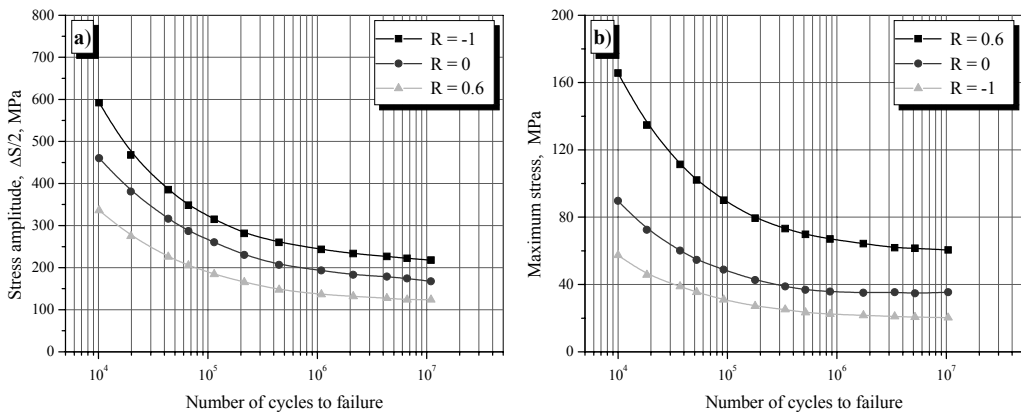


Figure 2: The influence of method of S - N data presentation on the effect of R ($=S_{min}/S_{max}$) value. Stress amplitude S_a vs. number of cycles N (left), maximum stress S_{max} vs. N (right) /10/

For general consideration of mean stress effects, various models of the mean-amplitude response have been proposed. A commonly used presentation is the Goodman line, although other models are possible (e.g., Gerber and Soderberg). The conventional plot associated with this problem is produced using the Haigh diagram, with the Goodman line connecting the ultimate strength on S_{max} , and the fatigue limit, corrected fatigue limit, or fatigue strength, on S_a . This line then defines the boundary of combined mean-amplitude pairs for anticipated safe-life response. The Goodman relation is linear and can be readily adapted to a variety of manipulations.

In many cases Haigh or constant-life diagrams are simply designed, using the Goodman presentation approximating actual response through the model of the behaviour. For materials that do not have a fatigue limit, the fatigue strength at a given

number of cycles can be applied for the intercept on the stress-amplitude axis. Examples of the Haigh and constant-life diagrams are shown in Fig. 3 and 4. Figure 4 is of interest also because of its design in terms of ultimate tensile strength percentage for the strength ranges included. This diagram is for average test data for axial loading of polished specimens of AISI 4340 (DIN 40 NiCrMo6) steel (ultimate tensile strength, UTS, 850 to 1250 MPa) and is applicable to other steels (e.g., AISI 2330, 4130, 8630) /11/.

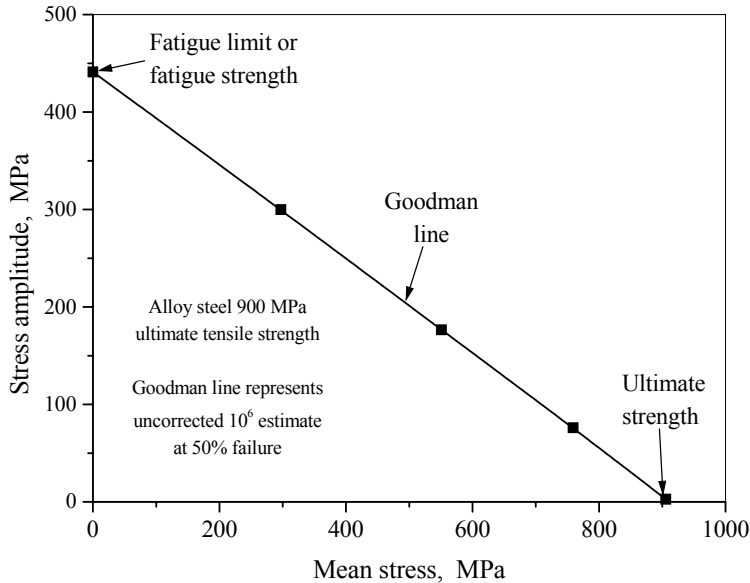


Figure 3: Haigh diagram based on employed approximations for the axes intercepts and using the Goodman line to establish the acceptable envelope for safe-life, infinite-life combinations

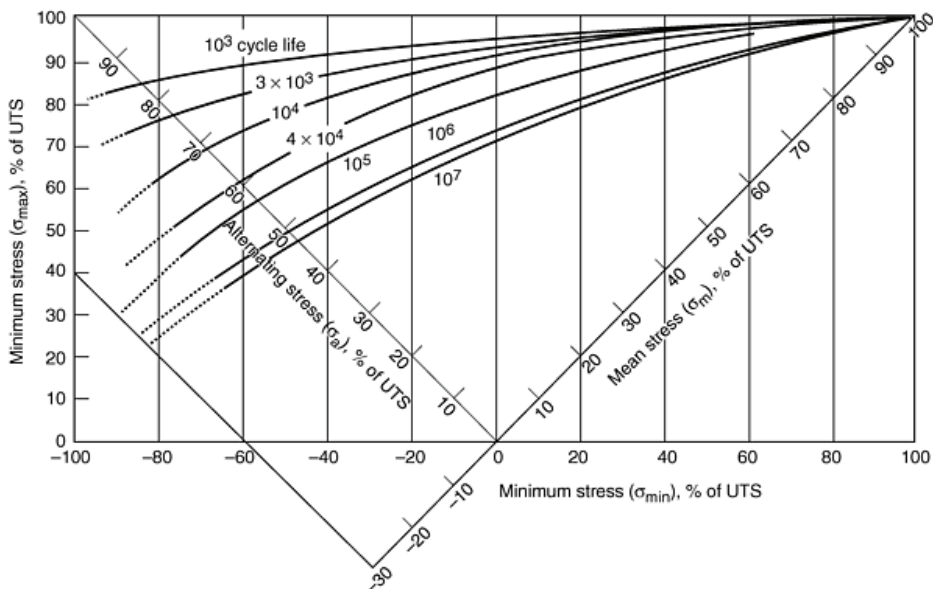


Figure 4: A constant-life diagram for alloy steels that provides combined axes for more ready interpretation. Note the presence of safe-life, finite-life lines on this spot.

Other examples of metallic response to cyclic loading in this regime are also interesting, like the behaviour of an aluminum alloy 2219-T85 (Fig. 5), showing a S_{max} versus $\log N$ plot, with the supporting data shown /12/. This is a typical S-N diagram, showing the fitted curve as the actual data that support the diagram. This is the currently required approach for representing this type of information in the handbook /12/.

Plastics and polymeric composites are interesting materials for different responses under mechanical loading, including dynamic excitation. The nature of hydrocarbon bonding results in substantially more hysteresis losses under cyclic loading and a greater susceptibility to frequency effects. An example of $S-N$ results for a variety of materials is given in Fig. 6. Also, different specifications are used for fatigue testing of plastics /13/. The plastics industry also employs tests to determine a "static" fatigue response, which is a sustained load test similar to a stress-rupture or creep test of metallic materials.

In application, this method is in its simplest form for steels in a neutral environment. The task is to compare the S_a determined in the part to a S_a vs. N curve at the necessary R value. Acceptable safe-life, infinite-life situation exists if the applied S_a is less than the fatigue limit. In a slightly more complex scenario, the S_m, S_a pair applied in a component is compared to the properly determined Goodman line on a Haigh diagram with two possible results: on or under the Goodman line indicate an acceptable safe-life, infinite-life situation, and results above the Goodman line indicate a finite-life situation that can be managed if the general boundary conditions of the method are not abused.

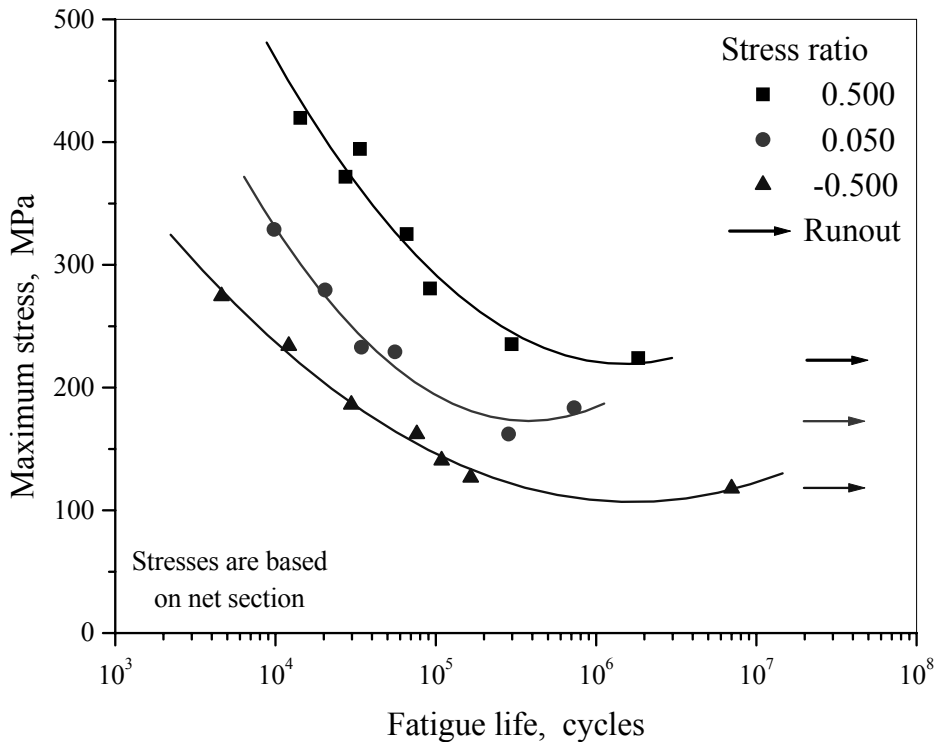


Figure 5: Best-fit S/N curves for notched, 2219-T851 aluminium alloy plate in longitudinal direction, with stress concentration factor $K_t = 2.0$

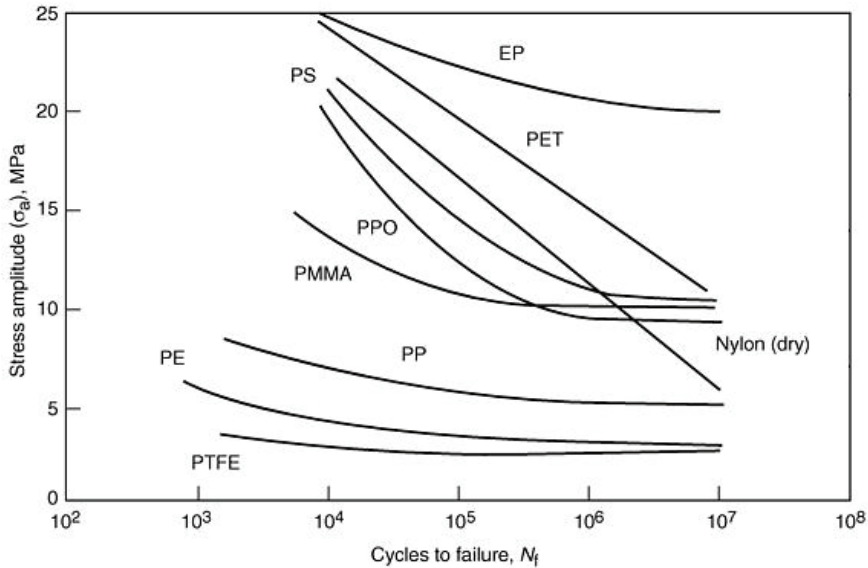


Figure 6: Typical fatigue-strength curves for different polymers (30 Hz test frequency) /14/

In multiaxial stress states the difficulty occur in identifying an appropriate "stress", and the stress-life technique offers then a variety of advantages. Its extension using strain as a controlling quantity is a natural progression of technology.

4. DAMAGE TOLERANT CRITERION: FRACTURE MECHANICS IN FATIGUE

The $S-N$ and $\epsilon-N$ techniques are usually appropriate when a component or structure can be considered a continuum (i.e. "no cracks" assumed). they can't be applied when a crack-like discontinuity is present. The fact that components with "cracks" may continue to bear load is generally not acceptable using either $S-N$ or $\epsilon-N$ methods.

One reason is the inability of the controlling quantities to allow the presence of a crack. A brief review of basic elasticity calculations shows that both stress and strain become infinite at a crack due to elastic stress concentration. Even induced plasticity still leaves low tolerable loads. An alternative concept and controlling quantity is required. That quantity is *stress intensity*, a characterization and quantification of the stress field near the crack tip, base of linear elastic fracture mechanics (LEFM). It recognizes the singularity of stress at the tip and provides measurable material property.

The development of fracture mechanics has roots in the early 1920s and mainly has developed since the late 1940s and early 1950s. A very basic expression for the stress intensity is its determination for a semi-infinite center-cracked panel having a through-thickness crack of length $2a$ in a uniform stress field σ that is operating normal to the opening faces of the crack. The resulting stress intensity factor K_I is as follows /15/:

$$K_I = \sigma \cdot \sqrt{\pi \cdot a} \tag{1}$$

where is the far field stress responsible for opening mode loading (mode I) and a is the crack depth in from the edge of the plate.

This formula allows an appreciation of the combined influence of stress and crack length. Stress intensity depends directly, but not singularly, on stress, and it depends on crack length. In a more general format, stress intensities might be expressed as:

$$K_I = \sigma \cdot \sqrt{\pi \cdot a} \cdot Y \quad (2)$$

where Y is a geometric factor allowing the representation of other geometries.

In fact, a stress can never be applied, but a load can. Stress is a resultant and determined quantity; it is not measurable. It is a mathematical tool of useful characteristics and provides interpretations and insights, especially in reflecting an areal rationalized force (load) path through the structure. Structures and materials, however, only experience loads (mechanical, thermal, chemical) and respond with displacements and strains.

In some cases, however, where complexity precludes a simple "stress" approach, analytical techniques do allow the calculation of stress intensity factors under the imposed loads. The connection of stress intensity, K_I , as a controlling quantity for fracture is a direct consequence of a physical model for LEFM under plane-strain conditions. Its limit is K_{Ic} , the critical plane-strain fracture toughness. The use of the stress intensity range, ΔK_I , as a controlling quantity for crack extension under cyclic loading is simply by correlation. The ability of the stress intensity to reflect crack-tip conditions remains mathematically correct, but the correlation of ΔK_I to crack growth is successfully demonstrated. By altering Eq. (1) using $\Delta\sigma$ instead of σ , ΔK_I results in:

$$\Delta K_I = \Delta\sigma \cdot \sqrt{\pi \cdot a} \quad (3)$$

The stress intensity factor range to a certain extent simply reflects an extension of the stress-based practices. However, the testing to support fracture mechanics-based fatigue data is done differently than in the $S-N$ or $-N$ methods because of the necessity to monitor crack growth. Crack growth testing is performed on samples with established K_I vs. a relation. Under the controlled load specified using two dynamic variables, the crack length is measured at successive intervals to determine the extension over the last increment of cycles. Crack length measurement can be done visually or by mechanical or electronic devices using established techniques that allow for automation of the process.

The result from the testing is not crack growth rate, da/dN , but a versus N . Next numerical differentiation of the $a-N$ data set using provides da/dN versus a . Coupling this latter data with a stress intensity factor expression (K_I as a function of load and crack length) for the specific sample results in the final desired plot of da/dN versus ΔK_I . This process is shown schematically in Fig. 7. The da/dN versus ΔK_I curve has a sigmoidal shape, and a full data set covers crack growth rates that range from fatigue crack threshold to fracture. It is to note that this data represents only "long crack" behaviour; that is, the cracks are substantially greater in size than any controlling microstructural unit (e.g. grain size) and typically exceed several millimeters in length. A second important assumption is that of a plane-strain stress state; therefore, a plane-stress descriptor is not required.

A real test of modelled da/dN vs. ΔK_I expressions is whether, under reintegration, the original $a-N$ data will be reproduced. The generation of da/dN vs. ΔK_I data is obviously more involved than either $S-N$ or $\epsilon-N$ testing. It does have the advantage, however, of producing multiple data points from a given test. Figure 8 reflects interesting features at each extreme of the da/dN vs. ΔK_I curve. First, at the upper limit of ΔK_I , it reaches the point of instability and the crack growth rate become very large as fracture is approached.

The second point of interest is the lower end of the ΔK_I range where crack growth rate essentially decrease to zero; this is identified as the fatigue crack growth threshold, $\Delta K_{I, th}$.

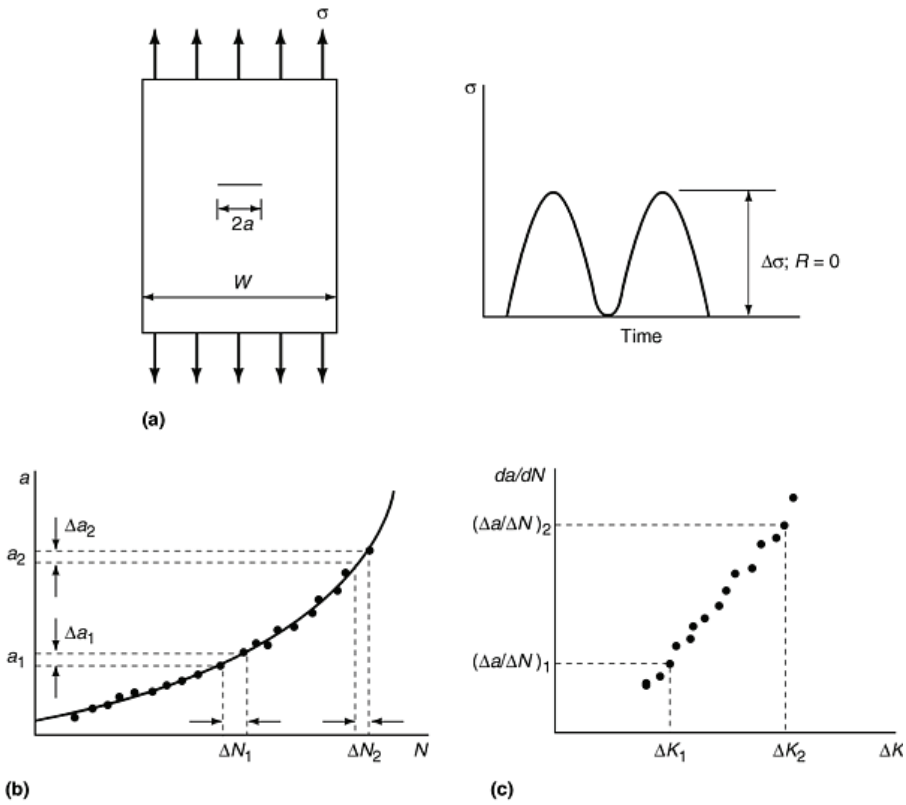


Figure 7: (a) Specimen and loading in modelling process for generating fatigue crack growth rate (da/dN vs. ΔK). (b) Measured data. (c) Rate data /15/

The existence of threshold behaviour at low ΔK_I values is analogous, in some senses, to the fatigue limit of some ferrous materials in $S-N$ response. If, with the appropriate R ratio, the stress intensity factor range is below the threshold value, $<\Delta K_{I, th}$, cracks will not extend under the applied load. Thus, an assessment of nonpropagating crack can be made.

A reflection on failure criterion is appropriate here. Much as K_I is a quantity for assessing the point of unstable fracture initiation, $\Delta K_{I, th}$ is the limit for the initiation of crack growth (for "long" cracks) under cyclic loading. Above $\Delta K_{I, th}$ and below instability, the criterion for subcritical extension is satisfied and the rate is as determined by the curve.

4.1. Correlation between da/dN and ΔK

Linear elastic fracture mechanics is an analytical procedure that relates the magnitude and distribution of stress in the vicinity of a crack tip to the remote nominal stress applied to the structure, to the size, shape, and orientation of the crack, and to the crack growth and fracture resistance of the material. The procedure is based on a single parameter, K , called the stress-intensity factor, derived from the mathematical analysis of stress-field equations, in the region of a crack tip. This same procedure is used to characterize fatigue crack growth rate (da/dN) in terms of the cyclic stress-intensity factor range (ΔK).

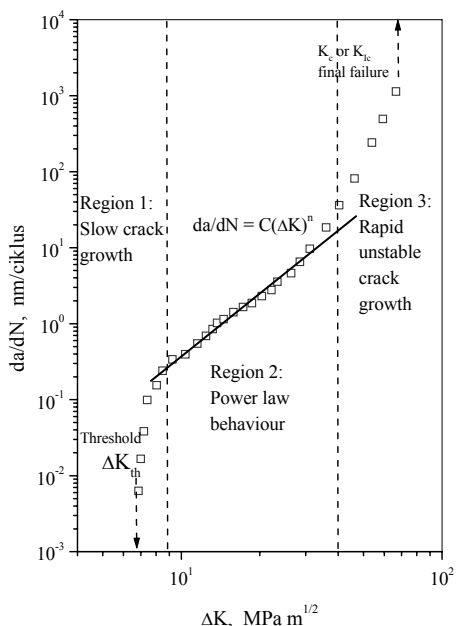


Figure 8. Asymptotic behaviour of da/dN vs. ΔK plot for 13 CrMo 4 4 steel at either end and a linear portion in the central part /16/

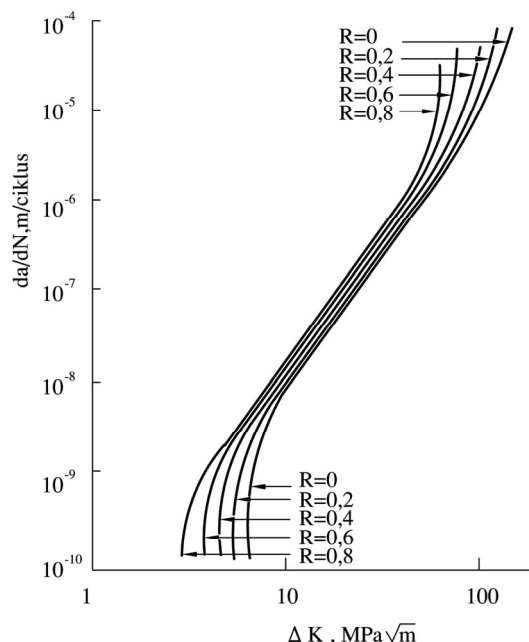


Figure 9. The influence of R value on the fatigue crack growth characteristics of a steel /17/

The crack length (a) increases with the number of fatigue cycles, N , when a component or a specimen containing a crack is subjected to cyclic loading, if the load amplitude (ΔP), load ratio (R), and cyclic frequency (ν), are held constant. The crack growth rate, da/dN , increases as the crack length increases during a given test and in structure. The da/dN is higher at any given crack length at higher load amplitudes. Thus, the following functional relationship can be derived from these observations:

$$\left(\frac{da}{dN}\right)_{R,\nu} = f(\Delta P, a) \quad (4)$$

where the function f is dependent on the geometry of the specimen or component, the crack length, the loading configuration, and the cyclic load range. This general relation is simplified with the use of the ΔK parameter as summarized below.

In 1963, Paris and Erdogan /18/ published an analysis with sufficient fatigue crack growth rate (FCGR) data, deriving a correlation between da/dN and the cyclic stress intensity parameter, ΔK . They argued that ΔK characterizes the magnitude of the fatigue stresses in the crack tip region, characterizing the crack growth rate in agreement with the relationships of Eq. (4). The parameter ΔK accounts for the magnitude of the load range (ΔP) as well as the crack length a and geometry. Later studies /19/ has confirmed the findings of Paris and Erdogan. The data for intermediate FCGR values can be represented by the simple mathematical relationship, commonly known as the Paris equation:

$$\left(\frac{da}{dN}\right) = C \cdot (\Delta K_I)^n \quad (5)$$

where C and n are constants that can be obtained from the intercept and slope, respectively, of the linear log da/dN versus log ΔK plot (Figs. 8 and 9).

It has been shown that specimen thickness has no significant effect on the FCGR behaviour /20/, although that is not always the case. The ability of ΔK to account for so many variables has tremendous significance in the application of the data. Thus, the FCGR behaviour expressed as da/dN versus ΔK can be regarded as a fundamental material property analogous to the yield and ultimate tensile strength, or plane strain fracture toughness, K_{Ic} , /21/. Knowing this property, prediction of the crack length vs. cycles behaviour of any component using that material and containing a preexisting crack or crack-like defect can be obtained, as long as the fatigue stresses in the component are known and a K expression for the crack/load configuration is available.

This is a simple exponential relation that can readily be curve fit to the desired data portion, Fig. 9. Stress or load ratio affects crack propagation data as well. The influence is that increasing R (here $R = K_{min}/K_{max}$) decreases both the threshold value at the low end and the instability at the up end of the da/dN vs. ΔK curve (Fig. 10 /22/, Fig. 11 /8/).

Like other mechanical properties, microstructure affects also fatigue crack growth characteristics. An example, given in Fig. 12, shows the combined influence of both gamma prime and grain sizes on fatigue crack propagation in Waspaloy.

Plastics also can be analysed using this technique. Figure 13 shows a variety of materials that are displayed in the conventional form. Many polymeric materials exhibit substantial frequency effects, and this should be considered in the generation of data.

In application, use of da/dN versus ΔK_I is completely different than either the $S-N$ or $\varepsilon-N$ continuum method. Instead of providing an immediate life estimate in association with a given stress or strain combination and a test coupon's modelled failure criterion, a more complicated determination is required. Using the a versus ΔK_I relation in the part, the applied loads are employed to assess crack extension over incremental changes in length, and they are continuously summed to reflect the total increase. In essence, this is the regeneration of the $a-N$ curve for the specific part. Crack growth can be assessed until fracture (achieving a critical crack size) or some other intermediate point.

It is common in several industries to use the above technique to determine intervals between inspections to ensure structural integrity. So formulated inspection schedules maximises the probability to detect discontinuity only in an extended, critical stage, enabling to use advantages of the damage tolerant approach. Even on this technique, a crack, once discovered, can't necessarily be left. Removal or structural modification may be the only acceptable alternative (e.g. in airframes). The predictive aspects of the technique can justify continued operation under full or derated conditions till requested replacement parts or with a stated finite-life limit for the unit (extra inspections may be required). By probabilistic methods a quantified risk assessment can be assessed.

4.2. Test procedure

American Society for Testing and Materials (ASTM) Standard E647 /25/ is the accepted guideline for fatigue crack growth rate (FCGR) testing and is applicable to a wide variety of materials and growth rates. The testing consists of several steps, starting with selecting the specimen size, geometry, and crack length measurement technique. When planning the tests, the investigator must respect of the application of FCGR data. Testing is often performed in laboratory air at room temperature; however, any gaseous or liquid environment and temperature may be used to determine the effect of temperature and corrosion on cyclic loading. Cyclic loading also may involve various waveforms for constant-amplitude loading, spectrum loading, or random loading.

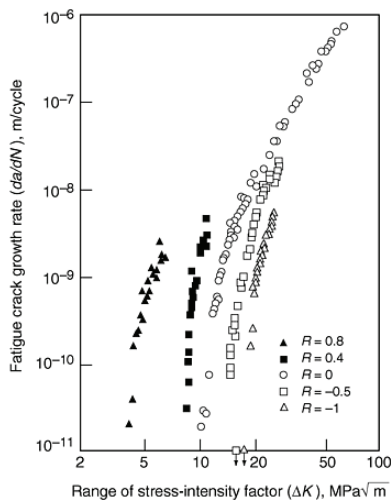


Figure 10: The effect of R value on the fatigue crack growth of a steel St 42-2 (DIN) /22/

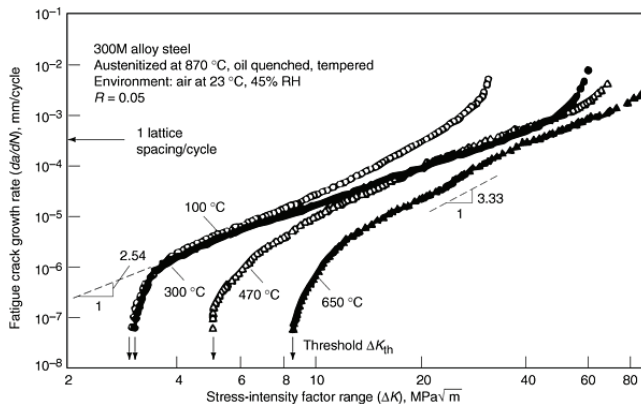


Figure 11: R value effects on threshold and fracture instability behaviour of 300M steel /8/

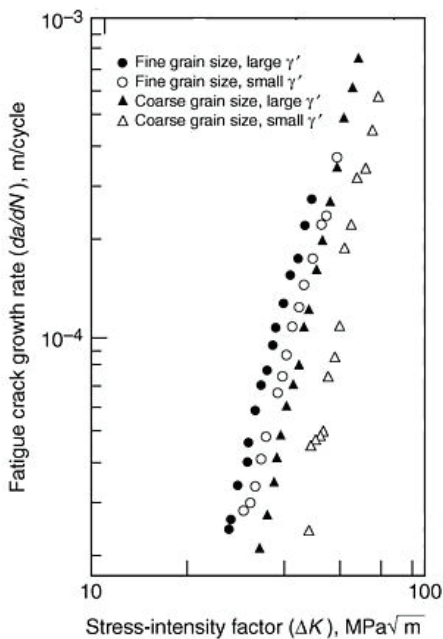


Figure 12: Effect of grain size on fatigue crack growth of Waspaloy super alloy /23/

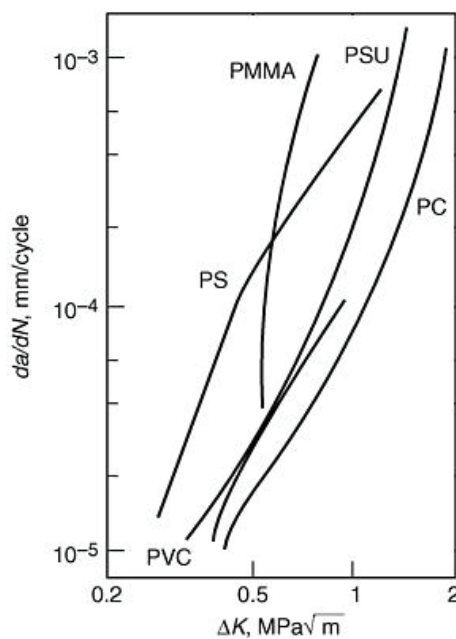


Figure 13: Fatigue crack propagation behaviour of various polymers /24/

In addition, many of the conventions used in plane-strain fracture toughness testing, ASTM E-399 /26/, are also used in FCGR testing. For tension-tension fatigue loading, the K_{Ic} loading fixtures frequently can be used. For this type of loading, both the maximum, P_{max} , and P_{min} , minimum loads in a cycle are tensile, and the load ratio, $R = P_{min}/P_{max}$, is in the range $0 < R < 1$. A ratio of $R = 0.1$ is commonly used for comparative purposes.

In the threshold and the low-growth regime FCGR testing (region I in Fig. 8) acquisition of valid and consistent data is complicated, since the crack growth behaviour is more sensitive to the material, environment, and testing procedures. Within this regime, the material fatigue mechanisms that slow the crack growth rates are more significant.

It is expensive to obtain a true value of ΔK_{th} . In some materials it does not even exist. Designers are more interested in the fatigue crack growth rate at threshold regime, e.g. ΔK corresponding to a fatigue crack growth rate 10^{-8} to 10^{-10} m/cycle. Because the duration of the tests increases for each decade of near-threshold data (10^{-8} to 10^{-9} to 10^{-10}), the precise requirements should be determined before the test. ASTM Standard E- 647 addresses these requirements, but the methods for fatigue crack threshold test may differ.

In all areas of crack growth rate testing, the resolution capability of the crack measuring technique should be known, what is more important in the threshold regime. The smallest amount of crack length resolution as possible is desired, because the rate of decreasing applied loads (load shedding) is dependent on how easily the crack length can be measured. The minimum amount of change in crack growth that is measured should be ten times the crack length measurement precision. It is also recommended that for non-continuous load shedding testing, where $[(P_{max} - P_{min})/P_a] > 0.02$, where mean value is accepted as $P_a = (P_{min} + P_{max})/2$, the reduction in the maximum load should not exceed 10% of the previous maximum load, and the minimum crack extension between load sheds should be at least 0.50 mm.

4.2.1. Specimen type selection

In selecting a specimen, the resolution capability of the crack measuring device and the K -gradient (the rate at which K is increased or decreased) in the specimen should be known. If the measuring device is not suitable, the threshold crack growth rate may not be achieved before the specimen is fractured. When a new crack-length measuring device is applied, a new type of material used, or some factor is different from previous testing, the K -decreasing portion of the test should be followed with constant load amplitude (K -increasing) to make the methods comparable. With consistency achieved, constant-load amplitude testing at the low crack growth rate is not necessary in similar conditions.

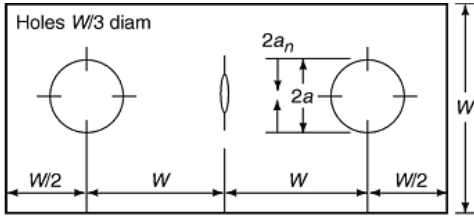
Three types of specimens used in FCGR testing are commonly used: pin-loaded (Figs. 14, 15), bend-loaded (Fig. 16.a) and wedge-gripped specimens (Fig. 16.b, c, d). Precisely machined specimens are essential, and ASTM E 647 specifies the tolerances and K -calibrations for compact-type C(T) and middle-tension M(T) geometries. Single-edge bends SE(B), arc-shaped A(T), and disk-shaped compact DC(T) specimen geometries and their K -calibrations are discussed in ASTM E 399. Similar tolerances should be specified for "nonstandard" specimens. The selection of an appropriate geometry depends on material availability and form, desired loading condition, and equipment limitations.

The most widely used types of specimens are M(T) (Fig. 14), and C(T) specimens (Fig. 15). However, any specimen configuration with a known stress-intensity factor solution can be used in fatigue crack growth rate testing, assuming that the appropriate equipment is available for controlling the test and measuring the crack dimensions.

4.2.2. Specimen size, crack length and microstructure consideration

The applicable range of the stress-intensity solution of a specimen configuration is very important. Many stress-intensity expressions are valid only over a range of the ratio of crack length to specimen width (a/W). The expression given in Fig. 14 for C(T)

specimen is valid for $a/W > 0.2$, and for M(T) (Fig. 15) for $2a/W < 0.95$. The use of stress-intensity expressions outside prescribed region can produce errors in results.



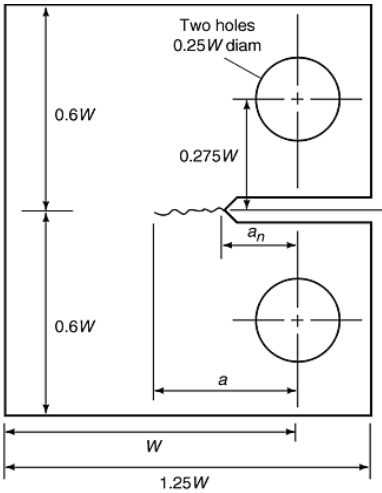
Center-cracked tension specimens ΔK value

$$\Delta K = \frac{\Delta P}{B} \sqrt{\frac{\pi a}{2W}} \sec \frac{\pi \alpha}{2}$$

$$\alpha = 2a/W$$

Expression valid for $2a/W < 0.95$

Figure 14: Standard center cracked tension - Middle-tension M(T), and ΔK solution



Compact-type specimens ΔK value

$$\Delta K = \frac{\Delta P(2+a)}{B\sqrt{W}(1-\alpha)^{3/2}} \left(0866 + 4.64\alpha - 13.32\alpha^2 + 14.72\alpha^3 - 5.6\alpha^4 \right)$$

$$\alpha = a/W$$

Expression valid for $a/W < 0.2$

Figure 15: Standard compact-type specimen - C(T), and ΔK value /25/

The size of the specimen must also be appropriate. To follow the LEMF rules the specimen must be tested in elastic range. However, unlike the requirements for plane-strain fracture toughness testing, the stresses at the crack tip do not have to be in a plane-strain state, but stress state should be controlled by test variable, according to material properties, specimen size, crack length, and applied load. Since the loading modes of different specimens vary, each specimen geometry must be considered separately.

For the center-cracked tension M(T) specimen, it is required that:

$$W - 2a \geq \frac{1.25P_{max}}{B\sigma_{YS}} \quad (6)$$

where $W - 2a$ is the uncracked ligament of the specimen (Fig. 14) and σ_{YS} is the 0.2% offset yield strength at the temperature corresponding to the FCGR data.

For the compact-type C(T) specimen, it is required that:

$$W - a \geq \frac{4}{\pi} \left(\frac{K_{max}}{\sigma_{YS}} \right)^2 \quad (7)$$

where $W - a$ is the uncracked ligament (Fig. 7). For C(T) specimen, the size requirement in Eq. (7) limits the monotonic plastic zone in a plane-stress state to about 25% of the uncracked ligament. For both Eqs. (6) and (7), the size requirements are appropriate for

low-strain hardening materials ($\sigma_{UTS}/\sigma_{YS} \propto 1.3$), where σ_{UTS} is the ultimate tensile strength, and ASTM E 647 recommends the use of the monotonic yield strength. For higher-strain hardening materials, Eq. (6) and (7) may be too restrictive, and the criteria may be relaxed by replacing the yield strength, σ_{YS} , with the effective yield strength, σ_F :

$$\sigma_F = \frac{(\sigma_{YS} + \sigma_{UTS})}{2} \quad (8)$$

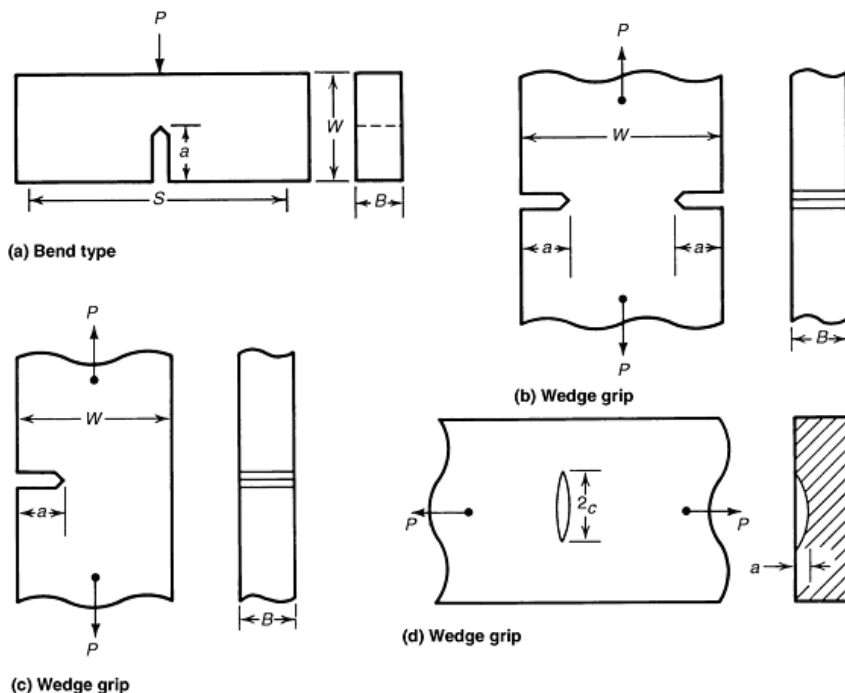


Figure 16: Alternative geometries of crack growth test specimens: a) Single-edge-crack bending. b) Double-edge crack tension. c) Single-edge-crack tension. d) Surface-crack tension.

Fatigue crack growth rates are relatively insensitive to stress state (i.e. plane-stress or plane-strain), there are some practical limitations on specimen thickness. ASTM E 647 recommends C(T) specimen thickness (B) range between 5 and 25% of width ($W/20 \leq B \leq W/4$), and M(T) specimens may have thicknesses up to 12% of width ($W/8$). For center-cracked tension specimens, thickness should not exceed 25% of width. Similar ranges for the thicknesses should be employed for other specimen types.

Although specimen thickness can vary, the amount of crack curvature in the specimen will increase as the thickness increases. Because stress-intensity solutions are based on a straight through-crack, a significant amount of curvature, if not properly accounted for, can lead to an error in the data. Crack-curvature correction calculations are detailed in ASTM E 647. The minimum allowable thickness depends on the gripping method used; however, the bending strains should not exceed 5% of the nominal strain in the specimen.

The material and its microstructure play an important role in the selection of specimen geometry. Materials with anisotropic microstructures due to processing (rolling, forging) may show large variations in fatigue crack growth rates in different directions [27]. If the experimental crack growth rate data are to be used for life estimates, the orientation of the specimen should be selected to represent loading orientation expected in service.

In order to eliminate grain size effects, it is usually recommended that the specimen thickness, B , be greater than 30 grain diameters [28, 29]. In some cases, such as in large-grain (~ 3 mm) lamellar γ - α_2 Ti-Al intermetallic or α - β titanium alloys, the required specimen sizes would be too expensive, test loads very high, and the component dimensions probably be less than 30 times the grain size. Then, testing should be performed on thickness representative of the component. Curvature of the crack front and side-to-side variation in crack length due to thickness can be a problem in thick specimens.

4.2.3. Specimen pre-cracking

The method by which a notch is machined depends on the specimen material and the desired notch root radius (ρ). Saw cutting is applicable to aluminium alloys, but for a notch root radius of $\rho = 0.25$ mm milling or broaching is required. In low- and medium-strength steels notch can be produced by grinding, but for high-strength steels, nickel-base super alloys, and titanium alloys electrical discharge machining may be necessary.

The specimen might be side polished to allow monitoring of crack growth, using standard metallography practices, if possible, sometimes followed by etching. For is too large or small specimen hand grinders, finishing sanders, or handheld drills can be used with pieces of polishing cloth to apply the abrasive and create a satisfactory viewing surface. These techniques are quick and easy to apply, and they are often used when visual measurements are made only during precracking and subsequent measurements are made by automated techniques such as electric potential or compliance.

The K -calibration functions from ASTM E 647 and E 399 are valid for sharp cracks within the range of crack length specified. Consequently, before testing begins a sharp fatigue crack that is long enough to avoid the effects of the machined notch must be present in the specimen. The process that generates this crack is termed precracking. Loads for precracking should be selected such that the K_{max} at the end of precracking does not exceed levels expected at the start of a test. For most metals, precracking is a simple process that can be performed under load or displacement control, with moderate growth rates (10^{-5} m/cycle) using ΔK from growth curves in the literature. To decrease the precracking time, common practice is to initiate crack at a load above that which will be used in test, and after that reduce it. Crack growth can be arrested above the threshold stress-intensity factor value due to formation of the increased plastic zone ahead of the tip of the advancing crack. The loads should be shed no faster than 20% (per increment of crack extension) from the previous load increment. As the crack approaches the final size, this percentage can be decreased.

The amount of crack extension between each load decrease must also be controlled. If the step is too small, the influence of the plastic zone ahead of the crack may still be present. To avoid transient (load-sequence) effects in the test data the load range in each step should be applied over a crack-length increment of at least $(3\pi) (K'_{max}/\sigma_{YS})^2$, where K'_{max} is the terminal value of K_{max} from the previous load step. This requirement ensures that the crack extension between load sheds is at least three plastic zone diameters.

The influence of the machined starter notch must be eliminated so that the crack tip conditions are stable. For C(T) and M(T) specimens the final precrack should be at least 10% of the thickness of the specimen or equivalent to the height of the starter notch.

Two additional considerations regarding crack shape are the amount of crack variation from the front and back sides of the specimen and the amount of out-of-plane cracking. Due to microstructural changes through the specimen thickness, residual stresses

(particularly in weldments), or misalignment of the specimen in the grips, the crack may grow unevenly on the two surfaces. If a fatigue precrack departs more than $\pm 5^\circ$ from the plane of symmetry, the specimen is not suitable for subsequent testing.

Brittle materials, such as intermetallic and ceramics, can be very difficult to precrack. Frequently initiated flaw immediately propagates to fracture. This is due, in part, to the increasing K gradient found in FCGR specimens and the relatively narrow range of ΔK for stable crack growth. Chevron-notched specimens (Fig. 17) are used for determining the fracture toughness of brittle materials that are difficult to fatigue precrack. Chevron notches generate decreasing K -gradients at the start of precracking and may be machined as part of the specimen, or they may be added just prior to testing using a thin diamond wafering blade. The maximum slope of the chevron notch should be 45° . Precracking of brittle materials should be performed under displacement control conditions, so that as the crack extends, the load and the applied K decrease. Lastly, the loads should be increased slowly from low levels due to the stochastic nature of crack initiation in these materials. If initiation is especially difficult, compressive overloads may assist the process. It is also helpful to monitor the initiation process with a method other than optical observation, electric potential techniques and back face strain compliance.

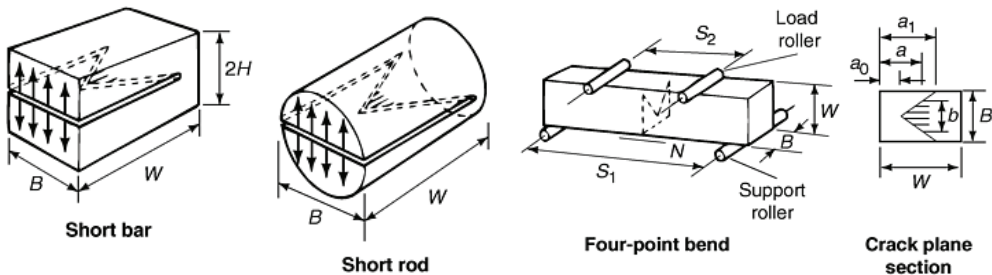


Figure 17: Chevron notch in fracture mechanics specimens - the shaded area (b) is the crack area

Once precracking has been completed, an accurate optical measurement of the initial crack length, a_0 , must be made on both sides of the specimen to within 0.10 mm or $0.002W$, or to within 0.25 mm for specimens of $W > 127$ mm. If the crack lengths on the two surfaces differ by more than $0.25B$, then the test will not be valid, because K -calibration functions presume the existence of a straight crack front. Once the precrack has been measured and side-to-side variation and distance from centerline have been established, testing may start.

4.2.4. Equipment

Specimen size and geometry can also be influenced by laboratory equipment such as the load frame, load cell, existing loading fixtures, testing environment, and even the crack length measurement device, and available tools and equipment should be used.

Most modern mechanical testing laboratories exclusively use electrical servo hydraulic load frames for FCGR investigations. Current controls and data acquisition technology of hydraulic load-frames are more versatile than the electromechanical systems used in previous years. When selecting a specimen geometry and size, one must be aware of the load capacity of the actuator and load-frame. Loads that are too high cannot be applied, and those that are too low cannot be controlled with the required accuracy ($\pm 2\%$). In addition, the load cell to be used during testing must be able to

measure the maximum applied load and resolve the lowest expected amplitudes, as specified in ASTM E 4.

When testing in environments, specimens fit inside furnaces or cabinets with ample space left for clevises, cantilever beam clip gauges, and other hardware.

Gripping of the specimen must be done in a manner that does not violate the stress-intensity solution requirements. In grips that are permitted to rotate, such as the compact-type specimen grip, the pin and hole clearances must be designed to minimize friction. The alignment of the system should be checked carefully to avoid undesirable bending stresses and uneven cracking. Alignment can be easily checked using a strain gauge specimen. Gripping arrangements for compact-type and center-cracked tension specimens are described in ASTM E 647 /25/.

4.2.5. Loading

The loading conditions play an important role, and load ratio, R , residual stresses, K -gradients, and small-scale yielding (SSY) should be considered. All specimen geometries are well suited for tension-tension ($R > 0$) testing. However, tests that call for negative R are restricted to symmetric, wedge-grip loaded specimens, like the middle-tension specimens, sensitive to compressive loads and moving through zero loads.

Residual stresses in the material have a marked effect on FCGR and if they are through the thickness, perpendicular to the direction of crack growth, may accelerate or retard crack growth. When these stresses are not uniform, the ASTM E 647 recommends a reduction of the thickness-to-width ratio (B/W).

The rate at which K increases as the crack extends at a constant-load amplitude is given by the geometry function $f(a/W)$ and may be considered when selecting the most appropriate specimen geometry. Figure 17 shows the effect of geometry on the K -gradient through a variety of specimen geometries. Specimens with shallower K -gradients are preferable for brittle materials, while the opposite is true for ductile materials.

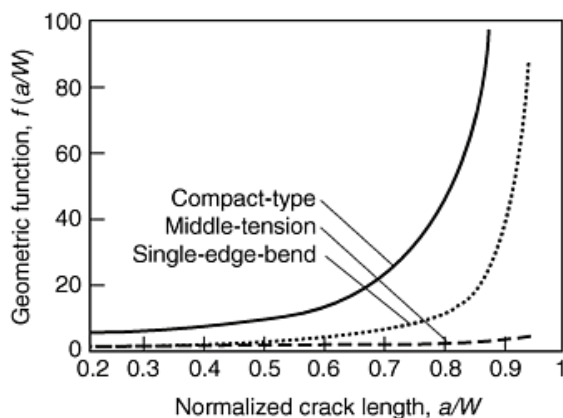


Figure 17: K-gradients for a number of fatigue crack growth specimens

4.2.6. Crack length measurement

Precise measurements of fatigue crack extension are crucial for the determination of reliable crack growth rates. ASTM E 647 requires a minimum resolution of 0.1 mm in crack length measurement. Various crack measurement techniques have been applied, including optical (video, visual and photographic), ultrasonic, acoustic emission, electrical, and compliance (displacement and back face strain gauges) methods.

4.2.7. Analysis of crack growth data

The two major aspects of FCGR test analysis are to ensure suitability of the test data and to calculate growth rates from the data. The analysis also may require the calculation of fatigue crack closure level and the analysis of fracture surface and metallography. It is essential that computer-controlled tests generate records of a vs. N and FCGR. It is prescribed to ensure the validity of the test data and make corrections to the crack length, if necessary (ASTM E 647).

At the end of the test, the final crack length is measured on both sides of the specimen. The error between the final measured and predicted crack size is linearly distributed over the crack extension range. If periodic optical measurements were made during the test, other more appropriate correction procedures can be used.

REFERENCES

1. D.W. Cameron, and D.W. Hoepfner, *"Fatigue and Fracture"*, ASM Handbook Vol. 19, 2005.
2. A. Wöhler, Versuche über die Festigkeit der Eisenbahnwagenachsen, Zeitschrift für Bauwesen, 1860.
3. *"Dynamically Loaded Structures"*, AWS Structural Welding Code, ANSI/AWS D1.1-92, American Welding Society, 1992, p 185-201.
4. C. Lipson, G.C. Noll, and L.S. Clock, *"Stress and Strength of Manufactured Parts"*, McGraw-Hill, 1950.
5. J.E. Shigley and L.D. Mitchell, Mechanical Engineering Design, McGraw-Hill, 4th ed., 1983.
6. H.O. Fuchs and R.I. Stephens, Metal Fatigue in Engineering, John Wiley and Sons, 1980.
7. J.A. Bannantine, J.J. Comer, and J.L. Handrock, *"Fundamentals of Metal Fatigue Analysis"*, Prentice-Hall, 1990.
8. Fatigue Design Handbook, Society of Automotive Engineers, 2nd ed., 1988.
9. ASTM E 468-90, *"Standard Practice for Presentation of Constant Amplitude Fatigue Test Results for Metallic Materials"*, Annual Book of ASTM Standards, Vol 03.01, ASTM, 1995.
10. M. Burzić, MSc Thesis, Faculty of Technology and Metallurgy, Belgrade, 2001.
11. R.C. Juvinall, *"Engineering Considerations of Stress, Strain, and Strength"*, McGraw-Hill, 1967, p 274.
12. MIL-HDBK-5D, *"Military Standardization Handbook"*, Metallic Materials and Elements for Aerospace Vehicle Structures, 1983, p 3-164.
13. ASTM D 671-93, *"Test Method for Flexural Fatigue of Plastics by Constant-Amplitude-of-Force"*, Annual Book of ASTM Standards, Vol 08.01, ASTM, 1995.
14. A. Moet and H. Aglan, *"Fatigue Failure, Engineering Plastics"*, Vol 2, Engineered Materials Handbook, ASM International, 1988, p 742.
15. D. Broek, *"The Practical Use of Fracture Mechanics"*, Kluwer Academic Publishers, 1989, p 52.
16. M. Burzić, PhD Thesis, University of Novi Sad, Faculty of Technical Sciences, Serbia, 2008.
17. M. Burzić, R. Prokić-Cvetković, B. Grujić, I. Atanasovska, Ž. Adamović, *"Safe Operation of Welded Structure with Cracks at Elevated Temperature"*, Strojniški Vestnik - Journal of Mechanical Engineering, 2008, Vol. 54, No. 11, pp. 807-816.
18. P.C. Paris, and F. Erdogan, J. Basic Eng. (TRANS. ASME), Series D, Vol. 85, 1963, p.528-534.
19. P.C. Paris, Proc. 10th Sagamore Conf., Syracuse University Press, 1965, p. 107-132.
20. J.R. Griffiths and C.E. Richards, Mater. Sci. Eng., Vol. 11, 1973, p. 305-315.
21. M. Burzić, Ž. Adamović, *"Experimental Analysis of Crack Initiation and Growth in Welded Joint of Steel for Elevated Temperature"*, Materials and Tehnology, 2008, Vol .42 No. 6, pp. 263-271.

22. J.M. Barsom and S.T. Rolfe, *"Fracture and Fatigue Control in Structures"*, Prentice-Hall, 1987, p 299.
23. S.D. Antolovich and J.E. Campbell, *"Fracture Properties of Super alloys, Application of Fracture Mechanics for Selection of Metallic Structural Materials"*, American Society for Metals, 1982, p 271.
24. A. Moet and H. Aglan, *"Fatigue Failure, Engineering Plastics"*, Vol 2, Engineered Materials Handbook, ASM International, 1988, p 747.
25. ASTM E 647-03, *"Standard Test Method for Measurement of Fatigue Crack Growth Rates"*, Annual Book of ASTM Standards, Vol, 03.01, 2003, ASTM, p. 674-701.
26. ASTM E 399-91, *"Standard Method for Plane-Strain Fracture Toughness of Metallic Materials"*, Annual Book of ASTM Standards, Vol 3.01, 1992, ASTM, p. 569-596.
27. K.T. Venkateswara Rao, W. Yu, and R.O. Ritchie, *Metall. Trans. A*, Vol. 19A (No. 3), March 1988, p. 549-561.
28. A.W. Tompson and R.J. Bucci, *Metall. Trans.*, Vol 4, April 1973, p. 1173-1175.
29. G.R. Yoder and D. Eylon, *Metall. Trans.*, Vol 10A, Nov 1979, p. 1808-1810.

THEORETICAL BASIS OF STRUCTURAL INTEGRITY AND LIFE

Dražan Kozak

*University of Osijek, Mechanical Engineering Faculty in Slavonski Brod, Croatia
dkozak@sfsb.hr*

Nenad Gubeljak

University of Maribor, Faculty of Mechanical Engineering, Maribor, Slovenia

1. INTRODUCTION

Any structure, especially a welded structure contains the defects. These defects in welded structure can appear as a consequence of materials defects (like non-metallic inclusions) or, more often, as defects in the welded joints (like misalignment, distortion, root defects, slag, pores, inclusions, cracks). A crack can increase from such an initial defect to critical crack size. Crack growth frequently takes place in structures subjected to loads which are lower than nominal design load. The question how to ensure the structural integrity and reliable work of the structural components through their complete life, starting with design, through fabrication and exploitation) is continuously open and is the matter of many investigations. For that it is important to know more details about structure behaviour regarding when the working conditions are influencing factor of prime importance. The time interval of crack growth from defect to critical crack size can be considered as the safe service lifetime. The safe use and full function of a structure is possible during this time. Total loading capability and the reliable usage of a structure are the main concern of the investors and the users of a structure.

In this regard key questions are:

- How is the usage of the structure reliable?
- Is it possible to extend service-life-time of the structure?

This article gives the main principles for the safe and reliable use of structures. On the basis of the proposed principles, it is possible to achieve maximum and efficient use of a structure. Corresponding procedure is applicable during the stage of design, manufacturing and maintenance of a structure. The best effect can be achieved if the testing of materials and the stress analysis are performed parallel to design and manufacture, followed by required structure testing. The preparation and manufacturing of specimens should be taken in account also for next testing during the service lifetime.

The presented procedure principles can be applied for structures in service, although it is not certain that reliable materials input data are always available, as required /1/.

2. BASIC PRINCIPLES

The procedure for designing against fracture is based on generally accepted standards for material testing (like ASTM E 1820 /2/, BS 7448 /3/), verified structure design procedures (EN Eurocode 3 /4/) and procedures for structural integrity assessment (like BS 7910 /5/, API 579 /6/, R5 /7/, R6 /8/, SINTAP /9/, ETM /10/).

Some important factors regarding the basic principles like:

- Common experience of structural component producer and of user as well.
- Knowledge about new research results.

- Data about the structure reliability in the concept stage of design and in operation, have to be included when prescribing for a procedure designing against fracture.

Unified procedure for designing against structural fractures, based on principles of safe use of structures and presented in Fig. 1, is accepted in the framework of the FITNET project /11/, funding by EC.

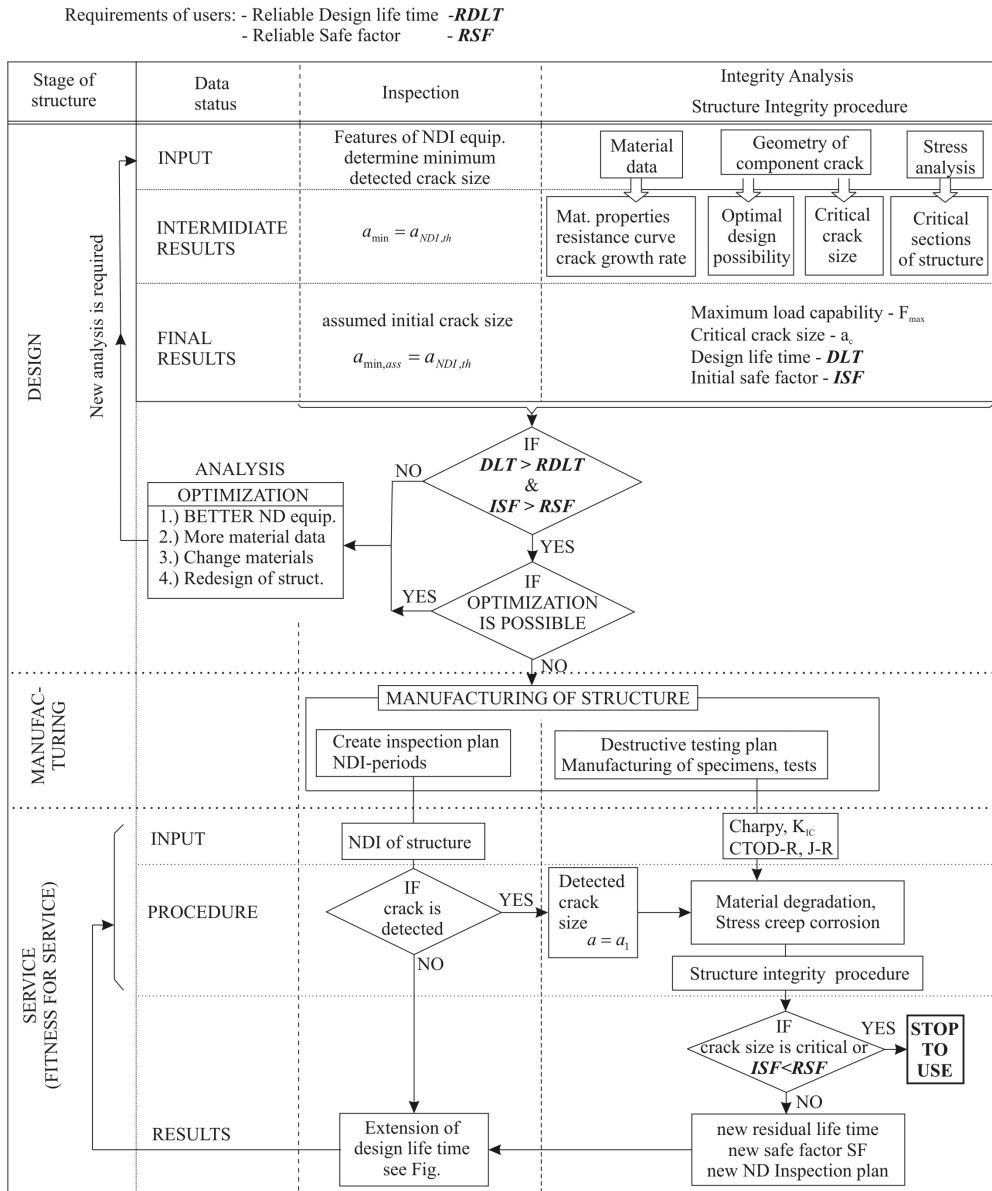


Figure 1: Procedure for design against failure of a structure

Figure 1 shows all steps in the procedure for designing against structural fracture. The application of this procedure starts at the structure design stage, and it should be applied during manufacturing and service until the final usage. The final stop of structure usage is determined by increased risk of failure, for a value higher than the reliable safety factor.

It is possible to use this procedure for any single component of a structure, and in this manner to reduce the number of critical components in a structure. Specifying real critical components it is also possible to reduce the number of necessary inspections, since for less critical components the frequency of inspection might be reduced. In this way, the expenses for non-destructive inspection (NDI) testing could be reduced without increasing risk for fracture, enabling in the same time servicing lifetime extension.

It is to notice that applicable testing for structural integrity are non-destructive (like ultrasonic, radiography, magnetic particles, visual) for detecting defect shape, size and position, and destructive for determination of material properties, and material resistance to crack initiation and propagation. The resistance to the crack propagation should be measured under the same condition (environment and loading) to which a structure is exposed in service. A unified approach does not exist on how to achieve safe usage of a structure. The main problem is the number of different structures with many different components and critical parts, most dangerous of can cause failure of the structure.

3. DESIGN STAGE

In the design stage, two basic activities run together. The first activity is connected with crack detection and its significance assessment. It is important here to recognize the exact capabilities and sensitivity of the non-destructive testing (NDT) equipment, which determine minimum detectable crack size, important for consideration in design. It is clear that postulated crack size in design is limited by the sensitivity of NDT equipment. The servicing lifetime lasts corresponds to the time from crack growth, from postulated to critical crack size. Here are most interesting cracks which can grow in fatigue or in creep, and for that specimens for crack propagation have to be subjected to the same loading conditions and environment as the structure. The effects of sensitivity and the quality of the NDT equipment on designed lifetime are shown in Fig. 2.

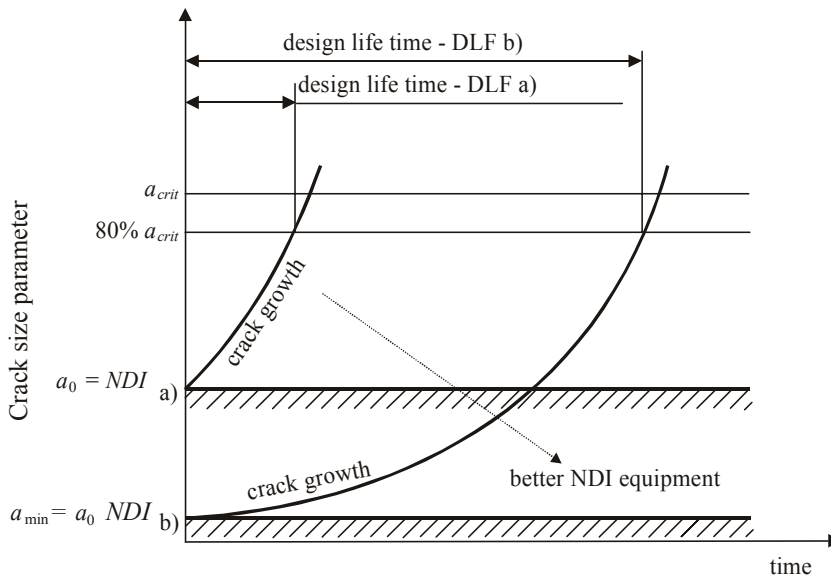


Figure 2: Effect of NDI equipment quality on design lifetime of structure

The second activity set consists of material testing, stress analysis and determination of critical structural sections of structures, necessary from the very beginning of design.

The results of this stage can be expressed in following data:

- The postulate assumed crack size,
- The maximum loading capacities of the structures,
- The servicing critical crack size,
- Design lifetime.
- Initial safety factor.

Next analysis, using these data, should give the answers to the following questions:

- Is calculated design lifetime (DLT) longer than the required design lifetime (RDLT)?
- Is initial safety factor (ISF) greater or equal to the required safety factor (RSF)?

Algorithm for this procedure is presented in the Fig. 3.

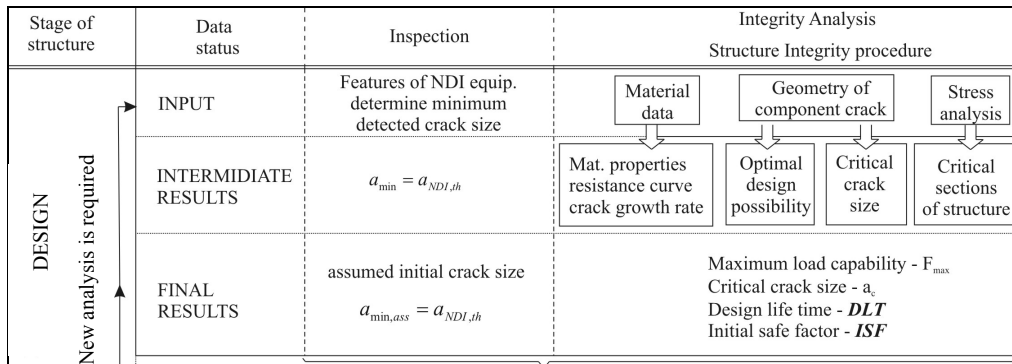


Figure 3: Algorithm for design lifetime estimation of a structure

In the case that the answers to both mentioned questions are positive, it is justifiable to continue to the next step, to the manufacturing of a structure. It is also desirable to optimize the design, e.g. to reduce the weight of a structure, if possible.

In the case of negative answers, the optimization is obligatory and the complete procedure has to be repeated. Optimization generally includes:

- Selection of NDT equipment of higher quality;
- More complete data about material properties, or
- Selection of more suitable materials, and
- Redesign of structure.

4. MANUFACTURING STAGE

Parallel to the structural manufacture, it is necessary to make an NDI plan with a reliable number of inspections during service (Fig. 4). The initial inspection NDI (“0”) is necessary immediately after the manufacturing or assembling of a structure, as the initial usage of the structure. During structural manufacture, the specimens for mechanical and fracture-mechanical testing are necessary (Fig. 4). These specimens should be subjected in testing to the same loading and environmental conditions as critical structural components are exposed to in service. This procedure is already well-established in the nuclear power plant industry.

During the exploitation NDI plan should foreseen at least 3 inspections during the lifetime of structure. It is also desirable, for responsible structures, that critical location be continuously monitored, applying convenient system by strain gauges, or introducing the system of new generation, which includes up-dated devices based on television recording and corresponding computer analysis.

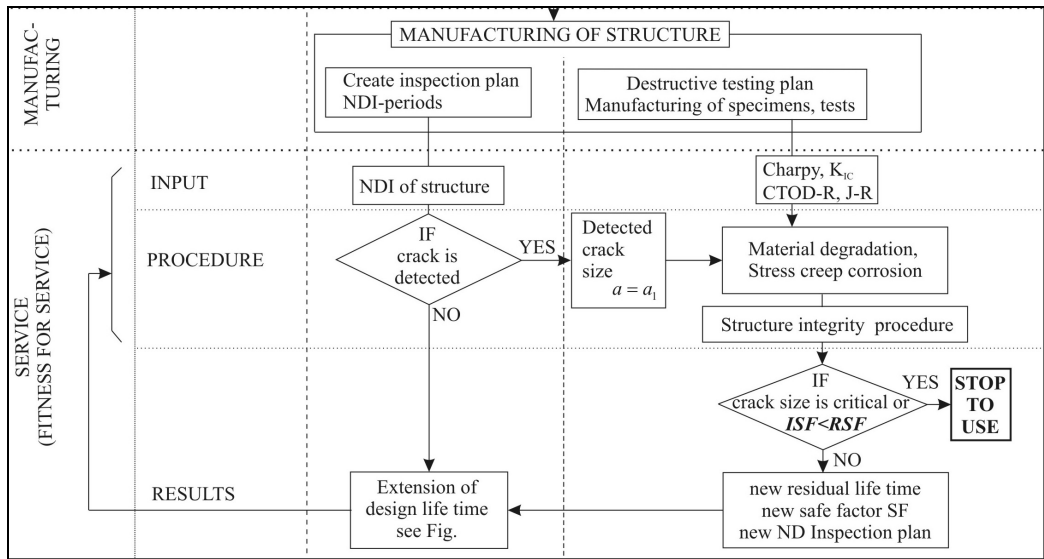


Figure 4: NDI plan and plan of specimen's producing in the manufacturing stage

5. OPERATIONAL STAGE

During the service of a structure it is necessary to follow specified NDI plan. As input data for structural integrity assessment, NDI plan always contains input data about a crack (shape, size, location and orientation). In a case of no detected crack, the residual service lifetime is usually equal to the design lifetime, and the safe usage period is extended for last period inspection. However, in this case the checking of structure wall thinning should be done, in order to prevent plastic collapse.

In a case of detected crack (Fig. 5), or established wall thinning, it is necessary to consider the possibility of structural component replacement. When structural component replacement is impossible, then a structural integrity procedure should be applied. In this case, it is also necessary to perform fracture toughness and mechanical testing of the prepared specimens. They have to be made from the same materials and exposed to the same or similar loading conditions applied for components. This testing is of special importance, because the obtained results will show the effect of environment and degradation of the material during usage.

The material degradation and thinning have an effect on crack growth law, as is schematically shown in Fig. 6. Degradation of material properties reduces service lifetime. Therefore, it is necessary to determine actual material properties, as bases for new service lifetime determination. If the new safety factor is found to be lower than the required safety factor (RSF), then the structure should be repaired or usage arrested.

In a case, where new safety factor (NSF) is higher than or equal to the required safety factor (RSF), then the new NDI plan has to be specified. After every NDI the whole structural integrity assessment procedure should be performed. Each time the new safety factor (NSF) is to be determined and compared to the required safety factor (RSF).

Some level of conservatism should be kept in each performed analysis. This leads to the service lifetime extension, as is shown in Fig. 7. In some cases, this extension can be an even longer than the designed lifetime. It enables reliable structural usage during full service lifetime.

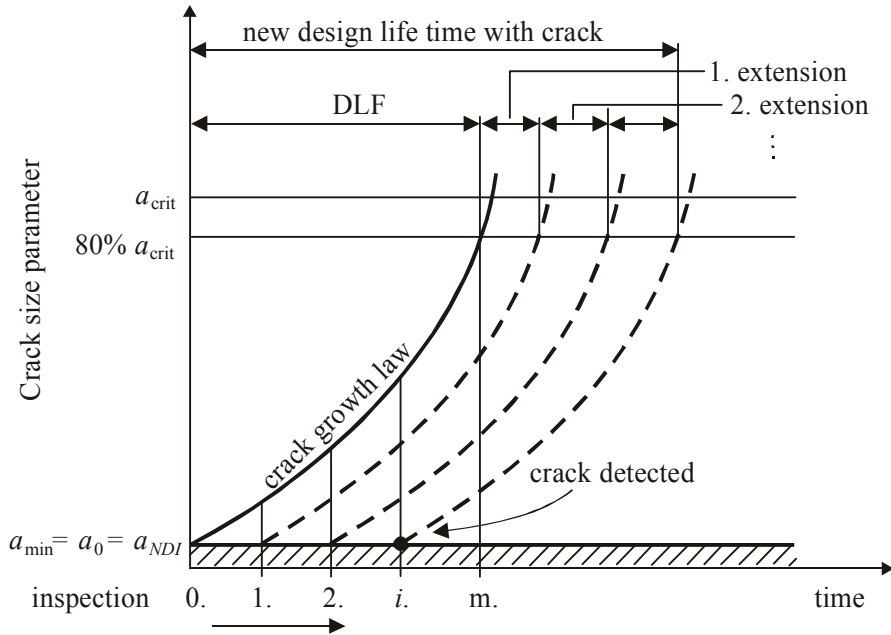


Figure 5: Extension of service life time until the crack is not detected

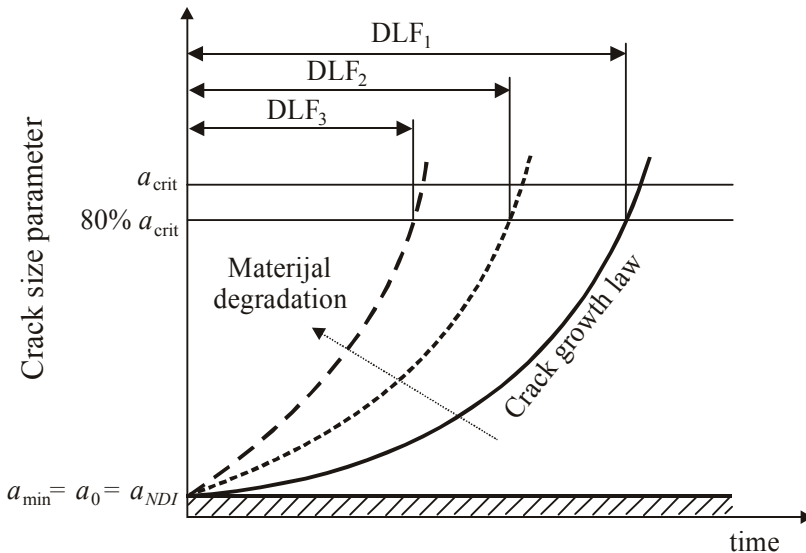


Figure 6: Effect of material properties degradation or wall thinning on service lifetime

However, the proposed principles are also applicable for materials of dropped properties when the risk of the structural failure is not increased. On the basis of the performed testing, it is possible to assess new values of critical crack lengths and new service lifetime limited by the safety factor of reliable structure use. New stress analysis is not required, if the results are available from the 1st stage (Fig. 7) and the wall thinning is negligible. Therefore, only in a case, where the geometry (e.g. thickness of component exposed to corrosion) changes should stress analysis be performed.

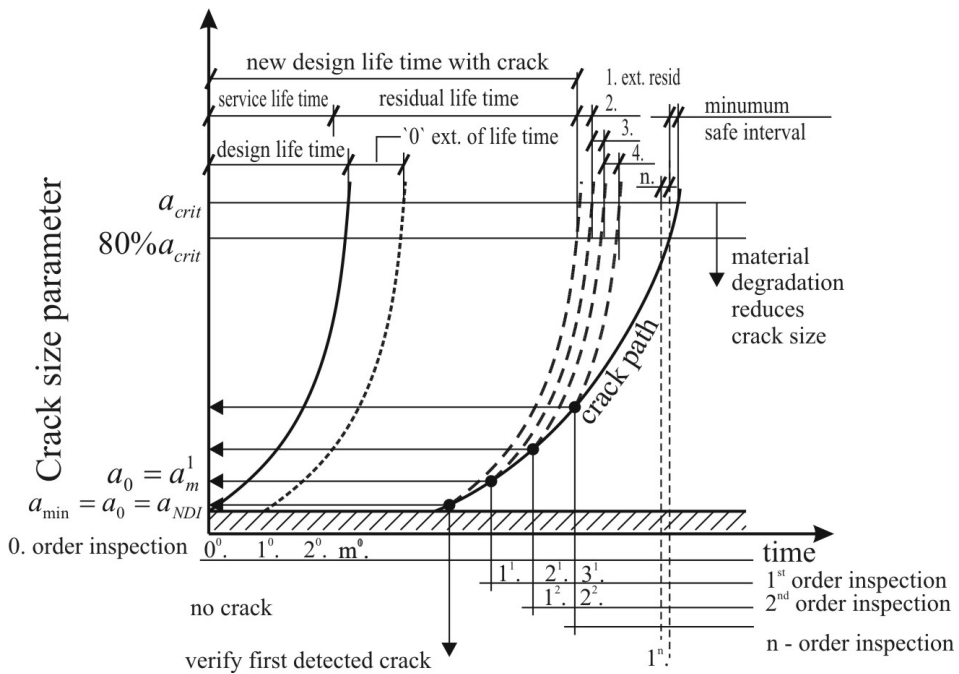


Figure 7: Extension of service lifetime of structure during crack propagation

6. INTRODUCTION TO SINTAP

The Structural Integrity Assessment Procedure (SINTAP) is one of a most comprehensive assessment procedure, very popular in practice. The SINTAP accepted the basic principles of R6 /8/ and ETM /11/, and extended use of fracture mechanics (Fig. 8).

Basic features of this procedure are:

- Assessment for inhomogeneous configurations, like strength mismatched weldments,
- Taking into account effect of residual stresses,
- Application in the ductile-to-brittle material behaviour transition temperature range.

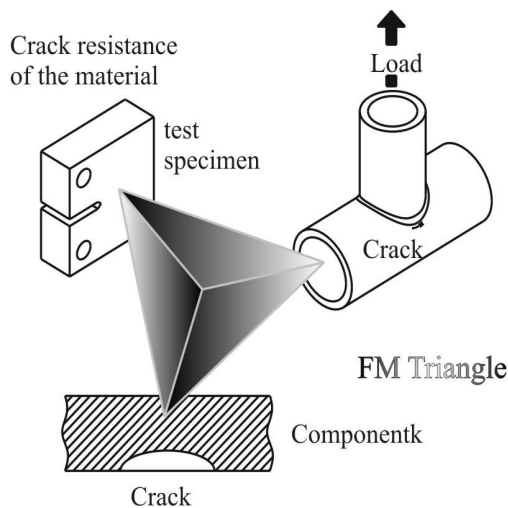


Figure 8: Triangle of the fracture mechanics approach

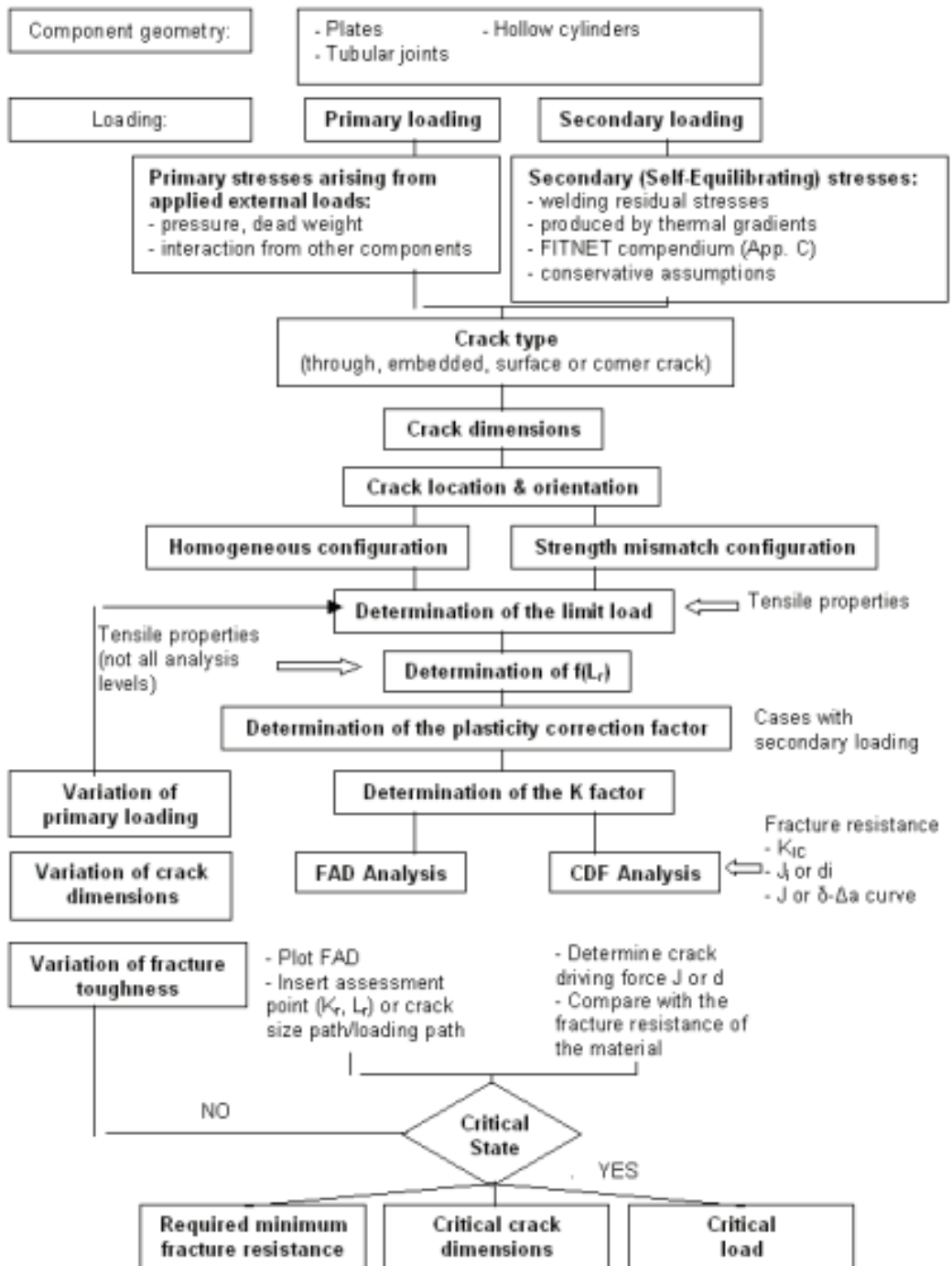


Figure 9: Overall flow chart of the FITNET FFS Failure Mode Module /12/

There are four levels of analysis within the SINTAP defect assessment procedure. An increase in level corresponds to increased complexity and needs more detailed data, but for that leads to improved accuracy. Overall structure of the SINTAP procedure has been depicted in Fig. 10.

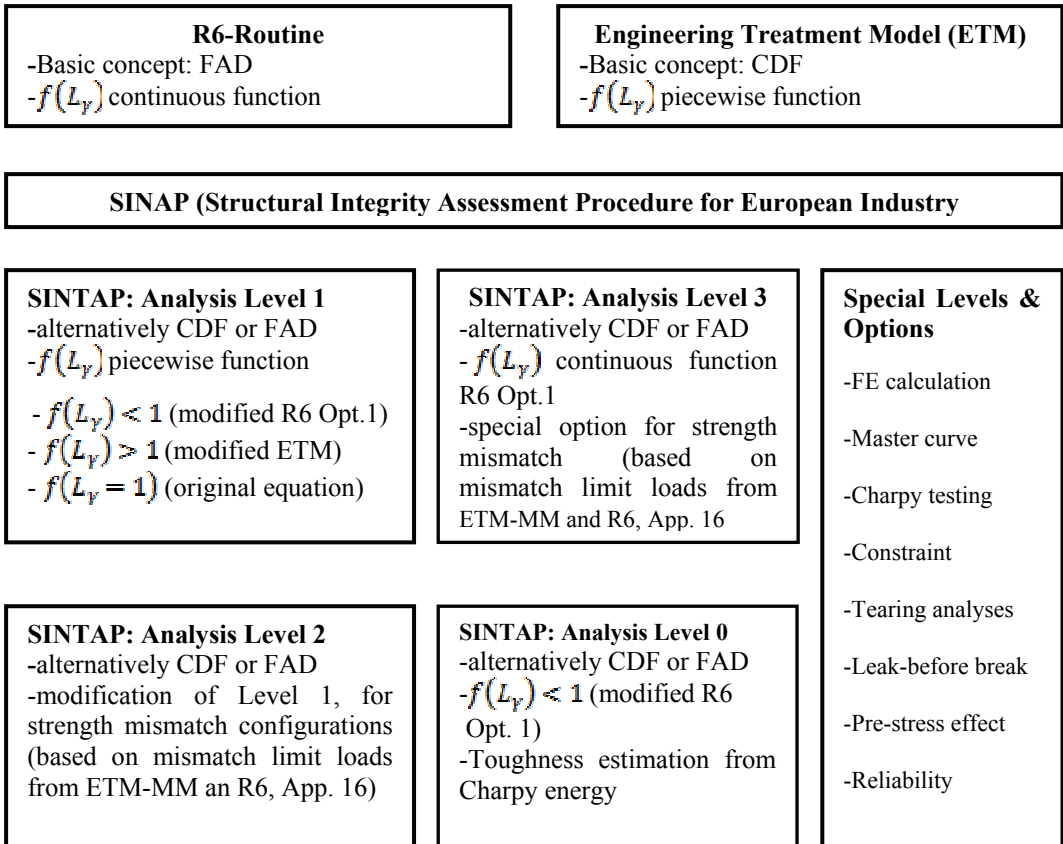


Figure 10: Analysis levels of the SINTAP procedure

In order to determine a critical crack size the following input data are required:

- Geometry and dimensions of the component,
- Applied loading including secondary load components, such as residual stress,
- Information on crack type and orientation, and
- The stress-strain curve and fracture toughness of the material.

6.1. Geometry and dimensions of the component

This data can be found in different handbooks. As an example, in Fig. 11 radial (a) and longitudinal (b) cracks in a disk are presented.

6.2. Applied loading including secondary load components

The applied load can be introduced as:

- Single load such as a tensile force,
- Bending moment or
- Internal pressure.

Hence, the stress profiles over the thickness of primary, σ_1 , and secondary, σ_2 , stresses, neglecting the effect of a crack and determined by a finite element analysis, are presented in the Fig. 12.

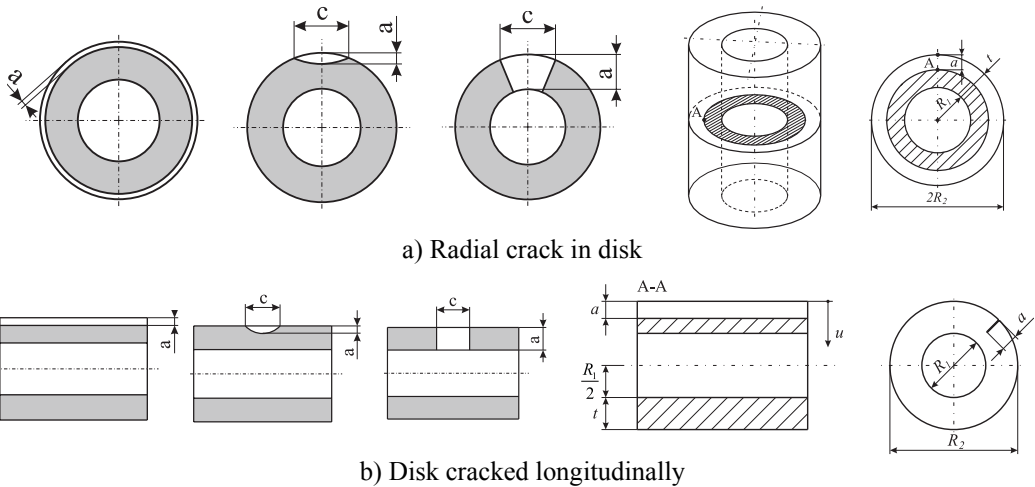


Figure 11: Radial (a) and longitudinal (b) cracks in a disk

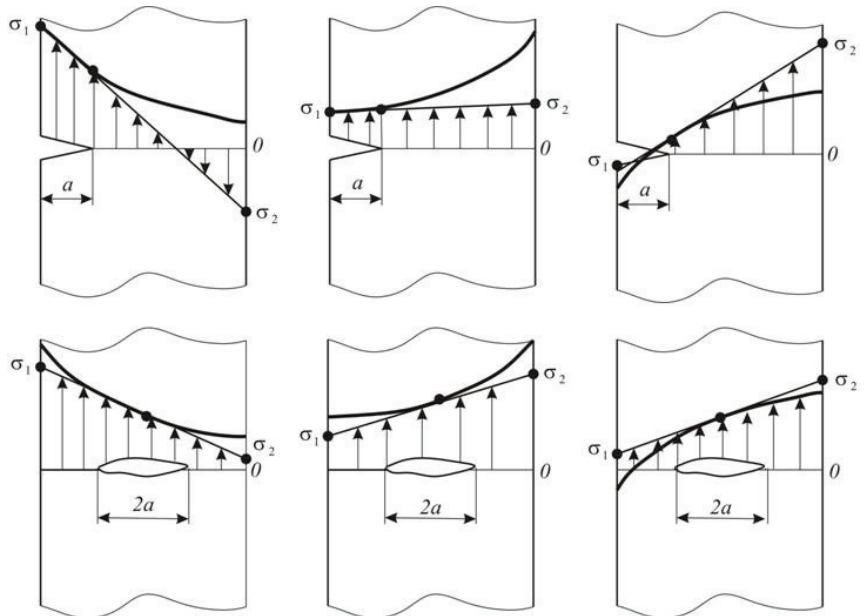


Figure 12: Stress profile through the thickness determined by finite element analysis /12/

Membrane and bending stress components are calculated from the principal stresses normal stresses, σ_1 and σ_2 :

Membrane stress component

$$\sigma_m = \frac{1}{2}(\sigma_1 + \sigma_2)$$

Bending stress component

$$\sigma_b = \frac{1}{2}(\sigma_1 - \sigma_2)$$

If the cross section contains a crack, the secondary stresses can be a major loading component (typical secondary stresses are welding residual stresses). Secondary stresses are taken into account in determining the K factor, but not in determining the limit load, FY, or the degree of ligament plasticity, Lr.

In the case of linear-elastic deformation behaviour, the crack tip loading can be determined by superposition the K factor due to primary and the K factor due to secondary stress:

$$K_r = \frac{K_I^p + K_I^s}{K_{mat}} + \rho \quad (1)$$

and in the CDF route as,

$$J = \frac{1}{E'} \times \left[\frac{K_I^p + K_I^s}{f(L_r) - \rho} \right]^2 \quad (2)$$

$$\delta = \frac{1}{E' \cdot \sigma_Y} \times \left[\frac{K_I^p + K_I^s}{f(L_r) - \rho} \right]^2 \quad (3)$$

The quantity ρ characterizes the difference between the actual crack tip loading and the crack tip loading which would result from simple superposition of K_{Ip} and K_{Is} . Using

$$L_r = \frac{\sigma_{ref}^p}{\sigma_Y} \quad (4)$$

it is dependent on the ligament of plasticity, L_r (which is a function on primary loading, on the magnitude of the secondary stress, and on the equation applied for $f(L_r)$). Therefore, the correction term ρ can be determined from the plot given in the Fig. 13.

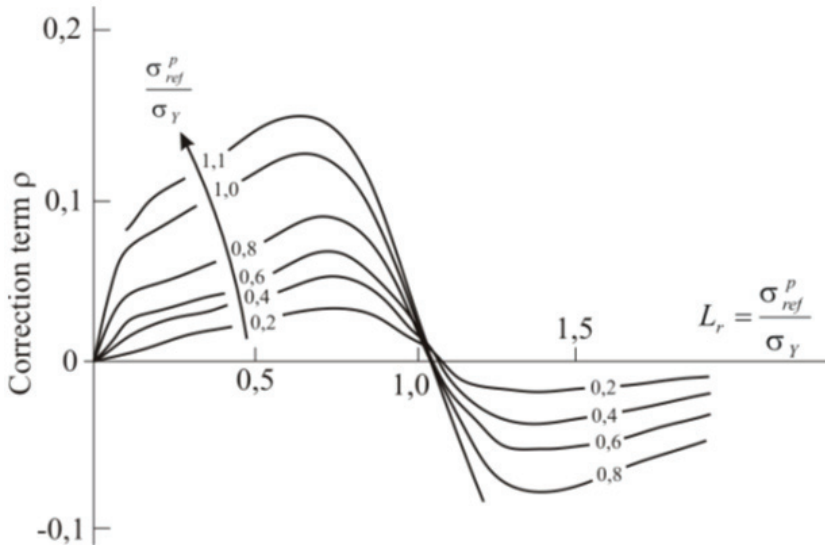


Figure 13: Correction term ρ in function of L_r

6.3. Crack type and orientation

Real flaw shapes are idealized by substitute geometries such as rectangles, ellipses and semi-ellipses (Figs. 14 and 15). The idealization has to be done such that the crack tip loading will be overestimated.

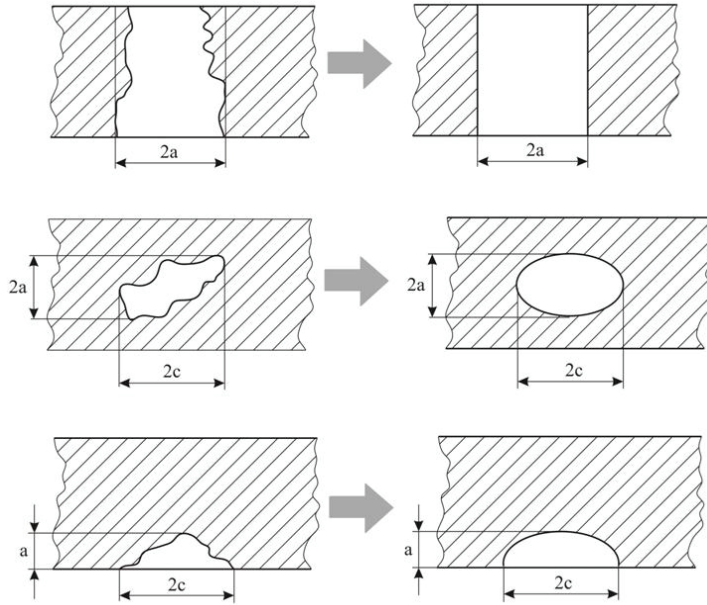
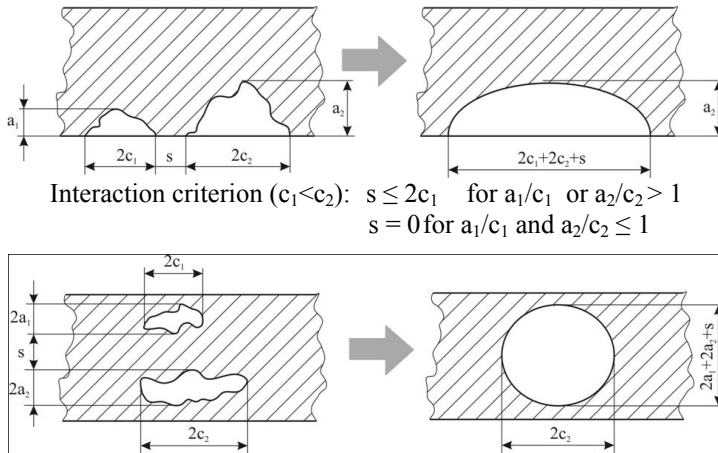


Figure 14: Flaw shape idealization /12/

In the same way multiple interacted flaws could be idealized as one flaw:



Interaction criterion ($c_1 < c_2$): $s \leq 2c_1$ for a_1/c_1 or $a_2/c_2 > 1$
 $s = 0$ for a_1/c_1 and $a_2/c_2 \leq 1$

Interaction criterion: $s \leq (a_1 + a_2)$

Figure 15: Planar flaws interaction rules /12/

6.4. Homogeneous and strength mismatched configuration

If difference is less than 10%, the use of SINTAP procedure for homogeneous material based on the base plate properties is recommended. In any another case the strength mismatched configuration should be take in account. Hence, the base material properties are kept constant, while the weld metal properties vary. This variation is described by mismatch factor:

$$M = \frac{\sigma_{YW}}{\sigma_{YB}} \quad (5)$$

where σ_{YW} and σ_{YB} present the yield strength of the weld metal and of base metal, respectively. The weld metal is commonly produced with yield strength higher than that of the base plate; this is known as overmatching (OM) with the mismatch factor $M > 1$. An increases use of high strength steels forces the fabricator to apply a consumable of lower strength to comply toughness requirements, this is undermatching (UM), $M < 1$.

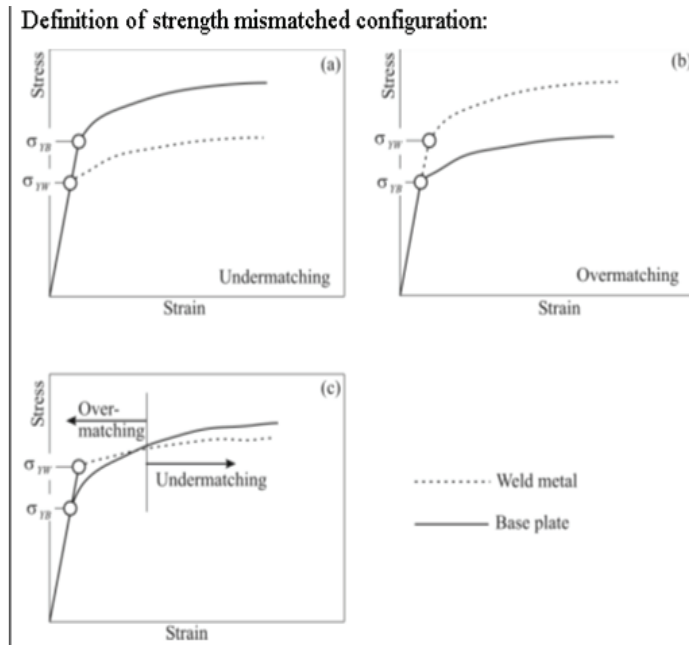


Figure 16: Strength mismatch definition /12/

The mismatch plays an important role for:

- fracture toughness of material (weld metal and base metal), K_{mat} , J_{mat} , $CTOD_{mat}$;
- stress intensity factor solution (K_I) in linear-elastic and elastic-plastic ranges; and
- limit load solution given by appropriate terms, like plastic limit load F_Y .

Undermatching (UM) gives rise to a strain concentration in the weld metal, while overmatching (OM) reduces the strain in the weld metal as compared to the base plate. The SINTAP procedure offers separate assessment options for the analysis of such cases.

6.5. Plastic limit load F_Y

The plastic limit load of the component with crack is one of the key parameters of the SINTAP analysis. Limit load is a net section yield load which refers roughly to that load of still unbroken ligament ahead of the crack is first fully plastic and the local load-deformation curve becomes non-linear. In a fracture mechanics analysis it has to distinguish a plastic collapse load which is identical to the maximum load which the structure with crack can sustain and a net section yield load. Within the SINTAP procedure a compendium of limit loads is provided and a loading parameter L_r is used, defined as the ratio of the applied load F and the limit load F_Y or respectively as the ratio of an applied net section stress σ_{ref} and the yield strength of the material, σ_Y :

$$L_r = \frac{F}{F_Y} = \frac{\sigma_{ref}}{\sigma_Y} \tag{6}$$

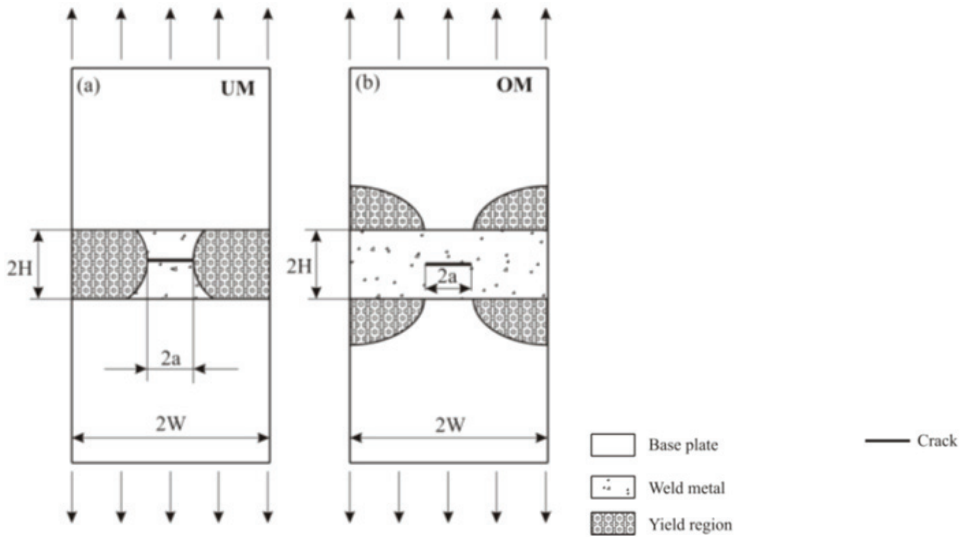


Figure 17: The mechanical consequences of strength mismatch

the latter given as $\sigma_Y = R_{eL}$ for materials with Lüders plateau, and $\sigma_Y = R_{p0.2}$ without it.

6.6. Stress intensity factor K

The SINTAP procedure provides an own compilation of stress intensity factor, K , and limit load solutions. Stress intensity factors can be determined for single load, like force, bending moment, internal pressure, as well as for stress profiles. The latter alternative allows consider geometrically complex components by using substitute structures, i.e. the stress profile is determined for the real structure without crack, whereas the determination of the K -factor is based on a simpler geometry like a plate or a cylinder.

6.7. Correction function $f(L_r)$

Under conditions of small scale yielding (roughly up to 0.6 times the limit load) a fracture mechanics analysis can be based on the linear-elastic K factor. For contained and net section yielding where the plastic zone is no more limited to a small region ahead of the crack tip, the application of the K concept would lead to a significant underestimation of the real crack tip loading in terms of the J -integral or CTOD. Irrespective of this general statement the application of a formal K concept becomes possible when the linear-elastic K factor is corrected with respect of the yield effect. This is the essential of the correction function $f(L_r)$. With respect of $f(L_r)$ the SINTAP procedure is structured in a hierarchic manner consisting of various analysis levels constituted by the quality and completeness of the required input information. Higher levels are more advanced than lower levels: they need more complex input data, but the user is "rewarded" by less conservative results. An unacceptable result provides a motivation for repeating the analysis at the next higher level rather than claiming the component to be unsafe.

Default level

The corresponding equations for $f(L_r)$ for ferritic steels without Lüders plateau are:

$$f(L_r) = \left[1 + \frac{1}{2} L_r^2 \right]^{-1/2} \times \left[0,3 + 0,7 \exp(-0,6 L_r^6) \right] \quad \text{for } 0 \leq L_r \leq L_r^{max} \quad (7)$$

$$L_r^{max} = 1 + \left[\frac{150}{R_{p0.2}} \right]^{2,5}, \quad \text{where } R_{p0.2} \text{ is in MPa} \quad (8)$$

The fracture toughness is estimated in a conservative way from Charpy data by:

$$K_{mat} = \left[\left(12\sqrt{KV} - 20 \right) \times \left(\frac{25}{B} \right)^{1/4} \right] + 20 \quad (9)$$

on the lower shelf and by:

$$K_{mat} = K_{J_{0,2}} = \sqrt{\frac{E \cdot \left(0,53 \cdot KV^{1,28} \right) \times 0,2^{(0,133 \cdot KV^{0,256})}}{1000 \cdot (1 - \nu^2)}} \quad (10)$$

on the upper shelf (K_{mat} , MPa \sqrt{m} ; specimen thickness B , mm; Charpy energy KV , J).

In addition, SINTAP offers a correlation for the ductile-to-brittle transition based on the Charpy transition temperature for 28 J.

Basic level

$$f(L_r) = \left[1 + \frac{1}{2} L_r^2 \right]^{-1/2} \times \left[0,3 + 0,7 \exp(-\mu \cdot 0,6 L_r^6) \right] \quad \text{for } 0 \leq L_r \leq 1 \quad (11)$$

with

$$\mu = \min \begin{bmatrix} 0,001 \cdot \frac{E}{R_{p0.2}} \\ 0,6 \end{bmatrix} \quad (12)$$

$$f(L_r) = f(L_r = 1) \times L_r^{(N-1)/2N} \quad \text{for } 1 \leq L_r \leq L_r^{max} \quad (13)$$

$$N = 0,3 \cdot \left[1 - \frac{R_{p0.2}}{R_m} \right] \quad (14)$$

$$L_r^{max} = \frac{1}{2} \left[\frac{R_{p0.2} + R_m}{R_{p0.2}} \right] \quad (15)$$

with L_{rmax} being the limit against plastic collapse.

Advanced level

$$f(L_r) = \left[\frac{E \cdot \varepsilon_{ref}}{\sigma_{ref}} + \frac{1}{2} \frac{L_r^2}{(E \cdot \varepsilon_{ref} / \sigma_{ref})} \right]^{-1/2} \quad \text{for } 0 \leq L_r \leq L_r^{max} \quad (16)$$

where

$$L_r^{max} = \frac{\sigma_f}{\sigma_Y} \quad \text{with } \sigma_f = \frac{1}{2} (\sigma_Y + R_m) \quad (17)$$

Different to the Levels above, $f(L_r)$ is a continuous function, which follows point-wise the true stress-strain curve. Each value of σ_{ref} is assigned to an L_r value by

$$\sigma_{\text{ref}} = L_r \cdot \sigma_Y \quad (18)$$

The corresponding reference strain ε_{ref} is obtained from the true stress-strain curve. No distinction is necessary between materials with and without a Lüders plateau. On the other hand $\sigma_{\text{ref}}/\varepsilon_{\text{ref}}$ values have to be available at $L_r = 0.7; 0.9; 0.8; 1; 1.02; 1.1$ and other values of L_r .

6.7. The true stress-strain curve of the material

The reference strain, $\varepsilon_{\text{true}}$, for the assessment of the normalized load, can be determined from the true stress-strain curve. With engineering stress, σ , and strain, ε , (Fig. 18), true stress and strain values, σ_t and ε_t , are defined by:

$$\varepsilon_t = \ln(1 + \varepsilon) \quad \sigma_t = \sigma(1 + \varepsilon) \quad (19)$$

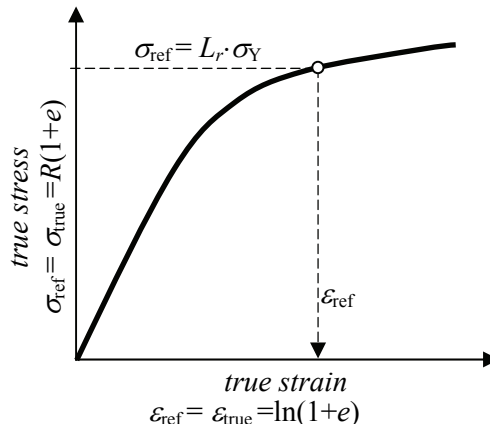


Figure 18: True stress – true strain curve

6.8. Comparison of crack driving force (CDF) and fracture analysis diagram (FAD)

Applying the fracture analysis diagram (FAD) philosophy a failure line is designed by normalizing the crack tip loading with the material's fracture resistance (Fig. 19). The assessment of the component is then based on the relative location of a geometry dependent assessment point with respect to this failure line. In the simplest application the component is regarded as safe as long as the assessment point lies within the area enclosed by the failure line. It is potentially unsafe if it is located on or above the failure line. Basic relations are presented by Eqs. (20) to (24).

Failure assessment curve:

$$K_r = f(L_r) \quad (20)$$

$$L_r = \frac{F}{F_Y} = \frac{\sigma}{\sigma_Y} \quad (21)$$

Loading path:

$$K_r = \frac{K_I(a, F)}{K_{\text{mat}}} \quad (22)$$

$$K_{\text{mat}} = \sqrt{\frac{J_{\text{mat}} \cdot E}{1-\nu^2}} = \sqrt{\frac{\sigma_Y \cdot \delta_{\text{mat}} \cdot E}{1-\nu^2}} \quad (23)$$

Failure criteria:

$$f(L_r) < \frac{K_I(a, F)}{K_{\text{mat}}} \quad (24)$$

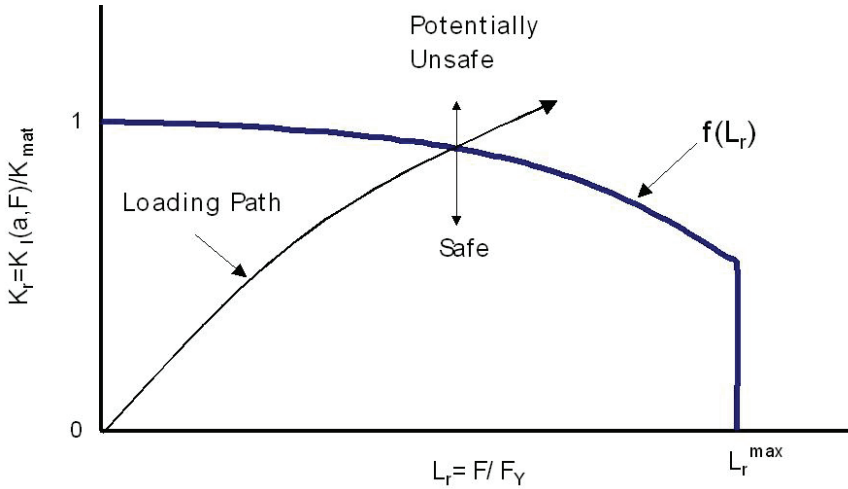


Figure 19: Failure assessment diagram based on a FAD philosophy

In contrast to this in the crack driving force (CDF) route the crack tip loading in the component is determined in a separate step. It is then compared with the fracture resistance of the material. If the crack tip loading is less than the fracture resistance the component is safe, otherwise it is potentially unsafe. The basic relations are given by Eqs. (25) and (26), and in next text for limit toughness and failure criteria.

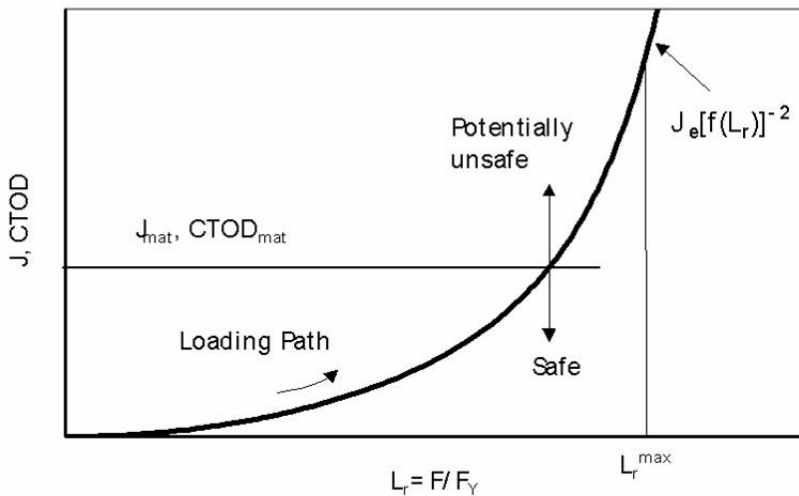


Figure 20: Failure assessment based on a CDF philosophy

Loading path = Crack driving force:

$$J = J_e [f(L_r)]^{-2} \quad (25)$$

$$J_e = \frac{K_I(a, F)^2}{E'} \quad (26)$$

Limit toughness: J_{mat}

Failure criteria: $J_{\text{mat}} < J$

6. Conclusions

Basic principles of structural integrity assessment have to be taken into account already in the design stage of a structure. Available procedures enable reliable usage of fracture mechanics to assess the component integrity. SINTAP, as one of a most comprehensive assessment procedure, uses the basic principles of R6 and ETM. Integrity assessment is based on the estimation of maximum allowable loading or maximum allowable crack size in unfavourable crack tip location and orientation. This lecture gives the basis of procedure for design against fracture not only in-service, but also in design and manufacturing phases.

REFERENCES

1. ASME, 1998, "ASME Boiler and Pressure Vessel Code, Section XI: Rules for In-service Inspection of Nuclear Power Plant Components", American Society for Mechanical Engineering
2. ASTM E 1820-99a, 2000, "Standard Test Method for Measurement of Fracture Toughness", Annual Book of ASTM Standards
3. BS 7448, 1997, "Fracture mechanics toughness tests; Part 2. Method for determination of K_{IC} , critical CTOD and critical J values of welds in metallic materials"
4. Eurocode, 1993, "Design Manual for Steel Structures and Building", Brussels
5. BS 7910, 1999, "Guide on methods for assessing the acceptability of flaws in fusion welded structures"
6. API 579-1/ASME FFS-1, 2007, "Fitness-For-Service", Second Edition, American Petroleum Institute, Washington, D.C.
7. R5, 2003, "Assessment Procedure for the High Temperature Response of Structures", Issue 3, British Energy
8. R6, 2003, "Assessment of the Integrity of Structures containing Defects", Revision 4, British Energy
9. SINTAP, 1999, "Structural Integrity Assessment Procedure", Final Revision. EU-Project BE 95-1462. Brite Euram Programme
10. Schwalbe, K. H. and Zerbst, U, 2000, "The Engineering Treatment Model", International Journal of Pressure Vessels and Piping, Volume 77, Issues 14-15, 2000, pp. 905-918.
11. FITNET, 2006, "European Fitness for Service Network", Final technical report, GTC1-2001-43049, Contract No. GIRT-CT-2001-05071, www.eurofitnet.org

SIMPLIFICATIONS FOR CONSERVATIVE STRUCTURAL INTEGRITY ASSESSMENT

Petar Agatonović

D-85244 Röhrmoos, Deutschland

P.Agatonovic@t-online.de

1. INTRODUCTION

Stress analysis is very important topic for design and fracture mechanics. From the beginning of the so-called industry revolution, the concern against structure integrity has lead to its great progress. From Hook (1578) up today the stress analysis has developed to include theories of material strength and elasticity, visco-elasticity and plasticity. Rapid increase of computer capacity brought to the further large progress in using numerical methods for the calculation and analysis of stresses with finite elements. At the same time the knowledge concerning material behaviour brought to the new constitutive theories as dislocation theory, theory of plasticity and failure mechanisms. This demanded the development of new disciplines, like fracture mechanics, fatigue of materials, corrosion theory and non-destructive examination methods. Simultaneously with this, new and stronger materials were developed and their resistance to fracture have been improved by alloys design, production processes and heat treatment.

All these advancements will remain inconceivable without simplifications of the corresponding problems to find out practical solutions. In accordance to the definition, under the notion of the simplification one understands the reduction of given conditions with the aim to get of some acceptable approximate solution of the problem. Even though the consequence of the simplifications is the getting away from the reality, they help by arriving to the solution, to better understand the corresponding relationships and correct assess the importance and ways of acting of different parameters. Under this condition, the simplifications are necessary and desirable.

Although the area of fracture analysis looks as the new research discipline, people were confronted for ages with this problem. However, the processes met in solid body fracture are so complicated and diverse that one can't expect that the corresponding phenomena will be described by simple formulas and criteria. Because of this, the development of fracture mechanics was falling back in some way behind other disciplines. But, today very abundant information concerning different fracture aspects exists, obtained through broad theoretical and experimental researches. This knowledge allows designer to deal with the problem of the structures safe against fracture in a more rational ways than it was possible in the past. Especially in the last 15 years extensive progress has been reached in the development and application of the fracture mechanics in design with light and high strength materials. At the same time, broad experiences show that the treatment of such structures without fracture mechanics is insufficient and can lead to the unexpected failure due to neglecting of unavoidable defects.

Accordingly, for the purposes of the safety of the metal structures, it is necessary to accept that as the result of production cycles in structural components crack-like defects always exist, at least at the size not detectable by non-destructive-inspection (NDI) methods applied, due to limited sensitivity of these methods. These cracks can lead to the

structural fracture at the maximum loading from the beginning of service or after some periods of service during which the crack can grow up to the critical size for nominal durable loading of the structure.

This also illustrates non-adequacy of conventional design praxis for the realization of fracture safe structures of their integrity guaranteed in service, which neglects the existence of cracks and the possibility of their growth to the critical size, and in this way the possibility of the unexpected fracture in spite of applied recommended safety factors against the yield strength or similar parameters of “ideal” structure material.

The aim of this paper is short but sufficiently detailed review of fracture mechanics and their applications, exhibiting exceptional power and potential, but at the same time is susceptible to the accepted restrictions, based on the simplifications allowed by theoretical solutions used.

2. BASIC ELEMENTS OF FRACTURE MECHANICS

Although the calculations for the evaluation of basic fracture mechanics parameters are complex, they nevertheless do not take into account all aspects of the problems. These calculations are only 2-dimensional, do not take into account redistribution and load relaxation around the crack tip due to the material plasticity and accept the assumption of material homogeneity. In addition, they started from an inherent assumption that the crack driving force can be quantitatively characterised by only one parameter (stress intensity factor, K , path independent J integral or crack opening displacement, δ). All these assumptions are only partially fulfilled and can lead, in the dependence of the actual case, to the significant errors in application, if the corresponding limits were not considered. However, the latest is not always so simple.

In spite of this, the fracture mechanics became important discipline in the praxis. Although not perfect, it offers many answers to the engineering practical problems that were until now not attainable. Awkwardness due to the possible errors (of course not these concerning wrong data for calculation and pure calculation) should not influence the fracture mechanics application. Is it in this respect more favourable to calculate beam with elastic stresses and with the addition of the safety margin declare it as safe, as has been done more or less successfully during last hundred years? Of course, this elastic calculation does not give exact results concerning the actual beam stresses, but was successful after long-standing application and corresponding experiences. However, for current conditions of light structures, high strength materials and tightness requirements concerning both economy and performances are no more satisfied.

In all that we are confronted with the notorious fact of the selection between accurate solution far from the reality and approximate solution satisfying practical requirements.

The solution for Hutchinson-Rice-Rosengren (HRR) problem appeared to be important, because it established J -integral as the most convenient fracture mechanics parameter, taking in consideration elastic-plastic material behaviour at crack tip, but, in addition by recognised difference between plane stress and plane strain conditions. HRR calculations have found that the stresses in the plastic zone are much higher in plane strain than in plane stress condition, what is the theoretical explanation for empirically observed thickness effects to the 2D-parameters of fracture mechanics. The LFM solution based on K do not apply this difference – the stresses are the same for both cases.

However, the HRR-solution is not complete and it is subjected to the corresponding limitations. Just near the crack tip, at the distance $r \rightarrow 0$, the solution is invalid because it

neglects finite geometry changes at the crack tip based on its blunting. The validity of the solution is loosed already before the end of plastic zone. When the contribution of the higher order terms in the series become significant, this isolated parameter is no more sufficient for the more accurate evaluation of the stresses in the section, but also for the assessment of the important effects based on constraint, like geometry parameters of the cracked body (this means not only constraint due to the wall thickness). This led to the so-called two parameters fracture mechanics, of which the most known are T for the correction of K and Q for the correction of J-integral.

The dependence on the geometry in LEFM conditions emphasize the importance of another aspect, not sufficiently respected up to now. Theoretical analysis of notch or crack starts from the assumption of endless contour in the space (Fig. 1). Nominal stress is evaluated independently of the crack effect.

In the reality the solid is always of limited size, and for the purpose of evaluation under the real conditions different corrections are introduced, like that for plate width and back wall. Unfortunately, this kind of correction is developed only for LEFM and is inaccurate under the yielding conditions. The corresponding solutions are in general not analytical, but based on finite element calculations or experiments. As already shown, at very short distance from the crack tip the solutions based on K and J is no more valid and significant differences appear here, depending on local geometry. In addition, significance of the stress in the cross-section weakened by the crack is obvious having in mind that for the evaluation of the collapse or pure plastic failure must be considered, although the definition of the corresponding stress is often not simple and accurate.

Elastic-plastic fracture analyses such as given in the EFRI or R-6 methods assume net-section yielding in the structure. According to the definition, L_r is the ratio of the applied load to the load which produces plastic yielding of the cracked structure, so that the weakening of the section by the crack must be considered.

However, in the calculation of the Fracture-Analysis-Diagram (FAD) it is usual to take the ratio of equivalent applied stress to the material's yield or proof strength, and not the section forces, so the smallest section is compelling. The solutions for K values are standardized in the fracture mechanics, considering stress in the section without crack.

Similar problem is well known by the treatment of material fatigue (Fig. 2).

Under the condition of local plasticity the evaluation of maximal stresses and strains due to the stress concentration caused by notch or hole in the plate is based on the stress, reached in the section reduced by the hole or notch, calculated for a particular loading with stress distribution across the section obtained for a uniform geometry. This is especially important when, for example, the mean stress effect has to be considered. Because of this following question is reasonable: why the stress in critical section is not calculated based on elastic-plastic fracture mechanics?

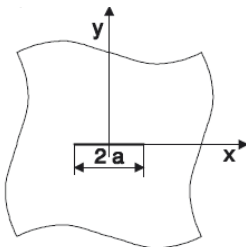


Figure 1: Crack theoretical model

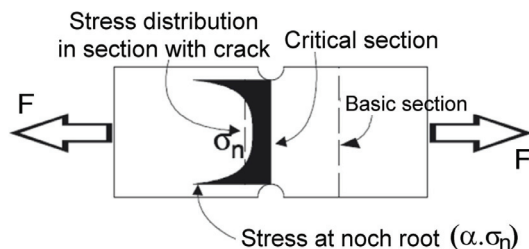


Figure 2: Presentation of stress concentration effect

Not only that this treatment is desirable for the unification, but this will lead to the more direct and less exposed to the errors, consideration of the corresponding conditions.

But, when the reduction of the section due to the crack is significant, the application of the values calculated for remote section without crack is risky, since is not on the safe side. This is significant in Elastic-Plastic-Fracture-Mechanics (EPFM), because the plastic effect in the section reduced by the crack occurs earlier, with very high intensity.

Researches in EPFM range were very successful by establishment of the parameters that characterise process of ductile fracture. The experimental methods adequate for the evaluation of fracture resistance and analytical methods for the fracture conditions have been developed. However, the corresponding methods require very complex analyses that can be conducted only with the help of advanced finite element methods, what can be expensive, time consuming and require high level of corresponding skills for the realisation. That certainly represents one of main obstacles to the extension of the EPFM methods for the structural integrity evaluation.

To overcome these obstacles, that additionally reduce general applicability of EPFM, so-called engineering approach (like that developed by EPRI) is developed for use, also based on simplifications which require no finite element analysis and in this way make this kind of analysis attainable to the engineering community. Unfortunately, application of this method is also followed with the limitations and the question arose whether it is superior knowing the current level of finite elements methods and computers capacity.

Looking on the different solutions for the calculation of crack parameters (K , J), it is to notice that cracks always have an ideal form. Natural defects are not of such a form and their contours are usually irregular and for that they cannot be examined by standard procedures. On the other hand, it is well known that these defects after growth under fatigue loading gradually convert into the typical semi-elliptical form. Based on this, the procedure is developed assuming that all natural defects are of simple form of plane or elliptical contour, convenient for next consideration. Certainly, the idealized or effective cracks are not real cracks, but only simplified representation of their complex real form enables their treatment by the fracture mechanics procedures.

Rules for this idealization (so-called reconsideration) of real cracks are developed in details from different codes. In Fig. 3 is, as an example, shown one method of treatment. The trend with this is obvious, that end forms are on the safe side, although there is no definite evidence in this respect. Initial natural defect is in all cases completely contained in the new effective contour, whose area is then larger.

Necessity to use finite elements, particularly in EPFM, has been several times already emphasized. Also in this area different simplification were necessary to enable the simulation of condition at the crack tip. For the adequate calculation of stresses and strains with the help of finite elements it is necessary to reproduce corresponding singularity in accordance with the theoretical solution of fracture mechanics. As known there are two tips of singularity; $1/\sqrt{r}$ for elastic material behaviour, and $r^{-n/n+1}$ for elastic-plastic material, whose behaviour is described by the exponent relationship. In the last case, by elastic perfectly plastic materials ($n \rightarrow \infty$) the singularity takes value r^{-1} . Besides, the changes in the crack tip geometry due to blunting must be taken into account.

The field of deformations is modelled by the polynomials using standard finite elements, and with those elements modelling of singularity is not possible. Therefore simple conventional elements cannot be used for crack modelling.

Requirements in this respect are realised by the modification of standard isoparametric elements in adequate way. Elastic singular behaviour $1/\sqrt{r}$ is presented by the isoparametric finite elements (with 8 nodes in 2D and 20 nodes by 3D) if the mean node at element side is moved in direction of crack tip at quarter position. Additionally, to consider the plasticity, two corner nodes and mean nodes at crack tip must have identical position from the beginning (the corresponding element edge collaborates in point, in which way the element passes from rectangular in triangle – from there the name), but under loading influence they may, to realistically represent crack blunting, be separated. Because that these collaborate rectangular elements include $1/\sqrt{r}$ and r^{-1} terms, it is assumed that they will sufficiently accurate describe the behaviour at crack tip in combination with the standard description of material law in exponential form.

Accordingly, there are three different kinds of elements for crack tip modelling:

- Deformed „quarter-point“ element: by this element elastic singularity $1/\sqrt{r}$ is accurately described.
- Collaborated element (from rectangular to triangle) that posses 3 different nodes at crack tip. With this element r^{-1} singularity is realised, which corresponds to elastic-ideal plastic materials.
- Element that combines both above changes and in this way includes $1/\sqrt{r}$ and r^{-1} singular terms.

If such elements are used for crack modelling, then a couple of their nodes at crack tip share the same position. When the model is loaded the elements at tip are deformed and these nodes starts to separate. This leads to crack blunting and realistic modelling of crack tip behaviour, as shown in Fig. 4.

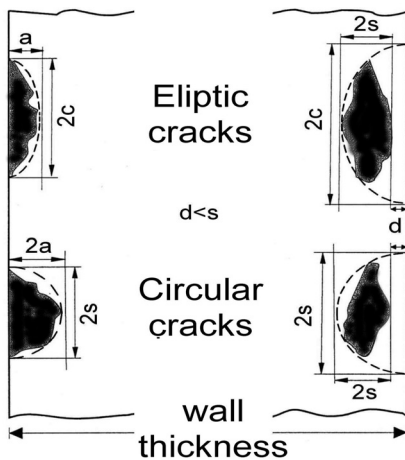


Figure 3: Idealization of surface and embedded cracks

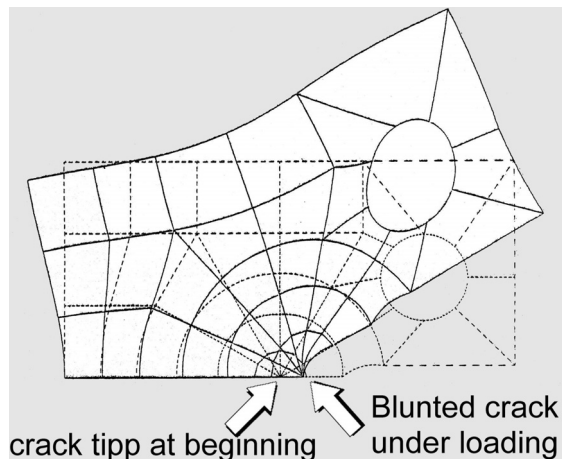


Figure 4: Crack tip simulation with the finite element method

Using finite element method the evaluation of stress intensity and J -integral values for 3D-geometries of structures and cracks becomes possible. Independence on integration contour is principally only valid for 2D case. By 3D-geometry, as in the case of surface crack (Fig. 5) the independence is only approximative and the deviation is more expressed with the growing distance from crack tip.

3. VOLUME (THREE-DIMENSIONAL) CRACKS

Next important deviation on theory side is associated with the crack geometry. Analytical solutions of fracture mechanics concentrate on 2-dimensional problems and two limit cases of plane stress and plane strain conditions. Although the real fracture mechanics problems surround crack areas which are curved with stress field in three dimensions, simply only possible analysis and corresponding solutions are limited to the 2-dimensional idealisation. Solutions based on this idealisation enable further treatment by fracture mechanics. Here, it should be mentioned that this 2-dimensional approach is not only limited to the analytical solutions, but is also completely transmitted to the experimental evaluation of the material parameters. Moreover, the material properties, as K_{Ic} , J_{Ic} , and crack opening displacement (COD) are evaluated on through crack specimens. Accordingly, one of the basic problems in fracture mechanics is, how on the basis of knowledge, acquired with the help of 2-dimensional specimens with through cracks, assesses the behaviour of real 3-dimensional structures, e.g. with the surface crack (Fig. 5).

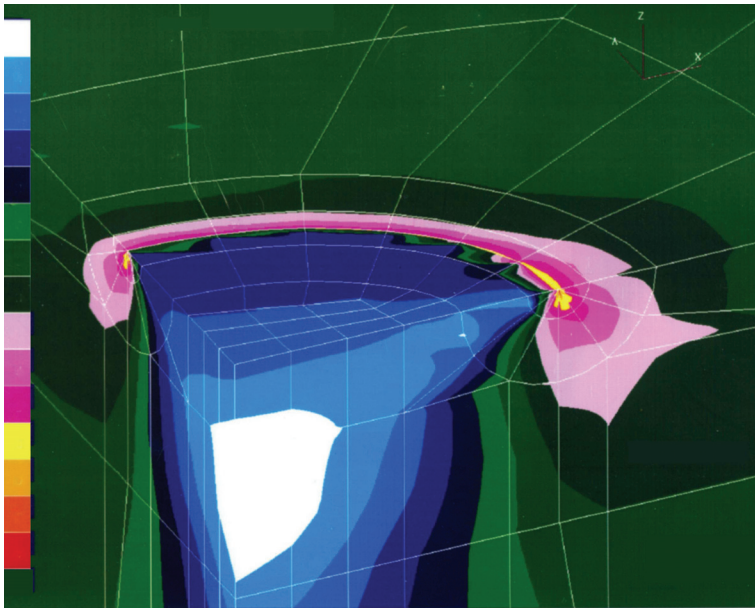


Figure 5: Stress distribution at surface crack tip

Practical experiences show that initiation and growth of fracture in the engineering structures can be mainly attributed to the surface cracks. Therefore, the surface cracks in structure are of great practical importance. Especially in thin wall structures with crack the plastic collapse of the ligament is the most frequent cause for the failure. Except this, as the through crack causes leakage, the damaged components can be timely excluded from operation or unloaded, such cracks are in practical application less dangerous. For that, residual strength of the surface crack ligament and the evaluation of crack critical length for wall penetration are the most important criteria for the guarantee of “leak-before-break (LBB)”. Therefore, study of the formula relating to the maximal loading of the surface crack ligament is an important task of the fracture assessment, especially for the case of pressurised structures.

It is important to note, that the surface cracks are of small dimensions, always smaller than wall thickness and are more dangerous, especially when the bursting of vessel may

precede the leakage, since it is difficult to detect them. Apart from this, surface cracks are space (volume) cracks, what means that the relationships are complex. Numerical investigations have shown not only the increase of J -integral due to the plasticity but also redistribution along of the crack contour compared to the linear elastic solution. Since the constraint is near to the crack tip weaker, material is here more liable to the yielding. By it, based on redistribution, the conditions inside of the crack surface get worse, and this can lead to the accelerated breakage in this part of the crack. Significant differences in the behaviour compared to the through crack require the application of material of special characteristic, but the use of such materials is due to the significant dependence on geometry and test conditions unreliable.

The aim of the problem for surface crack in space treatment, starting from the fact that for the fracture assessment under plasticity conditions, both the stresses and strains must be considered, new method has been developed by the author, already presented at previous IFMASS's. This approach will be presented here by the design of Fracture Analysis Diagram (FAD). The FAD application, which combines the corresponding criteria of pure brittle and pure plastic fracture, although of different origin, is included in many codes, like in R-6, API 679, BS 7910 and SINTAP. Differently to classical form of interpolation between these limit cases, the points of new proposed diagram solution are calculated starting from the relationship based only on fracture mechanics.

Starting from the known relationship between J and K that after substitution

$$J = K_{\sigma} K_{\varepsilon_{ref}} \quad (1)$$

holds its validity in all ranges between elastic to the plastic, it follows, in the design of FAD, for an engineering material stress-strain curve described in form $\sigma = B_F (\Delta\varepsilon_{pl})^n$

$$K_r = \sqrt{\frac{L_r \sigma_Y}{E \varepsilon_{ref}}} \quad \text{with} \quad \varepsilon_{ref} = \left[\frac{L_r \sigma_Y}{E} + \left(\frac{L_r \sigma_Y}{B_F} \right)^{1/n} \right] \quad (2)$$

On the basis of given relationships the curve in Fig. 6 is designed. For the comparison the curve obtained with R-6 method using the same material properties is presented.

Noticeable is considerable difference between the two lines. This is not surprising, having in mind that the R-6 curves is designed with the idea „safe rather than accurate“ (and to avoid possible errors on the side of lower safety).

The resistance curve path shows that up to the stress level in cracked cross section (net-section) at 70 % of the yield strength the available plasticity is sufficient to held, on the basis of crack tip blunting, the material resistance at the same level as without crack. After that the plasticity starts to be consumed through the deformation in the volume outside of the crack, and this act negatively to the residual strength.

The accuracy of the calculation based on new method is verified through the series of test on surface crack specimens and massive cylinders with the equal wall thickness and crack size (Fig. 7). Comparison with the results obtained by R-6 (Fig. 8) convincible demonstrates the advantages of new method not only due to the simplicity but also regarding the reliability. Details of the calculation by new method are given in /3 to 7/.

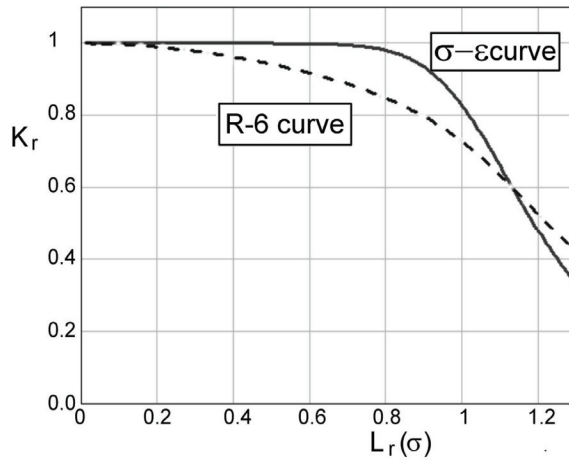


Figure 6: Example of the Fracture Analysis Diagram (FAD)

Using FAD it is possible to evaluate conditions for fracture, but also to assess the importance of the corresponding material characteristics and the features of structures. Figure 9 shows which of these subjects are dominated in elastic, plastic and plastic collapse characteristics.

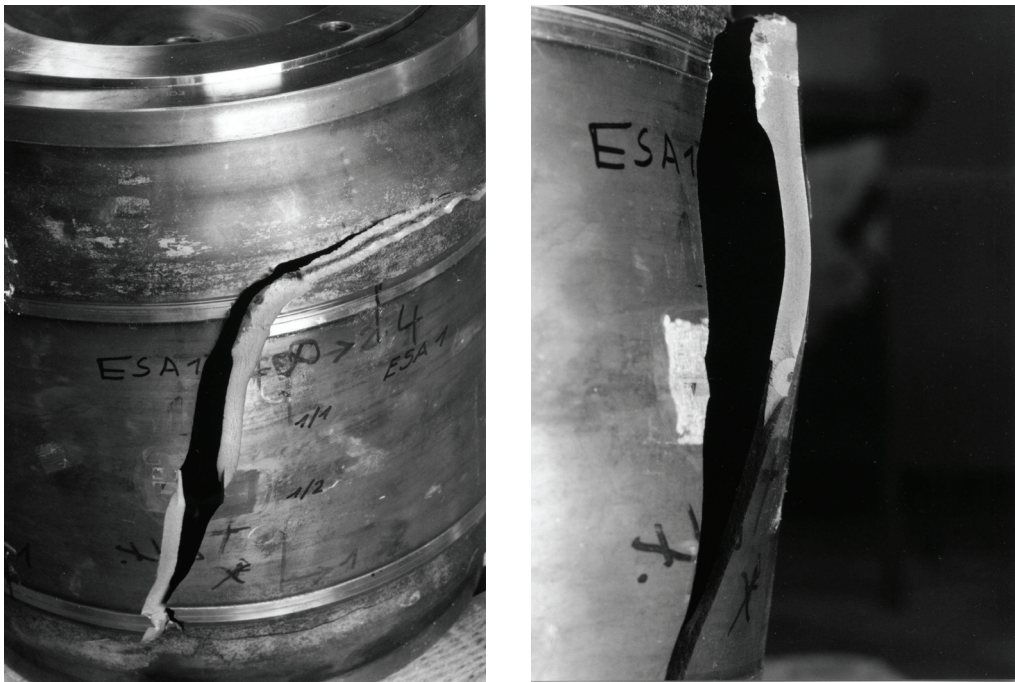


Figure 7: Pressure vessels after failure

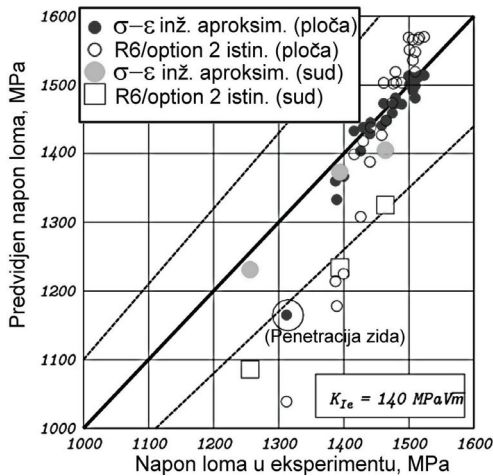


Figure 8: Comparison of test results for the validation of σ - ϵ -method

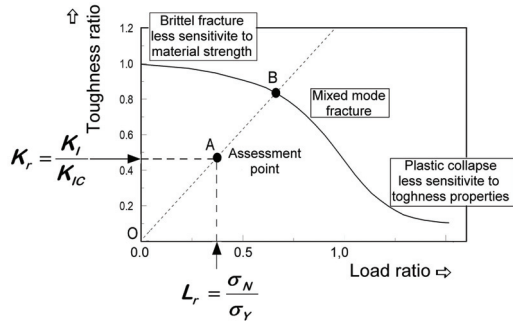


Figure 9: Different areas for FAD influence parameters

4. METHODS AND PROCEDURES

Limitation with which is confronted the user by application of fracture mechanics are not only based on theoretical solutions. Often the largest problems appear by the preparation of data necessary for calculation, as for example is the real crack size, whose measurement based on limited sensitivity of equipment very soon became uncertain. This means that the defects below some size cannot be detected reliably, and for that they must be tolerated. It is the question, what to do if the existence of those defects is evident, although they can not be detected? The answer to this question is found in method that at the beginning had simply named “crack tolerance”, but with the time is developed in a complex method, like “fitness-for-purpose” (FFP) or “retirement-for-cause”, included in modern codes. In codes as API 579, BS 7910 and R6 description in detail of application procedures are given, requiring calculations by complex models based on finite elements.

This kind of approach allow the optimisation of equipment management based on planned inspections, maintenance, repairs, life extension, stop the operation and eventual component retirement before its fracture can cause failure of equipment and unplanned long-term and expensive outage of service. This approach enables to extend the life of equipment, far above nominal calculated life of components.

Defects that appear in structural components are of different kind, each with its own distribution regarding the size and number (Fig. 10):

- Defect that are the result of the material production process, as porosity, micro-cracks, inclusions and surface pits. This kind of discontinuities is usually below the typical NDT detection capability, and requires design fully tolerating them.
- Defects that are introduced during fabrication: machining marks, scratches or any type of damage that could produce a crack like discontinuity. They are often large enough to be detected by standard NDT and repaired.
- Discontinuities that are formed in service. They include cracks formed by fatigue, corrosion, creep and impact damage. Their origin can be any of the previously cited defects. These discontinuities must be under the full control of damage tolerance requirements and this means that they must be discovered in time and tracked during

service. The problem is that the quality of inspection might be poor and the conditions in service stronger than in production, so the larger defects can pass unnoticed.

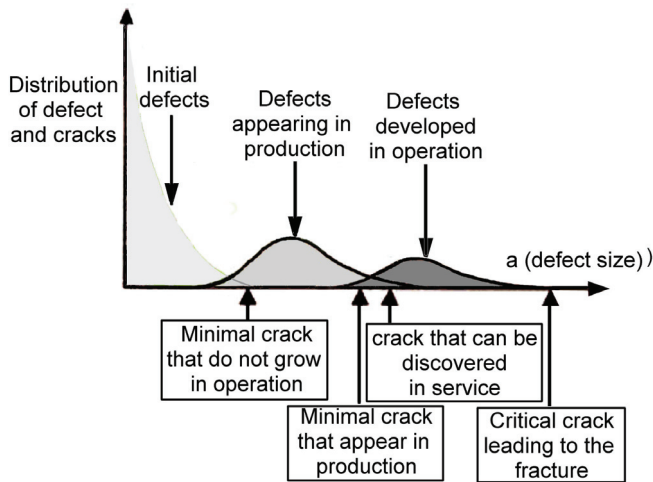


Figure 10: Defect distribution and limit values

Principle FFP-method will be demonstrated on one example whose details are shown in Fig. 11. Calculated expected design life without cracks is amounted 6000 hours. Performed analysis showed that crack sized $a_i = 1.5$ mm may stay undetected by applied inspection sensitivity so that it can grow up to the critical value $a_{kr} = 3$ during 2800 hours. For that the first inspection must be carried out by 50% of calculated life based on crack growth, or after 1400 hours. If by this first inspection the crack still cannot be detected, its initial size is again assumed to be 1,5 mm and the procedure is repeated. In this way designed life will be achieved after four inspections. The number of inspections can be reduced, supposing that the sensitivity of the first inspection is higher. For example, after production the cracks size of 1 mm can be reliably detected, and in this case can be added to the life tile first inspection is also half of life corresponding to the crack growth from 1 to 1,5 mm. Even better is if the inspection sensitivity in service can be improved. Direct saving is measured in this case based on inspection cost reduction, slowdown in exploitation and the like.

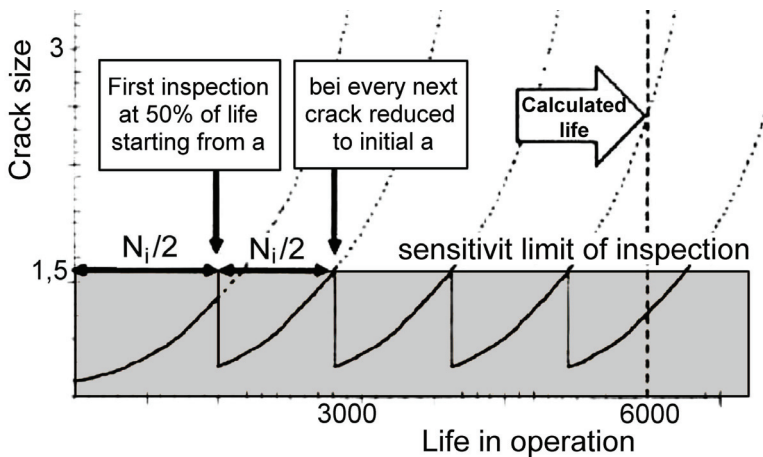


Figure 11: Safe life based on possible crack tolerance

Against this method of “safe life” there is the “fail safe” method. This is the case when designing the structure in which one component may fail without causing the failure of the structure, because the other components are capable to maintain structural integrity of the system when the new load (stress) for the failed condition is applied at least up to the next inspection. This is the case like bolt connection with several bolts. Similar concept refers to the combat aircraft that have two jet engines, so that in case of one failed down or being stroked the aircraft can fly back to the basis with the power of only one engine.

It can be seen from these examples that the practical application of the method is based more on technical disciplines and management, that unavoidable involves the risk. Reduction of the risk requires good knowledge of all processes based on technical disciplines significant for the case. Decisions in this respect are always made based on fundamental concepts and considering total cost. The latter is hard to calculate, when not only the cost of exploitation but also of unexpected and fateful accidents are considered.

On the other hand, equipment owners today all over the world, especially in energy branch, require assessment based on „fitness-for-purpose“ and corresponding confident safety in application, what is reasonably based on solid experiences in this respect.

When the available inspection methods are not sufficient, other methods can be used, which are also based on fracture mechanics. For pressure equipment is usual to perform the test by overpressure before the service, to prove the structural integrity under the pressure and temperature in operation. Praxis of this proof test with some overpressure before involve the equipment in service is recognised as „good design praxis“. Behind this stands the fact, that the endurance in the proof test conditions provides increased safety that the component can be reliably exposed to lower loading level in service for long time. On the other hand, the improved reliability of the structure was exhibited, because during proof test components, which are not adequate, can be removed from operation, without affecting the reliability of the components which survive the test.

However, formal application of this test do not attain full profit, because, in spite of all advantages quantitative data regarding important parameters are missing, as presence and size of cracks and discontinuities in component, lifetime of safe exploitation without failure risk after some period, actually required level of loading in test and the real risk of failure during the test itself. Direct benefit of this test, not limited to pressure components and pressure loading, can be significantly increased applying the fracture mechanics in preparation and execution of test optimisation and after that, since successful test enables to determine safe operational conditions for the definite period of next operation.

The principle of fracture mechanics application for proof pressure testing is shown in Fig. 12 for the case of brittle materials and single loading in test. Here is a_0 maximal crack dimension with which the loading P_0 can be applied in test without failure. The reason of proof test suppose the worst case scenario, and this means that the crack of size a_0 is certainly present in tested component and it is taken as initial size for the evaluation of safe life in operation after this test. For a_0 evaluation upper values of material toughness has to be taken giving conservative (down) values in life calculation.

Although the knowledge about the existence and distribution of remaining cracks is limited, after successful test it is supposed that no one crack exist larger than a_0 in the critical location and in the weak material. Guaranteed life is than evaluated based on calculated crack growth under service conditions based on expected mechanisms (fatigue, corrosion, creep) up to the maximal allowed crack size a_k calculated for maximum expected service loading P_{kr} . It is to note, that in proof test the failure must not mean

catastrophic failure, but any significant indication of inadequacy for practical use. For example, the leakage in service may cause the dangerous presence of inflammable or toxic gases. In this case the wall penetration by the crack in proof test must be treated as complete failure, even the accident did not occur and the crack behaviour was stable.

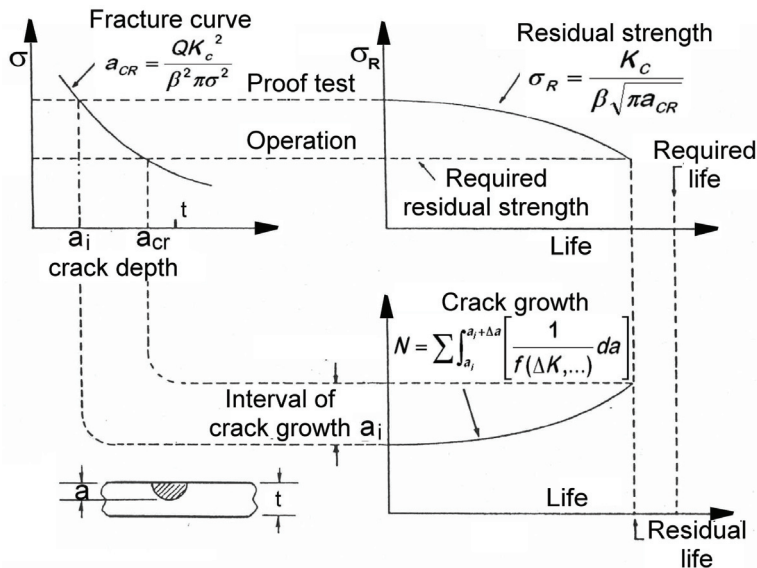


Figure 12: Schematics of proof test by fracture mechanics

It is important to understand that the crack size a_0 in the proof test is assumed on the calculation base, what means that this crack may not exist in reality and must be not detected during NDI (embedded crack). In general, the determination of a_0 is more simple than of a_{kr} , because the condition for proof test performance is very well known and controlled and, of course, less complex than the conditions in service.

Proof test philosophy is most simple for the brittle materials, where there are no difficulties connected with the stable crack growth before fracture. In addition, since the crack tolerance of brittle materials is lower, crack maximum size for fracture is lower. This allow higher a_{kr}/a_0 ratio for given P_0/P_{kr} than for ductile materials, and this allows longer residual life. It is advantageous to perform the test at the temperature at which the ductility of the material is lower than in service conditions, although the cost of the test due to higher probability of fracture can be higher. In ductile materials crack of corresponding size can grow during test without fracture, so that condition after test become worse and the component can also be less reliable in service than without this test. In order to prevent this, the inspection after test (and during the test) is requested, and this can make the all procedure more expensive.

Although a_0 may not be size of real crack, its application does not mean reduction of the available life. In contrast, by this procedure only the definite period of use without risk is guaranteed, and the further life extension is after repeated proof test, in order to again confirm applicability of components for next extended service. Moreover, in this way the real life capacity (above minimal calculated life) based on random scatter of the items distribution can be suggested. At the same time this means that the worst case scenario is temporary and only valid up to the next inspection and repeated proof test.

Proof test can be applied as the alternative for non-allowed crack detection (for example, if the complex component form do not allow efficient NDI application), but also as additional mean to the NDI. The reliability of components will be certainly increased by the strategy of combined inspection using both proof test and NDI. NDI can be carried out with this before or after the test. NDI before test has advantage since it reduce the risk of failure during test, and when the position of the crack become in this way known, its evaluation and calculation difficult, it is possible to measure the crack opening and possible growth during the test using gauges (Fig. 13) for control and prevention of fracture during test. If the NDI is executed after test, crack detection is significantly improved because crack opening based on its blunting.

Finally, proof test opens the possibility of stress measurements during test for testing of calculated values. This is very important, because the accurate evaluation of stresses under operational conditions for the accurate evaluation of fracture mechanics behaviour and prove of structure reliability is necessary. Consequently, the most important by the proof test project is, beside the fracture avoidance through the overloading, to avoid the non-necessary permanent damage of component. Damage can appear during test from many reasons. For example, if the test is performed under the conditions that material is regarding toughness significantly weaker than under the service conditions, the crack can develop (due to overloading) even when it would be not appear under normal conditions. More frequent failures in test can emerge if the a_0 size is small compared to the typical manufacturing defects. Accordingly, although conditions tightening and increase of proof test numbers may increase reliability in service of structures that survived this test, this may unnecessary increase fractures during test by the cracks, smaller than cracks growing up to the critical size for the fracture in service. The optimisation is here necessary.

Projecting of proof test is serious task and it is only possible based on detailed investigation of design, its loading and operational conditions. Since the calculation of pressure containing components is usually based on more complex methods, e.g. finite elements, for pipes simplified methods are often applied. The widely used formula for the evaluation of pipe bursting pressure (plastic collapse) of wall thickness h through axial crack is

$$P_{kr} = \frac{\sigma_F \cdot h}{m \cdot R_m} = \frac{P_B}{m} \quad (3)$$

Here R_m is the mean pipe radius and σ_F flow strength, based on yield σ_R and fracture σ_K strengths

$$\sigma_F = k \cdot (\sigma_R + \sigma_K) \quad (4)$$

Experimental values for k vary between 0.5...0.6. At high temperatures, where the strain hardening is lower, this value tends to 0.5.

Pressure necessary for unflawed pipe bursting is marked as P_B , and the required correction m due to the presence of crack is

$$m = 0.614 + 0.481\lambda + 0.386\exp(-1.25\lambda) \quad \lambda = \left[12(1-\nu^2)\right]^{1/4} \frac{c}{\sqrt{R_m h}} = \frac{1.82c}{\sqrt{R_m h}} \quad (5)$$

with $2c$ axial length of crack and λ as pipe shell parameter.

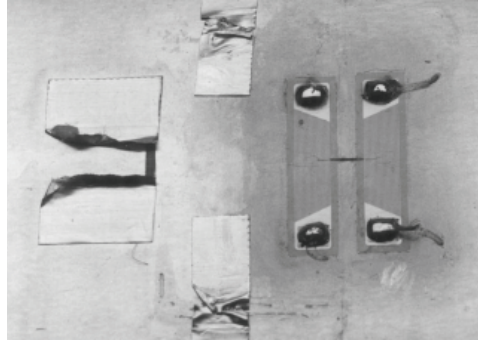


Figure 13: Measurement of crack opening by special gauges

For the case of part-through axial surface crack of depth a pressure necessary for the penetration of remaining ligament may be calculated from an empirical equation

$$p_{sc} = \frac{\sigma_F h}{m_p R_m} = \frac{p_B}{m_p} \quad \text{where} \quad m_p = \frac{1 - \frac{a}{m \cdot h}}{1 - \frac{a}{h}} \quad (6)$$

In accordance with this two formulas, if $p_{kr} > p_{PP}$ wall penetration is stable and does not lead to the pipe bursting (since for it higher pressure is necessary), but to the leakage. In contrary, the wall penetration is unstable. For the case of penetration ($a/h = 1$) more accurate formula is

$$m_p = \frac{1 - \alpha \frac{a}{m \cdot h}}{1 - \frac{a}{h}} \quad \text{with} \quad \alpha = 1 + 0.9 \left(\frac{a}{h} \right)^2 \left(1 - \frac{1}{m} \right) \quad (7)$$

The effect of circumferential crack depends on support condition, which may vary between two extreme cases: free-bending and clamping.

$$p_{kr} = \frac{2\sigma h}{R_m} \left(1 - \frac{\theta}{\pi} - \frac{2\beta}{\pi} \right) \quad (8)$$

Herein the last term $\beta = \sin^{-1} \left(\frac{\sin \theta}{2} \right)$ according to the angle length of crack $2 \cdot \theta$ adds only in the case of the free bending. To the praxis corresponds best the solution somewhere between the two extremes.

Under the effect of service conditions (loading, temperature, environment) surface crack in the vessel wall might grow under pressure and this can lead to the wall penetration or bursting of the vessel. In case of wall penetration, it comes to the internal fluid release, what either leads to vessel unloading or can be observed in time by regular inspections. Based on this, concept of Leak-before-Break (LBB) has been developed, which is derived from the idea that the failure of the component containing fluid under the pressure will be manifested by the leakage and in this way being under the full control. Accordingly, if the necessary conditions, examined by fracture mechanics, are fulfilled, growth of the crack initiated from any defect in the structure will always lead to the wall penetration and leakage and never to the vessel bursting. Such a defect can be

detected during inspections before pass through the wall. In practical application LBB must have sufficient life safety for the safe execution of the necessary action of leakage establishment, component unloading and necessary repairs. If this is fulfilled LBB can be accepted as the method of preventing failure or accident in equipment.

Today is the LBB important element of the general approach to the equipment safety, which is applied to tolerate existing or assumed cracks in a structure for definite period of operation. The starting point of the LBB procedure is normally a surface crack, which is in the state for the wall penetration of the pressure containing component. To prove LBB case for this type of the crack it is necessary to show that:

- crack breaks the pressure barrier before it may cause fracture,
- resulting leakage through the wall breakthrough is of sufficient rate, so that its recovering is possible before crack reaches its critical size leading to the failure

Behaviour of the structure and corresponding relationships can be shown on LBB-diagram, Fig. 14.

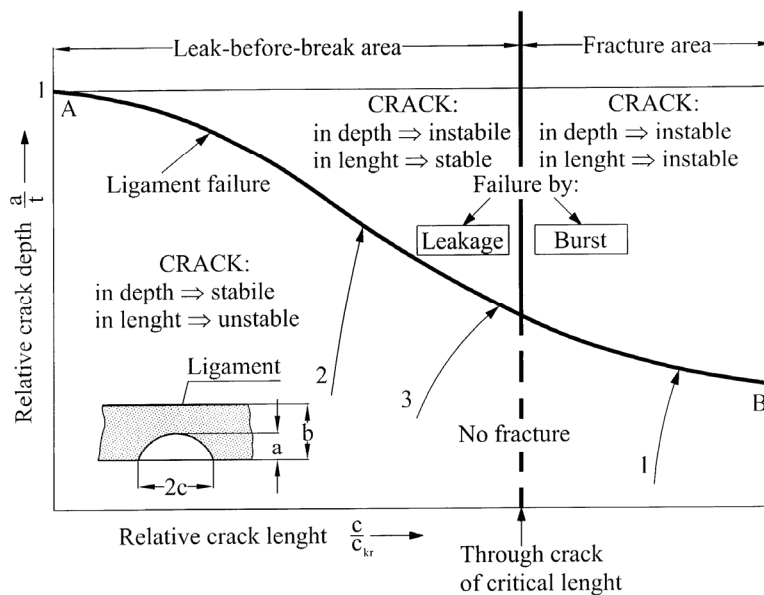


Figure 14: Presentation of the LBB-method (LBB-diagram)

Axes of this diagram are: relative crack depth a/t and the relative crack length in proportion to its critical length c/c_{Kr} . Curve AB defines fracture initiation (crack growth) for the surface crack. Vertical line at $c/c_{Kr} = 1$ separates the regions of through crack, which length is below and above critical size and, because of that, the safe area. However, surface crack which is longer than c_{Kr} may not cause failure if below of the ligament line. But if this crack grows in depth (Fig. 14, arrow 1) due to the fatigue or stress corrosion, it will certainly cause unstable fracture, and for such crack is the LBB-concept not applicable. Structure remains safe only if the crack growth is limited to the area below AB. In second example (arrow 2) the line of ligament penetration is achieved by crack growth, and after wall penetration the conditions for leakage can be realised through the further crack growth along the surface, until the crack opening become sufficient for noticeable leakage, before the critical length is achieved. The latest is only possible if the crack growth route (arrow 3) is near to the limit ($c = c_{Kr}$) in which case catastrophic failure may

appears and not leakage. Obviously, after leakage appearance, the fracture can only be avoided in case of pressure release or if the leakage is discovered in time and necessary action, to avoid further growth, were carried out. If anything exists that disrupt leakage or its detection (like insulation) than safety can not be guaranteed by LBB.

In codes is also mentioned NHLBB (NH = Non Hazardous). In general, an insulated NHLBB vessel is assumed to leak down to zero pressure without any further cycling, which assures that the crack cannot subsequently grow to critical size (rupture). Vessels that can have the pressure cycled or have significant externally applied loads after developing a leakage are not NHLBB.

Review of the LBB-diagram shows that the application of this concept requires precise analysis using fracture mechanics methods that include following important aspects:

- Investigation of conditions that must be fulfilled to apply LBB-concept in actual case.
- Evaluation of the critical size of the through crack for different crack position, taking in consideration actual loads and their combinations.
- Calculation of the leakage intensity starting from the minimal size of the actual crack, i.e. the control of the crack opening characterizing the leakage rate. The values must be conservatively evaluated (minimal expected) for leakage conditions to be fulfilled.
- Cracks discovering through the LBB approach (including proof test)
- Crack growth analysis.
- Ascertain the leakage discover in the inspection system.

Discover of cracks and leakage in pipelines is often complicated, as the number of pipes is high and the elbows additionally loaded by the moments. For the vessels is the definition of loading simpler and the crack discovery easier. Difficulties, of course, appear at the connections and supports, especially if the cracks caused by residual stresses after inspection. However, the LBB-method is of special benefit for the components that are not accessible for NDI inspection. Although the LBB procedure is now improved, there are still different problems to be considered in actual application:

Leakage region. For the evaluation of leakage area local loading and corresponding conditions must be considered, in the case of elevated temperatures to include also creep effect. The crack opening under load can be evaluated, e.g. based on EPRI-Handbook data for plate with mean through crack. For the case of pipe, it can be assumed that the plate is endless, and this means that the function h_2 is taken for $a/b = 0$:

$$\delta = \alpha \varepsilon_0 c h_2(0, n) \left(\frac{\sigma}{\sigma_Y} \right)^n \quad (9)$$

for material obeying the law

$$\frac{\varepsilon}{\varepsilon_Y} = \alpha \left(\frac{\sigma}{\sigma_Y} \right)^n \quad (10)$$

Crack position. All positions on component must be considered, but it is not sure which one is the most important. Situation is complicated, since the position of expected maximal crack growth in normal operation does not always coincide with the position of critical crack size for the lowest overloading in operation.

Stress state. Stresses at the considered positions are based on combination of different loading that may change in dependence of crack development, especially in creep.

Sensitivity of leakage detection. Different conditions affect leakage detection. Leakage effect may be reduced if the fluid evaporates or enters to the chemical reaction.

Material data. Frequently the material data are insufficiently known, especially for the welded joints where the safety evaluation by crack opening becomes more difficult.

Anyhow, LBB method is successfully applied in general, because it offers important technical advantages and economy.

Stored energy in a vessel under pressure is calculated based on formula

$$E = \frac{P_u \cdot V}{\kappa - 1} \left[1 - \left(\frac{P_{sp}}{P_u} \right)^{\frac{\kappa - 1}{\kappa}} \right] \quad (11)$$

where p_u and p_{sp} are internal pressure and pressure acting outside vessel, respectively, V is vessel volume and κ gas constant (ratio of specific heats = $\frac{c_p}{c_v}$, for air 1.4). The containment is a pressure vessel if the calculated energy is 20 kJ or more,.

5. CONTROL AND VALIDATION OF CALCULATION RESULTS

Understanding of the basic relations of the critical structures integrity was the stimulus in the development of engineering analysis methods starting with Galileo's investigation of beam bending resistance in 17th century. One of the most important goals in modern metallic structures design is the optimisation of useful weight and the application of high strength materials in order to achieve high economic efficiency. Besides this, certain structures, as for example space vehicles, can be only realised if, based on available driving power, are capable to carry, not only dead weight but also the weight of necessary fuel and useful load, and this means, they should be light structures. It is possible only applying new developed analysis methods, in which fracture mechanics has the decisive role in assessing reliability and residual life of structures (power plants, transport systems, including pipelines, process equipment and mechanical plants of different kind, during their life subjected to complex loading and conditions). Common problem of such structures is large financial load to community of their retirement. Having in mind shortage in capital, and the growing risk caused by the aging of this infrastructure, ability to fast and efficient assess structural integrity and the priority of repair and retirement with the minimum costs at acceptable risk is of great importance for national economy.

As by all calculation tied to the structure integrity, also the fracture mechanics data must produce some uncertainty. For that it is recommended to apply the data that, with possible deviations, in all cases produce conservative results. Still it is necessary to apply some safety margin calculated as the ratio of maximal load (force) that structure can carry without failure and the real applied maximal loading of the structure. The safety factor in fracture mechanics can be assessed using FAD, as ratio between lines OB/OA (Fig. 9).

This leads to conservative results, because it is usual to select minimal values of material characteristics. According to the MIL-standard, for example, two options are allowed, "A" or "B". "A" value corresponds to the material characteristic that must be fulfilled in 99 % cases with the confidence level of 95 %, and are applied if the fracture of considered element leads to the overall system failure. If the fracture of the element leads to the load redistribution to other joined elements it is possible to apply "B" value, with the probability of 90 % (with same confidence). The selection is based on the experiments

and depends on number of specimen in test (Table 1). If the number of specimens is too low the corresponding value can be even lower than the minimal value in experiments.

However, valid functional relationship is important if the safety factor is assessed in relation to other parameters. For example, safety factor in relation to the crack size must consider that the crack growth is exponentially dependent on crack size, so that the linear relationship is no more typical, i.e. cannot be compared with the safety factor based on force (load) ratio. Usual praxis of crack tolerance, where the time of next inspection is proposed after 50 % of calculated life to the critical size, does not mean the safety factor of 2 relative to the crack size. On the contrary, calculations and the measurements of crack growth show that after half of life the crack growth is usually within 15-30 %.

Table 1: Evaluation of minimal values for the case of normal distribution

$allowable = \bar{m} - k \cdot s$		
where $\bar{m} = \frac{\sum x_i}{n}$ mean value $s = \sqrt{\frac{\sum (x_i - \bar{m})^2}{n - 1}}$ and k from table		
k (confidence level 95 %)		
Number of tests n	99 % of probability (A values)	90 % probability (B values)
5	5.75	3.42
6	5.07	3.01
8	4.46	2.58
10	3.98	2.36
15	3.52	2.07
20	3.30	1.93
30	3.06	1.78
50	2.86	1.65
100	2.68	1.53
200	2.57	1.45
500	2.48	1.39
∞	2.33	1.28

However, safety factor based on load ratio can also be too conservative for the structural components under strain control, and not by constant, in the range of plasticity. In such cases is recommended to carry out “sensitivity” analysis that should show the level of change in safety factor in dependence of influence parameters. In calculation are all parameter varied, but so that their values stay real and, based on this the changes in safety factor are calculated. Different codes, like BS7910, R6 and R5, SINTAP, describe this procedure in detail. Usually is said that the safety factor has to cover all real possible variation. Problem is that in this way can be considered only known, expected variation, but not the unexpected one. The same problem occurs if the safety factor is assessed based on probability and random parameters that considers random but not systematic deviations. Independently, the factor of safety in case of fracture mechanics can never be larger that one applied on the structure or component without crack.

Application of high safety factor brings serious problems concerning economy and carrying capacity, as already mentioned. However, there are some situation in which factor of safety must be higher to achieve the needed safety, like in situation of:

- Frequent cause is uncertainty concerning material characteristics that appear due to the insufficient number of experiments, non-homogeneity of material structure (welding

structures), working temperature near to the brittle-ductile transition, indirect evaluation of fracture characteristics, as e.g. by impact testing.

- Scheme for the evaluation of operational loads deviate from real one, which is too complex to be applied.
- Uncertainties exist concerning the application of NDI and its sensitivity.
- Characterisation of crack is difficult and the calculated values are uncertain.
- Time in service can affect the parameters, as it is the case with material properties
- Loading condition change.
- Failure consequences are unacceptable.

6. CONCLUSION

Almost two thirds of the respondents reply positively in an inquiry to the question: should there be a professional qualification for competence in the application of fracture mechanics method as fitness-for-service (FFS) technology? Due to the complexity of materials and high number of simplifications, of which every one introduces some limits in the application of fracture mechanics methods, proper training and the experience is certainly necessary. Since the knowledge is not only possessing of information about certain problem, but creative and responsible approach to the application of available information (know-how), become clear that frequently opposing information and requirements should be treated of, adequate experiences and skills are necessary.

Procedures within the structural integrity analysis are techniques by which the fitness-for-purpose of elements and structures carrying the load and reliable equipment operation are evaluated. Used an appropriate and correct way these procedures increase general efficiency preventing excessive sizing and redundant inspection and repairs, providing balance between economy and the safety requirements for the environment, which are jeopardized by the consequences of fracture and failure in structure operation.

REFERENCES

1. P. Agatonović.: Fracture Case Studies – Basic Principles, in: From Fracture mechanics to Structure Integrity Assessment, 8th International Fracture Mechanics School in Belgrade/YU 23-27 June 2003. Ed. S. Sedmak and Z. Radaković pp. 159 – 192.
2. Agatonović, P.: Različite strategije određivanja preostale čvrstoće i veka, Integritet i vek konstrukcija (2/2001), str. 75-89.
3. Agatonović, P.: Die Restfestigkeit bestimmen, Spannungs-Dehnungs-Annäherung – ein neues Verfahren, Materialprüfung 41(1999), pp. 24-30.
4. Agatonović, P. : KI mittels Spannungs-Dehnungs-Annäherung abschätzen: Verifikation des Verfahrens, Materialprüfung 41(1999), pp. 77-84.
5. Agatonović, P.: Development of residual strength evaluation tool based on stress-strain Approximation, International Journal of Fracture 98, pp. 129-152, Kluwer Academic Publishers, the Netherlands.
6. Agatonović, P. and T.K.Henriksen: “*Development of Residual Strength Prediction Tools for the Structure Integrity of Launchers Based on Elasto-Plastic Fracture Mechanics*”, Conf. on Spacecraft Structures, Materials and Mechanical Testing, 27-29 March 1996, Noordwijk, The Netherlands, ESA/ESTEC.
7. Agatonović, P. and M. Windisch: MARC Anwendung zur Untersuchung des Versagensangerissener Bauteile, MARC Anwendertreffen, 14/15.9.94
8. Agatonović, P. and U. Clormann: “*Analytical Prediction and Test Verification of the Multiaxial Behaviour of High-strength Steel for Lightweight Structures*”, Proc. Int. Symp.

- “Advanced materials for lightweight structures” ESTEC, Noordwijk, The Netherlands, 25-27 March 1992 (ESA SP-336, Oktober 1992).
9. Agatonović, P. and M. Windisch: “*Role of Combined Numerical and Experimental Investigation in the Justification of the Structure Integrity and Damage Tolerance of Space Structure*”, ESA Int. Symp. on spacecraft Structures and Mechanical Testing, Noordwijk (NL), 24-26th April 1991.
 10. Agatonović, P. at all.: “*Anwendung kleiner Proben mit Oberflächenriss zur Vorhersage der Tragfähigkeit von rissbehafteten Bauteilen*”, In Werkstoffprüfung 1990, Bad Nauheim DVM Dezember 1990, pp. 213-222.
 11. Agatonović, P. and M. Windisch: “*Non-Linear Fracture Analysis of Specimens and Components with Surface Cracks*”, 5th Int. Conf. Numerical Methods in Fracture Mechanics, 23-27 April 1990 in Freiburg.
 12. Agatonović, P, H. Kordisch and E. Sommer: “*Justification of Dimensioning Criteria for a Rocket Motor Case Using Fracture Mechanics*”, in “*Element of Defect Assessment*” European Symposium on EPFM, October 9-12 1989 in Freiburg.
 13. Anderson, T. L.: ELASTIC - PLASTIC FRACTURE MECHANICS: A CRITICAL REVIEW, (PART 1) SSC-345, SHIP STRUKTURE COMMITTEE, April 1990,
 14. Chell, G. at all: Significant Issues in Proof testing: “*A Critical Appraisal*”, NASA CR-4628, 1994.
 15. Mirzaei M.: Fracture Mechanics Lecture Notes: 3, Dept. of Mechanical Eng., TMU, <http://www.modares.ac.ir/eng/mmirzaei/FM.htm>
 16. Grüter, L. at all: “*Leak-Before-Break Considerations for LMFBR Structures*”, International Journal of Pressure Vessels and Piping, Febr. 1986.
 17. Wilkowski, G.M. at al: “*State-of-the-Art Report on Piping Fracture Mechanics*”, NUREG/CR-6540 1997.
 18. Zehnder, A.L.: “*Lecture Notes on Fracture Mechanics*”, Dept. of Theoretical and Applied Mechanics, Cornell University, Ithaca, NY 14853, January 7, 2008.

SIGNIFICANCE OF FRACTURE MECHANIC TESTING FOR STRUCTURAL INTEGRITY OF WELDED JOINTS

Vencislav Grabulov, Dejan Momčilović***

Institute for testing of materials IMS, Belgrade, Serbia

** vencislav.grabulov@instiutims.rs ** dejan.momcilovic@instiutims.rs*

1. INTRODUCTION

Welding technology has had a significant impact on industrial development. Fabrication by welding is an effective method to reduce production and fabrication costs and can be mechanized, computer controlled, and incorporated in assembly lines. Welding fabrication has revolutionized many industries, including shipbuilding and automotive production, and has resulted in the development of various products, such as pressure vessels, that could not otherwise have achieved their present functions. Welding technology is complex and fabrication by welding encompasses properties that should be understood to different levels by the design engineer, the fabricator, and the welder. Some of these properties pertinent to the theme are residual stresses, imperfections, and stress concentration. Failures of engineering structures occur predominately at welded joints, even in structures designed, fabricated, and inspected according to appropriate standards and codes. For example, fatigue cracking in bridges, ships, offshore structures, pressure vessels, and buildings occurs, almost without exception, at the welded joints and attachments, like cover plate fillet welds, stiffeners, backing bars, and seam and girth weld toes.

2. WELDING AND RESIDUAL STRESSES

Residual stresses are those that exist in a component free from externally applied forces. They are caused by non-uniform plastic deformations in neighbouring regions. These regions can be small, as occurs within weldment, or large, as may occur in curving or straightening a beam or a shell during fabrication. Furthermore, residual stresses are always balanced so that the stress field is in static equilibrium. Consequently, wherever tensile residual stresses occur, in neighbouring region compressive residual stresses exist. Residual stresses can be either beneficial or detrimental to the behaviour of components. For example, controlled thermal or mechanical residual stresses are used to curve or straighten large components. Also, compressive residual stresses are used to minimize environmental effects on component surfaces and to improve their fatigue initiation resistance. Because fatigue life is governed by the stress range rather than the magnitude of the static or steady-state, applied or residual stresses, tensile residual stresses usually have only a secondary effect on the component fatigue behaviour. On the other hand, excessive tensile residual stress can also initiate unstable fracture in materials of low-fracture toughness. For that, the magnitude of unfavourable residual stresses should be controlled, especially in thick, highly constrained weldments of low fracture toughness.

In addition, residual stresses can be induced by thermal, mechanical, or metallurgical processes. Thermal residual stresses are caused by non-uniform permanent (plastic) deformations when a metal is heated, then cooled under restraint. Unrestrained expansion and contraction do not generate residual stresses. However, restrained expansion and contraction induce permanent deformation (strains) and corresponding residual stresses.

Mechanically induced residual stresses are caused by non-uniform permanent deformation when a metal is mechanically stretched or compressed under restraint. The occurrence of mechanically induced residual stresses requires the presence of both. Permanent mechanical deformation and restraint, that prevents the deformed metal from contracting or expanding to its new unrestrained equilibrium dimension. In general, the sign (tension or compression) of mechanically induced residual stress is opposite to the sign of non-uniform plastic strain that produced the residual stress. This process is used to mechanically curve or straighten components and, as in peening, which produce a compressive stress layer on the component surface to improve its fatigue or corrosion behaviour.

Fabrication by welding usually results in stresses that are locked into the fabricated assembly. These stresses are either residual stresses or reaction stresses, or both. Residual stresses are caused by the inability of the deposited molten weld metal to shrink freely as it cools and solidifies. Reaction stresses are caused by the inability of assembly components to move relative to each other during thermal expansion and contraction of the deposited weld metal, or the molten base metal for autogenously welded joints and surrounding base metal. Contraction of solidifying weld metal is restricted by adjacent materials, resulting in three-dimensional residual stresses. The magnitude of these stresses depends on several factors, like size of the deposited weld bead, weld sequence, total volume of the deposited weld metal, weld geometry, and strength of the deposited weld metal and of the adjoining base metal. Often, the magnitude of these stresses exceeds the elastic limit of the lowest strength region in the weldment.

Methods for measuring residual stresses are sectioning, drilling hole, and X-ray diffraction. The sectioning method is a destructive test in which residual stresses are determined by removing slices from the member and measuring the resulting strain. Drilling hole is a semi-destructive test for measuring residual stresses near the material surface; it involves placing strain gauges on the surface and measuring strain relaxation by drilling hole in the vicinity of the gauges. The X-ray diffraction method is a non-destructive test in which surface residual stresses are determined by measuring the change in the lattice spacing of the material; only surface residual stresses are measured in a localized area.

Development of residual stresses in a groove welded joint is shown in Fig. 1 /1/.

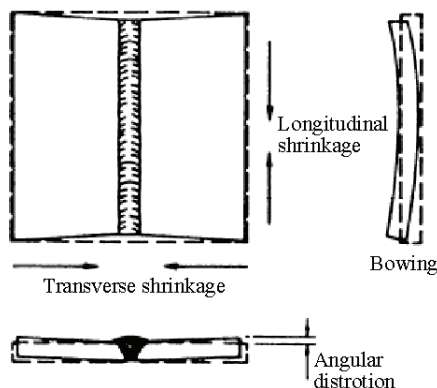


Figure 1: Residual stresses for a butt-welded plate /1/

As the deposited molten metal cools, it contracts longitudinally along and transversely across the weld, Fig. 1. Surrounding base metal prevents the contraction, producing residual tensile (+) and compressive (-) stresses. These stresses may cause distortion,

deformation in post-weld machining, stress corrosion cracking and fracture /2/. The tensile and compressive stresses are balanced in neighbouring areas to be in equilibrium.

2. WELD DISCONTINUITIES AND THEIR EFFECTS

Different discontinuities and cracks in the deposited weld metal (WM) or in the heat-affected-zone (HAZ) of the base metal (BM) can occur in produced welded joints /1, 3-4/. They introduce stress concentration regions, shown in Fig. 2 for different types of weldments. Codes and specifications define acceptance levels for discontinuities in terms of their type, size, orientation, and distribution. Usually, cracks and crack-like discontinuities are not acceptable. Discontinuities are designated as defects only when their size, orientation, and distribution exceed specification limits and their presence affects the integrity of the component, making it unsuitable for its intended application.

Various types of weld discontinuities, cracks, and imperfections, their causes and methods to avoid them are considered in many references. In general, the weld discontinuities might be caused by: (1) improper design that restricts accessibility for welding; (2) incorrect selection of a welding process or welding parameters; (3) improper handling of consumables, and (4) other causes including welding performance. These observations are cited to emphasize that quality assurance in welding requires considerations and proper decisions, starting with the design stage and continuing throughout the entire fabrication process. Weld discontinuities can be classified in three basic groups:

1. Crack-like discontinuities (cracks, lack of fusion, lack of penetration, overlap)
2. Volumetric discontinuities (porosity, slag inclusions)
3. Geometric discontinuities (undercut, incorrect profile, misalignment)

Most frequent defects and crack-like discontinuities in weldments are shown in Fig. 3.

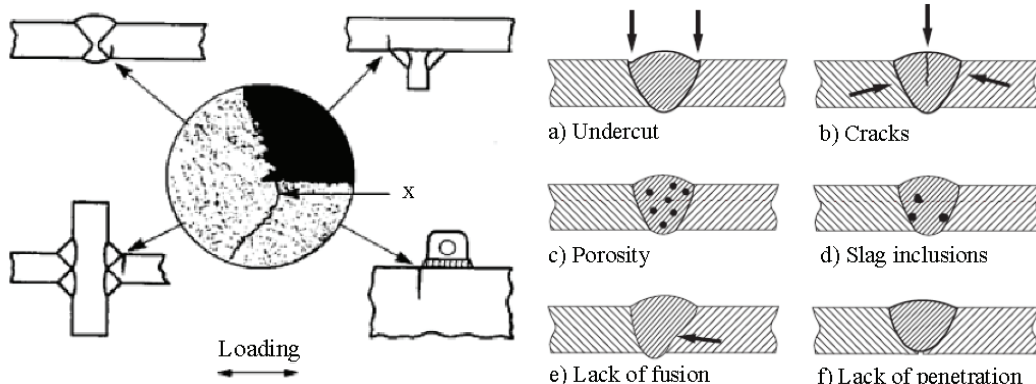


Figure 2: Stress-concentration regions weldments Figure 3: Defects and cracks in welded joint

The mere existence of discontinuities does not indicate a loss of product's fitness for a given application. Product suitability for service is based on the severity of the discontinuity, depending on their size, shape, and orientation, assessed according to applicable specifications and analyses, and on the magnitude and direction of applied stresses. The severity of discontinuity increases with its size, when it is closer to planar form and loaded by perpendicular tensile stresses. Volumetric discontinuities are less injurious than planar, crack-like discontinuities. The discontinuities oriented in stress direction might be innocuous compared to that of same size perpendicular to the tensile stress, which can be dangerous. Surface discontinuity with plane perpendicular to the tensile stresses is more

severe than embedded one of the same size and similar shape. As stress raisers, the discontinuities affect fatigue and brittle fracture behaviour in their immediate vicinity.

Cracks are the main problem for structural integrity of welded structures, and fracture mechanics is inevitable tool, including testing of cracked specimens.

Cracks in welds can occur in welding manufacturing, or during service.

The cracking associated with the welding process can occur in deposited weld metal in the form of hydrogen attack, gas porosity and solidification cracks, at the fusion line like liquation cracks, HAZ burning or hot tearing and in HAZ in the form of lamellar tearing, cold or hydrogen induced cracks and reheat cracking (which can also occur in WM).

The most complex and severe are solidification and liquation cracks, lamellar tearing, cold and reheat cracks. The basis for discussion of the cracking mechanisms in different cases is the crack resistance of a material and how welding can affect this property /1,5/.

In-service cracks are produced by the effect of applied load, environment, vibration or service thermal cycling.

3. STRESS CONCENTRATION

Typical stress concentrations due to notches are shown in Fig. 4.

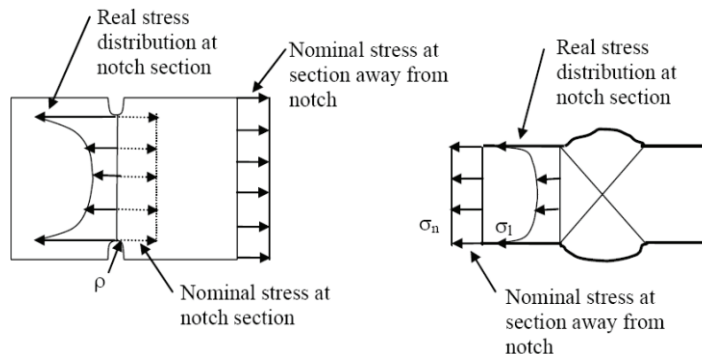


Figure 4: Stress concentrations at notches: plate with edge notches (left): butt welded joint (right)

In a plate with two edge notches, symmetrically disposed, the stress will increase slightly due to cross section reduction by notches, and much more by stress distribution caused by the local disturbance, dependent on the notch radius size ρ . When overloaded, cracks might appear in the root of notches. Similarly, in butt welded joint the reduction of cross section affects slightly, and much more is expressed the stress concentration by WM overfill at the transition between the BM and WM. These effects can be described by the stress concentration factor, k_t , expressed as the ratio of the maximum local stress, σ_{max} , and the nominal stress, σ , in remote cross section:

$$k_t = \frac{\sigma_{max}}{\sigma} \quad (1)$$

The maximum stress for a given planar discontinuity occurs when the plane of the discontinuity is perpendicular to the direction of the tensile stress and approaches zero as the plane of the discontinuity becomes parallel to it. The stress increase caused by a surface discontinuity is about twice compared to an embedded discontinuity of equal size and shape. The stress increase due to planar discontinuity whose plane is perpendicular to the direction of the tensile stress is higher compared to a volumetric discontinuity of equal planar size and shape projected.

Stress concentration has an important effect of fatigue, including welded joints /6/. The situations shown in Figs. 2-4 are typical locations for fatigue crack initiation, but also direction of loading is important. Thus, planar discontinuities, such as plate laminations, whose plane is parallel to the surfaces of a plate subjected to in-plane tensile stress fluctuations, rarely cause degradation in the fatigue life, but can be detrimental when the plate is subjected to tensile stress in the through-thickness direction. Also, unwelded regions loaded perpendicular to their plane in partial penetration groove welds or when lack of fusion occurs behave like cracks and, depending on the geometry of the weldment, can cause crack initiation and propagation from the weld root.

4. THE APPLICATION OF FRACTURE MECHANICS PARAMETERS

Fracture may be defined as the mechanical separation of a solid by applied stress. Fracture of engineering materials is classified as ductile or brittle. In a brittle material, like glass, the energy required for fracture is simply the intrinsic surface energy of the material. For alloys at room temperature, much more energy is spent for fracture because of plastic deformation preceding final separation of metallic materials.

The application of fracture-mechanics technology has significantly improved design of structures regarding safety and reliability, quantifying the parameters that affect structural integrity. These parameters include the magnitude and range of the applied stresses; the size, shape orientation, and rate of propagation of the existing crack; and the fracture toughness of the material. Linear-elastic fracture mechanics (LEFM) is applicable if the crack tip in a body is sharp and negligible plastic deformation preceded fracture, like in case of high-strength steels, titanium, and some aluminium alloys. Elastic-plastic fracture mechanics (EPFM) is used when the crack is not sharp, so crack-tip plasticity can produce crack tip blunting, for materials such as lower-strength, higher-toughness steels.

Toughness is defined as the ability of a material to absorb energy. It is characterized by the area under a stress-strain curve for a smooth tensile specimen loaded slowly to fracture. Notch toughness represents the ability of a material to absorb energy in the presence of a notch, usually by impact loading, using the Charpy V-notch specimen, the dynamic-tear specimen, and fracture-toughness specimens loaded quasi-statically (K_{Ic}) or dynamically (K_{Ia}). Traditionally, the notch-toughness of low- and intermediate-strength steels have been characterized in terms of the transition from ductile to brittle behaviour by decreasing test temperature /3,7,8/. Most structural steels can fail in either a ductile or a brittle manner depending on temperature, loading rate, and constraint. The ductile-to-brittle transition behaviour of steels is most frequently characterized by impact testing the Charpy V-notch specimen, ASTM E 23. Notch toughness at each testing temperature may be determined from the energy absorbed during fracture, from the present shear (tearing) or cleavage on the fracture surface, or lateral expansion. An example of the ductile-to-brittle transition with temperature for each of these parameters is presented in Fig. 5 /3/.

The rate of change from ductile to brittle behaviour depends on many parameters, including strength and composition of the material. It has been customary to define a single temperature, corresponding to consumed energy of 20 J, or to 50% of cleavage.

Fracture-toughness behaviour, or the ability of cracked material to withstand fracture, is established by using fracture-mechanics concepts, in the form of stress-intensity factor:

$$K = C\sigma\sqrt{a} \quad (2)$$

where C is a constant, depending on specimen and crack geometry, σ , MPa, is nominal stress, and a , mm, is crack size. One of the basic principles of fracture mechanics is that unstable fracture occurs when the stress-intensity factor reaches a critical value, Table 1.

For mode I loading (opening, tensile mode) and for negligible crack-tip plastic deformation (plane-strain conditions), the critical stress-intensity factor for fracture instability, K_{Ic} , represents the inherent ability of a material to resist tensile crack extension. However, this fracture-toughness property varies with constraint, and like other material properties such as yield strength, varies with temperature and loading rate as follows.

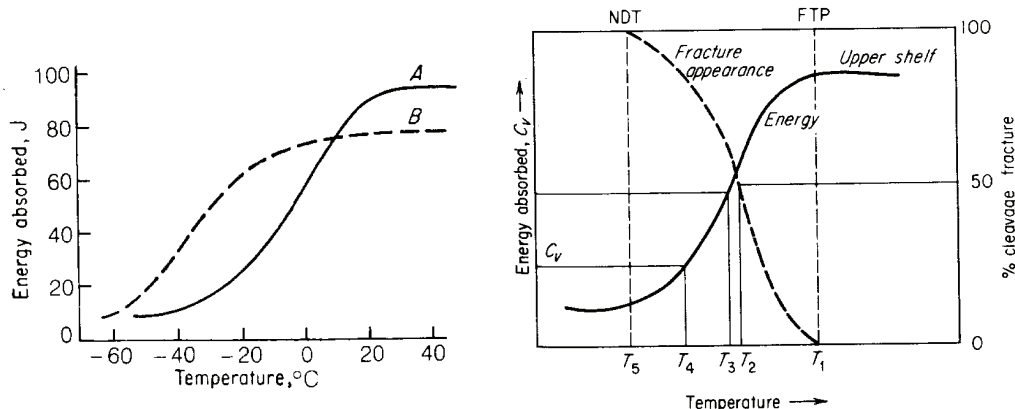


Figure 5: Transition-temperature curves for two steels, showing fallacy of depending on room-temperature results (left), various criteria of transition temperature obtained in Charpy test (right)

Table 1: Stress-intensity factors

K_c	Critical stress-intensity factor for static loading and plane-stress conditions of variable constraint. This value depends on specimen thickness and geometry, and on crack size.
K_{Ic}	Critical stress-intensity factor for static loading and plane-strain conditions of maximum constraint. This value, a minimum value for thick plates, is material property.
K_{I_d}	Critical stress-intensity factor for dynamic (impact) loading and plane-strain conditions of maximum constraint.

Each value from Table 1 (K_c , K_{Ic} , K_{I_d}), is also a function of temperature, particularly for structural materials exhibiting a transition from ductile to brittle behaviour [9,10, 11].

Knowing the critical value of K at failure (Table 1) for a given material of a particular thickness and at a specific temperature and loading rate, the designer can determine flaw sizes that can be tolerated in structural members for a given design stress level. Conversely, the designer can determine the design stress level that can be safely used for an existing crack, present in a structure. In general, the relationship among fracture toughness (K), stress (σ), and crack size (a) is shown schematically in Fig. 6 for through thickness crack in a plate. The figure shows that there are for particular material many combinations of stress and crack size (σ_f , a_f) that may cause fracture, and many of them (σ_0 , a_0) when fracture will not take place, under slow loading and at given test temperature.

High-toughness structural materials undergo extensive plastic deformation prior to fracture, and for them EPFM parameters are applicable. Crack-tip opening displacement (CTOD), corresponding to slow loading rates is also applicable in LEFM, and the J-integral, as an energy criterion for slow loading rates, is used in EPFM.

Based on either of them, crack resistance curve (R-curve) is defined, indicating fracture resistance of material to stable crack growth.

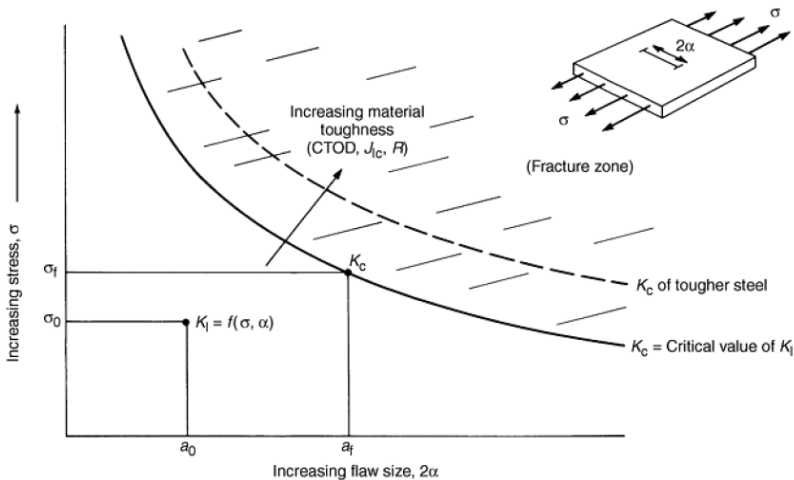


Figure 6: Relationship among stress, flaw size, and material toughness /12/

As discussed, crack resistance can be evaluated by different fracture mechanics parameters. Three of them are in general use: the stress intensity factor K , the crack opening displacement (COD), and the J integral. Their critical values: plane strain fracture toughness K_{Ic} , critical COD (δ_c), and J_{Ic} , a measure of fracture toughness, can be used as material properties of homogeneous materials. However, there are many problems in testing and evaluation of results for welded joints connected with the properties of the WM and the heterogeneous microstructure of the HAZ.

5. FRACTURE MECHANIC TESTING OF WELDED JOINTS

The weld metal and adjacent HAZ have heterogeneous microstructures, with regions of different strength and toughness, that affects fracture behaviour. Welding residual stresses have also to be taken into account in fracture consideration. This situation makes fracture testing of welded joints to be complex. Fracture testing, using slow loading and precracked specimen, allows determination of only the crack initiation portion of the fracture toughness. Charpy testing determines a combination of crack initiation, propagation and arrest properties. Fracture initiation testing of welded joints thus is even more sensitive to the local microstructure ahead the crack tip than Charpy tests are to the microstructure at the notch. Heterogeneity also causes welds to be particularly sensitive to the rules for data interpretation for fracture initiation tests. Fatigue precracks are less likely to be straight in a heterogeneous material. Tests may have multiple events of crack initiation and arrest in local areas (“pop-ins”). Different strengths may cause validity criteria based on yield strength and specimen size to give ambiguous results. Each of these issues must be accounted for in a test protocol appropriate to welds. Fracture toughness specimens can be taken from welded joints in several orientations as shown for compact tension specimens in Fig. 7. These orientations can be designated by two-letters: first letter is the direction normal to the crack plane, while the second letter is the direction in which the crack will propagate. The letter choices are L - longitudinal direction; T - long transverse direction (the weld width direction); and S -, short transverse direction (the through thickness direction). Care should be taken that the orientation letters describe the weld area, because different combinations of these letters may be applied to the same orienta-

tion for base metal specimen. For instance, in a girth weld of a pipe, the long direction of the weld is the pipe hoop direction, not the longitudinal or axial direction of the pipe.

Fracture toughness testing of HAZ presents particular problem, because several different microstructures can cluster in the HAZ, based on the different heating histories in different locations from the welding. A fracture toughness measured in the HAZ is likely to be affected both by the properties of the several HAZ microstructures that the crack tip passes through and by the properties of the adjacent WM and BM.

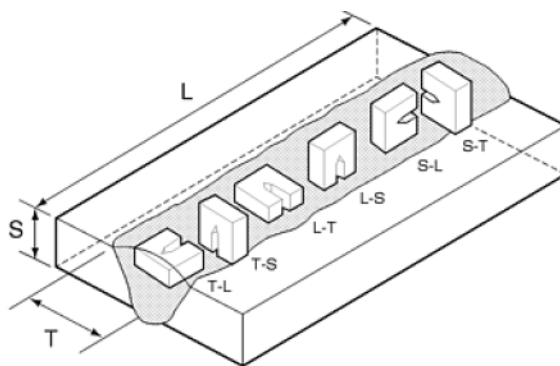


Figure 7: Orientations of toughness specimens relative to weld. L - longitudinal direction; T - long transverse direction (weld width); S - short transverse direction (weld thickness). In the two-letter code, the first letter designates the direction normal to the crack plane, and the second letter designates the expected direction of the crack plane /12/

Fracture initiation toughness is measured using the stress intensity factor, K , the J -integral, J , or the crack tip opening displacement (CTOD). All these parameters are applied to welded joints. CTOD measurements are specified in welded regions rather than in base metal, since this test was originally developed for welded joint. Conversions between K , J , and CTOD can be performed but with limited accuracy.

Fracture toughness testing of welds may require precise positioning of the notch to test the microstructure of interest (Fig. 8). Testing of welds may also require some modification of the test specimen. Anyhow, the choice of particular specimen geometry depends on testing purpose and requirements.

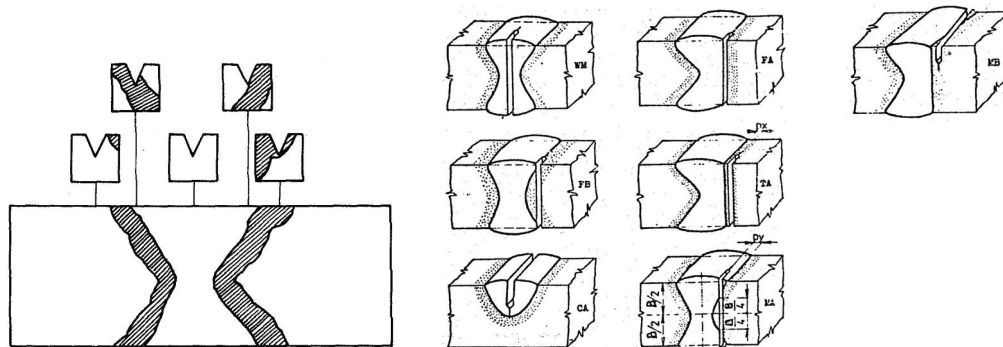


Figure 8: Typical notch positions in fracture mechanics specimens of welded joint

Significant differences in toughness also may be attributed to differences in the fracture criteria. Data obtained as the CTOD or J integral evaluate the fracture toughness of ductile materials after significant crack extension, in plastic range. Consequently, the

toughness values for the same material are higher than those obtained as K_{Ic} or J_{Ic} values. Advantages and disadvantages of fracture toughness tests are listed in Table 2 /8-14/.

The three-point bend and compact specimens (standardized in ASTM E 399 and E 813) are recommended for general laboratory materials evaluation, because K and J calibrations for these specimens are known and relatively low loads are required during testing. Data obtained with non-standard specimens must be evaluated carefully to ensure that the same fracture criteria are used, such as the onset of cracking.

Table 2: Fracture toughness tests

Method	Advantages	Disadvantages
K_{Ic} , ASTM E 399	This method is the most reliable to get fracture toughness values at lower temperatures. The success of all other methods is based on their ability to give data comparable to this method.	The high cost of testing the large specimens at high temperature tends to reduce the number of data points. Linear extrapolation from valid K_{Ic} at lower to higher temperature is conservative. No valid K_{Ic} values at high temperature.
J -integral, ASTM E 813	Provides fracture toughness values that agree with K_{Ic} value. Fracture toughness data at high temperature are realistic. Sound theoretical basis permits evaluation of stable crack growth. The value dJ/da is a measure of the resistance to continued crack propagation. Testing a series of small J specimens provides an indication of material toughness variation.	It is not possible to evaluate irregular crack propagation due to residual stress or at HAZ near welds. Not accurate enough at low temperatures. Measurements are inaccurate due to irregular crack fronts. Not valid for thin materials where K_J is $2.5 K_{Ic}$. When heat tinting is used, the additional number of specimens increase testing costs.
CTOD, BS 7448	Provides fracture toughness values that agree with K_{Ic} method. Fracture toughness data at high temperature are realistic. CTOD results are consistent and comparable with the values of other methods. Simultaneous measurement of CTOD and J integral is possible.	Variations in the measurement of CTOD (δ) results in variations of K_{Ic} up to a factor of 2. This method is restricted to temperatures above -60°C .

A proper use of fracture-mechanics methodology for fracture control of structures necessitates the determination of fracture toughness for the material at the temperature and loading rate representative of the intended application. The morphology of fracture surfaces for steel can be understood by considering the fracture-toughness transition behaviour under static and impact loading, depicting the mode of crack initiation at the crack tip for static, and the mode of crack propagation for dynamic loading.

This is to emphasize that one of the key problems regarding accuracy of fracture mechanic testing of welded joints specimens is notch positioning, Fig. 8 /15/.

Experimental work experienced in methodological approach can help, as an example, to understand better fracture mechanics parameters for BM, HAZ and WM, determined as static and impact crack properties of high strength steel welded joint were tested /16 - 20/.

6. EXPERIMENTAL INVESTIGATION

Experimental investigations of the static and impact properties have been performed with high strength (HSLA) steel NIONIKRAL 70 (NN70) of nominal yield strength 700 MPa, designed for pressure equipment in process industry and in shipbuilding, e.g. for submarines. This is a quenched and tempered (Q&T), low alloy, Ni-Cr-Mo steel (Table

3), produced in an electric furnace and subsequently slab-rolled to 18 mm thick plates. After hot rolling, the steel is quenched in water from 890°C and tempered at 660°C. The properties (Tables 4 and 5) were obtained by combining classic quenching and tempering with grain refinement, micro alloying and suitable precipitation.

The aim of this investigation was to determine the toughness and fracture properties of the constituents of a welded joint (BM, WM and HAZ) and to assess any reduction of these properties caused by welding. The chemical composition and mechanical properties of NN70 steel are given in Tables 3 and 4, respectively; Charpy V energies obtained at different temperatures are listed in Table 5.

The high strength of NN-70 steel is accompanied by good impact toughness in both orientations (total impact energy greater than 65 J down to -80°C, Table 3) and a low nil-ductility transition temperature (below -120°C for 50% Charpy V energy, -103°C in the drop weight test, ASTM E208), significant crack initiation energy and resistance to crack propagation at all testing temperatures. This combination of strength and toughness is favourable for pressure equipment application.

Table 3: Chemical composition of NIONIKRAL 70 steel, %

C	Si	Mn	P	S	Cr	Ni	Mo	V	Al
0.1	0.2	0.23	0.009	0.018	1.24	3.1	0.29	0.05	0.08

Table 4: Mechanical properties of NIONIKRAL 70 steel

Specimen orientation	Yield stress	Tensile strength	Elongation	Contraction
	$R_{p0.2}$, MPa	R_m , MPa	A , %	Z , %
Parallel to rolling	780	820	19	66
Perpendicular	770	810	20	74

Table 5: Charpy V absorbed energy of NIONIKRAL 70 steel

Specimen orientation	Energy J	Testing temperature, °C							
		20	-20	-40	-60	-80	-100	-120	-140
Parallel to rolling	Total	108	106	107	100	98	78	64	30
	Initiation	41	40	42	36	36	33	29	23
	Propagation	67	66	65	64	62	45	35	7
Perpendicular	Total	81	80	81	76	65	49	46	28
	Initiation	30	29	28	24	23	23	23	22
	Propagation	51	51	53	52	42	26	23	6

Because of low sulphur content, steel NN-70 is guaranteed without cracks, A class. The applied CaSi treatment resulted in globular MnS, without MnS inclusions shape responsible for lamellar tearing, enabling to apply NN-70 steel also for welded T joints.

The weldability and cracking susceptibility of high strength steels can be serious problems in application [21-23], requiring the consideration of the risks of cracking during fabrication and of failure during service. The most important aspects of weldability are the sensitivity of the WM and the HAZ to any type of cracking during or after welding, behaviour related to brittle fracture and the mechanical and technological properties of the welded joint, macro- and micro-analysis of the BM, HAZ and WM. In spite of precautions taken in the first stage of the weldability analysis of NN70, it was not possible to avoid cracks, because experience with the welding of HSLA steel was limited. A hot crack which developed inter crystal line between the dendrites in the cast structure of the WM, is presented in Fig. 9. A cold crack (Fig. 10) occurred in the transition fusion region in the cast structure of the weld metal and in the HAZ region of dominant coarse-

grained microstructure, where the development was trans crystal line. The occurrence of these cracks required the application of empirical formulae for weldability assessment and numerous technological tests (FISCO, CTS, Window, Tanaka, Y test) /20/. The tests showed that NN70 is not prone to hot cracking if the electrodes and welding regime are properly chosen. Although an applied under matching can prevent the occurrence of cold cracks, they were found at the fusion line (Fig. 10) if the samples had been preheated below 130°C, so proper welding procedure and its control was necessary.



Figure 9. Hot crack in weld metal

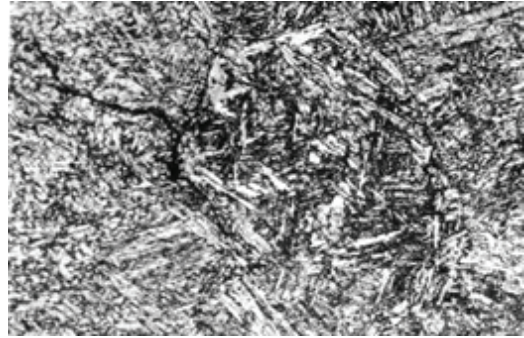


Figure 10. Cold crack at the fusion line

After experimental analysis, applying three different levels of heat input and an analysis of the HAZ width and the obtained microstructure, it was possible to define a proper Welding Procedure Specification (WPS) and produce defect-free welded joints. The analysis included the determination of the nil ductility transition temperature. This temperature was -74°C for the welded joint, according to ASTM E-208, and -85°C for the HAZ and -25°C for the WM, according to the 50% Charpy energy.

6.1. Preparation of welded samples and qualification of the welding procedure

The welding technology and regime were chosen in accordance to the properties and basic microstructure of NN70 steel. The shape of the welded joint was designed to simulate the best stress distribution in real structures. Samples for experimental investigations were prepared by manual arc welding (MAW) of the metal following a defined WPS. Two plates of NN 70 steel, 18 mm thick, prepared for an asymmetric 2/3 X welded joint by edge machining (Fig. 11), were welded with a 2 mm gap. The chemical composition and mechanical properties of the applied electrode EVB 75 (according to EN 757: E 69 4 Mn2NiCrMo B 42) are shown in Tables 6 and 7, respectively. Welding was performed in six passes, with the heat inputs given in Table 8. Specimens of the welded joint, WM and HAZ were machined from the welded plates for qualification (Fig. 12).

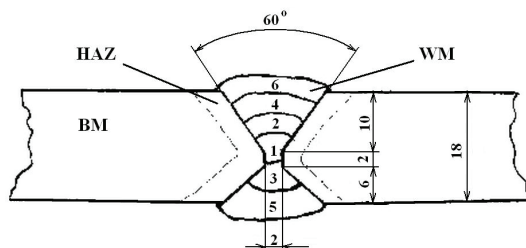


Figure 11: Welded samples were produced in six passes

The results of the tensile tests of the welded joint are shown in Table 9. The specimens started to yield at about 700 MPa and fractured in the WM, indicating that strength under matching of the welded joint was obtained (compare Table 4.).

The results of guided bend tests according to EN 910 (Welded butt joints in metallic materials - Bend test) are given in Table 10, as bending angle and fracture initiation location. They show a limited deformation capacity of the welded joints. Cracks occurred at the fusion line and in the WM for specimens bent around the face side (i.e. the side of pass 6, Figs. 11 and 12). Better results were obtained for specimens bent around the weld root, since the weld face side was wider and did not contain a critical region of the HAZ with a dominant coarse-grained microstructure, close to the fusion line.

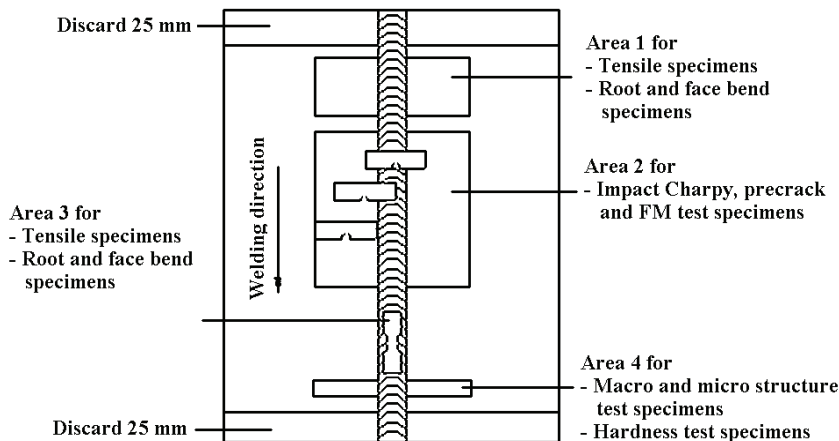


Figure 12: Welding direction and specimen positions in the sample plate

Extended instrumented Charpy V-notched specimens tests of the WM and HAZ were performed according to ASTM E23-86 at different temperatures. The position of the V-notch in the specimen, determined following Fig. 8, is presented in Fig. 15. The results in Table 11 present the total impact energy and the parts for crack initiation and propagation. The maximum load is accepted for the calculation of the crack initiation energy.

Comparison with the results for the BM (Table 4) show that the WM has lower impact energy at all temperatures, with a higher transition temperature. Although the energy values for the HAZ are acceptable, the significant scatter of the results required a detailed analysis of the effect of microstructure.

Coarse-grained regions (Fig. 10) contributed to the reduced impact toughness of some specimens in Table 11. The effect of low toughness is localized by multipass welding, producing regions of lower impact toughness as narrow segments in the HAZ, surrounded by metal of higher toughness, in which crack growth will be arrested.

Table 6: Chemical composition of the weld metal, %

Electrode	C	Mn	Si	Cr	Ni	Mo
EVB 75	0.06	1.65	0.3	0.55	2.0	0.35

Table 7: Mechanical properties of the weld metal according to specification

Electrode	Yield stress	Tensile strength	Elongation	Contraction	Impact energy, J		
	$R_{p0.2}$, MPa	R_m , MPa	A , %	Z , %	+20°C	-40°C	-60°C
EVB 75	710-770	770-830	18-20	110-140	50-80		35-65

Table 8: Welding parameters for manual arc welding (MAW) of NN 70 steel

Base metal	Electrode	Pass	Diameter, mm	Heat input, Q , J/cm
NN70	EVB 75	1	3.25	16.9
		2	3.25	15.1
		3	4	19.4
		4	4	20.4
		5	4	18.9
		6	4	19.0

Table 9: Tensile properties of the welded joint specimens.

Electrode	Tensile strength, R_m , MPa	Contraction, Z , %
EVB 75	766	68.8
	759	67.7

Table 10: Results of guided bend test of welded joints

Specimen	Thickness, mm	Filler metal	Bending angle	Bending on	Fracture position.
7B2	18	EVB 75	30°	Face	Fusion line
7B20	18	EVB 75	180°	Root	Fusion line
7B3	18	EVB 75	30°	Face	Weld metal
7B30	18	EVB 75	180°	Root	No fracture

Table 11: Charpy energy (V-notch) of welded joint constituents

Notch position	Charpy energy, J, at											
	20°C			- 60°C			- 100 °C			- 140°C		
	t	ini	pr	t	ini	pr	t	ini	pr	t	ini	pr
Weld metal	47	17	30	23	14	9	7	4	3	5	2	3
	40	12	28	16	6	10	10	6	4	8	5	3
	43	19	24	16	7	9	7	4	3	6	2	4
Heat-affected-zone	64	35	29	53	43	10	99	89	10			
	123	80	43	91	51	40	48	27	21			
	64	47	17	72	50	22	58	37	21			

t – total energy; ini – energy for crack initiation; pr – energy for crack propagation

6.2. The effect of microstructural heterogeneity on notch and crack resistance

The testing results obtained with V-notched and pre-cracked specimens depend on the position of the notch root and the crack tip in the microstructure (Fig. 8). Although different, the microstructures of the BM and WM are homogeneous and the scatter of the obtained test results was not significant. However, the scatter of the results obtained for the HAZ (Table 11) was significant due to microstructural heterogeneity and required detailed analysis. The transition region at the fusion line, presented in Fig. 13, is positioned between the cast microstructure of the WM, left, and the coarse-grained (CG) HAZ region, right. On the other boundary of the HAZ (Fig. 14), there is a transition region between the directed fine grains (FG) of the rolled BM, left, and the fine grains of the tempered HAZ, right. Although the microstructure of the WM (Fig. 9) is a cast one, it presents a continuous homogeneous metal of sufficient volume, enabling the determination of the WM properties, including notch and crack resistance. This is not the case with the HAZ. Exposed to successive heat inputs, the microstructure of the HAZ in the regions between two boundaries, given in Figs. 13 and 14, changed during welding. The details of this microstructure are presented in Fig. 15 along the crack tip in a pre-cracked specimen.

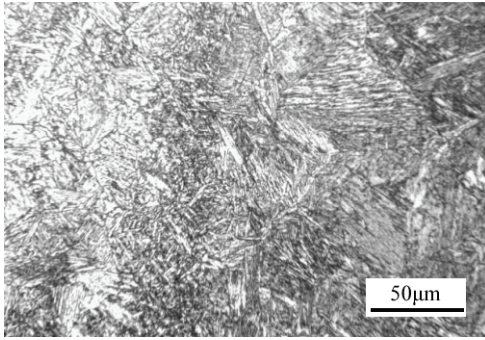


Figure 13: Transition region at the fusion line: WM cast microstructure, left, and coarse-grained HAZ region, right, with a visible fusion region between them

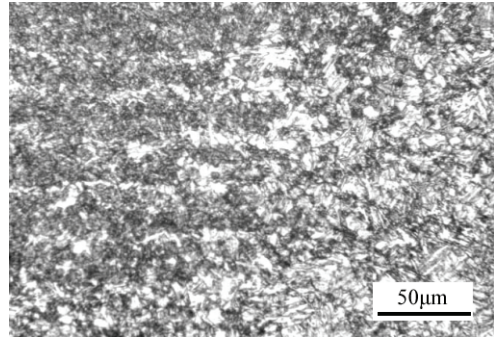


Figure 14: Transition region between the directed fine grains of rolled BM, left, and the fine-grained bainite of the tempered HAZ, right

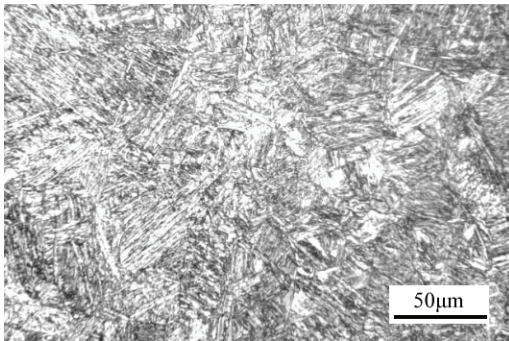
The size of the HAZ is limited and the regions of different microstructures too small for an evaluation of their mechanical properties. In the case of NN70 steel, the HAZ microstructure consisted of bainite of different grain sizes. Upper bainite of CG (location 1) in the vicinity of the fusion line (with an eventual martensite region, but not clearly recognized here) is followed by lower bainite (location 2) and FG tempered bainite similar to the BM (location 3) in the middle, and by lower bainite at the end (location 4, Fig.15). It should be noticed that the transition between the bainite regions is smooth. Due to different microstructures in the regions, the mechanical properties, including impact toughness and crack resistance, can differ significantly, affecting the overall response of a welded joint specimen.

Regarding structural integrity, the response of the HAZ as a whole is important and the obtained HAZ microstructure, being of the same type, is favourable, in spite of its complexity caused by the differences in the size of the grains. Welded joint design has to accommodate as much as possible to the expected service loading and an X-shaped welded joint, (Fig. 15), is recommended and accepted here for welding qualification and WPS. For this reason, the notch root in Charpy V and the crack tip in pre-cracked specimens were located as presented in Fig.15. The obtained results represent an average response of the loaded HAZ to the involved stress concentration and local constraint.

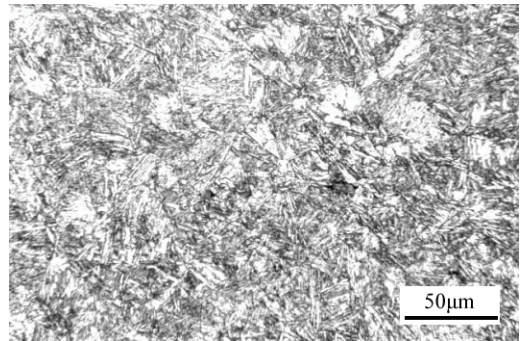
An evaluation of the mechanical properties is possible by HAZ simulation, which enables samples of sufficient size (11x11x55 mm) to be obtained. It was successfully applied to different steels of increased strength for pressurized equipment /21/. The performed analysis with normalized V micro alloyed NIOVAL 47 steel of TSt 460 class (nominal yield strength 460 MPa) revealed the presence of a very brittle CG region in the HAZ close to the fusion line, which resulted in a loss of structural integrity of spherical storage tanks by crack initiation and growth during service /22/. The differences in the microstructure in the HAZ were not so expressed, and only an average response regarding local properties, such as crack resistance and impact energy, of the HAZ as a constituent of welded joints was required.

Applying the approach, proposed by Kfoury /23/, which demonstrated that a fracture process could be discontinuous, to the complex HAZ microstructure (Fig. 15), it can be supposed that the final stretch zone, as well as the process zone is not uniform along the crack tip, being dependent on the local microstructure. It is to expect that these zones are

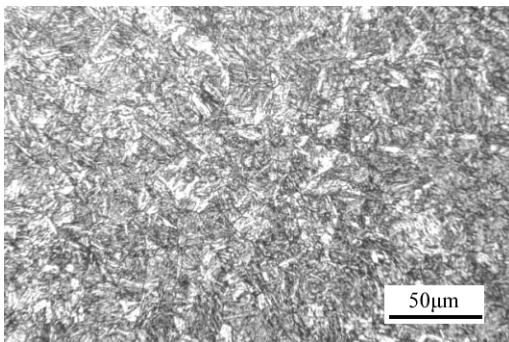
smaller for the CG regions and extended for the FG regions, and fracture will propagate in some locations, and in others will be arrested. The total energy released for fracture is related to the crack front microstructure, representing the overall response of the HAZ.



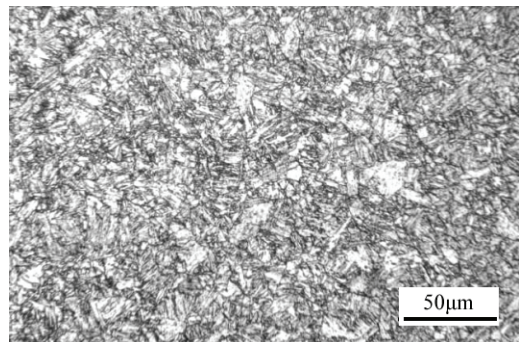
Location 1 – Coarse-grained - upper bainite



Location 2 - Lower bainite



Location 3 – Fine-grained - tempered bainite



Location 4 - Lower bainite

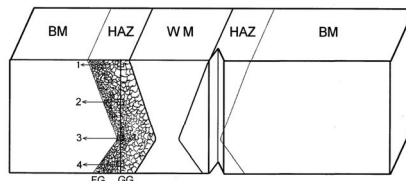


Figure 15: Microstructures along the crack tip in a fracture mechanics specimen produced from a welded joint sample

It is also to expect that the response in the case of V-notch and crack tip will not be the same since the involved stress concentration is not of the same level and different volumes of metal are involved in the fracture process. If brittle behaviour prevails and causes the crack occurrence, the structural integrity will be endangered, as experienced with spherical storage tanks [24,25]. Otherwise, the structure can be considered as service-safe.

6.3. Determination of crack sensitivity and fracture toughness

To understand and evaluate the degradation of the BM properties caused by welding, specimens with a V-notch, machined in the BM, WM and HAZ were pre-cracked by fatigue (Fig. 16) and tested.

The crack tip in the HAZ specimens were located as indicated in Fig. 15, hence, due to the X shape of the welded joint in, some cases, it could also encompass the BM or WM. From the experimental point of view, a K-shaped welded sample is better [26], since

crack tip can be located more accurately in the same microstructure, but an X-shaped sample was selected because it describes the crack response in a real structure better.

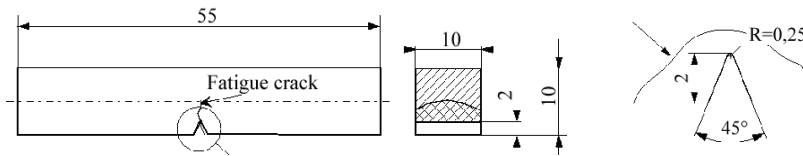


Figure 16: Pre-cracked three-point bend specimen SE (B) applied for impact and J integral testing

It should be mentioned that the specified requirements regarding strength, ductility and toughness were fulfilled. However, an additional consideration of the significantly reduced impact energy of the WM was necessary. It was argued that, if required, an electrode of better toughness, with a higher Ni content, producing a lower nil ductility transition temperature, could be applied. However, the HAZ behaviour still requires analysis, bearing in mind that the application of a better electrode would not affect the microstructure and properties of the HAZ. The microstructure of the HAZ region where a crack was initiated can be revealed on a broken specimen, after the test.

Fracture mechanics tests performed with the J -integral enabled the picture of the crack behaviour of the constituents of welded joints to be completed. Single Edge (SE), three-point bend (B) specimen, pre-cracked in the BM, WM and HAZ, (Fig. 16), were tested in a support span, $S = 40$ mm, following the single specimen compliance technique according to ASTM E1737. Typical $J - \Delta a$ curves, obtained for the BM, WM and HAZ in the tests, are presented in Fig. 17.

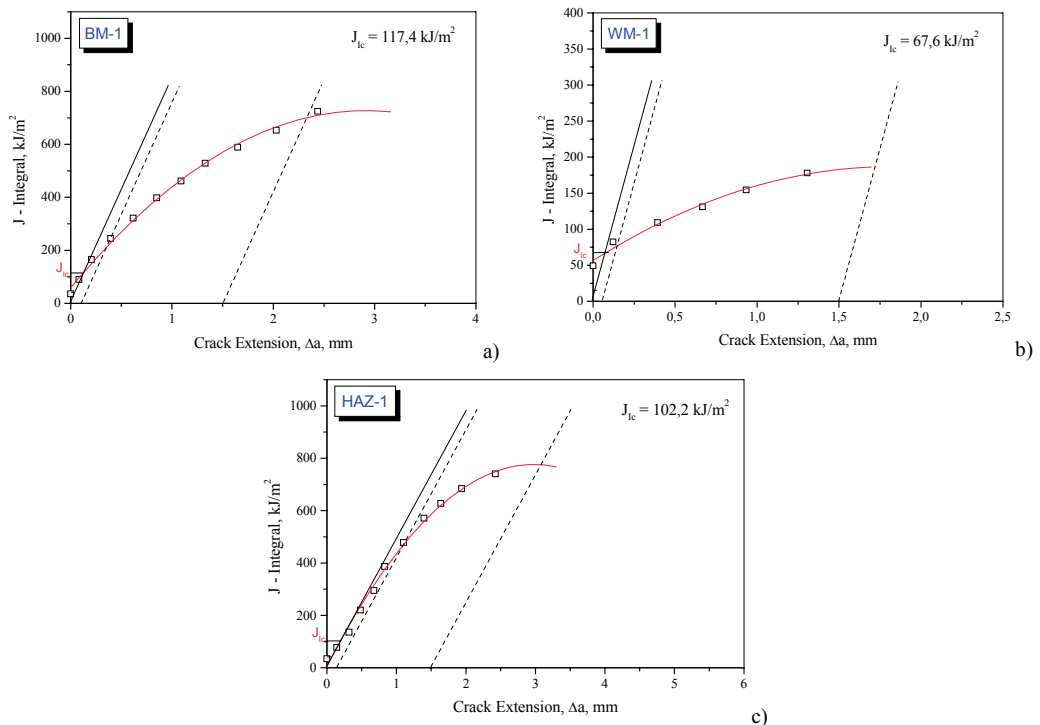


Figure 17: $J - \Delta a$ diagrams (crack resistance curves) for SE(B) specimens: a) BM-1, b) WM-1 and c) HAZ-1.

They allow the determination of J_{Ic} , a measure of fracture toughness, which is used for the calculation of the critical stress intensity factor, K_{Ic} :

$$K_{Ic} = \sqrt{\frac{J_{Ic} \cdot E}{1 - \nu^2}} \quad (3)$$

where E is the elasticity modulus, and ν the Poisson ratio. The obtained results for J_{Ic} and K_{Ic} are summarized in Table 12. The differences in the crack resistance of the BM, WM and HAZ are clear. Similar relations were obtained with dynamic J-R curves /27/.

Table 12: Results of testing the critical J-integral, J_{Ic} , and the critical stress intensity factor, K_{Ic} .

Specimen No.	Critical J-integral,	Critical stress intensity factor,
	J_{Ic} , kJ/m ²	K_{Ic} , MPa√m
BM-1	117,4	157,7
BM-2	124,6	162,5
WM-1	67,6	119,7
WM-2	63,7	116,2
HAZ-1	102,2	147,2
HAZ-2	97,5	143,7

7. DISCUSSION AND CONCLUSION

The presented analysis was performed in the scope of the qualification of a welding procedure for NN70 steel, with the aim of understanding the degradation of the properties caused by welding. The slight under matching in the strength of the WM (Tables 4; 7; and 9), did not significantly affect the tensile strength of the welded joint.

The effect the size of the specimens and how the obtained results can be transferred to the welded joints of a real structure require more attention. The relations of the values of the critical J-integral, J_{Ic} , and critical stress intensity factor, K_{Ic} , for the BM, WM and HAZ (Table 12.) just confirm that the fracture mechanic approach is significant tool in structural integrity assessment of welded joints /20/.

Finally, this lecture and conclusions clearly confirm that fracture mechanics testing of welds are significant for structural integrity of structures with welded joints.

REFERENCES

1. K. Easterling, *Introduction to the Physical Metallurgy of Welding*, Butterworth – Heinemann ltd., ISBN 0 7596 0399 1, second edition, Oxford, GB, 1992, pp42, 191 - 239
2. Barsom, J.M, Rolfe, S.T, *Fracture and Fatigue Control in Structures: Applications of Fracture Mechanics*, 3rd ed, ASTM, 1999 pp 237 – 250
3. George Dieter, *Mechanical Metallurgy*, SI Metric Edition, McGraw-Hill, 1988, pp 474 - 477
4. *The Welding Engineer's Current Knowledge*, DVS Duisburg, 1999
5. ASM Handbook Volume 11, *Failure Analysis and Prevention*, ASM International (2002)
6. Lassen T, Recho N, *Fatigue life analyses of welded structures*, ISTE Ltd, 2006, pp 20-22
7. Grabulov V., *Contribution of the evaluation of brittle fracture behaviour of high strength pressure vessels steels weldments*, International conference "Pressure Equipment Sector in Europe and Reflections in The Republic of Macedonia - Quality Assurance and Integrity Assessment", Skopje, 2005, Collection of invitation papers,p.119-127
8. D. Momčilović, I. Atanasovska, V. Grabulov, *Behavior of Metals under Impact Loading*, Proceedings of 1. International Congress of Serbian Society of Mechanics, Kopaonik, 10-13.04.2007., ISBN 978-86-909973-0-5. COBISS.SR-ID 138952460, Serbian Society of Mechanics, Belgrade, pp. 1053...1058

9. V. Grabulov, I Blačić, A. Radović, S.Sedmak, *Loading rate effect on HSLA steel welded joints fracture resistance*, Proceedings, ECF Conference, Alexandroupolis, Grece, 2006, pp.234-241
10. Pluvinage G, *Fracture and Fatigue Emanating from Stress Concentrators*, Springer Science + Business Media, Inc, (2004)
11. ASM Metals Handbook Volume 20, *Materials Selection and Design*, ASM International, USA, (1997)
12. ASM Handbook Volume 8, *Mechanical Testing and Evaluation*, ASM International, USA, (2000)
13. ASM Handbook Volume 19, *Fatigue and Fracture*, ASM International, USA, (1997)
14. Annual Book of ASTM Standards, ASTM Volume 03.01 Metals -- Mechanical Testing; Elevated and Low-Temperature Tests; Metallography, 2004
15. Grabulov, V., Burzić, Z., Momčilović, D., Significance of mechanical testing for structural integrity, The Challenge of Materials and Weldments - Structural Integrity and Life Assessments, International Fracture Summer School 9, (2009) pp121-151
16. M. Zrilić, V. Grabulov, Z. Burzić, M. Arsić, S. Sedmak (2007), *Static and Impact Crack Properties of high Strength Steel Welded Joint*, International Journal of Pressure Vessels and Piping, Volume 84, Issue 3, March 2007, Pages 139-150
17. Sedmak S., Grabulov V., Momčilović D., Chronology of lost structural integrity initiated from manufacturing defects in welded structures, Structural Integrity and Life, Vol 9, No 1, (2009) pp39 – 50
18. G. Adziev, A. Sedmak (2003), *Integrity assessment of spherical storage tank*, Structural Integrity and Life, Vol. 3, No 2. pp. 93-98.
19. V. Gliha, D. Rojko, T. Vuherer (2004), *The properties of the HAZ and weld metal in a multi-pass joint of microalloyed steel* (in Serbian), Zavar. & zavar. konstr., Vol. 49, No 3, pp. 103-107.
20. V. Grabulov, et al. (2005), Weldability Testing of Micro alloyed Steel and Integrity Assessment of Welded Joint, *Welding in the World*, Vol. 49, pp. 464-477.
21. K. Gerić (2005), *Cracks in welded joints*, A monograph, FTN Publishing, Novi Sad, (in Serbian)
22. K. Gerić, S. Sedmak (1998), *Crack behaviour analysis in the heat-affected-zone of micro alloyed steels*, 12th European Conference on Fracture, ECF 12, Fracture from defects, Sheffield, pp. 2138-2143.
23. A. Kfoury (2006), *Characteristic crack-tip distances in fracture criteria. Is crack propagation discontinuous?* 16th European Conference on Fracture, ECF 16, Failure analysis on nano and engineering materials and structures, Alexandroupolis, p. 1089, (disc with full paper available)
24. V. Grabulov, I. Blačić, H.J. Mac Gillivray, S. Sedmak (2001), *Dynamic J-R curve evaluation applying a pre-cracked Charpy specimen*, Charpy Centenary Conference, D. Francois and A. Pineau (Eds.), Vol. 1, pp. 313-320.
25. U. Eisele, J. Schiedermaier (2004), Application of ductile fracture assessment methods for the assessment of pressure vessels from high strength steels (HSS), International Journal of Pressure Vessels and Piping 81, 879–887.
26. M. Zrilić, V. Grabulov, Z. Burzić, M. Arsić, S. Sedmak (2007), Static and impact crack properties of a high strength steel welded joint, International Journal of Pressure Vessels and Piping, Volume 84, Issue 3, March 2007, Pages 139-150.
27. V. Grabulov, I. Blacić, H.J. Mac Gillivray, S. Sedmak (2001), *Dynamic J-R curve evaluation applying a pre-cracked Charpy specimen*, Charpy Centenary Conference, D. Francois and A. Pineau (Eds.), Vol. 1, pp. 313-320.

PRACTICAL ASPECTS OF PRESSURE VESSELS INTEGRITY

Miodrag Arsić

Institute for materials testing - IMS, Belgrade. Serbia

m.arsic@verat.net

1. INTRODUCTION

Designing and manufacturing of pressure equipment (PE), according to Directive 97/23/EC – PED /1/, is carried in correspondence with technical and legal regulations, implementing harmonized standards for equipment manufacturers is optional. Directive (PED 97/23/EC) refers only to designing, manufacturing and compatibility assessment of pressure equipment and assemblies designed for maximal pressure greater than 0.5 bar.

Pressure equipment must be designed, manufactured, tested, equipped and installed in such way that ensures safety during service, and it should be handled following manufacturer's instructions, in accordance with defined working conditions. Nondestructive testing of welded joints must be performed by qualified personnel. For the examination of the pressure equipment of higher categories, personnel must be authorized by the independent organization. Final inspection may be applied during manufacturing to any part of the equipment, internally and externally, if it is necessary from the safety aspect.

Structural integrity is new approach, which comprises state analysis and diagnosis of behaviour, life assessment and structure revitalization. Except common situation regarding life assessment after the imperfection has been detected by nondestructive testing, this approach includes stress state analysis. Precise and detailed distribution of strains and stresses, obtained in this way, enable to determine "weak" spots of the structure. This approach is important for highly loaded structures, such as pressure equipment.

This lecture gives an overview of new approach to standardization and technical harmonization for pressure equipment, which refers to structural integrity, i.e. on the fundamental safety requirements, calculations, design, strength testing and nondestructive testing (NDT). Methodological approach to modelling and strength calculation of pressure vessel structure by using the finite element method (FEM), calculation of fracture mechanics parameters for surface crack and state assessment by application of nondestructive testing methods, are also presented.

When pressure equipment is used in energy structures it may be classified in different directives. For example, compressor unit (Fig. 1), can be classified to PED 97/23/EC, but also to Simple Pressure Vessels Directive 87/404/EEC, Machinery Directive 98/37/EEC and Low Voltage Directive 2006/95/EC, because some parts of the unit (compressor, cooler, measuring devices, control devices, valves, electromotor and other components) they fall into corresponding directive. Directive 99/36/EC (TPED) is applied to Transportable Pressure Equipment. Manufacturer's and distributor's responsibility is that all parts of the unit comply with the requirements of relative directive /2/.

2. STRUCTURE AND CONTENT OF PRESSURE EQUIPMENT DIRECTIVE

The PED 97/23/EC was introduced into Serbian legislation by the Regulation of technical requirements for pressure equipment /3/. This regulation prescribes the requi-

rements to be fulfilled by design, manufacturing and compatibility assessment of pressure equipment and components for maximal allowed pressure above 0.5 bar.

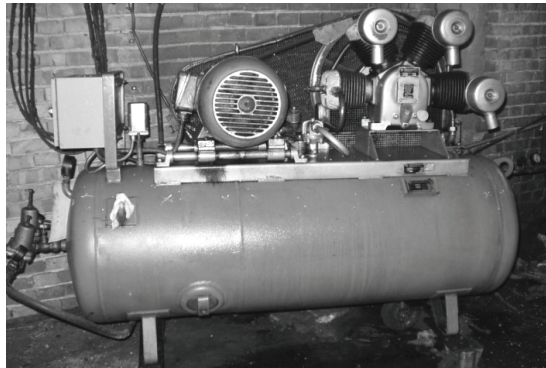


Figure 1: Compressor unit

In order to define the usage of the Directive to particular components of pressure equipment, manufacturer has to classify the equipment for evaluating the compatibility into one of the four categories (I – IV). The first category is concerned with the smallest, and the fourth category to the greatest danger of pressure /1, 3/.

The equipment with parameters beyond the first category is subject of the existing engineering practice and is not evaluated for compatibility.

To define category of pressure equipment, manufacturer should identify:

- category of equipment - vessel/steam generator/pipeline/safety equipment, Fig. 2;
- phase of fluid in the equipment - gas or liquid;
- group of fluid in the equipment - group 1 or group 2, Fig. 3.

Group 1 covers the fluids which are, according to EC Directive for classifying dangerous substances, marked as: explosive, extremely flammable, very flammable, flammable (with the maximum allowed temperature above the ignition point), very poisonous, poisonous, oxidising. Group 2 covers all other fluids, including water/steam.



Figure 2: Categorization of pressure equipment

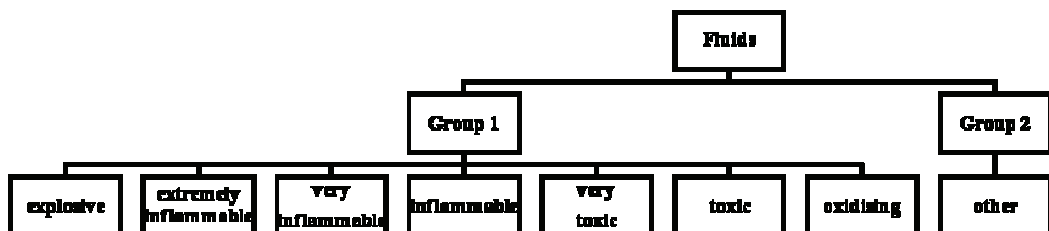


Figure 3: Subdivision of fluids

Directive demands that all the pressure equipment and assemblies be safe when putting them on the market and applied in service. The basic safety requirements and certificates are not requested for the group of the accepted engineering practice (EP).

Manufacturer is obliged to analyze dangerous situations which are relevant to the equipment. They have to design, produce and check the equipment in order to ensure its safety when exploiting it in certain conditions. Moreover, they have to show and apply the basic requirements by taking into consideration all possible circumstances.

Regarding the materials, manufacturer of pressure equipment has to fulfil basic safety requirements by using corresponding materials which are:

- in accordance with the European standards;
- covered by European approved materials;
- in accordance with the individual material specification.

Directive 97/23/EC relies on harmonized standards and supporting harmonized standards, as shown in Fig. 4 /4/.

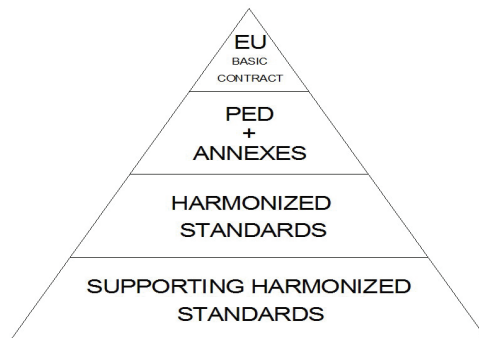


Figure 4: Relation between directive and standards /4/

Harmonized standards are standards about the same subject, approved by different institutions for standardization, which enable mutual substitution of products, processes and services or mutual acceptance of the tests results or giving information in accordance with standards JUS/ISO/IEC Instruction 2:2001.

Harmonized standards define technical requirements and define examination methods. Minimal safety conditions required by PED 97/23/EC are fulfilled by using of harmonized standards. Harmonized standards for equipment comprised by PED 97/23/EC are given according to category of the equipment, at this moment for:

- Unfired pressure vessels EN 13445 parts 1-6
- Shell boilers of high capacity EN 12953 parts 1-12
- Water-tube boilers and auxiliary installations EN 12952 parts 1-15
- Industrial piping, pipelines EN 13480 parts 1-6

Harmonized standards refer to area of supporting harmonized standards, which define requirements related to particular elements and details of methods. They are grouped to:

- Standards for nondestructive testing (NDT)
- Standards which define welding and allied procedures
- Standards for materials
- Standards for products (pipelines, forgings)
- Standards for threaded nozzles
- Standards for principle NDT method, connected with:
 - Radiographic testing - RT
 - Ultrasound testing - UT
 - Acoustic emission - AT
 - Eddy current testing - ET

Leak testing - LT

Magnetic particle testing - MT

Penetrating fluid test - PT

Visual testing - VT

Standards for NDT of welded joints include VT, ET, MT, PT, RT and UT.

3. DESIGN OF PRESSURE VESSELS

Pressure equipment must be designed for prescribed loading according to its purpose and other predictable conditions. In order to establish corresponding security limits for all possible errors general available calculation method and suitable safety coefficients should be used in design. Allowed stresses for pressure equipment have to be limited by operating conditions.

Given design requirements could be fulfilled by one of design methods or by their combination, corresponding to considered case, applying experimental method with empirical equations, analytical methods or using fracture mechanics approach.

3.1. Design using experimental method

Pressure equipment design evaluation, entirely or in parts, could be performed by using of adequate testing program on the representative equipment sample or equipment category. Program must define testing conditions and acceptance criteria for the design. Real values of basic dimensions and material properties must be established before testing. When risk of deformation or fatigue is present, adequate testing is defined based on equipment operating conditions, for example time of exposure to given temperature, number of cycles for determined load level. If necessary, additional testing concerning other factors such as corrosion or external damages could be required.

3.2. Design using analytical procedures

Design of pressure vessels by analytical methods implies for vessel and components shapes for which standard calculation methods and regulations are available.

Regulations in general comprise clauses which are obligatory for designer. Different influences which may appear in loadings and stresses of vessels are quoted, but designer is free to evaluate and consider all factors such as category, class, purpose, operating conditions. Procedure of analytical calculation of strength and stability of pressure vessels is defined by particular standards.

3.3. Design using of fracture mechanics

Design of pressure vessel by fracture mechanics approach includes designing for determined operating life, considering following operating life phases:

- Phase without fractures (initial fractures are not detected on the product)
- Fracture appearance in service (the appearance of the initial fracture)
- Fracture propagation (crack extension)
- Phase of operating life before fracture (fracture process phase)

The effect of individual phase till final fracture of pressure equipment is depended on service stress intensity, base material properties and structure design.

Design using the rate of crack growth is effective in the case of negligible effect of initial crack, high toughness of material, or high mean stress and low stress amplitude.

In pressure equipment the greatest significance have initial cracks (notches) induced by machining, heat treatment or welding, and in service the effect of variable stress amplitudes, affecting both crack initiation and crack extension.

Design of pressure equipment is greatly affected by success in analytical, numerical and experimental determining of linear-elastic or elastic-plastic fracture mechanics parameters. In the case of analytical and numerical determination parameter is crack driving force due to external load in experimental approach material crack resistance is obtained.

Cylinder or plate with surface crack is most important in practice, because imperfection in real structures can be presented in this form. There are analytical solutions for numerous cases depending to loading type (tension, flexion), imperfection position (surface or internal), imperfect shape (crack, semi-elliptical or semi-circular defect).

Analytical determining of stress intensity factor

In general case of cylinder with defect, solutions for stress intensity factor could be presented as /5/:

$$K_I = (\sigma_m + H\sigma_b) \sqrt{\frac{\pi a}{Q}} \cdot F\left(\frac{a}{t}, \frac{a}{c}\right) \quad (1)$$

where Q is imperfection shape factor, a - depth, $2c$ - length of defect, t - thickness, σ_m - tensile and σ_b - flexural component of stress, F and H are parameters which depend on ratios a/c and a/t . Dependence of factor Q on crack shape and applied stress level σ/σ_{ys} (σ is applied stress, σ_{ys} - yield stress) is shown in Fig. 5. This dependence implies Q tends to maximum unique value ($Q = 2.5$) for $a/2c \rightarrow 0.5$, changing the shape from elliptical to circular, saving in further growth that shape.

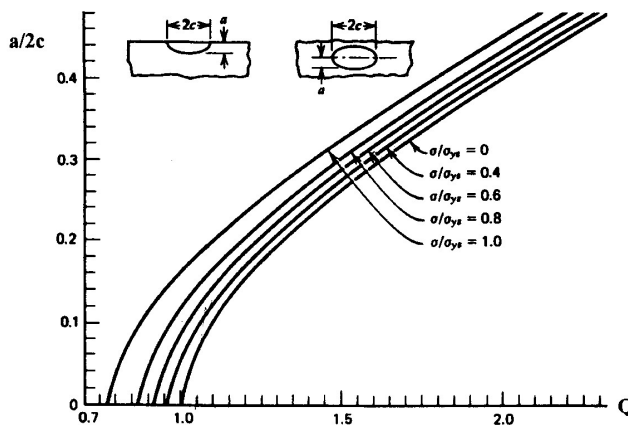


Figure 5: Imperfection factor Q dependence of on the crack shape and applied stress /5/

Analytical determining of CTOD and J integral

There are many analytical models for calculation of crack tip opening displacement, δ_t , (CTOD) and J integral /6/. They are based on empirical relations, like CTOD design curve and JWES empirical formulae, or on simplified mathematical models, ETM and EPRI as simple, and Read-King's and Ratwani-Erdogan-Irwin (REI) models as complex, but very efficient. They will be shortly presented in next text.

Empirical expressions which connect CTOD (δ_t) with a remote stress (as a loading measure) in elastic and plastic region are based on CTOD curve7/.

The simplicity of this approach is clear when, in addition to remote stress, σ , the residual stress, σ_{zn} is taken into account through the equivalent remote strain ε :

$$\varepsilon = (\sigma + \sigma_{zn}) / E \quad (2)$$

where E modulus of elasticity. Stress concentration factor, k_I , can also be included

$$\varepsilon = (k_I - 1)\sigma / E \quad (3)$$

Japanese Welding Society developed standard WES 2805 to assess the integrity of welded structures (JWES 2805 Procedure /8/), using elastic-plastic fracture mechanics and CTOD (δ) concept for estimating the significance of defects in welded joints.

Imperfection, detected by nondestructive testing, can be simplified by an ideal form, as semi-elliptic surface or elliptic embedded crack, and then use equivalent length of corresponding through crack based of the linear elastic fracture mechanics (LEFM). Significance of imperfection is evaluated by the condition:

$$\text{crack driving force} > \text{material crack resistance} \quad (4).$$

for possible crack initiation,

$$\text{crack driving force} < \text{material crack resistance} \quad (4a)$$

when crack effect might be neglected.

Crack driving force is determined by fracture mechanics formulae, and material crack resistance by CTOD standard testing /6/. Remote strain, ε , is determined by summing up the primary strain ε_1 (due to applied load), secondary strain ε_2 (due to residual stress and geometry irregularities) and secondary strain ε_3 (due to stress concentration).

Engineering treatment model (ETM)

This is EFAM ETM 97 procedure /9/, using expressions for determining CTOD based on elastic-plastic fracture mechanics (EPFM). This procedure was developed in GKSS, Geesthacht, Germany in 1997 and represents a part of methodology on determining the significance of imperfections, such as cracks, in welded joints.

In elastic range, when the load, F , is lower than net section yielding load, F_Y , $F < F_Y$, crack tip opening, defined as δ_5 , is presented as:

$$\delta_5 = \frac{\beta_1 K}{E} + \frac{K_{ef}^2}{mE\delta_Y^2} \quad (5)$$

where $\beta = 2.41 \sqrt{\text{mm}}$ and $m = 1$ for plane stress condition, or, $\beta = 2.09 \sqrt{\text{mm}}$ and $m = 2$ for plane strain condition, and K_{ef} is effective stress intensity factor corresponding to effective crack length, a_{ef} , defined as:

$$a_{ef} = a + \frac{1}{2} \frac{K_{ef}^2}{\pi\delta_Y^2} \quad (6)$$

Alternatively, J integral can be applied, introduced by the relation:

$$J = \frac{K_{ef}^2}{E} \quad (7)$$

where δ_5 can be defined through J -integral combining Eq. (7) and Eq. (5)

An important feature of ETM procedure is possible application to heterogeneous materials, that is, to welded joints with mismatch effect greater than 10%.

Engineering procedure of Electric Power Research Institute (EPRI)

In this procedure the analytical solutions for J integral, crack mouth opening and load-line displacements are included, for elastic-plastic material behaviour of cylinders with longitudinal and circumferential cracks, combining elastic and fully plastic regions /10/.

Ratwani-Erdogan-Irwin (REI) model

It deals with elastic-plastic analysis of a thin cylindrical shell with longitudinal crack, neglecting transversal shear, and to allow derived integral equations /11/ simplify as
– the shape of the crack is rectangular (crack depth c is a constant);
– material ahead the crack tip is taken as perfectly plastic (no strain hardening), that means it obeys Dugdale’s model.

Model REI can be applied to any crack type (through, part-through or surface longitudinal crack) in cylindrical pressure vessel. Its main advantage is a simple use because all the necessary data for calculation are in normalized form. Here, it is applied for determining the crack driving force on welded joint of cylindrical vessels.

King’s model

It is based on the idea that a 3D problem can be solved by combing 2D problems of plane stress and plane strain state. Namely, if through-thickness crack is in question, the problem would be in 2D plane stress, and if the surface crack length is equal to the plate width, the problem would be of plane strain type. Since surface crack is between these to extreme cases, the solution can be found combining 2D problems. Plane stress problem must consider local membrane force N and moment M , because of existence of ligament length $t - c$, where t is plate thickness, c is crack depth /12/.

In fact, King’s model is a simplified line - springs model.

4. INTEGRITY ASSESSMENT OF PRESSURE VESSELS IN SERVICE

Figure 6 shows the scheme of activities in controlling and inspecting pressure vessels. Integrity assessment of pressure vessels in service primarily depends on capability of detecting and determining type, position and magnitude of imperfection in welded joints.

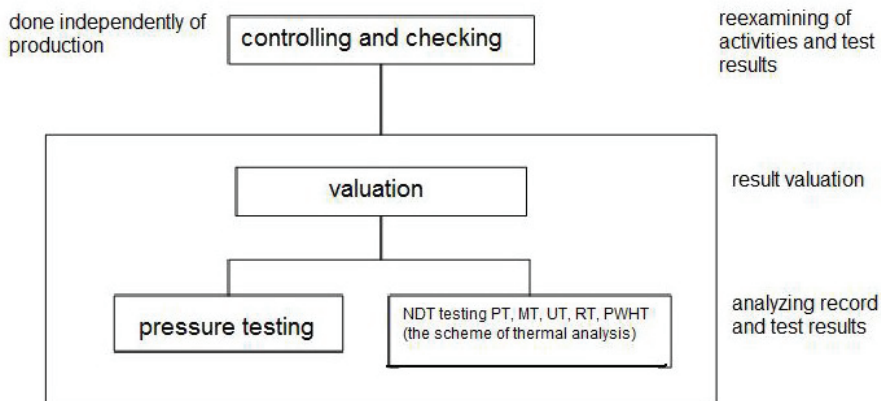


Figure 6: Examination activities and check-up scheme

Assessment of pressure equipment state in service applying NDT method can be classified into eight different activities:

1. Identification of labels
2. Measurement of dimensions and their evaluation

3. Determining material chemical composition
4. Determining material mechanical and physical characteristics
5. Micro-structural characterization of material
6. Detection of imperfections and assessment of their significance
7. Leakage detection and evaluation of its significance
8. Determining stress and dynamic response

Selection of appropriate or combination of NDT methods demands full understanding of problem, capacity and sensitivity of equipment, including skill and experience of personnel. The relation between imperfection size frequency and capacity of NDT methods is given in Fig. 7. Dye penetrant, magnetic particles and eddy current are mostly used to detect surface cracks, radiographic and ultrasound methods for embedded defects.

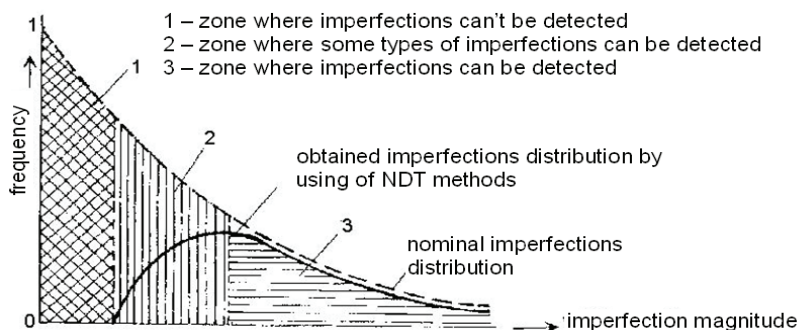


Figure 7: Distribution of imperfection magnitude frequency related to capability of NDT methods

When imperfection is found, it is to decide whether it has to be removed or not, since in case of welded joints imperfection presence does not mean explicitly loss of fitness for purpose and use of welded structure, here pressure vessel. It is to analyze the imperfection type, its size and frequency relative to vessel class and load condition. The decision should be made considering expected load, operating environment, the danger of fracture and possible consequences. The approach which determines these factors is known as “fitness for service” and has an advantage over experience indicators because:

- repairs can be expensive, especially if the assembling and service are in delay;
- the time for repair can be lower than the original production, since the repairs are often performed by local removing of imperfections and re-welding; anyhow, repaired seam can contain new defects, its toughness can be lower and residual stress can be involved, because stress release heat treatment is usually inappropriate on a local level and expensive for applying on a complex equipment.

Fitness-for-service in today’s practice presents a multi-process:

- Imperfections have to be characterized in respect to size and position by NDT methods and making decisions based on convenient assumptions.
- Determining the local stress distribution.
- Consideration of fatigue crack growth rate and the possibility of non-growing crack.
- Determining imperfection critical size before fracture. If imperfection critical size will be reached before next inspection, repair is necessary.

4.1. Pressure vessel modelling and calculation using Finite Element Method

Cylindrical horizontal welded storage tank (Fig. 8) from the manufacturing program of “GOŠA FOM” company falls in group of transportable vessels. It is designated for the

storage and transportation of liquid carbon dioxide. The tank is installed on prepared supports of road vehicle. Once installed, it is intended to be used during its operating life.

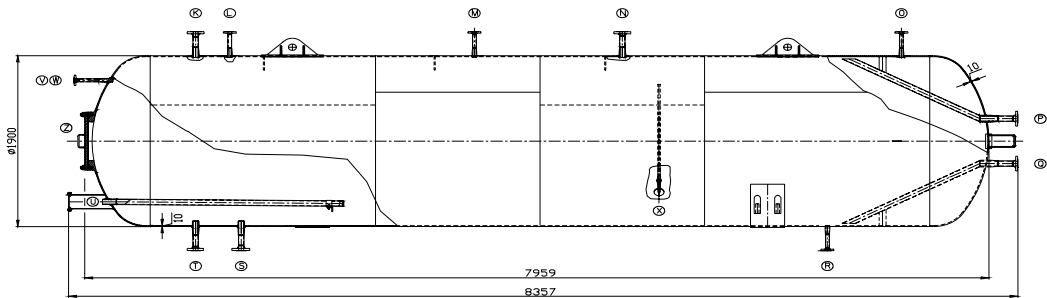


Figure 8: Transportable storage tank for liquid carbon dioxide

Technical characteristics of the tank are:

- Maximum allowed operating pressure 2.0 MPa
- Test proof pressure 2.6 MPa
- Range of service temperature $\pm 30^{\circ}\text{C}$ ($\pm 3^{\circ}$)
- Working medium non-toxic, non-flammable, non-explosive
- Capacity 21 m³
- Empty vessel mass 4400 kg
- Maximum mass of loaded vessel 24840 kg

According to general and location factors, the tank belongs to pressure vessels class II.

Loadings and stresses for calculation

Loadings of movable pressure vessel, given in corresponding standards, are defined for design, calculation and construction for liquid carbon dioxide. Depending on the type, purpose and class of the vessel, following loading has to be taken into consideration:

1. uniform loadings caused by internal pressure,
2. dynamic and impact loadings including rapid pressure changes,
3. loadings induced by static effect of working fluid,
4. loadings by mass of vessel and the mass of working and test fluid,
5. loadings induced by pipelines, accessories and insulation,
6. loadings induced by wind,
7. loadings induced by earthquake,
8. thermal stresses,
9. local stresses on the places of nozzles or supports,
10. loading induced by the elevation of empty tank.

During its working life, this tank is exposed to all cited loadings, but dominant loading are under 1, 3, 4, 9 and 10. The rest, because of their small impact on strength, toughness and stability of the tank, are not taken for calculation.

As uniform loadings by internal pressure is taken only test proof pressure of 2.6 MPa.

Loadings by dead weight of vessel and the mass of working and test fluid of 24840 kg (4400+20440), in addition to effect of internal pressure (2.6 MPa) are used in item 4.

Local stress distribution on the locations of nozzles or supports, item 9, is partly taken according specific modelling concept of the tank, with possible upgrading of existing nozzle for more accurate calculation, overcoming stress concentration effect.

Dead weight of vessel (4400 kg) is used at elevation of empty tank by shrouds under the angle of 45°, item 10.

Allowable deformations and stresses

The highest allowable deformation is defined by the request that applied loadings must not produce permanent deformation, according to selected material of the vessel, fine grained structural steel TStE355, Table 1.

Table 1: Mechanical characteristics of TStE355 steel

Young modulus	Yield strength	Tensile strength	Elongation	Impact toughness, J, at	
E , MPa	R_{eH} , MPa	R_m , MPa	$L_o = 5d$, %	-20°C	-50°C
200000	414 - 436	574 - 582	28-30	176-200	50-53

For adopted safety factor $S = 1.1$ allowable stress σ_{al} and elongation l_{al} are:

$$\sigma_{al} = R_{eH} / S = 414 / 1.1 = 376 \text{ MPa} \quad l_{al} = \sigma_{al} \times L / E = 376 \times 835.7 / 200000 = 15.7 \text{ mm}$$

Model of tank structure

Strength calculation is made by finite element method (FEM) in KOMIPS program.

In static calculation tank is considered as a space structure of connected plates elements (quadratic and triangular) with variable cross section. The whole bearing structure is reduced to middle plane of shell and front and rear lids. All the connections are reduced to one of considered planes. Accepted model, Fig. 9, consisted of 3242 nodes and 3308 plate elements /13/. This calculation is used to derive requested conclusions.

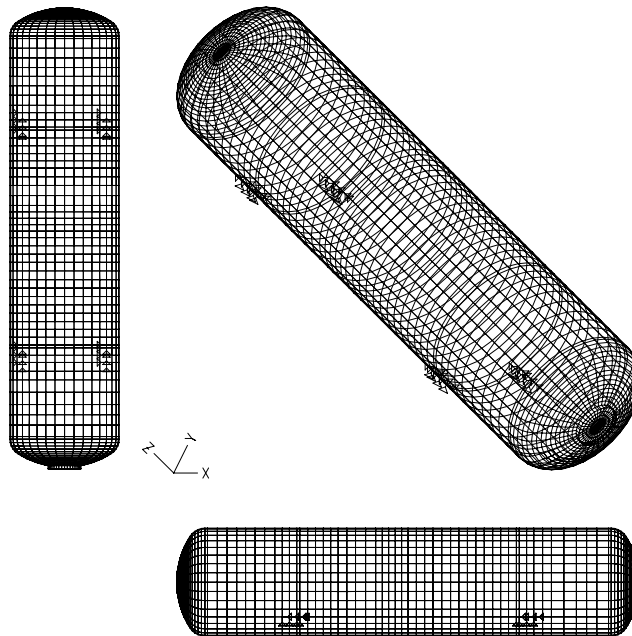


Figure 9: Accepted finite elements model of tank used for calculation

For plate elements, maximum equivalent stresses and strains in considered section have been calculated using suitable software modules. Displacements of the nodes for typical and critical loadings by mass of vessel and the mass of working and test fluid are shown in Fig. 10, with stresses calculated from strains.

For the loading by mass of vessel and the mass of working and test fluid, the greatest displacements took place in front and back lids in the region of nozzles U, X, Z and P, Q, and the values are within the allowed limits. Stresses in nozzles U, X locations are very close to the material allowed stress, Fig. 11.

Surface elements exposed to compression or shear should satisfy stability conditions. Stability of shell element is checked on the mantle surface between the lugs for dimensions: wall thickness $h = 10$ mm, section length $a = 4300$ mm, section width $b = 335$ mm.

Critical normal, σ_{cr} , and shear stresses, τ_{cr} , are obtained using the expressions:

$$\sigma_{kr} = K_{\sigma} \cdot E \cdot \left(\frac{s}{b}\right)^2 \quad \tau_{kr} = K_{\tau} \cdot E \cdot \left(\frac{s}{b}\right)^2 \quad (8)$$

For the ratio $b/a = 335/4300 = 0.078$ contour condition coefficients for fixed edges of mantle elements are $K_{\sigma} = 3.8$ and $K_{\tau} = 8$, so critical stresses are:

$$\sigma_{kr} = 3.8 \cdot 210000 \cdot \left(\frac{1.0}{33.5}\right)^2 = 711.1 \cdot MPa \quad \tau_{kr} = 8 \cdot 210000 \cdot \left(\frac{1.0}{33.5}\right)^2 = 1497.0 \cdot MPa$$

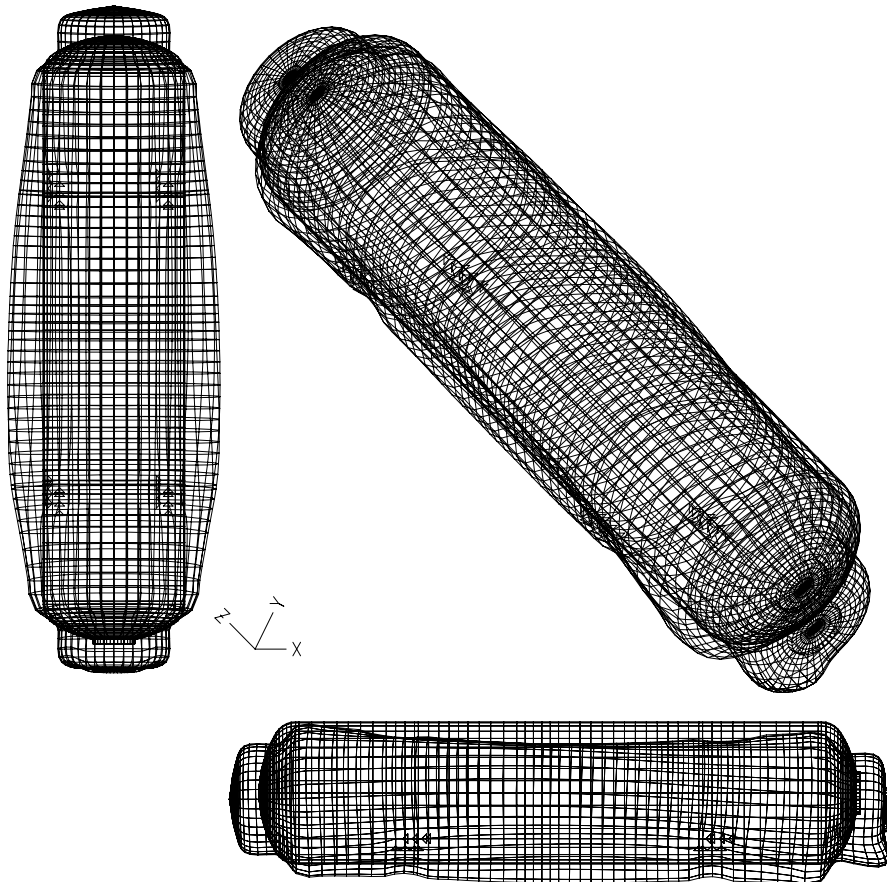


Figure 10: Displacements of the nodes or the one of the loading cases

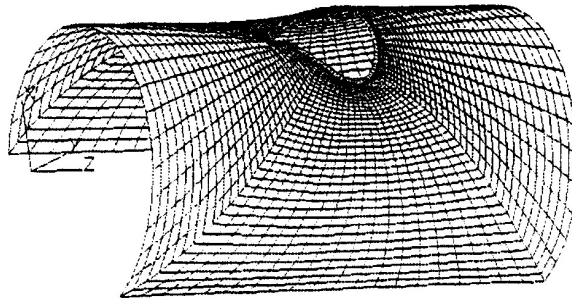


Figure 11: View of deformed nozzle region

Structural stability is assured, since stress and strain values are in allowable limits.

This calculation is an example of general approach in new regulations to technical harmonization of pressure equipment (PED 97/23/EC), which are related to structural integrity, i.e. to basic strength safety, calculation and design conditions.

4.2. Analysis of axial crack in welded thin cylindrical shells by REI model

Elastic-plastic analysis of thin cylindrical shells with an axial crack can be analysed by REI model, with basic assumptions helped to formulate and solve equations:

- crack shape is rectangular (crack depth is constant) (Fig. 12. a);
- there is no transversal shear (Kirchhoff's assumptions for thin shells hold good);
- material is ideally plastic (there is no strain hardening).

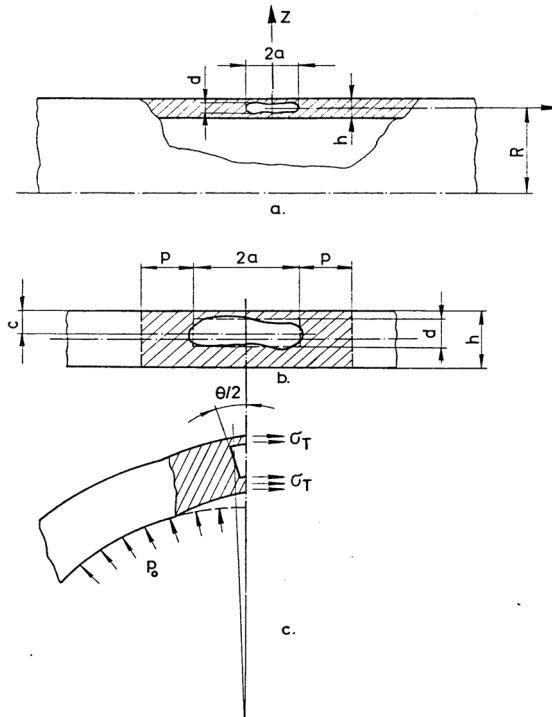


Figure 12: Internal crack in shell with fully plastic ligament

In addition, it is adopted that net cross section, for $-a < x < a$, is fully plastic and it transmits only membrane stresses close to yield stress value (Fig. 12. c). It is also adopted

that plastic deformations have been extended beyond crack on the distance p (Fig. 12. b) and that plastic region can be presented as plastic strip, Barenblat-Dagdale's model.

With these assumptions Dagdale's model of plastic strip can be used. The solution of this problem defined is given as a function of crack tip opening displacement, δ_t ,

$$\delta_t(X, Y) = \delta(X, 0) + Z\theta(X) \quad (9)$$

The main advantage of REI model is his simple usage since necessary data are given in non-dimensional form for characteristic size of non-dimensional shell parameter λ :

$$\lambda = \sqrt[4]{12 \cdot (1 - \nu^2)} \cdot \frac{2a}{\sqrt{R \cdot h}} \quad (10)$$

where R is shell radius, and ν Poason's coefficient. REI model can be applied to any axial crack in cylindrical pressure vessel.

Equation for J integral with certain simplifications is:

$$\frac{J \cdot E}{4 \cdot a \cdot R_{eh}^2} = J^* = m \left[\frac{\delta_0}{d_1} + \frac{\theta_2}{d_2} \cdot \left(0,5 - \frac{d}{h} \right) \right] \quad (11)$$

For calculating shell parameter, λ , in this case the value a_p should be applied as crack length in Eq. (10).

The parameters of plastic zone $\alpha = a/a_p = \lambda/\lambda_p$, necessary for calculating, is taken according to diagram (Fig. 13) where a correlation between zone α and load normalised by applied pressure p is used

$$N_0 / (hR_{eh}) = (pR) / (hR_{eh}) \quad (12)$$

to obtain the values

$$\sqrt{J^*} = \sqrt{\frac{J \cdot E}{4aR_{eh}^2}} \quad (13)$$

for different parameter sizes λ_p .

The values of J^* integral are calculate for different ratios of crack depth d and vessel wall thickness h , d/h (Fig. 12.b), and in Fig. 13 presented for typical parameter values λ_p (0; 1; 2; 3) /14, 15, 16/. Obtained diagrams are used for predicting fractures of cracked cylindrical pressure vessel.

The effect of welding residual stresses and imperfections on the behaviour of crack in pressure vessel is experimentally investigated /17, 18/, testing four plate samples, welded of microalloyed T.St E460 steel. Surface cracks tips were located in the HAZ of samples, as presented in Fig.14. In order to analysed the effect of residual stresses, two plates were post-weld heat treated (P1 and P2), and two were not (P3 and P4). The imperfections in geometry were found in all four plates in such a way that plates P1 and P3 were distorted up (the crack tip is directed to convex side), and plates P2 and P4 distorted down (the crack tip to the concave side), for an angle of 1° in both cases, Fig.15. It was concluded that the most favourable situation regarding fracture mechanics parameter is for plate P2 (post-weld heat treated, crack tip on concave side), whereas plate P3 presented the worst case. Experimental results of J integral direct measurements from Ref. /18/ as relationship J integral vs. remote stress σ are compared here with the results obtained applying REI model, as presented in Fig.16.

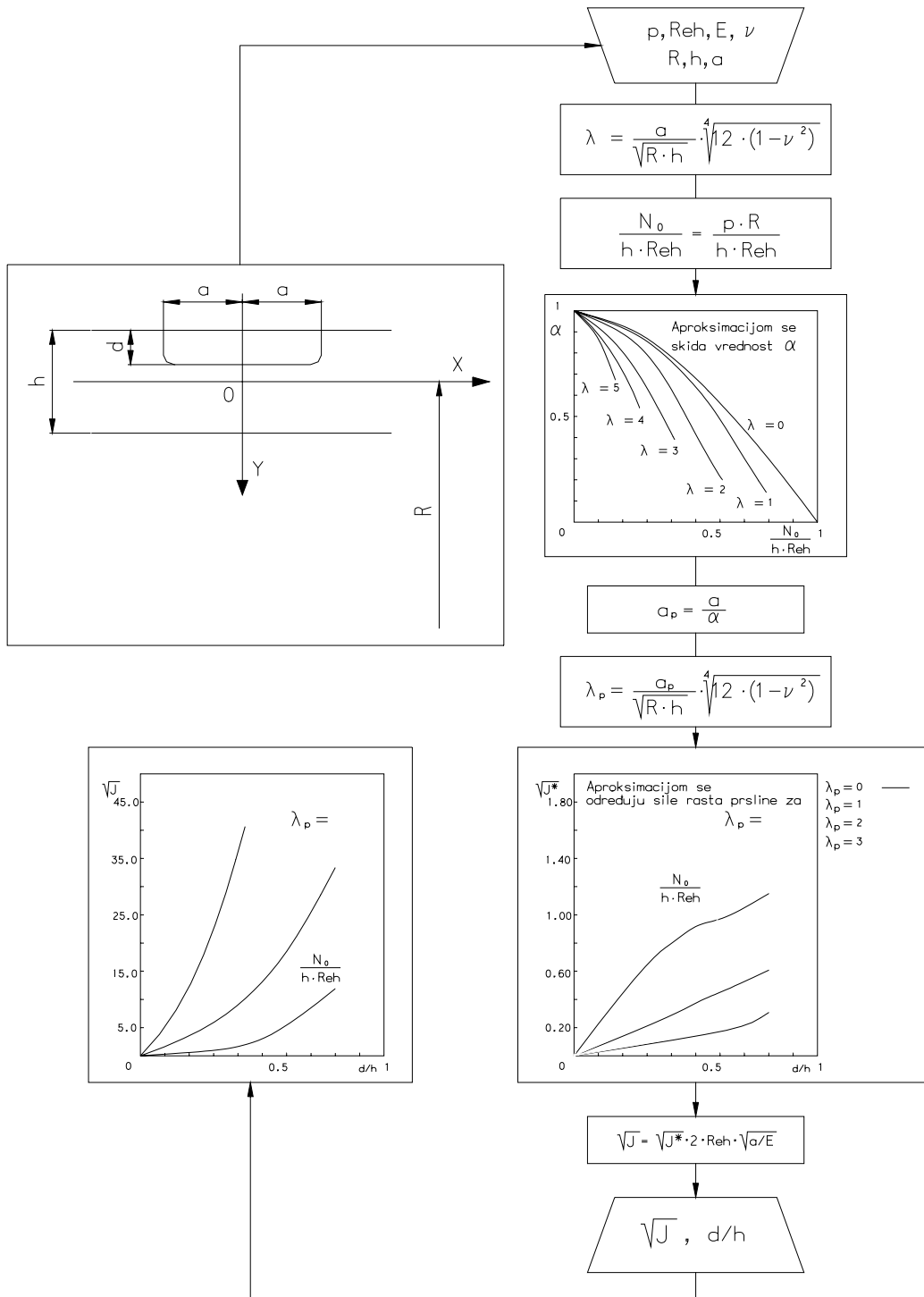


Figure 13: Algorithm for creating REI0 and modified REI models /14/

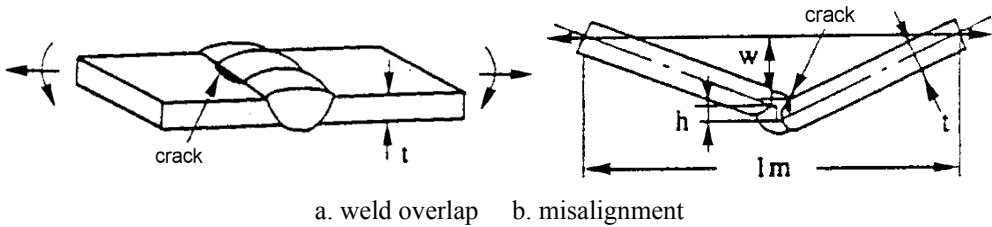


Figure 14: Crack occurrence due to stress concentration from defects in butt welds

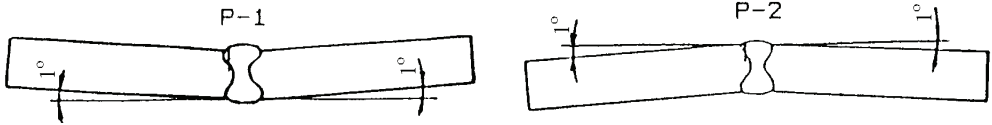


Figure 15: Effect of angular distortion

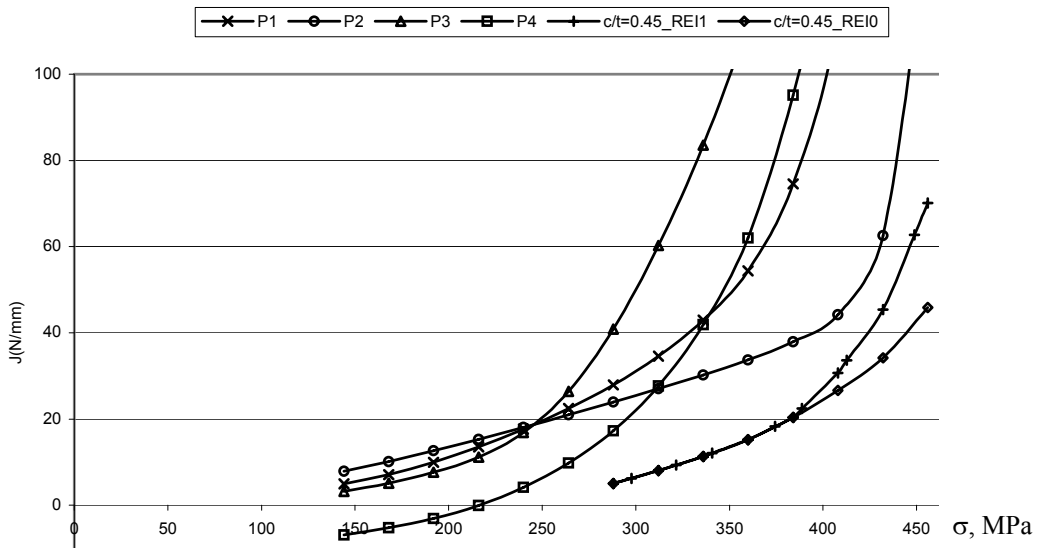


Figure 16: Comparison of experimental results and results obtained by REI method.

Results obtained by REI method are given in two variants, the first one by an original procedure REI0, and the other by modified variant REI1, where the yield condition is replaced by a condition used in the King model /19/. Since it is not possible to consider residual stresses and geometry imperfections in the REI method, results presented in Fig.16 clearly show that the best agreement is obtained for plate P2, and that the modified REI1 model variant exhibited better agreement than the original procedure REI0.

ACKNOWLEDGEMENT

This lecture contains a part of results obtained in the project 14014 “Research and development methods for estimate integrity and reliability of welded pipelines in oil industry” supported by Ministry of Science and Technological Development of Serbia.

REFERENCES

1. The Pressure Equipment Directive (97/23/EC), on Internet

2. Guide to the implementation of directives based on the New Approach and the Global Approach, European Commission Directorate – General for Enterprise and Industry, Danish Technological Institute – DTI, (2000).
3. Pravilnik o tehničkim zahtevima za opremu pod pritiskom, Službeni glasnik –Official journal L 181, (1997) (in Serbian). (Regulation of technical requirements for pressure equipment)
4. Arsić, M., Kurai, J., Aleksić, V., “*European pressure equipment directive and non-destructive examinations in structure integrity assessment*“, International Conference „Pressure equipment sector in Europe and the reflections in The Republic of Macedonia“- Quality assurance and integrity assessment, Skopje, (2005), pp. 35-42.
5. Hertzberg, R.W., „*Deformation and Fracture Mechanics of Engineering Materials*“, John Wiley & Sons, New York, (1996).
6. Sedmak, A., „*Primena mehanike loma na integritet konstrukcija*“, Univerzitet u Beogradu, Mašinski fakultet, Beograd, (2003). (in Serbian) (The application of fracture mechanics to structural integrity)
7. Burdekin, F.M., Dawes, M.G., „*Practical Use of Linear Elastic and Yielding Fracture Mechanics with Particular Reference in Pressure Vessels*“, Proc. of the Institute of Mechanical Engineering Conference, London, (1971), pp 28-37.
8. Japan Welding Engineering Society Standard "Method of Assessment for Flaws in Fusion Welded Joints with respect to Brittle Fracture and Fatigue Crack Growth"; WES 2805, (1997).
9. Schwalbe, K.H. et al, EFAM ETM 97 „Method for assessing the significance of crack-like defects in engineering structures“, GKSS report, Geesthacht, Germany, (1997).
10. Kumar, V., German, M.D., Shih, C.F., „An engineering approach for elastic-plastic fracture mechanics analysis“, Report EPRI, NP-1931, RP 1237-1, General Electric, Schenectady, (1981).
11. Erdogan, P., Ratvani, M.M., Irwin, G., „Fracture Propagation in a Cylindrical Shell Containing an Initial Flaw“, Lehigh University, Research Report, (1974).
12. King, R.B., "Elastic-plastic analysis of surface flaw Using a Simplified Line-spring Model", Eng. Fracture Mech. 18, (1983), pp. 217-231.
13. Aleksić V., Arsić M., Sedmak S.: “*A methodology approach in modelling and calculating the strength of a mobile pressure vessel by finite element method*”, VII Int. science meeting on achievements in the power and machine industry DEMI 2005, Banja Luka, (2005), pp. 29- 34.
14. Petrovski, B., „*Određivanje preostale nosivosti suda pod pritiskom sa površinskom prslinom*“, doktorska disertacija, Tehnološko-metalurški fakultet, Beograd, (1985). (in Serbian) (Residual strength assessment of a pressure vessel with surface crack)
15. D.T.Rid, „*Analiza mehanike loma i krive dopuštenih veličina greški za površinske prsline u cevovodima*“, III letnja škola mehanike loma, Arandelovac, (1984). (in Serbian) (Fracture mechanics analysis and curves of allowable defect sizes for surface cracks in pipelines)
16. Aleksić, V., Arsić, M., „*Procena čvrstoće zavarenih spojeva na tankim cilindričnim ljuskama oslabljenim aksijalnom prslinom, modifikovanom REI metodom*“, Procesna tehnika, 1/ 2002, pp. 123 – 126. (in Serbian) (Assessment of welded joint strength on thin cylindrical shells weakened by axial crack, applying REI model)
17. Adžiev, T., “Contributions in the research of residual stress effects on the fracture resistance of welded structure with a crack” (in Macedonian), Doctoral thesis, Faculty of Mechanical Engineering, University of Skopje, (1988).
18. Adžiev, T., “*Zaostali naponi od zavarivanja – uticaj na ponašanje posude pod pritiskom sa prslinom*”, IFMASS 6, GOŠA-TMF, (1994), p. 127. (in Serbian) (Residual stresses from welding – effect on the behaviour of a pressure vessel with crack)
19. Sedmak, A., Burzić, Z., Aleksić, V.: “*Inženjerske metode za proračun parametara mehanike loma zavarenij spojeva*”, IFMASS 7, TMF-JSZ-GOŠA, 2000, p. 305. (in Serbian). (Engineering methods for calculating fracture mechanics parameters of welded joints)

MICROSTRUCTURAL ANALYSIS OF CRACK TIP REGION

Katarina Gerić

Faculty of Technical Sciences, Novi Sad, Serbia

gerick@uns.ns.ac.yu

1. INTRODUCTION

The fracture develops from the crack tip. The investigation of crack propagation, the analysis of the stress fields ahead the crack tip, and the microstructural analysis, including fracture surface are inevitable parts in understand fracture process.

2. BRITTLE FRACTURE

The fracture is usually initiating from crack already present in material and developed by crack growth. Local stress increase, caused by flaws in the material, significantly contributes to fracture development. When the development of deformation is restrained the fracture of metals is of brittle type in the Griffith sense. Anyhow, metal does not behave in an ideally brittle manner and the plastically deformed zone on the crack tip occurs. When its size is neglectible compared to component dimension and crack size, resulting fracture can be considered as a brittle one. It is to underline that once started brittle fracture will developed by cleavage mechanism, with no additional energy consumed.

Cleavage involves breaking bonds: the local stress must be sufficient to overcome the cohesive strength of the material, which is higher than the remote stress required to cause fracture. In order to initiate cleavage, there must be a local discontinuity ahead of the macroscopic crack, sufficient to exceed the bond strength. Sufficiently sharp micro crack can produce local stress concentration. Cottrell suggested that micro cracks by dislocation interaction form at intersecting slip planes. However, more common mechanism for micro crack formation in steel is connected with inclusions and second-phase particles.

Figure 1 shows scanning electron microscope (SEM) fractograph of a cleavage fracture in high-strength low-alloy (HSLA) steel [1].

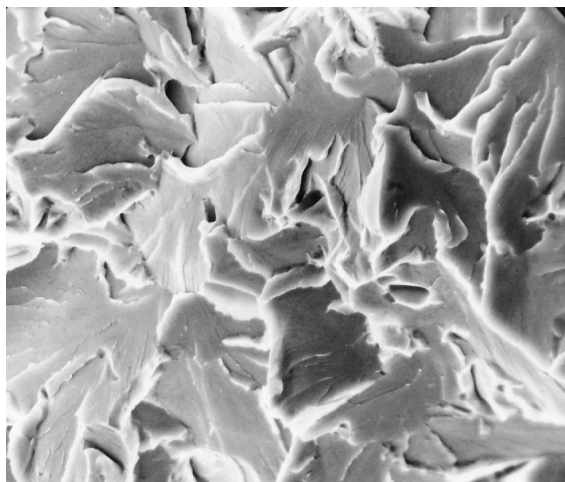


Figure 1: SEM fractograph of cleavage in steel (2000x)

The multi faced surface is a typical cleavage, each facet indicates single grain. The “river patterns” on each facet are typical of cleavage fracture, indicating that multiple lines converge to a single one, like river confluents.

Ritchie, Knott and Rice /2/ introduced a simple model to relate fracture stress to fracture toughness, explaining why brittle steel does not fracture upon a minimal load is applied. They postulated that cleavage fracture occurs when the stress ahead of the crack exceeds σ_f over the characteristic distance, Fig. 2, which equals to two grain diameters.

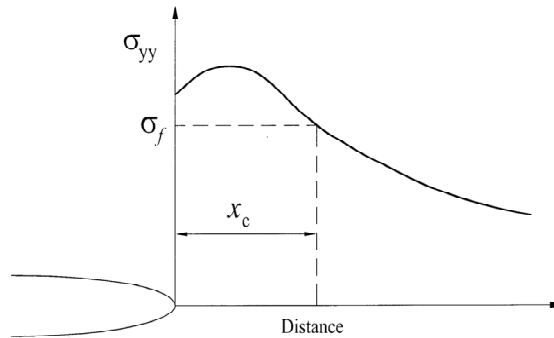


Figure 2: Ritchie-Knott-Rice model for cleavage fracture: failure is assumed to occur when the fracture stress is exceeded over a characteristic distance x_c /2/

3. PLASTIC ZONE

Linear elastic stress analysis of sharp cracks predicts infinite stresses at the crack tip. In real metals, however, stresses at the crack tip are of finite value due to the crack tip blunting of finite radius size took place, followed by plastic (yielding) zone. The plastic zone size estimation for plane stress conditions is

$$r_y = \frac{1}{2\pi} \frac{(K_I)^2}{(\sigma_{YS})^2} \quad (1)$$

where K_I is stress intensity factor and σ_{YS} is yield stress.

If strain hardening effect is neglected, the stress distribution for $r = r_y$ can be presented by horizontal line at $\sigma_{yy} = \sigma_{YS}$, Fig. 3. The stress singularity is truncated by yielding at the crack tip. When the yielding occurs, the plastic zone radius r_p became twice as large as r_y .

In plane strain yielding is suppressed by the triaxial stress state, and the Irwin plastic zone is smaller by a factor 3.

The effective crack length is defined as the sum of the actual crack size a and plastic zone correction r_y

$$a_{eff} = a + r_y \quad (2)$$

The nonlinear material deformation is limited to a small region around the crack tip in linear elastic fracture mechanics (LEFM). In elastic-plastic fracture mechanics (EPFM) material exhibits time independent, nonlinear behaviour (i.e. plastic deformation).

Wells noticed that crack faces moved apart prior to fracture /3/. Plastic deformation had blunted an initially sharp crack, Fig. 4. The blunting level is strongly dependent on the toughness of the material. This observation led Wells to suggest that the crack tip ope-

ning displacement (CTOD) can serve as a measure of fracture toughness, expressed in the form of finite displacement δ at the crack tip.

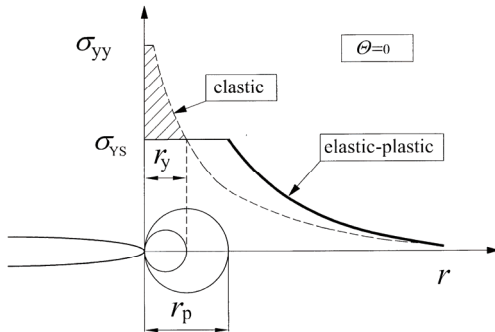


Figure 3. First order and second order estimates of plastic zone size (r_y and r_{p_2} , respectively) /4/

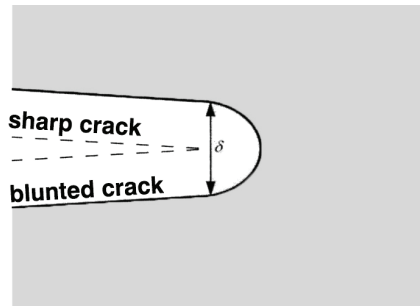


Figure 4. Initially sharp crack blunts by plastic deformation, resulting in a finite displacement (δ) at the crack tip

4. STRETCH ZONE

In linear-elastic fracture-toughness testing crack initiation is easy to detect because of its brittle nature. In contrast, a crack in a ductile material will first blunt, extend virtually, and then grow continuously in a stable manner, Fig. 5, exhibiting different stages of crack extension in a ductile material. The effect of described behaviour on crack resistance curve (J-R curve) for ductile material is presented schematically in Fig. 6 by the change of J integral with crack extension. The R curve is nearly vertical in the first phase of deformation and there is a small amount of apparent crack growth due to blunting. As J increases, the material at the crack tip fails locally allowing the crack to advance further. Because the R curve is rising, the initial crack growth is usually stable. Some experience is necessary to determine the crack-initiation toughness in elastic plastic materials, as there is no straightforward procedure for evaluating a single correct ductile fracture toughness value.

Before stable tearing, virtual crack extension in ductile materials leaves a signature of the crack-initiation and blunting phenomena called the stretch zone. This featureless region lies between the fatigue precrack front and the onset of ductile tearing, Fig 7 /5/. The formation, shape, and size of the stretch zone are characteristics of the material /6, 7/. In highly ductile materials, the stretch zone would normally have two components: a horizontal component called the stretch-zone width (SZW) and a vertical relief of the crack front called the stretch-zone depth (SZD), as depicted in Fig. 8. Both the SZW and SZD are closely related to the fracture toughness of a ductile material, and many attempts have been made to measure the characteristic stretch-zone parameters on the fracture surface of specimens and use them as an aid in determining the critical fracture toughness. The measured SZW or SZD values can be used as convenient indicators for identifying the crack initiation point on the experimentally generated crack-growth-resistance (R) curve. There is no consensus among researchers whether ductile fracture toughness should be estimated using SZW or SZD. Some of them use the SZW, while others argue that SZD measurement is more appropriate than SZW for obtaining fracture toughness of ductile materials /8/.

An advantage of SZW is that it can be measured directly on the specimen fractured surface using a scanning electron microscope (SEM), whereas SZD measurements are

more difficult to perform, mainly due to the problems associated with identifying the various stages of the fracture process.

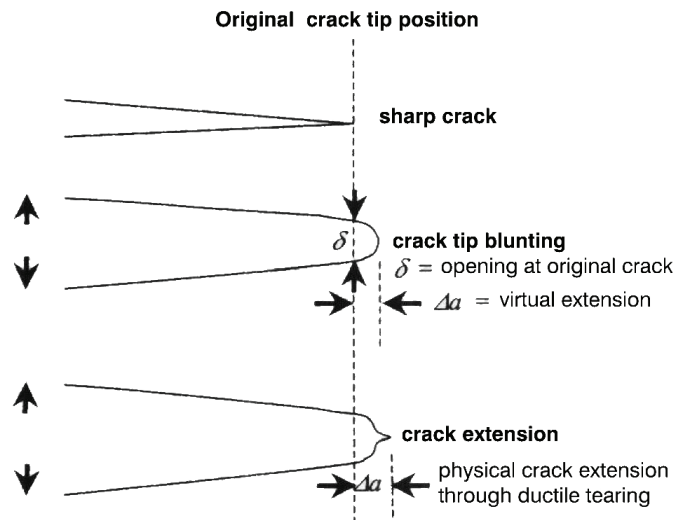


Figure 5: Schematic of crack extension process in a ductile material

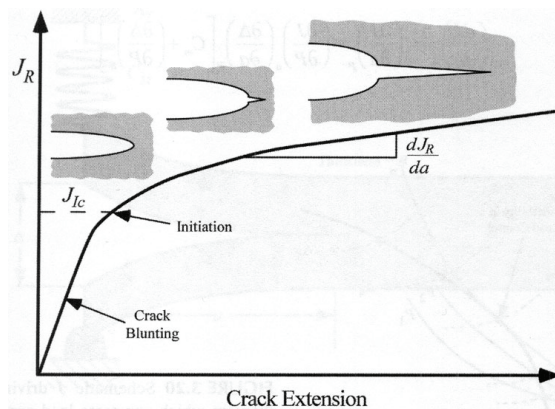


Figure 6: Schematic J integral vs. crack extension for ductile material - resistance curve

Thus, if a SZD measurement is going to be used, it is necessary to specify clearly the methodology. Apart from accuracy in determining the fracture toughness of ductile material, it is sometimes necessary to examine the nature of the variation when factors affecting the toughness, such as the yield strength and strain-hardening exponent, can vary. Literature which considers the convenience of the SZW or SZD in predicting the nature of the variation in fracture toughness with material properties is limited.

5. METODOLOGY FOR STRETCH GEOMETRY MEASUREMENT

Stretch-zone depth (SZD) measurements are not straightforward, but rather the values have to be calculated from indirect measurements [9]. A blunted crack configuration is shown in Fig. 9.a. In the figure, the SZW is the projected length (w) of the stretch zone when viewed at 90° to the crack plane. In Fig. 9.b the specimen is tilted through an angle α and stretch zone projection on the plane normal to the viewing direction is observed.

The geometric inter-relation between w and t is shown in Fig. 9.c. With reference to these figures, it can be written that

$$OC = OB \cos \alpha = t \cos \alpha \quad \text{since } OB = t, \text{ and}$$

$$DB = AC = OC - OA = t \cos \alpha - w \quad \text{since } OA = w$$

Similarly,

$$DA = BC = OB \sin \alpha = t \sin \alpha, \text{ and}$$

$$FD = \frac{DB}{\operatorname{tg} \alpha} = \frac{t \cos \alpha - w}{\operatorname{tg} \alpha}$$

Here, F denotes the point at which the stretch zone ends and ductile tearing starts, as shown in Figure 9.b. Hence, FA is the SZD of height h , and therefore

$$\text{SZD} = h = FA = FD + DA$$

$$\text{SZD} = h = \frac{t \cos \alpha + t \sin \alpha \operatorname{tg} \alpha - w}{\operatorname{tg} \alpha}$$

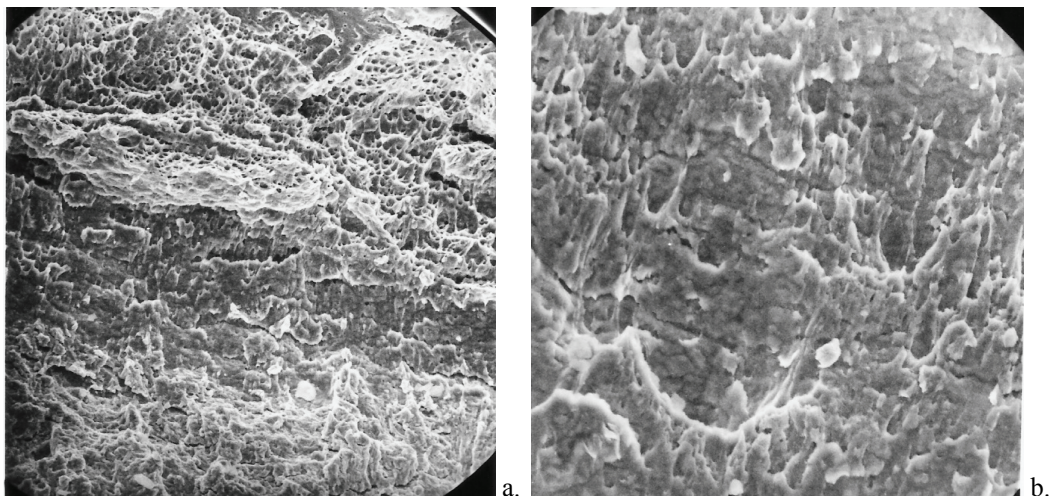


Figure 7. Scanning electron microscope (SEM) pictures of (a) fracture surface and (b) stretch zone

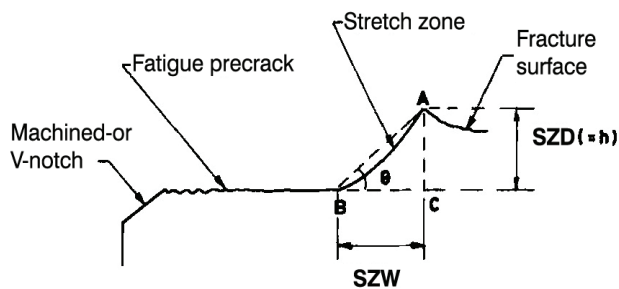


Figure 8: Schematic of the crack profile depicting the stretch zone components
SZW - stretch zone width, SZD - stretch zone depth

If the specimen is tilted through an angle of $\alpha = 45^\circ$, then

$$\text{SZD} = h = 2t - w \quad (3)$$

Using the identities specified above, the SZD of the stretch zone produced during fracture can be calculated starting from values of w and t .

From the aforementioned scheme, it can be seen that if an error in accuracy is made when identifying the true plane of fracture, the error in the calculation of h is given by the product of the angular error between the true and actual reference frames and the stretch-zone width (SZW). Similarly, the error made in the determination of w is equal to the product of angular error and h .

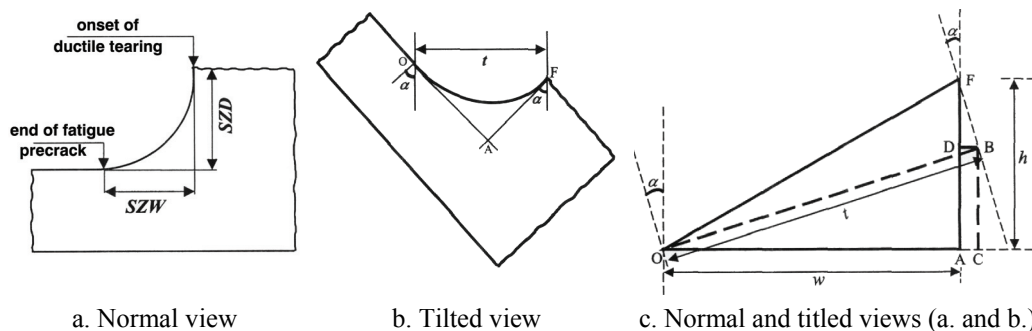


Figure 9. Schematic view showing the geometric inter-relationship between the untilted and tilted configurations of the stretch zone dimensions

6.1. Practical measurements of stretch zone geometry

The fractured surfaces were first extracted from the tested specimens and placed on the stage of the scanning electron microscope (SEM), aligning the plane of fracture to be normal to the electron beam, Fig. 10. This is ensured by measuring the size of a linear feature of known length, like the notch.

At tilt position fixed to 0° , a representative stretch feature was recorded with a sufficiently high magnification to be able to identify local features within the stretch zone, while making sure that the whole width of the stretch zone was contained in the field of view. In order to demarcate the stretch zone limits easily, efforts were made to ensure that a good contrast was achieved.

Secondly, the SEM stage was tilted so that the fracture surface was rotated through 45° about an axis through the crack front, and the features recorded at the same magnification. While tilting, it was important to ensure that there was no lateral shift of the specimen, in order to view the same area of fracture surface previously examined.

Whilst it is true that the fracture features of the steels provide excellent contrast to confidently demarcate the stretch zone, establishing the actual end of the stretch zone was nonetheless difficult in the 0-deg tilt condition, due to the near vertical relief in this region. Correspondence with features in the 45° tilted view, in which the end of the stretch zone was more easily discernible, was therefore sought for identification of stretch-zone limits. Such features are marked as A, B, and C in the fractographs, Fig. 11, obtained in testing HSLA steel of 800 MPa nominal strength. As shown in Fig. 9, w and t were measured from tracings of the start and end of the stretch zones in 0° and 45° tilt images on transparency grids. The correspondence between w and t was ensured through identifiable features in both tilt conditions. Both halves of the specimens were measured at least 30 times along the thickness direction. From each measurement of w and corresponding t , the h value of the SZD was calculated using Eq. (3).

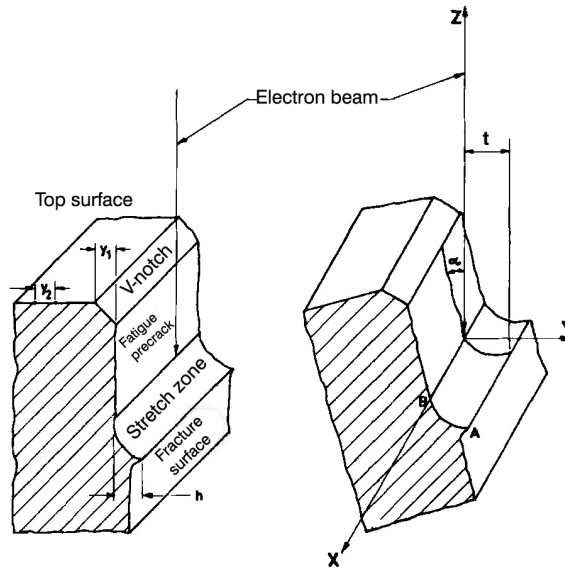


Figure 10: Fracture surface of the specimen in the tilt stage on scanning electron microscope

Visual examination of the highly magnified specimen, Fig. 11, gives the impression that the stretch zone was uniform in the specimen midthickness. However, after measuring the stretch-zone dimensions w and t , as discussed, it was obvious that the magnitude of these values, as well as the magnitude of h , vary across the crack front. A typical variation of w , t , and h across the specimen thickness is shown in Fig. 12. Although the stretch zone appears uniform macroscopically, the variation in local microstructure and alteration in local deformation characteristics as the crack tip blunts leads to differences in w and t values and hence, in the magnitude of h .

The experimental measurements [10] were made on high strength Mo-Nb microalloyed steel NIOMOL, with 0.06% C (Fig. 13). The investigation was carried out on a welded joint, and the results presented here are the measurements made on 10 mm wide samples from the heat-affected-zone (HAZ). Seven fractographs were made by SEM, which were then used to measure the width and the depth of the stretch zone [11]. Five measurements were made per each fractographs, using Texture Analysis System, i.e. TAS plus. Typical variation in the measured w , t and h in performed experiments is presented in Fig. 14.

6.2. Fracture toughness obtained measuring stretch zone width and depth

The method for obtaining the J integral by measuring the stretch-zone width (SZW) is based on the fact that SZW is equivalent to the critical virtual crack extension (Δa_{cr}) prior to the onset of ductile tearing, a vertical line drawn at $\Delta a = \text{SZW}$. The J corresponding to the intersection of this vertical line with the J-resistance curve is taken as J_{SZW} , Fig. 15.

For determination of J from the SZD, two methods were used.

In the first method, the CTOD calculated as per standard, was plotted against Δa , and a line at $\delta = 2\text{SZD}$ is drawn to intersect the $\delta - \Delta a$ curve. The Δa value corresponding to the intersection was labelled Δa_{cr} . The intersection of Δa_{cr} on the corresponding J- Δa curve is labelled J_{SZD} , Fig. 16.a. In the second method, the J - δ data are plotted, and a vertical at $\delta = 2\text{SZD}$ is drawn. Intersection on J - δ curve is labelled J_{SZD} , Fig. 16.b.

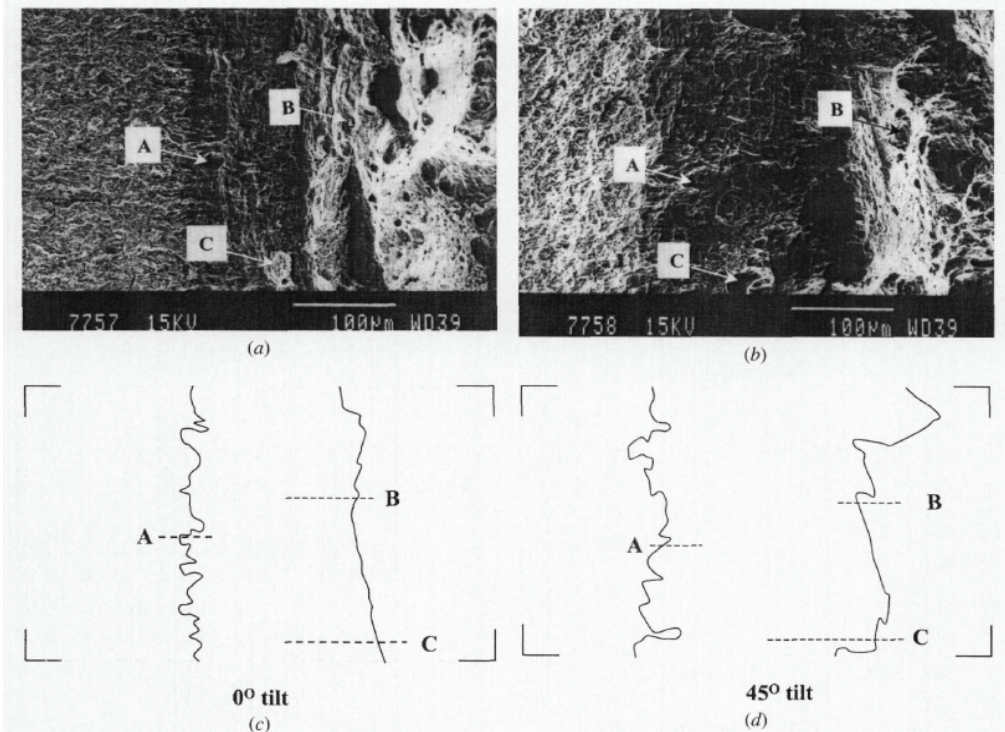


Figure 11: Methodology used for the stretch zone geometry measurement /9/

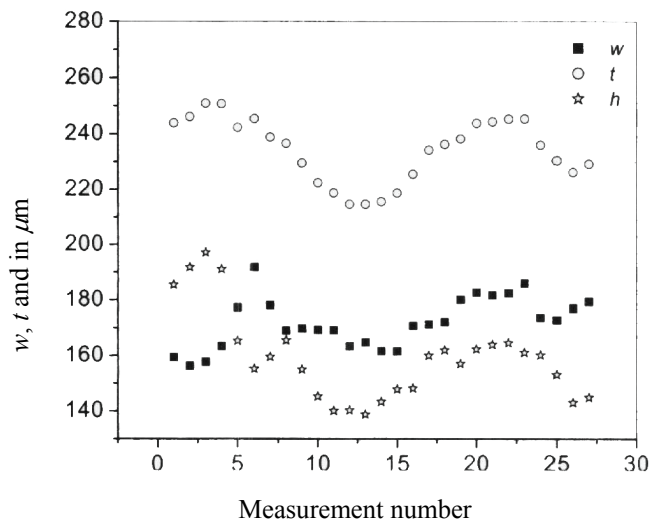


Figure 12: Typical variation in the measured w , t and h /9/

7. FATIGUE CRACK

Under certain conditions, fatigue crack can also be characterised by the stress intensity factor. Consider a growing crack in presence of a constant amplitude cyclic stress intensity, Fig. 17. At the tip of a crack subjected to variable load, a variable plastic zone is formed, which is the largest when the force is the maximal, i.e. when the load is highest, and smaller for lower loads.

A cyclic plastic zone forms at the crack tip and the growing crack leaves behind the plastic wake. If the plastic zone is sufficiently small, that it is embedded within an elastic singularity region, the conditions at the crack tip are uniquely defined by current K value, and the crack growth rate is characterized by K_{max} and K_{min} (Fig. 17). Fatigue cracks propagation is often followed by striations on a fracture surface. Striations are small registered perpendicular to the direction of crack propagation.

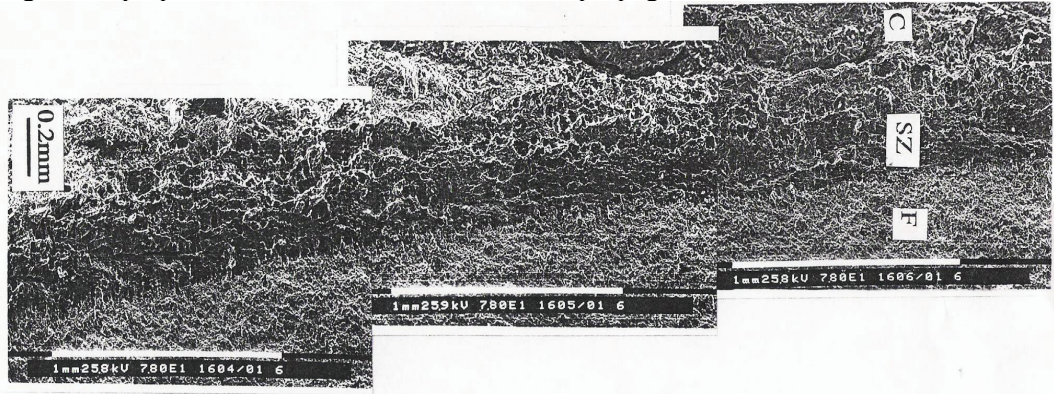


Figure: 13. Fractograph of NIOMOL (F- fatigue, SZ- stretch zone, C- cleavage) /12/

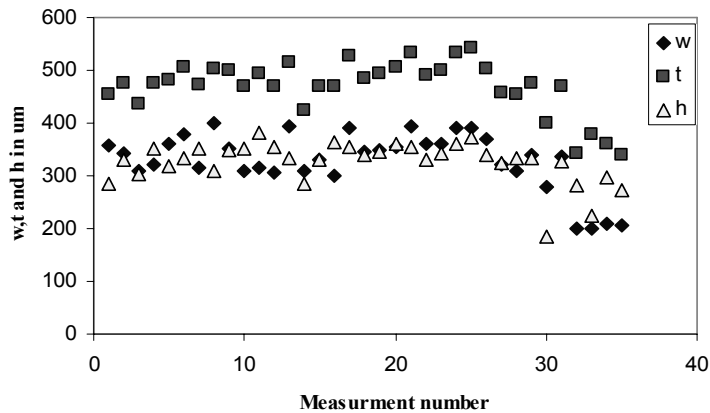


Figure 14: Typical variation for NIOMOL in the measured w , t and h /12/

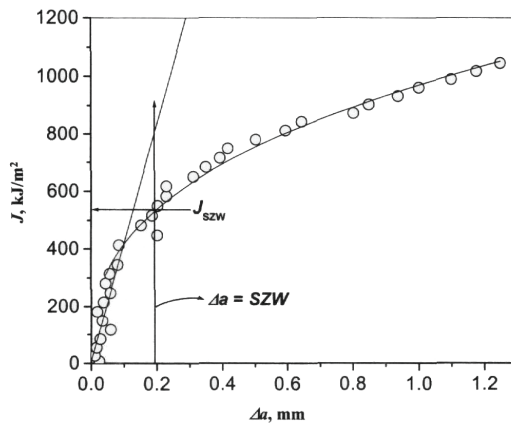


Figure 15: A schematic showing the method for determination of J_{SZW} using SZW

One mechanism proposed for striation formation during fatigue crack growth is illustrated in Fig. 18. The crack tip blunts as the load increases, and an increment of crack growth occurs as a result of the formation of a stretch zone. Local slip is concentrated at 45° from the crack plane. When the load decreases, the direction of slip is reverse, and the crack tip folds inward. The process is repeated in subsequent cycles, and each cycle produced a striation on the upper and lower crack faces. Width of striation depends on fatigue crack growth rate in 7000 aluminium alloys with different content of (Fe+Si), Fig. 19. For the same ΔK , a greater striation spacing confirm the faster crack grow in the alloy with maximum impurities content, Fig. 19.a, than in its high-purity versions, Fig. 19.b /9/.

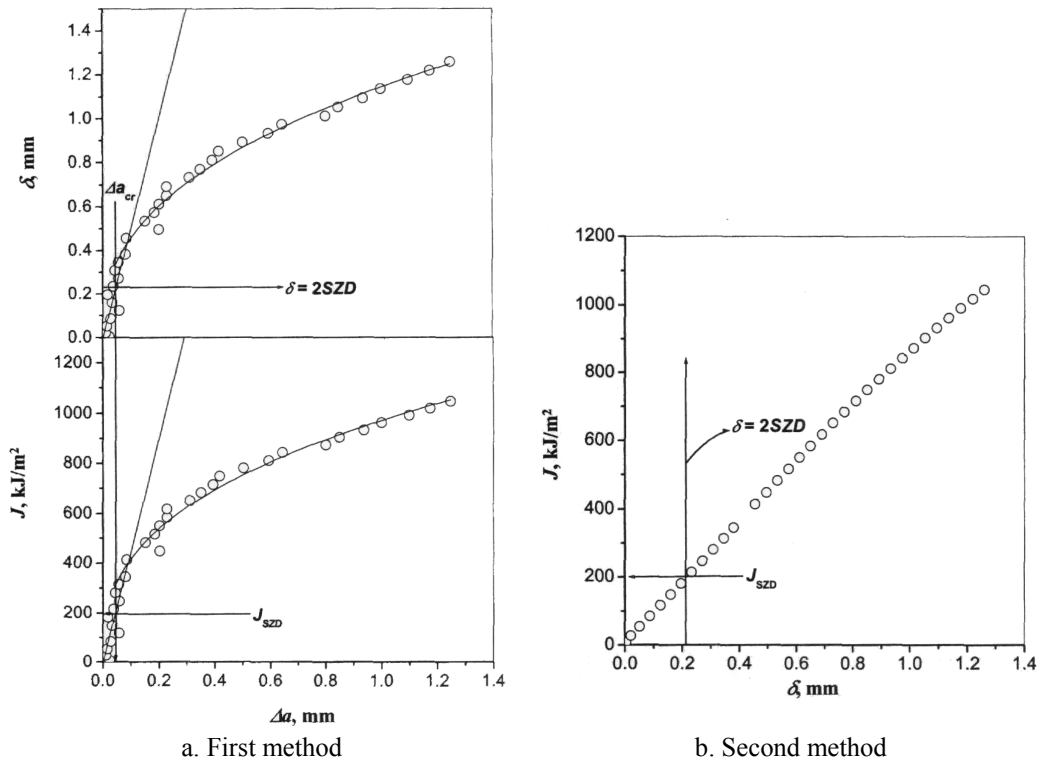


Figure 16. Determination of J_{SZD} from SZD /9/

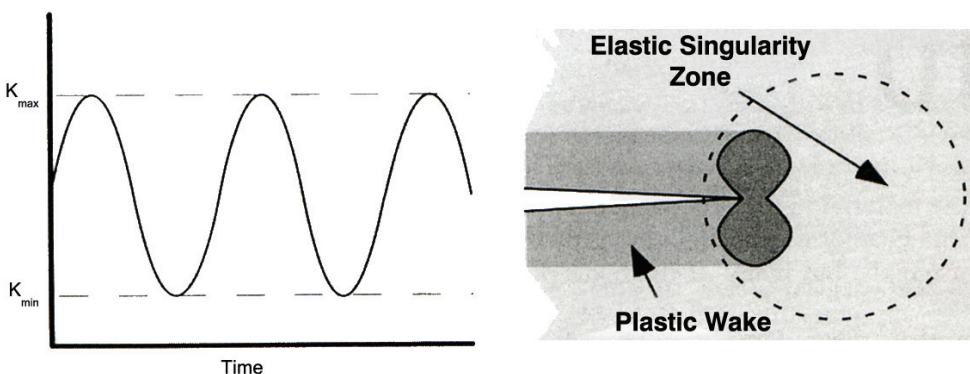


Figure 17: Constant amplitude fatigue growth under small-scale yielding conditions

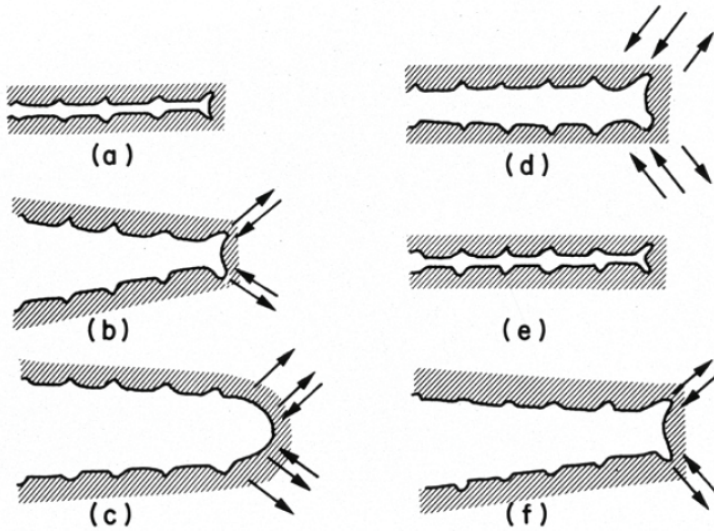
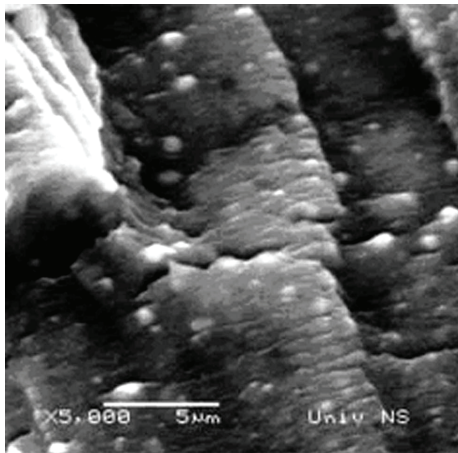
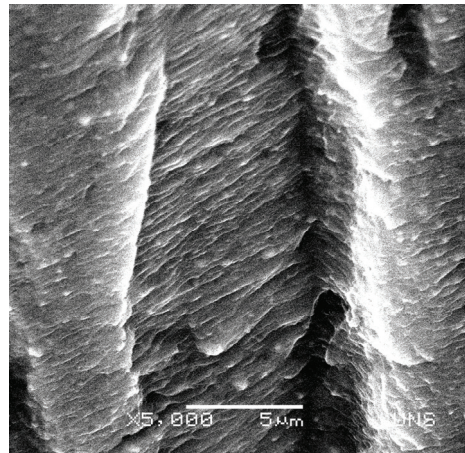


Figure 18: The crack blunting mechanism for striation formation during fatigue crack growth /13/



a.



b.

Figure 19: Fractographs fatigue fracture surface of 7000 aluminium alloys on SEM /14/

9. CONCLUDING REMARKS

The type of fracture caused by load application depends on the stress state on the crack tip. When the plastic zone on the crack tip is small, as considered in LEFM, a cleavage fracture occurs, whereas a ductile fracture occurs when the plastic zone on the crack tip is large, considered in EPFM, producing different fracture morphology.

The width of the stretch zone when testing fracture toughness in EPFM conditions provides a useful parameter for determination of J integral. The J value obtained by measuring SZW is considered not to have ligament size effect. It must be taken into account that the slope of the blunting line is sensitive to the microstructure and the loading rate, and for that it is better to determine both width (SZW) and depth (SZD) of stretch zone.

Since SZD measurements are not straightforward, but rather have to be calculated from indirect measurements, the described methodology used in literature is verified for the specimens of HSLA steels.

Condition of the crack tip is also significant for fatigue fracture, as crack propagation rate depends on whether there are second phase particles of impurities ahead of a crack tip. These particles accelerate the crack propagation and influencing the spacing between striations, thus affecting the appearance of fracture surface.

REFERENCES

1. Geric, K., *The cracks in welding joints*, The Monograph, Faculty of Technical Science, University of Novi Sad, (2005) (in Serbian)
2. Ritchie, R.O., Knott, J.F., Rice, J.R., *Journal of the Mechanics and Physics of Solids*, Vol- 21, (1973), pp. 395-410.
3. Wels, A.A., *Proceeding of the Crack Propagation Symposium*, Vol. 1, (1966), paper 84, Cranfield, UK
4. Anderson, T.L., *Fracture Mechanics*, Taylor and Francis (2005)
5. Glavardanov, I., Gerić, K., *Application of SEM for fracture toughness estimation*, 6th Symposium on Electron Microscopy, Sarajevo, (1989), pp. 277-279. ?
6. Gerić, K., Glavardanov, I., Sedmak, S., *Estimation of J integral and stretch zone in HAZ*, *Proceeding 24th Conference of production engineering*, Novi Sad, (1992), pp. 31-38. ?
7. Gerić, K., Sedmak, S., Glavardanov, I., *Application of SEM for final stretch zone definition*, 3th Symposium on Electron Microscopy, SEM92, Niš, (1992), p. 140. ?
8. Blumenauer, H., Ude J., *Stretch zone measurement on ductile steel*, ECF9, Volume II, (1992), pp. 871-874.
9. Das, S.K., Sivaprasad S., Das, S., Chatterjee S., Tarafder S., *Materials Science and Engineering A 431*, (2006), pp. 68-79.
10. Gerić, K., IFMASS7, Monograph, Faculty of Technology and Metallurgy, Belgrade, (2002), (in Serbian), pp 271-279.
11. Gerić, K., Sedmak, S., *The evaluation of final stretch zone by scanning electron microscopy*, *Proceeding of I Congress on Electron Microscopy*, Novi Sad, (1994), pp. 265-266. ?
12. Gerić, K., Sedmak, S., *Final stretch zona size evaluated by scanning electron microscopy*, *Fortschritte in der Metallographie*, Sonderband der Praktischen Metallographie, (1995), 483-486.
13. Laird, C., *Fatigue and microstructure*, ASM, Metals Park, OH, (1979), pp. 149-203.
14. Cvijović, Z., Vratnica, M., Gerić, K., *Fractographic analysis of fatigue damage in 7000 aluminium alloys*, *Journal of Microscopy*, Vol. 232, (2008), pp. 589-594.

APPLICATION OF NON-DESTRUCTIVE TESTING PROCEDURES FOR STRUCTURAL INTEGRITY ASSESSMENT

Stevan Kuzmanović

Energoinvest-IMQ, Sarajevo, Bosnia and Herzegovina

s.kuzmanovic@lsinter.net

Abdulah Koro, Nedžib Njuhović

Energoinvest-IMQ, Sarajevo, Bosnia and Herzegovina

1. INTRODUCTION

Non-destructive testing methods are used for detection of discontinuities, defects and imperfections in products, primarily in casings, forgings, plates, pipes, and weldments.

In general, these deficiencies can be divided in that developed:

1. in casting process of raw material;
2. during manufacturing by rolling, forging, cutting, welding;
3. in exploitation of components and equipments.

Detrimental effects can be avoided or significantly reduced if deficiencies are detected in an early stage of manufacturing or service. For that, the role of non-destructive testing (NDT) is of high importance for structural integrity and life of equipment in service.

Basic knowledge about NDT methods and procedures can be found in textboxes and literatures, including many lectures held in the previous International Fracture Mechanics Summer Schools (IFMASS). With this in mind, in addition to classification of imperfections and defects, state-of-the-art in the improvement of NDT performance in practice will be presented here, followed by the examples of recent NDT applications.

2. IMPERFECTIONS AND DEFECTS

Most important deficiencies in equipment and their components are imperfections and defects. Short overview of them can help to follow next text in an easier way.

2.1. Classification of imperfections

In general, imperfections are classified depending on manufacturing process, type of material, thickness and other factors. So, in steel castings to 50 mm thick, discontinuities detectable by radiography are grouped in ASTM E446 standard as follows:

- A – gas porosity,
- B – inclusions of slag and sand,
- C – shrinkage cavity,
- D – cold crack,
- E – hot crack,
- F – inserts,
- G – marble air.

Geometrical imperfections in metallic materials, formed in arc melting process, are classified in EN ISO 6520-1 as follows:

- 100 – cracks,
- 200 – voids,
- 300 – inclusions of solids,

- 400 – lack of fusion and incomplete penetration,
- 500 – imperfections in shape and dimensions,
- 600 – other imperfections.

1.2. Assessment of imperfection effect

The assessment of imperfections significance for product function capacity, when fracture mechanics analysis is missing, is performed at:

- nominal level (product is accepted or rejected without analysis),
- ordinal level (products are classified based on drawings, photographs, radiograms, replications and similar documents taken from corresponding catalogues),
- metrics(metrification) level (measuring dimensions, location of discontinuity, occurrence frequency and other actions).

At the nominal level are mainly assessed planar discontinuities: cracks, lack of fusion, incomplete penetration, notjoined inserts. Ordinal level is applied mainly for castings, and metrification level for welded joints and forgings.

1.3. Defects

Under the term "defect" unacceptable imperfections and discontinuities in material and product are comprised. In general, the defects can be repaired by grinding and/or welding, but defective object will be frequently rejected. In special cases defect can be accepted under the condition of regular inspection or monitoring in service.

2. LAST CHANGES IN NON-DESTRUCTIVE INSPECTION PERFORMANCE

In past fifteen years a significant changes took place in non-destructive testing practice. The changes are the result of impressive development of electronics, informatics and material's design, but more important is the fact that non-destructive tests present a powerful tool for quality assurance of products, thus for security and reliability of equipment in service, and for the maintenance. This is followed by intensive standardization of the equipment and materials, on one side, and by training, qualification and certification of personnel in non-destructive testing, on the other side.

The Directive 97/23/EC – PED ("Pressure equipment") has obliged in a proper way the owners, users and manufacturers of equipment to apply and obey corresponding standards and codes, and the authorised accredited national bodies and independent accredited and notified inspections and certification bodies to verify their application.

2.1. Equipment and devices for non-destructive testing

Regarding the function the standard equipment for NDT does not passed significant changes, but a row of improvements have been involved.

X – Ray devices are operating with ceramic tubes. Control unit is now digitalised and can memorise several programs, including default program for x-ray tube warming-up. It controls tube temperature, and switch off the device, if necessary.

Gamma defectoscopes are in general protected from depleted uranium. New isotope Se-75 is available for testing steel in thicknesses 10 to 40 mm. It is to notice that Ir-192 is not used anymore to test steel bellow 20 mm in thickness.

Illuminators and densitometers belong to the x-ray devices requiring regular inspection. The films are classified based on sensitivity and granularity. Manual processing of films is not anymore in use, dominantly automatic device are used for processing.

Ultrasonic devices are digitalised, so it is almost impossible to find an analogue device on the market. These are the devices of significant capacity in programming. When the sound velocity, distance range and detection sensitivity are known the device can be set by only one referent reflector. DGSreference curve can be directly downloaded from the memory, and a digital-to-analogue converter (DA) curve can be saved in the memory and called in testing procedure.

Modern devices for eddy current testing, for acoustic emission testing and visual control are also digitalised. In the videoscope is the chipis applied at the tip of the sensor, and the signal is digitalised in the control unit connecting video chart and monitor.

2.2. Calibration of the equipment

Being the measuring devices the NDT equipment has to be calibrated.If the standard does not prescribe calibration intervals, then the equipment user has to do this. The equipment and devices are to be calibrated in national institution for measures, at equipment producers or in non-destructive testing laboratory, following the accepted procedure.

High voltage in x-ray equipment is to be checked using one of three procedures accepted in European Standards and the focal (point) following one of five prescribed procedures. The amperage of the tube and exposition time can be checked by the NDT laboratory itself.

The dimensions of the isotope are to be checked by x-ray method.

For the illuminator light diffusion, illumination uniformity and screen temperature are to be checked.

According to ASME, Sec. V, Part. 2, densitometer should be calibrated every 90 days using gradually darkened bands traceable to NIST.

For ultrasonic devices and testing sensors European Standards prescribed checking of series of parameters, what can be performed in general only at device producer. Non-destructive testing companies have to check by them own

- Daily: index of a head,beam angle, physical state and outer aspects,

-Weekly:time base linearity,amplification linearity,sensitivity and the relation signal noise, impulse duration.

Working characteristic (relationship voltagevs. amperage) and ampermeter accuracy have to be checked in current sources for testing by magnetic particles.

Electrical magnetic yoke is to be checked by the test of lifting plateof specified mass or measuring tangential field capacity in the middle of poles distance.

All instruments for measurement of testing parameters have to be calibrated as well, as this the case with UV meter, instrument for measurement of magnetic tangential field capacity, thermometer, chronometer, manometer.

2.3. Testing media

Testing media (suspension of magnetic particles and components of dye penetrant system have to pass specified testing and testing of each batch. Batch testing certificate must be enclosed todelivered material; certificate of specified testing should be requested.

2.4. Documentation requested before testing

Testing bidder in stage of ordering should supply to tester a row of data about tested subject, among other the requested quality level of the tested subject, preferably in the specificationform, for examplefor welding joint EN ISO 5817 quality level C, for

plates EN 10160 quality class S2 – E3, and for castings EN 12680–1 severity level 3. Testing techniques and scope can be specified based on product quality and acceptance level.

2.5. Testing procedure specified in written form

ASME, Sec. V and majority of European Standards (EN 12062: 2002 "Common rules for non-destructive testing of metallic materials") request to present written procedure – specified instruction for tested subject inspection by selected testing method. Instruction should define testing techniques and parameters.

Program for the instruction composition for welded joints testing by x-ray, which includes all the limitations, is available in EN 1435: 2003.

It might be requested to deliver the instruction for verification or to be presented to the purchaser representative or authorised inspector.

2.6. Verification of testing parameters

Testing parameters have to be verified during procedure and proof the testing quality before the decision of tested subject is made. For example:

- In ultrasonic testing, in addition to parameters cited in a part "Calibration of the equipment" every four hours must be controlled distance range and sensitivity settings, and in case of excessive deviation all tests performed after last control must be repeated.

- In the magnetic particles inspection should be controlled: particles concentration in the suspension, suspension susceptibility (using control block No. 1 or No. 2), tangential magnetic field capacity and/or magnetisation amperage, illumination of testing surface or UV radiation and testing surface back illumination.

- In the x-ray testing it is to control: the level of backside radiation (lead number "B" on the cassette back side), film chemical procedure (using in advance exposed band), the existence of requested marks on the radiograph, the existence of artefacts in considered zones, radiograph darkness, and image quality value, and if some of these parameters deviates of allowed value, the radiograph can't be used for evaluation of tested subject.

2.7. Testing performance

Different testing levels might be applied according to required quality level of product. For example, when testing welded joints:

- In x-ray tests two levels are defined, class A – base techniques, and class B – advanced techniques. These classes differ in the value of minimal distance between source and film, quality of used film and requested image quality value.

- In the ultrasonic tests four testing levels (A, B, C and D) are specified. The increased probability of detection from level A to level C is achieved by increased covering that is by scanning number (more scanning directions, more angles propagation, and surface flattening). Testing level D is aimed for special applications.

2.8. Personnel in non-destructive testing

The greatest contribution in non-destructive testing is achieved by the request that only personnel qualified and certified by corresponding standard can perform the testing. In Europe it is EN 473: 2000 "Qualification and certification of NDT personnel" (harmonized standard of EC 23/97 directive).

Personnel in NDT are classified at three levels:

- Level 1: testing performance according to written instruction.
- Level 2: performance and evaluation of testing finding, selection of testing techniques, instruction creating.
- Level 3: performance and evaluation of testing finding, selection of testing techniques, instruction, specifications and procedures producing, standard interpretation.

Training of personnel is to be performed according to the programs accepted by The International Committee for Non-destructive Testing and valid standards. Training duration is prescribed depending of testing level and method.

The personnel qualification comprises successful passing the examination for the method and in manufacturing or industrial sector. The exams of levels 1 and 2 include:

- basic exam (basic postulates of testing method),
- specified exam (knowledge of standards, procedures, codes)
- practical exam (skill in testing performance according to standards)

The examination for level 3, in addition of such an exam for method, includes so called cognition of common knowledge at least of 4 methods for the level 2 and the cognition of product material and manufacturing technology.

The exam for qualification is considered as passed if in each part of examination the result achieved is minimum 70% and the total mark is at least 80%.

The trainings and examinations are held in Exam Centres of Certification Body by authorised examiner, which did not train the candidates. Examination questions with multiple selection and the samples are provided by the Certification Body from its collection of randomly selected secret questions and samples.

Certification body is an institution accredited according to EN ISO/IEC 17024 and is under continuous surveillance of national Accreditation Body. In Europe is generally accepted accreditation of Certification Body if The Accreditation Body is a permanent member of European Accreditation and a signatory of Multilateral Agreement, accepting the surveillance of other members of European Accreditation.

Directive EC 23/97 requires that Certification Body is also notified, that means under the surveillance of Pressure Equipment Committee of European Commission.

Competitiveness Certificate is delivered based on the documents which confirm:

- necessary minimum industrial experience,
- minimum required training for method, level and industrial sector,
- successfully passed qualification exam, and
- eye sight capacity.

Education and necessary industrial experience are interlinked only at level 3.

Eye sight capacity comprises the ability of close sight and differing of colours and for VT might be requested ability of sight at distance, and for RT the differing of grey nuances. Eye sight capacity is to be checked once a year. .

Certification renew is termed at every fifth year, and re-certification at every ten years.

2.9. The report of examination

After performed testing a written report is to be delivered (including RT). In corresponding standards the content of the report is specified, and in some of standards document form for the report is available.

It is to take care that signatories of the report be the persons accomplished the testing and evaluating the results, which overtake in this way direct responsibility for testing performed and on this base evaluated product quality.

2.10. The position of non-destructive testing in industrial production

In the standards harmonised with Directive (PED 97/23/EC) directive for tube boilers (power plant boilers), mantled boilers (boilers for district heating), pressure vessels and industrial piping the requirements relating to the inspection and destructive and non-destructive are contained in the same part of corresponding standard.

It is similar for gas supplying systems, but they also include requirements for welding.

In the standard inducing common rules for non-destructive testing of welding joints is specified:

"The organisation which performs the testing has to be organised independently of production and its activities have to be controlled by quality assurance system.

If an external testing organisation is requested for inspection, it has to be accredited according to EN ISO/IEC 17025".

Standard EN ISO/IEC 17025 includes common requirements for competitiveness of laboratories for testing and calibration. European Accreditation issued the document EA-4/15:2003 "Accreditation of bodies which perform non-destructive testing".

3. INSPECTION FOR MAINTENING OF EQUIPMENT IN FUNCIONAL STATE

Available thermal power plant equipment in our region is close to or beyond the prescribed operating life. For that it is required to be regularly inspected regarding the state of materials and components in order to save their functionality. Generally, in Bosnia and Herzegovina the power plants should be inspected every second year, and retrofitted every fourth year. The inspection programs for power plants maintenance are defined by national electrical companies.

As an example for maintenance program ASME Code, Sec. XI, can serve, as generally available standards, which includes the inspection programmes for nuclear power plant components supervised by the Authorised Inspection Agency, but also the programmes of German Thermal Power Plants Association can serve for this purpose.

To achieve relevant data about material and component state all available NDT methods are used. As an example for the retrofit of turbine in block 7 of Thermal Power Plant "Kakanj" was included visual examination, ultrasonic testing, testing by magnetic particles and by dye penetrants, and also metallographic analysis of material micro-structure by replication, ultrasonic thickness measurement and hardness measurements in selected regions of the component. This will be illustrated by examples in next text.

3.1. Components state inspection

Enormous number of reports about extended equipment inspection are generally stored not systematically and often they are not available, making difficult, or even impossible, to follow the changes of equipment during lifetime.

Gathered experience have shown that sometimes the original testing base data are missing, like quality of component material, not to mention parameters and findings of previously performed testing. This is specially the case when the tests are performed by external institutions, including component manufacturer.

Today achieved level of computers and informatics allows developing software in which following data might be stored, like:

- original initial data about component,
- maintenance programmes,
- location, type, applied procedures parameters and findings of testing,

- performed repairs and replacements,

The application of software of that kind and data base might be the great contribution to a reliable operation of the equipment. This can be well supported by the possibility of software to warn on eventual failure.

3.2. Continuous monitoring of component state

In addition to continuous monitoring of process parameters of equipment, like temperature and pressure, continuous monitoring of component state can be beneficial.

Many different sensors are capable, when involved in corresponding system, to assure useful information and warnings about equipment component state, like: strain gauges, piezoelectric transducers, acoustic emission sensors, electrical magnetic transducers, CCD cameras, lasers diodes, and infrared cameras.

4. APPLICATION OF NON-DESTRUCTIVE TESTING IN PRACTICE

Different are causes of structural damage of components. Most important of them are: overloading, mechanical and thermal fatigue of material, creep, wear, corrosion (stress, intercrystalline, general), and erosion.

Different methods are applied to detect defects in components during periodical inspection or overhauls. Some examples from that experience are presented in next text.

4.1. Steam pipeline in Thermal Power Plant "Kakanj", unit 7

Steam line in unit 7 (230 MW, operating pressure 174.5 bar at 545°C), had been inspected in November 2001 (Fig. 1, Fig. 2).

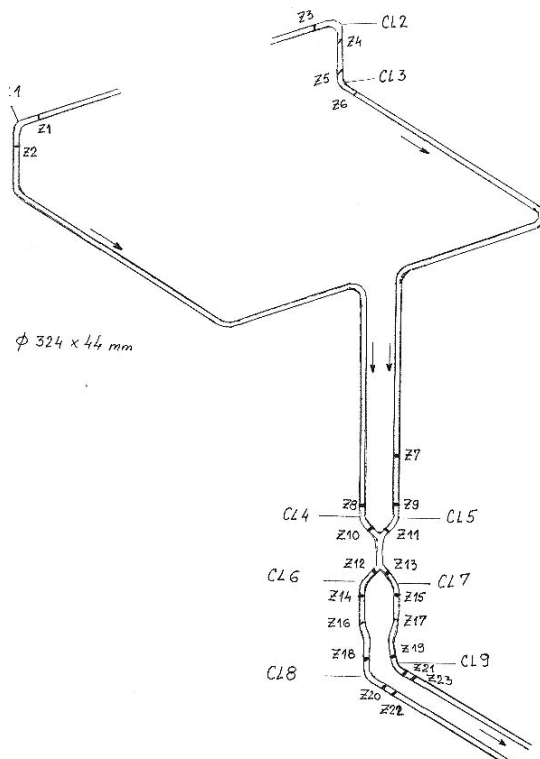


Figure 1: Line of fresh steam – knees and welds

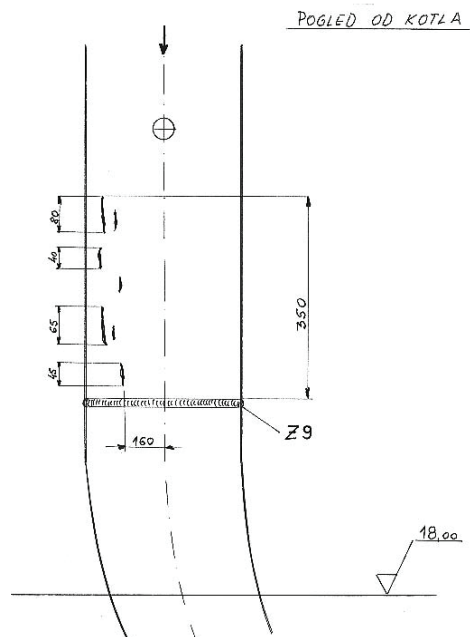


Figure 2: Defects close to welded joint Z9

For this complex inspection following NDT methods had been applied: dimensional measurement on specified locations and control of diameter and wall thickness at knees, visual control of steam line and of steam line supports, metallographic analysis applying the replication of the location of knees, magnetic and ultrasonic testing of welded joints, hardness measurement of welded joints, and geodetic measurement of steam line in cold and warm state.

Serious linear indications had been detected on pipes close to welded joints Z1 and Z9, only by incident, since magnetic particles testing of pipes had not been specified.

The defects on the pipe in the vicinity of Z1 had been grinded out 6 to 7 mm in depth and repaired by welding. The pipe segment close to welded joint Z9 was cut out in length of 2200 mm and this segment was replaced by a new one. Chemical composition, checked by stiloscop analysis, was found to be the same for old and new segments.

4.2. Turbine unit 7 in Thermal Power Plant "Kakanj"

Turbine of unit 7 had been inspected in March 2005, during general surveillance of turbine components according to NDT programme. Outer casings of high and medium pressure turbines (castings, material ČSN 422744.1) were examined by visual inspection (Fig. 3), and magnetic particles testing of dividing plane and transition radiuses (Fig. 4).

On the bottom part of high pressure outer casing, cracks, 420 and 30 mm in length, were detected (Fig. 5). The photograph taken after initial grinding, obtained by magnetic particles testing, is shown in Fig. 6, and by dye penetrant in Fig. 7. The crack 420 mm long had been root out after grinding 100 mm in depth of wall 140 mm thick (Fig. 8).

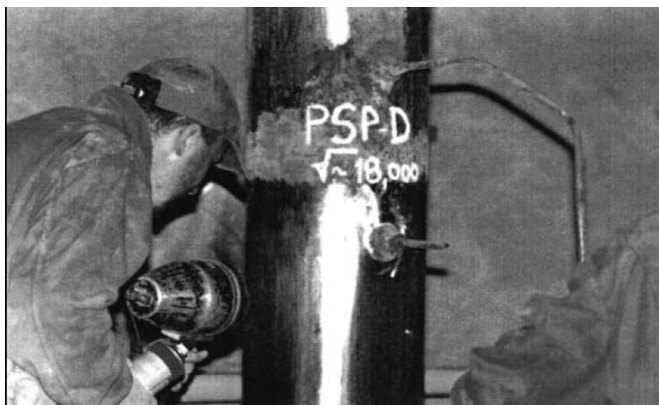


Figure 3: Visual inspection of pipes in the vicinity of weldment Z9

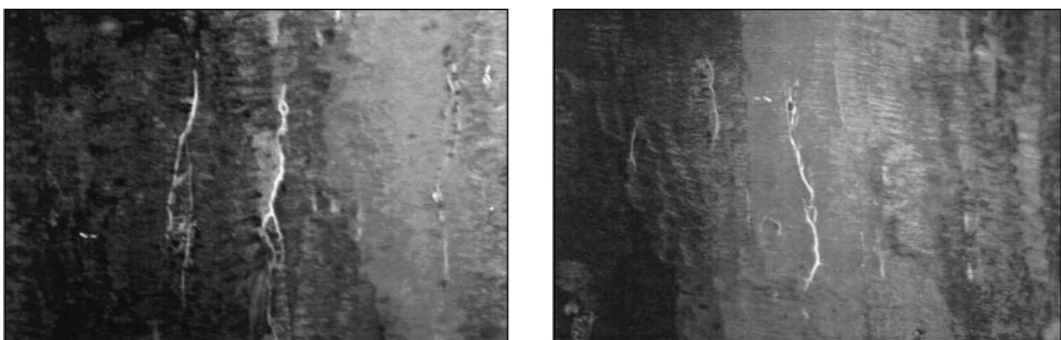


Figure 4: The records of magnetic testing indications (Z9)

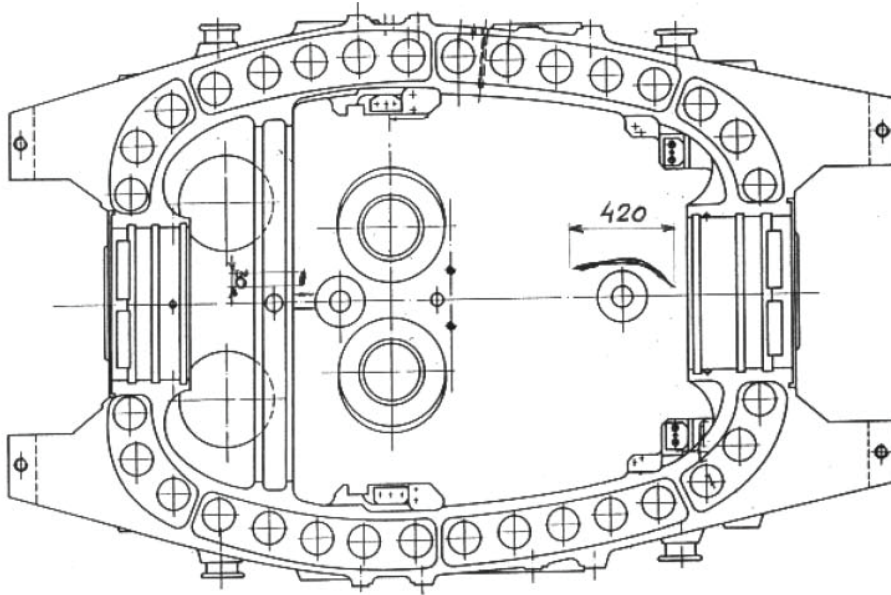


Figure 5: Location of cracks on the bottom part of high pressure outer casing

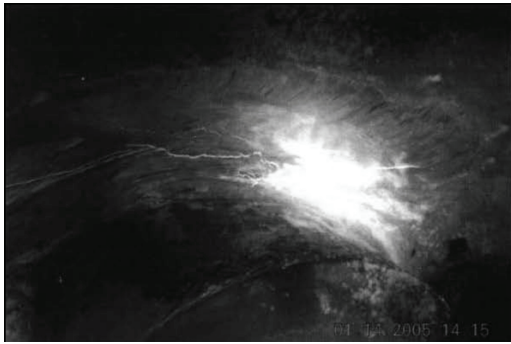


Figure 6: Indication 420 mm long obtained by magnetic particles testing



Figure 7: Indication 420 mm long obtained by dye penetrant testing

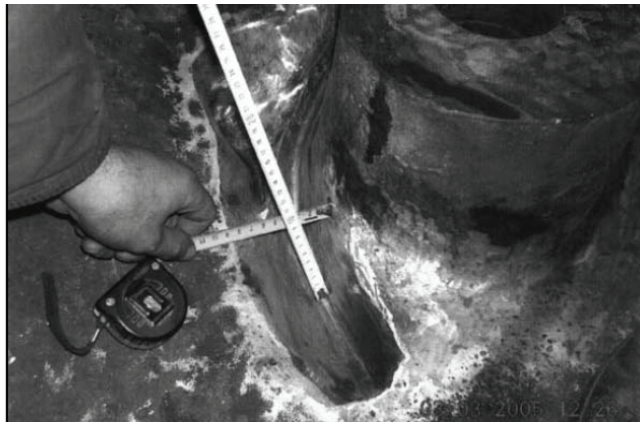


Figure 8: The crack 420 mm long had been eliminated after 100 mm deep grinding

4.2. Turbine unit 6 in Thermal Power Plant "Kakanj"

Turbine unit 6 of 110 MW had been inspected in July 2001. Following tests were applied for inspection of medium pressure turbine rotor:

- visual inspection,
- magnetic particles testing of blades, stiffeners and rivets, of rotor axes body, discs, shafts and couplings,
- ultrasonic testing of shafts and coupling front side, of disc fang on regulation wheel, of contact surface of discs and axes body on last four pressed discs,
- hardness measurement on the location of replication,
- testing by videoscope of central hole.

By magnetic particles testing linear indications of net type had been detected on transition radiuses, discs 17, 18 and 19 (forgings. material ČSN 15.320.9) (200 to 300 indications), 1 to 10 mm long, in the regions 500 mm long and 40 mm wide (Figs. 9, 10).

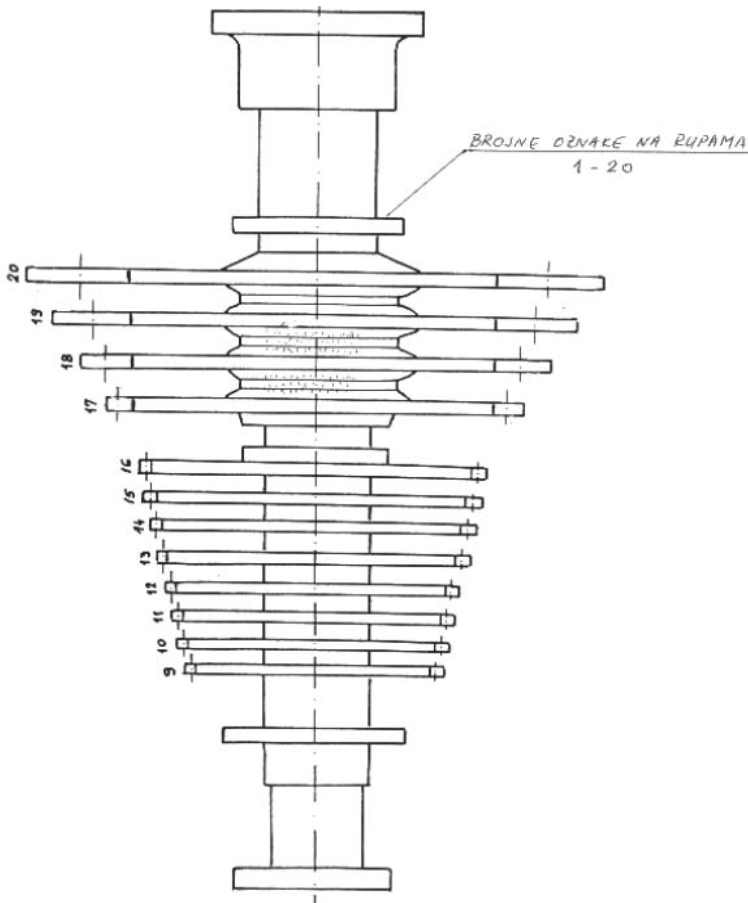


Figure 9: Distribution of discontinuities of medium turbine rotor

After rotor machining on the turning lathe for 1.8 mm in diameter, new testing revealed reduced number of indications for 10 to 15%. This was not accepted and the discs were replaced by new discs.

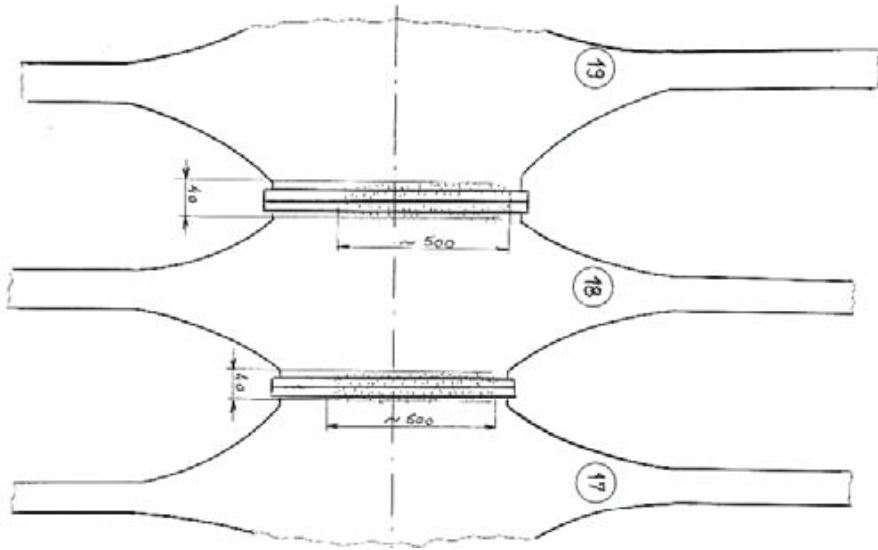


Figure 10: Distribution of discontinuities on discs 17, 18 and 19 of medium turbine rotor

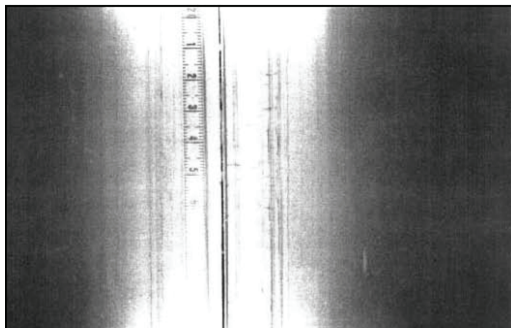


Figure 11: Indication on discs 17 and 18 obtained by dye penetrant testing

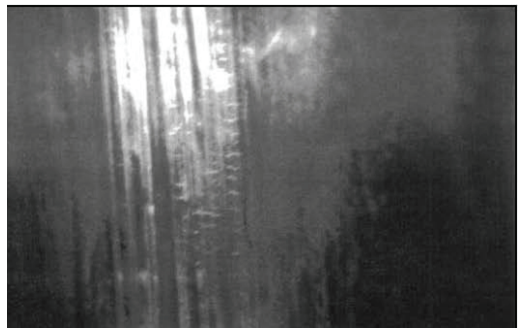


Figure 12: Indication on discs 17 and 18 obtained by magnetic particles testing

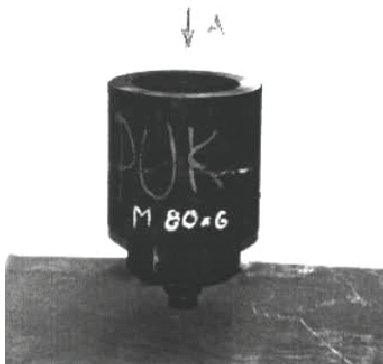


Figure 13: Nut M 80X6

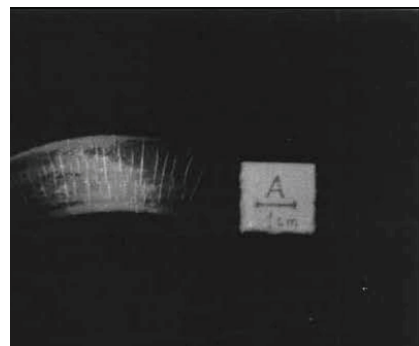


Figure 14: Indication on contact surface obtained by magnetic particles testing

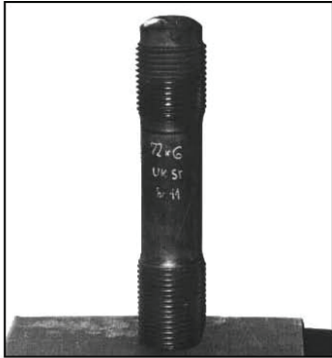


Figure 15: Bolt M 76X6 No 11 of inner casing of medium pressure turbine

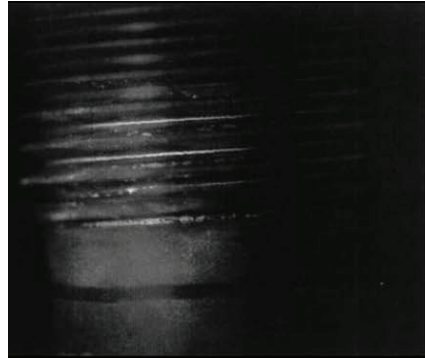


Figure 16: Indication on thread of bolt M 76X6 No 11, obtained by magnetic particles testing

4.3. Turbine unit 5 in Thermal Power Plant "Kakanj"

In turbine unit 5 (110 MW) in the scope of general inspection according to specified programme, 576 nuts and 315 bolts had been examined in July 1998, by:

- visual inspection of bolts and nuts,
- magnetic particles testing of bolts and contact surfaces of nuts,
- hardness measurement of bolt head and corresponding nuts.

The cracks were detected on the contact surface of 8 nuts M 80x6 and 3 nuts M 64x4. Cracks were detected on the bolt No 11 M 72x6 thread of medium pressure casing.

CONCLUSION

During last fifteen years an impressive improvement in non-destructive testing device has been achieved, following the more and more strict requirements from the industry regarding the quality, structural integrity and life extension. The improvement are presented for frequently used methods, and examples of own experience are presented and discussed.

REFERENCES

1. SECTOR Cert, 53840 Troisdorf, Kirchstrasse 12: Manual for NDT personnel training, (1996-2006)
2. CEN, Rue de Stassart 36, B-1050 Brussels: European standards regulating non-destructive testing (1993-2007)
3. ASME Code, Sec. V i Sec. XI, Edition(1993-2004)
4. AEA, Beč, Non-destructive testing Manuel for industrial management and quality control personnel, (1999).
5. ASTM: Manual for non-destructive testing, Second edition, Volume 10: Review of non-destructive testing, (1996)

THE ANALYSIS OF THE STRESS-STATE IN CONSTRUCTIONS IN EXPLOATATION

Taško Maneski

*University of Belgrade, Faculty of Mechanical Engineering, Belgrade, Serbia
tmaneski@mas.bg.ac.rs*

Vesna Milošević-Mitić

University of Belgrade, Faculty of Mechanical Engineering, Belgrade, Serbia

1. INTRODUCTION

The analysis of the constructions behaviour exposed to thermo-mechanical loading is presented. Calculations were done using finite element (FE) method, Program Package KOMIPS (author T. Maneski /1/). The basic elements for this analysis are disposition of loading, distribution of membrane and bending stresses and distribution of deformation energy. Membrane and bending stress might be calculated by beam and plate finite elements. Relations between these two types of stresses in all elements of considered construction are given for critical cross sections. Distribution of the deformation energy across the groups of finite elements (elements of structure) is effective indicator for the applicability of considered construction. Energy method in analysis is effective for the selection of the reconstruction of the structure, if required.

Program package KOMIPS is presented here as applied for the analysis of stress and strain fields, fields of deformation energy and eigen-frequencies of different structures. Following examples are presented:

1. Thermo-mechanical calculation of the reactors
2. Calculation of the strength of the claws
3. Thermo-mechanical calculation of the strain of the gas pipeline RTB BOR
4. Stresstate in the construction of an autoclave
5. Numerical and experimental diagnostic of the behaviour of the palet-pack machine
6. Diagnostic of the dynamic behaviour of a drive unit.

2. THERMO-MECHANICAL CALCULATION OF THE REACTORS

Models of different constructions of reactors (pressure vessel) were considered using FE of thin plate. Consideration is performed for two loading situations:

1. combined effect of working pressure, weight and temperature;
2. pressure in hydraulic proof test and weight.

The appropriate values of pressure are presented in Table 2.1.

Dynamic calculation of eigen-oscilations had been performed for all types of analysed reactors.

Reactors DC-301 and DC3-3, as typical, are presented and discussed more detailed.

Table 2.1: Working pressure and proof test pressure of analysed reactors

Reactor	DC-301	DC-302	DC-303	DC-304	DC-401
Working pressure,bar	50	35	25	26	671
Proof testpressure, bar	106,9	108	109,39	108	112

2.1. Reactor DC-301

Obtained results for reactor DC-301 are presented in Fig. 2.1. Maximum deformation in working conditions is expressed by displacement, found to be $f_{max}=0.85$ cm.

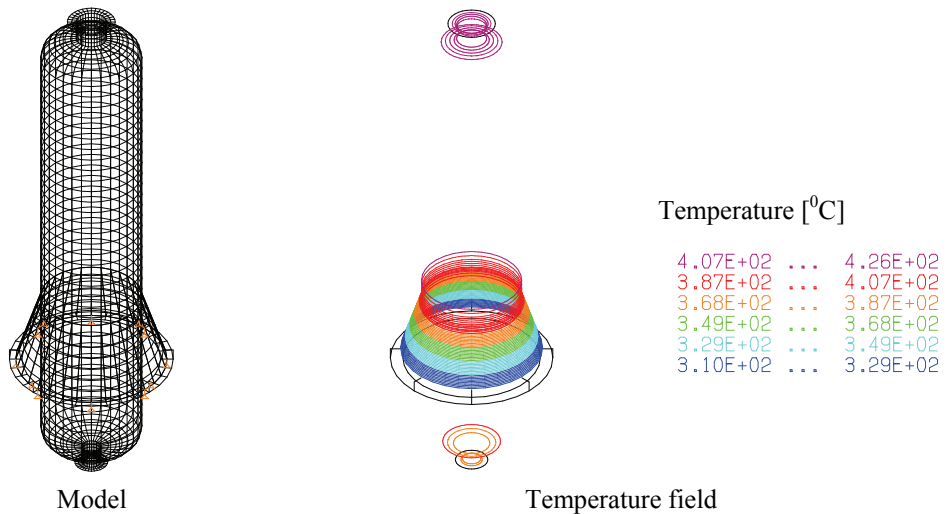


Figure 2.1: Model for calculation and temperature field of the reactor DC-301

Distributions of displacement, equivalent stress and deformation energy during hydraulic proof pressure test are presented in Fig. 2.2.

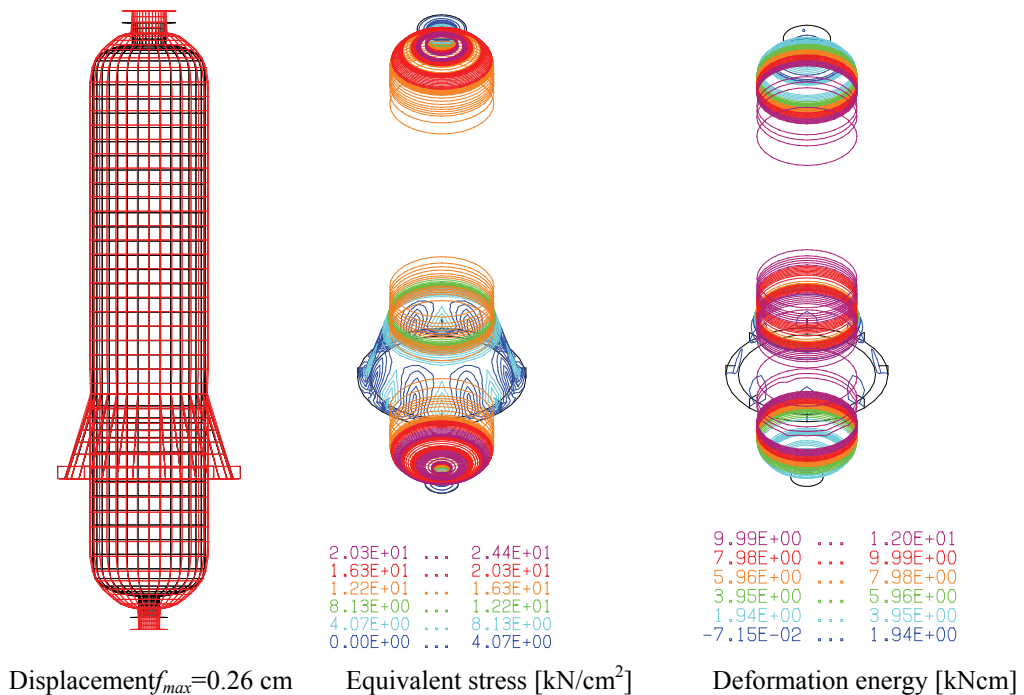
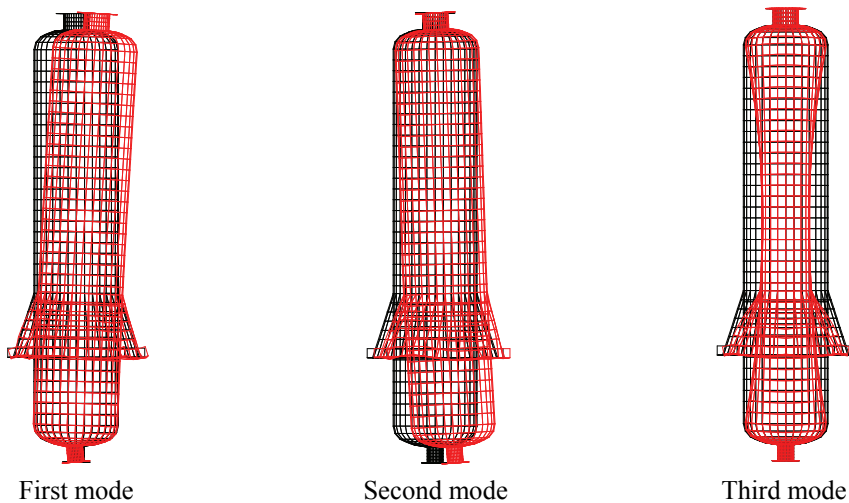


Figure 2.2: The behaviour of reactor DC-301 in hydraulic proof pressure test

The amplitudes of first three modes of displacements are presented in Fig.2.3.



First mode

Second mode

Third mode

Figure 2.3: Shape of first three modes of the reactor DC-301 construction

2.2. Reactor DC-303

FE model of reactor DC-303 and deformation field are shown in Fig. 1.4, equivalent stress and deformation energy in proof test in Fig. 1.5, first three modes shape in Fig. 1.6.

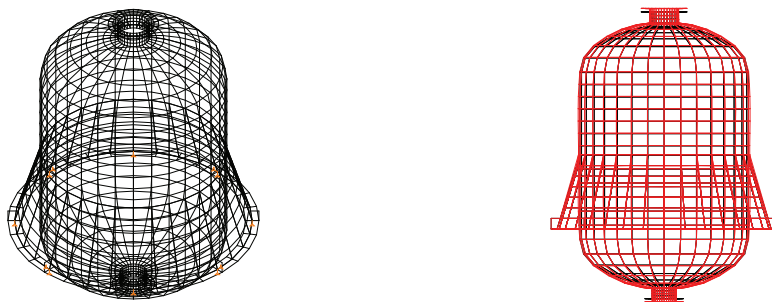


Figure 2.4: Model for calculation of the reactor DC-303 and obtained deformation field

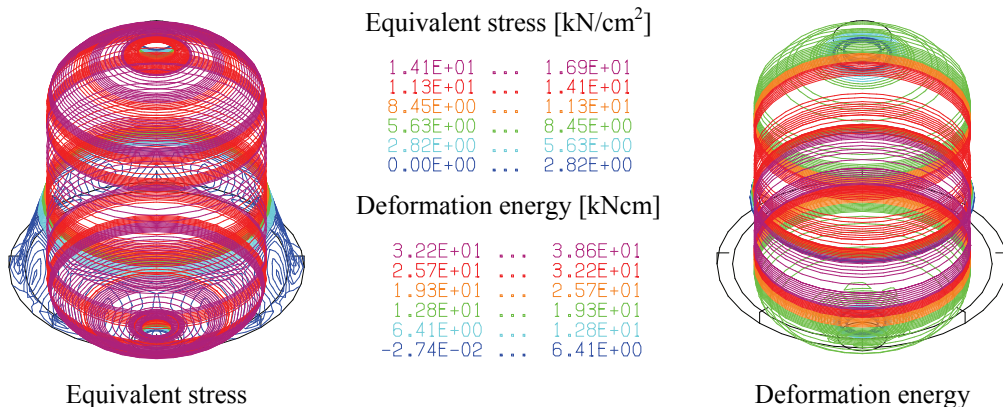
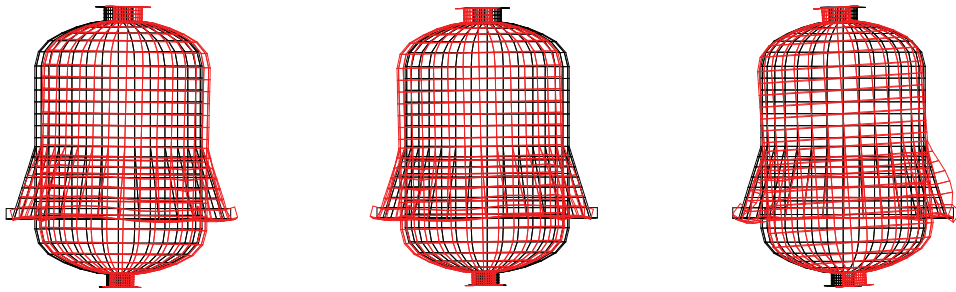


Figure 2.5: Behaviour of reactor DC-303 inhydraulic proof pressure test



$f_{01} = 29,4 \text{ Hz}$, $A = 0,009 \text{ cm}$ $f_{02} = 29,5 \text{ Hz}$, $A = 0,009 \text{ cm}$ $f_{03} = 42,4 \text{ Hz}$, $A = 0,01 \text{ cm}$

Figure 2.6: Shape of first three modes of the reactor DC-303 construction

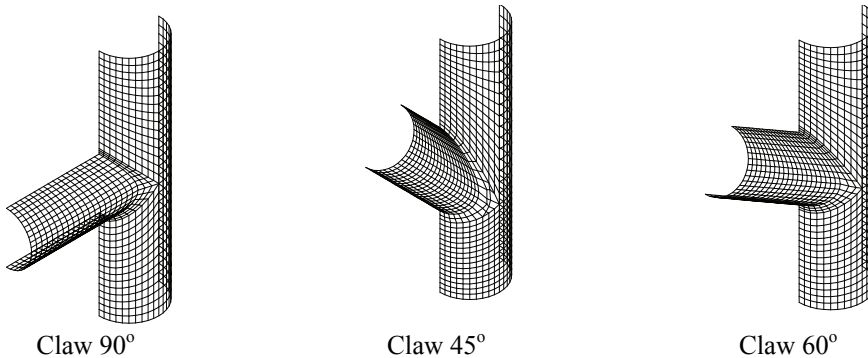
In Table 2 eigen-frequencies of all reactor-constructions, obtained from dynamic finite element analysis, are listed.

Table 2.2: Eigen-frequencies of the analysed reactors

Reactor	First mode	Second mode	Third mode
DC-301	20,6 Hz	42,5 Hz	64,1 Hz
DC-302	40 Hz	81,5 Hz	140,5 Hz
DC-303	29,4 Hz	29,5 Hz	42,4 Hz
DC-304	26,6 Hz	26,7 Hz	30 Hz
DC-401	17,9 Hz	18 Hz	50,3 Hz

3. CALCULATION OF THE STRENGTH OF THE CLAWS

FEM models of the claws of different shapes are presented in Fig. 3.1. As examples, in Fig. 3.2 behaviour of the claw 90° is shown, in Figs. 3.3 and 3.4. of the claw 45° .



Claw 90°

Claw 45°

Claw 60°

Figure 3.1: FEM models of the claws

Table 3.1: Dimensions and pressures for calculation

	Pressure	Dimensions
Claw 90°	$p=35 \text{ bar}$	pipe $\phi 267 \times 12,5 \text{ mm}$ in pipe $\phi 317 \times 14,2 \text{ mm}$
Claw 45°	$p=25 \text{ bar}$	pipe $\phi 267 \times 12,5 \text{ mm}$ in pipe $\phi 317 \times 14,2 \text{ mm}$
Claw 60°	$p=35 \text{ bar}$	pipe $\phi 267 \times 12,5 \text{ mm}$ in pipe $\phi 317 \times 14,2 \text{ mm}$

3.1. Claw 90°

Nominal stress in section remote from gap, at the pressure 0.35 bar, is for:

- Pipe $\phi 317 \times 14.2$ - $\sigma_1 = pR_1/t_1 = 0.35 \cdot 15.85/1.42 = 3.91 \text{ kN/cm}^2$,
- Pipe $\phi 267 \times 12.5$ - $\sigma_2 = pR_2/t_2 = 0.35 \cdot 13.35/1.25 = 3.74 \text{ kN/cm}^2$.

Maximal equivalent stress in the zone of gap, calculated by FEM for the claw without reinforcement is $\sigma_{e1} = 13.3 \text{ kN/cm}^2$, so applied stress concentration factor is

$$k = \sigma_{e1} / \sigma_2 = 13.3/3.74 = 3.56.$$

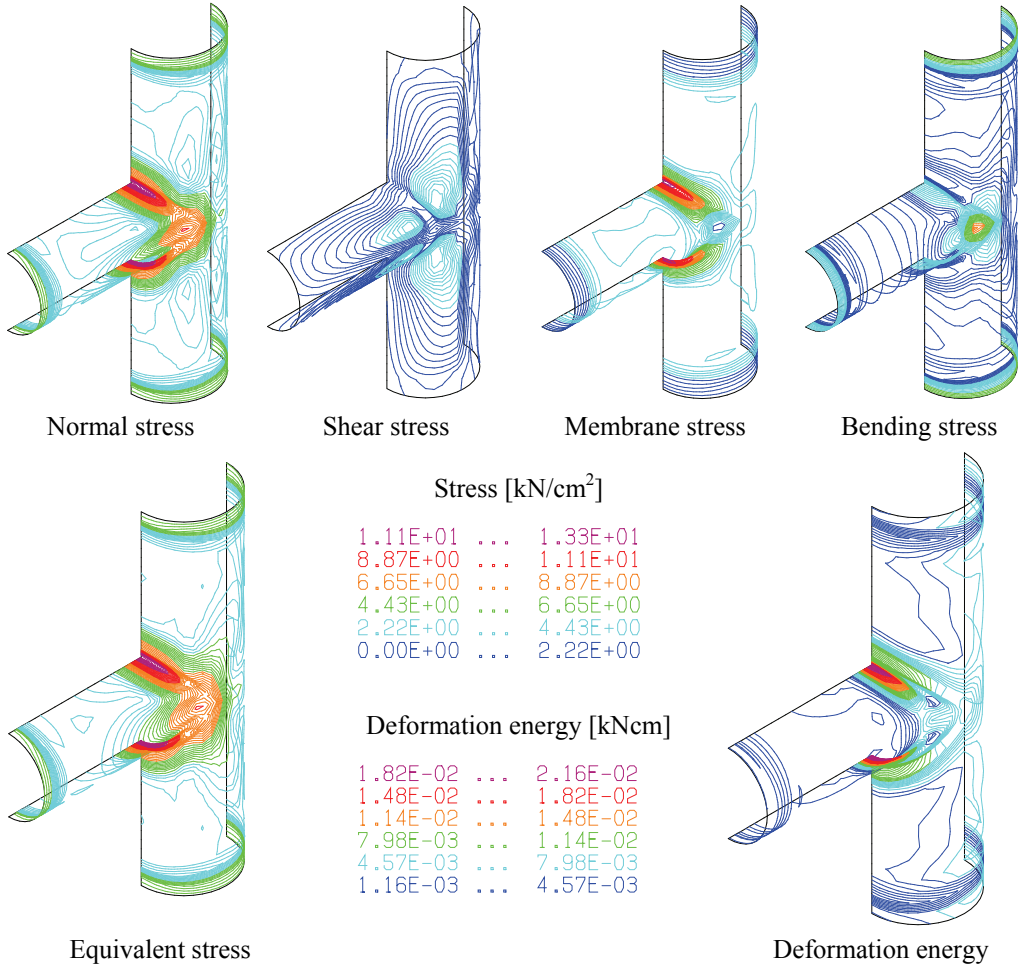


Figure 3.2: Behaviour of the claw 90° without reinforcement

Claw 45°

Nominal stress in section remote from gap, at the pressure 0.25 bar, is for:

- Pipe $\phi 317 \times 14.2$ - $\sigma_1 = pR_1/t_1 = 0.25 \cdot 15.85/1.42 = 2.79 \text{ kN/cm}^2$.
- Pipe $\phi 267 \times 12.5$ - $\sigma_2 = pR_2/t_2 = 0.25 \cdot 13.35/1.25 = 2.67 \text{ kN/cm}^2$.

Distribution of stress components and deformation energy is presented for claw 45° without reinforcement in Fig. 3.3, and with reinforcement in Fig. 3.4.

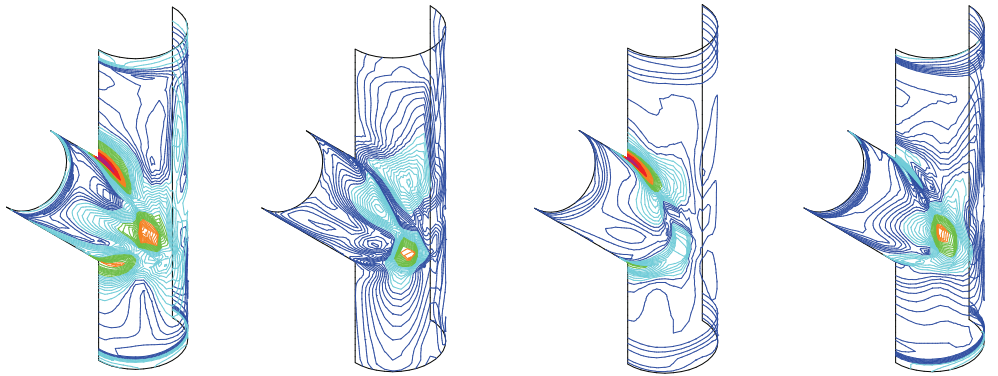
Maximal equivalent stress in the zone of gap in FEM calculation for the claw without reinforcement is $\sigma_{e1} = 20.4 \text{ kN/cm}^2$, for the claw with reinforcement $\sigma_{e2} = 10.6 \text{ kN/cm}^2$.

Applied stress concentration factor in the first case (without reinforcement) is

$$k = \sigma_{e1} / \sigma_2 = 20.4/2.67 = 7.64$$

and in the second case (with reinforcement) is

$$k = \sigma_{e2} / \sigma_2 = 10.6/2.67 = 3.93.$$

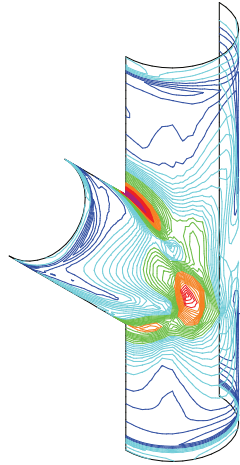


Normal stress

Shear stress
Stress [kN/cm²]

Membran stress

Bending stress

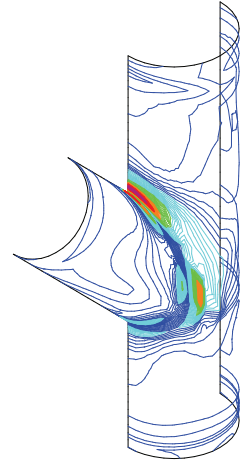


Equivalent stress [kN/cm²]

1.70E+01	...	2.04E+01
1.36E+01	...	1.70E+01
1.02E+01	...	1.36E+01
6.80E+00	...	1.02E+01
3.40E+00	...	6.80E+00
0.00E+00	...	3.40E+00

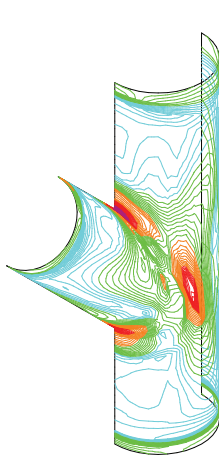
Deformation energy [kNm]

3.00E-02	...	3.60E-02
2.41E-02	...	3.00E-02
1.82E-02	...	2.41E-02
1.23E-02	...	1.82E-02
6.33E-03	...	1.23E-02
3.96E-04	...	6.33E-03



Deformation energy [kNm]

Figure 3.3: Behaviour of the claw 45° without reinforcement



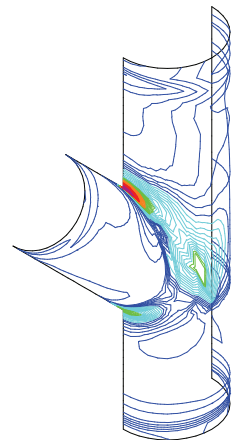
Equivalent stress [kN/cm²]

Stress [kN/cm²]

8.83E+00	...	1.06E+01
7.07E+00	...	8.83E+00
5.30E+00	...	7.07E+00
3.53E+00	...	5.30E+00
1.77E+00	...	3.53E+00
0.00E+00	...	1.77E+00

Deformation energy [kNm]

2.14E-02	...	2.56E-02
1.72E-02	...	2.14E-02
1.30E-02	...	1.72E-02
8.76E-03	...	1.30E-02
4.55E-03	...	8.76E-03
3.34E-04	...	4.55E-03



Deformation energy [kNm]

Figure 3.4: Behaviour of the claw 45° with reinforcement

4. THERMOMECHANICAL CALCULATION OF THE GAS PIPELINE

The complete gas pipeline in the company RTB BOR is considered through selected 15 functional parts. Each part represents independent complex regarding loading. Between two parts the functionless compensator is placed to accept transversal force.

The pipeline geometry and design conditions were taken of Mašinoprojekt KOPRING.

Following pipeline segments are considered: rapid gas line (segments 1-8), adsorb collector (segments 9-11), oblique bypass 1 (segments 12-15), bypass 2 (segment 16).

Two cases of loading were analysed:

- mechanical loading (weight of a construction, of a dust and of an isolation),
- thermo mechanical loading (weight and design temperature).

Segment 1 – Ø1400x6

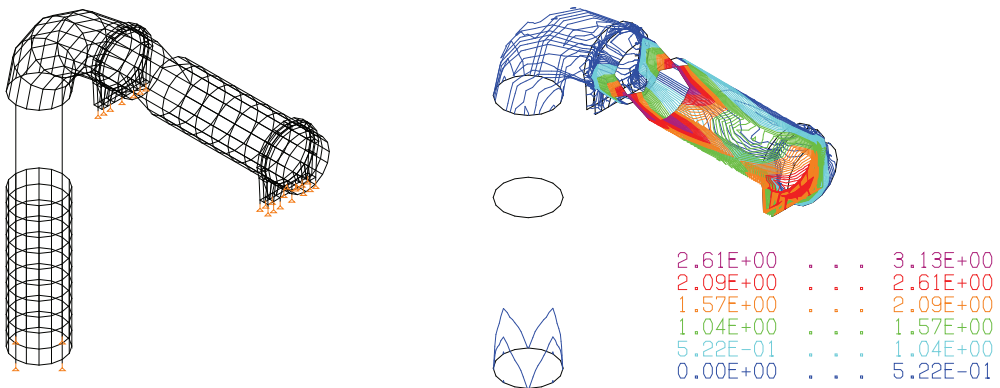


Figure 4.1: Model and stress-field of segment 1 caused by thermo-mechanical loading [kN/cm²]

Maximal deformation of the segment 1, due to the mechanical loading only is $f_{max}=1.14\text{cm}$, and due to thermo mechanical loading is $f_{max} = 4.54 \text{ cm}$.

Segment 2 – upper and lower entrance line (Ø1400x6)

Two cases of loading were considered, active upper and lower parts of gas pipeline.

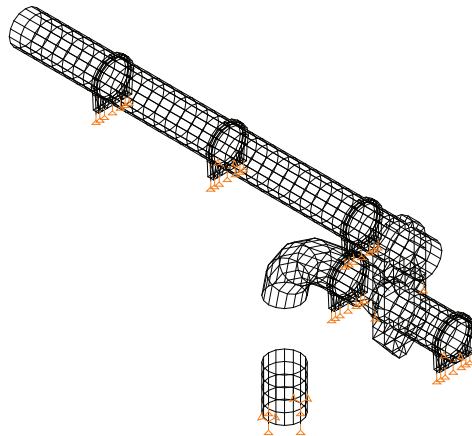


Figure 4.2: Model and supports of segment 2

Maximal deformation of segment 2 due to mechanical loading in the first case, for active upper part is $f_{max} = 4.02$ cm and due to thermo mechanical loading is $f_{max} = 8$ cm, and for active lower part is $f_{max} = 3.86$ cm and $f_{max} = 5.18$ cm, respectively. Stress distribution is presented in Fig. 4.3.

In both cases of working conditions and both cases of loading TD compensator is disburden and HS compensator is loaded. Behaviour of segment 2 is satisfactory.

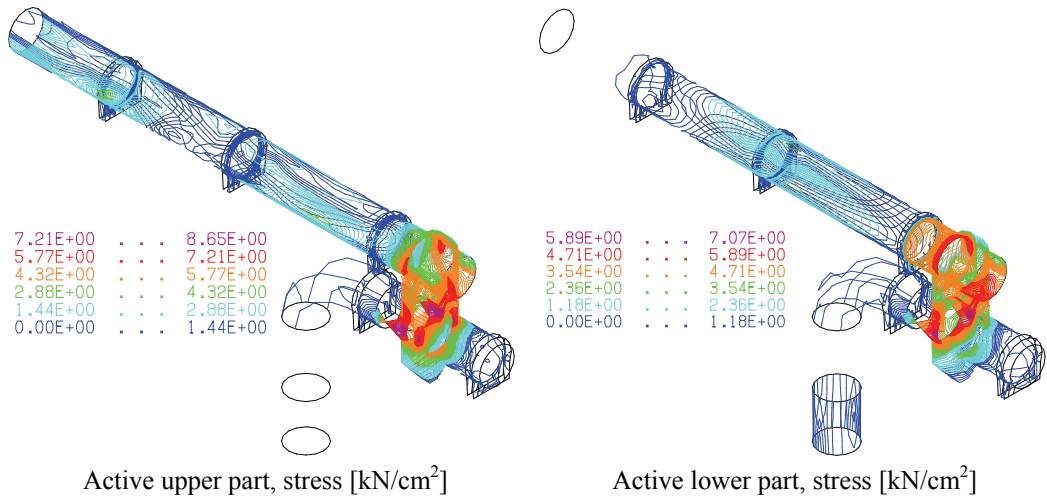


Figure 4.3: Stress in segment 2 due to thermo mechanical loading

Segment 4 – a part of the pipe-line of 17.6m between two fixed segments - Ø1400x6

Stress distribution in segment 4 due to thermo mechanical loading is shown in Fig. 4.4.

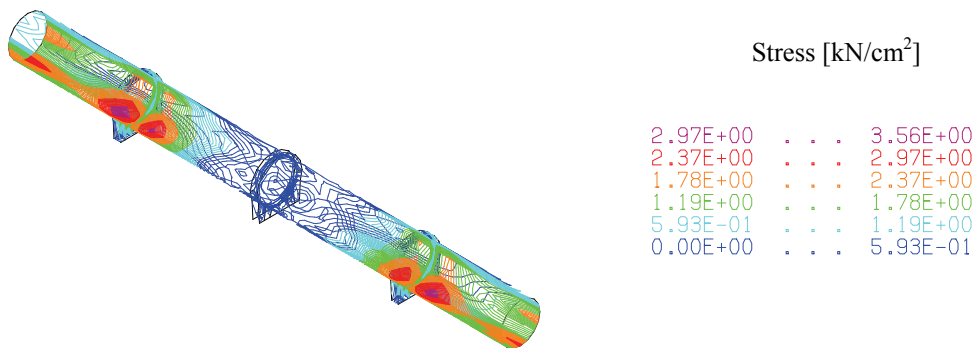


Figure 4.4: Stress distribution in segment 4 due to thermo mechanical loading

Segment 9 – adsorbed (entrance part) - Ø3000x8 / Ø2000x8

Stress distribution in segment 9 due to thermo mechanical loading is shown in Fig.4.5.

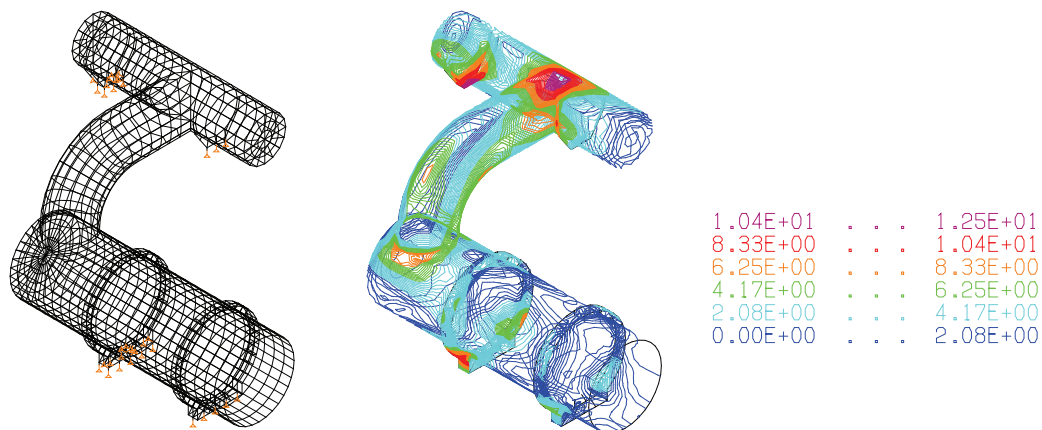


Figure 4.5: Stress due to thermo mechanical loading [kN/cm²]

Maximal deformation of segment 9 for thermo mechanical loading is $f_{max} = 3.89$ cm.

Segment 16 – bypass 2 Ø2000x8 / Ø4000

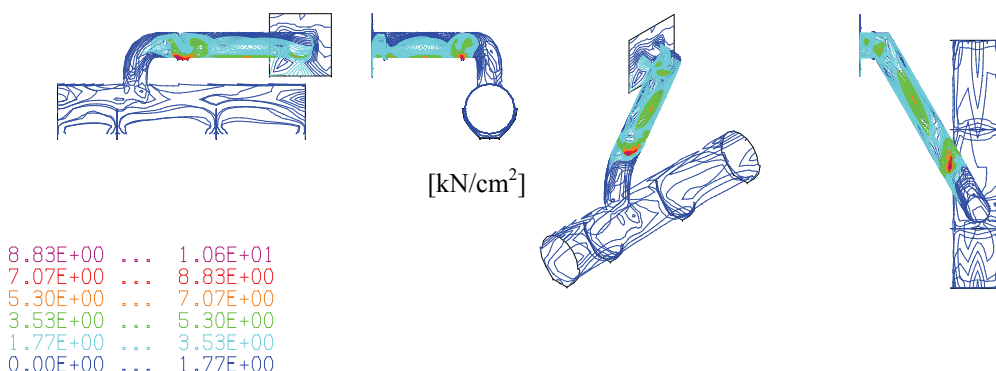


Figure 4.6: Stress distribution at the temperature 250°C for the pipe diameter Ø4000 mm

Performed analysis of complete gas pipeline in the company RTB BOR allowed to derive following conclusions:

1. Analysis were done for temperatures higher then operating, assuming that the temperature field in one segment is homogeneous.
2. Calculated results present maximal stresses at stress concentrations sites; calculated values of stresses are lower than allowed stress values for corresponding temperature.

The behaviour of gas pipeline as a whole is assessed as satisfactory.

Regular inspection of the construction and supports state has been recommended. Thermal dilatation of fixed supports should be provided.

5. STRESS ANALYSIS OF AN AUTOCLAVE CONSTRUCTION

Upon the request of the company Kolubara Prerada - Vreoci the project of overhaul and reconstruction of autoclave was realised in cooperation with the Welding Institute, Beograd.

The autoclave consists of several sub-structures:

- top spherical lid, connectors for opening the vessel top lid,;
- top cone shell above the support,
- middle cone shell and support;
- bottom cone shell, zone of emptying device, device segments, limiters and draining boards;
- spherical bottom lid, connectors, device for opening the bottom vessel lid.

5.1. Problems in the construction of autoclave during the service

Next problems were established (Fig. 5.1):

- the geometry of the segment support allowed to form coal deposits in the support zone until it is completely blocked;
- coal particle movement has caused removal of the basic material in this zone,
- cracks occurred due to high stress concentration, and support blockage reduced shell thickness in the segment support zone, and imperfections in welded joints.



Figure 5.1: Cracks, damages and fracture of autoclave components during the service

5.2. Design calculation of autoclave vessel

Autoclave vessel is modelled by thin plate finite elements, while the supports were modelled using volume finite elements (Fig. 5.2).

Calculations of existing vessel were performed for a pressure 0.3 kN/cm^2 and temperature 200°C , with a difference of 20°C .

The existing autoclave vessel design was examined for two situations: with no blockage and with a blockage in the support zone with two neighbouring device segments. Blockage of the area between two slant plates resulted in fluid pressure only from one side. This enabled following conclusion for the calculation of the existing autoclave vessel, when blocked in the segment support:

- vessel deformation in the segment support zone increased significantly, followed by an unfavourable shape;
- the maximum stress value acts in the whole shell zone around the segment support, reaching the value 19.8 kN/cm^2 ,
- exaggerated stress concentration affected complete autoclave shell around the segment support.

5.3. Calculation of redesigned autoclave vessel

Calculation of no blocked vessel revealed the state of strains and stresses in regular service conditions, and for the vessel blocked in the segment support zone possible occurrence of cracks was indicated. Redesigned model indicated an important improvement in stress distribution (Fig. 5.3).

5.4. Defining activities required for evaluation of the remaining autoclave

The proposed improvement of vessel design required overhaul and reconstruction of segment supports and segments of the emptying device should assure an extension of continuous autoclave operation in the redesigned zone for a long service life.

Proposed project of autoclave vessel service life extension should be based the assessment of remnant operating life, through an experimental-numerical procedure:

- select one autoclave as a representative for the assessment of the remnant life;;
- visual inspection of the complete autoclave vessel;
- inspection with the testing of all welded joints;
- measuring plate thickness of the whole autoclave vessel;;
- determination of parameters for the fracture mechanics;
- experimental dynamic measurement of strain and temperature during service;

numerical procedure for calculating of the remnant operating time based experimental procedures.

6. NUMERICAL AND EXPERIMENTAL DIAGNOSTICS OF THE BEHAVIOUR OF THE PALETTE-PACK MACHINE

Considered machine packs one palette in eight cycles, each with five sacks of 50 kg. Packing of the tours is in cross positions. One cycle is consisted of following operations: lifting with rotation of the palette to the position for packing, moving 5 sacks from the transporter to the palette, descending the palette and lifting to the position for removing air from sacks and descending the palette for the beginning of the next cycle. The whole palette is packed in minimum 40 seconds.

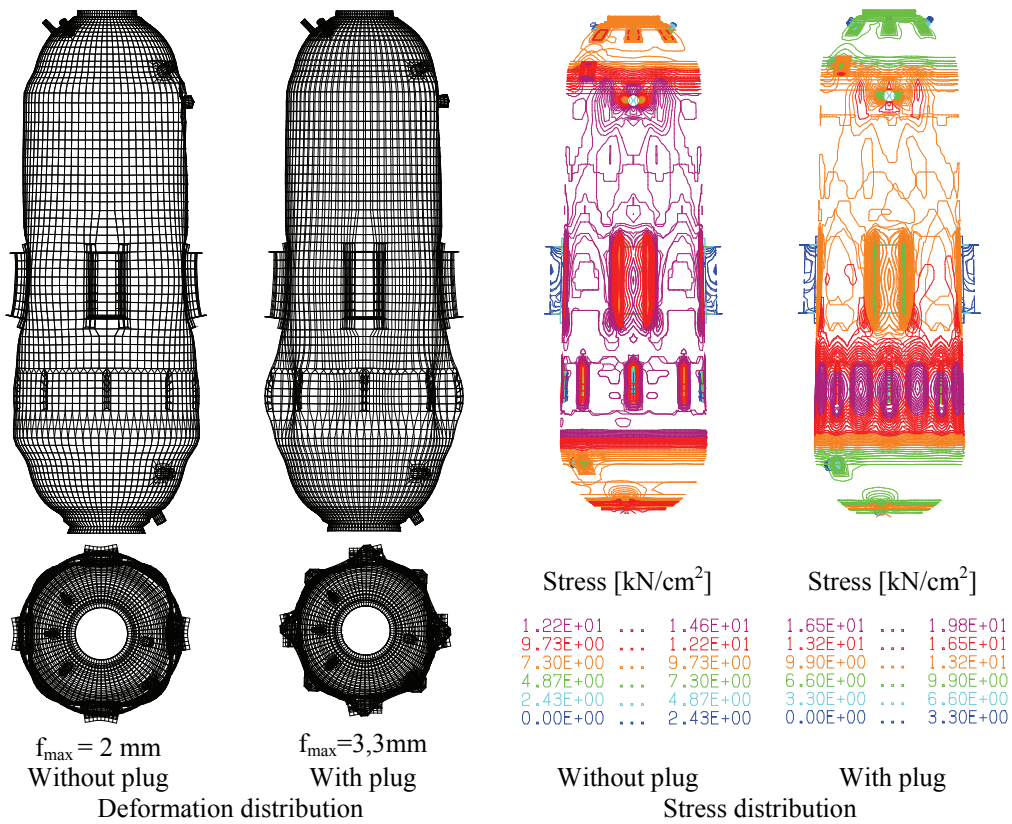


Figure 5.2: Deformation and stress distribution of the existent autoclave construction

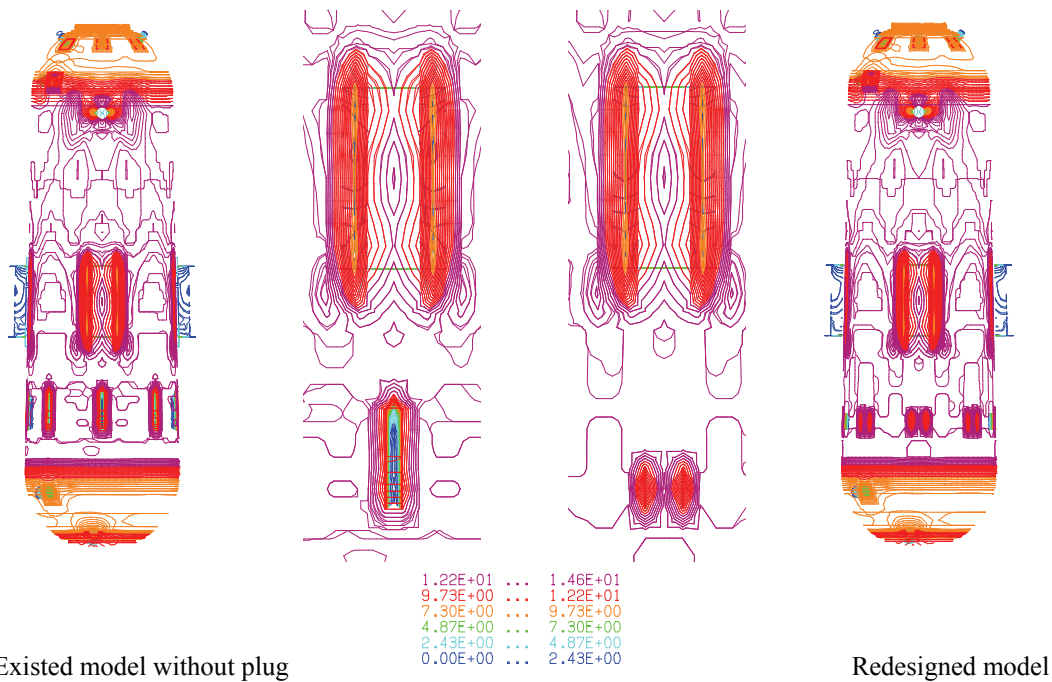


Figure 5.3: Stress fields of the existed and redesigned model, equivalent stress [kN/cm²]



Figure 6.1: Palette-pack machine



Figure 6.2: In-service crack and failure

The drive-unit consists of an electromotor, angular velocity 730 rot/min, gear box, catenary and chain linked to the structure of palette. During operation, the failure was observed in diagonals of palette, on the frame and in the nexus which was moving the palette (Fig. 6.1, Fig. 6.2). It repeated about every 30 days of service, with fractured nexus, palette or the frame. The problem had to be analysed by both numerical and experimental approach.

As the electromotor frequency is 12.2Hz, behaviour of the frame is satisfactory in both cases.

6.1. Finite element analysis

The view of frame and the palette, with corresponding FE models, are presented in Figs. 6.3 to 6.9.

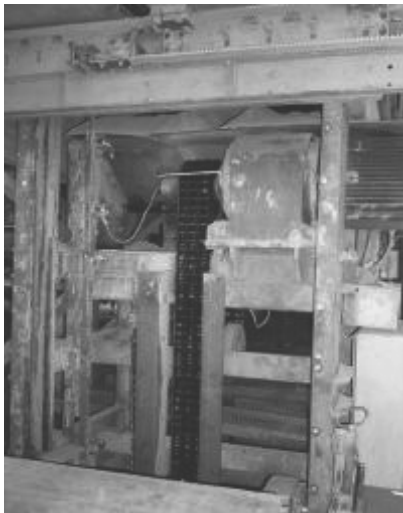


Figure 6.3: Frame

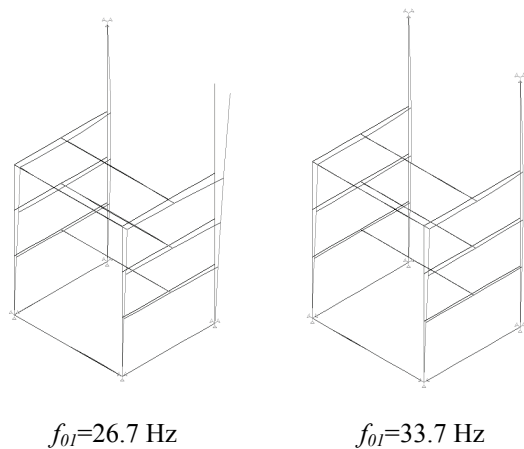


Figure 6.4: Dynamic behaviour of the frame



Figure 6.5: The construction of the pallet

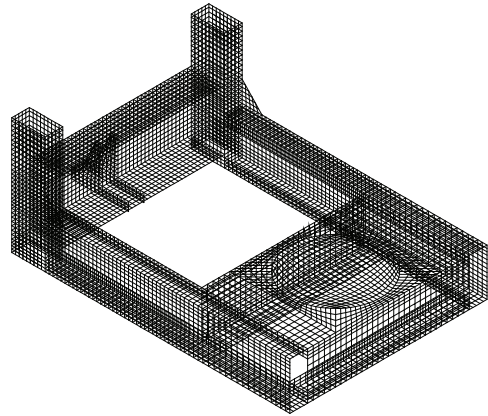


Figure 6.6: Model of the pallet in isometric

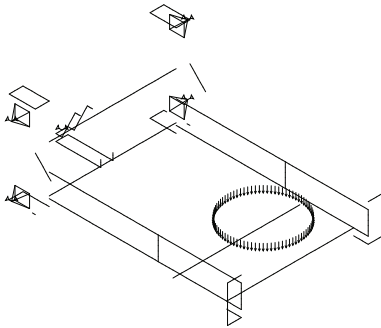


Figure 6.7: Loading and supports

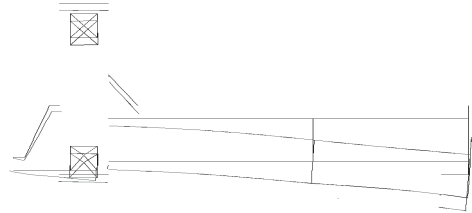
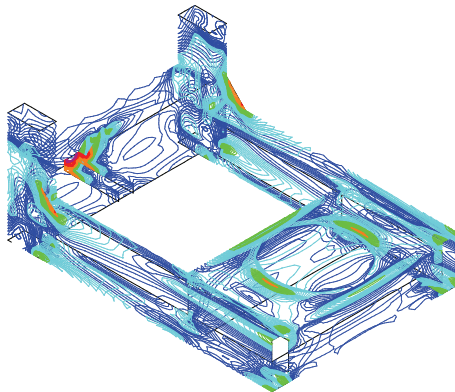


Figure 6.8: Deformation of pallet, $f_{max} = 0.45$ mm

Figure 6.9: presents the pallet stress field calculated by FEM for the loading of 10 kN.



2.17E+00	...	2.60E+00
1.73E+00	...	2.17E+00
1.30E+00	...	1.73E+00
8.67E-01	...	1.30E+00
4.33E-01	...	8.67E-01
0.00E+00	...	4.33E-01

Figure 6.9: Stress field in the pallet [kN/cm^2]

In the same case, the strain gauge was placed on one part of the pallet surface. The stress at this location is calculated to be $0.7 \text{ kN}/\text{cm}^2$ for loading of 10 kN. For maximum load of 2 tons of cement, the stress on the strain gauge location would be $1.4 \text{ kN}/\text{cm}^2$. The maximum stress calculated was $26 \text{ kN}/\text{cm}^2$, or in service $52 \text{ kN}/\text{cm}^2$ in diagonal elements.

The chain finite element calculation was performed in two steps: the static calculation for one shackle of the chain and the dynamic calculation for the whole chain.

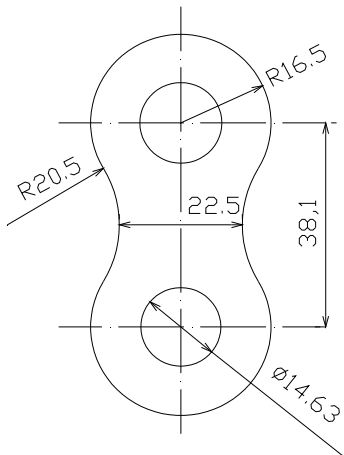


Figure 6.10: One shackle

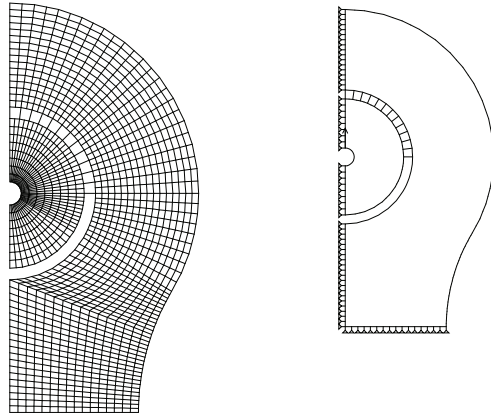


Figure 6.11: Model of the shackle

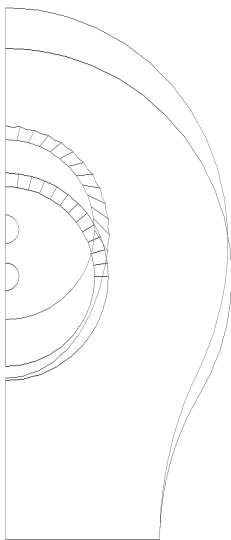
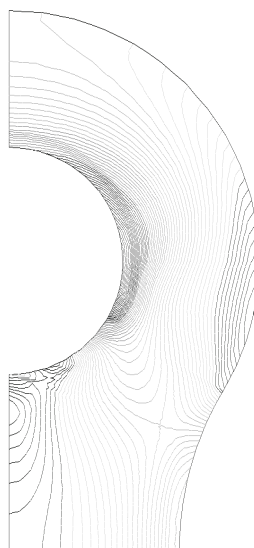


Figure 6.12: Shackle deformation



5.40E+00 ... 6.48E+00
 4.32E+00 ... 5.40E+00
 3.24E+00 ... 4.32E+00
 2.16E+00 ... 3.24E+00
 1.08E+00 ... 2.16E+00
 0.00E+00 ... 1.08E+00

Figure 6.13: Stress field[kN/cm²]

Table 6.1: Eigen-oscillations

	Angular frequency [s ⁻¹]	Frequency [Hz]	Period [s]
1.	253.28	40.31	0.024807
2.	255.40	40.65	0.024602
3.	594.13	94.56	0.010575

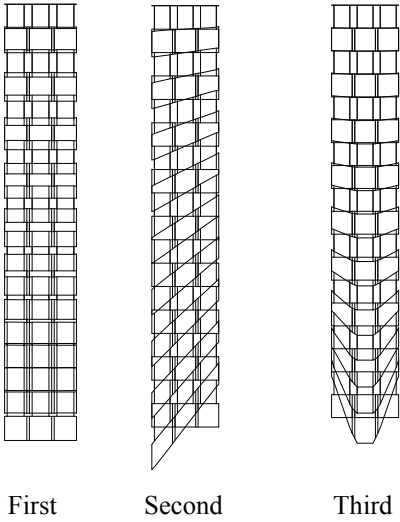


Figure 6.14: First three modes of oscillations

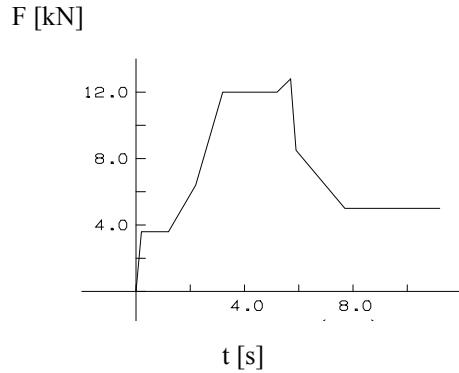


Figure 6.15: The function of the compulsive force

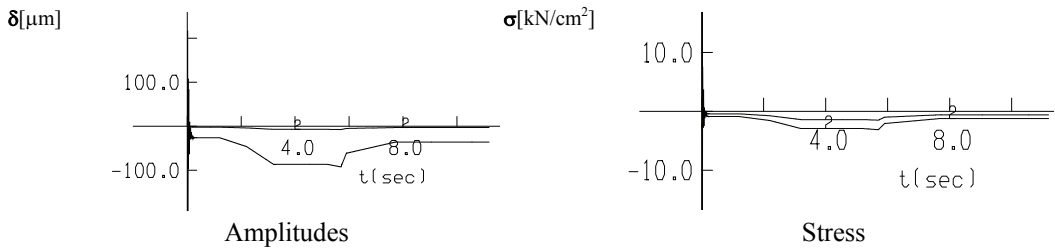


Figure 6.16. Response on the left shackle of one row

The smaller stress amplitude curve corresponds to the upper row of shackles.

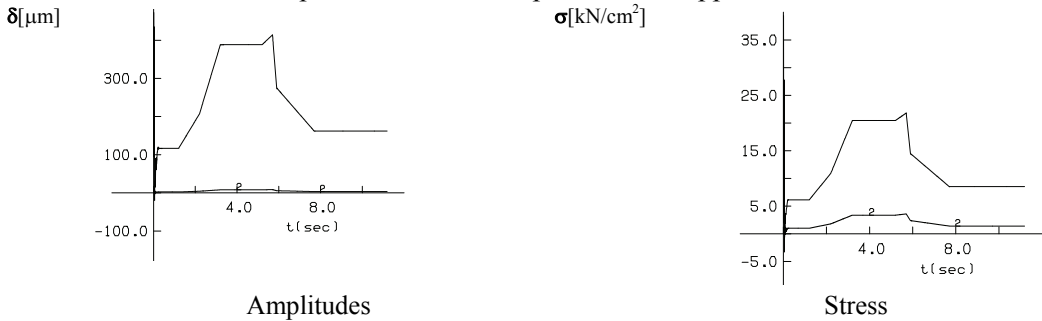


Figure 6.17. Response on the right shackle of one row

The influence of the compulsive force is reported for the right shackle of the chain. The lower row of the shackles is carrying impulsive force.

6.2. Experimental results and repair

Several strain gauges had been applied to measure the dynamic stresses on the frame and palette in the experimental testing (Fig. 6.18), and the clearly expressed neck followed by final fracture was found on the shackle (Fig. 6.19). Test was performed

during the operation under maximum loading of 2 tones. Lower line represents the stress values on the palette, and the upper line represents the stress on the neck of the right shackle in lover row (Fig. 6.20, Fig. 21).



Figure 6.18. The positions of the gauges

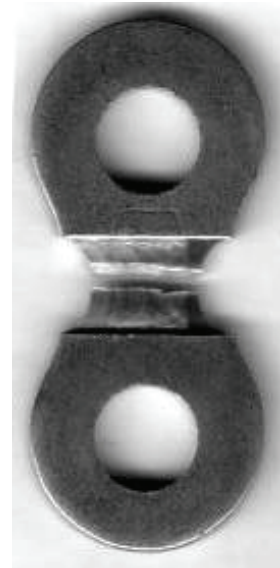


Figure 6.19. Fractured shackle

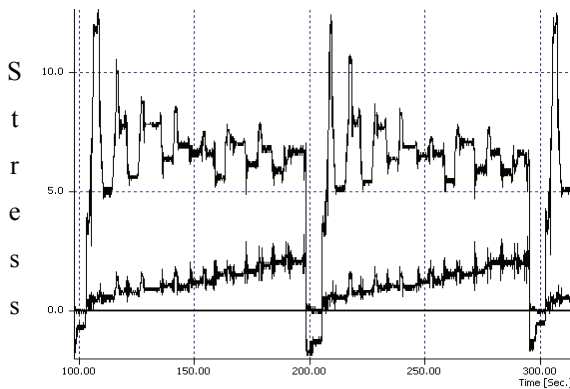


Figure 6.20: Dynamic stress on the shackle and the palette [kN/cm²]

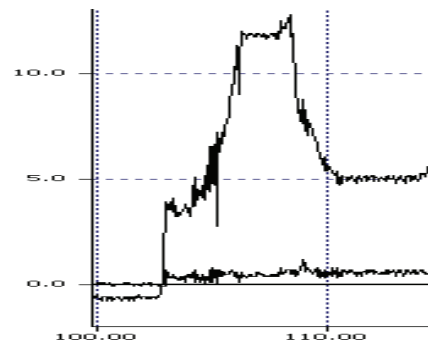


Figure 6.21: First impulse of one cycle, stress [kN/cm²]

The stress of 15 kN/ cm² in dynamic test,at the beginning of loading impulse, was found in the middle of the shackle and the maximum stress was six times higher (90 kN/cm²). In tensile test of shackle sample ultimate tensile stress of 100 kN/cm² was found.

After performed analysis and redesign of critical elements, new chain was produced and built-in. Redesigned chain is presented in Fig. 62. It is in successful exploitation for satisfactory long time.

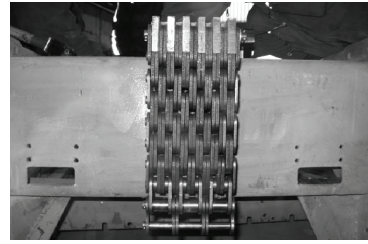
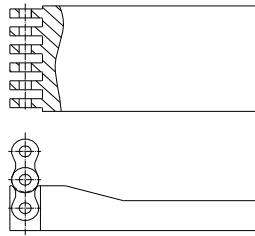


Figure 6.22: The change after reconstruction

7. DIAGNOSTICS OF DYNAMIC BEHAVIOUR OF DRIVE UNIT

Dynamic behaviour of drive unit B-1800 – Kostolac (Fig. 7.1) was performed in cooperation with the Faculty of Mining and Geology in Belgrade. Drive unit consists of three main parts: electromotor, gear box and momentum bar with corresponding supports.

Nominal power of the electromotor, produced by Sever – Subotica, is $P = 630$ kW, and the angular velocity is $n = 980$ o/min.



Figure 7.1: Drive unit B-1800 –Kostolac

7.1. Modelling and analysis of electromotor behaviour

Finite element model of electromotor is shown in Fig. 7.2, and found eigen frequencies are presented in Fig. 7.3. The influence of the coupling masses on the eigen-frequencies of electromotor, listed in Table 7.1, are used to draw diagram in. Fig. 7.3.

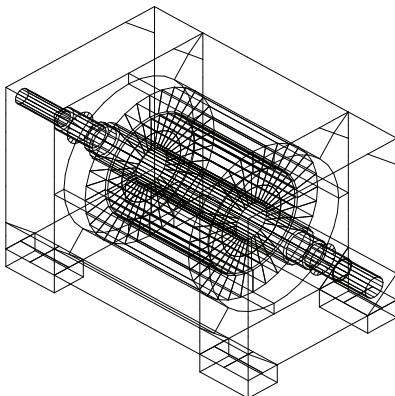


Figure 7.2: Model of electromotor

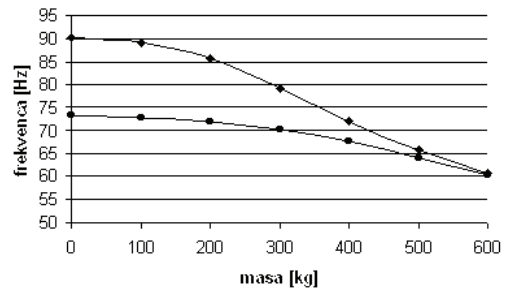
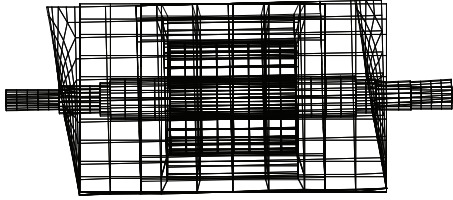


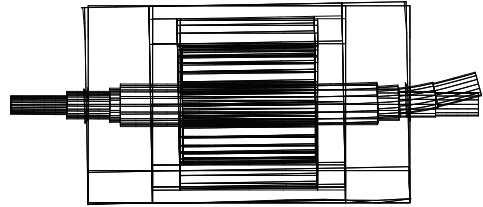
Figure 7.3: Eigen frequencies of electromotor as a function of coupling mass

Table 7.1: The influence of the coupling mass on the eigen-frequencies of electromotor

Mass	0 kg	100 kg	200 kg	300 kg	400 kg	500 kg	600 kg
First freq.	73.3 Hz	72.8 Hz	71.8 Hz	70.3 Hz	67.7 Hz	64.1 Hz	60.3 Hz
Second freq.	90.3 Hz	89.1 Hz	85.8 Hz	79.2 Hz	71.8 Hz	65.7 Hz	60.8 Hz



Coupling mass – 0 kg



Coupling mass –600 kg

Figure 7.4: Second mode of oscillation

Gear-box

Gear-box consists of: cover, input-shaft, middle-shaft and output-shaft. Dimension of the cover is 2550×1660×1060 mm.

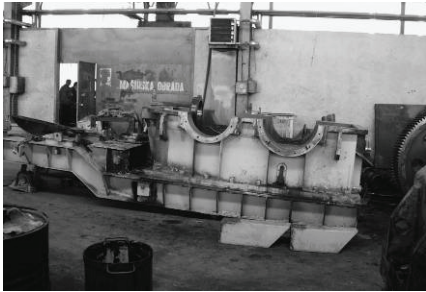


Figure 7.5: Lower part of the cover

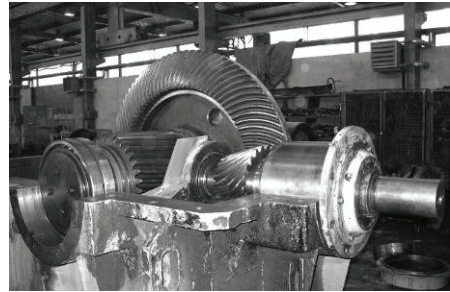


Figure 7.6: Shafts

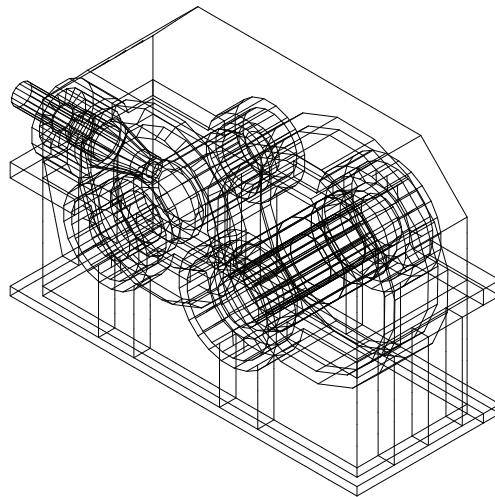


Figure 7.7: Model of the gear-box

Input-shaft of the gear-box is 960 mm length, changeable cross-section. Diameters on its ends are $\varnothing 150$ and $\varnothing 120$ mm.

Middle-shaft of the gear-box is 1100 mm length. Diameters of the shaft on its ends are $\varnothing 300$ mm and $\varnothing 290$ mm.

Output-shaft has length of 1050 mm and changeable cross-sections. Diameters of this shaft on its ends are $\varnothing 300$ mm and $\varnothing 390$ mm.

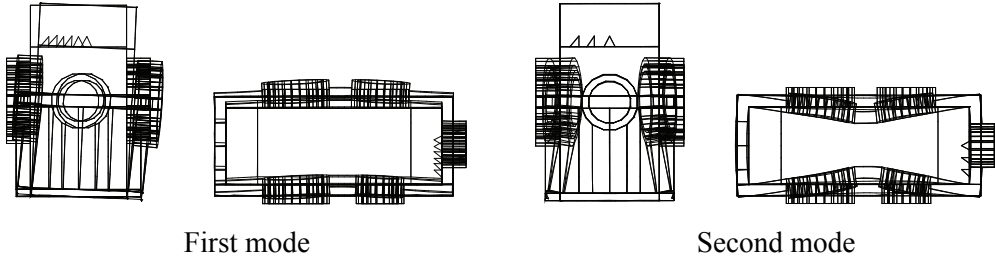


Figure 7.8: First and second mode of oscillations of the cover



Figure 7.9: First and second mode of oscillations of the input-shaft (coupling mass 500 kg)

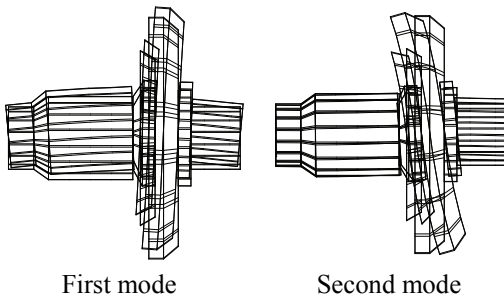


Figure 7.10: Amplitudes of middle-shaft

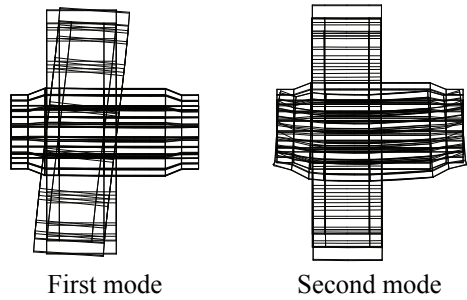


Figure 7.11: Amplitudes of output-shaft

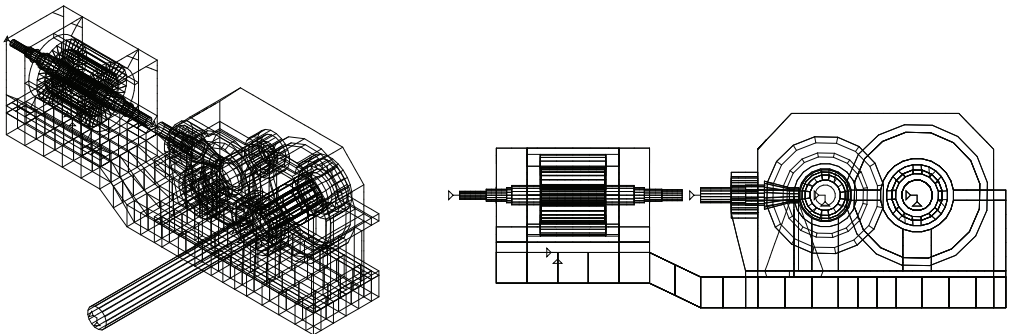


Figure 7.12: Drive unit

Table 7.2: Eigen frequencies of the elements of gear-box

Elements	Cover	Input shaft		Middle shaft	Output shaft
		0 kg	500 kg		
First frequency	15.8 Hz	165 Hz	3.5 Hz	89 Hz	61.2 Hz
Second frequency	23.6 Hz	303.6 Hz	25.1 Hz	139 Hz	110.8 Hz

The calculation was done for three cases:

1. without the influence of the couple,
2. a part of a coupling mass on the shaft of electromotor is 80 kg, and a part on a input-shaft of gear-box is 400 kg,
3. a part of a coupling mass on the shaft of electromotor is 100 kg, and a part on an input-shaft of gear-box is 500 kg.

Table 7.3: Eigen frequencies of the drive unit

	1. [Hz]	2. [Hz]	3. [Hz]	4. [Hz]	5. [Hz]
First case	23.7	27.4	33.3	35.5	36.8
Second case	14.2	20.3	22	23.3	27.3
Third case	13.2	18.9	20.4	23.3	27.3

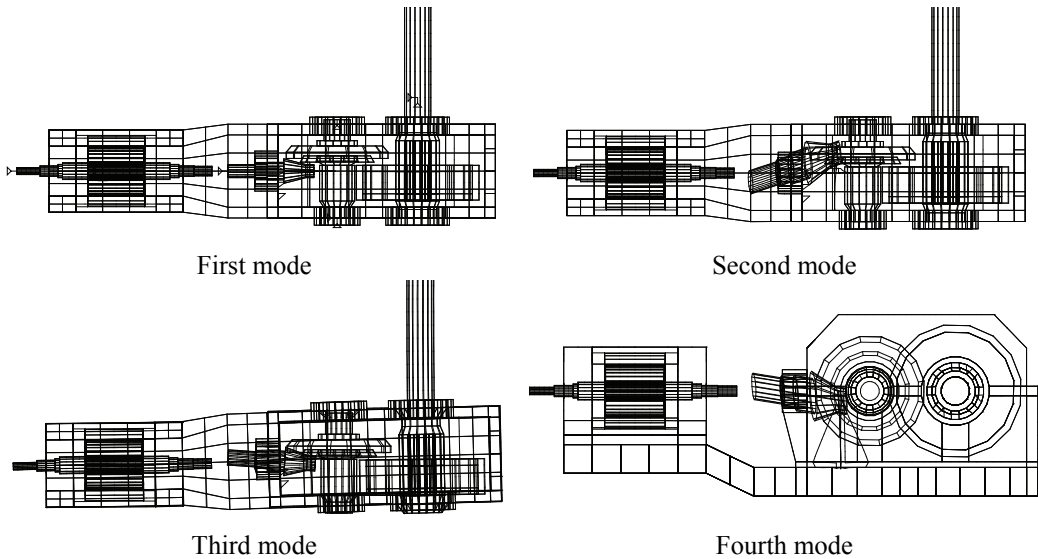


Figure 7.13: Amplitudes in first four modes of oscillations

CONCLUSION

Presented calculation is shown that the eigen frequencies of all shafts of a gear-box are high enough. Dynamic behaviour of electromotor is satisfied, as well behaviour of the momentum bar. The problem is immanent only in the input-shaft of the gear-box because of the influence of coupling. This influence is dominant in the first three modes.

REFERENCES

1. T. Maneski, 2008, Program Package "KOMIPS", Belgrade
2. T. Maneski, 1998, "Kompjutersko modeliranje i proračun struktura", Monografija, Mašinski fakultet, Belgrade
3. T. Maneski, V. Milošević-Mitić, D. Ostrić, 2002, "Postavke čvrstoće konstrukcija", Monografija, Belgrade
4. T. Maneski, 2002, "Rešeni problemi čvrstoće konstrukcija", Belgrade
5. [5] T. Maneski, 2004, "Stress Analysis for Structural Integrity Assessment", Paper in Monography IFMASS 8, From fracture mechanics to structural integrity assessment, editor S. Sedmak, Z. Radaković, DIVK and TMF, Belgrade
6. T. Maneski, D. Ignjatović, 2004, "Dijagnostika čvrstoće konstrukcija", Integritet i vek konstrukcija, Vol. 4, No. 1, Belgrade
7. T. Maneski, D. Ignjatović, 2004, "Sanacije i rekonstrukcije rotornih bagera", Integritet i vek konstrukcija, Vol. 4, No. 1, Belgrade
8. T. Maneski, D. Ignjatović, "Sanacije i rekonstrukcije transportera i odlagača", Integritet i vek konstrukcija, Vol. 4, No. 1, Belgrade
9. N. Andjelic, T. Maneski, V. Milošević Mitić, 2006, "The Influence of the Coupling on the Dynamic Behaviour of Electromotor", VII MAREN, Belgrade, pp. 336-341
10. V. Milošević Mitić, N. Andjelic, 2006, "Dynamic behaviour of the elements of gear-box", XVIII International Conference on "Material handling constructions AND Logistics", Belgrade, pp. 273-276
11. T. Maneski, V. Milošević Mitić, D. Ignjatović, N. Anđelić, 2007, "Diagnostic of the Dynamic Behaviour of Drive Unit; 1st International Congress of Serbian Society of Mechanics, Kopaonik, Proceedings, pp. 435-440
12. T. Maneski, V. Milošević Mitić, N. Andjelić, 2008, "Numerical and experimental diagnostics of the behaviour of the palette-pack machine", Section in Monography Machine Design 2008, ADEKO, Faculty of Technical Sciences, Novi Sad, pp. 133-13

DYNAMIC CHARACTERISTICS MODIFICATION IN THE MECHANICAL STRUCTURES REANALYSIS

Nataša Trišović

*University of Belgrade, Faculty of Mechanical Engineering, Belgrade, Serbia
ntrisovic@mas.bg.ac.rs*

1. INTRODUCTION

Dynamic response of mechanical systems depends of structural parameters. In mechanical structures reanalysis objective is to evaluate the structural response for successive modifications in the design avoiding the difficult solution of the modified equations. The structural modifications may be required by external factors or by the designer in order to improve the characteristics of structure response (eigenvalues and eigenvectors). Modification of dynamic characteristics means change of corresponding design variables to get desired dynamic behaviour of a structure. The design variables depend on the type of optimization problem. In the design of structural components, such as stiffened panels and cylinders, the design parameters represent the size and shape of stiffeners and their spacing, and the plates or shell thickness. The thickness of plates, cross-section areas of bars, and areas, moments of inertia, and torsion constants of beams represent the values which should be considered for modification. Joints and members could be eventually added or exuded during reanalysis process, modifying in this way the geometry of the structures. A simple scheme of dynamic modification during reanalysis is presented in Fig. 1.

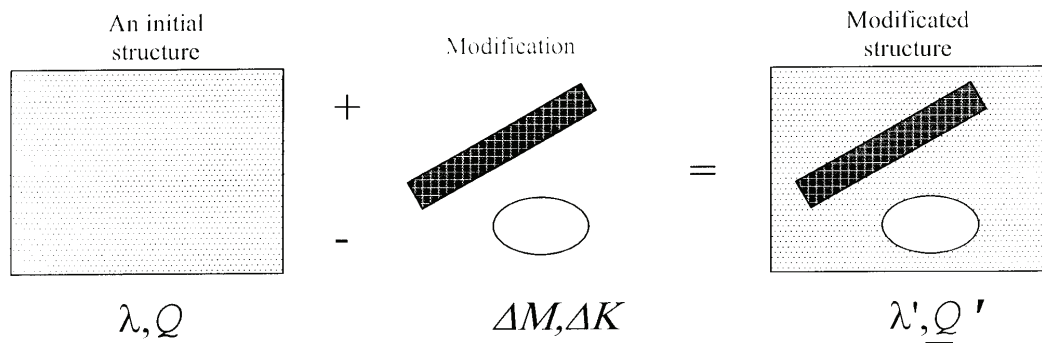


Figure 1: A simplified scheme of dynamic modification

Reanalysis methods might include following activities:

- (a) Modification in the geometry, with no further change in the number of degrees of freedom.
- (b) Modification of design variables (mass, damping and stiffness).
- (c) Increase or decrease of the number of degree of freedom (DOF) by changing the supporting system, and addition or deletion of joints and members.
- (d) Selection of new material for critical components, if possible.

Reanalysis methods mostly cannot involve the last two modifications, because they imply a change in the dimension of the system due to addition or deletion of degrees of

freedom or change of material. Several procedures for the dynamic reanalysis of structures concern the changes encountered by the dynamic properties of the structures when a modification is involved. Usually, the dynamic properties under consideration are the modal parameters, and for that several studies have been addressed to the modal reanalysis of linear structures. The perturbation approach has been utilized by Inamura /1/ and by Ki /2/ for the evaluation of the approximate eigen properties of the modified structural system. Rayleigh's method has been utilized by Wang and Pilkey /3/ and Hodges /4/ for the evaluation of the approximate eigenvalues and eigenvectors of the modified structure, taking into account the results of the initial modal analysis of the original structure. Nair, Keane and Langley /5/ proposed a method to improve first-order approximation of eigenvalues and eigenvectors. The reanalysis problems attract the attention recently, and many papers are devoted to this topic /6-28/.

The main goal of dynamic reanalysis is to provide numerical procedures to evaluate the structural response after modifications of design variables. The general problem of dynamic reanalysis is presented in Fig. 2 and consists of three important aspects.

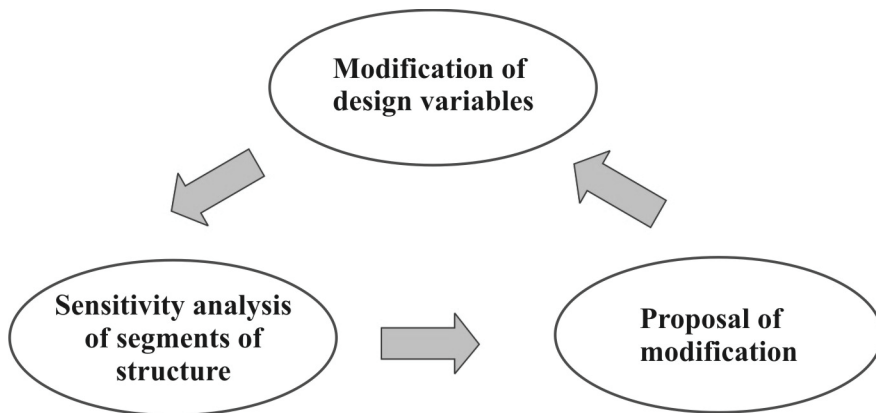


Figure 2: Triangle of dynamic reanalysis

The aim of this presentation is to show how the change of support conditions can improve dynamic characteristics of a structure. Structural model is the most important prerequisite for this analysis, because the distribution of potential and kinetic energy in every finite element (FE) of model is necessary for the evaluation of reanalysis success.

Appropriate finite element or analytical model of mechanical structure is important for the successful structural integrity analysis. In practice, a high degree of confidence can be achieved with such an analytical FE model when its dynamic response is confirmed by an experimental analysis. However, updating the FE model or identifying the analytical model directly is usually not the main objective of structural vibration analysis because there are many situations when the dynamic response of the mechanical structure does not satisfy the requirement specified by the structural analyst (designer). In such situations, the dynamic response of the mechanical structure has to be altered either by controlling the input data to the structure, or by changing the dynamic characteristics of the structure. The accepted inputs often result from interaction between the structure and environment and for that can't be easily controlled. When this is the case, the ability to alter the structural response by redesigning the dynamic characteristics of the structure is of prime significance. The use of structural reanalysis techniques to obtain the optimum condition of FE model of a mechanical structure has been extended considerably in recent years.

The optimal design of structures with frequency constraints is extremely useful in manipulating the dynamic characteristics in different ways. For example, in most low-frequency vibration problems, the response of the structure to dynamic excitation is primarily a function of its fundamental frequency and mode shape. In such cases, the ability to manipulate the selected frequency can significantly improve the performance of the structure. Similarly, the aero-elastic characteristics of an aircraft wing which primarily depends on its torsional and bending properties can be in best way studied by the torsional and bending modes.

Many different techniques are available, enabling successful application to the dynamic reanalysis of mechanical structures. One of the most popular is the sensitivity analysis which has been developed and applied by several experts in the general eigenvalue problem /29-34/, and, more specifically, in the applications of structural dynamic modification analysis, Ref. /35-38/.

The areas where sensitivity analysis has been successfully applied include

- system identification,
- development of insensitive control systems,
- use in gradient-based mathematical programming methods,
- approximation of system response to a change in a system parameter, and
- assessment of design changes on system performance.

In this area, both first- and higher-order eigenvalue and eigenvector sensitivities have been investigated in order to improve the prediction regarding the response of a modified structure based on known of its spatial and modal original properties, or initial, unmodified, state. The sensitivity analysis of a mechanical structure is based on a Taylor's expansion of eigenvalues and eigenvectors of the unmodified structure. Traditionally, a truncated Taylor or matrix power series evaluated at a nominal design point is used to approximate the eigen parameters of modified structures /21,22/. Previous studies indicated that the computation of the higher-order terms of these series is difficult and time consuming, so the effectiveness of this method is limited to small modifications. Even the use of higher-order terms in the local approximation series can't guarantee convergence for moderate to large perturbations in the structural parameters. The implication of this observation in the context of structural optimization is that limits posed at severe level have to be imposed additional troubles to ensure requested convergence in design. Very few studies in the literature have addressed the structural dynamic reanalysis problem for moderate to large modifications in the structural parameters. Direct and iterative approaches present two classes of them, currently mostly applied. The objective of most direct approaches is to increase the range of validity of local approximation techniques. Inamura /1/ proposed an approximate procedure in which the eigen pair perturbation equations are interpreted as differential equations in terms of the perturbation parameters. A procedure using the eigen sensitivity equations was developed by Pritchard and Adelman /24/ based on a similar approach.

The sensitivity method is a best representative of the updating approach which allows selection of updating parameters, but does not require full experimental evidence. For that, this method seems to be suitable for updating of large models. Also, it is worth noting that updating models based on control methods, such as eigen structure assignment method proposed by Minas and Inman /39,40/ are quite promising since they can be defined so that full experimental mode shape matrix is not requiring. The generally accepted perturbation procedure is presented in a diagram form in Fig. 3.

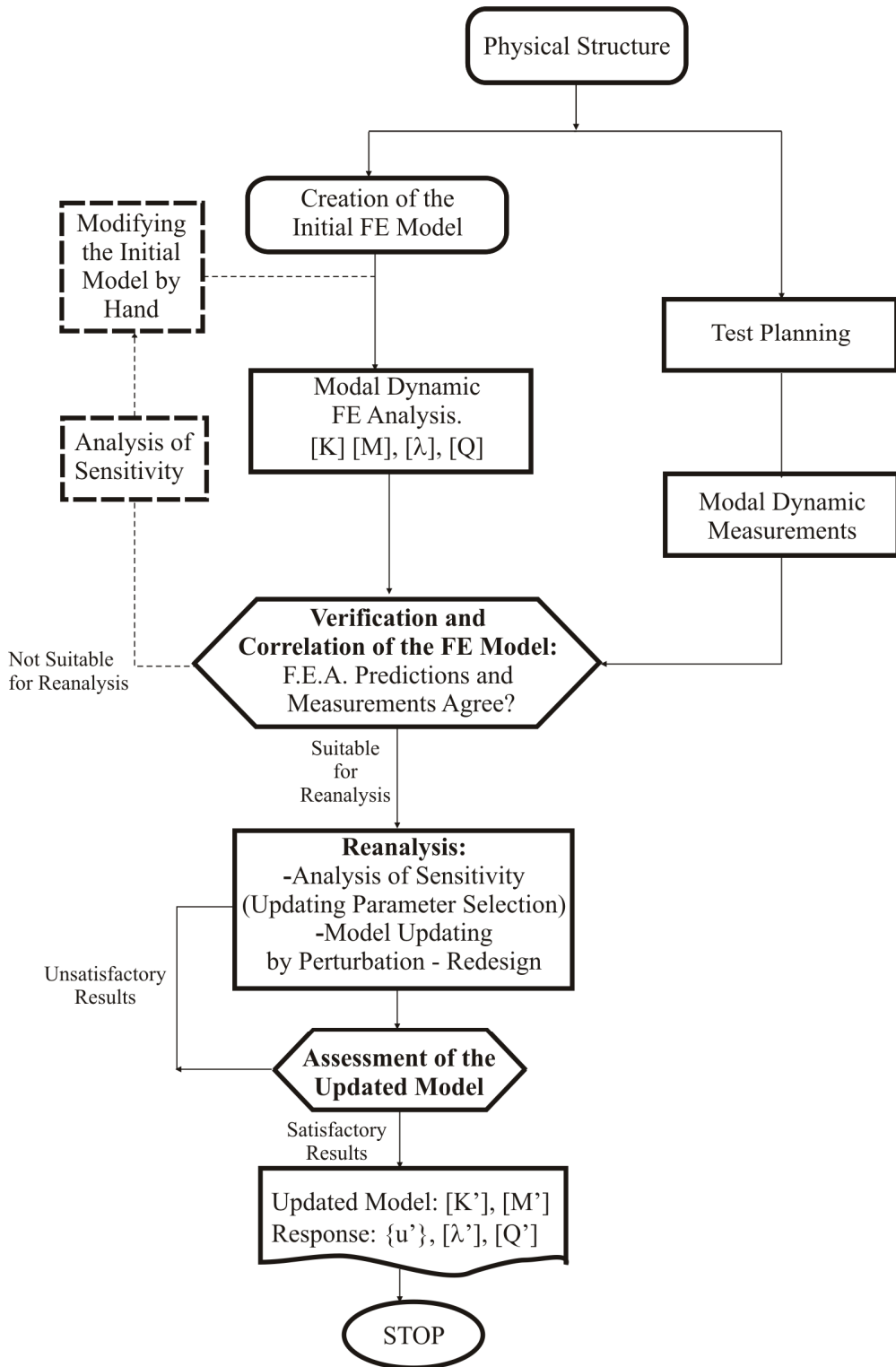


Figure 3: Flowchart of general perturbation

2. MODAL SENSITIVITY ANALYSIS – BACKGROUND AND SURVEY

It is generally accepted that sensitivity analysis can be applied as a valuable tool in structural reanalysis when sufficient modal properties are known, either through theoretical or experimental analysis. Modal sensitivities are the derivatives of the modal properties of a dynamic system with respect to chosen structural variables. There are two primary applications in the modal analysis. In the first case sensitivity data are used solely as a qualitative indicator of the location and approximate scale of design changes to achieve desired structural properties. The consequences of candidate design changes would then be evaluated using more exact methods. The second strategy uses the design sensitivities directly to predict the effect of proposed structural changes. The use of sensitivities in this fashion relies on the Taylor's series expansion of matrix, with the usual implications of convergence and truncation errors. Use only of first order design sensitivities assumes implicitly that the second (and higher) order derivatives are negligible. The use of these second order sensitivities as suitable criteria for the acceptability of first order sensitivities for predictive analysis can be interesting in some detail. Sensitivity analysis may be applied to candidate design modifications distributed across a number of degrees of freedom of the structure, but is limited in scale.

Modal design sensitivities are the derivatives of the eigen system of a dynamic system with respect to those variables which are available for modification by the designer. A typical modification would be the change in diameter of a circular section. This would affect both the mass of the section, proportional to the square of the diameter, and its stiffness, which depends on the second moment of area of the section. The change in length would have a mass effect directly proportional to length, but a stiffness change depending on the cube of length. Changing material would similarly affect mass, stiffness and damping. Shape sensitivity analysis of physical systems under dynamic loads may be important from different points of view to:

- understand and model the system's behaviour better with respect to shape;
- optimize the physical shapes of desired systems responses in given time interval, or
- identify shapes by utilizing the system's response measured in time.

3. PROBLEM STATEMENT

One important task in design of structures exposed to dynamic load is to increase the eigen frequency values outside the frequency range of forced load, which can damage the structure by the effect of resonance. Consequently, the main goal of dynamic optimization is to increase natural frequencies and to enlarge the difference between them. Some information should be available before setting up the finite elements (FE) model. The first pack of information includes referent information about the structure: size, material, and boundary conditions. Using this information it is possible to form a final model with all elements, which is at the same time a FE model prepared to start in analysis.

An output there are i pairs of eigenvalues λ_i and eigenvectors $\{\underline{Q}_i\}$ which are very important for a dynamic analysis. It was already mentioned that eigenvalues and the oscillation shapes in some construction, which can be obtained from differential equations

$$[M] \cdot \left\{ \ddot{\underline{Q}}(t) \right\} + [K] \cdot \left\{ \underline{Q}(t) \right\} = \{0\}, \text{ in the form } ([K] - \lambda_i \cdot [M]) \cdot \left\{ \underline{Q}_i \right\} = \{0\} \quad (1)$$

are important for the analysis.

Distribution of kinetic and potential energy in the main mode shapes is the crucial for the modification. Therefore, it is necessary to know potential energy of the system

$$E_{p,r} = \frac{1}{2} \{\underline{Q}_r\}^T [K] \{\underline{Q}_r\} \quad (2)$$

and also kinetic energy
$$E_{k,r} = \frac{1}{2} \lambda_r \{\underline{Q}_r\}^T [M] \{\underline{Q}_r\} \quad (3)$$

for the r^{th} shape of oscillation.

Analysis is directed to the elements of structure which have the best energy percentage at some shapes, in order to be monitored. These elements are the most sensitive to the change of design parameters (especially the eigenvalues). In order to accurately diagnose this sensitivity for all elements, arbitrarily modified structural model is formed or the model of just one particular, the most sensitive element. The crucial condition of the statements is that these changes must be very small. These small changes purport the change of some structural variable in the respective elements, being most sensitive.

A series of structural variables depend on the kind of considered construction. This might be: thickness of the plate or beam, density of the material, length of finite element. Then, the expression for eigenvalue increment can be used with a sufficient confidence:

$$\frac{\Delta \lambda_i}{\lambda_i} = \frac{\frac{1}{2} \{\underline{Q}_i\}^T [\Delta K] \{\underline{Q}_i\} - \frac{1}{2} \lambda_i \{\underline{Q}_i\}^T [\Delta M] \{\underline{Q}_i\}}{\frac{1}{2} \lambda_i \{\underline{Q}_i\}^T [M] \{\underline{Q}_i\}} \quad (4)$$

Denominator in above expression remains constant, insomuch that increment of eigenvalue depends only on numerator that is the difference $\Delta E_{p,r} - \Delta E_{k,r}$. From this stage of the procedure next values can be determined:

- eigenvalues of the modified structure or respective element, λ_i' ; and
- eigenvectors of the modified construction $\{\underline{Q}_i'\}$; as well as

increments of the potential and kinetic energy, $\Delta E_{p,r} - \Delta E_{k,r}$

Dynamic analysis and model diagnostics include analysis and model behaviour explanation and its modification, if necessary. Analysing the effect of energy distribution on the main mode shapes of construction elements, few specific cases can be recognized. Using these cases, the algorithm for reanalysis of similar structure can be made /12/.

The specific cases can be classified in following groups:

(i) The elements with kinetic and potential energy, which values are negligible comparing to the other elements. These elements require a detailed analysis. It is important to say that these elements are not convenient for modification, since they are not sensitive to changes. The elements close to supports of a simple beam or thin plate supported in a simple way are typical example for this group.

(ii) Elements with the kinetic energy greater than the potential energy. These elements have large displacements, for example elements at the end of cantilever beam. It is recommended to place the new support, if it is possible, or decrease existing mass or select a new material of lower density.

(iii) Elements with potential energy greater than the kinetic energy. In this case stiffness should be increased, by increasing moment of inertia of corresponding section. Proper example here is fixed element. This change can produce appropriate eigenvalue.

(iv) Elements with kinetic and potential energy, which values are not negligible comparing to other elements. These elements are the most difficult to be reanalysed, but they are the most frequent. A simple supported beam between supports is typical example. Way of modification depends of the local situation. Based on analysed examples, one type of modification would be increasing stiffness on these elements without increasing mass, or just reducing mass, if possible. It is possible to achieve by involving elements with larger cross section moment of inertia without changing mass or involving elements with the same moment of inertia but allying another material. An alternative is to use new elements assuring increased stiffness, and with increased displacements the kinetic energy will be also increased. The basic aim of this modification is to enhance eigenvalues. If the energy increment is reduced, this procedure exhibited the convergence, as required as a proof for successful procedure.

4. EXAMPLES OF PERFORMED REANALYSIS

In this analysis thin plates have been considered. The plate, 100 cm x 100 cm in size, and 1 cm thick is considered as initial plate. It was supported by hinges on each side, (Fig. 3), or it was fixed along the sides (Fig. 4).

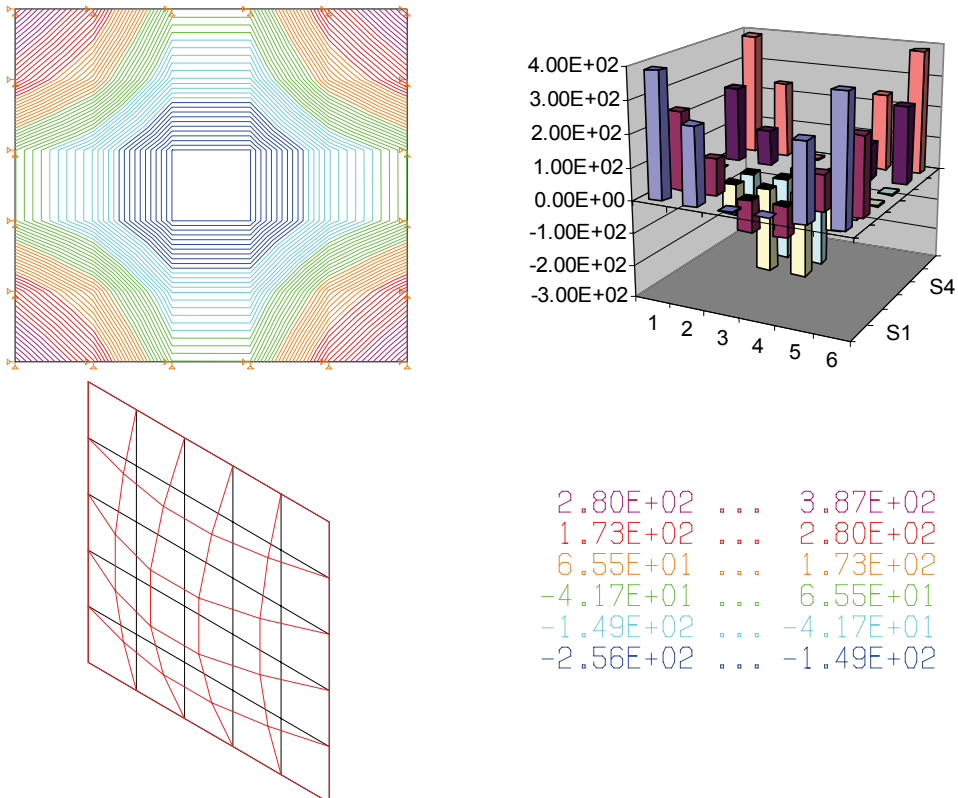
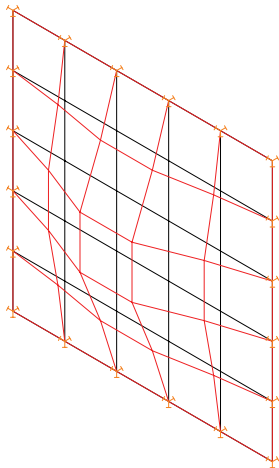
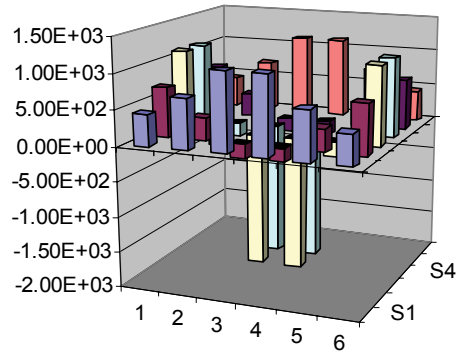
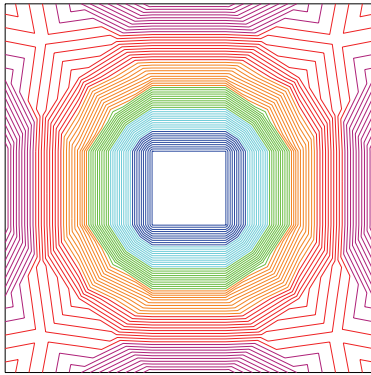


Figure 3: The square plate supported by hinges along the each side. Distribution of potential and kinetic energy increments, kNxcmm, for initial and arbitrary modified plate is presented. First frequency of the initial plate is $f_{01} = 48.63$ Hz, and for arbitrary modified plate $f_{01}' = 53.5$ Hz.



6.22E+02	...	1.12E+03
1.24E+02	...	6.22E+02
-3.74E+02	...	1.24E+02
-8.72E+02	...	-3.74E+02
-1.37E+03	...	-8.72E+02
-1.87E+03	...	-1.37E+03

Figure 4: The square plate fixed along the each side. Distribution of potential and kinetic energy increments, kNxcn, for initial and arbitrary modified plate is presented. First frequency of the initial plate is $f_{01} = 90.5$ Hz, and for arbitrary modified plate $f_{01}' = 99.6$ Hz.

The plate thickness was chosen as the design variable in the analysis, with the size 100 cm x 100 cm saved through the analysis. The effect of boundary condition was also considered, for both hinged (Fig. 3) and fixed supports (Fig. 4). Calculation of eigen pairs was performed using programme package KOMIPS /13/.

The modification consisted in arbitrary change of initial plate thickness uniformly by 10%. Potential and kinetic energies for modelled had been calculated using the Eqs. (1) to (4) and the differences in increment determined, as presented in Fig. 3 and Fig. 4. Based on obtained graphs for simple supported plate one can e concluded that elements near corners of the plate have the biggest positive difference, and by increased stiffness the dynamic behaviour is improved. The elements in the central part of the plate have the greatest negative difference. It can be noticed that both, potential and kinetic energies have the maximum values on this mode shape, what needs the more detailed reanalysis. However it can be proved that by increasing stiffness (increasing section thickness), and decreasing mass, the frequency will increase.

Analysing the fixed supported plate, stiffness should be increased on the elements which correspond the middle part of the side of square (the purple part on the graph, Fig.4), and at the central part of the plate, it is better to add elements with less mass and of greater stiffness.

The side walls of a plastic container used for transportation of parcels in aircraft industry prematurely failed due to excessive deflection (Fig. 5). In order to solve the problem dynamic behaviour of elements had been analysed on a proper model. The dimension of side wall were 295 x 142 x 196.5 mm. Performed analysis produced first three mode shapes (Fig. 5) of the plastic wall supported by hinges along the contour.

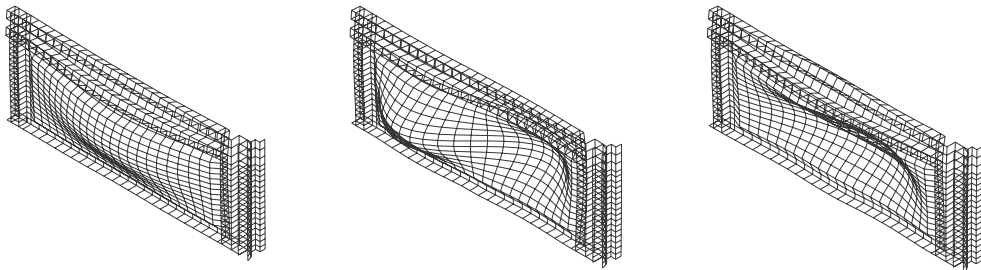


Figure 5: The first three mode shapes of the wall side of the container. Obtained frequencies are: $f_{o1} = 57.9 \text{ Hz}, f_{o2} = 97.4 \text{ Hz}, f_{o3} = 110 \text{ Hz}$

Two types of models were applied in the analysis. First one was initial, unmodified model, and second one was arbitrary uniformly modified model. It was required that the changes must be small. Distributions of the increment difference of potential and kinetic energies assessed by models in initial state and after arbitrary uniform modification of wall plate are shown in Fig. 6 for the first three mode shapes. This design of the wall enabled similar dynamic properties as in the thin plate and the introduction of fixed supports in different locations with the highest growth in kinetic energy enabled significant improved of dynamic behaviour of modified wall.

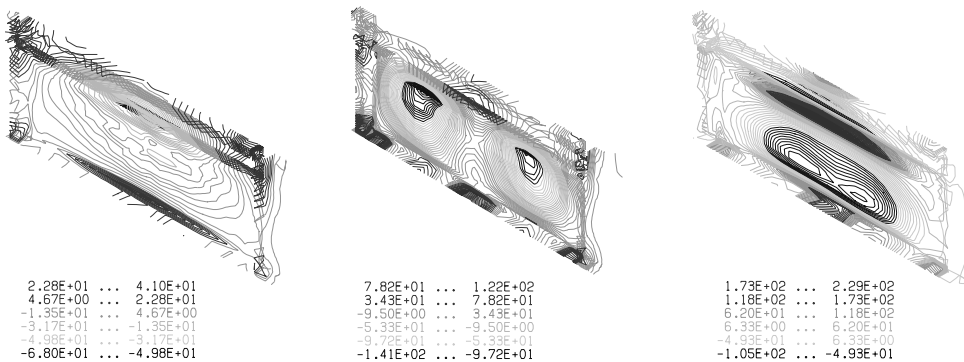


Figure 6: Distribution of potential and kinetic energies increments differences ($\Delta E_p - \Delta E_k$), in initial wall design and after arbitrary uniform modification for the first three mode shapes, kNxcmm

The next example of successful mechanical structure reanalysis is the dynamic behaviour of the intake structure of the piping system in a compressor station (Fig. 7).

Based on energy distribution in structural segments and by modification involved constraints it was possible to find out that unacceptable dynamic response of pipeline design is caused by several excitation frequencies closed to the natural frequencies, close to the resonant regime. Only a small disturbance is sufficient to produce the damage of steam line structure. The causes of unacceptable behaviour of the steam line in service were geometry design and applied supporting system. It was not possible to eliminate

completely unfavourable dynamic behaviour, but some improvement of the dynamic properties could be achieved changing the supporting system design, performed by modification of boundary conditions of the steam line structure.

The selected main mode shapes and the values of the natural frequencies of the pipeline structure in a compression station, obtained in reanalysis are shown in Fig. 7. The based excitation frequency produced by rotation of the compressor shaft is at the level of 7.2 Hz. It is to take care of derived excitations which obtained by an integer multiplier from the basic eigenvalue.

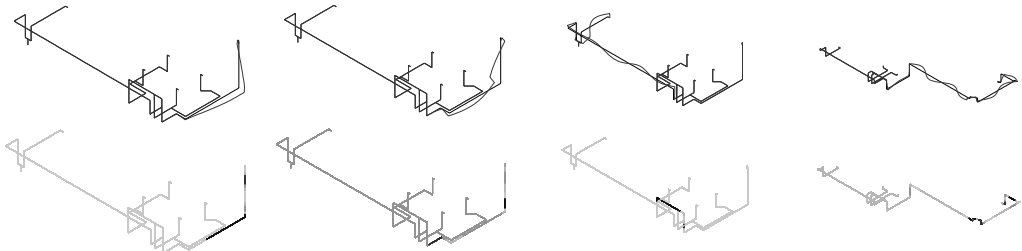


Figure 7: Sixth, seventh, sixteenth and seventeenth mode shapes of the intake structure of the piping in compressor station and corresponding diagrams of increment difference distribution of potential and kinetic energies ($\Delta E_p - \Delta E_k$)

5. CONCLUSIONS

Critical structures regarding dynamic behaviour in service should be reanalysed in order to find out the best approach for properties improving. Studying the dynamic behaviour of structures the responses introduced by changes in its shape, size or selected elements materials can be predicted. The main goal of dynamic optimization is to increase natural frequencies and to enlarge the difference between them. Especially, the lowest frequencies are the most interesting and with the values close to frequency excitation force in the system.

Presented approach is applicable for:

- I The elements with kinetics and potential energy, which values are negligible comparing to other elements.
- II Elements with the kinetics energy greater than the potential energy.
- III Elements with the potential energy greater than kinetics.
- IV Elements with kinetics and potential energy, which values are not negligible comparing to other elements.

Presented examples revealed the possibility to modify the system and improve its behaviour after detailed structural reanalysis, considering the graphs of potential and kinetic energy increment difference distribution and obtained modes shape, what could be significant help in dynamic structures service.

REFERENCES

1. Inamura, T., Eigenvalue Reanalysis by Improved Perturbations, International Journal of Numerical Methods in Engineering, Vol. 26, No. 1, 1988, pp. 167-181
2. Ki, I.K., Nonlinear Inverse Perturbation Method in Dynamic Redesign, PhD, Thesis, Michigan University, USA, 1983.
3. Wang, B.P., and Pilkey, W.D., Eigenvalue Reanalysis of Locally Modified structures Using a Generalized Rayleigh's Method, AIAA Journal, Vol. 24, No. 6, 1986, pp. 983-990

4. Hodges, D.H, Improved Approximations via Rayleigh's Quotient, *Journal of Sound and Vibration*, 1991, pp.155-164, 1997.
5. Nair, B.P., Keane, A.J., and Langley, R.S., Improved First-Order Approximation of Eigenvalues and Eigen Vectors, *AIAA Journal*, Vol. 36, No. 9, September 1998, pp. 1722-1727.
6. Grandhi, R.V., Structural optimization With Frequency Constraints – A Review, *AIAA Journal*, Vol. 31, No.12, December 1993, pp. 2296-2303.
7. Tong, W.H., Jiang, J.S., and Liu, G.R., Solution Existence of the Optimization Problem of Truss Structure with Frequency Constraints, *Int. Journal of Solids and Structures*, Vpol. 37., No. 30, 2000, pp. 4043-4060
8. Wang, D., Zhang, W.H., and Jiang, J.S., Truss Optimization on Shape and Sizing with frequency Constraints, *AIAA Journal*, Vol. 42, No. 3, 2004, pp. 622-630
9. Trišović, N., Sensitivity Analysis in Structural Dynamic, XXXII JUPITER Konferencija, Zlatibor, 09-11.05.2006.
10. Trišović, N., Maneski, T., Šumarac, D., Golubović, Z., An Example for Structural Dynamic Modification, Scientific Conference „Savremeni problemi u građevinarstvu“, Subotica, 02-03. June 2006.
11. Trišović, N., Maneski, T., Šumarac, D., Reanalysis in Structural Dynamics, SEECCM06, Kragujevac, 28-30 June 2006.
12. Trišović, N., Modification of the Dynamics Characteristics in the Structural Dynamic Reanalysis, PhD Thesis, Belgrade, November 2007.
13. Maneski, T., Contribution to Development of Design via Computational Modelling of Supporting Structure of Machine Tools, Faculty of Mechanical Engineering, Belgrade, PhD, Thesis, 1992.
14. N. Trišović, T. Maneski, D. Šumarac, Z. Golubović: “Beam Optimization on Shape and Boundary Conditions with Frequency Constraints“, In Proceedings:1st Int. Cong. of Serbian Soc. of Mech., Ed. D. Šumarac & D. Kuzmanović, pp.557-563, 2007.
15. N. Trišović, „Eigenvalue Sensitivity Analysis in Structural Dynamics“, *FME Transactions*, Volume 35, No 3, pp. 149-156, Beograd, 2007.
16. Trišović, N., “Modification of the Dynamics Characteristics in the Structural Dynamics Reanalysis”, *Facta Universities, Series Mechanical Engineering*, Vol.5, No 1, pp. 1 – 9, Niš, 2007
17. Trišović, N., Maneski, T., Šumarac, D., Golubović, Z.: “An Example For Structural Dynamic Modification“, *Savremeni problemi građevinarstva, Međunarodna konferencija, Građevinski fakultet Subotica*, 2, 3 jun, 2006.
18. Trišović, N., Maneski, T., „The Influence of the Weight of Coupling on the Dynamic Behaviour of Shaft of Electromotor“, *Proceedings of the VII International Symposium „MECHANIZATION AND AUTOMATION IN MINING AND ENERGETICS“*, Belgrade, September, 28-29, 2006.
19. Trišović, N., “Modal Sensitivity Analysis. Theoretical background”, *Proceedings of the 6th International Conference “Research and Development in Mechanical Industry”*, RaDMI 2006.,13-17. September 2006, Budva, Montenegro
20. Trišović, N., Maneski, T., Šumarac, D., Golubović, Z.: The Influence of the Supporting Manner to the Dynamic Behaviour of the Mechanical Systems, *SEECCM 2009, 2nd South-East European Conference on Computational Mechanics*, An IACM-ECCOMAS Special Interest Conference, M. Papadrakakis, M. Kojic, V. Papadopoulos (eds.), Rhodes, Greece, 22–24 June 2009
21. Nataša Trišović, Taško Maneski, Aleksandar Sedmak, Dragoslav Šumarac, Modification of the Dynamics Characteristics in the Structural Dynamic Reanalysis, *7th EUROMECH Solid Mechanics Conference*, J. Ambrósio et.al. (eds.), Lisbon, Portugal, September 7-11, 2009
22. Khot, N.S. *Optimization of Structures with Multiple Frequency Constraints*, *Computers and Structures*, Vol. 20, No. 5, 1985, pp. 869-876.

23. Levy, R., and Chai, K., *Implementation of Natural Frequency Analysis and Optimality Criterion Design*, Computers and Structures, Vol. 10, 1979, pp. 277-282.
24. Pritchard, J.I., and Adelman, H.M., *Differential Equation Based Method for Accurate Modal Approximations*, AIAA Journal, Vol. 29, No.3, 1991, pp. 484-486.
25. Sadek, E.A., *Dynamic Optimization of Framed Structures with Variable Layout*, International Journal for Numerical Methods in Engineering, Vol. 23, No. 7, 1986, pp. 1273-1294.
26. Young, J.W., and Christiansen, H.N., *Synthesis of a Space Truss Based on Dynamics Criteria*, Journal of the Structural Division, ASCE, Vol. 92, No. ST6, Dec, 1966.
27. Chattopadhyay, A., and Walsh, J.L., *Minimum Weight Design of Rotor Blades with Frequency and Stress Constraints*, AIAA Journal, Vol. 28, No. 3, 1990, pp. 565-567.
28. Cheng, K., and Gu, Y., *Sequential Quadratic Programming and Dynamic Optimal Design of Rotating Blades*, Journal of Structural Mechanics, Vol. 11, No. 4, 1983-84, pp. 451-464
29. Rosenbrock, H.H., *Sensitivity of an Eigenvalue to Changes in the Matrix*, Electronics Letters, Vol. 1, 1965, pp. 278-279
30. Reddy, D.C., *Sensitivity of an Eigenvalue of a Multivariable Control System*, Electronics Letters, Vol. 2, 1966, pp. 446
31. Rogers, L.C., *Derivatives of Eigenvalues and Eigenvectors*, AIAA Journal, Vol. 8, 1970, pp. 943-944
32. Vanhonacker, P., *Differential and Difference Sensitivities of Natural Frequencies and Mode Shapes of Mechanical Structure*, AIAA Journal, Vol. 18, 1980, pp. 1569-1572
33. Brandon, J.A., *Strategies for Structural Dynamics Modifications*, John Wiley, New York, 1990.
34. Plaut, R.H. and Huseyin, K., *Derivatives of Eigenvalues and Eigenvectors in Non-Self-Adjoint Systems*, AIAA Journal, Vol. 11, 1973, pp. 250-251
35. Rudisill, C.S., *Derivatives of Eigenvalues and Eigenvectors for a General Matrix*, AIAA Journal, Vol. 12, 1974, pp. 721-722.
36. Belle, H.V., *Higher Order Sensitivities in Structural Systems*, AIAA Journal, Vol. 20, 1982, pp. 286-288.
37. Skingle, G.W. and Ewins, D.J., *Sensitivity Analysis using Resonance and Anti-resonance Frequencies – A Guide to Structural Modification*, Proc. of the 7th Int. Modal Analysis Conf., 1989.
38. Lim, K.B., Junkins, I.L. and Wang, B.P., *Re-examination of Eigenvector Derivatives*, AIAA I. Guidance, Vol. 10, 1987, pp. 581-587.
39. Minas, C. and Inman, D.J., *Matching Finite Element Models to Model Data*, ASME Journal of Vibration and Acoustics, Vol. 112, 1990.
40. Inman, D.J. and Minas, C., *Matching Analytical Models with Experimental Modal Data in Mechanical Systems*, Control and Dynamics Systems, Vol. 37, 1990.

MODERN APPROACH TO CONTROL AND NONDESTRUCTIVE TESTING METHODS

Miodrag Kirić

Innovation Center of Mechanical Engineering Faculty, Belgrade, Serbia

mkiric@mas.bg.rs

Milesa Srećković

Business and Technology Incubator of Technical Faculties, Belgrade, Serbia

1. INTRODUCTION

Non-destructive inspection (NDI) is an important procedure for quality control and safe operation of structures and also for the assessment of its life span. Important defects may be cracks or corrosion pits in welds and castings, or variations in material properties that can lead to loss of strength or in-service failure.

Improper design may lead to excessive stress in component. Variable and impact loadings must also be considered since they contribute to failure by fracture or fatigue.

Classical non-destructive testing (NDT) methods have been properly applied for inspection during manufacturing, maintenance and repairing of structures and equipment in Serbia. Anyhow, permanent development offers new NDT methods. Special attention is paid here to three of them: global positioning system (GPS), ultrasonic testing (UT) and laser techniques, but some other are also discussed.

The construction of planned structures in Belgrade and Serbia, such as high buildings, bridges and metro, as well their maintenance, demand for monitoring using proven, but also some new techniques. The primary function of monitoring is to ensure the safety and long life of a structure, including high management and maintenance level. Monitoring must enable the timely detection of any damage of the structure, assess its significance and, if necessary, to implement corrective measures. The monitoring program is also important in construction phase, enabling verification of design concept and construction process, having in mind that defects are induced mostly during construction. Frequently, monitoring data are necessary for controlled life extension of structures approaching the end of their use or in the case of major repair, enabling safe operation of structures and the postponement of major investments.

Accordingly, monitoring includes various NDI methods during:

1. construction of a new structure;
2. testing for the structure acceptance;
3. exploitation for regular and requested exceptional inspection;
4. disassembling of the structure.

The choice of NDT and NDI methods should take into the account the structure type, loads and materials used. In the case of bridges, introducing data today are based almost entirely upon a visual inspection. In that, deterioration that does not manifest visible form is neither detected nor quantified. Quantitative data of NDT and NDI about structure state are required in the form which can be transmitted wireless to the server. This is important for hidden damages, like corrosion of reinforcement in concrete or cumulative fatigue cracks in steel bridges. Vibrations, deflection and distorsion should also be monitored.

Large structures, e.g. long bridges, towers and tall buildings, may be exposed to vibration and displacement during the earthquake, temperature change, variable or impact loading and strong wind, like typhoon. Climate changes are also important. To measure the structural vibration and displacement some classical measurement methods, such as accelerometer, strain gauges, linear variable displacement transducers (LVDT) and total stations are common tools for experts involved in monitoring. Laser interferometer and electronic distance measurement instruments are also adopted for this purpose. Bridge monitoring is now very important to transportation authorities in all countries.

Monitoring of structure is evidently important, for both safety and planning of maintenance and repair. The structures and equipment are today exposed to high loading in order to regain cost competitiveness: trains are designed for higher speeds, requiring that the tracks conform to more severe standards for rail alignment, mechanical loads and working pressures in internal combustion engines are increasing and the requirements for pressure equipment are very strict. According to the Pressure equipment directive (97/23/EC) the products should not endanger working personnel, environment and population. A crack in a welded joint can lead to a critical failure with a tremendous destroying capacity for a large vessel, and heavy consequences to humans, property and natural environment. Pressure equipment must be designed, manufactured and checked, applicable equipped and installed in such a way as to ensure its safety when put into service in accordance with the manufacturer's instructions, or in reasonably foreseeable conditions. On the other hand, mechanical loads and working pressures in pressure vessels are increasing for higher energy efficiency and cost competitiveness.

2. GLOBAL POSITIONING SYSTEM (GPS) TECHNIQUE

Global positioning system (GPS) is a satellite-based navigation system made up of a network of 24 satellites placed into orbit by the U.S. Department of Defence (NAVSTAR is the official U.S. Department of Defence name for GPS). It was originally intended for military applications, but in the 1980s, the government made the system available for civilian use. System works in any weather conditions, anywhere in the world, 24 hours a day. There are no subscription fees or setup charges to use GPS.

Sensor systems which monitor the geometry and deformations of large civil structures are not new. Most conventional bridge monitoring systems rely on a fixed network of sensors that transmit their data back to a central site for processing and analysis. Instead, the emerging GPS application of structural deformation monitoring is used. Recent advances in GPS technology have made it a cost-effective tool for safety monitoring.

The receiver of GPS tracks the satellite signals and computes the range and phase measurements. It uses triangulation to calculate the user's exact location. Essentially, the GPS receiver compares the time a signal was transmitted by a satellite with the time it was received. The time difference tells the GPS receiver how far away the satellite is. Now, with distance measurements from a few more satellites, the receiver can determine the user's position and display it on the unit's monitor /1/.

The use of classical methods is connected with some inconvenience and difficulties. For example, accelerometer cannot measure the swing of total vibration of structure because acceleration cannot be obtained properly when structure moves slowly. It requires direct contact with the structure as well wiring to link it to a central recording unit. The wiring can be easily damaged. Use of laser interferometer and electronic distance measurement instrument is limited by climate condition, i.e. clear line of sight is

the basic condition under which they can work. In addition, when the measurements in different measuring points are not synchronous, it is difficult to measure large displacement and to get the observations in real time. The measurement by laser interferometer is used to measure the distance changes between the measurement point and the reference point. To achieve this goal, a prism or reflective film must be mounted at the measurement point. The distance change versus time can be collected and be further analysed to determine dominant frequencies and corresponding amplitudes. This method offers high accuracy, but it is difficult to catch the measurement point when structure vibrations or shake are too expressed. So, all these traditional methods are of limited capacity regarding continuity, real time and automatization for monitoring large structures in real conditions

A GPS system also includes communication elements and monitoring center, Fig. 1. A GPS reference station tracks all GPS satellites that are in view at its location, and all antennas in remote stations simultaneously receive satellite signals from several satellites. A GPS receiver must be locked on to the signal of at least three satellites to calculate a 2D position (latitude and longitude) and track movement. With four or more satellites in view, the receiver can determine the user's 3D position (latitude, longitude and altitude). At the reference station, the difference information is generated and transmitted to the remote stations in real time. In the remote station, the signal received from the satellites is corrected by the difference information from the reference station. The remote 3D coordinates of a station are calculated in real time using Differential GPS (DGPS) software, Fig. 2. The coordinates are then transmitted to the GPS monitoring center and are further processed so as to get the displacements of a structure in three directions.

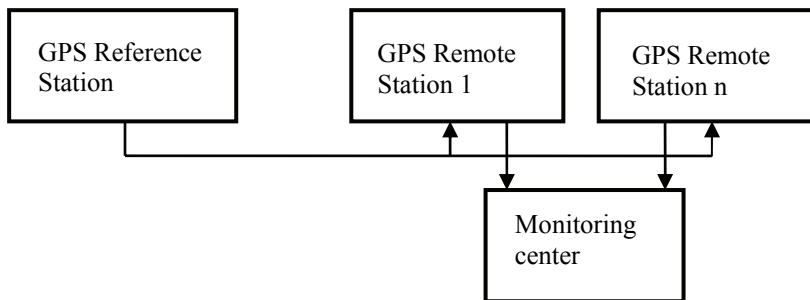


Figure 1: Simplified block scheme of GPS monitoring system

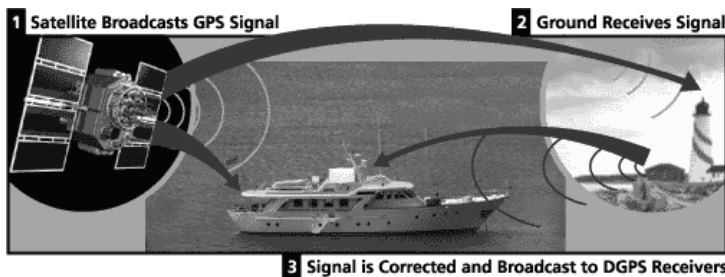


Figure 2: The scheme of the Differential GPS (DGPS)

Once the user's position has been determined, the GPS unit can calculate other information, such as speed, bearing, track, trip distance, distance to destination. Each of those timing signals is going to have some error or delay depending on what sort of perils

have befallen it on its trip down to the earth. However, the satellites are so far out in space that the little distances between receivers on earth are insignificant. Thus, the signals that reaches both of receivers will have travelled through virtually the same slice of atmosphere, and so will have virtually the same errors. The reference receiver is on a point that's been very accurately surveyed and is kept there. This reference station receives the same GPS signals as the roving receiver but instead of working like a normal GPS receiver (using timing signals to calculate its position), it uses its known position to calculate timing. The difference between calculated and received timing signal is an "error correction". The stationary receiver transmits this error information to the roving receiver so it can use it to correct its position measurements. Briefly, differential GPS (DGPS) is a technique that uses data from a receiver at a known location to correct the data from a receiver at an unknown location. The DGPS corrected solution is much more accurate than a normal GPS solution. DGPS involves the cooperation of two receivers, one that's stationary and another that's roving around making position measurements. DGPS can eliminate all errors that are common to both the reference receiver and the roving receiver on the ship, Fig. 2. Most systematic errors can be eliminated using a DGPS, but not errors due to environmental factors or receiver design. DGPS allows to obtain high accuracies e.g., positioning of a few meters /1/.

GPS technology not only overcomes the limitation of climate, but also measures the structure displacement in three-dimensional directions. The accuracy of a few milimeters can be obtained by using a DGPS carrier-phase approach, and the sampling frequency of 10 Hz or even 20 Hz is now available, providing higher accuracy.

Each GPS satellite transmits on two frequencies, L1 (1.575 GHz) and L2 (1.227 GHz). L1 is the primary signal used for most civilian applications, and L2 is used for computing ionospheric corrections in some cases. The L1 signal can be divided into three components: carrier wave, tracking codes, and navigation message. Information about the satellite positions (or orbits) is contained in the navigation message. Each satellite transmits its navigation message with at least two distinct spread spectrum codes: the Coarse / Acquisition (C/A) code, which is freely available to the public, and the Precise (P) code, which is usually encrypted and reserved for military applications. Both the C/A and P(Y) codes impart the precise time-of-day to the user. The C/A code is a 1.023 with 1.023 million rectangular pulses (chips) per second so that it repeats every millisecond. Each satellite has its own C/A code so that it can be uniquely identified and received separately from the other satellites transmitting on the same frequency. Both the navigation message and tracking codes are modulated on the carrier wave, a continuous radio signal at the L1 frequency. As with the tracking codes, the GPS receiver can correlate to the carrier wave to gather ranging information to each satellite. Because the frequency of the carrier wave is much higher than the frequency of the code chipping rate (2 MHz for the C/A-code vs. 1.575 GHz for L1), its cycles are much shorter, and thus, it is possible to make more accurate satellite ranging measurements using the carrier wave component of the satellite signal. However, this method is significantly more complex.

GPS tracking codes are designed so that when the code is successfully correlated in the receiver, an unambiguous range to the satellite is derived. The receiver knows exactly how far through the long code sequence it currently is. For carrier wave tracking, it is not so simple. Every wavelength looks exactly like every other one and each is about 20 cm long only. The receiver can determine the phase angle of the current cycle - but not how many cycles lie between it and the satellite. Because the receiver directly measures the

phase angle of the carrier wave, satellite ranging measurements derived from this procedure are called "phase" data. It is to note that most low-cost GPS receivers used for navigation applications produce only range data and positions derived from these measurements. Higher cost surveying and geodetic GPS receivers produce range and phase data.

The higher accuracy of positioning is achieved by using Real-Time Kinematic (RTK). RTK uses the satellite's carrier wave as its signal, not the messages contained within. In practice, RTK systems use a single base station receiver and a number of mobile units (rovers). The units calculate their relative position to millimeters, although their absolute position is accurate only to the same accuracy as the position of the base station. The typical nominal accuracy for these dual-frequency systems is $1 \text{ cm} \pm 2 \text{ parts-per-million (ppm)}$ horizontally and $2 \text{ cm} \pm 2 \text{ ppm}$ vertically. RTK GPS is being used together with sophisticated software to model the 3D position of a structure, and control the precise placement of this structure. This accuracy of GPS can be obtained using principles of interferometry - a measurement technique based on the fact that two waveforms will constructively or destructively interfere with each other if they arrive slightly out of phase. It compares carrier signals using these effects rather than signals themselves. Interferometric GPS is a technique which employs measurements of carrier phase difference to provide highly accurate relative position measurements. The differencing inherent in the interferometric approach leads to cancellation of many errors including ionospheric and tropospheric errors, ephemeris errors, and the effects of selective availability. Interferometric GPS uses the measurements at multiple antennae mounted on rigid baselines to provide orientation information. In the interferometric GPS technique, phase from a satellite is measured at two or more receiving locations and differenced. The carrier phase difference yields the distance between the two receiving sites projected along the propagation direction. This is a triangulation, the measurement which uses angle measurements together with at least one known distance. Figure 3 represents a snapshot in time of the transmitted wave's amplitude from a single satellite. Receiver 1 intercepts a particular wavefront (determined by the perpendicular projection of the receiver 1 measurement onto the line of sight). At this same instant in time, receiver 2 measures a different wavefront (determined by perpendicular projection). The difference in phase between the two wavefronts, $\Delta\phi$, is a direct measure of the propagation distance.

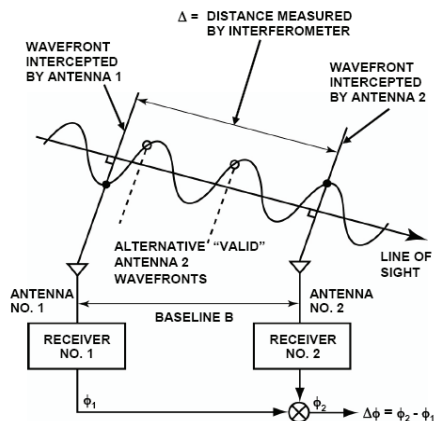


Figure 3: Example of Simplified GPS Interferometry /2/

Since the lever arm between the receiving antennae is known, the angle between the lever arm vector and the line-of-sight vector in the plane containing the satellite can be found. This process may be extended to received signals from multiple satellites (with multiple lines of sight) and to multiple receivers enabling the determination of all attitudes. The distance Δ involves the phase difference $\Delta\phi$ and can be calculated as follows:

$$\Delta = k \Delta\phi + N\lambda \text{ cm} \quad (1)$$

$$k = 19 \frac{\text{cm}}{360^\circ} = 0,053 \frac{\text{cm}}{\text{deg}} \quad (2)$$

Here λ is wave length; it can be $\lambda \approx 19 \text{ cm}$, as in Ref. /2/.

GPS is a form of information technology using systems of hardware, software and information (time and ephemeris) transmitted from satellites to provide derived information (time, position, and velocity) to users. The derived information may be combined with other systems to perform a variety of tasks. As a distribution system for precision time signals GPS helps to synchronize global information networks of fiber optics, communication satellites, radio, coaxial cable, and copper wire.

2.1. The applications of global positioning system

GPS has been tested for surveying large structures since the late 1980s. The past ten years have seen dramatic reductions in hardware cost coupled with significant increases in performance, so market pressure caused manufacturers to focus more attention on the development of low-cost, high-accuracy GPS antennas, and prices are greatly reduced during last two decades /3/. Recent advances in GPS technology have made it a cost-effective tool for monitoring safety and performance of bridges: the price of the GPS receivers employed in structural monitoring systems is below \$5,000.

Fields of GPS application are now numerous. GPS is used in all phases of *highway construction*. Survey data is used to design construction projects. Real-time GPS data is used to provide precision management of heavy machinery during construction. *Bridge monitoring* is becoming increasingly important for traveler safety and for maintenance during life of bridge. The problem is ageing of bridges, since many of them are carrying greater loads than predicted by design. High accuracy GPS survey receivers are installed at critical locations on bridges to measure deflection and deformation. This data is used to ensure bridge integrity and safety. *Train control and collision avoidance* is being implemented in the United States through the deployment of a nationwide differential GPS network based on vacated Air Force emergency communication sites. A GPS-based separation system is being developed that will help trains avoid collisions. Using GPS information, the fully automated separation system will activate a warning the trains that they are too close to one another. *Earthquake monitoring and prediction* is the next field of successful application of GPS system. High-accuracy GPS surveying receivers are being used to monitor the earth's crustal movements preceding earthquakes. In Japan, a network of hundreds of GPS stations is monitoring shifts of a few millimeters in fault lines. In the United States, GPS systems gather data for geology research projects related to land mass movement. GPS is applied for *mining and infrastructure* development and/or management in order to obtain public safety, precise location for mine surveying, cost-cutting and increased productivity in open cut mines, precision location for mining explosives, oil pipeline development and monitoring. *Public safety and emergency services* are benefiting from GPS through better resource management and vehicle dispatch. GPS

tracking and navigation reduces response times and enables more efficient utilization of expensive vehicles used by such as police, fire, and search and rescue. GPS can also be combined with communications to coordinate the actions of multiple ground, sea, and air emergency vehicles. DGPS systems can also be deployed to emergency locations to guide individuals, like firemen in a burning building or expeditions to South Pole.

Because atmospheric and orbital errors increase with the distance between the reference and the remote station, it is better to set up the reference station at a relatively small distance from the remote station. When the distance is 1 km or less the atmospheric and orbital errors are expected to be about a millimeter. The remote station should be located at the measurement point, the biggest deformation point or the feature point of a structure.

Mobility is a basic characteristic of field tasks. Location-Based Computing (LBC) is an emerging discipline focused on integrating geoinformatics, telecommunications, and mobile computing technologies. LBC utilizes geoinformatics technologies, such as Geographic Information Systems and tracking methods, such as GPS, in a distributed real-time mobile computing environment. In LBC, elements and events involved in a specific task are registered according to their locations in a spatial database, and the activities supported by the mobile computers are aware of the locations by suitable positioning devices /4/.

2.2. The experience with the application of GPS system to bridges

It turned out that the performances of GPS system are very suitable for bridge behaviour monitoring. At long-span cable supported bridge, for example, the remote points are located in the middle of the bridge deck, or on the top of the bridge tower. One of important applications of GPS is monitoring of cable-supported bridges by vibration and strain measurement and for real time monitoring of other structural vibrations. Inertial sensors such as accelerometers and gyros can be added to the GPS antenna assembly to further increase positioning accuracy.

Using the displacements of measurement points in special directions, vertical, lateral and longitudinal, the analyses includes the temperature dependence, the wind velocity dependence, or load dependence of displacement. The data processing includes coordinates transformation, spectral analyses, data extraction and structures health assessment.

The different information about the lifecycle of a bridge (e.g. construction, inspection and maintenance schedules) integrated to the 3D model of the bridge, result in 4D models /5/. 4D models will allow for spatial-temporal visualization and analysis that are not possible with present bridge management systems. Present methods of capturing location information using paper or digital maps, pictures, drawings and textual description can lead to ambiguity and errors in interpreting the collected data.

There are two system architectures for structural monitoring with GPS, one based on a fixed network of sensors, Fig. 4, and the other based on mobile sensors. Fixed network of sensors are mounted on the structure at sites of interest /6/. Each bridge deformation monitoring system sensor node consists of a GPS receiver, microcontroller, and data radio. The GPS receiver tracks the satellite signals and computes necessary data on range and signal phase, which are transmitted by radio to the central processing unit.

GPS, like any other technology, has limitations for measuring deformations of large civil structures. However, it is today a powerful and cost-effective tool for monitoring some types of structural deformation and performance. Foundation settlement, creep, and different movements generally occur over relatively long periods of time. Therefore, averaging times of a few hours can be used, producing positions with millimeter-level

accuracy. On the other side, motion due to wind loading is cyclic with frequencies of a few hertz. Little or no averaging can be done, positioning accuracy is about centimeter.

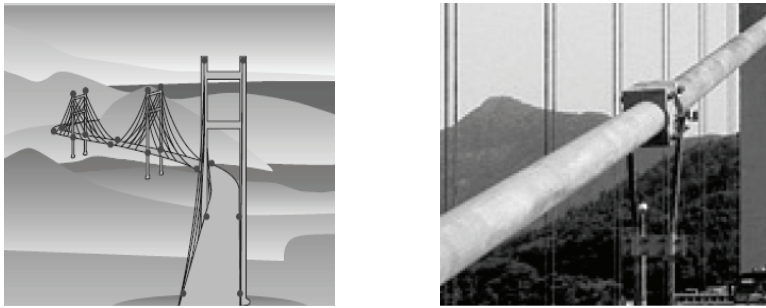


Figure 4: Critical points whose positions are measured occasionally (left) and continuous deformation monitoring of bridge component (right) /7/

This restricts the utility of GPS for monitoring short-term motion to more flexible structures. Because vibrations of rigid structures are small, it is difficult to monitor them using GPS. GPS is in common use to monitor the flexible structures, such as long-span cable-supported bridges, high buildings and large objects. Examples are bridge 'Gazela' and designed bridge over Ada Ciganlija in Belgrade, Fig. 5.



Figure 5: Model of designed bridge over river Sava at Ada Ciganlija in Belgrade

The experience with system for real-time displacement monitoring of a large-span bridge, which allows recording its fatigue history is described here first (Fig. 6). The system is applied to the Tsing-ma Bridge of Hong Kong and Humen Bridge of Guangdong in China /8/. Three basic elements included are: GPS receiver, Data transmit system and Data manage and real-time monitoring system. The sampling frequency of GPS receiver can reach 20 times per second, while the location precision can approach 5~10 mm. So the GPS can be used in the displacement monitoring of large structure.

Following requirements had been fulfilled in system design:

- The basic vibration period of Tsing-ma Bridge is 8~14s, the basic vibration period of the towers is about 4s. The sampling frequency has to be above 1 Hz under typhoon, and after it should be > 4 Hz, and these can be modified artificially.

- The time lag to apply the wind load displacement of bridge should be < 10~15s.
- The accuracy of displacement should be 1~2 cm.
- The data are processed in the central control room.
- Data should be transmitted in wireless way.
- The data needed include: 1. displacement real-time record; 2. time-displacement curve (t-x, t-y, t-z); 3. 2-D deformation figure; 4 rotation of the tower; 5 dynamic vibration simulation animation; 6 frequency spectrum analysis.

The components of here applied GPS automatic monitoring systems are:

- GPS monitoring station.
- Hardware: NOVATEL RT-12, 12-channel GPS receiver, which can process double frequency kinematic monitoring. The difference accuracy is 1~2 cm, the data output frequency is 4 Hz, and the antenna can avoid multi-path effects.
- Monitoring software: developed by Tsinghua University can accomplish the parameter setup of GPS real-time carrier phase difference; datum station difference signal transmit monitoring and satellite situation monitoring.
- Data transmitting system: wireless multi-to-one communication method is adopted. The difference signal sent from the datum station is 279 bits; the sampling frequency of flowing station is 0.25 Hz. The signal sent back is 35 bits per group.
- Software system includes four softwares: for database management, for bridge displacement real-time monitoring, for bridge safety analysis and for general control.
- The time-displacement curves are plotted each day. It was found a linear regression between displacement and temperature.

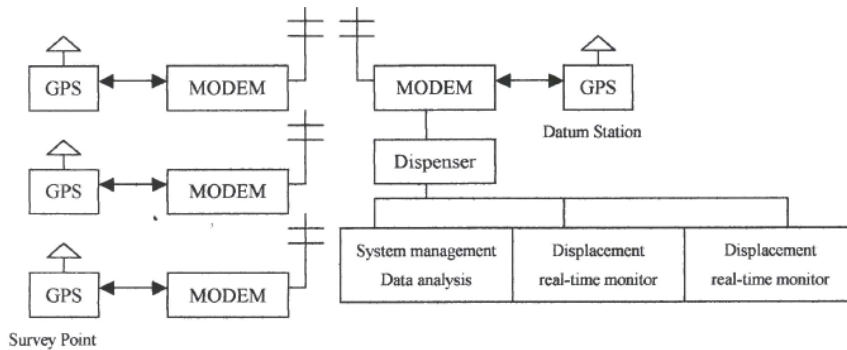


Figure 6: GPS displacement monitoring system in real time /8/

As concluded, GPS is an effective method for the safety monitoring of large span bridges and has advantages as real-time, distinctness, and no influence to the traffic. Cost of GPS and total station is compared in Table 1. GPS is proven that can work under any weather condition including fog, rain and typhoon.

Table 1: Comparison of cost between GPS and former total station method in yuans, CNY, /8/

Item cost ($\times 10^4$ CNY)	GPS method	Total station method
Equipment	220	25
Labor	2	6
Traffic stop	0	400 (8 nights)
Total cost	222	431

CNY (1 chinese yuan) = \$US 0.146156 on 2008.12.12

The second example of experience refers to an investigation of GPS application to measurement of suspension bridge movement using pseudolites (PS), Fig. 7. This information can be used to warn of dangerous conditions and estimate the long-term deterioration of the structure. Additionally, this information is of value to bridge designers and for traffic management. It is known that when using GPS, the accuracy, availability, reliability and integrity of the position solutions is very dependent on the number and geometric distribution of the available satellites. One option to improving the satellite geometry is to use ground-based transmitters of GPS-like signals, “pseudolites” (PLs). PLs can be properly located to provide additional ranging information, and therefore improve the positioning precision. In situations with limited or no visibility of the GPS satellites, ground transmitters that emulate the signal structure of the GPS satellites (PLs) can be used as additional or replacement signal sources. The measurements to test the suitability of a PL-augmented GPS system for bridge monitoring, were conducted at the Wilford suspension footbridge over the river Trent in Nottingham, UK on 16 October 2002 /9/.

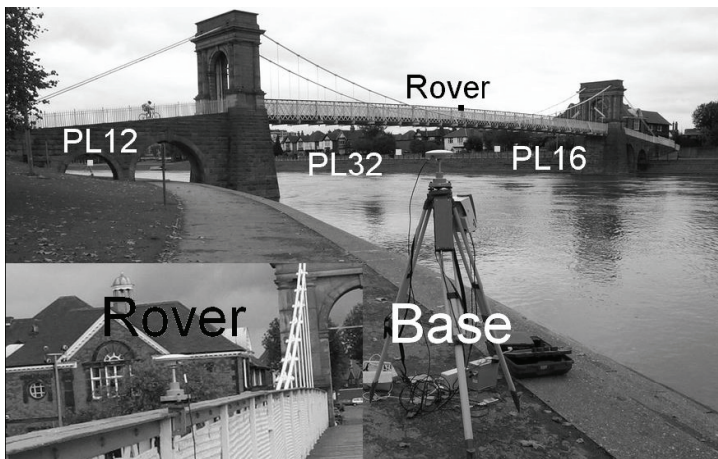


Figure 7: Pseudolite (PL) locations in relation to base and rover GPS receivers /9/

Pseudolites are ground-based pseudo-satellite transmitters which initialise carrier-phase DGPS navigation systems (CDGPS) in seconds to perform RTK measurements with error of about 1 cm. Also are used synchronolites (synchronized pseudolites) which derive their timing from individual GPS satellites; they can replace the CDGPS reference station and data link and simultaneously initialize CDGPS navigation.

The equipment used for the measurements consisted of two types of GPS receivers used in the trial, and connected to the same Leica AT502 antenna via a splitter /9/. The low-cost (few hundred \$US) single-frequency Canadian Marconi Corp. (CMC) Allstar receivers were used to track the PL and GPS signals, while the Leica SR530 receivers tracked only the GPS satellite signals. The Allstar receiver allows the user to request particular PRN codes (12, 16 or 32) to be tracked, and this is a basic requirement for a PL-tracking GPS receiver. The Leica receivers were used to provide an independent check on the quality of the GPS data from the CMC receivers and their dual-frequency capability would enable ambiguities to be resolved cinematically On-The-Fly (OTF). The three pseudolites were located on the river bank footpaths, Fig. 7.

By data processing of GPS-PL positioning it was found out that in the vertical component time series the standard deviation was 7.2 mm (sub-cm) and smaller than the

GPS-only solution by 31%. It has been demonstrated that when GPS is augmented with PLs similar positioning precision (sub cm) can be obtained for both the horizontal and vertical components. The low-cost single-frequency CMC Allstar receiver provided good quality GPS measurement data and tracked the pseudolite signals for the entire trial without difficulty. These GPS receivers therefore have the potential to be used in a low-cost system for deformation monitoring. Also, it was necessary to resolve carrier phase ambiguities by appropriate software, which was developed.

2.3. Modal analysis of bridge vibrations

The structural modal parameters: resonant frequencies, mode shapes and modal damping are determined from dynamic measurements of structures like buildings, towers and bridges. The modal parameters can be used for a variety of purposes: active control, if the design requirements have been respected, and to update numerical models for better understanding the dynamic behaviour of the structure under the dynamic loads - operative or exceptional loads, produced by earthquakes or winds. Moreover, periodic monitoring of the modal properties can be used to determine the structural integrity of investigated structure. Structural vibrations have to be measured at different ambient excitations, such as traffic, wind, earthquake and their combination. In this case, only response data of ambient vibrations are measurable and the detailed loading conditions are unknown. For most of the structures under natural operating conditions the loads are nonstationary, cannot be easily measured, and the ambient excitation is taken as unobserved white noise.

Structure dynamic testing is considered as a procedure for determining the resonance (natural) frequencies of a structure. The identified vibration mode shape for each natural frequency corresponds to the deflected shape when the structure is vibrating at that frequency. Each vibration mode is associated with a damping value which is a measure of energy dissipation. The natural frequency, vibration shape and damping value are referred to as the modal parameters of the particular mode. Dynamic tests involving identification of modal parameters are also known as modal tests or modal surveys.

Full-scale dynamic testing of structures can provide valuable information on the service behaviour and performance of structures. With the growing interest in the structural state of highway bridges, dynamic testing can be used as a tool to assess the integrity of bridges. From the measured dynamic response, induced by ambient or forced excitation, modal parameters (natural frequency, mode shape and modal damping value) and system parameters (stiffness, mass and damping matrices) can be obtained. These identified parameters can then be used to characterize and monitor the performance of the structure. Analytical models of the structure can also be validated using these parameters.

Two different techniques can be used to extract the modal properties of a structure such a bridge under ambient vibration: eigensystem realization algorithm (ERA), from early 1980s, and a new method based on wavelet transform (WME). Both techniques need free-decay signals to extract the modal parameters. At this aim a random decrement technique (RDT) has been used to process the environment-excited signal. These techniques were applied to determine modal properties of the Nottingham Wilford suspension bridge, (Fig. 7), under ambient vibration [9]. This footbridge exhibits large deflections (decimeter range) under normal environmental loading. Its span is held up by two sets of suspension cables restrained by two massive masonry anchorages. The span sidewalk is 3.65 m wide and 68.58 m long is composed of a steel deck and wooden floor.

The GPS sensors were employed for the acquisition of ambient excited signals, being strongly polluted by GPS noise. A pass band filter was applied to the signals acquired in the attempt to clear out those frequencies mainly due to electromagnetic interferences.

The GPS receivers and antennas, Fig. 8, employed to monitor the displacements of the Wilford Bridge were provided by Leica Geosystems Ltd., and were capable to acquire the real time absolute three-dimensional positions at 2 mm positioning accuracy and a rate of 10 Hz. This meant that according to theory, the extractable modal properties should have a frequency smaller than 5 Hz. The bridge ambient vibrations have been detected using a network of GPS sensors installed on the bridge. The FFT analysis shown that not all the random noise was taken out by the RDT process. Both the techniques employed, ERA and WME, extracted only one vibration mode, the frequency and the modal damping are listed in Table 2. The results showed that the two techniques used provided very similar results in the estimation of the first natural frequency with a difference of 1%.

Table 2: Modal properties of the Nottingham Wilford bridge /10/

Extraction technique	Frequency (Hz)	Modal damping
ERA	1.74	0.025
WME	1.72	0.019

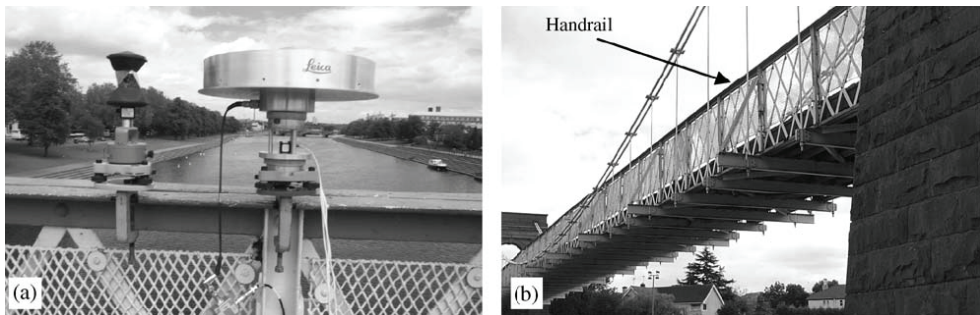


Figure 8: GPS positioning at the Wilford Bridge /10/

The real-time kinematic global positioning system (GPS), installed on the bridge for on-line monitoring of bridge deck movements, has shown the potential of using GPS sensor to monitor and measure the vibration properties of medium span suspension bridge in the low-frequency range; the data can be used for extracting modal properties from in-service-loads induced low-frequency vibration (< 5 Hz) by processing the signal with the wavelets transform. This was applied to the Tsing Ma long suspension bridge in Hong Kong and described in detail in Ref. /11/.

The instrumentation for bridge monitoring in many cases consists of a mix of dual and single frequency GPS receivers, triaxial accelerometers, pseudolite transmitters and GPS/pseudolite compatible receivers and a digital weather station.

The features of single and dual frequency GPS receivers are pointed out, including instrument price and the time required for resolving integer ambiguities. A single frequency GPS receiver is about half the price of a dual frequency receiver. Whilst a dual frequency GPS receiver fixes digital ambiguity in nearly real-time, a single frequency receiver has to take about half of an hour to achieve a fixed solution. Anyhow, research reveals that for bridges that only have limited movements of a few cm the achievable positioning accuracy with a single frequency receiver can be at least as good as that of a more

expensive dual frequency GPS receiver but its sampling rate can reach 100 Hz. But, there is problem in achieving a cm RTK GPS positioning with single frequency GPS receivers.

3. APPLICATION OF NEW NON-DESTRUCTIVE TESTING TECHNIQUES

Several new developed non-destructive-testing methods are now in use for covering extended demands regarding flaws and damages detection.

3.1. Contactless ultrasonic method

For solving the problem of surface state effect on NDT results the contactless ultrasonic (UT) procedure is developed. The influence of the surface condition on UT can be described as the echo amplitude changing with the probe replacement over the surface. It is expressed as the sensitivity variation and it may amount a couple of dB, thus the flaw size can be wrong estimated dependent on surface preparation. For that the flaw estimation becomes uncertain and greater flaws can be estimated as acceptable. One way to avoid the problem is surface preparation before UT, in accordance with recommended procedures, the second is the use of water jet or other more dense media, like a thin layer of grease, for improving acoustical contact between the ultrasonic probe and test surface. For these reasons great attention is paid to the development of portable contactless ultrasonic devices based on the electro-magnetic acoustic transduction. The problem can be solved using contactless, hand-held probes, Electromagnetic Acoustic Transducer (EMAT). This new innovative inspection technique is already accepting in many industries. A comparison of piezoelectric UT and EMAT device is given in Fig. 9.

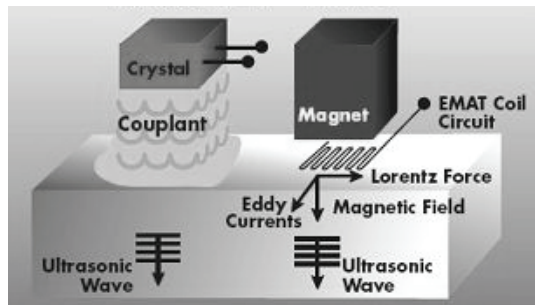


Figure 9: A comparison of piezoelectric UT (PET) and EMAT UT

The basic structure of an EMAT consists of a magnet (a permanent or an electro-magnet) and a meander shaped wire, located above the metal surface in the magnetic field, as presented in Fig. 9. In this case, the eddy currents are periodic and flow in a uniform magnetic field. The spacing between adjacent wires makes this type of coil particularly sensitive to waves of length twice the spacing between the wires. Here, the eddy currents under the coil find themselves subjected to a periodic magnetic field. This form of periodic magnetic field and uniform eddy current generates or detects shear horizontal (SH) waves whose wavelengths are twice the width of the individual magnets. The physical principles are based on the same electromagnetic induction processes that govern electrical motors and generators. A wire carrying an alternating current and held close to a conductor will induce eddy-currents in the conductor. If a large magnetic field also floods the area of the eddy-current, Lorentz forces are generated in the conducting surface by electric motor action and these launch acoustic waves into the conductor at the same frequency as the current that drives the wire. The acting Lorentz force is the vector

product of vector of eddy current in metal and vector of magnetic field. When used as a receiver, acoustic vibrations inside the conductor move the surface under the wire. In the presence of a magnetic field, this motion produces an eddy current in the conductor surface that produces a magnetic field extending across the air gap to induce a current in the near-by wire connected to a preamplifier.

The advantages of the EMAT are:

- The lack of immediate contact implies an air gap next to the surface part and, thus, no coupling liquid or grease layer is present to restrict the range of temperatures or inspection speeds available for testing.
- The transduction process takes place within a thin layer at the surface part allows the time-of-flight (or phase) of the ultrasonic wave to be measured with great accuracy so that dimensions and physical properties of materials enable quality assurance purposes.
- The shape of the coil and the direction of the magnetic field allow the type (shear or longitudinal) and direction of wave propagation to be controlled by the transducer design.
- Special wave types (e.g., shear horizontal, Lamb, Rayleigh) are readily available to satisfy unusual inspection problems.
- Coils that are large or contoured to fit odd shapes are inexpensive and extend the range of part geometries available for inspection.

The sensitivity of EMAT is often expressed by transfer impedance between a transmitter and a receiver pair: it is defined as the impedance of the voltage output at the receiver coil's terminals divided by the current being driven through the transmitter's coil. Thus, its unit is ohm. Under convenient conditions (magnetic fields of the order of 5,000 gauss and many turns in the EMAT coils), the output voltage can be as large as a millivolt when the transmitter current is 100 A – and transfer impedance is 10 $\mu\Omega$. Achieving these levels of current in the transmitter coil and amplifying the receiver voltages with a minimum of noise requires careful electronic design.

Besides more comfort testing, EMAT enables the application of different wave modes, such as Lamb, shear or surface (Rayleigh) waves dependent on product geometry, such as plate, bar and pipes. By directing waves circumferential around the surface of the bar, a measure of the amplitude of the waves after each trip around the bar, can be used to determine the apparent surface wave attenuation of the ultrasonic surface wave on the bar surface. This quantity is determined by the beam spread, the microstructure of the material and by scattering from any defect on the surface. For longitudinal laps and seams, the scattered amplitude and hence the attenuation can be shown to be a universal function of the wave length of the surface wave and the depth of the flaw.

The analysis of the EMAT sending and reception with the help of existing transducers on the base of constant magnets has shown, that their main disadvantage is the low transduction coefficient at testing objects from ferromagnetic materials attacked by corrosion. Thus it appears necessary to increase the pulsing energy and magnetic field induction. Anyhow, this leads to the increase of power consumption, sizes and weight of EMAT and to limitation at work on steel objects, because of the damage danger.

There are known the EMATs, which work as a part of stationary plants and provide high sensitive welds testing with Lamb waves, using the pulse magnetic field. But this kind of EMAT was not used in the devices with off-line power supply, because of its big sizes and large power consumption.

The examples of EMAT application are: monitoring of the billet temperature during continuous casting of steel, on-line measurement of the wall thickness of seamless steel tubing, inspection of buried gas pipelines, flaw detection by special wave modes in plates, pipes and bars, long range inspection of railroad tracks, inspection of pipes by guided, circumferential waves, inspection of piping using axial propagating transversal wave, which can reach very long distances through the pipe wall, and many others.

Other application of EMAT is residual stress measurement in railroad wheels /12/ (acoustoelastic stress measurements). It is also used for high temperature measurements, bolt-axial stress and grain-size measurements, monitoring fatigue and creep, surface flaw detection, corrosion detection, long-range detection of flaw in wires.

3.2. Magnetic particle testing methods

Besides UT, for surface and subsurface cracks detection the magnetic particle testing (MT), Fig. 10, is in permanent use. MT is based on magnetic flux leakage. Liquid particle MT is found to be more sensitive than dry particle MT. Both can use fluorescent particles when black light is required.

For NDT of pipes made of broadly applied low alloyed steels are, MT magnetic flux leakage methods, and UT, contact and contactless methods.

The measured flux leakage in MT is dependent on material properties, wall thickness, stress in pipeline, and flaw size. Induction coil method and Hall sensor method are used. The equipment for the MT method is known as pipe scan. It is an easy to use, cost effective, portable, magnetic flux leakage inspection system for the detection of random internal corrosion in pipes. The special, advanced magnetic material coupled with unique mechanical design enable coverage of all pipe diameters from 50 mm to 2.4 m, with a limited number of scanning heads. Unlike some inspection methods, magnetic flux is not affected by fluid streaming through the pipeline, so surveys can be carried out both on-line and off-line. Use of pipe scan of high probability of detection, to locate actual internal corrosion, coupled with A scan ultrasonic monitoring of corrosion growth, provides a cost effective accurate system for the determination of piping integrity.

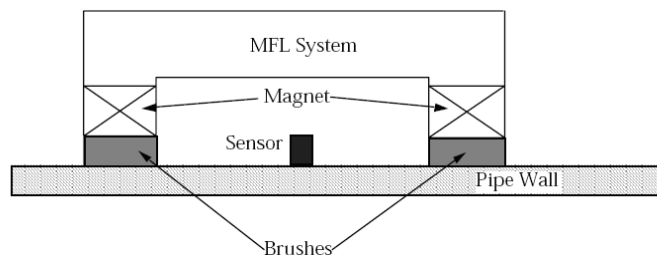


Figure 10: The estimation of the size of surface cracks using Hall sensor

Applicable contact ultrasonic methods are piezoelectric (PET), shear and Lamb wave techniques, and for contactless testing EMAT, magnetostrictive sensor, longitudinal, shear wave and Lamb wave techniques are used.

3.3. Special applications of ultrasonic and magnetic particle testing methods

One of popular UT technique is long range ultrasonic testing. It has been introduced commercially in early 1998 for the in-service monitoring of pipes and pipelines. It is predominantly used by the oil and gas industry for detection of corrosion and other metal

loss defects, and is becoming widely accepted as a valid means of assessing the condition of pipes and pipelines, particularly where they are difficult or expensive to access for inspection. Today it is broadly applied in identifying corrosion in different situations in pipes diameter range 50 mm to 1200 mm and for assessment of pipes state.

A non-contacting ultrasonic probe, placed inside a pipe, which operates in light liquid product lines, can be realized as a movable test system. It is known as a pipe-inspection-gear (PIG). The ultrasonic head comprises a fixed centrally mounted ultrasonic probe whose signal is projected along the pipe axis on to a 45° angle reflector rotating at speeds up to 1000 rpm. The forward speed is in the range of 1 m to 3 m per minute. The signal is transmitted through the liquid to and from the outer pipe wall. The return signal is captured for subsequent analysis. PIG can pass through a 1.5D bends (D is pipe outside diameter) and can be pulled back to its launcher or move in free mode (autonomous device for detecting flaws and leakage in pipes). With the captive PIG the power is supplied along the umbilical and results returned on line. Such test systems can be used in pipeline for transporting natural gas. They are exposed to aging, and the integrity has to be monitored frequently. Stress corrosion cracks (SCC) can be easily detected using liquid fluorescent magnetic particle inspection. However, this technique is not practical for in-line inspection of pipes. Up-dated technology for pipeline inspection uses the MT is capable to measure the local changed magnetic field on the inside pipe wall using sensors. It is required that in-line inspection technology enables to locate the flaws without having to resort to excavation. SCC is usually oriented along the pipe and may remain undetected. It can occur in a range of pipeline field conditions including soil type, stress, cathode potential, coating conditions and temperature. Axial magnetic field in-line inspection PIG, extensively used for pipeline inspection, is convenient for detecting corrosion damage or circumferentially oriented defects inside a pipe, but not surely flaws or cracks in the axial direction. For that EMAT is better. Two EMATs can be used in the pitch-catch disposition to send and receive longitudinal or shear waves perpendicular to the longitudinal weld joint. EMAT is a vital NDT tool for an early location of SCC and other defects, like corrosion, welding cracks, pits. It is important that such NDT tool is capable to detect SCC accurately, without false signals, to characterize to some extent the defect size. Although EMAT is in use for more than a decade, some further research work is still necessary. Properly designed, EMAT can be positioned anywhere inside the pipe, in a way that can send and receive confined acoustic waves for detecting flaws and leakage in pipes.

Long range ultrasonic testing is also applied for detection of circumferential cracks under the supports of long tubes in heat exchangers, inspection of railroad tracks, especially welded rails, inspection of wire cables and piping at pipe supports.

The next UT method in use is the phased array inspection. It is an advanced technique for volumetric assessment and flaw detection, applicable for discontinuity detection in thick steel plate or vessels, longitudinal and butt weld testing, stress corrosion cracking in pipes and in turbines, nozzle corrosion testing, and hydrogen induced cracking.

. Phased array consists of a number of ultrasonic elements arranged in a single instrument. The multiple elements are used to create an ultrasonic beam. The beams can be “steered” to optimize their orientation to the tested object, increasing the probability of detection of flaws, for example in longitudinal welds in piping. The beams can be scanned over the object in order to produce an image. By adjusting the individual

elements electronically, the beams also can be focused to yield clearer and less uncertain results /13/. The sum of delayed signals is given by

$$V(t, \tau) = \sum_n v_n(t - n\tau) \quad (3)$$

where $v_n(t)$ is the signal from the n -th transducer and τ is the delay time. The result is the summed signal dependent on delay time τ . These summed signals are plotted in Fig. 11, showing the determination of the delay time between transducers. A maximum amplitude is obtained when all signals add coherently at $\tau = 330$ ns.

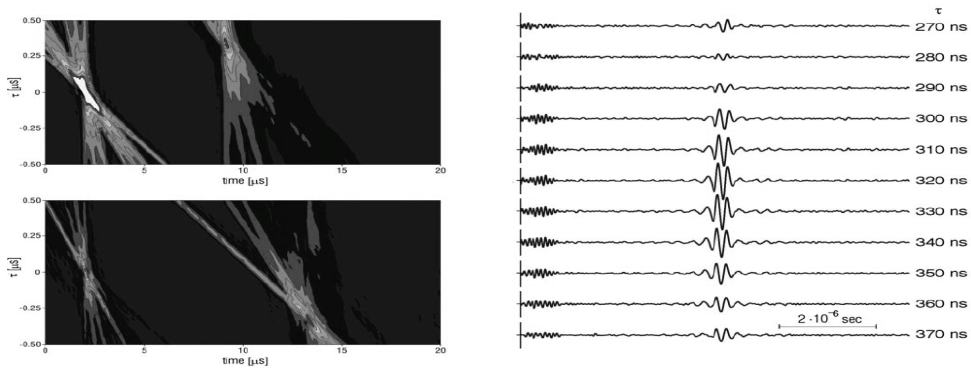


Figure 11: Two illustrations of the phased array technique: the contours of ultrasonic beams at two locations (left) and sum of delayed signals as a function of the delay time τ (right) /13/

Portable phased array ultrasonic instruments offer advantages over conventional single-element UT, particularly in testing of automated welds in piping. When operating in scanning mode and using the electronic focusing capabilities of these systems, phased array ultrasonic systems are significantly faster than single-element systems.

3.4. Acoustic emission

Acoustic emission is a technique to monitor in services or laboratories initiation of defects and failures in structural materials, applied in structural components (steam pipes and pressure vessels), and in the investigation of rocks, composite materials, and metals. Acoustic emissions (AEs) are the stress waves produced by the sudden internal stress redistribution due to changes in material structure, caused crack initiation and growth, crack opening and closure, dislocation movement, twinning, and phase transformation as well as fiber breakage and fiber-matrix debonding in composites, Fig. 12. AE is found to be an effective way of detecting fatigue and fracture behaviours of materials, too.

AE technique detects the activities inside the materials, through the input of one small sensor on the material surface in-service or laboratory operation, enabling to monitor continuously damage development and an early warning of possible failure, including fatigue damage, but does not produce quantitative results. Since service environments are generally very noisy, and the AE signals are very weak, signal discrimination and noise reduction are very difficult, yet extremely important for successful AE application.

Possible sources of AE signals are crack initiation and growth induced by stress corrosion cracking and hydrogen embrittlement; dissolution of metal; hydrogen gas evolution; the breakdown of thick surface-oxide films and the fracture or decohesion of

phases, such as precipitates. High-sensitivity AE sensors can pick up signals at an early stage of fatigue crack initiation, such as dislocation movement and slip-band formation.

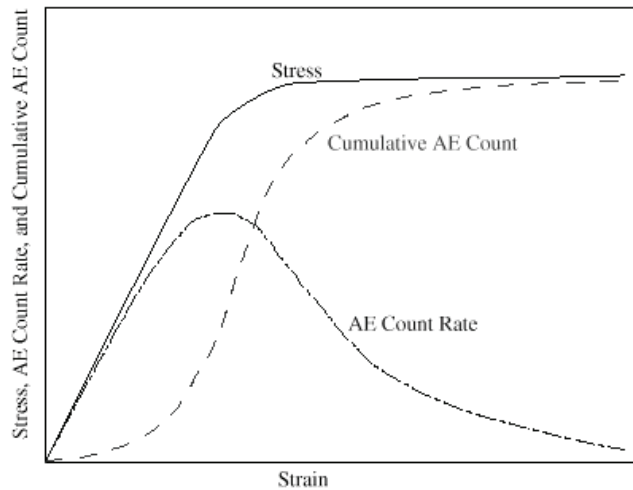


Figure 12: The illustration of AE: A tensile stress-strain curve and AE signals /14/

AE is used for testing of composite materials. Because of more complex damage mechanisms, such as reinforcement (fibers or particles) failures, delamination, matrix cracking, and debonding of the fiber and matrix, composite materials provide a greater variety of AE sources in fatigue and fracture experiments. AE signals resulting from different damage mechanisms often vary significantly. Most of the composites consist of at least one hard or brittle phase, which causes stronger AE signals. On the other hand, because of the homogeneity and simplicity of metals, the wave propagation in metals should not be as complex as in composites and rocks, since there are less reflections, diffractions, and scattering in metals. Therefore, metals represent a good subject for studying source-function and waveform analyses using AE.

New AE systems enable to locate and characterize the nature of AE sources captured.

4. LASERS IN NON-DESTRUCTIVE INSPECTION AND TESTING DEVICES

Reviewing of various references one can reveal that the topics concerning application of lasers in NDI are: analytical methods for linear and nonlinear systems, prediction and simulation, system identification, implementations of contemporary numerical systems (like finite elements method - FEM, boundary elements method - BEM) /15/, experimental methods, correlation methods, structural dynamics in different environments, noise and vibration monitoring, failure detection, sensors and transducers, signal processing /16, 17/. In many of these tasks lasers are applied in developed devices, schemas and complete systems. Some examples are presented here.

4.1. The application of laser Doppler vibrometer (LDV)

Bridge structures are exposed to different external loads (traffic, earthquakes, impacts, and random variable loads) during lifetime. This may cause structures unexpected damage in service, which may lead to failures with loss of human lives and costly repair.

Structural health monitoring has become an important inspection and research topic for damage assessment and safety evaluation of structures, and it is possible to be done by

measurement the displacements of bridges. It is a difficult task, since bridges are designed to overpass some distance, mostly over the sea or the river. The use of accelerometer base measurement technique for evaluating bridge forced vibrations or to perform bridge modal analysis is already established. The value of acceleration amplitude can be very low at low frequencies. The limitations with accelerometer application are linked with transducer types. Installation of the conventional devices for displacement measurement is difficult and expensive. In addition to already presented global positioning system (GPS) development and experience for bridge structural health monitoring, Laser Doppler Vibrometer (LDV) have been suggested as an alternative for displacement measurement on bridges, producing valuable information for structural integrity assessment.

LDV includes: a laser, a mirror, three beam splitters, a Bragg cell, and a photo detector, Fig. 13. The mirror reflects the reference beam of laser frequency f_0 which passes through the upper beam splitter and adds to the beam from Bragg cell, $f_0 + f_b$ and adds also to the beam obtained from the target, $f_0 + f_b + f_d$. The mixture is detected by the photo detector and analysed to give velocity as the result /18/.

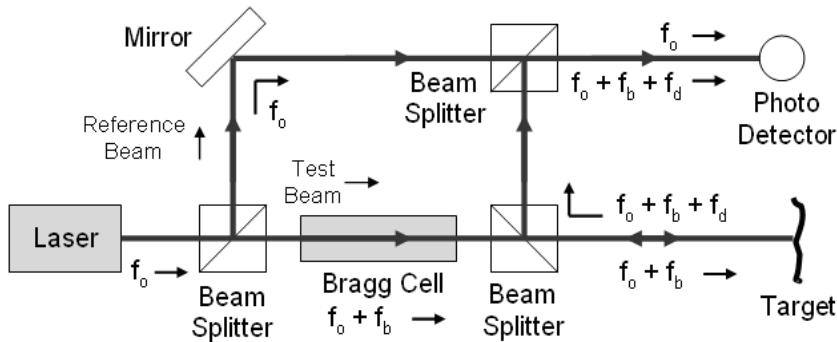


Figure 13: Scheme of Laser Doppler Vibrometer (LDV) /18/

Digital image processing techniques as innovative, highly cost-effective and easy to implement, still maintaining the advantages of dynamic measurements and resolutions. At first, the measurement point is marked with a target panel of known geometry. A commercial digital video camera is installed on a fixed point beyond the bridge (e.g. on the coast) or on a pier (abutment), which can be regarded as a fixed point. Then, the video camera takes a motion picture of the target marked at the measurement point. Meanwhile, the displacement of the target is calculated using the image processing techniques, which require the texture recognition algorithms, projection of the captured.

The displacement measurement is more appropriate. Used locations of a bridge for this purpose can be different, depending on the bridge design, e.g. the lower deck of bridge can be used, Fig. 14. LDV detects relative vibrations as opposed to the absolute measures of accelerometer. Some results in field measurements on a highway little bridge excited by traffic under normal operating systems will be presented through some pictures. The accelerations measurements were performed by accelerometer for civil engineering structures and by LDV with a fringe counter board in terms of velocity and displacement, and have been compared as calculated from LDV signals and the one directly measured by the accelerometer. The advantages of the laser devices at lower frequencies are clear and new possibilities are opened to analyse bridge loads in operating conditions, monitor bridge health, predict fatigue life and improve bridge design.

Figure 15 shows the measurement point for LDV as well for the accelerometer. The measurement head and the entire LDV measurement system are shown in Fig. 16 /19/. LDV head must be mounted on a stable holder not connected with a structure.



Figure 14: The lower deck of the bridge, possible location for displacement measurement



Figure 15: The measurement point /19/

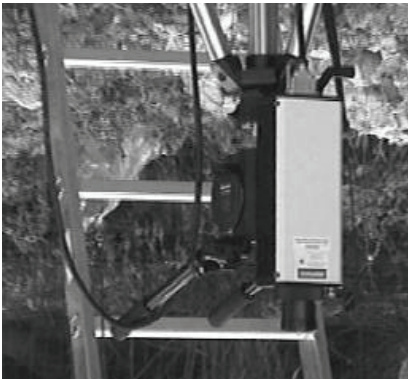


Figure 16: LDV measurement head (left) and LDV measurement chain (right) /19/

The analytical solution of bridge dynamic response under moving loads is complex task, affected by many factors /20/. The basic geometry of the model is given in Fig. 17. The length of the beam is l and a moving harmonic force $P(t)$ is assumed with constant velocity V_0 . The solutions for the midpoint displacement depend on Ω - the frequencies of the exciting force $P(t)$. Three cases are considered (Fig. 18): Ω lower than the first beam resonance frequency (a), equal to it (b), and higher than it (c).

In Fig. 19 two direct measurements by LDV and accelerometer, showing variations of displacement vs. time (up), its second derivative, a measure of the acceleration (middle) and accelerometer signal (down). The accelerometer signal also follows variations of the displacement and its second derivative, but LDV signals are more clear and useful/20/.

4.2. Electronic speckle pattern interferometry (ESPI)

While laser interferometer measures only one point at time, electronic speckle pattern interferometry (ESPI) laser allows taking snapshot of vibrations of complete 2-D plane and immediately shows the result of huge area as an image /21/. The disadvantage is that the system is large and heavy, applicable only in the laboratory. The ESPI system produces two short flashes immediately after each other, records these diffractions by a CCD

camera and then compares (subtracts) both images. The resulting image corresponds to the vibrations of the surface. The diagrams in Fig. 20 left correspond to two states of a surface, in non deformed state (up), and in the deformed surface (down) /22/. Phase shift Δ between the reference and the object wave is caused by the deformation /23/.

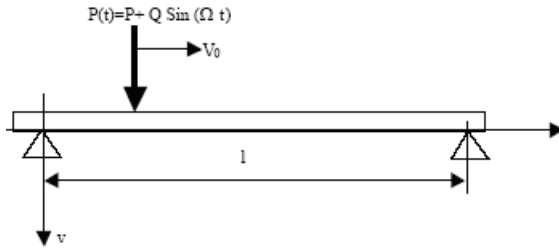


Figure 17: Theoretical model of the beam forced vibrations

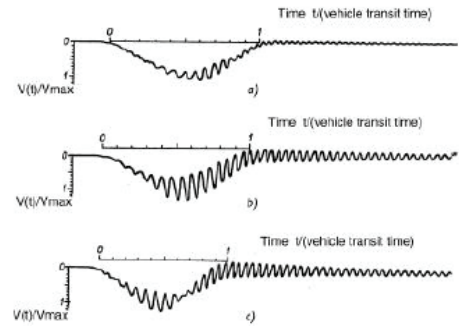


Figure 18: Theoretical solution for beam midpoint displacement

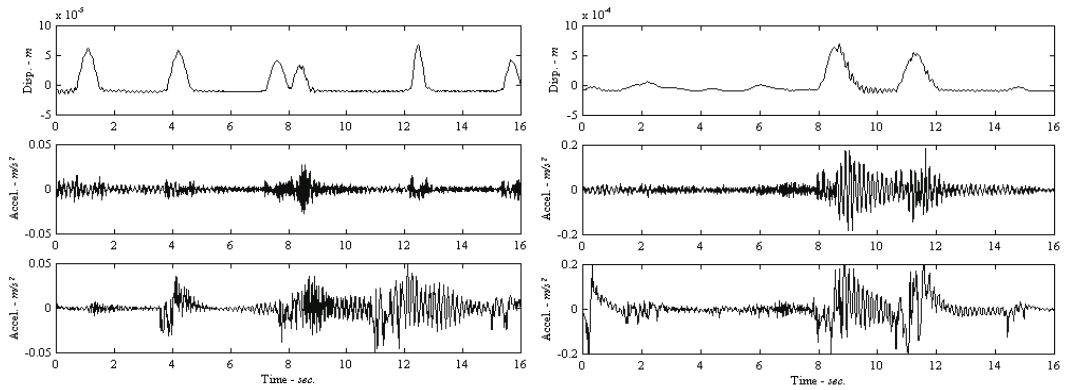


Figure 19: Comparisons of two direct measurements of displacement by LDV (up), the second derivatives (middle) and accelerometer signals (down)

Speckle techniques include holographic interferometry, (ESPI, also named television, electronic, video or digital holography) and shearography. These interferometric techniques require two steps: recording of the object surface, and a second one after applied stress to the object (e.g. by pressure or thermal stress). After applied stress, displacement and strain can reveal discontinuities or flaws (as delamination, disbonding or crack).

Laser testing solution for 3D contactless stress and vibration analyses is Vibro-ESPI-System Q-500 system. It enables highly sensitive full field measurement of harmonic vibration of component surface. It assures both, static and dynamic, deformation measurements. Ruby laser and three cameras enable various applications (brake squeal, car body vibration, engine vibrations, shock waves, explosions). Fiber flexible glasses are used and 1 m² area can be analysed. Light modulator and trigger system produce stroboscopic laser illumination, synchronized to the vibration frequency of the test object /24/. It is best suited for the development and testing of complex components and structures in acoustics and stress/strain analysis of electronics, vehicle design, and aerospace. It can be used for the experimental verification of analytical and numerical calculation techniques.

A review of laser vibrometer types and their applications is given in Table 3.

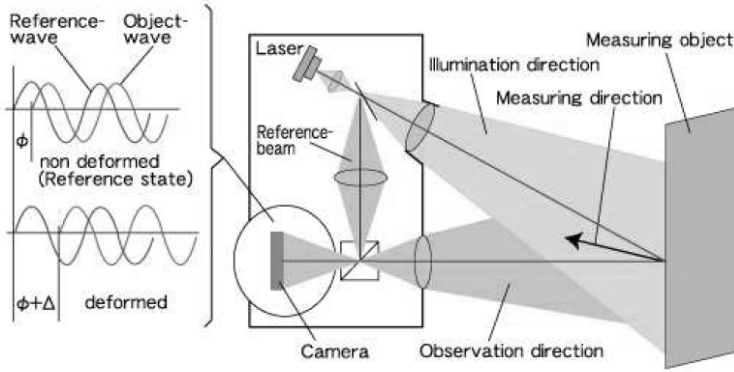


Figure 20: The principle of an electronic speckle pattern interferometry (ESPI system) /22/

Table 3: Laser vibrometers and their applications

Vibrometer type	The application
Standard Optic Vibrometers:	Standard optics high sensitivity single point vibrometers
Fiberoptic Vibrometers	Single point, differential and dual channel fiberoptic vibrometers
Scanning Vibrometers	For full field vibration measurements
Rotational Vibrometers	For angular vibration measurements on rotating structures
In-Plane Vibrometers	For 1-D in-plane vibration measurements
Production Vibrometers	Ruggedized industrial type compact vibrometer sensors
3D Vibrometer	For single point simultaneous X,Y and Z measurements
Compact Vibrometers	Compact high sensitivity vibrometers
Digital Vibrometers	Optimized digital decoding techniques for theoretical limit performance and traceable calibrations
Portable Digital Vibrometers	Portable& affordable
High Speed Vibrometers	For measurements at high vibrational velocities

The examples of ESPI laser interferometry typical results are given in Fig. 21.

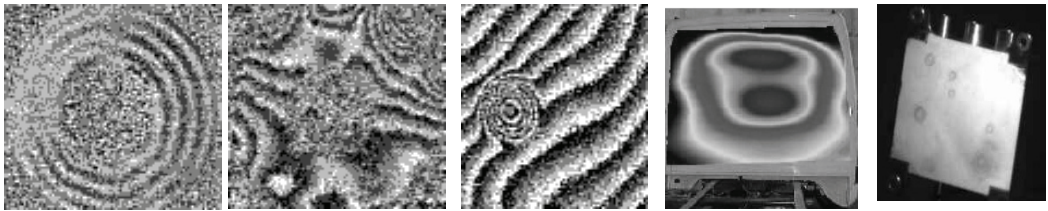
Vibration demonstration is typically for loud speaker, different figures can be observed according to the eigen modes, frequency and amplitude (a). The results obtained with an excitation frequency ≈ 10 kHz. High frequency mode is prevalent for small separation between the two shots ($40 \mu\text{s}$). The second picture is obtained for few seconds separation of a pulse. A sandwich sample (aluminium skin, honeycomb core) has been tested for skin-core debonding (b). Defects could be detected with a thermal loading of the sample. The record of vibration of a truck cabin is given in (c). Electrical casing is small Al part with rubber coating (d). Bonding quality is tested with artificial defects.

4.3. Laser shearographic system

Modern phase stepping optical systems used for aircraft industry have higher sensitivity and signal-noise ratio (SNR) in interferometric methods. Phase stepping optical configuration (real-time phase, phase circulation and display) enable wrapped phase mapping of surface deformation. Obtained data serve for signal processing and flaws detecting. Proper filtering is introduced for better results.

Transferring compact measuring system Q 800 for full field represents contactless NDT inspection for different materials (composite materials fiber glass reinforced plastics, bonded composite materials). Delaminations, cracks, voids, impact damage, defects

in repaired areas and stressed components can be recognized. To stress the component various loading are applied (thermal loading, vacuum, heating and vibration excitation).



a. Loud speaker, Ø 30, CCD camera - pulse separation 40 μ s (left) and few s (right) b. Honeycomb/skin debonding c. Truck cabin Vibration analysis d. Artificial defects in Al casing

Figure 21: The examples of ESPI laser interferometry application in industrial environment

Sensor head can be of small weight and had robotic production inspection system. For inspections in daily circumstances Nd³⁺:YAg is used as a source. The surface of 1 m² can be inspected and obtain data for deformation and /or stress distribution on the surface. Technical details are: resolution 768x582 pixels, mount lens, zoom 1 4/6 -12mm.

DISCUSSION AND CONCLUSION

Presented NDT methods are modern in the world, although used for more then one decade. Some of these methods, GPS and AE, enable global inspection and monitoring, during building and maintenance of structures, and the others, improved UT and MT, enable reliable testing of structural components. Recently developed laser metrology for different purposes also contributes to better testing and inspection.

One point of view would be to make transformation to nowadays the most accurate measurements according to defined theoretical evaluations; the other would be related to development methods in particular industrial branches: railways, shipbuilding, masonry, mechanical and electrical engineering, from heavy industry demands to micro or nanotechnologies. The approach could be described as: techniques used in standard methods of verification and the other still undeveloped methods but very prospective.

Productivity increase, consumer satisfaction and safety require that manufacturing products or structures be thoroughly inspected and characterized during fabrication, after fabrication and in service, along the lifespan. There is broad selection of procedures serving to assess: shape, thickness, composition, microstructure, surface and inner defects, which may affect structural integrity (delaminations, cracks, porosity, disbonds). Due to increased number of investigated items and constructions, ageing effects and new materials and manufacturing processes, innovative inspection concepts strongly needed to reduce the human factor and to increase throughput and sensitivity. Practical examples are sophisticated sensors, adapted loaded mechanisms, data evaluation and presentation.

The last drawbacks of conventional holographic methods have been suppressed with the substitutions of photographic plates and thermo graphic cameras by CCD cameras. Some results show that current limitations are the capability of laser and CCD cameras, demanding further research and development.

REFERENCES

1. http://www.google.com/url?sa=t&source=web&ct=res&cd=4&url=http%3A%2F%2Fen.wikipedia.org%2Fwiki%2FGlobal_Positioning_System&ei=Nv5FSf7JEZWgQeKe4NII&usq=AFQjCNGrf5XrBYp--JY37hZQqJE1_JIGEA&sig2=eoJvrrFw67vkYP-4Tc9Eew

2. Charles Lee and Robert Buchler, Design and Test of a Synergistic Interferometric GPS-INS, Paper No. 24239, Northrop-Grumman, Scott Pace, James E. Wilson, Global Positioning System, Market Projections and Trends in the Newest Global Information Utility, The International Trade Administration - Office of Telecommunications - U. S. Department of Commerce, September 1998, GPS-space.commerce.gov.pdf
3. M. Kirić, The application of information-technological standards to control and maintenance of bridges using non-destructive testing, *IVK*, Vol. 7, No.3 (2007), pp. 177-187.
4. Data of f. Leica (TPS2000_brochure_en.pdf)
5. M. Kirić, On the application of a database model to non-destructive testing of bridges (in Serbian), *Materijali i konstrukcije*, Vol. 51, No.1 (2008), pp. 32-40.
6. A. Hammad et al, Mobile Model-Based Bridge Lifecycle Management Systems, www.blackwell-synergy.com/doi/abs/10.1111/j.1467-8667.2006.00456.x
7. J. Jianjing et al, Study for Real-time Monitoring of Large-Span Bridge Using GPS, Proc. ISSST 2002, "Progress in Safety Science and Technology", Beijing/New York: Science Press, Huang P., Wang Y.J., Li S.C., Qian X.M., eds., Taiwan, Sep. (2002). pp. 308-312.
8. N. Raziq, P. Collier, GPS deflection monitoring of the West Gate bridge, *Journal of applied geodesy*, Walter de Gruyter, ed. ,Vol. 1, 05/2007, pp. 35-44.
9. J. Barnes, et al, The Monitoring of Bridge Movements using GPS and Pseudolites, *Proceedings, 11th FIG Symposium on Deformation Measurements*, Santorini, Greece, 2003.
10. M. Meo, et al, Measurements of dynamic properties of a medium span suspension bridge by using the wavelet transforms, *Mechanical Systems and Signal Processing*, Volume 20, Issue 5, July 2006, Pages 1112-1133, [99994&view=c&wchp=dGLzVtz-zSkzk&md5=5b313999bfad27ddd746085d7b974e51&ie=/sdarticle.pdf](http://www.sciencedirect.com/science/article/pii/S0888327006009994&view=c&wchp=dGLzVtz-zSkzk&md5=5b313999bfad27ddd746085d7b974e51&ie=/sdarticle.pdf)
11. Y. L. Xu, J. M. Ko and Z. Yu, Modal analysis of tower-cable system of Tsing Ma long suspension bridge, *Engineering Structures*, Vol. 19, No. 10, pp. 857-867, 1997.
12. C. Lonsdale, F. Demilly, V. Del Fabbro, Wheel rim residual stress measurements, <http://www.standardsteel.com/rdpapers/RWMEC.pdf>
13. <http://www.ece.cmu.edu/~dwg/research/IEEE%20sensors.pdf>
14. M. Huang, et al., Using Acoustic Emission in Fatigue and Fracture Materials Research *JOM*, November 1998 (Vol. 50, No. 11)
15. R. Gospavić, M. Srecković, A. Milosavljević, R. Radovanović, A. Kovačević, A. Bugarinović, S. Babić, *Laser Material Interaction, Proceedings of 2nd DAAAM International Conference on Advanced Technologies for Developing Countries*, Tuzla, June 25-28, 2003, pp. 177-182. (15)
16. M. Srećković, S. Ristić, D. Družijanić, Ž. Tomić, R. Gospavić, J. Ilić, N. Milošević, V. Popov, Z. Burzić. Aspects of the Theory and Praxis on Laser Interaction with the Material for Special Construction, *Proceedings of the 4th DAAAM International Conference, ATDC 05*, Ed., M.Kljajin, Sept. 21-24, 2005, pp. 321-327. (16)
17. J. Ready, *Industrial laser Application*, Mir, Moscow, 1981. (17)
18. http://commons.wikipedia.org/wiki/File:LDV_Schematic.png (18)
19. *Laser Metrology Handbook, Laser Metrology and Machine Performance VI*; Ford, D. G.; Ed.; Wit Press: Southampton, UK, 2003. (19)
20. M. Gioffrè(*), V. Gusella(*), R. Marsili(°), G. Rossi (°), Comparison between accelerometer and laser vibrometer to measure traffic excited vibrations on bridges (20)
21. http://books.google.com/books?id=LtIFcoeIP-UC&pg=PA562&lpg=PA562&dq=ESPI+system+interferometry+%22Q+500%22&source=bl&ots=a1_eNCLxiQ&sig=BcLEk_-h6mfLDVc6XdUHV2S-xRg&hl=en&ei=__KSSZamHJKU-ga20JGmCw&sa=X&oi=book_result&resnum=4&ct=result#PPA529,M1 (21)
22. <http://zvuk.hamu.cz/studio/dokumenty/Lit145.pdf> (22)
23. <http://www.ndt.net/search/docs.php3?showForm=off&Country=-1&date=-1&DocGroup=-1&Method=&MainSource=29&language=E&MediaType=&restrict=keywords&searchmode=AND&instID=-1&KeywordID=170> (23)
24. <http://www.dantecdynamics.com/Default.aspx?ID=856> (24)

CONTINUOUS MONITORING AND STRUCTURE INTEGRITY ASSESSMENT

Nenad Gubelj, Jožef Predan

*University of Maribor, Faculty of Mechanical Engineering, Maribor, Slovenia,
nenad.gubelj@uni-mb.si*

Tomaž Valh, Drago Valh

Walch d.o.o., Maribor, Slovenia

1. INTRODUCTION

The Structural INTeegrity Assessment Procedure (SINTAP) represents with its sequential approach an ideal basis for computer manipulation. The procedure might be seen as a collection of recommendations mainly for engineering purposes in industry, for engineers with practical experiences but limited knowledge of fracture mechanics. This application provides a fracture assessment procedure useable as the basis of a structural integrity management system. Several assessment levels are offered, from simple but conservative approaches, with limited available data, to accurate and complex approaches.

Standard levels of SINTAP procedure are “Level 0”, “Level 1”, “Level 2”, “Level 3”. When increasing the level, the demand for the entry parameters of the material increases. There's also another issue, on which the application depends in addition to the standard SINTAP procedure. This is the Engineering Treatment Model (ETM) method for assessing the significance of crack-like defects in engineering praxis that offers the results of the stress intensity factor and limit loading for different configurations. The application already contains an example of lift car fork plus twelve loading configurations.

The main requirement when planning the application was the universality and openness of the tool for manifold of elementary configurations in addition to already included ones. One should also be able to export the results, data and graphs in standard formats into other standard applications.

Though the SINTAP procedure is standardised, each solution holds for an individual configuration, on the other hand. Its result in the simplest form is only information whether is the identified damage in the construction safe or is there a potential danger for a failure (fracture). This is basic information only. Consider that a crack can be safe for the prescribed load but unsafe in case of overloading. The application enables repeating the calculations with different properties of the crack or different loadings for that purposes. It remains up to the user to decide which is the critical parameter. In the context of obtained results should be understood that the approaches described in this procedure are not intended to supersede existing methods, particularly those based on workmanship. They should be seen as complementary, the use of which should be aimed at ensuring safe and efficient material's selection, structural design, operation and life extension.

1.1. Applicability

The procedure described is based on fracture mechanics principles and is applicable to the assessment of metallic structures containing actual or postulated flaws. The purpose of the procedure is to determine the significance, in terms of fracture and plastic collapse, of flaws present in metallic structures and components.

The procedure is based on the principle that failure is deemed to occur when the applied driving force acting to extend a crack exceeds the material's ability to resist the extension of that crack. This material property is called the material's fracture toughness or fracture resistance.

The procedure can be applied in the design, fabrication or operational stages.

1.1.1. Design stage

The method can be used for assessing hypothetical planar discontinuities at the design phase in order to specify the material properties, design stresses, inspection procedures, acceptance criteria and inspection intervals.

1.1.2. Fabrication stage

The method can be used for fitness-for-purpose assessment during the fabrication. However, this procedure shall not be used to justify shoddy workmanship and any flaws occurring should be considered on a case by case basis with respect to fabrication standards. If non-conforming discontinuities are detected, which cannot be accepted to the present procedure, the normal response shall be:

- (i) correcting the fault in the fabrication process causing the discontinuities, and
- (ii) repairing or replacing the faulty product.

1.1.3. Operational stage

The method can be used to decide whether continued use of a structure or component is possible and safe despite detected discontinuities or modified operational conditions. If during in-service inspection discontinuities are found which have been induced by load fluctuations and/or environmental effects, these effects must be considered using suitable methods which may not be described in the present procedure. The procedure may be used to show that it is safe to continue operation till a repair can be carried out in a controlled manner. Further applications of the method described are the provision of a rationale for modifying potentially harmful practices and the justification of prolonged service life (life extension).

1.2. Approach

The approach used in this application is suitable for the assessment of structures and components containing, or postulated to contain, flaws. The failure mechanisms considered are fracture and plastic collapse, together with combinations of these failure modes. The philosophy of the approach is that the quality of all input data is reflected in the sophistication and accuracy of the resulting analysis. A series of levels is available, each of increasing complexity and each being less conservative than the next lower level; consequently 'penalties' and 'rewards' accrue from the use of poor and high quality data, respectively. This procedural structure means that an unacceptable result at any level can become acceptable at a higher one. The user should perform the work necessary to reach an acceptable level and need not invest in unnecessarily complicated tests or analysis.

Due to the hierarchical structure of data and assessment levels, path selection through the procedure is made based on the relative levels of contribution of brittle fracture and plastic collapse in overall failure. Qualitative and quantitative guidance is provided for the user in the direction that will yield most benefit in terms of data improvement.

The basis for this is the location of the initial analysis point in terms of brittle fracture and plastic collapse. This can be assessed by either the Failure Assessment Diagram (FAD) or the Cracking Driving Force (CDF) curve. The methods can be applied to

determine the acceptability of a given set of conditions, determine the value of a critical parameter, assess the safety margins against failure or determine failure probability.

In order to facilitate the route through the application, information is grouped according to five parts:

- (I) Description of the configuration
- (II) Material inputs
- (III) Geometrical inputs
- (IV) Additional inputs and description
- (V) Calculation

The flow chart (Fig. 1) shows the structure and the operation of the application.

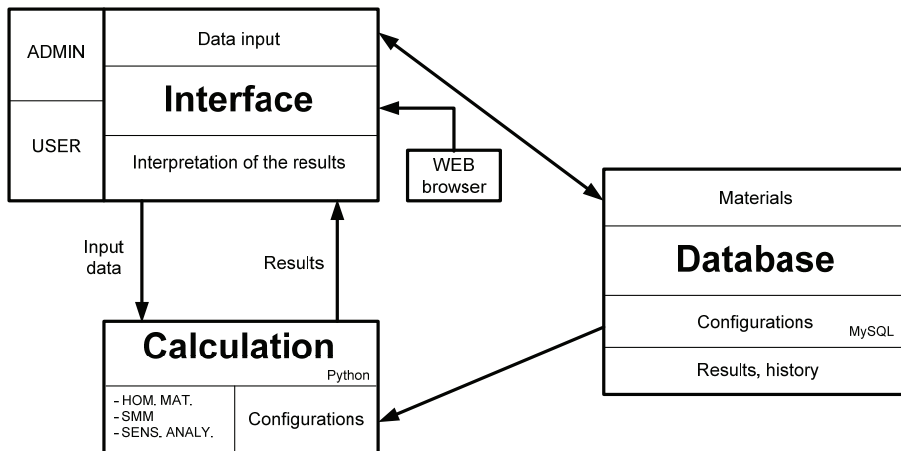


Figure 1: Structure and operation of the application

The application is build up from several program languages that coincide with the philosophy of universality of the tool with respect to the user and configurations. The graphical interface is developed using Typo 3 and CMS technology. The configuration is realized using PHP, html and Javascript. The data and results are stored by MySQL. Python is used for loading additional geometrical and loading configurations. The calculation is performed in two phases. The first one is the preparation of the stress intensity factor and limit loading. The second phase is a standard SINTAP-FRACTURE MODE procedure carried out in FAD or CDF diagram.

2. THE SINTAP APPLICATION

2.1. Running the program and entry check-up

The SINTAP is a web application started typing <http://mostis.structures.ws/> to the default web browser and click Login after applied username and password (Fig. 2).

2.2. File

After the login, a new form displays, where a Project is chosen. Every user has own personal username and password given by the administrator.

There are three possibilities after Login available:

- To open a new project by clicking New
- To open an existing project by clicking Open
- To edit an existing project by clicking Edit

If New is chosen, a new project is loaded. One only has to fill up the following fields (Fig. 3); only Name is obligatory, others are optional and provide additional information

- Date,
- Project status,
- Location,
- Description.

Login

User login

Enter your username and password here in order to log in on the website:

Username:

Password:

[Forgot your password?](#)

Figure 2: Login form

New

Name:
Please enter new name.

Date:
Enter date (dd.mm.YYYY).

Project status:

Location:
Please enter location information.

Description:
Please enter description.

Figure 3: New project form

If there are already existing projects, they can be manipulated by clicking Open. One chooses the desired project from the list on the left side, Fig. 4, by clicking the text with the mouse.

2.3. Configuration

2.3.1. Configuration

Selection of the geometrical and loading configuration is the basis for the calculation. The geometrical and loading configuration is selected, when is marked with the mouse (Fig. 5). Its picture appears below together with description of the configuration, load units, crack units, availability of the stress distribution, description of the component geometry, crack geometry, loading, in addition availability of the strength mismatch and sensitivity analysis. The desired configuration is selected by clicking »Submit«. The

SINTAP procedure level is selected with respect to the availability, quantity and quality of the material properties. The application supports three levels of SINTAP procedure: Default, Basic, Mismatch and Advance level, as shown in Fig. 6. The most basic or default level 0 is also called "the level of insufficient material knowledge".

Open			
Name	Date	StatusLocation	Description
<u>C001-level 0-hom</u>	24.10.2007	Active	Primer konfiguracije: konfiguracija 001 homogen material Sintap nivo 0
<u>C001-level 0-hom</u>	24.10.2007	Active	
<u>C002-level 1-hom</u>	25.10.2007	Active	Konfiguracija 2 SINTAP level 1 Homogen material
<u>C002-level 1-hom</u>	25.10.2007	Active	Konfiguracija 2 SINTAP level 1 Homogen material
<u>C005</u>	30.11.2007	Active	
<u>C017</u>	26.11.2007	Active	C017-Test
<u>C021</u>	27.11.2007	Active	Test configuration 1.21
<u>Crane double crack</u>	10.12.2007	Active	Belgrade main site centreA double edge crack was discovered on the support pillar no. 3 of the crane serial number SE378872652 on july 36 2007.....
<u>Crane double crack</u>	10.12.2007	Active	Belgrade main site centreA double edge crack was discovered on the support pillar no. 3 of the crane serial number SE378872652 on july 36 2007.....
<u>DeleteMe</u>	25.03.2008	Active	Will be deleted!
<u>DeleteME2</u>	26.03.2008	Active	

Figure 4: Open existing project form

Another dialog is loaded showing the list of available configurations.

2.3.2. Procedure level

The Advance level is upper an engineering level, based on compendia solutions for Stress-intensity factor - SIF and Limit Load Solution. It's also the most sophisticated (advanced) level. It gives most accurate and least conservative results, but it requires the knowledge about the complete stress-deformation curve from uniaxial tensile test. The Mismatch level is equivalent to the Basic level and it is in use when difference between yield strength of weld metal and base metal are greater than 10%.

Advanced level offers also the calculation of Sensitivity analysis if the latest is available within the configuration.

The selected options are accepted by clicking »Submit«.

2.3.3. Configuration details

Configuration details form doesn't enable entering any data but provides some additional information about the loading case.

The Advance level is upper an engineering level, based on compendia solutions for Stress-intensity factor-SIF and Limit Load Solution. It's also the most sophisticated (advanced) level. It gives most accurate and least conservative results, but it requires the knowledge about the complete stress-deformation curve from single axis tensile test. The Mis-match level is equivalent to the Basic level and it is in use when difference between yield strength of weld metal and base metal are greater than 10%.

Advanced level offers also the calculation of Sensitivity analysis if the latest is available within the configuration.

The selected options are accepted by clicking »Submit«.

Configuration details form doesn't enable entering any data but provides some additional information about the loading case.

Configuration

Configuration filter

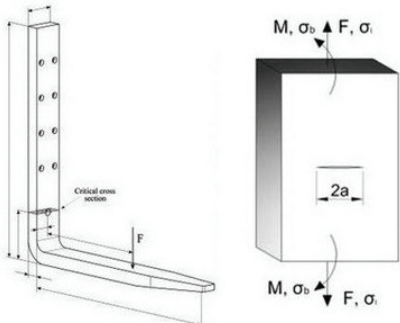
Component geometry: -- display all --
 Crack geometry: -- display all --
 Loading: -- display all --

Available configurations

- Axial Surface Cracks in Pipe Elbows (Internal Pressure)
- Centre (Through) Cracks in Plates (Combined Tension and Bending)**
- Centre (Through) Cracks in Plates (Tension Loading)
- Chordal Cracks in Round Bars (Bend Loading)
- Chordal Cracks in Round Bars (Tension Loading)
- Circumferential Surface Cracks in Tubes (Tension Loading)
- Double Edge Cracks in Plates (Tension Loading)
- Elliptical Embedded Cracks in Plates (Combined Tension and Bending)
- Full Circumferential Surface Cracks in Tubes (Tension Loading)
- Internal Corner Cracks in Pipe Nozzles (Internal Pressure)

Submit

Summary



The figure shows two diagrams. On the left, a 3D perspective view of a pipe elbow with a crack. A force F is applied at the end, and a 'Critical cross section' is indicated. On the right, a 2D perspective view of a rectangular plate with a central crack of length $2a$. The plate is subjected to a bending moment M and a tensile force F , resulting in stresses σ_b and σ respectively.

Centre (Through) Cracks in Plates (Combined Tension and Bending)
Load unit: kN
Crack unit: mm
Stress dist.: no
Component geometry: Plates
Crack geometry: Single Edge Crack
Loading: Combined Tension and Bending
Homogeneous material: available
Joints with strength mismatch: not available
Sensitivity Analysis: not available

Figure 5: Configuration form

Procedure level

Material configuration: Homogeneous material
 Joints with strength mismatch

SINTAP Procedure level: 0
 1
 2
 3

Sensitivity Analysis:

Submit

Figure 6: Procedure level form

2.3.4. Strength mismatch: Crack locations

A welded joint is heterogeneous in both deformation properties and microstructure. The first causes a variation of strain and hence driving force, and the latter causes a variation of fracture properties across the weld. The weld metal is represented by a strip

and is commonly produced with yield strength, σ_{YW} , greater than that of the base plate, σ_{YB} , the case is designated with the mismatch factor

$$M = \frac{\sigma_{YW}}{\sigma_{YB}} \quad (1)$$

Undermatching ($M < 1$) gives rise to a strain concentration in the weld metal and it is therefore good practice to avoid undermatching since the local ductility in the weld metal can be exhausted at low global deformations. Overmatching ($M > 1$) reduces the strain in the weld material as compared to the base plate, thus shielding a defect in the weld metal.

This option is only available if Strength mismatch is more than 10% ($M < 0.9$ or $M > 1.1$). Its appearance depends on the selected configuration and normally requires the following data (Fig. 7):

- The stress-strain condition
- Dimensions of the joint
- Position of the crack according to the welding material

Strength mismatch: Crack locations

Strength mismatch, Stress-Strain condition:: Plane Strain
 Plane Stress

Joint or Weld geometry

2H [mm]:

H_1 [mm]:

Crack and component geometry regarding possible crack locations within the weld metal, including an interface crack. Select the correct crack configuration::

CENTRE CRACKED TENSILE PLATES: CCT

Figure 7: Crack location form (welded joints)

2.4. Material properties

The next step is to fill up the forms about the material properties.

2.4.1. Material # 1: Base

Several parameters are required accordingly to the selected procedure level, Table 1.

The dialog contains different fields to enable entering the material properties. There are several options which depend on the level of SINTAP procedure. In addition to other

material parameters, the information about the shape of stress-deformation curve has to be given (whether material exhibits continuous yielding or Lüders plateau).

The »Advanced level-A« demands a Stress-Strain curve that has to be added as two columns of points as an R-e curve respectively (Fig. 8). Columns are separated by 'tab' or »;«. The decimal delimiter is dot ».« or comma »;«. The Stress-Strain curve can be described as an Engineering curve, an Engineering curve where a Ramberg-Osgood approximation shall be performed or, as a true stress-strain curve. The Ramberg-Osgood approximation can be used if one doesn't have enough points of the engineering R-e curve. The minimal number of curve points is ten. However, the approximation is highly recommended for such a small number of points in order to avoid the unusual shape of the failure acceptance curve in FAD. That would make it useless for failure assessment.

2.4.2. Material # 2: Weld

If »Strength mismatch« was chosen, the »Material #2: Weld« is enabled and requires the data to be filled in the same manner as in case of »Material #1: Base«. Consider that only fields of Advanced level are enabled.

Table 1: Material properties for different procedure levels

Description	Default value	Unit	Level			
			0	1	2	3
Young's Modulus of Elasticity (E)	210	GPa	✓	✓	✓	✓
Poisson's ratio (ν)	0,3	-	✓	✓	✓	✓
Plastic constraint factor (m)	1,5	-	✓	✓	✓	✓
R_{el}	-	MPa	✓	✓	✓	✓
$R_{p0.2}$	-	MPa	✓	✓	✓	✓
R_m	-	MPa		✓	✓	✓
$K_{mat}, J_{mat}, \Delta_{mat}$	-	-		✓	✓	✓
Charpy impact energy (Cv)		J	✓			
or		-	-	-	-	-
Working temperature (T)		°C	✓			
Temperature at 28J of Charpy impact energy (T_{28J})		°C	✓			
Probability of failure (P_f)		%	✓			
Yield strength at 0.2% plastic strain ($R_{p0.2}$)		MPa	✓	✓	✓	✓
Tensile strength (R_m)		MPa		✓	✓	✓
Crack fracture resistance in terms of K , J or δ ($K_{mat}, J_{mat}, \delta_{mat}$)		$N/mm^{1.5}$, N/mm, mm		✓	✓	✓
Engineering stress-deformation curve from single axis tensile test (R-e)		File				✓
Stress-strain curve type	-	-				✓

2.4.3. Sensitivity analysis

The variability influence of the maximum number of reached loading cycles on the variability of input random quantities is studied by means of the sensitivity analysis. There takes place an increase of crack initiation a_0 to critical size a_{cr} .

The R-curve can be described in three ways. As a CTOD- Δa curve, as a J- Δa or in a form of three parameters: A, C and D. In that case the parameters are entered in the field »Crack growth fracture resistance data« in the forms using »=«, 'tab' or »;« as delimiter.

The order of the parameters is not important, but the names must be »A«, »C« and »D«. See an example in Figs. 9 and 10. One can use either ».« or »<« as a decimal delimiter.

The calculation of the curve from the parameters is performed by the Ref. /7/.

The equation fitted to the crack extension data ($y_i, \Delta a_i$) has a general form

$$y = A + C \cdot \Delta a^D$$

where y is either J or CTOD, Δa is the crack extension, A , C and D are constants.

Stress-Strain curve:

0	0
520.791	0.002557912
521.3092	0.003550025
523.5393	0.004533163
529.3008	0.00549884
539.7729	0.008421755
555.0227	0.010326896
569.1632	0.013218031
575.679	0.015154222
608.8896	0.019898854

Please enter Stress-Strain curve data or choose file for upload.

Stress-Strain curve type:

- Stress-Strain (R-e), Engineering curve
- Stress-Strain (R-e), Engineering curve + Ramberg Osgood approximation
- Stress-Strain (R-e), True curve

With second option the engineering curve will be calculated using Ramberg-Osgood equation.

Figure 8: Stress - strain data form

If Δa^D is substituted with $x = \Delta a^D$, A and C can be evaluated using linear regression. Then, the value D is chosen so as to maximise the correlation coefficient.

One takes the values of D from 0 to 1 in steps of 0.01. For each value of D , the $x_i = \Delta a_i^D$ and the correlation coefficient r are calculated:

$$r = \frac{S_{xy}}{\sqrt{S_{xx} \cdot S_{yy}}} \quad (2)$$

where

$$S_{xx} = \sum X_i^2 - \frac{(\sum X_i)^2}{N} \quad S_{yy} = \sum Y_i^2 - \frac{(\sum Y_i)^2}{N} \quad S_{zz} = \sum Z_i^2 - \frac{(\sum Z_i)^2}{N} \quad (3)$$

for the N data points.

Sensitivity analysis

Load data from material

Crack growth fracture resistance data:

A	0
C	0,015
D	0,63

Please enter R-curve data or choose file for upload.

Type of R-curve:

- CTOD - delta a
- J - delta a
- Offset power law fit parameters

Crack growth fracture resistance curve or R-curve.

Figure 9: Fracture resistance curve form

Sensitivity analysis

Load data from material

Crack growth fracture resistance data:

Please enter R-curve data or choose file for upload.

Type of R-curve: CTOD - delta a
 J - delta a
 Offset power law fit parameters

Crack growth fracture resistance curve or R-curve.

Type of specimen: CT
 3PBS
 M(T)

Optional parameter for information only.

Crack Extension, delta a:

Crack Extension with R-curve according to definition of crack size at stable crack growth.

Increasing the Load: Automatically set the parameters
 Manually set the parameters

Please note: When manually setting the parameters the application WILL NOT seek the critical crack size and critical load.

Starting load:
 Should be higher than zero load size.

Maximum load:
 Should be higher than nominal load.

Loading step:
 Please note: Setting the loading step too small can produce large number of curves.

Figure 10: Sensitivity analysis form

The value of D which maximises r should be chosen. The corresponding A and C are evaluated from

$$C = \frac{S_{xy}}{S_{xx}} \text{ and } A = \bar{y} - C \cdot \bar{x} \quad (4)$$

where

$$\bar{x} = \frac{\sum x_i}{N} \text{ and } \bar{y} = \frac{\sum y_i}{N}$$

The load can be increased manually or automatically. If one chooses the »Manually set the parameters« option, an appropriate number of curves is drawn, the user has to choose change manually parameters to achieve the critical curve. In that case, the »Starting load«, »Maximum load« and »Loading step« are enabled. If one chooses »Automatically set the parameters«, the program finds automatically the critical curve, there are also the critical parameters, obtained by Sensitivity analysis, printed.

Thus two additional diagrams are obtained at the end of the procedure (see chapter 3. Assessment). The load curves are calculated up to the 90% of the physical or validity condition limitation. FAD diagrams for automatically and manually set parameters are shown in Figs. 11; 13 and 14.

FAD diagram

There were two boundary conditions evaluated:

1. The curve lies under the FAD diagram break (at $L_{r \max}$)
2. The curve lies above the FAD diagram break (at $L_{r \max}$)

The latter case usually leads to inadequate results, one should account more on results obtained from the CDF diagram.

Both boundary conditions are evaluated first by finding a knee point of the load curves. The knee point is defined as the point, where

$$\frac{\Delta K_r}{\Delta L_r} \approx 1 \tag{5}$$

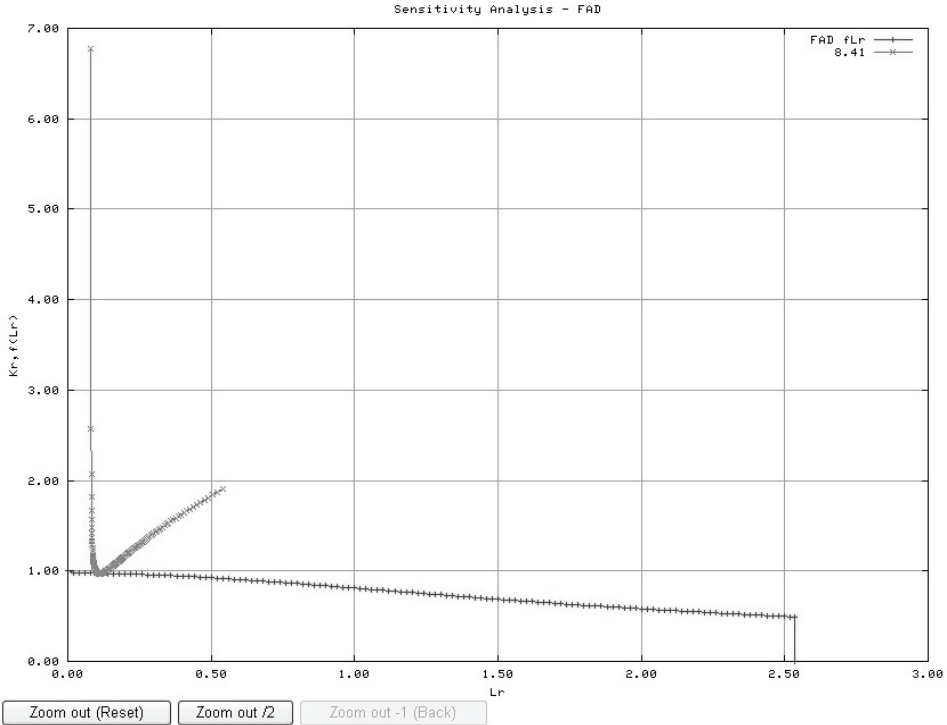


Figure 11: FAD diagram, automatically set parameters

The comparison is made whether the line through the break point of the FAD is above or under the line through the knee point of the loading curves, as shown in Figure 15.

1. The critical curve lies under the FAD diagram break

In that case the critical curve is suppose to touch the break point of the FAD ($L_r\ max, K_r$), see Fig. 16. Let the line through (0,0) and ($L_r\ max, K_r$) be called a »FAD line«.

Then, two curves are calculated: one with the load below and one with the load above the point ($L_r\ max, K_r$) that defines the critical load in that case. These curves are defined as Nominal Load * 0,5 and Nominal load * 1,5.

There's a linear dependency assumed between loads and same (L_r, K_r) pairs on different load curves. The critical L_r is assumed to be an $L_r\ max$. The critical load can therefore be calculated from:

$$F_{critical} = F_i = k_c \cdot L_r\ max + n_c \tag{6}$$

where

$$k_c = \frac{F_{i-1} - F_{i+1}}{L_r\ i-1,j - L_r\ i+1,j} \quad n_c = \frac{L_r\ i-1,j \cdot F_{i+1} - L_r\ i+1,j \cdot F_{i-1}}{L_r\ i-1,j - L_r\ i+1,j}$$

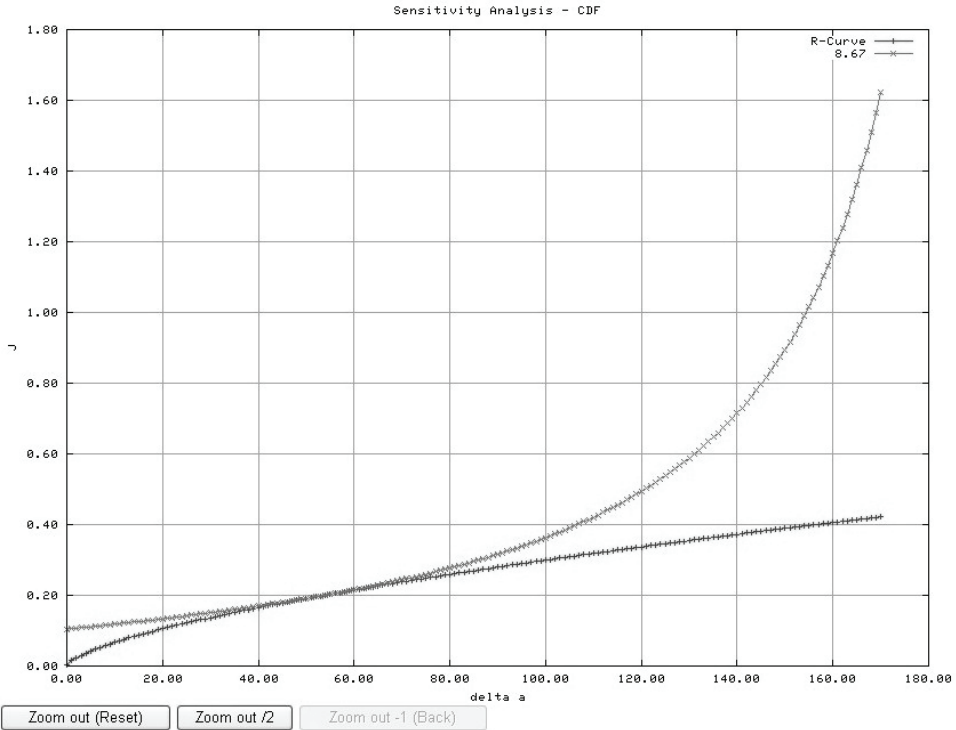


Figure 12: CDF diagram, automatically set parameters

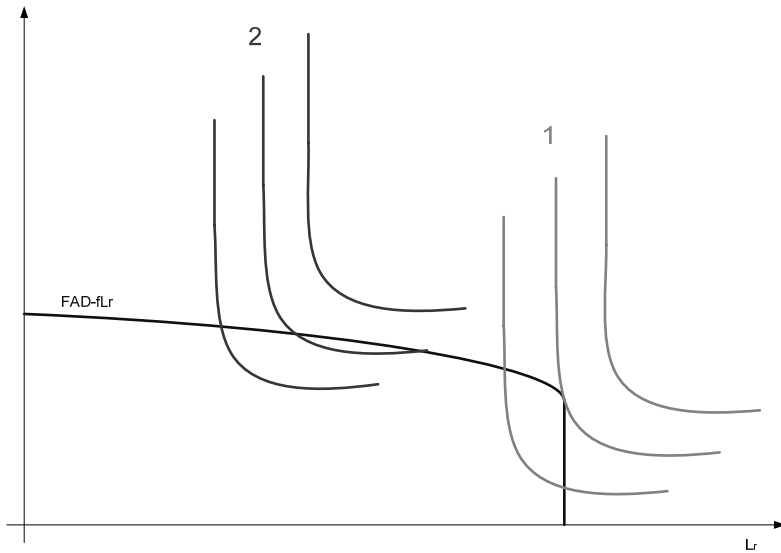


Figure 13: FAD diagrams (critical curves lay above or below the diagram break)

Each point of each loading curve meets a specific crack size. If there is a sufficient density of points, a linear approximation can serve to obtain an excellent result.

$$Crack_{critical} = Crack_j = k_{cr} \cdot L_{rmax} + n_{cr} \quad (7)$$

where

$$k_{cr} = \frac{Crack_{j-1} - Crack_{j+1}}{L_{r\ i,j-1} - L_{r\ i,j+1}} \quad n_c = \frac{L_{r\ i,j-1} \cdot Crack_{j+1} - L_{r\ i,j+1} \cdot Crack_{j-1}}{L_{r\ i,j-1} - L_{r\ i,j+1}}$$

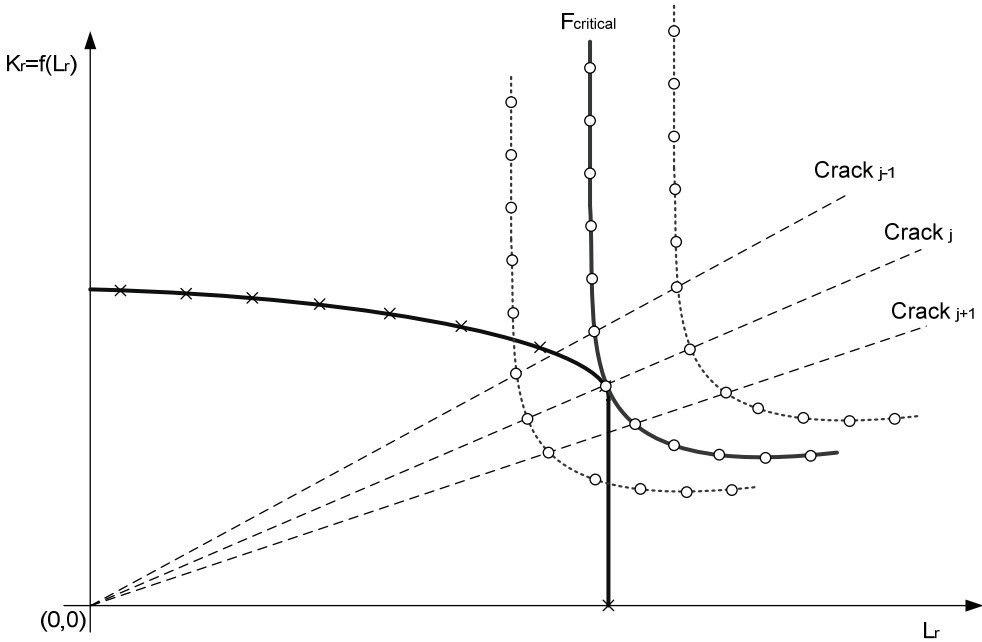


Figure 14: FAD diagrams (critical curve lies below the diagram break)

2. The critical curve lies above the FAD diagram break

First a cross-section between the FAD - $f(L_r)$ and a straight line through the knee of a load curve is calculated (Fig. 15). Two additional curves are calculated in addition. Taking a linear dependency between load and a same crack size, the critical load is calculated as the knee point was the critical point. Then a short check up is performed if all the points are really under the FAD - $f(L_r)$ curve. If the crack extension goes lower than the knee, this is usually not the case. This depends on the user, how he or she sets the crack parameters. Then, the maximum distance between the straight line between two neighbouring points of FAD - $f(L_r)$ right to the knee of the load curve and the line through the points of the load curve and (0,0) is calculated:

The load curve is moved in the direction of decreasing the dist to zero, the critical load can be calculated by taking into account the linear dependency between the load and the distance of the curve from (0,0). The critical crack value is defined by the point (crack) that defines the maximum distance *dist*.

$$dist = \max_{i,j} \left(\sqrt{(x_i - x_j)^2 + (y_i - y_j)^2} \right) \quad (8)$$

There exists a local minimum of the load curve. At that point the load curve will touch the R-Curve when a proper loading is applied, as shown in Fig. 16. The local minimum is calculated by differentiation of the load curve.

$$\frac{d(J)}{d(\Delta a)} = \min \quad (= 0) \quad (9)$$

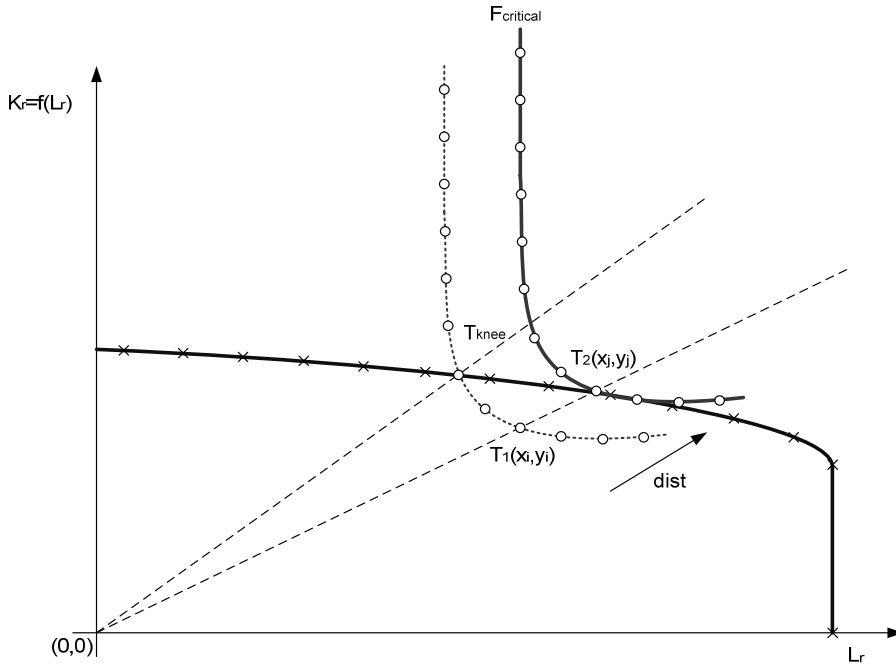


Figure 15: FAD diagrams (critical curve lies above the diagram break)

CDF diagram

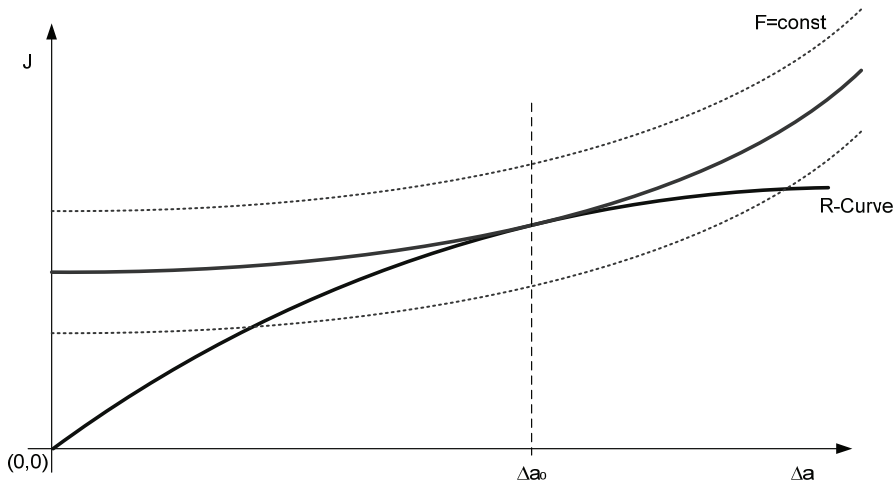


Figure 16: CDF diagram

If latter one defines the critical load at Δa_0 , the critical load curve can be calculated.

Usually, the stress intensity factor, K_I , is proportional to the loading and geometry depended, a function of the crack size.

$$K_I = F \cdot f(a) \quad (10)$$

where:

F applied load

$f(a)$ non-linear function of crack (variable) and dimensions (constant)

At a certain crack size ($a=const$), one can write

$$K_I|_a = F \cdot \alpha \tag{11}$$

Thus at every point α can be calculated from the following equation which combines the R-Curve and the load curve as looking for the critical loading:

$$K_I = \sqrt{J \cdot E} = F \cdot f(a) \Rightarrow F = \frac{\sqrt{J \cdot E}}{f(a)} \tag{12}$$

where $f(a)$ is calculated from the geometrical configuration $f(a) = \frac{K_I(a)}{F_j}$ taking into account that $F_j = const$ along a load curve j. In fact, this is the curve that touches the R-Curve. Now calculating $\frac{d(F)}{d(\Delta a)}$ from the obtained points, one obtains the critical crack

Δa_0 and critical load $F_j = F_{critical}$ at that point.

2.4.4. Strength mismatch: Deformation pattern

This option is available only if Strength mismatch was chosen. Here, the deformation pattern is to be selected from the dialog shown in Fig. 17.

Strength mismatch: Deformation pattern

Shape of deformation zone:

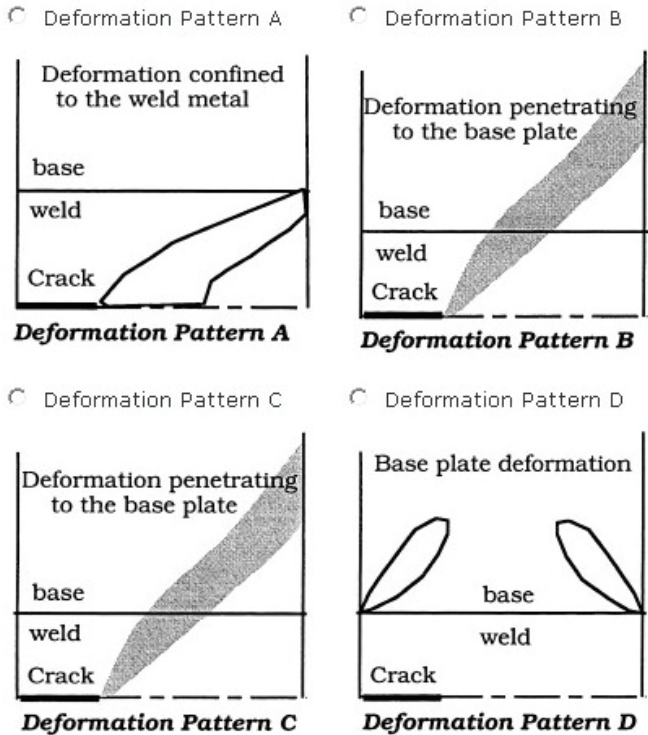


Figure 17: Deformation patterns for strength mismatch

2.4.5. Material editor

Choose Material editor and click “Add new material” (Fig. 18). In addition to the “General info”, there is also the “Material numerical data” which is the same as “Material #1: Base” for instance.

To edit or add the material curves, one need to simply click “Edit curves” after the material is selected or a new one added (Figures 19 and 20). The list of curves is shown. To edit the already existing curves, one needs to click on its name. In order to add the new curve, “Add new curve” needs to be clicked.

Material editor

Add new material	Delete this material	Edit curves
-------------------------	-----------------------------	--------------------

General info

Short name:
Please enter material short name.

Long name:
Please enter material long name.

Description:
Please enter description.

Purpose:
Please enter material purpose.

Data source:
Please enter data source.

Standard:
Please enter standard.

Standard label:
Please enter standard label.

Optional description standard:
Please enter standard description.

Available For:

Verified:

Data level:

Lover temp [C]:

Upper temp [C]:

Owner:

Owner group:

Date added:

Figure 18: Material editor form (1)

Material editor

Selected material: Material 1 - Level 3

Add new curve

Curve type	Short description
<u>Offset power law fit parameters</u>	
<u>Stress Strain R-e (eng) curve</u>	<u>Stress-Strain eng 1</u>

Figure 19: Material editor form (2)

Material editor

Selected material: Material 1 - Level 3

Back to curves table Delete this curve

General info

Short description:

Please enter short description.

Description:

Please enter description.

Data source:

Please enter data source.

Type of specimen: CT
 3PBS
 M(T)
Optional parameter for information only.

Remarks:

Remarks.

Curve type:

Curve:

0	0
520.791	0.002557912
521.3092	0.003550025
523.5393	0.004533163
529.3008	0.00549884
539.7729	0.008421755
555.0227	0.010326896
569.1632	0.013218051
575.679	0.015154222
608.8896	0.019898854

Please enter curve data or choose file for upload.

Figure 20: Material editor form (3)

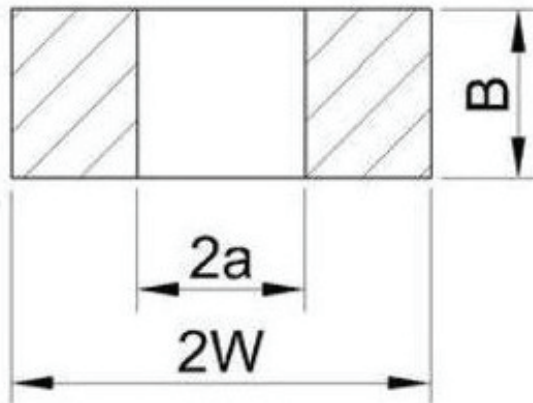
There are six types of curve possible “Curve type”. First three are valid for Sensitivity analysis, second three for SINTAP level 3.

- R curve (CTOD - delta a)
- R curve (J - delta a)
- R curve (Offset power law fit parameters)
- Stress - strain, R-e (Engineering) curve
- Stress - strain, R-e (Engineering + RO) curve
- Stress - strain, R-e (True) curve

2.5. Geometry

The geometrical parameters of the crack and component are filled into appropriate fields shown in Fig. 21. The meaning of the parameters is seen from the picture. One must consider that geometry parameters cannot take values ≤ 0 and that crack cannot be ≤ 0 and it also cannot be greater than the geometrical parameter in which direction it grows.

Geometry



Crack geometry

$2a$ [mm]:

Component geometry

$2W$ [mm]:

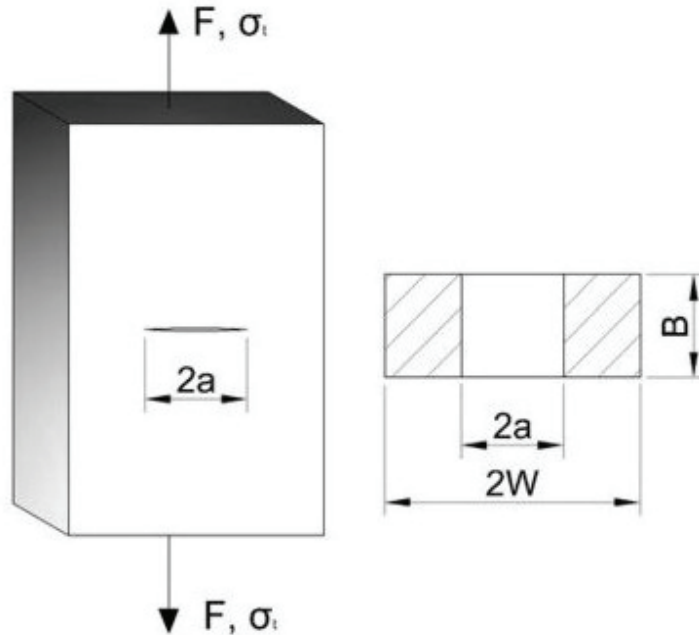
B [mm]:

Figure 21: Geometry form

2.6. Material primary stresses

Here, the primary stresses in appropriate units are entered (Fig. 22).

Primary stresses



Simple external loading

F [kN]:

Figure 22: Primary stresses form

2.7 Additional

2.7.1 Selectable boundary conditions

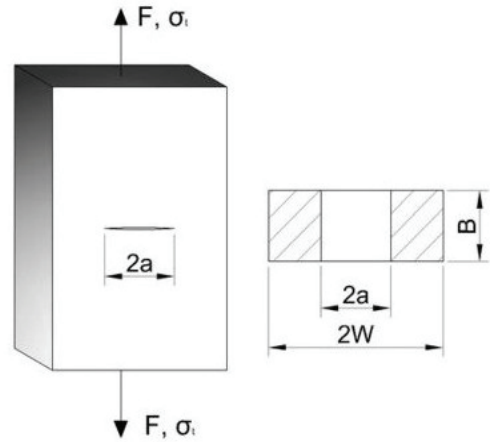
There are several boundary conditions available (an example is given in Fig. 23). These options must not be left empty.

2.7.2 Calculation parameters

This dialog enables decision about the assessment with respect to the critical load or critical crack (Critical value assessment), as shown in Fig. 24. The calculation is repeated with only one parameter being changed, while other remains constant. Thus the loading curve or the crack growth curve is drawn. This method enables to determine not only the operating or nominal point, but also the critical or failure point. There are two parameters that define the increase of selected value, these are steps for increasing the load or crack length and the maximum load or crack length. The lower limit of the increasing parameter is selected as a small positive number. The step for increasing the normalized load L_r has

to be given, too. The lower limit of the increasing normalized load is always zero, while the plastic collapse limit defines the upper limit. With this dialog the final act of the parameter entry is presented. It preserves the parameters of previous calculations as being part of the opened project, if they exist.

Selectable boundary conditions



Plane Stress/Strain condition, valid for calculation of Stress Intensity Factor and Limit (Yield) Load:: Plane stress
 Plane strain

Figure 23: Selectable boundary conditions form

Calculation parameters

Type of Stress-Strain response: Crack length (Load = const.)
 Load (Crack length = const.)

Starting crack size:
 Should be larger than zero crack size.

Maximum crack size:
 Should be larger than nominal crack size.

Step for increasing the crack size:

Starting load:
 Should be higher than zero load size.

Maximum load:
 Should be higher than nominal load.

Step for increasing the load:

Step for increasing the Normalized load (L_r):

Figure 24: Calculation parameters form

In short, one chooses between the stress-strain response to the increasing Load or Crack. In the first case, the minimum and maximum loads are entered in addition to the step for increasing the load. In the second, the minimum and maximum crack has to be entered, including the step for increasing it. The default value of Step for increasing the Normalized load (L_r) is 0.02.

3. Assessment

The calculation is initiated by clicking »Start«. There are Critical and Nominal points obtained by FAD and CDF procedure displayed separately. There are also the Critical load and Nominal load and crack displayed. If Sensitivity analysis was performed and automatically set the parameters selected, there are also results of SA visible. An example of the report is given in Fig. 25.

3.1. Graphical representation of the results

The basic purpose of the SINTAP-FRACTURE MODE procedure and the graphical representation of the results is assessment of the structural integrity of the component. The location of two points is determined with the use of a various calculation methods. The first point is called the nominal or operating point, while the second is known as a critical or failure point. Both are presented in both graphs (FAD and CDF) and should give identical or comparable results. The position of the nominal point with respect to the failure curve is of our interest. This describes the failure safety of the structural component. The failure point expresses the critical state, this state has two parameters: critical crack length and the failure load.

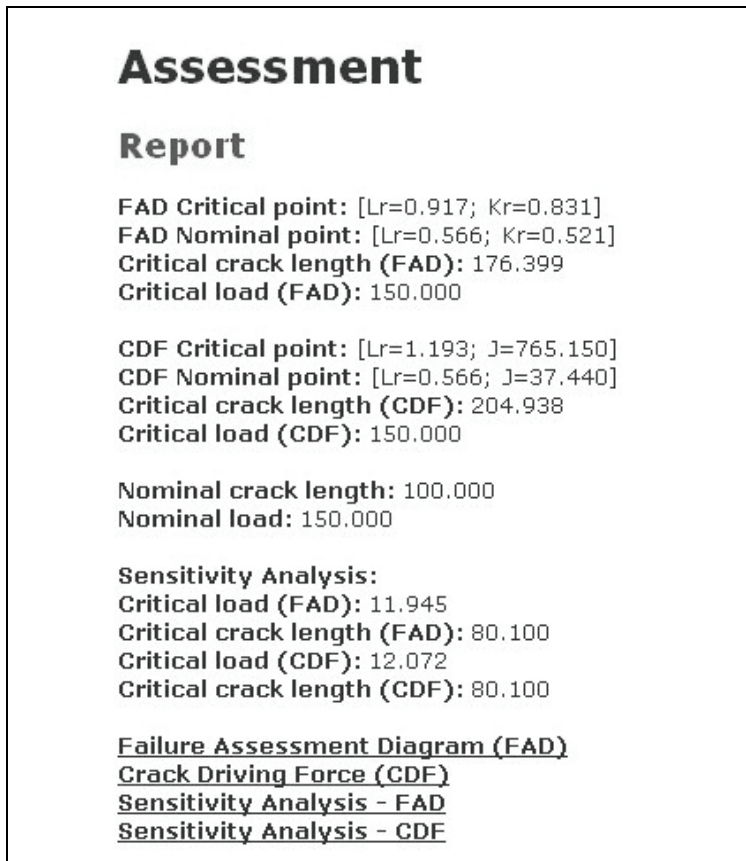


Figure 25: Report form

After the last dialog is confirmed, the SINTAP-FRACTURE MODE calculation is performed in two steps. The first stage is performed in Python environment. Firstly, the selected parameter is increased, and then the calculation of stress intensity factor, limit load, reference stress and normalised load is performed. The data is transferred into the main application before the second stage follows. The second stage is the standard SINTAP-FRACTURE MODE procedure with prescribed equations. Their selection depends on the level of the procedure and on the type of material yielding (Lüders plateau).

There are three “zoom controls”:

- Zoom out (Reset) *resets all zooms*
- Zoom out /2 *zooms the area marked with the mouse*
- Zoom out -1 (Back) *returns picture to the previous zoom*

Each diagram contains two curves.

The FAD diagram contains a curve, that originates from point (0, 1) and ends at the plastic collapse limit, as shown in Fig. 26. The curve is named a "Failure assessment curve" (also "Failure curve") and describes behaviour of the material. The area under the curve is considered as failure safe; the area above it is considered as "potentially unsafe". The second curve is called "Loading curve" (the load is increasing along this curve); it can also be named as "Crack growth curve" (the crack is growing along this curve). The nominal or operating point with an initial crack length at designed load lies at this curve. The intersection of both curves indicates the critical or failure point.

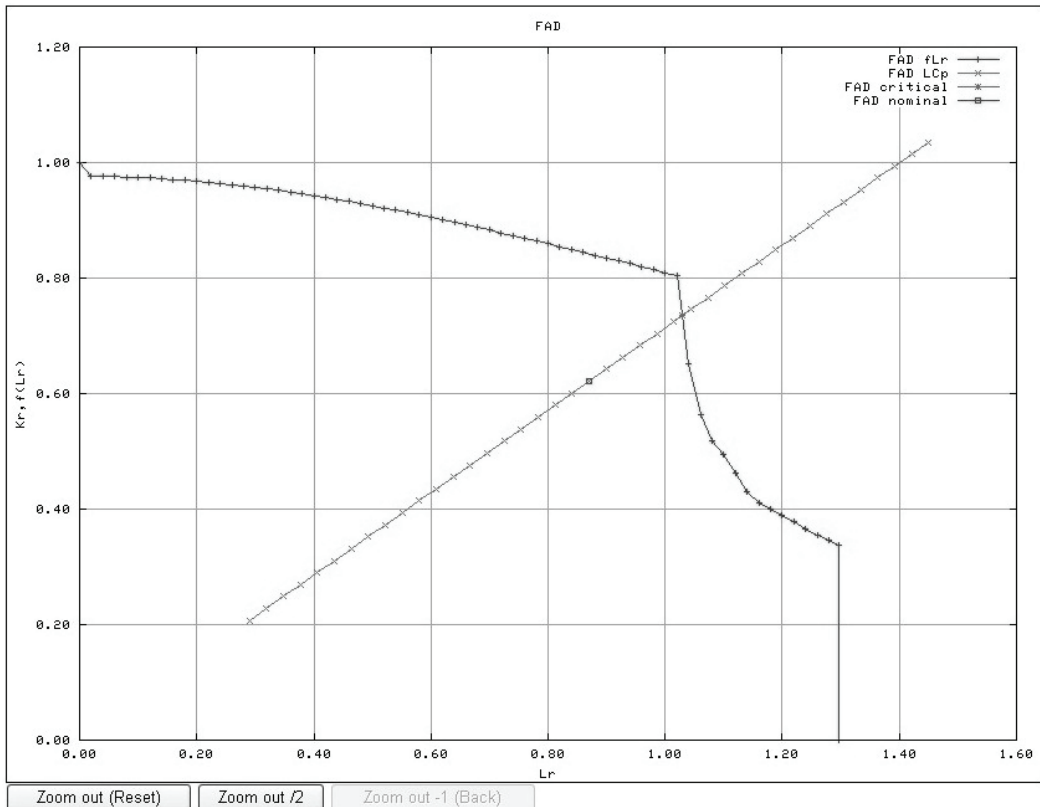


Figure 26: FAD diagram created from user input data

The CDF diagram (Fig. 27) also contains two main curves. The third curve is an additional vertical straight line originating from the x-axis at the plastic collapse limit. The first horizontal curve or line describes the fracture resistance J_{mat} as the property of the material in terms of J-integral. The area under the curve is considered as safe, the area above it is considered as a "potentially unsafe". The second curve is the "Loading curve" or the "Crack growth curve". It combines the properties of the material and developing load or growing crack and describes the "Crack driving force". The nominal or operating point with the initial crack length at designed load lies at this curve. The intersection of both curves indicates the critical or failure point. With developing load or growing crack the operating point slips from the "safe" towards the "potentially unsafe" region.

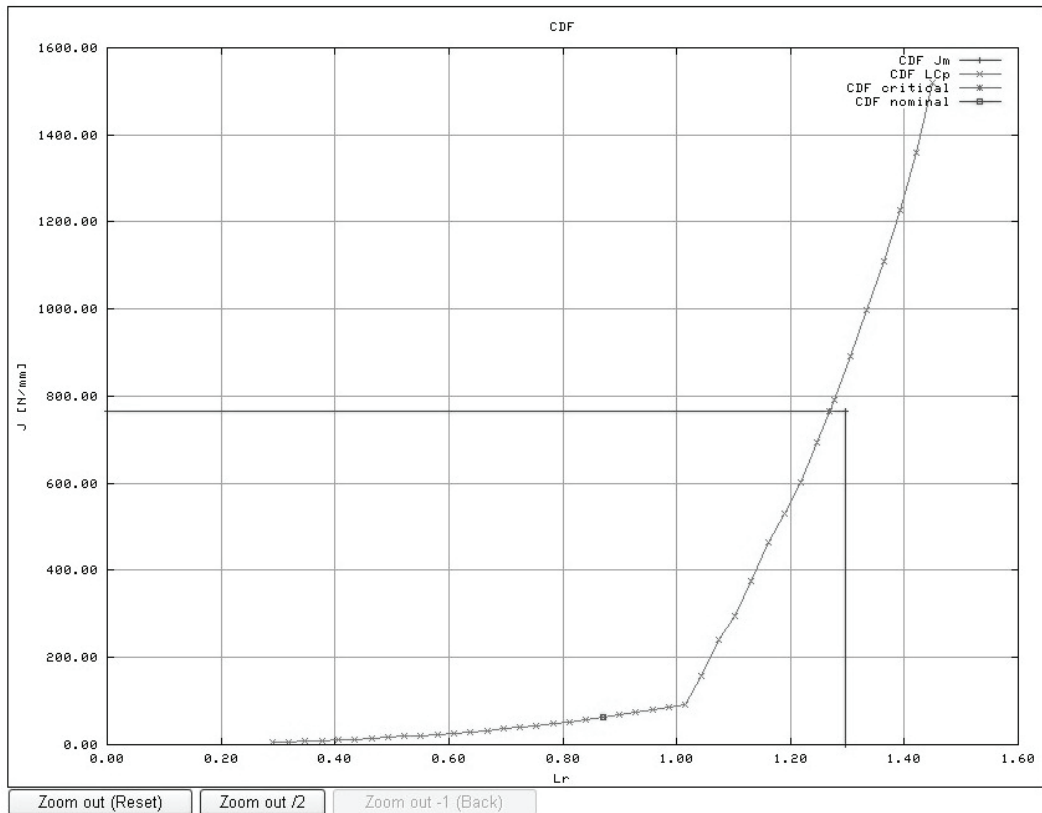


Figure 27: CDF diagram created from user input data

4 Conclusion

The application of the software of the Fracture module of the Procedure to real case gives simple single but important information about materials properties requirements. The software is possible to use in design stage (choice of right material) and using state. Software is established with module structure which incorporates each component as modul with known limit load solutions and stress intensity factor solution. In the software is SINTAP concept /2/ applied for structure integrity analysis. Software check valid conditions for solutions and provide possiblity to change stress intensity factor with new solution or add new component. Material modul includes rutine for input mechanical

properties and fracture toughness. Output routine enables print and save results as report or plots and text file appropriate for further analysis.

REFERENCES

1. T. Valh, Preračun celovitosti konstrukcijskih komponent z računalniškim programom po SINTAP postopku, Diplomsko delo, Univerza v Mariboru, Fakulteta za strojništvo, Maribor, 2004
2. U. Zerbst, C. Wiesner, M. Koçak, L. Hodulak, SINTAP: Entwurf einer vereinheitlichen europäischen Fehlerbewertungsprozedur-eine Einführung, GKSS-Forschungszentrum Geesthacht GmbH, Geesthacht, 1999
3. K.-H. Schwalbe, U. Zerbst, Y.-J. Kim, W. Brocks, A. Cornec, J. Heerens, H. Amstutz, EFAM ETM 97-the ETM method for assessing the significance of the crack-like defects in engineering structures, comprising the versions ETM 97/1 and ETM 97/2, GKSS-Forschungszentrum Geesthacht GmbH, Geesthacht, 1998
4. K.-H. Schwalbe, Y.-J. Kim, S. Hao, A. Cornec, M. Koçak, EFAM ETM-MM 96-the ETM method for assessing the significance of the crack-like defects in joints with mechanical heterogeneity (strength mismatch), GKSS-Forschungszentrum Geesthacht GmbH, Geesthacht, 1997
5. N. Gubeljak, Celovitost konstrukcij, Znanstvena monografija, Univerza v Mariboru, Fakulteta za strojništvo, Maribor, 2006
6. N. Gubeljak, Mehanika loma, Univerza v Mariboru, Fakulteta za strojništvo, Maribor, 2009
7. Neale B.K., On the best fit curve through crack growth fracture resistance data, *Fatigue Fract. Engng. Mater. Struct.*, 16(4), 465-472.

ROLE OF PARTICLES IN FRACTURE MECHANICS: EVOLUTION OF ONE APPROACH

Nenad Radović

*Department of Metallurgical Engineering, Faculty of Technology and Metallurgy,
University of Belgrade, Begrade, Serbia
nenrad@tmf.bg.ac.rs*

1. INTRODUCTION

Since the early days of fracture mechanics, the importance of the particles present in microstructure was greatly emphasized. The particles in steels are either impurities (sulphides, silicates, aluminates, oxides), or second phase particles (predominantly carbides and nitrides). To describe the role of the particles, it was necessary to take into account the chemical composition, shape and size distribution. Primarily, all particles were treated as stress concentrators, due to its sharp edges which were formed during solidification. Therefore, the main challenge for metallurgical engineers was how to avoid the presence of the sharp elongated particles in steels. The problem was mainly solved by increasing the steels purity; decrease in sulphur and phosphorous content is a permanent activity in steel production. Later, concurrently with the development of physical metallurgy, this approach was modified. The new approach was provided by achievements in industrial practice related to the possibilities of particles control. For that, the control of the particles had enabled two new different strategies:

- (i) control of the particle shape, and
- (ii) control of the particle chemical composition.

The shape control was applied primarily on sulphur based particles, mainly MnS. The addition of Ca led to the change in shape and increase of the Young's modulus. Therefore, MnS particles became spheroid and non deformable, i.e. MnS did not act as stress concentrator, in spite of the presence of sulphur. This approach was applied for the large particles (non-metallic inclusions). The other route was based on the knowledge of nucleation of the phases with high toughness. The nucleation of these phases preferentially starts on matrix/particles surface. Also, the relationship between particles and phases is well established. These particles are carbides, nitrides, oxides or carbonitrides of alloying elements, sub micrometer in size. Therefore, the control of particle precipitation will lead to the final microstructure with high toughness and/or very small grain size. This approach has successfully enabled the development of microalloyed steels and significant improvement of the toughness of the weld metal and welded joints.

Inclusions have undergone a long way from undesirable features in early days (stress concentrators) to beneficial factor for excellent toughness in steel. This evolution is the subject of this presentation.

For the last several decades, fracture mechanics had been one of the main tools for prediction the materials resistance to fracture. Equation 1 quantifies and correlates materials property, service conditions and the size of features that act as stress concentrators /1-3/.

$$K_{Ic} = \sigma \cdot \sqrt{\pi \cdot a} \quad (1)$$

where K_{Ic} is minimal, critical stress intensity factor - the material property, σ is design stress, corresponding to service conditions, a is allowable flaw size or by non-destructive testing (NDT) detected flaw size in a component.

Defects in material structure can be classified in two groups:

- (i) cracks (induced mainly by improper machining, heat treatment, welding, design);
- (ii) particles (introduced as the consequence of high level of impurities or second phase particles).

Each of these defects causes the inhomogenities in the stress field, leading to local stress concentration at the tip of the crack or sharp edge of the particle and resulting in stresses much higher than nominal. Also, in order to quantify the influence of the crack shape and its position, a geometrical factor is introduced. Finally, these defects will lead to considerable decrease of the toughness.

The effectiveness of the stress concentrator depends strongly on the shape. Figures 1 and 2 show the differences in normalized stress intensity for (1a) through thickness and (1b) cylindrical cavity with symmetrical cracks and (2a) disk shaped crack and (2b) spherical cavity with equatorial crack /4/. It is clear that when the stress concentrator is related to minimum surface (1b and 2b), the particle size is detrimental for crack initiation.

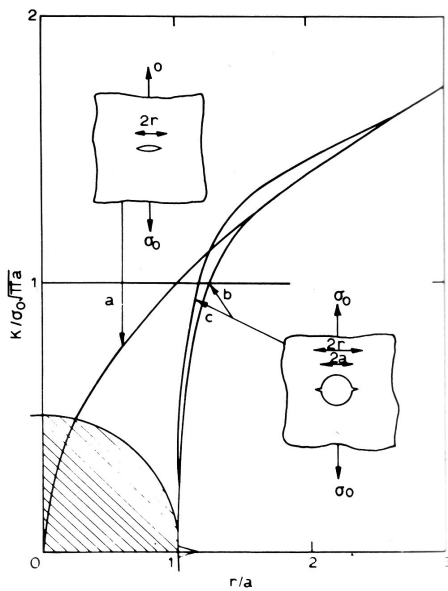


Figure 1: Normalized stress intensity factor for through thickness crack (a) and cylindrical cavity with symmetrical cracks (b) /4/

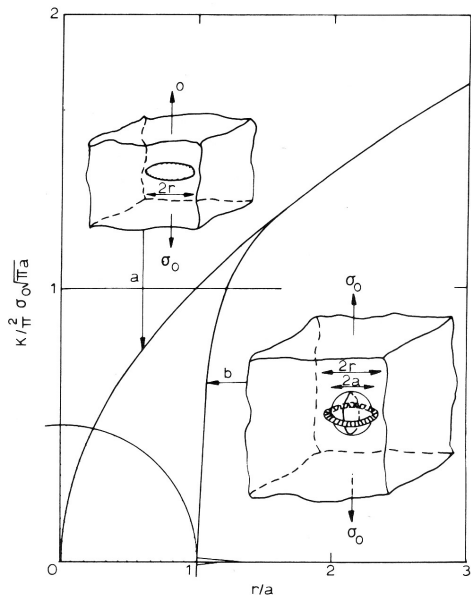


Figure 2: Normalized stress intensity factor for disc shaped (a) and spherical cavity with equatorial crack (b) /4/

2. NONMETALLIC INCLUSIONS

Non-metallic inclusions dominantly include sulphides, oxides, silicates, aluminates and their compounds or composites. They can be formed both in liquid and solid state. When formed in liquid state, the main challenge is to enable sufficient time for slag formation and physical removal. If they are not removed from the steel melt before solidification, they can cause defects in the casting products, give rise to processing difficulties and failures, decrease productivity, degrade product properties, and reduce

premium yield and cause serious problems in all steps in the production (deformation, machining, heat treatment and welding). Since their removal is mandatory during treatment of molten steel, they will not be discussed.

The main focus is related to the formation of non-metallic inclusions during cooling in solid state. Sulphides, carbides, and nitrides precipitate under normal conditions during cooling of steel below solidus temperatures.

The shape and chemical composition of inclusions can be very different by its shape. They can be formed of one or more chemical compounds, or can be spherically, cylindrically, cubically or else way shaped. Figure 3a shows schematically the complex oxide-sulphide inclusion. During steel production, oxide inclusion was first to be formed, usually because oxides have higher melting temperature in comparison to sulphides. With further cooling, the sulphides have been formed on already present oxides. The final chemical composition comprises the elements present in oxide and sulphide. Also, the shape is detrimental to the surface tension between sulphide and matrix, leading to the stress field around the inclusion, as presented in Fig. 3a. Figure 3b presents the stress field around one cylindrical inclusion /5/.

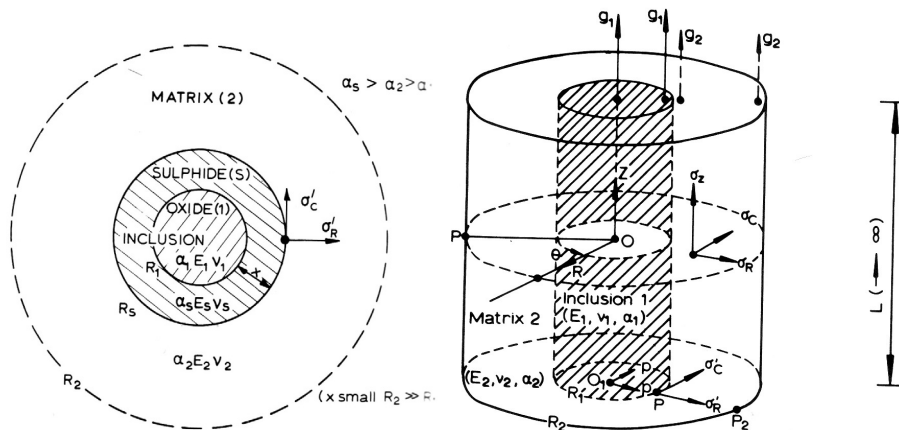


Figure 3: The shape, stress field and chemical composition of some inclusions: spherical duplex inclusion (left); cylindrical inclusion (right) /5/

Oxide inclusions arise from exogenous and indigenous origins. Exogenous inclusions are formed during the melt transfer by (1) reoxidation of deoxidized and refined steel melt when it comes into contact with air and oxidizing slag; and (2) entrainment of the reoxidation product, slag, and refractory. Indigenous inclusions form in the ladle from the reaction between oxygen dissolved in the melt and a deoxidizing element such as Al or Si added to the melt. In a deoxidized and refined steel melt, indigenous inclusions are usually small in size, and hence they are less harmful, provided that they do not agglomerate into large ones during the melt transfer. In contrast, exogenous inclusions often exist in large sizes shortly before the melt is delivered into the mould, have limited opportunity to be removed, and hence are more harmful /4, 5/.

The origin of sulphur in steel is predominantly from the coke. During ore reduction in blast furnace, large amount of sulphur gets dissolved in pig iron. During next production steps, ladle treatment of pig iron, steel production and ladle treatment of steel, one of the main goals is to decrease the overall content of sulphur /6/. If the sulphur is remained in steel in solid solution it can form the eutectic alloy with very low melting temperature

(close to 900°C), leading to melting on the grain boundaries followed by fracture. To avoid presence of sulphur in solid solution, the alloying with manganese was introduced. This approach was based on high affinity between manganese and sulphur, resulting in formation of manganese sulphide (MnS). MnS is a particle formed at temperatures close to solidification temperature and can be present both on grain boundaries and within the grains. In this way, the problems related to occurrence of low melting eutectic mixtures were solved. On the other hand, presence of particles had triggered new problems. MnS particles can be discussed in terms of stress concentration and influence on fracture toughness. Its influence on fracture toughness depends on overall presence of sulphur and the size and shape distribution of particles. Its surface is composed of large number of different planes, and basically MnS's influence depends solely on its size. Figure 4 shows the influence of the sulphur content on the toughness /7/.

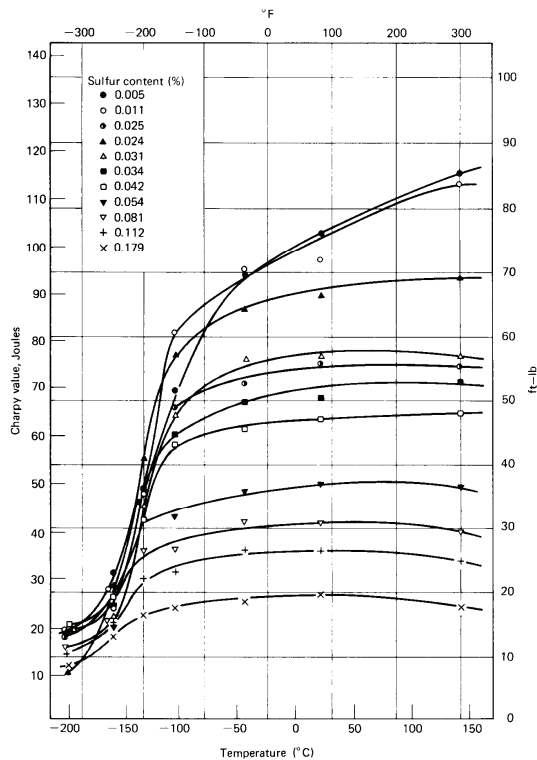


Figure 4: Influence of sulphur content on transition temperature in steels /7/

3. CONTROL OF MnS INCLUSIONS

This role of Mn ensured significant rise in toughness in low carbon steels, with exceptions of some medium carbon quenched and tempered steels. During further metal working, MnS inclusions can become elongated (rolling) or fractured and dispersed (forging). Presence of long elongated MnS inclusions in as rolled steels is very dangerous, since the edges behave as stress concentrators, leading to fracture or to lamellar tearing in welded constructions. Also, particles themselves can be fractured and can initiate the crack that can propagate through steel matrix and lead to fracture /4/. Figure 5 represents the elongated MnS inclusion after hot rolling in low carbon steel. The inclusion is placed within the ferrite microstructure.

The easiest and most pragmatic approach was to decrease the level of sulphur in steel as much as possible. To understand this approach, it is necessary to understand the origin of sulphur in steel. The dominant origin of sulphur in steel is from coke. Coal used for coke production can have up to 1% of S! Large amount of sulphur that is charged into blast furnace will be dissolved in pig iron. The most effective way to decrease sulphur content in steel is to add large amounts of Ca (as lime powder) during ladle treatment of both pig iron before steel production and ladle treatment of steel. The biggest obstacles for this activity are very large costs and sometime very high investment in new equipment. Figure 6 shows the change of sulphur and other impurities in steel for the period 1950-2000 /8/. The only problem to this approach was the extremely high cost for production of steel for mass applications. Therefore, in some respect, the whole approach had to be changed.

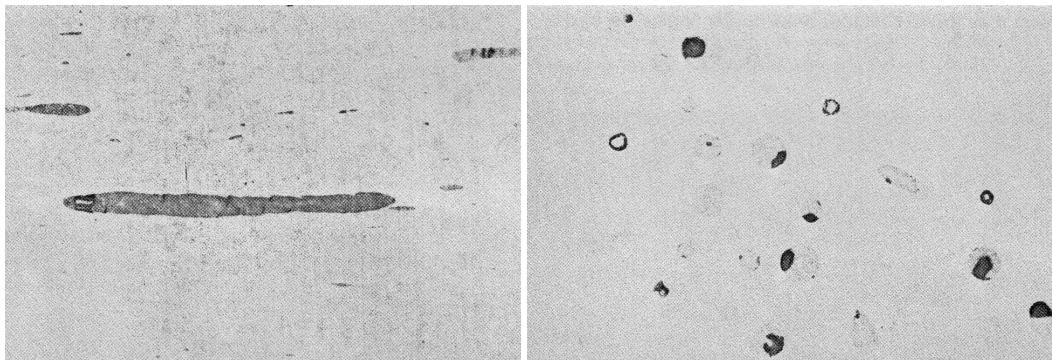


Figure 5: MnS inclusions with voids in low carbon steel: elongated MnS inclusion after hot rolling (left); refined and dispersed MnS inclusions after forging (right) /4/

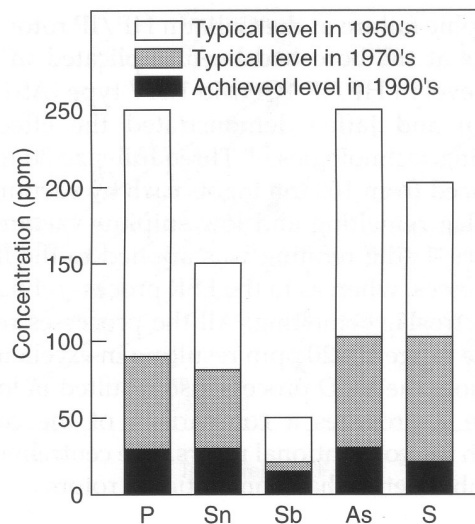


Figure 6: Trends in changing of impurity levels in Cr-Mo-V rotor steels /8/

One of the advantages was the knowledge from fracture mechanics, i.e. the application of a component with present crack in it. Therefore, the main goal was not to remove all sulphur from steel, but to make it non effective, i.e. to eliminate sulphides as critical particles. The solution was additional alloying with Ca or rare earth elements (RE).

Calcium injection in the ladle and tundish has been successfully attempted to:

(1) transform large alumina inclusion clusters into liquid calcium aluminates inclusions, which after solidification and during subsequent hot and cold rolling are elongated and fragmented into smaller sizes that do not impair steel properties;

(2) reduce nozzle clogging and eventual blockage by alumina inclusions, sustaining a consistent melt flow rate through the nozzle and a desired melt flow pattern in the mould to maintain productivity and cast product quality;

(3) convert dissolved sulphur into oxysulphide inclusions that are non-deformable during hot rolling, thus preventing the formation of deformable manganese sulphide inclusions in plate or strip; and

(4) improve the isotropy of mechanical properties and resistance to Hydrogen Induced Cracking (HIC) that are caused by the elongated manganese sulphide during hot rolling.

In MnS inclusion present Ca changes both the surface tension and Young's modulus. The increase in Young's modulus leads to high strength of particle that will not allow it to be deformed during rolling. Also, simply by changing shape from needle like (after rolling) to spherical (both before and after rolling), the stress concentration at the particle was significantly decreased. This improvement was directly based on knowledge provided by fracture mechanics, i.e. addition of Ca primarily influences the shape of MnS. This feature is shown in figure 7 /5/.

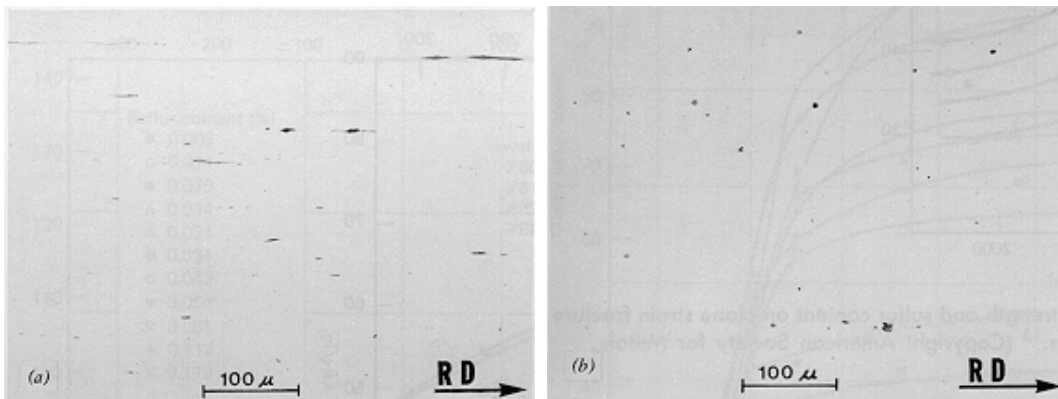


Figure 7: Shape of MnS after rolling: no Ca added (left); addition of Ca (right) /5/
RD → Rolling direction

Figure 8 shows the fracture surface by scanning electron microscope (SEM) in two steels: (a) Ca untreated and (b) Ca treated /9/. In the Ca untreated, the facets typical for brittle fracture are present together with elongated MnS inclusions. On the other hand, fractograph of Ca treated steel clearly show presence of spherical MnS particles with evidences of ductile fracture.

Finally, the usual amount of Ca addition in steel is approx. 40 ppm. It is easy to do it, not expensive and no degradation of any mechanical or technological property will occur. Also, this treatment has significantly improved weldability, because it had largely removed problems related to lamellar tearing.

4. BENEFICIAL ROLE OF PARTICLES

Experiences gained on the problems of inclusions control, parallel with understanding new phenomena in physical metallurgy, have triggered new ideas in order to use some

beneficial roles of particles. Their beneficial influence was basically oriented in two directions: (i) grain refinement in as-cast and thermo mechanically treated state /10-14/, and (ii) nucleation of tough phases during austenite decomposition /15-17/.

The formation of new phases of particles consists of two stages: a) nucleation of new phases (formation of nuclei) and (b) growth of new phase (nuclei growth) /11,14,17,18/. The size of the final product depends on the interrelationship between nucleation rate and growth rate. Therefore, two extreme situations are: (1) high nucleation rate and small growth rate - leading to very fine microstructure, and (2) small nucleation rate and high growth rate - leading to very coarse microstructure.

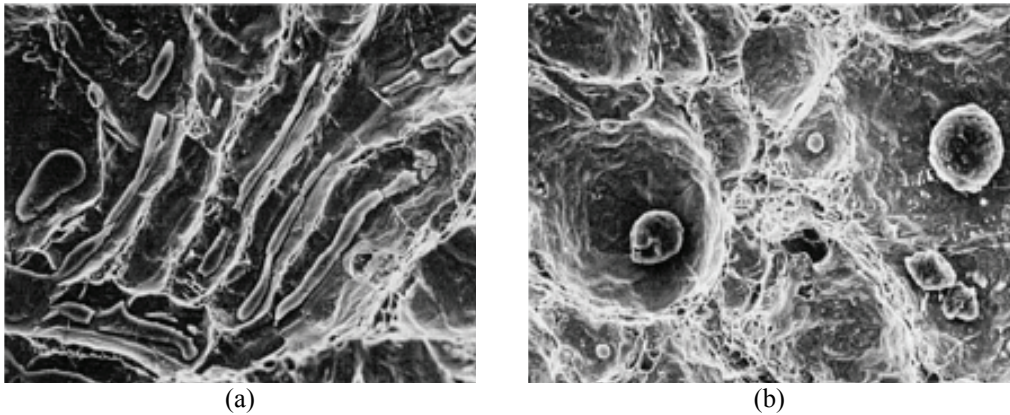


Figure 8: SEM fractographs showing the effect of calcium treatment on the fracture morphology of ASTM A633C steel impact specimens /9/
 (a) Untreated steel with elongated manganese sulphide inclusions
 (b) Calcium treated steel with spherical inclusions

The nuclei of new phase may be formed in the parent phase by thermally activated ‘random fluctuations’. The stability of such nuclei is dependent on the energy balance between the volume driving force and the surface energy term. Assuming a spherical nuclei of radius r , an energy balance for the surface energy (γ) created and the volume free energy (ΔG_v) change gives /11,14,17,18/

$$\Delta G_{total} = -\frac{4}{3}r^3\pi\Delta G_v + 4\pi r^2\gamma \quad (2)$$

The Eq. 2 describes the theoretical possibility for random-homogenous nucleation, i.e. nucleation can start in any point in volume with equal probability. In real systems, due to the presence of grain boundaries, surface of the casting mould, inclusions and particles. In the case of solidification, this equation is modified and new energetic balance is given in Eq. (3) and schematically shown in Fig. 9 /11,14,17,18/.

$$\Delta G_{total} = -V\Delta G_v + A_{SL}\gamma_{SL} + A_{SM}\gamma_{SM} - A_{SM}\gamma_{ML} \quad (3)$$

where V is the volume of the nuclei, A_{SL} is the surface (area) on the interface liquid/solid and γ_{SL} is surface energy on interface liquid/solid, A_{SM} – is the surface (area) on the interface mould/solid and γ_{SM} is surface energy on interface mould/solid, γ_{ML} is the surface energy on interface liquid/mould, and θ is the wettability angle (9).

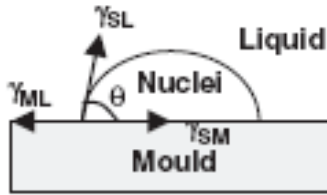


Figure 9: Heterogeneous nucleation during solidification on a mould wall. The designation on the figure is related to Eq. (3) /18/

The equal energetic balance is considered if instead of solidification, a precipitation occurs on present particle and grain boundary.

It is well known that at liquidus temperature, first fraction of metallic materials starts solidification. The nuclei are, in accordance to Eq. (3), formed on the wall of the mould, leading to formation of dendrites. Dendrites are characterized by its characteristic shape. They lead to chemical and structural inhomogenities. This type of microstructure has very low plasticity, relatively high hardness and strength, but very poor toughness. In order to increase the toughness of as cast microstructures, the main challenge was to decrease the size of dendrites. The main route was to introduce extremely large number of places on which the nuclei of the dendrites can occur. The best possibility was to make some modifications of the chemical composition of liquid metal, in order to obtain large number of particles. These particles are high temperature oxides or sulphides and they are formed within the liquid phase. From the start of cooling, each of them acts as example shown in Fig. 10, i.e. as a place for heterogeneous nucleation. In some cases, the classic dendritic solidification is not occurring, but formation of equiaxial grains. Therefore, within the equal volume, larger number of places for start of nucleation will lead to smaller dendrites. Smaller dendrites will improve mechanical properties, i.e. yield stress will be increased, together with toughness. Figure 10 shows the effect of modification of solidification microstructure due to phosphorus refinement on the microstructure of Al-22Si-1Ni-1Cu alloy. Figure 10.a show extremely large primary crystals, within the eutectic mixture. These large crystals actually serve as stress concentrators, resulting in very low toughness. Addition of phosphorus will modify the places for primary crystals solidification, Fig.10.b, i.e. their number is dramatically increased. Therefore, no large primary crystals can be observed and microstructure with higher toughness is obtained. Figure 10.c show the microstructure obtained after addition of phosphorus (molten in liquid phase) and use of flux. The particles of flux have the same role in refining the microstructure. Also, the best effect is achieved using combined treatment with both phosphorous and flux /9/.

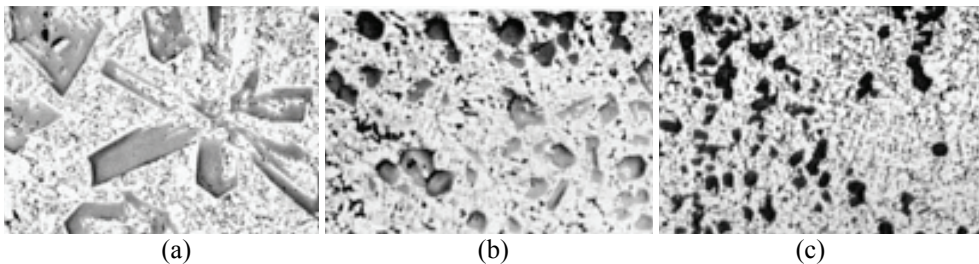


Figure 10: Effect of phosphorus refinement on the microstructure of Al-22Si-1Ni-1Cu alloy. (a) Unrefined. (b) Phosphorus-refined. (c) Refined and fluxed. All 100X /9/

This solution, originally developed for castings, had significant positive impact on improvement of welded structures. First, the toughness of weld metal was increased and secondly, the temperature interval for solidification was narrowed, leading to smaller chances for solidification hot cracking /19/.

4.1 Influence of particles on grain size

One of the most important problem in welding of low carbon steels was abnormal grain growth in the heat-affected-zone (HAZ). The weld pool, as the heat source, would rise the temperature of steel very close to melting point. In order to find practically applicable solution, the main idea was to modify the alloying and introduce elements that would produce precipitates on the grain boundaries. Once the particles that are present on the grain boundary would be able to suppress the grain boundary mobility and delay the grain growth to times much longer than time for welding. The solution was found in Ti addition /10-14,19/.

As indicated before, titanium is an element, which exhibits a strong tendency to form oxides and sulphides as well as nitrides and carbides. Titanium nitride, considering most typical nitrogen levels in steel, will be formed before or during solidification. Such particles, already formed in the liquid steel can be separated into the slag and have no effect on the properties of the steel. If not, they are relatively large as a result of their high formation temperature and must be considered as inclusions, having a ductility-impairing effect on the steel properties. With a larger particle size, the ability to refine the microstructure is diminished. However, a positive effect on the steel properties remains from the formation of TiO and TiN by the reduction of any free oxygen and nitrogen, which are harmful elements with regard of the toughness of steel /20/.

On very high temperatures in steel, atoms of titanium would react with atoms of nitrogen in solid solution. The newly formed precipitates will occur on the grain boundaries, since they are preferential places for precipitation, due to thermodynamic reasons (Eq. 3).

The solubility (maximal amount of nitrogen and titanium in solid solution at respective temperature) can be calculated using Eq. (4) /20-22/

$$\log [\text{Ti}][\text{N}] = \frac{A}{T} - B \quad (4)$$

where [Ti] and [N] are concentration of Ti and N in steel, respectively, in weight percents, T is temperature, K, A and B are constants. Their values depend on the temperature and state of steel (liquid or solid) /21,22/.

TiN particles decorate the austenite grain boundaries and mechanically block their movement. Only in the case of very high heat input (either high temperature or long time), TiN particles will start to coarsen. In the cast condition TiN particles are present in diameter 1 to 3 micrometer, which will hardly be dissolved during reheating. During the coarsening, small particles become dissolved, and large particles become even larger, coarser. During this process, some segments of grain boundaries can be TiN-free, and can start growth particularly in fusion zone /14, 19/.

4.2. Influence of particles on phase transformation

Influence of particles on phase transformations can be observed as: (i) influence on recrystallization and (ii) influence on austenite decomposition.

Influence on recrystallization

The influence on the recrystallization is the main feature characteristic for microalloyed steels. The interrelationship between deformation hardening in successive passes during hot rolling, suppression of recrystallization and cooling rate enables different thermomechanical processing routes for microalloyed steels, Fig. 11 /11, 14, 23, 24/.

Usual chemical composition of microalloyed steels comprises Ti (for improved weldability), Nb and V (for improvement of strength and toughness via grain refinement). Very effective particles for precipitation hardening are about 1 to 2 nm in diameter. The interface of such fine precipitates is coherent with the steel matrix. These particles are typically formed during or after the γ/α transformation in the ferrite phase. With the higher temperature of formation and a slower cooling rate the carbo-nitrides tend to grow and become incoherent with the steel matrix. The metallurgical mechanism of precipitation hardening changes from plastic deformation by cutting the particle to dislocation looping avoiding the particles. Such overaged particles are less effective in increasing the strength owing to both, their incoherent nature and the bigger particle size.

In addition to undissolved particles such as TiN, which may be as large as one micrometer, the precipitates formed during hot working or heat treatment in austenite are rather coarse, at around 20 nm in diameter. Thus they have only a limited effect for precipitation hardening and their major role is in refining the microstructure.

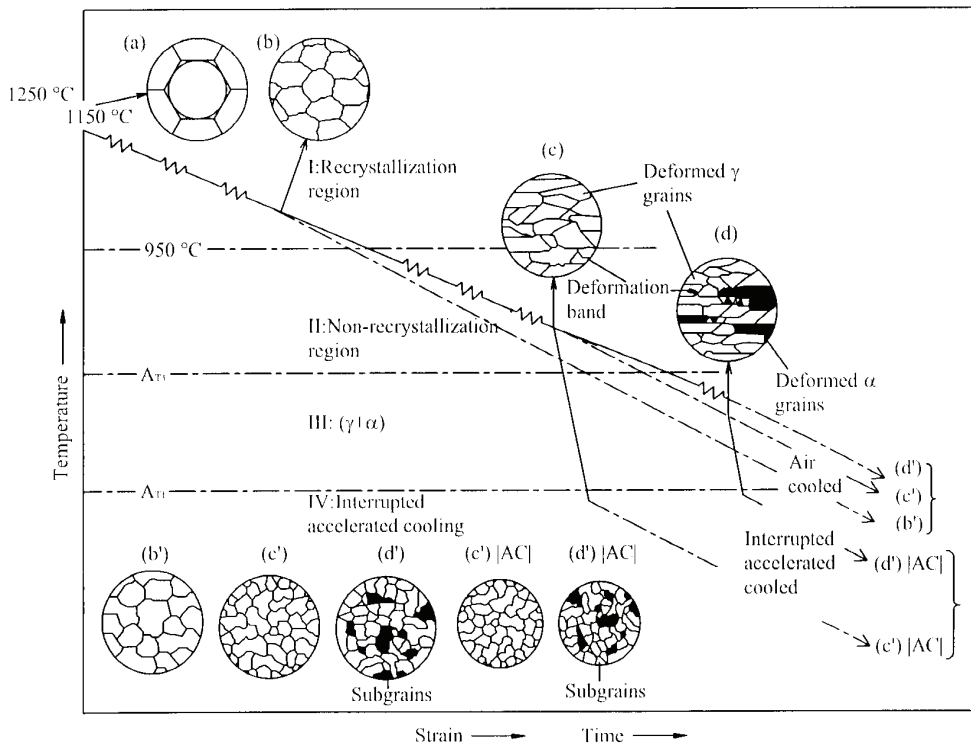


Figure 11: Schematic illustration of thermomechanical rolling of microalloyed steels /23/

Influence on austenite decomposition

During continuous cooling of medium carbon microalloyed steels, the main goal is to suppress the nucleation of bainitic microstructures and to enhance formation of acicular

ferrite and related microstructures, due to poor toughness of bainitic/martensitic microstructures /15, 16/. Since bainites and acicular ferrite nucleates in the same temperature interval, the main difference between them is related to nucleation places. While bainites nucleate on austenitic grain boundaries, acicular ferrite nucleates on the particles within the grains. Therefore, it is suggested that particles are necessary for nucleation of acicular ferrite. The extent of nucleation depends, among others, on composition, crystal structure, number, size and interparticle distance. Second condition is grain size on annealing temperature, i.e. grain should have some optimal size, rather larger than smaller, because larger grains will decrease temperature of austenite decomposition, to the temperature range in which acicular ferrite is a dominant structure. Hardenability has similar role. Second phase particles are usually oxides and nitrides or sulphides; MnS particles served as preferential places for precipitation of VN, which has great potential for nucleation of intragranular proeutectoid ferrite (intragranularly nucleated ferrite – INI), which in turn serves as nucleation site for acicular ferrite /15, 24/. Therefore, even considerably high content of sulphur (130 ppm) did not damaged toughness, i.e. nucleation of acicular ferrite would be not possible without MnS particles. This conclusion is very important for further practical design of materials /25/.

Service life with present crack, introduced in fracture mechanics has been adopted in materials science also, i.e. in spite of the presence of particles in steels, their control allow the application of materials. On the other hand, the requirement for clean steel is necessary, like in use of seamless tubes /26/. The benefit of carbides in wear resistant and tool steels/27/, and influence of impurities on deformation and fracture behaviour in aluminium 7000 series alloys /28/, although important are not discussed in this presentation.

5. CONCLUSIONS

Development of material that can meet all requirements together with reasonably low costs is the eternal question and challenge.

Based on knowledge of fracture mechanics, consideration of particles in steel is not only in direction of lower content of impurities, but more to CONTROL of shape and distribution of second phase particles. It is much easier and reasonably cheaper to control the shape of inclusions, than to produce super clean steel. If the shape of second phase is modified into sphere, than low stress concentration will occur. Also, by its influence on grain refinement and transformation behaviour, the presence of particles turned to be beneficial and unavoidable.

REFERENCES

1. R.W.Hertzberg, Deformation and Fracture Mechanics of Engineering Materials, J.Wiley and Sons, New York (1996)
2. J.F.Knott, Fundamentals of Fracture Mechanics, Butterworths, London (1973)
3. Dj.Drobnjak, Lecture Notes, Faculty of Technology and Metallurgy, Belgrade (1996)
4. Kiessling, R., Nordberg, H., *Influence of Inclusions on Mechanical Properties of Steel*, Production and Application of Clean Steels, Iron and Steel Institute, London (1972) p.179
5. Brooksbank,D, Andrews, K.W, *Stress Field Around Inclusions and Their Relation to Mechanical Properties*, Production and Application of Clean Steels, Iron and Steel Institute, London (1972) p.186.

6. N.Radović, Dj.Drobnjak, Development of Steels for fabrication of welded structures with improved safety, *Zavarivanje i zavarene konstrukcije*, XLVI (2001) 81
7. ASM HAndbook Vol1, Properties and Selection: Irons, Steels, and High-Performance Alloys, Metals Park, Ohio (1998)
8. Viswanathan, R., *Application of Clean Steel/Superclean Steel Technology in the Electric Power Industry – overview of EPRI Research and Products*, Clean Steel: Superclean Steel, The Institute of Materials, London (1996) p.1
9. ASM HAndbook Vol 15 Casting, Metals Park, Ohio (1998) p198
10. N.Radović, Dj.Drobnjak, Effect of interpass time and cooling rate on apparent activation energy for hot working and critical recrystallization temperatures of Nb-microalloyed steel, *ISIJ International*, 39 (1999) 576
11. Nenad A. Radović, Thermomechanical Treatment of Microalloyed Srteels, Monography (in Serbian), AMES, Belgrade (2007)
12. N.Radović, Correlation Between Apparent Activation Energy for Hot Working and Temperature of No Recrystallization in Microalloyed Steels, *Materials Science Forum*, 426-432 (2003) 1553-1558
13. Dj.Drobnjak, N.Radović, M.Andjelić, A.Koprivica, Effect of Test Variables on Apparent Activation Energy for Hot Working and Critical Recrystallization Temperatures of V-microalloyed Steel, *Steel Research*, 68 (1997) 306
14. T.Gladman, Physical Metallurgy of Microalloyed Steels, IOM, London (1996)
15. Dj.Drobnjak, A.Koprivica, Fundamentals and Application of Microalloying Forging Steels, Ed. Chester J.van Tyne, G.Krauss and D.Matlock, TMS, Warrendale, Pa (1996) 93-106
16. N.Radović, A.Koprivica, D.Glišić, A.Fadel, Dj.Drobnjak, Influence of V and N on Transformation Behaviour and Mechanical Properties of Medium Carbon Forging Steels, *Materials Science Forum*, in press
17. H.K.D.H. Bhadeshia, Bainite in Steel, the IOM Communications, London (2001)
18. Verlinden. B., et al., Thermo-Mechanical Processing of Metallic Materials, Pergamon Press, 2007
19. Kou.S., Welding Metallurgy, Second Edition, Wiley Inter-Science (2003)
20. K.Hulka, *Characteristic Feature of Titanium, Vanadium and Niobium as Microalloy Additions to Steel*, Niobium GMBH, Duesseldorf, available at:
<http://www.cbmm.com.br/portug/sources/techlib/info/charact/charact.htm>
21. Wan-Yi Kim et al., *Thermodynamics of Titanium, Nitrogen and TiN Formation in Liquid Iron*, *ISIJ International* 47 (2007) 1082
22. K.Inoue et al., *Solubility Product of TiN in Austenite*, *ISIJ International* 38 (1998) 991
23. T.Tanaka, Microalloying 95, Ed. M.Korchynsky, The Iron and Steel Society, Warrendale, Pa (1995) 165-181
24. A.Radović, N.Radović, *A Contribution of Fracture Mechanics to Materials Design, From Fracture Mechanics to Structural Integrity Assesment* – IFMASS-8 Eds. S.Sedmak and Z.Radakovic, DIVK-TMF, Beograd (2004) 61
25. R.Smallman, M., Bishop, R.J., Modern Physical Metallurgy and Materials Engineering Science, process, applications Sixth Edition, Butterworth-Heineman, (1999)
26. G. Simić, V. Lučanin, J. Tanasković, N. Radović, *Experimental Research Of Characteristics Of Shock Absorbers Of Impact Energy Of Passenger Coaches*, *Experimental Techniques*, 33 (2009) July/August 29-35
27. R.Čirić, K.Raić, N.Radović, V.Grabulov, Z.Odanović, *Analysis of Carbides and Carbide Phases Distribution in Friction Welded Joints*, *Welding in the World*, 49 (2005) 157-170
28. M.Vratnica, Z.Cvijovic, N.Radovic, *The Effect of Compositional variations on the Fracture Toughness of 7000 Al-alloys*, *Materijali in Tehnologije*, 42 (2008) 191-196

STEELS FOR ELEVATED TEMPERATURE APPLICATION: HEAT-AFFECTED-ZONE SPECIFICS

Ljubica Milović

*Faculty of Technology and Metallurgy, University of Belgrade, Belgrade, Serbia
acibulj@tmf.bg.ac.yu*

1. INTRODUCTION

Ferritic steel 9Cr-1Mo and its modified versions are currently favoured structural materials for steam generator applications as they offer useful combination of high temperature mechanical properties and corrosion/oxidation resistance. The arrivals of new generation power plants have increased the operating steam temperatures and pressures to achieve higher efficiency and better environmental protection. This has led to the development of modified versions of 9% Cr steels, with excellent combination of creep strength and ductility. These steels include plain 9Cr-1Mo steel initially modified by the addition of strong carbide forming elements such as Nb and V (9Cr-1Mo-V-Nb, designated as T91 or P91) and further modified by the addition of W (9Cr-0.5Mo-1.8W-V-Nb designated as T92 or P92), /1-3/.

Modified 9Cr-1Mo steel (T91/P91), with high creep strength, high thermal conductivity, low thermal expansion coefficient and good resistance to corrosion and stress-corrosion cracking, is widely used as a structural material in power generation and petrochemical industries. The alloy is recommended for use in the normalized and tempered condition. Because of the transformable nature of the ferritic alloy, it is susceptible to the formation of undesirable microstructures during fabrication and/or heat treatment processes.

The non-destructive characterization of this steel microstructure is important for quality control during fabrication and heat treatment, to ensure the desired microstructure and mechanical properties. The ultrasonic technique is promising tool (for characterization of microstructures, assessment of defects and evaluation of material properties), /4, 5/.

Tungsten-bearing 9Cr and 12Cr steels have been favoured as advanced ferritic heat-resistant steels with sufficient creep rupture strength for application to thick section boiler and turbine components of coal-fired ultra-supercritical (USC) power plants at temperatures higher than 600°C and to first wall and blanket structures of the fusion reactor. Recent trends to increase steam temperature over 600°C and pressure of boiler and turbine components enhance thermal efficiency, resulting in lower fuel consumption and lower CO₂ emission. Under these circumstances, the construction of USC plants operating at 650°C is planned in Europe, The United States and Japan. This requires the development of advanced ferritic heat-resistant steels with sufficient creep rupture strength at temperatures higher than 600°C. Tungsten-bearing 9Cr and 12Cr steels are also being considered as alternate candidate structural materials to austenitic type 316 stainless steel and conventional Cr-Mo steels for application to first wall and blanket structures of the fusion reactor, because of their higher resistance to swelling than type 316 stainless steel and because of their lower radio activation than Cr-Mo steels under high energy neutron irradiation, /6/.

2. MARTENSITIC STEELS

The demand for higher efficiency in fossil fired power plants lead to the development of new creep resistant materials during the last decades. They made it possible to increase the steam temperature up to range of 625°C for permanent service, using ferritic and martensitic materials.

Special attention was paid to the improvement of 9-10% Cr-steels martensitic steels. These grades had their basis in the well known grade T/P9 (X11CrMo9-1). As the next step forward, T/P91 (X10CrMoVNb9-1) was developed in the 1980th. To enhance its creep-rupture strength, the elements V, Nb and N were added to the alloy of T/P9.

During development of new base materials it is of great importance, that corresponding filler metals with matching creep strength properties will be developed simultaneously. Concerning the alloy concept, it is the easiest way that the chemical composition is identical to those of the base material. That is true for a great number of filler metals but not for all. Additional micro alloying elements and specialties concerning improvement of weldability and handling are the detailed knowledge of the individual development departments. Matching filler metals are developed for common used welding processes like GTAW, SMAW and SAW, /7/.

The martensitic steels are welded in the “martensitic range”, this means preheat- and interpass temperatures are between 200°C and 300°C. Due to the martensitic structure and the required toughness, great care is necessary during welding, regarding the thickness of individual weld layers, heat input and later with the post weld heat treatment (PWHT). In all cases, PWHT has two means: tempering and stress-relieving.

Rupture stress increases with preheat and interpass temperature. Since the problem arises from the heterogeneous microstructure of the HAZ it can be eliminated by a re-austenitisation and tempering heat treatment.

The problem of tempering during PWHT is to insure safe service conditions. Appropriate temperature of PWHT lasting for example 8 to 10 hours, permits to maintain the tensile properties above the requirements and gives toughness values at a high level at low temperatures.

Pure martensitic transformation result from wall thicknesses up to about 80 mm followed by air cooling and begins at temperatures about 400°C. With greater wall thickness ferrite and carbide will be formed due to the longer cooling periods. At these thickness accelerated cooling is necessary to maintain a pure martensitic structure. This is valid for P91, E911 and P92. After welding a PWHT is carried out at 760°C. Here after hardness is approximately 250 HV 10. The low hardness in these steels is caused by the reduced C content in P91, P92 and E911 (compared to X20) and it makes further processing easier. Directly after welding, the hardness in the weld metal is with approximately 400 HV 10 about 100 units below the hardness of the weld metal for X20. Therefore the risk of cold cracking is reduced, so that after welding and before PWHT, cooling down to room temperature is possible. It is important that the weld cools completely below martensitic temperature before heat treatment. This is to achieve total post weld tempering of all martensite through the ensuing heat treatment. The martensitic finish temperature (M_f) of P91, P92 and E911 is in the range of 150°C, so that cooling to at least 100°C is required. In dependence of the temperature during PWHT the toughness level can be influenced as a function of the holding time. The recommended temperature for these grades is 760°C, but under certain conditions, e.g. for dissimilar joints, a lower temperature could be necessary. In this case a longer holding time will compensate the lower temperature /7/.

3. TYPE IV DAMAGE OF WELDED JOINTS

The cracking of welded joints is typically classified according to crack position and orientation. The designations for the characterization of crack locations are illustrated in Fig. 1. The classification of cracks depending on location of a crack is given as Type I if the crack location is in the weld metal, Type II if the crack starts at the fusion line, Type III if the crack locates in the coarse grained heat-affected-zone (CG HAZ) and Type IV if the crack is in the fine grained HAZ (FG HAZ) or the intercritical zone (IC HAZ). Type IV cracks manifest only in welded joints of creep-resistant steels, /8-14/.

The manifestation of type IV cracking is characterized by higher rate of creep void formation in fined grained and intercritically annealed HAZ of the welds, what leads to failure earlier than in parent steel. These zones contain coarse carbide particles leading to reduction of creep strength; these particles also contribute to nucleate void formation. In a cross-weld test, the weakened Type IV region is sandwiched between stronger parent material and coarse-grained HAZ.

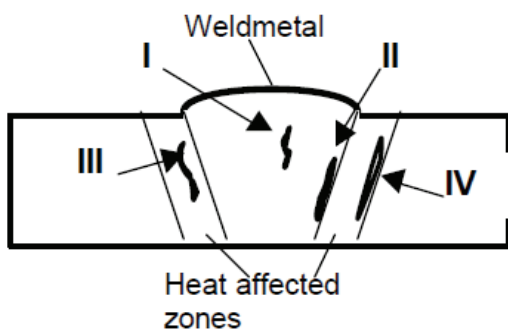


Figure 1: Classification of crack locations in welded joints

Figure 2 shows that although the Type IV failures started appearing after ~ 20000 hours, most of the failures in these steels appeared after 50000 hours of service i.e. the Type IV failures were a medium to long term service phenomenon.

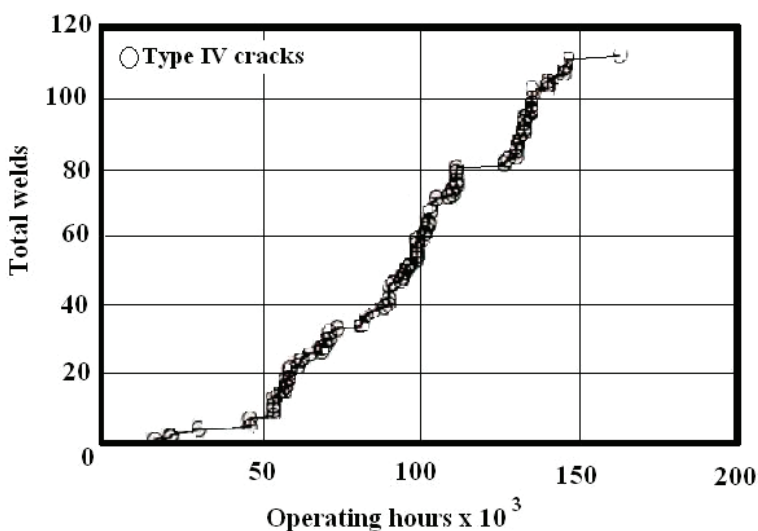


Figure 2: Type IV weld failures in conventional ferritic steels /15/

Figure 3 presents the different microstructures in the constituents of welded joint of 9-12% Cr steels (parent metal – PM, heat-affected-zone – HAZ, weld metal - WM) /16/.

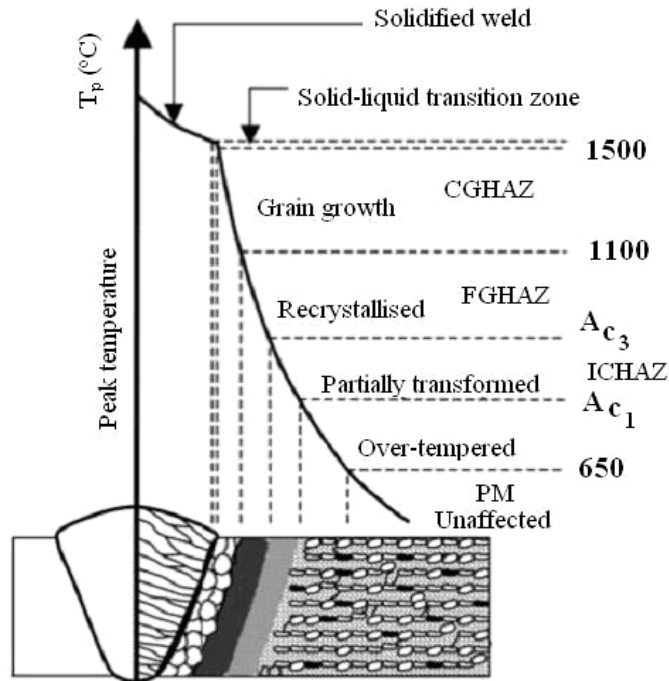


Figure 3: Typical microstructures HAZ of P91 steel formed during welding

Type IV damage, i.e. creep damage at the fine-grained HAZ (FG HAZ), usually appears at the interior of the thickness where the stress state is more complex than at the surface. Therefore, it is difficult to evaluate the remaining life by non-destructive techniques (NDT) which are applied for the outer surface, such as replication method.

After several incidences of failure in thermal power plants, Type IV damage has been the issue of many studies. The conclusion was that the damage was caused by lower creep strength of FG HAZ compared to that of CG HAZ in weld metal and parent metal.

4. HEAT AFFECTED ZONE SIMULATION PROCEDURES

In order to characterize different regions within the heat-affected-zone (HAZ) of a welded joint, HAZ simulation procedures are applied to parent material. It is generally intended to apply a temperature-time history as experienced in a distinct sub regions of the HAZ, which can be either measured by inserted thermocouples or predicted numerically (described in the German code SEW-088).

The mechanical properties and creep behaviour of the individual HAZ sub zones can be characterized on simulated specimens. It is important to check whether the creep fracture occurred in the homogeneous microstructural length of the specimen. One of the main points of creep testing simulated HAZ specimens is to find out the weakest sub region so called “soft zone”. Therefore is recommended to apply a series of different peak temperatures and to draw a plot of hardness or any creep test result as a function of the peak temperature and to compare it with the data of the parent material.

There are different methods in industrial use to apply the weld thermal cycle:

- Gleeble HAZ Simulation,
- induction heating and cooling in an oil bath and
- heating in a hot salt bath and cooling in a moderate tempered salt bath.

The main objective of all these techniques is to apply the weld thermal cycle as measurable in a distinct sub region of the HAZ to a sample with larger testing volume. In the following these methods are described, /17, 18/.

4.1. GLEEBLE welding simulation

Gleeble simulation is a very useful tool for the determination of the microstructure in the HAZ. By the controlled application of thermal and/or thermo mechanical cycles according to particular weldments geometry and the welding parameters, nearly every position in the weldments can be produced representatively and the microstructure can be investigated using conventional or sophisticated skilful techniques.

Due to the high electric power available (maximum current is about 6000 A), round (also rectangular) specimens up to diameter of 16 mm, about 140 mm long, can be used.

In order to determine a specific (creep) property of a particular region in the HAZ the weld thermal cycle is fed in the control computer and samples is heated up very rapidly (heating rates up to 10000 K/s) to the desired peak temperature by direct current flow with up to 6000 A. The cooling is very well controlled; faster cooling rates can be reached by reducing the free span between the jaws or by external gas cooling. The resulting microstructure in the middle of the test specimen, where the thermocouple is located, is then exactly the same as in real weldments at the considered position.

4.2. Induction heating and oil quenching

The HAZ simulation is performed by means of inductive overheating on 180 mm long round specimens \varnothing 20 mm. After heating up in a coil (heating time up to 1300°C is 35 s) and hold at peak temperature for several seconds, the specimens are dropped into an oil bath. The typical cooling time after 1300°C peak temperature is 10 s for the range from 800 to 500°C ($\Delta t_{8/5}$). The homogenous structure in the specimens has a length of 70 mm.

4.3. Salt bath heating and quenching

For the simulation technique of this kind a rough machined specimen is heated up by a hot salt bath corresponding to the desired peak temperature. After the specimen has reached the peak temperature, it is transferred to another salt bath having a much lower temperature (about 100°C). In order to get a specimen with uniform microstructure, different cooling times can be realized by variation of size and temperature of the second salt bath.

4.4. Comparison of the HAZ simulation techniques

The Gleeble HAZ simulation is most flexible (with the capacity for a larger range of heat inputs) and controllable method giving the best agreement with the actual weld thermal cycle. The length of constant microstructure is limited (about 10 mm), which has consequences with the respect to the gauge length.

The other two methods provide a uniform microstructure along the whole specimen length, the heating rate is much slower and the applicable cooling time is quite restricted. They are mainly used for larger testing samples and series or for first screening tests.

Small deviations may occur in situations where the time above A_{c1} - or A_{c3} -temperature has some effect on the resulting creep properties, like in cases of particle dissolution.

In the text below the literature example /17/ of Gleeble testing on 9-12% chromium steels will be shown.

5. GLEEBLE WELDABILITY TESTS ON 9-12% CHROMIUM STEELS

Gleeble simulations representing the shielded metal arc welding (SMAW) process were applied on specimens taken from pipes of P91 to produce HAZ simulated microstructures. The cooling time $t_{8/5}$ was 21.6 seconds. A special attention was laid on the evaluation of the soft zone in the HAZ by metallographic investigations using light microscopy and TEM, hardness tests and constant strain rate tests. The long-time creep rupture tests were performed to study the effect of the soft zone, which usually determines the location of creep fracture.

Fig. 4 shows comparison between the creep rupture behaviour of the parent steel P91 and X20CrMoV 12 1 with creep rupture strength of crossweld specimens made of the same materials. The creep rupture strength of crossweld specimens is significantly lower at higher temperature than that of parent steel.

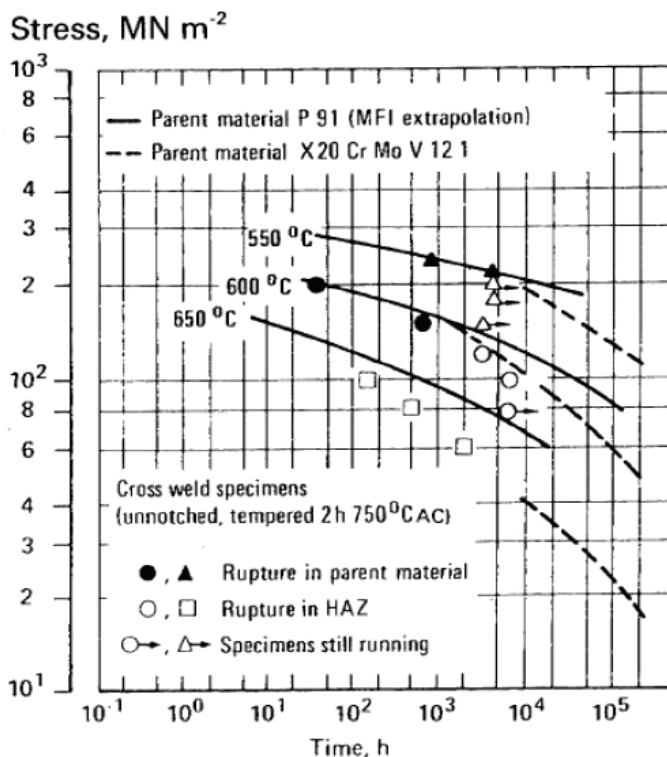


Figure 4: Creep rupture strength of parent steel and crossweld specimens of pipe steel P91 and X20CrMoV 12 1 /17/

5.1. Hardness profile

Hardness profiles across a weld seam of P91 show clearly a tendency to form a soft zone in the FG HAZ after post weld heat treatment (PWHT), Fig. 5. The hardness in this particular zone is about 20 HV lower than in the unaffected parent steel. The hardness

profiles of steel grades E911 and G-X12CrMoWVNbN 10 1 1 show a similar curve to that of P91. To define the zone in which maximum softening occurs, specimens were subjected to a HAZ simulation at different peak temperatures in the range between 760°C and 950°C. The hardness was tested in the as-welded, simulated and in the simulated PWHT conditions (760°C for 2 hours air cooled for P91 and E911 and 730°C for 12 hours for G-X12CrMoWVNbN 10 1 1).

The results of the hardness tests performed on the simulated microstructures of the three mentioned materials are presented in Fig. 6 as a function of the peak temperature for both, the as-welded and PWHT conditions. The beginning of α/γ -transformation as a function of heat cycles can be observed by the increase of hardness in the as-welded condition. After stress relieving, the hardening effect disappears and a small drop of about 10HV can be detected for peak temperatures between 850°C and 950°C.

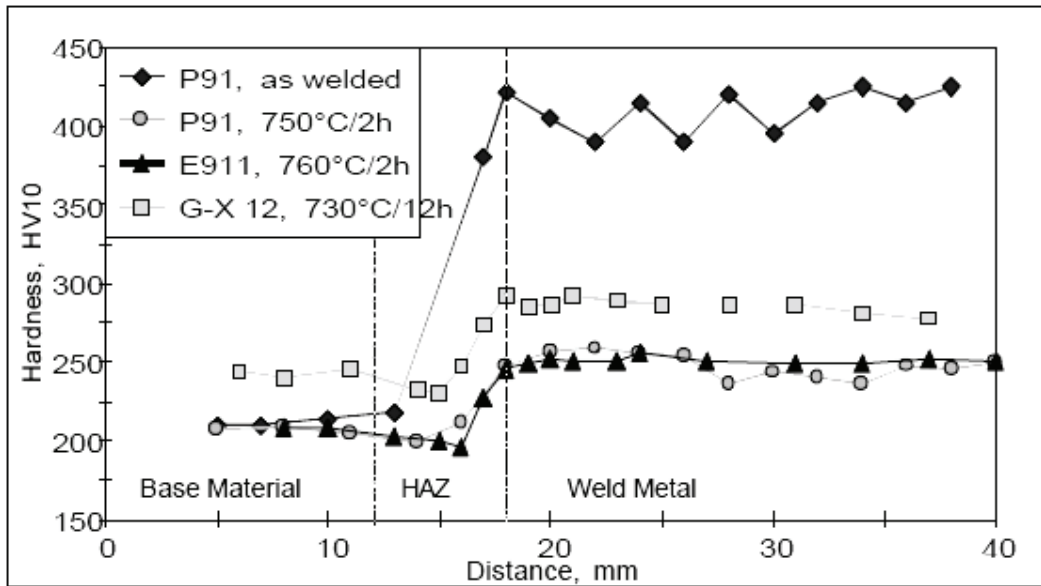


Figure 5: Hardness of weld seam in as-weld condition and PWHT of P91, E911 and G-X12CrMoWVNbN 10 1 1 /17/

5.2. Microstructural aspects

As described in /19-25/, the microstructure of the normalized and tempered P91 steel consists of tempered martensite with a large amount of $M_{23}C_6$ and MX precipitates. Microscopic examination of the specimen subjected to HAZ simulation thermal cycles revealed no significant change in the microstructures when the peak temperature did not exceed 850°C. When the peak temperature becomes higher than the A_{c1} temperature, depending on the shape of the thermal cycle, more and more austenite will be formed and transformed into martensite during cooling to room or preheating temperature. When heating up to 920°C, the amount of martensite which was found under given conditions of our tests is about 70-90%. At this temperature, slightly above A_{c1} and the short times caused by the weld thermal cycle, no significant amount of precipitates and hence carbon (C) and nitrogen (N) go into solution. Therefore, the martensite formed under these conditions lacks C. This is confirmed by the increase in hardness caused by higher peak temperatures. Since very small amounts of C go into solution at these peak temperatures,

the reprecipitation of $M_{23}C_6$ carbides and MX carbonitrides during the subsequent tempering treatment (PWHT) is very limited. In addition, the coherent MX particles coarsen and coagulate and lose their strengthening effect to a large extent. These effects also create a higher tendency towards recrystallisation in this area which, in connection with the overaging of the precipitates, results in a significant softening of these fine grained zones of the HAZ which were heated up to 900-950°C during the weld thermal cycle after PWHT, /17/.

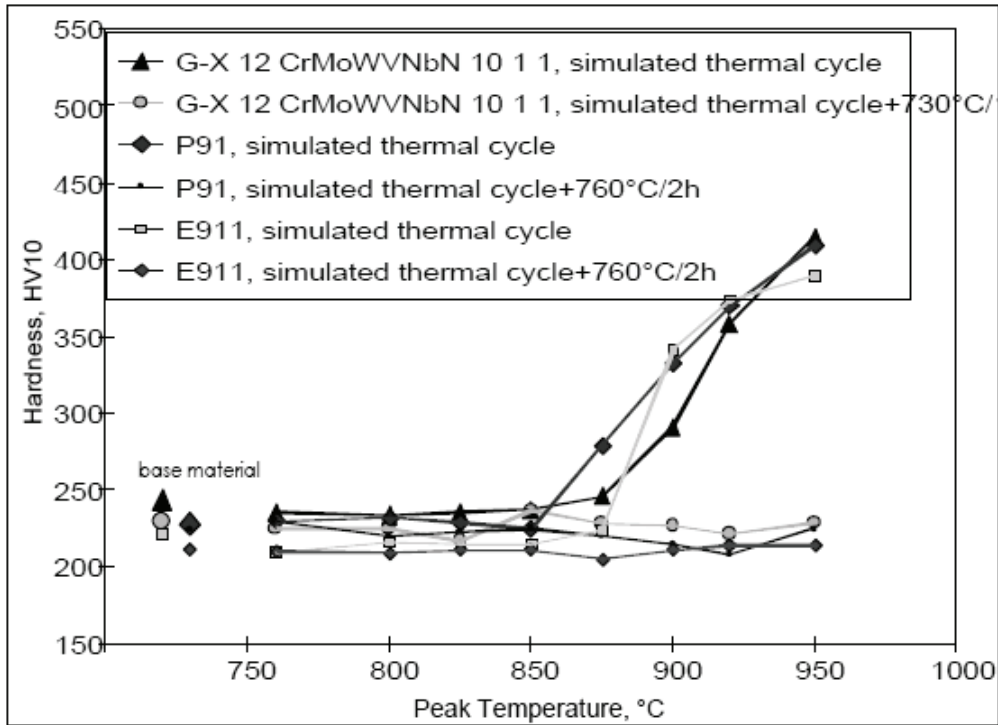


Figure 6: Results of hardness measurements on specimens of P91, E911 and G-X12CrMoWVNbN 10 1 1 subjected to weld thermal cycle simulations (determination of soft, intercritical zone) /17/

6. DETERMINING OF THE “SOFT ZONE”- CASE STUDY

For this investigation, a tube of steel P91, Ø 320 mm, with wall thickness of 14 mm and 140 mm long was used, /23/.

Typical temperatures of transformation during the welding cycle were determined from dilatometric curve, and these are $A_{c1}=835^{\circ}\text{C}$ and $A_{c3}=930^{\circ}\text{C}$, Fig. 7. Heating rate was 53.8°C/s . During cooling, formation of martensite started at temperature of 375°C , while martensite transformation completed at temperature of 210°C . Martensite formation was preceded by separation of a smaller quantity of bainite, /21/.

6.1. Simulation

For testing of the effects of various thermal cycles of welding on microstructure and mechanical properties of test material using thermal simulator SMITWELD, the specimens $11 \times 11 \times 70$ mm were used. Different HAZ regions were obtained by simulation of single-pass welding at temperatures of 1386°C , 1300°C , and 1250°C up to 950°C , graded by 50°C , 925°C , 900°C and 850°C and with cooling time between 800°C and

500°C, $t_{8/5}$, 40 sec. After welding, the samples were subjected to PWHT at 730°C for 1 hour. Then all samples were subjected to inspection of microstructure and measurement of hardness.

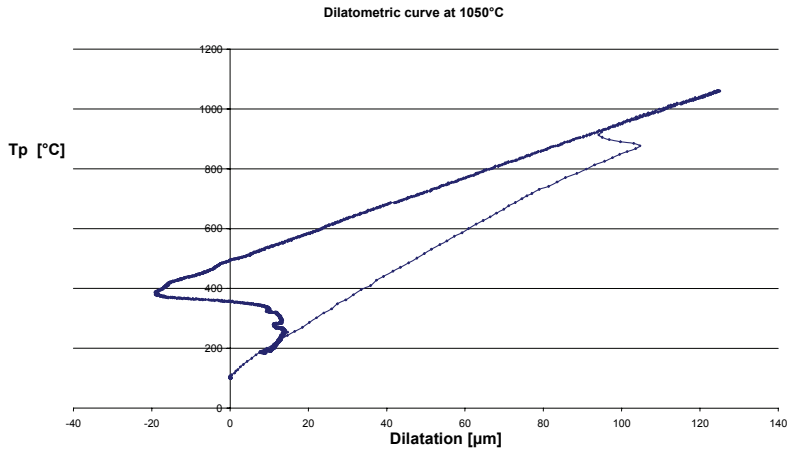


Figure 7: Dilatometric curve

6.2. Material

The appearance of microstructures at temperatures of 925°C, 1100°C, 1300°C and 1386°C is shown in Fig. 8. The microstructure corresponding to austenitisation temperature of 925°C, Fig. 8 a, consists of martensite with less prominent martensite laths. At some previous austenitic grain boundaries, the presence of coarser carbides above 1 µm was observed. The presence of the carbides is most probably the result of keeping at austenitisation temperature for a short time, considering that the carbides of $M_{23}C_6$ type completely dissolve at temperatures above 900°C [19].

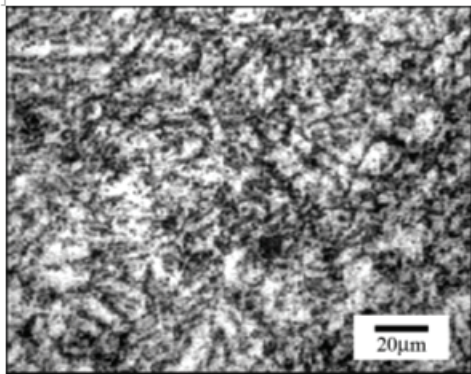
The microstructure corresponding to austenitisation temperature of 1100°C, Fig. 8 b, consists of tempered martensite with clearly visible martensite laths. Coarser carbide particles above 1 µm are still present.

The microstructure corresponding to austenitisation temperature of 1300°C, Fig. 8 c and 1386°C, Fig. 8 d, also represents tempered lath martensite. Carbide particles above 1 µm at the boundaries of previously austenitic grains practically are not present.

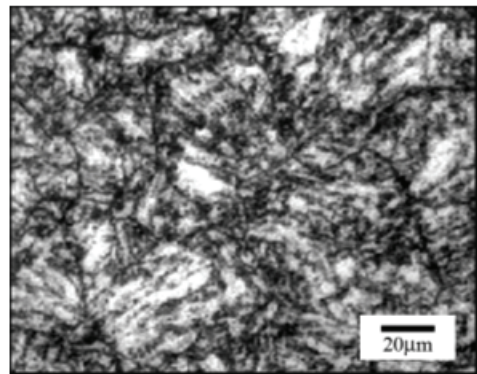
6.3. Hardness

Hardness of parent metal of 230 HV1 was measured. Variation of hardness of simulated samples with temperature of simulation showed a drop at 925°C, Fig. 9, and that is why this temperature of 925°C was chosen as representative of “soft zone”.

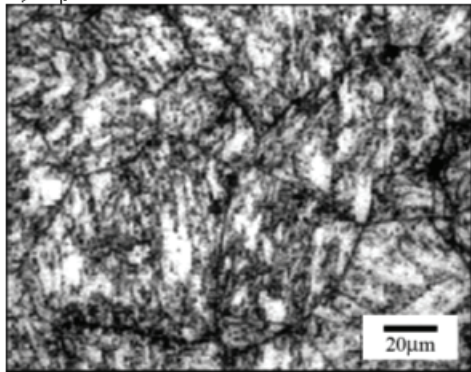
A significant drop of hardness of almost 40HV occurs at simulation temperature of 850°C that is somewhat above A_{C1} temperature. With an increase of simulation temperature, ferrite fraction transforming into austenite increases. At temperature of 925°C, this fraction was approx. 90%. At this temperature, there was no considerable dissolution of carbides and nitrides and transformation of C and N into solid austenite solution. Therefore, martensite formed at cooling had significantly lower content of C and N. Due to decreased content of C and N, repeated separation of $M_{23}C_6$ carbides and MX carbonitrides during subsequent heat treatment was limited resulting in hardness lower than that of base metal.



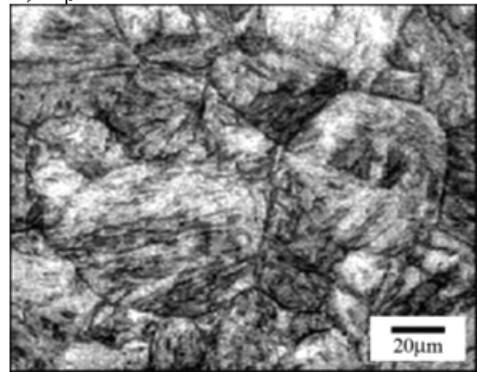
a) $T_p = 925^\circ\text{C}$



b) $T_p = 1100^\circ\text{C}$



c) $T_p = 1300^\circ\text{C}$



d) $T_p = 1386^\circ\text{C}$

Figure 8: Microstructure of simulated specimens (original magnification x 1000)

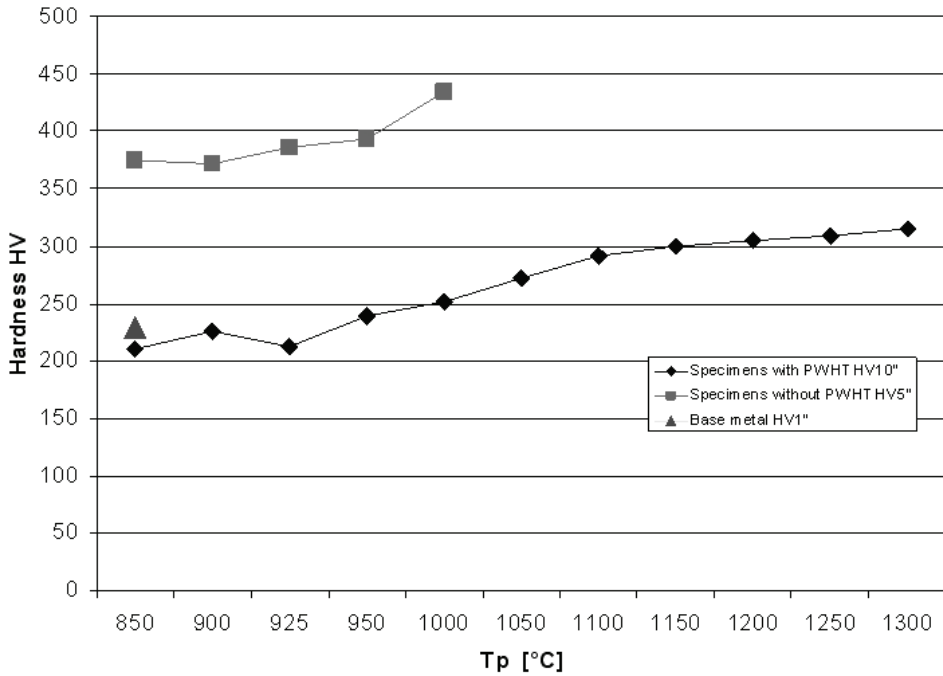


Figure 9: Measured hardness of tested specimens

Besides, carbonitrides precipitates MX coarse became rough and coagulated, which reduced their hardening effect. Due to the phenomena specified, FGHAZ corresponding to simulation-temperature interval from 900°C to 950°C had the smallest hardness. With an increase of simulation temperature above 950°C, hardness increased due to higher solubility of carbides.

7. CONCLUDING REMARKS

According to the investigations, the weldability of the heat resistant material P91 can be described as very satisfactory although there is a drop in the creep resistance in the HAZ. The investigations have shown that this drop in the creep resistance occurred in the FGHAZ where the peak temperature reached a level of about 900-950°C. At stresses lower than 150 MPa, the fracture location shifts from the parent steel into the softened FGHAZ. At operating temperature of 600°C, the data points of the weldments are below those of the parent steel by more than 25%.

This effect must be taken in account when designing the welded components made from P91.

REFERENCES

1. Francis, J. A., Mazur, W., Bhadeshia, H. K. D. H., *Type IV cracking in ferritic power plant steels*, Materials Science and Technology, 22(12): 1387-1395. (2006)
2. Albert, S.K. et al, *Microstructural investigations on type IV cracking in a high Cr steel*, ISIJ International, 42(12): 1497-1504. (2002)
3. Shibli, A., *Material Properties and Heat Treatment*, P91 Course, London. (2006)
4. Kumar, A. et al: *Comprehensive Microstructural Characterization in Modified 9Cr-1Mo Ferritic Steel by Ultrasonic Measurements*, Metallurgical and Materials Transactions A, 33A: 1617-1626. (2002)
5. Kumar, A. et al: *Characterisation of Microstructure in 9% Chromium Ferritic Steels using Ultrasonic Measurements*, Trans. Indian Inst. Met., 56(5): 483-497.(2003)
6. Abe, F.: *Effect of Fine Precipitation and Subsequent Coarsening of Fe₂W Laves Phase on the Creep Deformation Behaviour of Tempered Martensitic 9Cr-W Steels*, Metallurgical and Materials Transactions A, 36A: 321-332. (2005)
7. Heuser, H., Jochum, C., *Alloy design for similar and dissimilar welding and their behaviours*, 1st International Conference Super-High Strength Steels, Rome, Italy, proceedings on cd-rom. (2005)
8. Jallouf, S., Milović, Lj., Pluinage, G., Carmasol, A., Sedmak, S., *Determination of Safety Margin and Reliability Factor of Boiler Tube with Surface Crack*, Structural Integrity and Life, 5(3): 151-162. (2005)
9. Francis, J. A., Mazur, W., Bhadeshia, H. K. D. H., *Estimation of type IV cracking tendency in power plant steels*, ISIJ International, 44(11): 1966-1968. (2004)
10. Francis, J. A., Mazur, W., Bhadeshia, H. K. D. H., *Welding procedures and Type IV Phenomena*
11. Tezuka, H., Sakurai, T., *A trigger of type IV damage and a new heat treatment procedure to suppress it. Microstructural investigations of long-term ex-service Cr-Mo steel pipe elbows*, Int. J. of Press. Vess. and Piping, 82: 165-174. (2005)
12. Milović, Lj., *Significance of cracks in the heat-affected-zone of steels for elevated temperature application*, Structural Integrity and Life, 8(1): 41-50. (2008)
13. Milović, Lj., Zrilić, M., Putić S., *Primena visokohromnih čelika u termoelektranama*, 21. međunarodni kongres o procesnoj industriji PROCESING 2008, Subotica, Serbia. (2008)
14. Milović, Lj., Momčilović, D., Putić, S., Grujić, B., *Type IV Phenomena in Creep Resisting Steels*, 1st International Congress of Serbian Society of Mechanics, Kopaonik, Serbia. (2007)

15. Shibli, I. A., Performance of P91 Thick Section Welds Under Steady and Cyclic Loading Conditions: Power Plant and Research Experience, OMMI, 1(3): 1-17. (2002)
16. Mannan, S.L., Laha, K., Trans. Ind. Inst. Met., 49(4), 303-320. (1996)
17. Data Acceptability Criteria and Data Generation: Creep Data for Welds, ECCC Recommendations, 3(3). (2005)
18. Robertson, D., *Welding and Welded Component Behaviour*, P91 Course, London. (2006)
19. Milović, Lj., Doctoral thesis, Faculty of Mechanical Engineering, University of Belgrade. (2008)
20. Hald, J., Korcakova, L., *Precipitate Stability in Creep Resistant Ferritic Steels-Experimental Investigations and Modelling*, ISIJ International, 43(3): 420-427. (2003)
21. Milović, Lj., Vuherer, T., Zrilić, M., Momčilović, D., Putić, S., *Microstructural analysis of simulated heat affected zone in creep resisting steel*, Proceedings of the 3rd International Conference Deformation, Processing and Structure of Materials, Belgrade, Serbia: 215-222. (2007)
22. Seliger, P., Gampe, U., *Life Assessment of Creep Exposed Components, New Challenges for Condition Monitoring of 9Cr Steels*, OMMI, 1(2): 2-14. (2002)
23. Milović, Lj., Vuherer, T., Zrilić, M., Sedmak, A., Putić, S., *Study of the simulated heat affected zone of creep resistant 9-12% advanced chromium steel*, Materials and Manufacturing Processes, 23(6): 597-602. (2008)
24. Milović, Lj., Sedmak, A., Sedmak, S., Putić, S., Zrilić, M., *Numerical and Analytical Modelling of Elastic-plastic Fracture Mechanics Parameters*, Materials Science Forum, 555: 565-571. (2007)
25. Zrilić, M., Rakin, M., Milović, Lj., Burzić, Z., Grabulov, V., *Experimental and Numerical Evaluation of a Steam Line Behaviour Using Local Approach*, Journal "Metalurgija", 46(2): 87-92. (2007)

DISCRETE AND FRACTAL ASPECTS OF FRACTURE

Michael P. Wnuk

*College of Engineering and Applied Science, University of Wisconsin–Milwaukee,
USA*

mpw@uwm.edu

1. INTRODUCTION

Cohesive models of cracks have been remarkably successful in explaining certain essential features of fracture process such as a finite stress and non-zero crack opening displacement at the crack tip, and a certain equilibrium length of cohesive zone. This length increases with the applied load up to the point of incipient fracture and it serves as a measure of the material resistance to crack propagation. As a new approach, fractal and discrete nature of fracture occurring in real materials should be incorporated in cohesive model. Recent research on nano-cracks, Isupov and Mikhailov /1/, Ippolito et al /2/, indicate that the classic failure criteria break down for very small cracks. Such examples show the need for novel non-local failure criteria for design of structures, in which multiscale fracture mechanisms are present. It is proposed here, in order to refine available mathematical tools and to extend their validity for fractal (rough) cracks and for nano-scale to merge the basic concepts of the cohesive crack model with the fractal view of the decohesion process, employing the non-local criteria, which remain valid at atomistic or nano-scale levels. The present model is applied to define the cohesion modulus, which is used as a measure of material resistance to initiation and to propagation of fracture.

Fracture mechanics is developed based on two fundamental failure theories, proposed by Griffith /3/ and Barenblatt /4/. Griffith realized that brittle fracture happens as a result of competition between strain energy release and surface energy required to create new fracture surfaces. The interesting thing here is that there is no stress singularity. In the Griffith's theory it is predicted that for a given crack length there is a unique critical stress above which crack grows and below which crack remains in equilibrium. Barenblatt proposed the cohesive theory of fracture in which one assumes that there is a nonlinear region in the vicinity of the crack tip. Increasing applied loads increase separation of crack faces in the cohesive region and when the displacement is large enough the crack propagates.

The physically unacceptable singularities predicted by the classical fracture mechanics had been considered by Orowan /5/ and Irwin /6/. They proposed the “plasticity correction” term that was added in the equations describing the stress intensity factors for fracture of various modes, so that for the crack length approaching zero a finite stress resulted, corresponding to the local yield stress. Novozhilov /7/ suggested discrete nature of the crack propagation, introducing the concept of the minimum admissible growth step a_0 . This entity, known as “fracture quantum”, must be included in the energy criterion of Griffith - or an equivalent local stress criterion for fracture. Initially, the fracture quantum was identified with the interatomic distance b_0 in a cubic lattice. Similar concepts proposed Eshelby /8/.

The concept of discrete nature of fracture has been investigated by many researchers, beginning with Neuber /9/, Novozhilov /7/, Wnuk /10/, Seweryn /11/, Pugno and Ruoff /12/. Comparison of various fracture criteria used to describe discrete fracture process

suggests that a certain finite length parameter, determined either by the microstructural or atomistic considerations, must be introduced into the basic equations underlying the theory of fracture. Even though various names and symbols have been used in describing this entity, such as “Neuber particle”, “unit growth step” and “fracture quantum”, the physical meaning of these length parameters is the same, and it can be accounted for mathematically by a discretization technique, Wnuk and Yavari /13/.

The interest in understanding fracture on a more fundamental level indicates that some physics/mechanics coupled problems remain to be resolved. Many researchers have studied the problem at the lattice scale. Thomson, et al /14/ showed that in a very simplified 1D model for a range of stresses above and below Griffith’s stress crack becomes lattice trapped. Later Hsieh and Thomson /15/ extended their results to 2D. Esterling /16/, using a lattice statics method, studied similar problems for three dimensional cracks in a cubic lattice with nearest-neighbour interactions. Masudajindo, et al /17,18/ studied fracture of crystalline materials using the lattice Green’s function method. In particular, they showed that mode I and II crack problems are coupled in the lattice scale. There have been some very recent atomic-scale fracture studies (Marder and Liu /19/; Marder and Gross /20/; Marder /21, 22/).

Further developments are reported in papers given by Mattoni et al /23/, also Ippolito et al /2/, Pugno and Ruoff /12/, Cherepanov /24/; Taylor et al /25/, and Cornetti et al /26/. In this way, the “Quantized Fracture Mechanics” (QFM) was born.

A discretization procedure for the cohesive model of a fractal crack requires that all pertinent entities describing the influence of the cohesive stress that restrains opening of the crack, such as effective stress intensity factor, the modulus of cohesion, extent of the end zone and the opening displacement within the high-strain region adjacent to the crack tip are re-considered and replaced by certain averages over a finite length referred to as either “unit growth step”, cf. Wnuk /10/ or “fracture quantum”, cf. Novozhilov /7/. Thus, two novel aspects of the model enter the theory:

- (1) degree of fractality related to the roughness of the newly created surface, and
- (2) discrete nature of the propagating crack.

Both variables are shown to increase the effective fracture toughness.

The problem may be solved assuming a fractal crack is represented by a cohesive model and that propagation of fracture is not continuous but discrete. The present model yields the results identical to those known in classical fracture mechanics.

Recent work by Ippolito et al /2/ summarizes the pertinent results of the newly developed QFM model. This model is based on the hypothesis of discrete nature of crack propagation and it is used to explain the atomistic simulations data for nano-meter size cracks in β -SiC. The fracture quantum a_0 is seen to be a fraction of a nanometer. In addition to fracture quantum, the finite radius of curvature ρ found at the tip of a QFM crack has been considered as another length entity, resembling to blunt crack in linear-elastic fracture mechanics (LEFM). It turned out that not the fracture quantum alone but rather the ratio ρ/a_0 describes the microstructural behaviour of the material. The third important variable is the crack length itself, especially so in the nano-scale range, where fracture resistance is visibly sensitive to the crack length. Comparing the theoretical and atomistic simulations data Ippolito et al /2/ found that the best fit was obtained for both a_0 and ρ

being on the order of magnitude comparable with the interatomic distances in silicon carbide.

A new model, Discrete Fractal Fracture Mechanics (DFFM), is proposed here.

2. PRELIMINARIES. CLASSIC COHESIVE CRACK MODEL

When a cohesive model is designed, the length of the physical crack c is extended by an adding the cohesive zones at both ends of the crack (Fig. 1). Within these zones the restraining stress S counteracts the separation process. If the length of each cohesive zone is R , then the half-length of the extended crack becomes $a = c + R$. In order to solve the pertinent mixed boundary value problem one needs to assume the following distribution of pressure applied along the surface of the extended crack

$$p(x) = \begin{cases} \sigma, & 0 \leq x \leq c \\ \sigma - S, & c \leq x \leq a \end{cases} \quad (1)$$

This is later superposed with the uniform tension $p(x) = -\sigma$ thus generating a stress-free crack with two cohesive zones, in which the S -stress is present, Fig. 1. The second boundary condition is expressed in terms of the displacement component u_y , which is set equal zero along the symmetry axis outside the crack for $|x| \leq a$. The resulting solution is the familiar stress field, which in the vicinity of the crack tip contains the dominant term controlled by the stress intensity factor. This is the singular term, and it will be subject to annihilation. Such requirement of disappearance of the singular term is know as the “finiteness condition”.

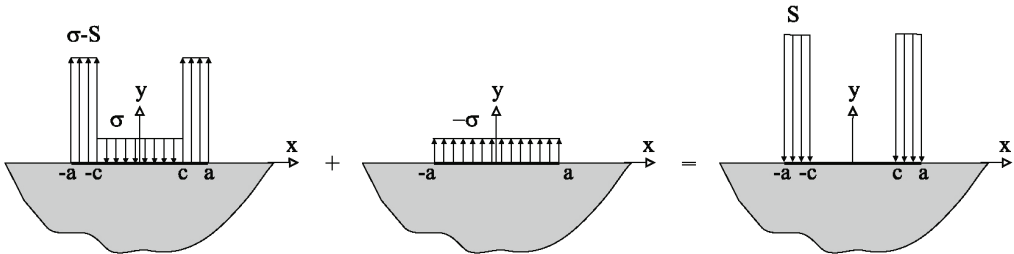


Figure 1: The distribution of pressure applied along the surface of the extended crack

Before proceed to set up such condition for the crack given in Fig. 1, K -factors associated with stresses σ and S should be evaluated. The well-known LFM expression

$$K_I = 2\sqrt{\frac{a}{\pi}} \int_0^a \frac{p(x)}{\sqrt{a^2 - x^2}} dx \quad (2)$$

is substitute (1) for the pressure $p(x)$ to obtain the stress intensity factor for cohesive crack

$$K_I = 2\sqrt{\frac{a}{\pi}} \left\{ \int_0^c \frac{\sigma dx}{\sqrt{a-x}} + \int_c^a \frac{(\sigma - S) dx}{\sqrt{a-x}} \right\} = 2\sqrt{\frac{a}{\pi}} \int_0^c \frac{\sigma dx}{\sqrt{a-x}} - 2\sqrt{\frac{a}{\pi}} \int_c^a \frac{S dx}{\sqrt{a-x}} \quad (3)$$

It is seen that both σ and S contribute to the total stress intensity factor. Notating as

$$K_\sigma = 2\sqrt{\frac{a}{\pi}} \int_0^c \frac{\sigma dx}{\sqrt{a-x}} \quad K_S = 2\sqrt{\frac{a}{\pi}} \int_c^a \frac{S dx}{\sqrt{a-x}} \quad (4)$$

the Eq. (3) is rewritten as follows

$$K_{TOT} = K_{\sigma} - K_S \quad (5)$$

With constant σ and S the integrals are easy to evaluate and the two K -factors become

$$K_{\sigma} = \sigma \sqrt{\pi(c + \tilde{R})} \quad K_S = 2S \sqrt{\frac{c + \tilde{R}}{\pi}} \cos^{-1} \left(\frac{c}{c + \tilde{R}} \right) = S \sqrt{\pi(c + \tilde{R})} \left[\frac{2}{\pi} \cos^{-1} \left(\frac{c}{c + \tilde{R}} \right) \right] \quad (6)$$

These two stress intensity factors remain in equilibrium $K_{\sigma} = K_S$ during the process of loading up to the point of incipient fracture. The function K_{σ}^2 can be thought of as a “driving force”, which forces the crack to open up, while K_S^2 represents material resistance. It is noted that K_S reduces to zero for a vanishing length of the cohesive zone. For a physically important case of R being small compared to the crack length c the second equation in (6) assumes a simple form

$$[K_S]_{\tilde{R} \ll c} = \sqrt{\frac{2}{\pi}} \int_0^{\tilde{R}} \frac{S d\lambda}{\sqrt{\lambda}} \Big|_{S=const} = \sqrt{\frac{2}{\pi}} S (2\sqrt{\tilde{R}}) \quad (7)$$

Variable λ represents the distance measured backwards from the outer edge of the cohesive zone. In this limiting case the cohesion modulus does not depend on the crack size. It is expressed in terms of the magnitude of the cohesive stress and the length R . Equating Eq. (7) with fracture toughness K_c and inverting the equation produce the ubiquitous result

$$\tilde{R} = \frac{\pi K_c^2}{8 S^2} \quad (8)$$

This formula defines the characteristic length parameter as determined through the cohesive model of fracture. Three essential variables are related via this simple equation, which is valid only when $R \ll c$. Otherwise, Eq. (6) must be used to define the length of the cohesive zone as a function of stress S and the crack size c .

Next the finiteness condition employed, which with (6) reads

$$\frac{\sigma\pi}{2} - S \cos^{-1} \left(\frac{c}{c + \tilde{R}} \right) = 0 \quad (9)$$

With Q denoting non-dimensional loading parameter, $Q = \pi\sigma/2S$, one can solve Eq. (9) for the length of the cohesive zone, namely

$$\frac{\tilde{R}}{c} = \sec Q - 1 \quad (10)$$

For small Q the right hand side reduces to $\frac{1}{2} Q^2$, and Eq. (10) reduces to Eq. (8).

3. DISCRETIZATION OF THE COHESIVE CRACK MODEL

In order to account for the discrete nature of fracture process all K -factors discussed above need to be replaced by their averages. Applying the scheme

$$K_{\sigma} \rightarrow \langle K_{\sigma} \rangle_{c,c+a_0} = \left[\frac{1}{a_0} \int_c^{c+a_0} K_{\sigma}^2 dc \right]^{1/2} \quad K_S \rightarrow \langle K_S \rangle_{c,c+a_0} = \left[\frac{1}{a_0} \int_c^{c+a_0} K_S^2 dc \right]^{1/2} \quad (11)$$

we proceed to evaluate the averages defined in (11). Symbol a_0 denotes the fracture quantum, which is used as a normalization constant for the length-like variables X and R ,

$$X = c / a_0 \quad R = \tilde{R} / a_0 \quad (12)$$

The results are

$$\begin{aligned}\langle K_\sigma \rangle &= \sigma \sqrt{\pi} \left[\frac{1}{a_0} \int_c^{c+a_0} (c + \widetilde{R}) dc \right]^{1/2} = \sigma \sqrt{\pi a_0} \left(c + \widetilde{R} + \frac{a_0}{2} \right)^{1/2} = \sigma \sqrt{\pi a_0} \left(X + R + \frac{1}{2} \right)^{1/2} \\ \langle K_S \rangle &= S \sqrt{\pi} \left(\frac{2}{\pi} \right) \left\{ \frac{1}{a_0} \int_c^{c+a_0} (c + \widetilde{R}) \left[\cos^{-1} \left(\frac{c}{c + \widetilde{R}} \right) \right]^2 dc \right\}^{1/2} \\ &= S \sqrt{\pi a_0} \left(\frac{2}{\pi} \right) \left\{ \int_X^{X+1} (X + R) \left[\cos^{-1} \left(\frac{X}{X + R} \right) \right]^2 dX \right\}^{1/2} = S \sqrt{\pi a_0} \left(\frac{2}{\pi} \right) I(X, R)^{1/2}\end{aligned}\quad (13)$$

The auxiliary integral $I(X, R)$ is defined as follows

$$I(X, R) = \int_X^{X+1} (X + R) \left[\cos^{-1} \left(\frac{X}{X + R} \right) \right]^2 dX \quad (14)$$

Substituting (13) into the equilibrium equation $\langle K_\sigma \rangle = \langle K_S \rangle$ yields

$$\frac{\sigma \pi}{2S} \left[X + R + \frac{1}{2} \right]^{1/2} = I(X, R)^{1/2} \quad (15)$$

One can readily solve this equation for the loading parameter Q as a function of X and R . To distinguish this solution from the classic Dugdale solution (10) the subscript D is used for ‘‘Dugdale’’ and the superscript ‘‘ d ’’ for ‘‘discrete’’. From (15) it follows

$$Q_D^d = \frac{I(X, R)^{1/2}}{\sqrt{X + R + \frac{1}{2}}} \quad (16)$$

An interesting simplification of Eq. (16) is obtained for the limiting case of small ratios R/X . For this case the integral (14) reduces to $2R$, and thus the Eq. (16) can be re-written as follows

$$\left[Q_D^d \right]_{R \ll X} = \sqrt{\frac{2R}{X + R + \frac{1}{2}}} \quad (17)$$

The inverse relationship can be readily provided

$$\left[R_D^d \right]_{X \gg R} = \frac{\left(\frac{1}{2} + X \right) Q^2}{2 - Q^2} \quad (18)$$

The other interesting result is obtained for the asymptotic case of $X \gg 1$, i.e., for the situation when the fracture quantum a_0 vanishes. When this case is tested numerically it transpires that the Eq. (16) reduces to a form identical with the Dugdale result (10). For $X \gg 1$ one gets

$$\left[Q_D^d \right]_{X \gg 1} \rightarrow Q_D = \cos^{-1} \left(\frac{X}{X + R} \right) \quad (19)$$

The inverse relation would agree with Eq. (10). The subscript D has been added to the symbol Q to identify it with the Dugdale result. It is therefore justified to conclude that

the results given for a discrete model of cohesive crack reduce to the known equations valid when discretization is removed. This is done by letting the fracture quantum approach zero and thus considering the range of $X \rightarrow \infty$. Figure 2 illustrates the differences and similarities between the solutions obtained from the discrete cohesive crack model and the classic Dugdale model. Examination of the graphs shown in Fig. 2 reveals that for a given external load Q , the nondimensional length of the cohesive zone R (which remains in equilibrium with the applied load) is greater for the discrete model. Thus the measure of the material resistance to crack initiation is enhanced when the discrete nature of fracture is taken into account. Naturally, the differences are more pronounced for the nano scale levels when the initial crack length is comparable to the magnitude of the fracture quantum; examine graphs (a), (b) and (c) in Fig. 2. The same conclusions would be drawn from examination of Fig. 3.

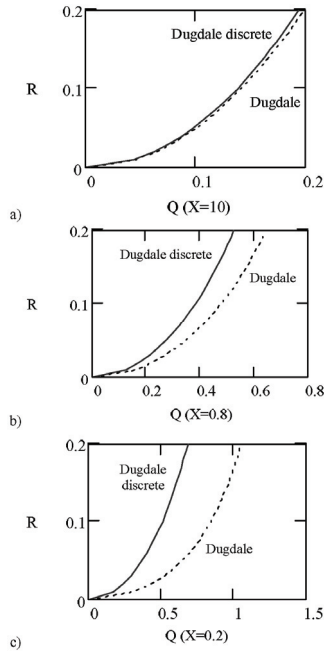


Figure 2: The comparison of discrete cohesive crack model and the classic Dugdale model

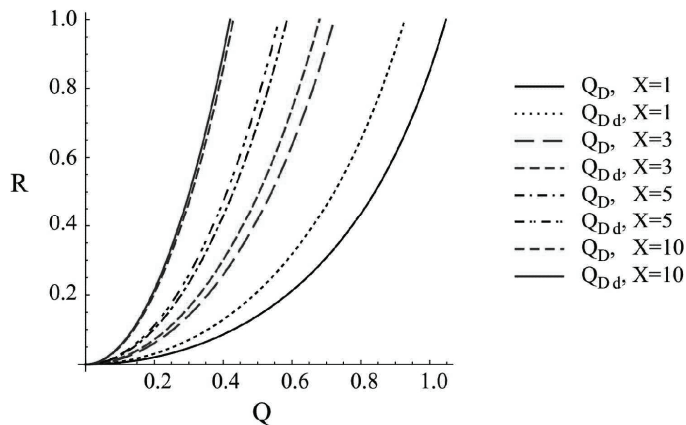


Figure 3: The analysis of graphs (a), (b) and (c) from Fig. 2

Let us look at the cohesion modulus of the discrete cohesive crack. From (13) it is

$$K_{coh}^d = \langle K_S \rangle = \frac{2}{\pi} S \sqrt{\pi a_0} I(X, R)^{1/2} \quad (20)$$

When the size of the cohesion zone is small compared to the crack length, the integral in the Eq. (20) reduces to $2R/a_0$, and simplified expression for the cohesion modulus is

$$\left[K_{coh}^d \right]_{R \ll X} = \frac{2}{\pi} S \sqrt{\pi a_0} \sqrt{\frac{2R}{a_0}} \quad (21)$$

This relation shows explicitly that the product $S\sqrt{R}$ determines material resistance to crack propagation. The problem faced by the material engineers consists in finding a right proportion between S and R ; there exists a conflicting trend between the magnitude of the cohesive strength (approximated by the inherent strength of the material) and length of the cohesive zone. Increasing S , by increasing strength without paying attention to cohesion toughness parameter, which describes the degree of ductility, lowers the length R and thus it may lead to undesirable effects of increased brittleness. This is where the theoretical considerations involving the fracture quantum and the resulting discrete nature of fracture at nano levels may prove to be useful in designing new materials. The formula (21) shows that indeed there is an additional length involved in defining the cohesion modulus. This is the length a_0 . As seen from (21) in addition to the inherent strength S there are two other factors that influence material toughness; these are the fracture quantum and the ratio of cohesive zone size to fracture quantum. This provides a material engineer with additional degrees of freedom to work with.

Yet another variable affecting the cohesion modulus and material toughness that should be considered is the roughness of the surface created in the fracture process.

4. DISCRETE COHESIVE MODEL FOR FRACTAL CRACKS

In this section two features typical of any fracture process are incorporate:

1. Roughness of the newly created surface due to varying degree of fractality (as opposed to the assumption of perfectly smooth surface employed in the classical LFM).
2. Discrete nature of the separation of two adjacent surfaces caused by decohesion (as opposed to continuous character of the propagation process commonly assumed in all local fracture criteria).

A fractal crack completed with the cohesive zone is considered. Therefore, all equations derived in the previous sections are used now and modify to fit the fractal model of Wnuk and Yavari /13/. That is the only model available at the present time, although it is only an approximation. The fractal crack model employed here is based on a simplifying assumption, in which the original problem is approximated by considerations of a smooth crack embedded in the stress field generated by a fractal crack, Wnuk and Yavari /27/.

The cohesive model implies existence of two stress intensity factors, one associated with the applied stress, K_{σ}^f , and the other K_S^f assigned to the cohesive stress. Superscript “ f ” emphasizes the fact that now fractal cracks are in question. When the discrete model is employed these two entities should be replaced by their averages taken over the interval $(c, c + a_0)$, where c denotes the half-length of the crack and a_0 is the fracture quantum. For each value of the applied load one can determine the corresponding equilibrium length of the cohesive zone. The calculation is using the finiteness condition

$$\langle K_\sigma^f \rangle - \langle K_S^f \rangle = 0 \quad (22)$$

One needs to evaluate both terms in Eq. (22), using a procedure similar to the one used in previous section for the averages. Now the following scheme is applied

$$K_\sigma \rightarrow \langle K_\sigma^f \rangle_{c,c+a_0} = \left\{ \frac{1}{a_0} \int_c^{c+a_0} [K_\sigma^f(c, \bar{R}, \alpha)]^2 dc \right\}^{1/2} \quad (23)$$

$$K_S \rightarrow \langle K_S^f \rangle_{c,c+a_0} = \left\{ \frac{1}{a_0} \int_c^{c+a_0} [K_S^f(c, \bar{R}, \alpha)]^2 dc \right\}^{1/2}$$

The resulting functions depend on the fractal exponent α and two length-like variables X and R . To calculate the K -factors for a fractal crack the expression given by Wnuk and Yavari /27 allows to obtain

$$K_\sigma^f = \frac{a^{\alpha-1}}{\pi^{2\alpha-1/2}} \int_0^a \frac{(a+x)^{2\alpha} + (a-x)^{2\alpha}}{\sqrt{a^2-x^2}} p(x) dx \quad (24)$$

In the first equation in (23) the substituting σ for $p(x)$ and $c+R$ for a leads to

$$K_\sigma^f(c, R, \alpha) = \chi(\alpha) \sigma \sqrt{\pi} (c+R)^\alpha \quad (25)$$

The scalar function appearing in this equation reads

$$\chi(\alpha) = \frac{1}{\pi^{2\alpha}} \int_0^1 \frac{(1+s)^{2\alpha} (1-s)^{2\alpha}}{(1-s^2)^\alpha} ds \quad (26)$$

Next evaluation of the average produces

$$\langle K_\sigma^f \rangle = \chi(\alpha) \sigma \sqrt{\pi a_0^{2\alpha}} \left\{ \frac{1}{a_0} \int_c^{c+a_0} (c+R)^{2\alpha} dc \right\}^{1/2} = \chi(\alpha) \sigma \sqrt{\pi a_0^{2\alpha}} \left\{ \int_X^{X+1} (X'+R)^{2\alpha} dX' \right\}^{1/2} \quad (27)$$

The integral is elementary and one can obtain

$$\langle K_\sigma^f \rangle = \chi(\alpha) \sigma \sqrt{\pi a_0^{2\alpha}} \frac{[(X+R+1)^{2\alpha+1} - (X+R)^{2\alpha+1}]^{1/2}}{\sqrt{2\alpha+1}} \quad (28)$$

It is readily observed that for the fractal dimension $D \rightarrow 1$ (or $\alpha \rightarrow 1/2$) expression (28) reduces to the equation valid for non-fractal discretized cohesive model

$$\langle K_\sigma \rangle = \sigma \sqrt{\pi a_0} \left(X+R+\frac{1}{2} \right)^{1/2} \quad (29)$$

Let us define the ratio of the last two K -factors

$$k_\sigma^f = \frac{\langle K_\sigma^f \rangle}{\langle K_\sigma \rangle} = a_0^{\alpha-1/2} \chi_\sigma(X, R, \alpha) \quad (30)$$

where the new scalar function is defined as follows

$$\chi_\sigma(X, R, \alpha) = \chi(\alpha) \left[\frac{(X+R+1)^{2\alpha+1} - (X+R)^{2\alpha+1}}{(2\alpha+1)(X+R+\frac{1}{2})} \right]^{1/2} \quad (31)$$

The plot of the function χ_σ vs. α is shown in Fig. 4. Since χ_σ depends also on crack length and the cohesive zone size, X and R , these two length-like variables are used as parameters to plot the graphs in Fig. 4. The discrepancies in the χ_σ function are particularly visible for the fractal dimension D approaching 2 (α converging to 0). This effect is reflected by the larger spread of function values at the vertical axis, where α equals zero.

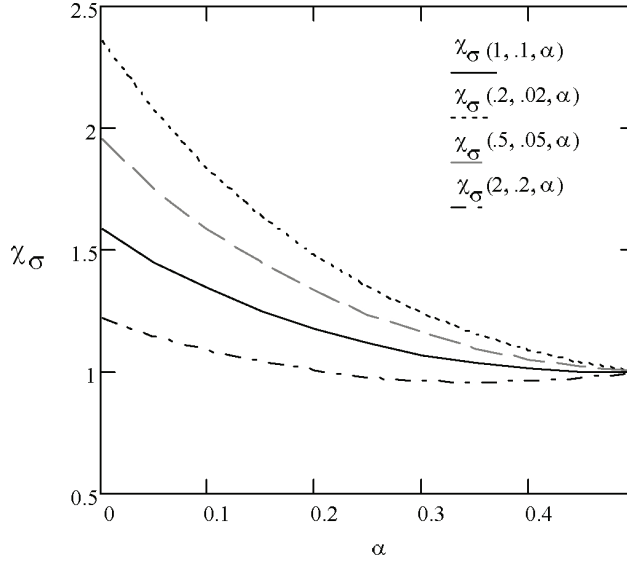


Figure 4: The dependence of function χ_σ vs. α

For the other limiting case of α approaching $\frac{1}{2}$, when a fractal crack reduces to a smooth crack, all curves shown in Fig. 3 converge to unity, which means that the effects of fractal nature of the crack disappear and the solution for the discrete cohesive model is recovered. It can also be seen that for the crack sizes comparable to fracture quantum the magnitude of the average $\langle K_\sigma^f \rangle$ is enhanced for any α , while for cracks much longer than a_0 the value of this average tends to drop below the value $\langle K_\sigma \rangle$ valid for a smooth cohesive crack. Therefore, one may conclude that both discrete nature of fracture and its fractal geometry alter the solutions obtained for the established cohesive crack models.

To emphasize this, the cohesion modulus $\langle K_S^f \rangle$ will be evaluated and discussed. This entity is a function of X , R and α , and its physical meaning is that of material resistance to initiation and propagation of cracks. Applying the second equation in (23) one obtains

$$\langle K_S^f \rangle = \frac{S}{\pi^{2\alpha-1/2}} \left\{ \frac{1}{a_0} \int_c^{c+a_0} (c+R)^{2\alpha} dc \left[\int_{\frac{c}{c+R}}^1 \frac{(1+s)^{2\alpha} + (1-s)^{2\alpha}}{(1-s^2)^\alpha} ds \right]^2 \right\}^{1/2} \quad (32)$$

Introducing the nondimensional variables X and R one obtains

$$\langle K_S^f \rangle = S\sqrt{\pi a_0^{2\alpha}} \left\{ \int_X^{X+1} (X'+R)^{2\alpha} dX' \left[\int_{\frac{X'}{X'+R}}^1 \Phi(s, \alpha) ds \right]^2 \right\}^{1/2} \quad (33)$$

With the inner integral denoted by $H(X, R, \alpha)$ and the auxiliary function Φ given as

$$\Phi(s, \alpha) = \frac{1}{\pi^{2\alpha}} \frac{(1+s)^{2\alpha} + (1-s)^{2\alpha}}{(1-s^2)^\alpha} \quad H(X, R, \alpha) = \int_{\frac{X}{X+R}}^1 \Phi(s, \alpha) ds \quad (34)$$

both integrals in (33) are evaluated numerically. With the notation (34) final expression for the desired average is obtained

$$\langle K_S^f \rangle = S\sqrt{\pi a_0^{2\alpha}} \left\{ \int_X^{X+1} (X'+R)^{2\alpha} H^2(X', R, \alpha) dX' \right\}^{1/2} \quad (35)$$

Written in a somewhat shorter form Eq. (35) becomes

$$\langle K_S^f \rangle = S\sqrt{\pi a_0^{2\alpha}} G_{coh}^f(X, R, \alpha) \quad G_{coh}^f(X, R, \alpha) = \left\{ \int_X^{X+1} (X'+R)^{2\alpha} H^2(X', R, \alpha) dX' \right\}^{1/2} \quad (36)$$

To verify the validity of Eq.(36) note that for $\alpha \rightarrow 1/2$ the function H reduces to

$$[H(X, R, \alpha)]_{\alpha=1/2} = \frac{2}{\pi} \cos^{-1} \left(\frac{c}{c+R} \right) \quad (37)$$

and the function G_{coh}^f becomes identical with the non-fractal result obtained previously for a discrete cohesive crack, namely

$$\begin{aligned} [G_{coh}^f]_{\alpha \rightarrow 1/2} &= \left\{ \int_X^{X+1} (X'+R) \left(\frac{4}{\pi^2} \right) \left[\cos^{-1} \left(\frac{X'}{X'+R} \right) \right]^2 dX' \right\}^{1/2} = \\ &= \frac{2}{\pi} \left\{ \int_X^{X+1} (X'+R) \left[\cos^{-1} \left(\frac{X'}{X'+R} \right) \right]^2 dX' \right\}^{1/2} = \frac{2}{\pi} I^{1/2}(X, R) \end{aligned} \quad (38)$$

Thus, as expected, the cohesion modulus for $\alpha > 1/2$ acquires the form

$$\langle K_S^f \rangle_{\alpha=1/2} = S\sqrt{\pi a_0} \left[\frac{2}{\pi} I^{1/2}(X, R) \right] \quad (39)$$

The effects of fractality and discrete aspects of fracture on the cohesion modulus let us examine the ratio

$$\chi_S = \frac{\langle K_S^f \rangle}{\langle K_S \rangle} = \frac{G_{coh}^f(X, R, \alpha)}{\frac{2}{\pi} I^{1/2}(X, R)} \quad (40)$$

Figure 5 provides the diagrams illustrating the dependence of this function on the fractal exponent α and the two length-like variables X and R . Best way to visualize the effect of these variables is to think of the ratio R/X . As seen from the graph in Fig. 5 the

material toughness measured for fractal and discrete fracture, as given by Eqs. (36), (40), can be either enhanced or reduced when the set of the independent variables (X , R , α) is modified. The range of $\chi_S > 1$ corresponds to an enhancement of material resistance to crack initiation due to variations in the degree of fractality of crack surface. The enhancement is seen to occur for the fractal dimension D approaching 2 and crack sizes small in comparison to the constant a_0 . The effect is pertinent to nano-cracks.

Now all the entities needed to set up the finiteness condition are available. Recalling the equality $\langle K_\sigma^f \rangle = \langle K_S^f \rangle$ and using Eqs. (28), (36) it is arriving at

$$\chi(\alpha)\sigma\sqrt{\pi a_0^{2\alpha}} \left[\frac{2\alpha + 1}{(X + R + 1)^{2\alpha+1} - (X + R)^{2\alpha+1}} \right]^{1/2} = S\sqrt{\pi a_0^{2\alpha}} G_{coh}^f(X, R, \alpha) \quad (41)$$

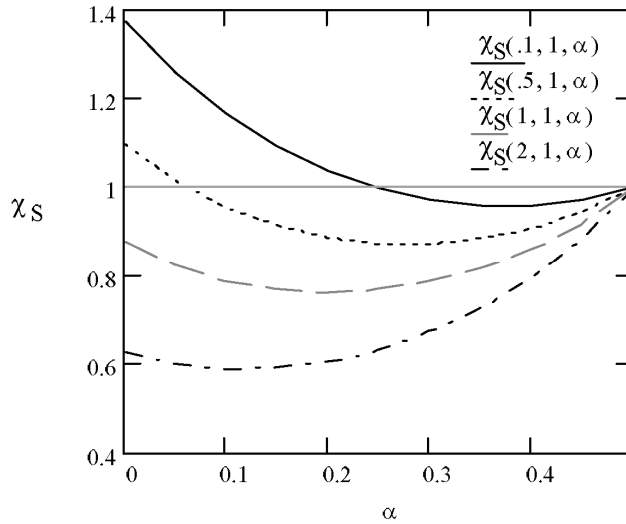


Figure 5: Dependence of function χ_S on fractal exponent α and two length-like variables X and R

This can be solved implicitly for the loading parameter $Q_f (= \pi\sigma_f / 2S)$ as a function of X , R and α . The solution is

$$Q_f = \frac{\pi}{2\chi(\alpha)} G_{coh}^f(X, R, \alpha) \left[\frac{2\alpha + 1}{(X + R + 1)^{2\alpha+1} - (X + R)^{2\alpha+1}} \right]^{1/2} \quad (42)$$

5. CONCLUSIONS

Relations between applied load and the equilibrium length of the cohesive zone have been established for three different mathematical representations of the crack, as follows:

1. Cohesive crack model of Dugdale-Barenblatt for a smooth crack described by two K -factors K_σ and K_S corresponding to the applied and the cohesive stress, respectively,
2. Discrete cohesive crack model described by the averages $\langle K_\sigma \rangle_{c+a_0}$ and $\langle K_S \rangle_{c+a_0}$.
3. Discrete and fractal cohesive crack model involving the fractal equivalents of the averages, namely $\langle K_\sigma^f \rangle_{c+a_0}$ and $\langle K_S^f \rangle_{c+a_0}$.

In a classic LEFM crack model there is no cohesive zone, and the crack itself provides a mechanism for relaxing the high stresses in the vicinity of a stress concentration. Therefore, this representation may be thought of as a limiting case of a more general and refined mathematical formulation involving cohesive zone associated with a crack. For such a representation the equilibrium between the driving force K_{σ}^2 and material resistance K_S^2 defines a unique relation between the length of the cohesion zone, say R , and the applied load, say Q . The equilibrium between $R (= R/a_0)$ and Q is maintained during the loading process up to the point of incipient fracture.

Cohesive zone generated prior to fracture has two important aspects. It measures the material resistance to fracture: the longer is the cohesive zone, the greater is the resistance. It also provides a mechanism for relaxing stresses prior to fracture in the immediate vicinity of a stress concentrator.

Figure 6 shows schematically four sketches of a crack represented by four different mathematical models.

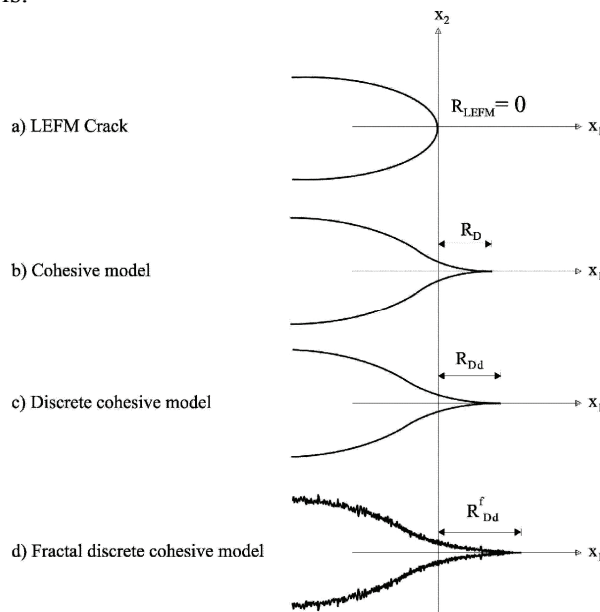


Figure 6: Schemes of mathematical models for crack representation

- (a) the LEFM concept of a Griffith crack embedded in a linear elastic solid,
- (b) Dugdale-Barenblatt cohesive model;
- (c) discretized cohesive model and;
- (d) a fractal cohesive and discrete model.

The very first crack shown in Fig. 6 has no cohesive zone at all, and the stresses are singular at the tip of the crack. In this case fracture toughness must be measured by employing the ASTM standards that make no mention of cohesion. The second crack in the figure corresponds to a cohesive model suggested independently by Barenblatt /28/ and Dugdale /29/. With cohesion included a better insight into material response to fracture is involved by visualizing the effect of the cohesive zone. As it turns out, it is a certain integral of the cohesion stress $S(x)$ over the zone R . For a constant S and under the restriction of $R/X \ll 1$ this integral reduces to a product of S and the square root of length R . This is the Barenblatt cohesion modulus, which determines material resistance to onset and propagation of fracture. Here, this expression is generalized for a discrete fracture

and with the fractal geometry taken into account. Thus, our most advanced model incorporates the discrete nature of fracture process and its fractal geometry at the same time. Two new variables enter the theory:

(1) fracture quantum a_0 ,

(2) fractality degree, measured by the fractal dimension D or by the fractal exponent α .

It is noteworthy that each of the successive models listed in Fig. 6 predicts for a given level of the applied load successively larger cohesive zone, namely

$$R_{Dd}^f \geq R_{Dd} \geq R_D \geq R_{LEFM}$$

The interpretation of the subscripts is as follows: f - fractal, Dd – Dugdale discrete, D – Dugdale. Of course, the LEFM value of R is zero, but using the K_c value obtained from the tests specified by ASTM one could, in a hindsight, define an equivalent length R that could be associated with a LEFM crack.

At the micro- and nano-scale the size of the Neuber particle, or process zone in a more updated nomenclature, becomes important not only for mathematical treatment of the problem, but also for the physical interpretation of the decohesion phenomenon at the atomistic scale.

REFERENCES

1. Isupov, L.P. and Mikhailov, S. E. (1998) A comparative analysis of several nonlocal fracture criteria. *Archive of Applied Mechanics*, 68:597-612.
2. Ippolito, M., Mattoni, A., Colombo, L. and Pugno, N. (2006) Role of lattice discreteness on brittle fracture: Atomistic simulations versus analytical models. *Physical Review B*, 73:104111.
3. Griffith, A.A. (1920), "The Phenomena of Rupture and Flowing Solids", Phil. Trans. Royal Soc. (London), Vol. A221, pp. 163-198.
4. Barenblatt, G.I. (1962) The mathematical theory of equilibrium of crack in brittle fracture. *Advances in Applied Mechanics*, 7:55-129.
5. Orowan, E. (1955) Energy criteria of fracture. *Welding Journal*, 34: S157-S160.
6. Irwin, G. R. (1958). Fracture I, *Handbuch der Physik VI*, Flu"gge Ed., 558–590, Springer.
7. Novozhilov, V.V. (1969) On a necessary and sufficient criterion for brittle strength. *Journal of Applied Mathematics and Mechanics-USSR*, 33:212-222.
8. Eshelby, J. D. (1957) The Determination of the Elastic Field of an Ellipsoidal Inclusion, and Related Problems. *Proceedings of the Royal Society of London Series A*, 241:376-396.
9. Neuber, H. (1958), *Theory of Notch Stresses*, Springer-Verlag, Berlin.
10. Wnuk, M.P. (1974) Quasi-static extension of a tensile crack contained in a viscoelastic-plastic solid. *Journal of Applied Mechanics*, 41:234-242, 1974.
11. Seweryn, A. (1994) Brittle-Fracture Criterion for Structures with Sharp Notches. *Engineering Fracture Mechanics*, 47:673-681.
12. Pugno, N. and Ruoff, R.S. (2004). Quantized fracture mechanics. *Philosophical Magazine* 84(27),2829–2845.
13. Wnuk, M.P. and Yavari, A. (2005) A correspondence principle for fractal and classical cracks. *Engineering Fracture Mechanics*, 72:2744-2757.
14. Thomson, R., Hsieh, C. and Rana, V. (1971) Lattice trapping of fracture cracks. *Journal of Applied Physics*, 42:3154-3160, 1971.
15. Hsieh, C. and Thomson, R. (1973) Lattice Theory of Fracture and Crack Creep. *Journal of Applied Physics*, 44:2051-2063.
16. Esterling, D.M. (1976) Lattice Theory of 3-Dimensional Cracks. *Journal of Applied Physics*, 47:486-493.

17. Masudajindo, K., Tewary, V.K. and Thomson, R. (1991) Theoretical-Study of the Fracture of Brittle Materials - Atomistic Calculations. *Materials Science and Engineering A-Structural Materials Properties Microstructure and Processing*, 146:273-289.
18. Masudajindo, K., Zhou, S.J., Thomson, R. and Carlsson, A.E. (1994) Atomic Theory of Fracture of Crystalline Materials - Cleavage and Dislocation Emission Criteria. *Materials Science and Engineering a-Structural Materials Properties Microstructure and Processing*, 176:255-261.
19. Marder, M. and Liu, X.M. (1993) Instability in Lattice Fracture. *Physical Review Letters*, 71:2417-2420.
20. Marder, M. and Gross, S. (1995) Origin of Crack-Tip Instabilities. *Journal of the Mechanics and Physics of Solids*, 43:1-48.
21. Marder, M. (1999) Molecular dynamics of cracks. *Computing in Science & Engineering*, 1:48-55.
22. Marder, M. (2004) Cracks cleave crystals. *Europhysics Letters*, 66:364-370.
23. Mattoni, A., Colombo, L. and Cleri, F. (2005) Atomic scale origin of crack resistance in brittle fracture. *Physical Review Letters*, 95:115501.
24. Cherepanov, G.P. (1990), Quantum fracture mechanics, *Strength of Materials*, 22(2): 155-163.
25. Taylor, D., Cornetti, P. and Pugno, N. (2005) The fracture mechanics of finite crack extension. *Engineering Fracture Mechanics*, 72:1021-1038.
26. Cornetti, P., Pugno, N., Carpinteri, A. and Taylor, D. (2006) Finite fracture mechanics: A coupled stress and energy failure criterion. *Engineering Fracture Mechanics*, 73:2021-2033.
27. Wnuk, M.P., and Yavari, A. (2003). On estimating stress intensity factors and modulus of cohesion for fractal cracks. *Engineering Fracture Mechanics* 70,1659–1674.
28. Barenblatt, G.I. (1959), "The Formation of Equilibrium Cracks During Brittle Fracture, General Ideas and Hypothesis. Axially-Symmetric Cracks", *J. Appl. Math. Mech.*, Vol. 23, pp. 622-636, English translation from *PMM*, Vol. 23 (1959), pp. 434-444.
29. Dugdale, D.S. (1960), "Yielding of Steel Sheets Containing Slits", *J. Mech. Phys. Solids*, Vol. 8, pp. 100-104.

CRACK ANALYSIS AT NANO LEVEL

Sedmak Stojan

*Faculty of Technology and Metallurgy, University of Belgrade, Serbia
sedmak@divk.org.rs*

1. INTRODUCTION

Two main contributions of fracture mechanics (FM) in the development of engineering structures are connected with fracture itself (prevention and analysis) and development of new materials based on specification with defined FM parameters. In this way structural security, safety and reliability have been significantly improved.

The introduction of nano structures can be considered as an important extension in the area of engineering structures, and the benefits of this extension are well recognized. The application of experience gathered with FM parameters is natural, since the requirements regarding security, safety and reliability are very important for nano structure /1/.

Some retrospect of FM development and review of its parameters /2, 3/ can help to understand the dilemmas and limitations in FM application to nanostructures, but the size effect should be recognized first, Fig. 1 /4/. Although this figure might request extended description, one also must have in mind the size of non-included huge structure, for which is FM of high interest, like sea platforms, ships, bridges, TV towers, new designed buildings, which extend the scheme in Fig. 1 at least for three orders of magnitude.

Depending on the application, crack and its tip can be considered at different levels. In a structure of macro size deeper knowledge of structure composition, up to the nano level, gathered by the application of modern testing devices and modelling can help to obtain more accurate assessment of crack significance, assuring in this way not only the security but also the economy. Introduced materials and structures of nano size appeal to assess their integrity and reliability in service, and this is next request to analyse crack behaviour at nano level. This is the purpose of this lecture.

2. REVIEW OF FRACTURE MECHANICS PARAMETERS DEVELOPMENT

Extensive investigation and experimental testing performed after the incident with Liberty ship (Fig. 2) /5/ which fractured in 1943 in an inexplicable way for that time, are the fundamentals of FM developments, although FM is not established as a direct result. This is one illustrative and well documented case study. Studying this failure the experts turned from experience aspect to experimental and theoretical aspects. From the standpoint of here considered topic, the most important finding was that unknown material properties, impact toughness and nil-ductility transition temperature were identified as responsible. Gathered new experience was of prime interest for improvement in design of structure and materials, extended the problem to practical solution, which allowed prescribing more convenient codes and standards regarding the security. But still this was not fracture mechanics approach.

It is to recall that the ship was a welded structure and that time it was allowed to strike the arc on a plate (Fig. 3) /6/. The plasticity of parent metal was sufficient to arrest crack growth through different microstructures in the heat-affected zone (HAZ).

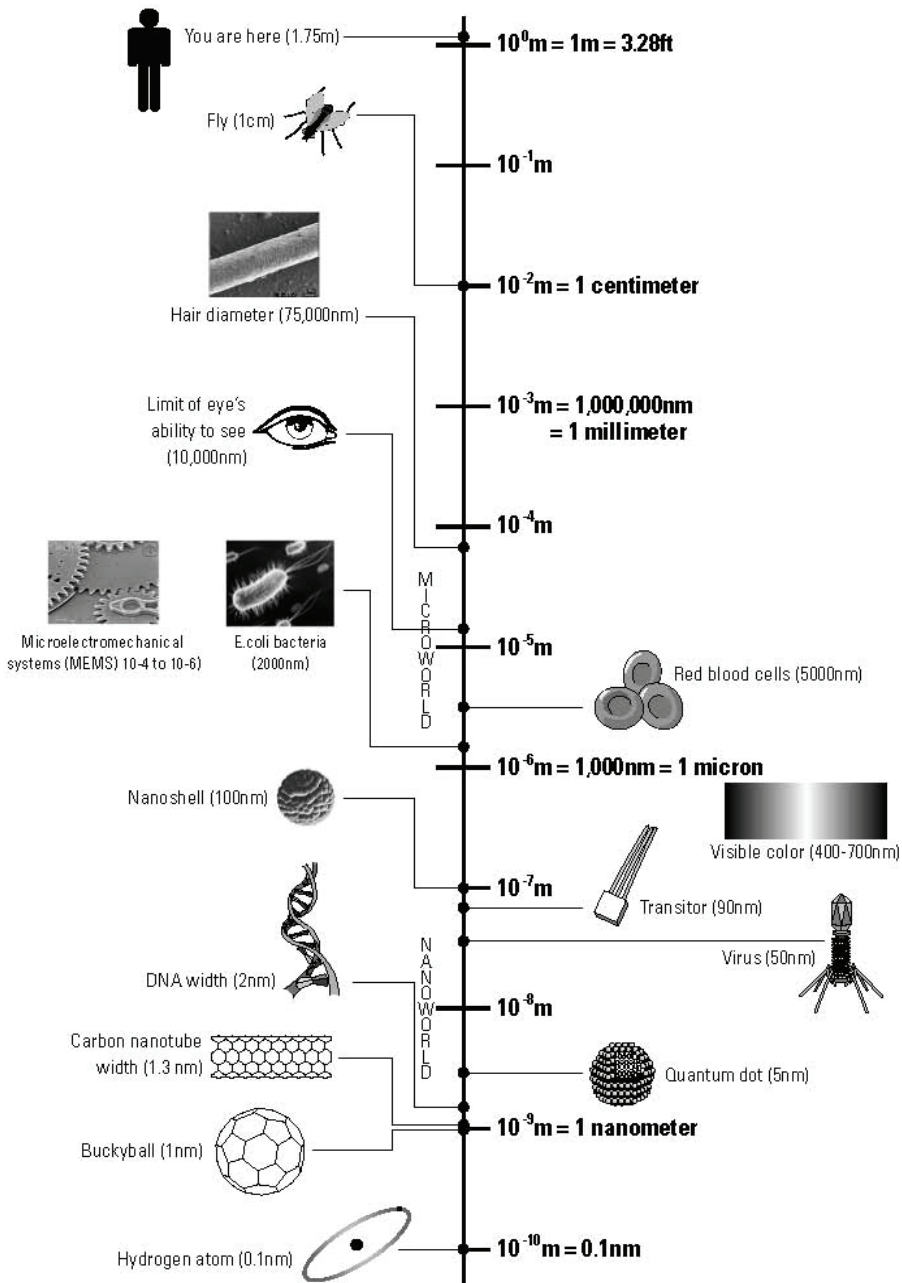


Figure 1. The scaling of solid body phenomena – a modern view /4/

So, parent metal properties enabled to neglect the effect of inevitable welded joint imperfections and heterogeneity in microstructure and mechanical properties. The problem of brittle fracture occurred only when the temperature was below the nil-ductility transition. Only the emerged in water bottom plating held, being capable to arrest fast growing crack. In time of ship failures stress concentration /7/ and fracture /8/ were already theoretically recognized, but did not attract required attention. They became interesting later, in FM development process.

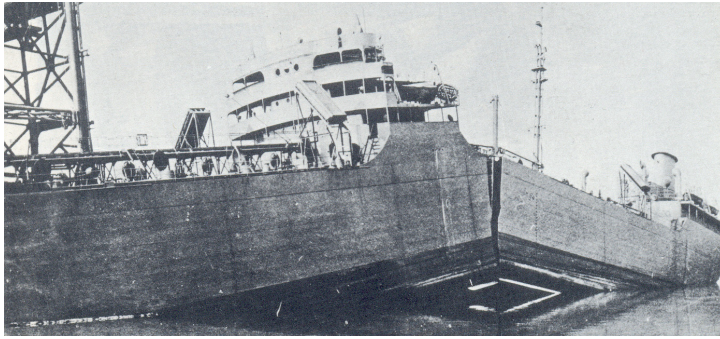


Figure 2: Failure of Liberty type ship “Schenectady” /5/

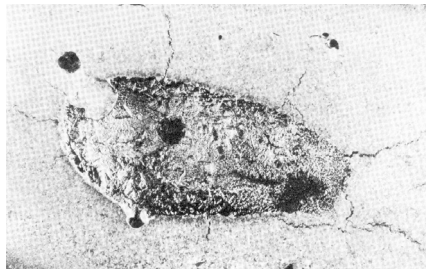


Figure 3. Welding arc strike. Cracks about 2 mm in size developed in hard heat-affected-zone (HAZ) surrounding fusion starter /6/

2.1. Linear elastic fracture mechanics (LEFM)

Considering the crack in homogeneous material, FM developed models for description of stress and strain distribution ahead the crack tip, the singular location in the field, and corresponding parameters for mathematical analysis. Intensive theoretical and experimental, and later on numerical investigation of stress concentration in elastic range around geometry transition and defects in loaded components enabled to involve crack and its size in the stress analysis. This was done for elastic behaviour (linear-elastic fracture mechanics – LEFM), using primarily the results of Griffith /8/ and of Irwin and Kies /9/. In this way theoretically supported crack analysis allowed to define crack parameters for plain strain condition, corresponding to generally accepted material properties expressed in strength parameters.

In the analysis of fracture strength Griffith /8/ recognized that it is possible to derive a thermodynamic criterion for fracture by considering the total energy change with increasing crack length in a cracked body. Only if the total energy decreased would the crack extend spontaneously under the applied stress. Using energetic approach in the body as a whole, it is possible to neglect local stress concentration around the crack tip and derive a useful expression for the fracture stress. The analysis performed by Griffith is based on the situation shown in Fig. 4. He analyzed the changes in energy, which occur if the crack is infinitesimally extended. New crack surfaces are created and since the stresses and displacements immediately ahead of the infinitesimally extended crack tip are identical to those ahead of the initial crack tip, the energy increase during crack extension is simply the unit "work to fracture", 2γ , multiplied by the area of produced new crack surfaces. Based on that, Griffith proposed that the crack driving force (CDF) is involved by the difference between the energy released for crack extension and that

needed to create new crack surfaces. The calculation applied by Griffith is complicated, but the same result is obtained by simplification using concept of stress-lines, Fig. 5 /10/.

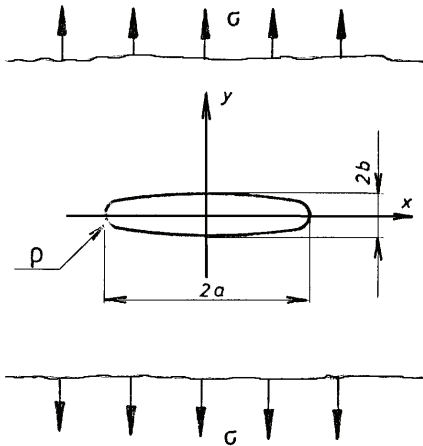


Figure 4. Griffith's crack: geometrical configuration

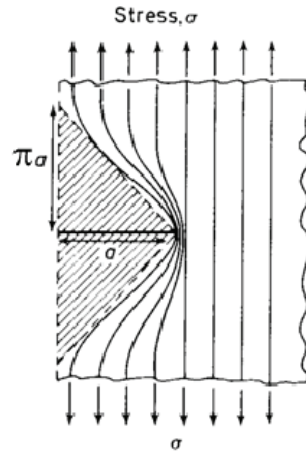


Figure 5. Simplified model for approximate calculation of strain energy release rate /10/

Two half-crack lengths a and $(a + \delta a)$ are considered under fixed-grip conditions, exposed to applied stress σ . The stress-free regions above and below the crack can be roughly triangular in shape and extended to a height π . Then, for a length a , the strain energy release U per unit thickness ($B = 1$) is given in plane stress by $\frac{1}{2} \times \text{stress} (\sigma) \times \text{strain} (\sigma/E) \times \text{area} (\pi a^2)$, i.e.

$$U = -\frac{1}{2} \sigma \cdot \frac{\sigma}{E} \cdot \pi a^2 \quad (1)$$

thus, for a length increase da , the decrease of the strain energy is

$$dU = -\frac{\sigma^2}{E} \cdot \pi a da \quad (2)$$

In plane strain, the tensile strain is given as $\sigma (1 - \nu^2)/E$ (ν is Poisson's ratio) instead σ/E , and the change in energy with crack length, $\partial U/\partial a$, is:

$$\frac{\partial U}{\partial a} = -\frac{\sigma^2}{E} \pi a \quad (\text{for plane stress}) \quad \frac{\partial U}{\partial a} = -\frac{\sigma^2(1-\nu^2)}{E} \pi a \quad (\text{for plane strain}) \quad (3)$$

In order to verify the results of Griffith, crack is modelled in an ideal crystalline body by increased atom distance at the tip under applied remote stress σ (Fig. 6), considering the change in crack-driving force F with the crack extension at atomic level /10/.

The strength is taken as a tensile stress σ , which must be applied to cause the fracture across a particular crystallographic plane of cubic lattice with initial atomic spacing b_0 . Stress σ is simply the sum of the forces, F , acting between successive pairs of atoms. To a first approximation, the value of F required to cause fracture corresponds to that needed to separate an isolated pair of atoms such as AB. For a pair of atoms, such as AB, CD,...PQ it is possible to draw a curve to represent their energy of interaction as a function of distance of separation b (Fig. 7). The resultant energy, U , exhibits a minimum at the equilibrium lattice spacing b_0 . Some energy must be spent to increase the

distance between atoms b , and the total energy, necessary to separate the two atoms to infinity, is given by U_o . The derivative of this curve is force – displacement curve, with initial slope equal to elasticity modulus E and total area under it is equal to twice the surface tension, 2γ , considering both sides of extended crack.

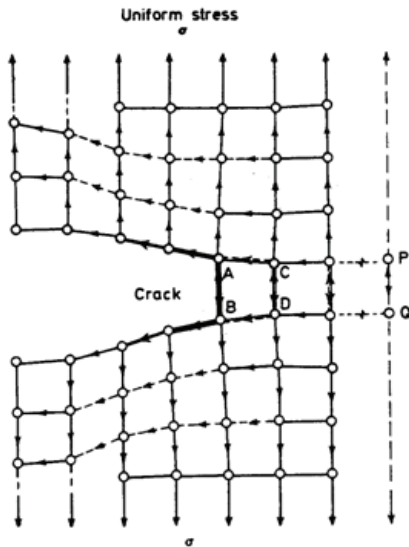


Figure 6. Development of a crack in an atomic model

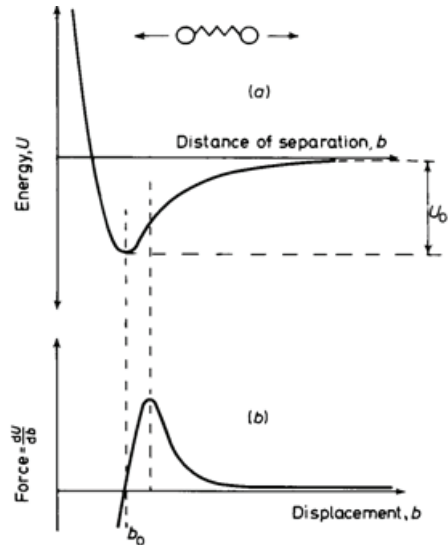


Figure 7. Bonding energy vs. distance of separation (up) and force vs. displacement (down)

Next approximation enables to derive the relationship /10/

$$\sigma_{max} = \sqrt{\frac{E\gamma}{b_o}} \quad (4)$$

where σ_{max} is ideal strength of material, and approximate fracture stress.

Fracture stress value of the order of $E/10$ may be estimated from Eq. (4), using the value of γ of the order $0.01 \cdot Eb_o$, applicable to many metals. The strengths of crystals and glasses in practice tend to be lower than this value by two orders of magnitude. Griffith /7/ first suggested that a macroscopically homogeneous sample might contain small defects, a cause of discrepancy between predicted and actual values because ideal fracture stress can be attained only locally in the sample.

To understand the fracture stress let us suppose an infinite body with a defect of elliptical shape (Fig. 4), with major axis $2a$ and minor axis $2b$, lying normal to the applied stress, σ . The concentrated value of stress at the ellipse ends would be /7/

$$\sigma_{yy} = \sigma_{max} = \sigma \left(1 + \frac{2a}{b} \right) = \sigma \left[1 + 2 \left(\frac{a}{\rho} \right)^{1/2} \right] \quad (5)$$

where $\rho = b^2/a$ is the radius of the ellipse tip. For crack-like defect, a value for ρ is taken as the lattice spacing b_o . Then, since $2\sqrt{a/b_o} \gg 1$ one would obtain:

$$\sigma_{yy} = \sigma_{max} \cong 2\sqrt{\frac{a}{b_o}} \sigma \quad (6)$$

Comparing Eq. (4) and Eq. (6) following stress at fracture σ is obtained:

$$\sigma = \sqrt{\frac{E\gamma}{4a}} \quad (7)$$

It can be seen immediately that, putting $\gamma = 0.01 \cdot Eb_o$, as before, a defect length $2a$ of $5000b_o$, say $1 \mu\text{m}$, is sufficient to lower the fracture strength by two orders of magnitude.

The Eq. (5) for the stresses around an elliptical hole was derived on the basis of linear elasticity. The Eq. (4) is based on supposed sinusoidal atomic stress-strain curve /10/. So, one has to have in mind that the macroscopic applied stress is correlate here to the atomic force-displacement laws.

As it is said, these values of $\partial U/\partial a$ also represent the decrease in potential energy, released when a crack extends by an infinitesimal amount δa under constant load.

The Griffith criterion for fracturing a body with crack of half length a may be visualised, Fig. 8.a, drawing the way in which energy changes with crack length. The total energy, W , consists of potential energy, U , and surface energy, S , and in plane stress:

$$W = U + S = -\frac{1}{2} \cdot \frac{\sigma^2 \pi a^2}{E} + 2\gamma a \quad (8)$$

The maximum in the total energy curve is given by a $\partial W/\partial a = 0$, i.e.

$$\frac{\sigma^2 \pi a}{E} = 2\gamma \quad (9)$$

This is depicted in Fig. 8.b, where the intersection of the line $-(\partial U/\partial a) = \sigma^2 \pi a/E$ with that of 2γ is shown. The positive value of the slope $(\partial U/\partial a)$ is defined as the potential energy release rate for crack extension under constant load for unit thickness and signed as G , presenting crack driving force. Comparing with Eq. (3) one can derive for a given crack length a the Griffith's fracture stress:

$$\sigma_F = \sqrt{\frac{2E\gamma}{\pi a}} \quad (\text{in plane stress}) \quad \sigma_F = \sqrt{\frac{2E\gamma}{\pi(1-\nu^2)a}} \quad (\text{in plane strain}) \quad (3a)$$

These expressions are similar in form to that derived for the crack tip using the solution for stress concentration /7/. Griffith's approach ignores the details of the fracture process at the crack tip, representing completely different procedure. Because it considers only the initial and final states and is not concerned with the details of fracturing over the length δa , it represents only a necessary condition for fracture, which may or may not be sufficient. Griffith's approach could treat the change in energy involved with the extension of a rather blunt elliptical hole and conclude that the total energy of the system would decrease, yet the hole would not extend if there were not sufficient stress concentrated at its end to attain the local fracture stress. The most important aspect for next development of fracture mechanics is that the crack size, a , is related to applied load, expressed through stress, σ , and material property, in the form of surface energy, γ .

The basic parameter of fracture mechanics, stress intensity factor K , is defined as

$$K = Y\sigma\sqrt{\pi a} \quad (10)$$

where Y presents a factor of geometrical shape and final sizes of considered component.

The critical K value, K_{Ic} , is material characteristics and can be determined experimentally using corresponding standard, e.g. plane strain fracture toughness, ASTM E399. It is to mention that plane strain condition must be fulfilled in K_{Ic} testing, and for that two requirements are prescribed in standard: very sharp crack with plane strain state at the tip (fatigue crack), and sufficient thickness of specimen to prevent plane stress state and shear lips. The required thickness for brittle material is small, but size for ductile material could be so large that can not be tested on available equipment.

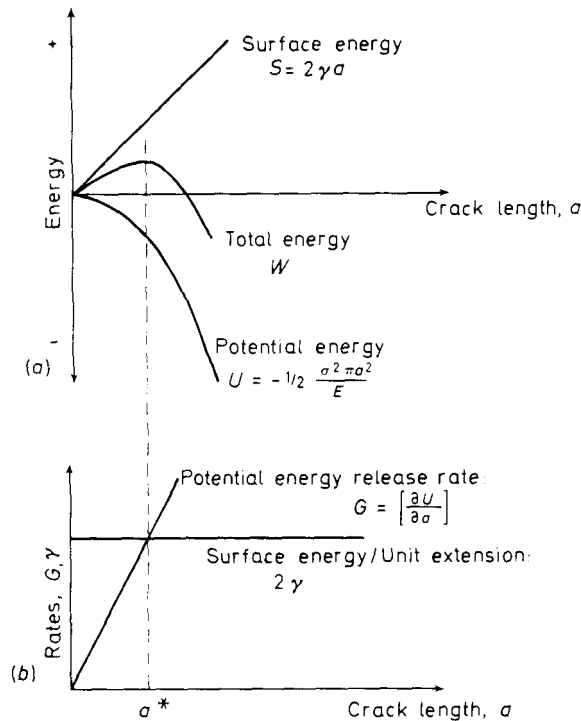


Figure 8: Variation of energy with crack length (a) and of energy rate with crack length (critical Griffith's crack length is denoted by a^*)

Structure is safe and reliable if the applied stress intensity factor K is less than plane strain fracture toughness K_{Ic} of material:

$$K \leq K_{Ic} \tag{11}$$

Linear elastic fracture mechanics can be applied to problems in which the plastic zone ahead the crack tip is small compared to the crack length. Fracture is then characterized by the plane strain fracture toughness, K_{Ic} , and the decisive value for brittle fracture is surface energy γ . In circumstances dominated by plane stress, the plastic zone is larger; nevertheless, if failure still occurred at net section stress levels which are much lower than the yield stress, problems may still be tractable by LEFM based methods /11/.

2.2. Elastic-plastic fracture mechanics (EPFM)

Since the fracture in steel and metallic materials frequently occurs after significant plastic deformation, a different approach was then necessary. Introducing path independent contour integral (J integral), defined by Rice /12/, it was possible to extend the fracture mechanics to elastic-plastic behaviour (elastic-plastic fracture mechanics – EPFM).

In that case significant energy γ_p is spent for development of plastic deformation before final fracture, even greater than surface energy γ . Orowan /13/ proposed the extension of basic formula of Griffith in the form:

$$\sigma_F = \sqrt{\frac{2E(\gamma + \gamma_p)}{\pi a}} \quad (12)$$

The expression $\gamma + \gamma_p$, called the fracture energy, can include plastic, viscoelastic or viscoplastic effects, depending on the material type.

The efficient parameter in describing crack in plane stress condition with expressed plastic deformation is path independent, contour J integral /12/. It is also possible to apply it as a measure of fracture toughness, J_{Ic} , according to ASTM E813 and similar later introduced standards, enabling to cover a wide range of stress conditions by only one parameter.

By definition J integral (Fig. 9) is an energy criterion, given in the form:

$$J = \oint_{\Gamma} \left(W dy - T_i \frac{\partial u_i}{\partial x} ds \right) \quad (13)$$

with $W = \int \sigma_{ij} d\varepsilon_{ij}$ - strain energy density (σ_{ij} is stress tensor, ε_{ij} strain tensor); Γ - integration path; ds - element of segment length; $T_i = \sigma_{ij} n_j$ - traction vector on the contour; u_i - displacement vector, n_i - normal unit on contour Γ . Rice has shown that J integral is path independent /12/ for two-dimensional plane problems with no volume and inertial forces, and for non-linear elastic material, homogeneous at least in crack growth direction. In that case J integral can be presented as the energy, released on crack tip for unit area crack growth, Bda , e.g. following expression is valid

$$JBda = B \oint_{\Gamma} W dy da - B \oint_{\Gamma} T_i \frac{\partial u_i}{\partial x} ds da \quad (14)$$

where B is specimen thickness. The member $B \int W dy da$ denotes the energy obtained (and released) along the contour Γ for crack increase, da . Second member in Eq. (14) represents the work of traction forces on contour displacement for crack growth da . As an energy criterion (the value $JBda$ is the total energy at crack tip available for crack growth Δa), it can be related to the Griffith's energy G , and stress intensity factor, K , so:

$$J = G = \frac{K^2}{E'} ; E' = E \text{ (plane stress)} \quad E' = E / (1 - \nu^2) \text{ (plane strain condition)} \quad (15)$$

The behaviour of elastic-plastic material during stable crack growth can be described by diagram $J-\Delta a$, (J-R curve), where Δa stands for crack extension, Fig. 10.

Generally, J integral is seen to be the potential energy difference between two bodies having identical boundary tractions, and incrementally different crack lengths. This is expected, since in J integral the energy terms are considered, similar as in Griffith's approach, in which the total energy of cracked body is calculated. It has been proved experimentally that J integral is path independent also in the plastic range. Therefore, J integral can be used as a general FM parameter, in both, elastic and plastic ranges, and the procedure for J - R curve determination is accepted in ASTM E1152 standard.

It is to mention that crack opening displacement (COD) is another popular FM parameter in elastic and in plastic range, applied for welded structures.

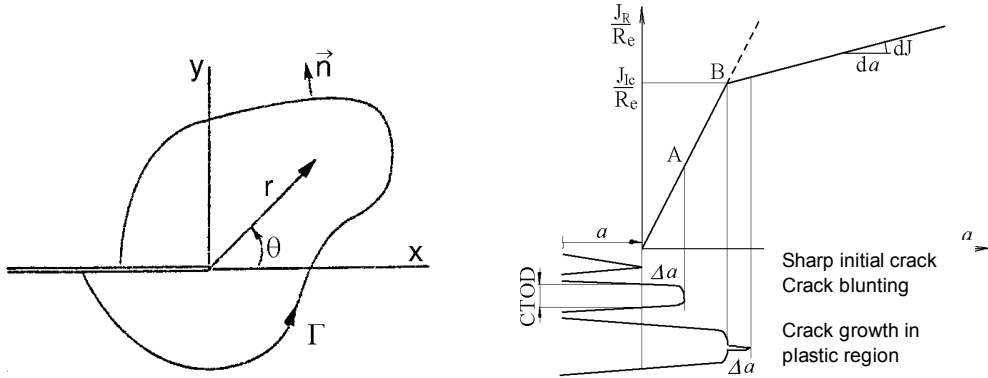


Figure 9. Arbitrary contour path for J integral Figure 10. Stable crack growth defined by J integral

When a large stretch zone at crack tip is developed, the crack-opening stress must exceed the yield stress to cause plastic fracture and stable crack growth. If a small degree of crack tip blunting is developed, the fracture is of elastic-plastic type. The elastic term signifies that the fracture is developed for elastic crack-opening stresses, up to the point B in Fig. 10, which indicates the final stretch zone, next FM parameter. Figure 11 illustrates that the crack tip blunting is the result of plastic slip within the grains. That is, slip is developed prior to micro cracking of the grains. In the case of welded joint differences in fractograms (Fig. 12) indicate the complexity of the problem.

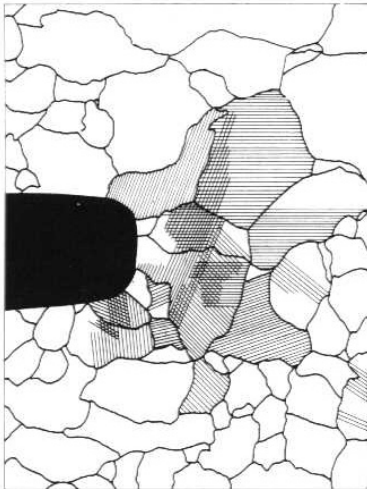


Figure 11: Mechanism of crack tip blunting

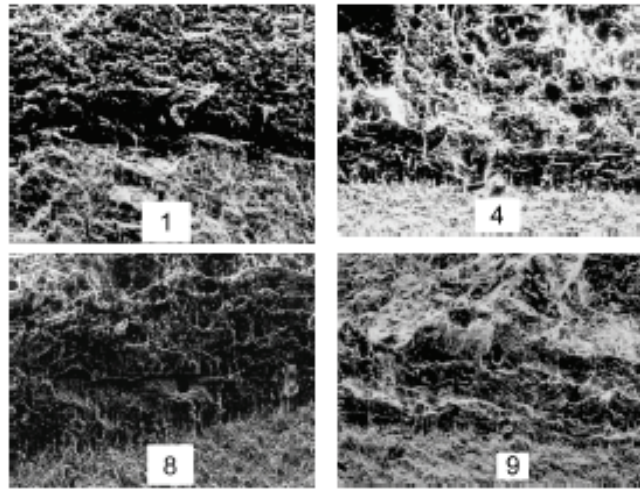


Figure 12. Final stretch zone recognized after point B in Fig. 11 for different regions in welded joint (see Table 1)

Table 1: Final stretch zones for weld metal and heat-affected-zone /14/

Sample	Position	Temperature	Final stretch zone
1	Weld metal	20°C	0.14 mm
4	Heat-affected-zone 0.5 mm from fusion line	20°C	0.19 mm
8	Heat-affected-zone 0.2 mm from fusion line	-60°C	0.44 mm
9	Heat-affected-zone 0.5 mm from fusion line	-60°C	0.23 mm

Constraint capacity corresponds to enforcing plane strain conditions, i.e. nil-levels of lateral contraction across the crack front. This definition is best understood in terms of the plastic zone developed at the crack front of a K_{Ic} specimen. If K_{Ic} can be measured, then the plastic zone is very small because of plane strain conditions. When constraint relaxation evolves, the plastic zone size increases and eventually becomes large related to the section size, Figs. 10 to 12. The complexity of the problem is indicated not only by different view of fractographs in Fig. 12, presenting final stretch zones for the weld and HAZ of the same steel, but also by the their values obtained at 20°C and at -60°C (Table 1). It is clear that micro structure in the region of crack tip is heterogeneous, and the response of material to the load is locally different. Crack tip is located in different micro structures and after blunting crack grows in different conditions. In this case structural integrity can be assessed by global consideration, i.e. energy dissipation.

2.3. Extension of application of fracture mechanics parameters

Once established, and supported by mathematical background, basic parameters of fracture mechanics, stress intensity factor, path independent contour integral (J integral) and crack opening displacement, have found the application also in the other fields. In addition to brittle behaviour, steel and metallic materials frequently exhibited significant plastic deformation, and the application to crack growth beyond yielding, (elastic-plastic fracture mechanics - EPFM) is helpful in this situation.

Well known Paris law based on stress intensity factor range, although empirical in its nature, is a powerful tool to solving the problems in fatigue. Looking for solutions of important problems with the crack in creep condition, C^* and C_t integrals are derived base on J integral. The crack problem in stress corrosion environment is also considered applying critical stress intensity factor, K_{Isc} .

It is to emphasize that performed extensions were possible only after introduction of series of assumptions, simplifications and approximations, necessary to cover uncertainties and shortage in knowledge.

Following the experience and using it in a similar way, fracture mechanics and its parameters are involved also for nano materials and nano structures /1/, but again with series of assumptions, simplifications and approximations, and applying broadly methods of simulations and modelling.

2.4. Structural integrity assessment by fracture mechanics

The achievement in fracture mechanics and numerical modelling of structures enabled the development of methods for reliability evaluation and structural integrity assessment. Applying these methods service safety of structures is increased and their life extended, allowing in the same time significant economical saving. Numerical modelling is today an inevitable tool in different structures design, manufacturing and use, like steel structures, power and petrochemical plants, aircrafts, machinery, vehicles, but also in the development of nano materials and structures. Welded structures have very important position in many of these sectors, requiring special attention. The reason is the possibility of crack occurrence in welded joints, which can endanger structural integrity and service safety /15/.

Fracture mechanics approach was applied and has been formally accepted in the case of Trans Alaska Crude Oil Pipeline /16/ for reliability assessment in the form of "fitness-for-purpose". The investigation defined theoretically and verified experimentally maxi-

mum allowable crack sizes before the procedure on when and how to repair cracks in welded joints was proposed. The most important conclusion of the study is that “fracture mechanics analysis is acceptable basis for allowable exception from valid standards under circumstances, under condition that this analysis provides clear and conservative structural integrity assessment”. Just to mention that similar approach can be applied in the case of nano materials.

The significance of detected or assumed crack in a structural component can be assessed by FM approach, applying developed procedures, e.g. SINTAP /17, 18/.

3. SCALE EFFECT AT THE CRACK TIP

Crack tip region requires special attention, as can be concluded referring to Figs. 3 to 6. It is also to underline that the model in Fig. 6 is based on many assumptions and simplification regarding structure of material, and it is easy to recognize how far from reality applied model is by comparing with fractographs in Fig. 12. More close insight at the crack can help in this situation.

The scale range within which continuum mechanics theories are applied is very narrow. All material properties differ when they are averaged over individual regions within each grain that can be traced to crystal lattices. In addition, when load is applied, pre-existing defects and imperfections can change their morphologies that can further add to the complexities of the analyses. As the scale size is reduced, these changes can occur continuously such that equilibrium may never be reached and the process is said to be in non-equilibrium. The use of ordinary continuum mechanics theories that assume equilibrium and material homogeneity fails.

Initially considered phenomena at the crack tip related to crack propagation within classic picture of metal structure are given in Fig. 13.

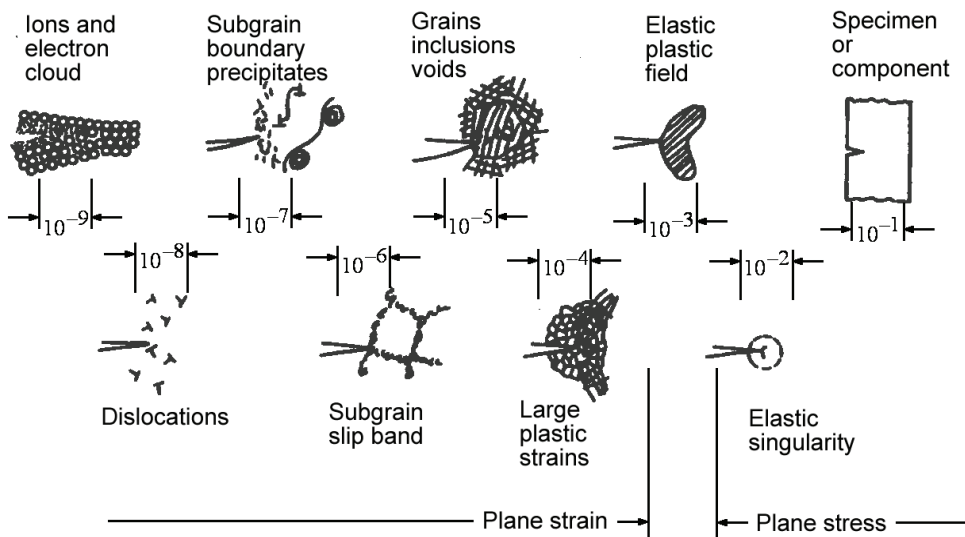


Figure 13: The sizes of phenomena in metals – a classical picture, presented in cm

Most important is that basic fracture mechanics formulae are developed for continuous and homogeneous material, and the consideration at the atomic force level just helped to confirm the applicability of obtained results, Fig. 6, Eq. (4), Eq. (7). The size of edge dislocations is about 10^{-8} cm, of sub-grain slip band 10^{-6} cm, while large

plastic strains extend to about 10^{-4} cm. Crack tip is connected with every picture in Fig. 13, so it can be attributed to all presented levels, but with different approaches. Intention to approach crack tip as close as possible enabled the development of new and more detailed models. An additional impression about the complexity of crack tip region and refinement of situation depicted in Fig. 13 can be obtained from Fig. 14 /19/.

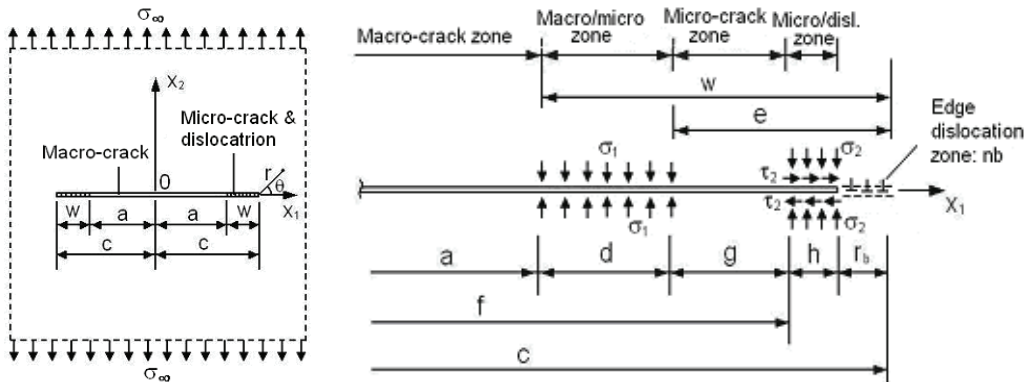


Figure 14. Presentation of macro/micro/dislocation model with one-half symmetry /19/

In the areas of material science and continuum mechanics, the field of mesomechanics /20/ attracted attention owing to the necessity of scaling shifting in size and time. The impetus of nanotechnology reached down the scale such that all disciplines would meet and benefit from one another. However, there are overwhelming difficulties associated with the discontinuities of results from the various scales, but also some basic notion connected with the stress and strength require more detailed and better definition when nano materials and structures are considered. Mesoelectronics has discovered that the heat transfer behaviour of small bodies is distinctly different and requires fundamental studies of electronics at the subatomic scale. New physical laws may have to be discovered to fill in the gaps. The final answer lies in multiscale where the results at the smaller scales must be translated to the macroscopic level. However this problem is well known even at the macro scale when the results obtained with small sized specimens should be applied to large components /21/.

For those problems where the physical process also calls for scaling in time such that chemical reactions at the microscopic scale will also have to be considered in conjunction with geometric continuum mechanics. Among the physical problems involved are aerodynamic stability of solids moving through fluid media in the transonic region where the traditional scaling scheme fails, like high speed projectile/target penetration with phase transition from solid to liquid to gas, the aging of polymeric and metallic materials where chemical reactions would alter the structural arrangements of the molecules owing to specimen size, time and temperature effects, and high temperature creep and combustion. The association of results at the atomic, microscopic and macroscopic scales has been made difficult because the possibility to transfer the results is questionable. All mentioned affects fracture behaviour considered at different scales.

Modern view on scaling of mater phenomena is presented in Fig. 1 /4/. Comparing Figs. 13, 14 and 1 one can conclude that usually accepted range of fracture mechanics application corresponds generally to the level of micro word and above it. Fracture mechanics eventually could be applied at the level of nano word, but additional consider-

ration about its validity should be necessary. First of all is how to define crack and its tip at nano level. It is visible in Fig. 1 that CNT is about 1.3 nm wide, the value not clearly contained in Fig. 13. Eventual defects are, of course, of lower size. It is difficult to find exact position for defects at nanoscale in Fig. 1.

It is clear that further consideration of structural integrity and reliability of nano material and eventual defects in it is necessary. This should include not only the state of stress and strain around defect boundary, but also many fundamental notions, such as strength and deformation parameters and properties.

4. NANO MATERIALS AND THEIR FRACTURE PROPERTIES

The development of nano materials is impressive, what is confirmed by the number of published papers devoted to performed research and achieved application, overpassing 2000 till the year 2006 /1/, extended eventually by exponential law. Today a spectrum of nano materials is available for different applications, exhibiting different properties.

First nano material obtained in controlled manufacturing in year 1991, carbon nano tube (CNT), attracted an enormous interest for the application in production of electronics and mechanics components. Single and multi wall CNT are accepted as super strong and stiff carbon fibres in developing new generation of composite materials. Monolayer of carbon atoms (graphene) and carbon nano tube are presented in Fig. 15 /1/. A cylindrical single layer of graphene or single-wall nanotubes (SWNT) represents the most elementary CNT. In cylindrical configuration the properties of graphene are conserved, especially those concerning the electrical and mechanical properties. A SWNT has the diameter of an order of 1-2 nm, capped with ends of, usually six, pentagonal cells. In this uniform arrangement of atoms the strength of structure is close to ideal since the full capacity of atomic bonds is seized. It reflects to fracture strength as well. As an illustrative comparison of modulus of elasticity and fracture properties of different materials are given in Table 2. The values in Table 2 should be taken only as informative, since the conditions for their determination can be very different. This should have in mind when the data given in Table 2 are used and compared /1/. In graphite, each carbon atom in a basal plane of compact packed hexagonal cell is strongly bonded (covalent sp^2) to the three neighbouring atoms while adjacent basal planes are bonded by weak van der Waals forces (π bond). For that, the elastic modulus of the graphite in the basal plane is very high while the strength of the graphite perpendicular on the basal planes is comparatively poor. In curved graphene sheets of CNT, the bonds are not purely of sp^2 or π type, but an admixture, hence, variation in mechanical properties may be a result.

Typical nano materials are ranged from 1 do 100 nm in size, Fig. 15d. The area to volume ratio is much higher than at micro and macro level. In addition to quantum effect, expressed already for several nm, this contributes to unexpected useful properties of nano materials. Nano crystalline materials are of extremely high strength and hardness, but they can also be very ductile and tough, resistant to fatigue, creep, erosion and corrosion, combined with high degree of electrical and thermal conductivity.

To use the benefits of obtained nano structures properties some comparison with macro scaled structures should be done.

Design, manufacturing and exploitation of structures on macro scale are all based on stress and strain parameters, comparing materials properties and corresponding values

found for structural components. In practice this is not sufficient for reliable service of structures and energy parameters should be used in addition, such as toughness.

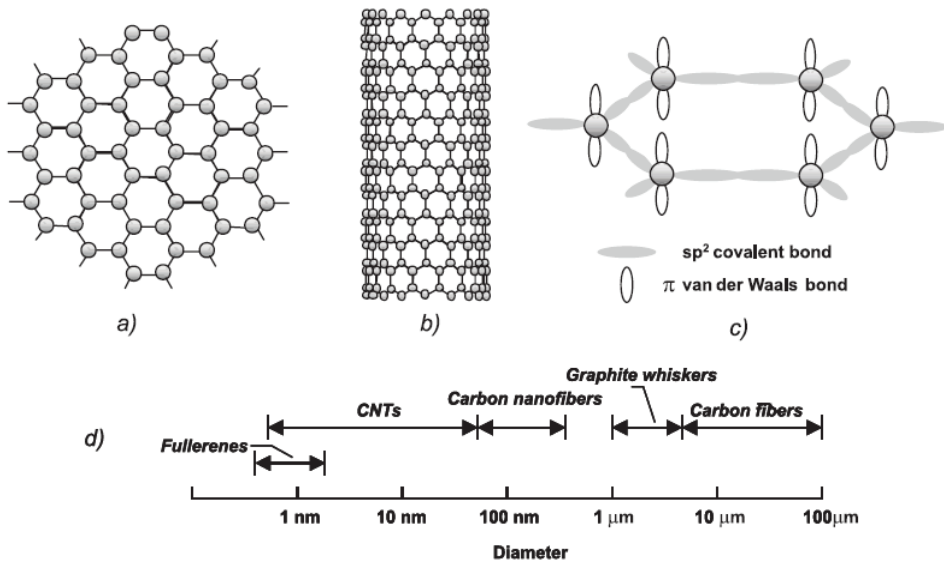


Figure 15: a. Monolayer of carbon atoms. b. Single-walled nanotube (SWNT). c. Covalent bond between basal carbon atoms and bond between basal planes. d. diameters of carbon materials

Table 2: Modulus of elasticity, fracture stress and strain for structural materials (based on [1])

Material	Modulus of elasticity, TPa	Fracture stress, GPa	Fracture strain, %
Steel 4340	0.207	1.6 ÷ 1.7	12
Tungsten	0.4	0.76	3.5
Zirkonia (ZrO ₂)	0.2	0.8 ÷ 1.5	-
Kevlar fibres	0.06 ÷ 0.15	3.6 ÷ 4.1	2.5 ÷ 1
Epoxy	0.0035	0.005	-
Diamond	0.7 ÷ 1.2	1.05	-
Carbon fibres	0.20 ÷ 0.75	4.0 ÷ 7.0	0.5 ÷ 1.8
Carbon nano tube	1 (0.50 ÷ 5.50)	15 ÷ 63	5 ÷ 15
Carbon multiwall nano tube	0.1 ÷ 1.2 (tension) 1.7 ÷ 2.4 (compression) 1.28 ± 0.59 (bending)	10 ÷ 66 100 ÷ 150 14.2 ± 0.8	- - -

Many assumptions and simplifications are induced for macro structures in order to achieve uniform interpretation of parameter values. Following facts should be respected:

Stress is defined as the relation between of applied load and cross section properties of component or specimen, neglecting the microstructure of material.

1. Stress and strain tensors, applied in mathematical structural analysis, are defined for a homogeneous continuum, and applied for inhomogeneous structure.
2. Yield strength of material, determined by standardized testing method, again with corresponding limitations, is generally accepted strength parameter in design.

Considering the dimension and composition of nano material it can be clear why the strength parameters data of nano materials are not yet completely available, especially those for CNT materials. In this case strength is also presented by the load in a moment

of noticeable changes (deformation) or breaking in material, but the structure of nano material (Fig. 15) requires to describe strength in a way different from that at macro scale. The problem is in fact that classical strength and strain parameters (yield strength, ultimate tensile strength, and elongation) are all defined for cross section and length dimensions, which are in nano materials small and not properly and completely defined yet.

Safe and reliable service of nano structures is of utmost importance since the consequences of failure can be very difficult, in many cases even catastrophic. Nano structure can also be defective, and assessment of defect significance is the subject of extended research and investigation. It is natural to apply gathered experience in the field that means to apply fracture mechanics approach for structural integrity assessment also at the nano level scale.

As an example, typical defects which can be introduced in CNT material by axial straining are presented in Fig. 16 /1/. They are caused

- a. by high axial straining ($\sim 15\%$) and low temperatures ($\sim 30\text{K}$), when longitudinal bonds can be broken producing conventional crack-like defect of length a , and
- b. by thermally activated accommodation to applied strain at higher temperatures producing carbon atoms re-arrangement in a distorted configuration of two pentagons and heptagons with the generation of an edge dislocation dipole.

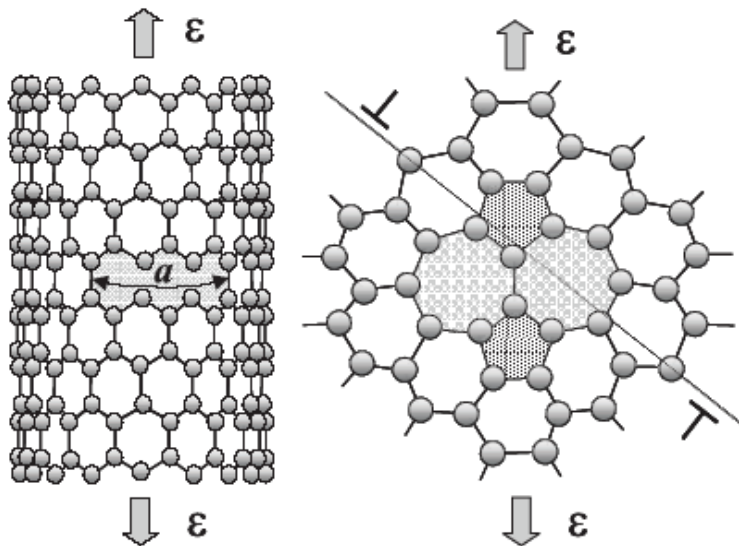


Figure 16: Defects generated in CNTs by axial straining: longitudinal bonds break producing a crack of length a (left) and thermally activated accommodation producing an edge dislocation dipole (right) /1/

The change of basic mechanical properties and material response to loading in this situation is inevitable.

Crack size and tip region are very small when considered in a sample of macro- up to the micro- scale (Fig. 13). This allows to treat material as continuous solid and apply the analysis of stresses, strains and cracks as defined in mathematical and numerical models, in spite of series of accepted simplifications. It is also possible to assume that crack tip exists as singular point in continuum solid, producing shortly described consequences on

loaded material behaviour. However, it is not easy to imagine crack tip as a point in Figs. 4 and 6, but also in Fig. 13 at magnification higher than micro level. For that the validity of applied formulae at macro scale is limited by the size of a structure, and simplifications of models in structural integrity and reliability analysis must be respected.

Development and introduction of nano materials and nano structures accentuate the necessity to assess the integrity and consider the effect of defects, since their application requires high level of reliability /22/. Important benefit of nano materials is high strength, achieved by perfect arrangement of atoms. Due to size effect failure consequences are different on macro/micro levels of that on nano level. The nano structure size is of similar order of magnitude as crack tip region considered at macro-scale (Fig. 16). The accuracy of the assessment of nano structure integrity is questionable having in mind that atomic distance in crystal is small (≈ 0.5 nm) and the defect (crack) can be also small (e.g. 10 nm).

5. DAMAGE AND FAILURE IN NANO STRUCTURES

Security and reliability of nano structures is of an utmost importance, because their damages and failures might be of catastrophic consequences. Complexity of this problem can be recognised from the scheme (Fig. 17) of computational modelling procedure /23/.

Anyhow, modelling of nano materials and nano structures is an inevitable step in modern procedures for development and improvement, with significant effects.

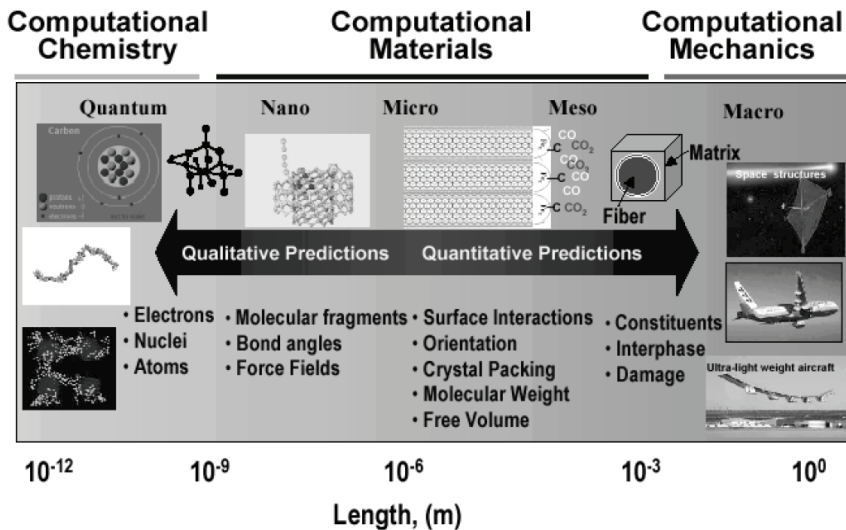


Figure 17: Length and time scales in material modelling /23/

5.1. Hierarchical integrated simulation models

Hierarchical simulation approach integrates information obtained from more detailed smaller-scale models into coarse-patterned, larger-scale models /1/. This approach has been proved successful when the physics at different scales are weakly coupled. It is feasible when, towards larger-scales, the information is passed via one or few common parameters, like inter-atomic potentials on molecular dynamics/quantum mechanics (MD/QM) interface, virtually decoupled from smaller-scale models. This is the base of so-called “ab-initio” method, which enabled to develop convenient algorithms, appli-

cable to the heterogeneous of engineering materials structures with various patterns by multi-field decomposition for describing the material deformation and, ultimately, the fracture. The potential energy of the system is formulated in terms of micro and macro stress tensors which account on the deformation gradients, body forces and couples. On the boundary, the forces and moments are specified together with the geometry and the volume of the simulation domain.

In this way ab-initio method underlying QM approximations (based on tight-binding approach) has been coupled with MD and, then, MD model is coupled to macro scale with continuum FE models. In this approach FE mesh size have been down-scaled to the interatomic distances range, compare Fig. 6.

The capacity of this approach is remarkable, as it can be seen from an example of modelling of deformation and fracture behaviour for material design purpose, applied in the case of Cybersteel for naval applications (Fig. 18). The steel has been conceived to contain particles at two different scale lengths. Primary inclusions, order of mean size 1 μm , and nano-secondary particles, order of 0.1 μm , have been considered. The former enhance the yield point and the tensile strength, the latter improve the ductility, implicitly the fracture toughness.

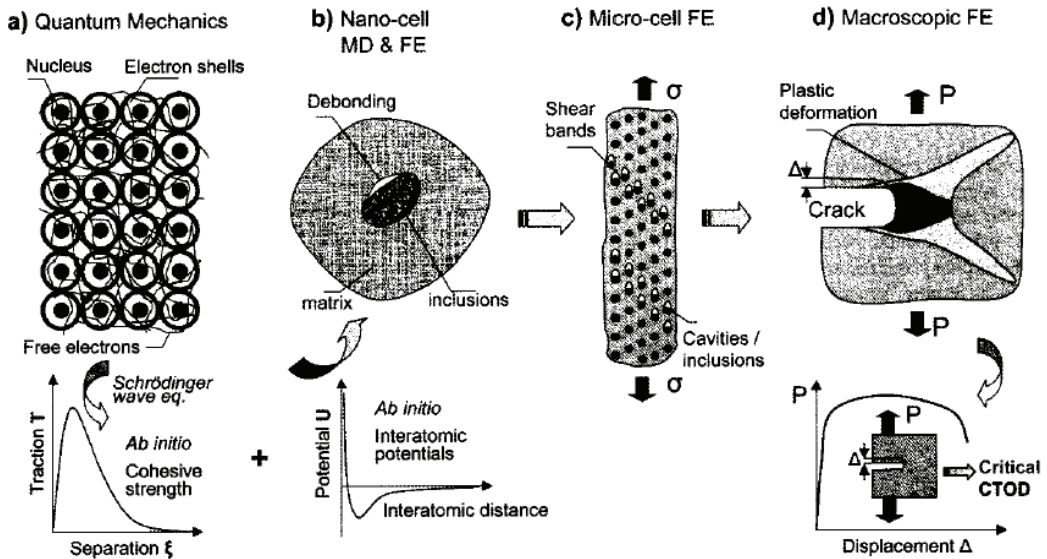


Figure 18: Example of hierarchical modelling: quantum mechanics simulation (a); molecular dynamics and finite elements models (b); macro-cell including nano-cell (c); macroscopic finite elements model for critical crack opening displacement assessment (d) /1/

For a proper description of localized gradients of deformation, higher-order terms are included into constitutive equations. The principle of virtual work enables to derive micro- and macro-scale governing equations. In hierarchical modeling the simulation is performed independently at every size-scale level by solving the scale-specific constitutive equation. The bridging between levels is achieved by embedding the information gained by fine-scale simulation into the model of a superior size-scale level.

Hierarchical in combination with concurrent simulation is adequate here since the failure occurs at several well defined size-scales. Failure initiated by particle-matrix debonding at quantum scale, void nucleation and growth is typical at mesoscale, shear

deformation localization appears within the shear bands at micro-scale and, finally, material separation by fracture occurs at macroscopic level. It is to mention that significant simplifications are necessary here, which have to be proved as conservative by experiments.

In Fig. 18 hierarchical simulation approach is presented, as devised for assessing and optimizing the mechanical behaviour of Cybersteel /1/. At quantum scale, the failure mechanism is initiated by bonds breaking at inclusions-matrix interface. The cohesive strength, in terms of atoms separation, as function of traction force, governs the atomic bonds breaking. The interface binding energy derived from this solution is regarded as key design parameter of Cybersteel (Fig. 18.a). At nano-scale, the debonding on inclusions-matrix interface is simulated by a concurrent method. The matrix and particles regions are modeled by finite elements and the interface is modeled by molecular dynamics. The debonding on interface triggers voids nucleation. Further, the dynamics of voids development, which is dependent on voids volume fraction and the distribution of nano-secondary particles, enables to simulate the constitutive law of deformation and plastic flow rule in a nano-cell (Fig. 18.b).

At micro-scale (Fig. 18.c), the constitutive equations of deformation and the plastic flow rule are simulated concurrently, similarly as in nano-scale cells, having incorporated the constitutive equations and plastic flow rule inherited and passed from nano-scale simulation. The deformation behaviour of the matrix, according to its constituency at micro-level, as well as of primary inclusions (of micro-size, by difference to secondary particles of nano-size) is simulated as a continuum by FE. The debonding on matrix/primary inclusions is simulated by MD with cohesive rule inherited from the simulation at QM level (Fig. 18.a). Subsequently, the growth and eventually the coalescence of voids, under increasing loading, are captured by FE simulation of the matrix. The observed shear bands, as prelude to final fracture, are simulated at this level. Under increased applied loading, continuum FE models of elastic-plastic fracture mechanics are applied (Fig. 18.d). After significant prior plastic deformation at macroscopic level, fracture appears as result of unstable plastic deformation, localized into a critical cross-section which is normal to the maximum of the applied principal tensile stress. Significant capacity of macroscopic plastic deformation under monotonously increased loading, owing to optimized size and nature of primary and secondary particles, coupled with high values of crack tip opening displacement demonstrated by simulation, confer, from design stage, high toughness to Cybersteel, which was fully confirmed by laboratory testing.

It should be remarked in this construct that the simulation of dislocations mechanisms, which are involved at mesoscopic level, has been circumvented owing to the lack of clarified physical models of dislocations, both as individual entities (e.g. the electrons configuration of the dislocations core) and as dynamic ensembles. However, the details of the physical process at mesoscopic scale are implicitly covered, globally, in the lower scale-sizes models at quantum mechanics and MD levels.

Presented approach can be considered as further and very detailed extension of previously developed crack significance assessment, involving high level of theoretically based knowledge gathered at different scales, but in fact it does not treat the situation at the crack tip. It demonstrates high level of applied theoretical background, capacity of modelling and numerical analysis and obtained practical effects, proved experimentally.

It is to notice assumptions involved at different scale, generally in tending to be sufficiently conservative to assure requested safety and reliability.

5.2. Reconsideration of Griffith's model

Since the size of the nano-structures becomes comparable to the size of the cohesive zone near a crack tip new approaches for the prediction of crack propagation are offered. In addition to the model presented in Fig. 14, next model is proposed by N. Pugno et al. /24/ as a modification of Griffith theory. If the load exceeds a critical value at which a crack of given length is stable, the energy-release rate per unit area of crack advance, G , becomes larger than the intrinsic crack resistance, G_c and as a consequence the crack propagates. In a perfect homogeneous solid in vacuum the crack resistance energy per unit surface is identified with the cleavage surface energy γ . Crack resistance is defined as $G_c = 2\gamma_c$. Within LEFM it is assumed that $\gamma_c = \gamma$. Quantized fracture mechanics (QFM), that modifies continuum-based fracture mechanics substituting the differential in Griffith criterion with finite difference has been formulated in /25/. This simple assumption has remarkable implications: fracture of tiny systems with a given geometry and loading conditions occurs at quantized stresses that are well predicted by QFM. The QFM theory introduces a quantization of the Griffith criterion to account for discrete crack propagation and discontinuous nature of matter at the atomic scale, and thus in the continuum hypothesis differentials are substituted with finite differences.

Simulations with nanocracks of length $2c_0 < 2a < 50c_0$, where $c_0 = 0.2644$ nm for silicon carbide matrix shown in Fig. 19, were performed using the Tersoff potential for calculation of inter-atomic forces /25/. Obtained results have shown a departure of 25% from the Griffith theory.

Modern atomistic methods and continuum methods for nanoscale modelling and simulation provide many insights about behaviour of the cracks on the nano-scale /16/. Continuum methods often start with extending the range of applicability of proven engineering methodologies to nanoscale phenomena. The recently developed Virtual-Internal-Bond (VIB) method is aimed to investigating fracture of such nano-materials. It is demonstrated that, at a critical length scale typically on the order of nanometer scale, the fracture mechanism changes from the classical Griffith fracture to one of homogeneous failure near the theoretical strength of solids.

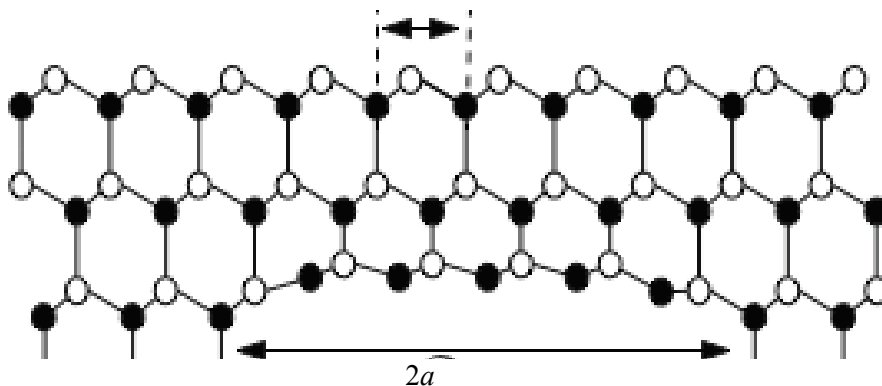


Figure 19: Geometry of the Griffith problem in the atomic-scale Full (open) dots represent carbon (silicon) atoms; the bond network is represented by sticks

Crack size and tip region are very small when considered in a sample of macro- up to the micro- scale (Fig. 13). This allows consider the material as continuous solid and apply stresses, strains and crack analysis as defined in mathematical and numerical models, in spite of series of accepted simplifications. It is also possible to assume that crack tip exists as singular point in continuum solid, producing here described consequences on loaded material behaviour. It is not easy to imagine crack tip as a point in Fig. 4 and Fig. 6, but also in Fig. 13 at magnification higher than micro level. For that the validity of applied formulae at macro scale is limited by the size of a structure, and simplifications of models in structural integrity analysis must be respected.

5.3. Transition of properties at nanoscale

Presented approaches can be considered as further and very detailed extension of previously developed crack significance assessment, including practical application, by involved high level of theoretically based knowledge gathered at different scales, but there are other influencing factors of high importance for material response and behaviour under loading. One of them is transition of properties at nanoscale, indicating that in fact material does not behave as expected, the problem similar to discovered nil-ductility transition temperature of steel, mentioned in Section 2. (in fact it does not treat the situation at the crack tip.

In yet another strangeness of the nanoworld, researchers at the National Institute of Standards and Technology (NIST) and the University of Maryland-College Park have discovered that materials such as silica that are brittle in bulk form behave as ductile as gold at the nanoscale /26/. Their results may affect the design of future nanostructures.

Pradeep Namboodiri, Doo-In Kim and colleagues from NIST first demonstrated the latest incongruity between the macro and micro worlds with direct experimental evidence for nanoscale ductility. Later on NIST researchers Takumi Hawa and Michael Zachariah and guest researcher Brian Henz shared the insights they gained into the phenomenon through their computer simulations of nanoparticle aggregates.

At the macroscale, the point at which a material will fail or break depends on its ability to maintain its shape when stressed. The atoms of ductile substances are able to shuffle around and remain cohesive for much longer than their brittle cousins, which contain faint structural flaws that act as failure points under stress.

At the nanoscale, these structural flaws do not exist, and hence the materials regarding the strength are nearly “ideal.” In addition, these objects are so small that most of the atoms that comprise them reside on the surface. According to Namboodiri and Kim, the properties of the surface atoms, which are more mobile because they are not bounded on all sides, dominate at the nanoscale. This dominance gives an otherwise brittle material such as silica its counterintuitive fracture characteristics. For that, they claim that “the terms ‘brittle’ and ‘ductile’ are macroscopic terminology”, probably not applicable at the nanoscale”. Accordingly, since crack size is defined at macro and micro level, its definition for the application at lower levels should be modified, what is also necessary for stress and strength, and many terms connected with them, like brittle and ductile, including also toughness /26/.

Using an atomic force microscope (AFM), Kim and Namboodiri were able to look more closely at interfacial fracture than had been done before at the nanoscale. They found that the silica will stretch as much as gold or silver and will continue to deform

beyond the point that would be predicted using its bulk-scale properties. Hawa, Henz and Zachariah's simulations reaffirmed their study and added some additional details. They showed that both nanoparticle size and morphology, whether the material is basically crystalline or amorphous, for example, have an effect on the observed ductility and tensile strength because those factors influence the mobility of surface atoms. In the simulations, the smaller the particles in the aggregate the more ductile the material behaved. Crystalline structures exhibited greater strength when stressed and deformed long after the critical yield point observed macroscopically.



Figure 24. NIST researchers have shown that silica that are brittle in bulk exhibit ductile behaviour at the nanoscale. Computer simulations demonstrate the material extension and necking that occurs during the separation of amorphous (top) and crystalline (bottom) silica nanoparticles /26/

9. DISCUSSION AND CONCLUSION

To understand better the approaches to damage and failure of structure as important for structural integrity, and their eventual application at nano scale, four key words require some consideration. These words are structure, integrity, crack and fracture. *Structure* is considered here as a composition designed and produced for requested purpose and use. It has to save the *integrity* during designed life even in the case of present defect, in the most danger form as a *crack*, which is considered as the locally separated material. Process of *fracture* is characterized by growing crack. Since the crack is considered as void area with boundary, its tip exists as a singularity, and for that tip is not a key word, although the region ahead the crack tip is of prime interest for fracture development. These definitions, apt to critic and open to comments, are accepted as a convention. Two remarks can be given here.

1. Initially, the discipline treating the crack was called Crack Mechanics, what is changed in Fracture Mechanics (FM).

2. When European Group of Fracture (EGF) changed its name, the form with more positive implication has been accepted – European Structural Integrity Society (ESIS).

Structural integrity assessment is based on inevitable simplifications. In that sense the problem can be considered as a specific approach to structural reliability. Basic presumption is the homogeneous microstructure, acceptable in some cases at macro and eventually at micro level, but it can not be applicable with a certainty at nano level. This assumption is far from being real even at macro level, i.e. for welded structures.

The way past to understand the fracture of structural components and its mechanisms is relatively long [3]. In the beginning of systematic analysis the knowledge about this matter was very limited and the problem is considered by gathering new experience and developing new theories, experimental and numerical procedures. But a lot has to be done more entering to nano level.

It is not an easy task to make the conclusion about this fast developing matter. Instead, some considerations from Ref. [26] are quoted. "At the macro scale, the point at which a material will fail or break depends on its ability to maintain its shape when stressed. The atoms of ductile substances can shuffle around and remain cohesive longer than brittle, which contain structural flaws acting as failure points. At the nano scale, these structural flaws do not exist. These objects are so small that most of the atoms reside on the surface. According to Namboodiri and Kim, the properties of more mobile surface atoms, not bounded on all sides, dominate at the nano scale. This dominance gives an otherwise brittle material (silica) its counterintuitive fracture properties".

The story about fracture, crack and crack tip is more and more far from its end by gathering more knowledge and applying more sophisticated approaches thanks to experimental and numerical methods, such as atomic force microscope and powerful computers and softwares. Considering crack surfaces as a typical kind of interface, it is necessary to find out actual limits that can help to understand fracturing process at different scales. Provisional and temporary conclusion about considered matter is explained probably in the best way in Ref. [27] in a way: "We can distinguish between interfaces in general and nano-interfaces as follows: Typically, an interface separates two bulk phases; we define, consistent with the above definition, a nano-interface as one in which the extent of one or more of the phases being separated by the interfaces is nanoscopic. In nanointerfaces we include nano-interconnects, which join two or more structures at the nanoscale. For nanointerfaces, traditional surface science is generally not applicable."

It is clear from ship fracture case study that some material property might be not discovered and that actual problem could be solved only if this property was recognised, characterised and specified for given circumstances. This could be more pronounced in the case of fatigue (e.g. for low cycle fatigue) or in the case of creep. Having in mind the development stage of nano structure, one can expect more uncertainties in the case of nano materials, suggested in performed research of the ductile behaviour found at nano level for material brittle at macro level [26].

Stress, defined as the ratio of load and the size of loaded area, is the fundamental value in engineering calculations. So defined, stress became most used value in structures for analysis and comparison with characterized material strength properties. However, the area is of final size at macro level under accepted assumptions, and this is not the case at nano level. Using the fracture atomic model (Fig. 6), stress at nano level could be considered as the sum of atomic forces rather than through area, difficult to be defined in model with distinct atoms arrangement.

The defects, including crack, can not be considered in the same way in macro and in nano structures. It is not possible to interpret crack tip and its severity in nano material,

since in this case the scale is on similar level, requiring for different definition of stress concentration, if any.

It is likely that another approach for calculation of loaded components is necessary at nano level, but before that or in the same time new properties should be discovered similarly to the case of ship.

The experimental technique and equipment, together with computers and softwares, achieved nowadays so impressive level that almost everything can be modelled and analysed virtually. But that implies necessary change of approach in regard security, safety and reliability, expressed already by the number of scientist and number of published papers in this range.

In this situation the problem how to transfer the fracture process characteristics to different scale (Fig. 1) became significant /1, 19, 21/.

REFERENCES

1. D. D. Cioclov: "Nanomechanics of Materials", Reprint from BID-ISIM "Welding and Material Testing", No 2; 3; 4/2007 and 1/2008, ISIM, Timisoara, 2008.
2. R.W. Nichols: "The use of fracture mechanics as an engineering tool", The 1984 ICF Honour Lecture, ICF 6, New Delhi, India, 1984.
3. S. Sedmak: "Crack problems in welded structures", IFMASS 9 monograph "The challenge of materials and weldments", Eds. S. Sedmak, Z. Radaković, J. Lozanović, MF, DIVK, TMF, Institut Goša, Beograd, 2008.
4. "The Hitchhiker's Guide to Nanotechnology" – Internet
5. M. Boyd: "Fracture design practices for ship structures" in "Fracture", Vol. V, edited by H. Liebovitz, Academic Press, New York, 1969.
6. W. S. Pellini: "Guidelines for fracture-safe and fatigue-reliable design of steel structures", The Welding Institute, Abington Hall, Abington, Cambridge CB1 6AL, England, 1983.
7. C.E. Inglis: "Stresses in a plate due to the presence of cracks and sharp corners", Transactions of the Institute of Naval Architects 55: 219, 1913.
8. A.A.Griffith: "The phenomena of rupture and flow in solids", Phil. Trans. Roy. Soc. London. A, 221: 163-198, 1920.
9. G.R.Irwin, J.A.Kies: "Fracturing and fracture dynamics", Welding Journal. Res. Sup. 31(2): 95s-100s, 1952.
10. J. F. Knott: "Fundamentals of fracture mechanics", Buthersword, London, 1973.
11. ESIS Procedure for Determining the Fracture Behaviour of Materials ESIS P2-92, TC1, 1992.
12. J.R. Rice: "Mathematical analysis in the mechanics of fracture", Fracture – an advanced treatise, Vol. II, H. Lieboviz (ed.), Academic, New York, pp. 191-308, 1968.
13. E.Orowan: "Energy criteria of fracture", Welding Journal. Res. Sup. 34(3). 1955. 157s-160s
14. K. Gerić: "Prsline u zavarenim spojevima" – Monografija, (Cracks in welded joints – Monograph), FTN Izdavaštvo, Novi Sad, 2005.
15. US-Yugoslav joint project "Fracture mechanics of weldments", Annual reports, Faculty of Technology and Metallurgy, Beograd, Principal investigator S. Sedmak, 1982-1992.
16. R.P. Reed, H.I. MacHenry, M.B. Kasen: "A fracture mechanics evaluation of flaws in pipeline girth welds", Welding Research Council Bulletin, No 245, 1979.
17. SINTAP: Structural Integrity Assessment Procedure, Final Report, EU-Project BE 95-1462. Brite Euram Programme, Brussels, 1999.
18. N.Gubeljak, U.Zerbst: "SINTAP- Structural INTeegrity Assessment Procedure", IFMASS 8 monograph "From fracture mechanics to structural integrity assessment", ed. Z. Radaković and S. Sedmak, DIVK, TMF, Beograd, 2004.
19. G.C.Sih: "Spatial and temporal scaling affected by system inhomogeneity: atomic, microscopic and macroscopic", ECF16, Alexandroupolis, 2006 (on disc)

20. Prospects of Mesomechanics in the 21st Century: Current Thinking on Treatment of Multiscale Mechanics Problems, in: G. C. Sih and V. E. Panin, *J. of Theoretical and Applied Fracture Mechanics*, 37(1-3), 1-410, 2001.
21. G. Pluinage: "Fracture transferability problem and mesofracture", in the IFMASS 8 monograph "From fracture mechanics to structural integrity assessment", ed. Z. Radaković and S. Sedmak, DIVK, TMF, Beograd, 2004.
22. B. Michel, T. Winkler: *MicroNanoReliability. Micromaterials and Nanomaterials*, Berlin, 2007.
23. T.S. Gates, G.M. Odegard, S.J.V. Frankland and T.C. Clancy, "Computational materials: Multi-scale modelling and simulation of nanostructured materials", *Composites Science and Technology*, **Volume 65, Issues 15-16**, pp **2283-2644**, **2005**.
24. N. Pugno, et al.: "Analytical approach versus atomistic simulations in fracture mechanics", ECF16, Alexandroupolis, 2006 (disc)
25. N. Pugno, R. Ruoff, *Quantized Fracture Mechanics*, *Philosophical Magazine*, 84/27 (2004) 2829-2845.
26. "Nanomaterials Show Unexpected Strength Under Stress" on Internet
27. "Theory and Modeling in Nanoscience", on Internet

